Quantum criticality in photorefractive optics: Vortices in laser beams and antiferromagnets

Mihailo Čubrović[*]

Scientific Computing Laboratory, Institute of Physics, University of Belgrade, Pregrevica 118, 11080 Belgrade, Serbia

Milan S. Petrović

Institute of Physics, P.O. Box 57, 11001 Belgrade, Serbia
and Texas A&M University at Qatar, P.O. Box 23874, Doha, Qatar

We study vortex patterns in a prototype nonlinear optical system: counterpropagating laser beams in a photorefractive crystal, with or without the background photonic lattice. The vortices are effectively planar and have two "flavors" because there are two opposite directions of beam propagation. In a certain parameter range, the vortices form stable equilibrium configurations which we study using the methods of statistical field theory and generalize the Berezinsky-Kosterlitz-Thouless transition of the *XY* model to the "two-flavor" case. In addition to the familiar conductor and insulator phases, we also have the perfect conductor (vortex proliferation in both beams or "flavors") and the frustrated insulator (energy costs of vortex proliferation and vortex annihilation balance each other). In the presence of disorder in the background lattice, a phase appears which shows long-range correlations and absence of long-range order, thus being analogous to glasses. An important benefit of this approach is that qualitative behavior of patterns can be known without intensive numerical work over large areas of the parameter space. The observed phases are analogous to those in magnetic systems, and make (classical) photorefractive optics a fruitful testing ground for (quantum) condensed matter systems. As an example, we map our system to a doped O(3) antiferromagnet with $\mathbb{Z}_2$ defects, which has the same structure of the phase diagram.

I. INTRODUCTION

Nonlinear and pattern-forming systems [1–3] have numerous analogies with strongly correlated systems encountered in condensed matter physics [4,5], and on the methodological level they are both united through the language of field theory, which has become the standard language to describe strongly correlated electrons [6,7] as well as nonlinear dynamical systems [8]. In the field of pattern formation, some connections to condensed matter systems have been observed; see, e.g., Ref. [4]. More recently, extensive field-theoretical studies of laser systems were performed, e.g., Refs. [9–12], and also compared to experiment [13]. However, this topic is far from exhausted and we feel many analogies between quantum many-body systems and pattern-formation dynamics remain unexplored and unexploited. In particular, nonlinear optical systems and photonic lattices are flexible and relatively cheap to build [3] and they can be used to "simulate" a broad spectrum of phenomena concerning band structure, spin ordering, and conduction in strongly correlated electron systems; some of the work in this direction can be found in Refs. [14,15].

Our goal is to broaden the connections between the strongly correlated systems and nonlinear optics and to put to work the mighty apparatus of field theory to study the patterns in a nonlinear optical system from the viewpoint of phase transition theory: Pattern dynamics in certain cases shows critical behavior which is analogous to phenomena seen in magnetic systems. To that end, we use the formalism of perturbative field theory and renormalization group analysis but we also perform numerical simulations from the first principles, i.e., directly integrating the equations of motion to provide an *independent*

check of our main conclusions. We also establish a connection to an O(3) antiferromagnetic model which is encountered in the study of strongly correlated electron systems. The analogy is not just qualitative: We construct the phase diagrams of both systems and find they have the same structure. Introducing disorder into the system further enriches the physics, and it is physically motivated: In optics, disorder is rooted in the imperfections of the photonic lattice, and in magnetic systems it comes from the quenched spin impurities which are regularly found in realistic samples. It turns out that in both cases a glassy phase arises. This is another important research topic and it is again appealing to realize glasses in photonic lattice systems, where the parameters are easy to tune.

A. On topology and vortices

The key phenomenon which governs the phenomenology of the systems studied is the existence of topologically nontrivial solutions or *topological solitons* [16]: These are the solutions which map the physical boundary of the system to the whole configuration space of the field, so one explores all field configurations by "going around the system." For example, in a two-dimensional system (in the x-y plane) with U(1) phase symmetry, the configuration space is a circle (the phase lies between 0 and 2π) and the boundary of the physical space (i.e., the two-dimensional plane) is again a circle, the "boundary" of the plane at infinity. The topological soliton is a pattern of the $U(1)$ field which spans the whole phase circle (its phase goes from 0 to 2π), as one moves around the far-away circle in the x-y plane. Of course, this is the vortex—the most famous and best studied topological configuration. Similar logic leads to the classification of topological defects of other, more complicated symmetry groups. A potential source of confusion is that in nonlinear dynamics and theory of partial

---

*mcubrovic@gmail.com

differential equations, the "integrable" solutions, i.e., linearly (often also nonlinearly) stable solutions which can be obtained by inverse scattering or similar methods and which propagate through each other without interacting, are also called solitons, or more precisely *dynamical solitons*. In optics, they are often called spatial solitons. Dynamical solitons in nonlinear optics are a celebrated and well-studied topic [17–22]; they show an amazing variety of patterns and phenomena like localization, Floquet states [14], etc. But in general they do not have a topological charge. In contrast, topological solitons carry a topological charge (winding number for vortices) and their stability is rooted in topological protection (conservation of topological charge).

The phenomenon of vortices is perhaps best known in three spatial dimensions. The phase of the wave function can wind, forming a vortex line. These vortices are stable when the phase symmetry is broken by magnetic field. Famously, vortices may coexist with the superconducting order ($U(1)$ symmetry breaking) in type-II superconductors or exist only in the normal phase, upon destroying the superconductivity (type I). The primary example in two spatial dimensions is the vortex unbinding phase transition of infinite order found by Berezinsky *et al.* for the planar *XY* model [23]. The formal difference between the two- and three-dimensional vortices is that the latter gives rise to an emergent gauge field; this does not happen in the *XY*-like system in two dimensions [24]. While the nonlinear optical system we study is three-dimensional, its geometry and relaxational dynamics make it natural to treat it as a $(2 + 1)$-dimensional system (the x and y coordinates are spatial dimensions, the z direction has the formal role of time, and physical time t has the role of a parameter). We therefore have a similar situation to the *XY* model: pointlike vortices in the plane (and no gauge field).

Vortex matter is known to emerge in liquid helium [25], Bose-Einstein condensates [26], and magnetic systems [27]. The basic mechanisms of vortex dynamics are thus well known. However, unusual physics can arise if the system has multiple components and each of them can form vortices which mutually interact. This is precisely our situation: We have a system of two laser beams propagating in opposite directions, and we will compare it to a two-component antiferromagnet. So far, such situations have been explored in multicomponent superconductors [28] which have attracted some attention, as they can be realized in magnesium diboride [29]. But these are again bulk systems, not planar. Vortices in planar multicomponent systems have not been very popular, an important exception being the two-component Bose-Einstein condensates of Ref. [30], which were found to exhibit complex vortex dynamics; in these systems, contrary to our case, the two components have an explicit attractive interaction, unlike our case where they interact indirectly, by coupling to the total light intensity (of both components).

B. The object of our study

In this paper, we study phases and critical behavior of topological configurations (vortices and vortex lattices) in a specific and experimentally realizable nonlinear optical system: laser beams counterpropagating (CP) through a photorefractive (PR) crystal. This means we have an elongated PR crystal

(with one longitudinal and two transverse dimensions) and two laser beams shone onto each end. We thus effectively have two fields, one forward propagating and one backward propagating. The optical response of the crystal depends nonlinearly on the *total* intensity of both beams, which means the beams effectively interact with each other. This system has been thoroughly investigated for phenomena such as dynamical solitons [17,31,32], vortex stability on the photonic lattice [18–20,33–36], and global rotation [37]. We will see that the CP beams are an analog of the two-component planar antiferromagnet, which can further be related to some realistic strongly correlated materials [38–40]. The two beams are now equivalent to two sublattices which interact through a lattice deformation or external field. The PR crystal is elongated and the axial propagation direction has the formal role of time, which has a finite span, the length of the crystal. For the antiferromagnet, the third axis is the usual imaginary time compactified to the radius $1/T$, i.e., inverse temperature. Both systems contain vortices as topological defects, i.e., solutions with integer topological charge. In the PR optical system, vortices arise as a consequence of the U(1) symmetry of the electromagnetic field. In the antiferromagnets we consider, the O(3) symmetry of the antiferromagnet gives rise to $\mathbb{Z}_2$-charged defects, which exhibit the same interactions as the vortices. The optical system is not subject to noise (i.e., it lives at zero temperature), and thus the criticality we talk about is obviously not the same as thermodynamic phase transitions. Phase transitions happen upon varying the parameters, not temperature, so they may be described as quantum critical phenomena in the broad sense taken in Ref. [38]—any critical behavior controlled not by thermal fluctuations but by parameter dependence.

In the PR counterpropagating beam system, our focus are the vortices but in order to study them we need to do some preparational work. We first recast the system in Lagrangian and then in Hamiltonian form so it can be studied as a field theory, which depends parametrically on the time t. Then we consider the time dynamics of the system and show that in a broad parameter range the patterns relax to a static configuration which can be studied within *equilibrium* field theory. Along the way, we also study the stability of topologically trivial (vortex-free) configurations and then consider the phases of the static vortex configurations. The analytical insight we obtain also allows us to avoid overextensive numerics—analytical construction of the phase diagram tells us which patterns can in principle be expected in different corners of the parameter space. By "blind" numerical approach, this result could only be found through many runs of the numerics.

In the antiferromagnetic spin system, the nontopological excitations are simple: They are spin waves, perturbed away from the noninteracting solution by the quartic terms in the potential. There are no dynamical solitons. But we will see that topological excitations lead to a phase diagram which, after reasonable approximations, can be *exactly* mapped to the phase diagram of the photorefractive crystal. The reason is that both can be reduced to an effective Hamiltonian for a *two-component* vortex system; i.e., every vortex has two charges or two "flavors." In the photorefractive crystal it happens naturally, as there are two beams, forward and

backward propagating. In the Heisenberg antiferromagnet it is less obvious and is a crucial consequence of the collinearity of the spin pattern. We will focus on common properties of the two systems and map the phase diagrams onto each other. In the antiferromagnetic system, different phases are separated by quantum phase transitions—phase transitions driven by the quantum fluctuations instead of temperature.

On disorder

It is known that impurities pin the vortices and stabilize them. This leads to frozen dynamics even though no symmetry is broken, the phenomenon usually associated with glasses. In simple systems such as the Ising model with disorder, one generically has two phases: The disordered (paramagnetic) phase remains and the ordered (magnetic) phase is replaced by a regime with algebraic correlations and no true order. In many cases, such phases are called glasses. The exact definition of a glass is lacking; normally, they show (i) long-range correlations, (ii) absence of long-range order, i.e., of a nonzero macroscopic order parameter, and (iii) "frozen dynamics," i.e., free energy landscape with numerous local minima in which the system can spend a long time [41,42]. While the most popular example are probably spin glasses in Ising-like models such as Sherington-Kirkpatrick and Edwards-Anderson models, glasses are also known to appear in the XY model with disorder in two dimensions, the Cardy-Ostlund model, which postulates both random couplings and a random magnetic field [43–45]. Our model is essentially a two-flavor generalization of the XY model, although in order to solve it we need to simplify it. According to Refs. [43–45], the details differ depending on how the disorder is implemented, but the two-phase system (paramagnetic, i.e., disordered, and glass) is ubiquitous. In the two-component version, the phase diagram becomes richer, and on top of the glassy phase and the insulator (disordered) phase we find a few other phases. In nonlinear optics, the topic of random lasers has attracted considerable attention [9–12,46]. Here one has a complex version of the XY model, with the additional complication that not only phase but also amplitude is free to vary, but only with random couplings (no random field). On top of the glassy and the disordered phase, one or two additional phases appear.

In the presence of disorder, the relation to magnetic systems in condensed matter physics is very inspiring, since a number of complex materials show different ordering mechanisms (spin and charge density waves, superconductivity, etc.) in parallel with significant influence of disorder. Just as in the disorder-free case, we are particularly interested in possible spin-glass phenomena in doped insulating O(3) antiferromagnets [39,40,47–49] and in the last section we will discuss also the spin-glass phase in such systems.

C. The plan of the paper

The structure of the paper is as follows. In the next section, we describe the dynamical system which lies at the core of this paper: counterpropagating laser beams in a photorefractive crystal. We give the equations of motion and repackage them in the Lagrangian form. In Sec. III, we study the vortex dynamics: We construct the vortex Hamiltonian and classify the order parameters. Then we study the renormalization group (RG)

flow and obtain the phase diagram. Finally, we discuss the important question of how to recognize the various phases in experiment: What do the light intensity patterns look like and how do they depend on the tunable parameters? Section IV brings the same study for the system with disorder. After describing the disordered system, we perform the replica trick for the disordered vortex Hamiltonian and solve the saddle-point equations to identify the phases and order parameters, again refining the results with RG calculations. The fifth section takes a look at a doped collinear antiferromagnet, a model encountered in the description of many strongly coupled materials, and shows how the dynamics of topological solitons is again described by a two-flavor vortex Hamiltonian. We discuss the relation between the phase diagrams of the two systems and the possibilities of modeling the condensed matter systems experimentally by the means of photorefractive optics. The last section sums up the conclusions. In Appendix A, we describe the numerical algorithm we use to check the analytical results for the phase diagram. In Appendix B, we show in detail that the CP beams are capable of reaching equilibrium (i.e., stop changing in time)—if they would not, the application of equilibrium field theory would not be justified. Appendix C discusses the stability of nonvortex configurations—although somewhat peripheral to the main topic of the paper, it is useful to better understand the geometry of patterns. In Appendix D, we give the (routine) algebra that yields the vortex interaction Hamiltonian from the microscopic equations. Appendix E contains an improved mean-field theory for the clean system, which we do not use much throughout the paper but we include it for completeness (we prefer either the simplest single-vortex mean-field reasoning or the full RG analysis, which are described in the main text). Appendix F discusses an important technicality concerning the CP geometry, i.e., the specific boundary conditions of the CP beam system where the boundary conditions for one beam are given at the front face and for the other at the back face of the crystal. Appendix G contains some details on mean-field and RG calculations of the phase diagram for the dirty system: The dirty case includes some tedious algebra we feel appropriate to leave out from the main text.

II. THE MODEL OF COUNTERPROPAGATING BEAMS IN THE PHOTOREFRACTIVE CRYSTAL

We consider a photorefractive crystal of length L irradiated by two laser beams. The beams are paraxial and propagate head on from the opposite faces of the crystal in the z direction. Photorefractive crystals induce self-focusing of the beams—the vacuum (linear) wave equation is modified by the addition of a frictionlike term, so the diffusion of the light intensity (the broadening of the beam) is balanced out by the convergence of the beam onto an "attractor region." The net result is the balance between the dissipative and scattering effects, allowing for stable patterns to form. The physical ground for this is the redistribution of the charges in the crystal due to the Kerr effect. The nonlinearity, i.e., the response of the crystal to the laser light, is contained in the change of the refraction index which is determined by the local charge density. A sketch of the system is given in Fig. 1. Before entering the crystal, the laser beams can be given any desirable pattern of both intensity
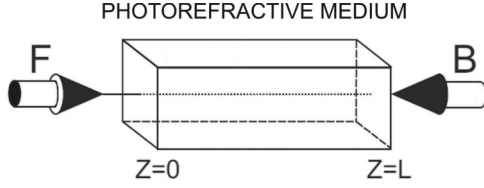
PHOTOREFRACTIVE MEDIUM

FIG. 1. Sketch of the experimental setup for the study of the CP beams in the PR crystal. The crystal has the shape of a parallelepiped, and the beams propagate along the longitudinal, z axis: the forward (F) beam from $z = 0$ to $z = L$, and the backward (B) beam the other way round. The intensity patterns are observed at the transverse faces of the crystal, at $z = 0$ and $z = L$.

and phase. In particular, one can create vortices (winding of the phase) making use of the phase masks [3] or other, more modern ways.

Assuming the electromagnetic field of the form $\mathbf{E} = e^{i\omega t + i\mathbf{q}\cdot\mathbf{r}}(Fe^{ikz} + Be^{-ikz})$, we can write equations for the so-called envelopes F and B of the forward- and backward-propagating beams along the z axis (the frequency, transverse, and longitudinal momentum are denoted respectively by $\omega, \mathbf{q}, k$). The wave equations for F and B are now

$$\pm i\partial_z \Psi_\pm(z; x, y; t) + \Delta\Psi_\pm(z; x, y; t)$$
$$= \Gamma E(z; x, y; t)\Psi_\pm(z; x, y; t), \quad (1)$$

where the plus and minus signs on the left-hand side stand for the forward- and backward-propagating component of the beam amplitude doublet $\Psi \equiv (\Psi_+, \Psi_-) \equiv (F, B)$, and Γ is the dimensionless PR coupling constant. The two beams (flavors of the field Ψ) will from now on be denoted either by F/B or more often by $\Psi_\pm$. We will use α as the general flavor index for summation, e.g., $\Psi_{1\alpha}\Psi_{2\alpha} = \Psi_{1+}\Psi_{2+} + \Psi_{1-}\Psi_{2-}$. The charge field E on the right-hand side of the equation is the electric field sourced by the charges in the crystal (i.e., it does not include the external electric field of the beams). Its evolution is well represented by a relaxation-type equation [17]:

$$\frac{\tau}{1 + I(z; x, y; t)}\partial_t E(z; x, y; t) + E(z; x, y; t)$$
$$= -\frac{I(z; x, y; t)}{1 + I(z; x, y; t)}. \quad (2)$$

Here, $I \equiv I_\Psi + I_x$ is the total light intensity at a given point, $I_\Psi \equiv |F|^2 + |B|^2$ is the beam intensity, and I_x the intensity of the fixed background. The meaning of I_x is that the crystal is all the time irradiated by some constant light source, independent of the counterpropagating beams with envelopes F, B. We will usually take a periodic lattice as the background, allowing also for the defects (missing cells) in the lattice when studying the effects of disorder. The relaxation time is τ. The time derivative $\partial_t E$ is divided by $1 + I$, meaning that the polarizability of the crystal depends on the total light intensity: Strongly irradiated regions react faster. In the numerical calculations, we solve Eqs. (1) and (2) with no further assumptions, as explained in Appendix A. For analytical results, we will need to transform them further, assuming a vortex pattern.

The equation for the charge field has no microscopic basis; it is completely phenomenological, but it excellently represents

the experimental results [3]. Notice that the derivative $\partial_t E$ in (2) is strictly negative (since intensity is non-negative): It thus has the form of a relaxation equation, and one expects that a class of solutions exists where $\partial_t E(t \to \infty) \to 0$, i.e., the system relaxes to a time-independent configuration. We show this in Appendix B; in the main text we will not discuss this issue but will simply take the findings of Appendix B for granted. Notice that there are also parameter values for which no equilibrium is reached [37,50,51].

For slow time evolution (in the absence of pulses), we can Laplace transform the equation (2) in time $[E(t) \mapsto E(u) = \int_0^\infty dt e^{-ut} E(t)]$ to get the algebraic relation

$$E(z; x, y; u) = -\frac{\Psi^\dagger\Psi + I_x - \tau E_0}{1 + \tau u + I_x + \Psi^\dagger\Psi}$$
$$= -1 + \frac{1 + \tau u + \tau E_0}{1 + \tau u + I_x + \Psi^\dagger\Psi}. \quad (3)$$

The original system (1) can now be described by the Lagrangian:

$$\mathcal{L} = i\Psi^\dagger\sigma_3\partial_z\Psi - |\nabla\Psi|^2 + \Gamma\Psi^\dagger\Psi$$
$$- \Gamma(1 + \tau E_0 + \tau u)\ln(1 + \tau u + I_x + \Psi^\dagger\Psi), \quad (4)$$

where σ_3 is the Pauli matrix $\sigma_3 = \text{diag}(1, -1)$. One can introduce the effective potential

$$V_{\text{eff}}(\Psi^\dagger, \Psi) = -\Gamma\ln\frac{e^{\Psi^\dagger\Psi}}{(1 + \tau u + I_x + \Psi^\dagger\Psi)^{1+\tau(E_0+u)}}, \quad (5)$$

so we can write the Lagrangian as $\mathcal{L} = i\Psi^\dagger\sigma_3\partial_z\Psi - |\nabla\Psi|^2 - V_{\text{eff}}(\Psi^\dagger, \Psi)$. This is the Lagrangian of a nonrelativistic field theory (a nonlinear Schrödinger field equation) in $2 + 1$ dimensions $(x, y; z)$, where the role of time is played by the longitudinal distance z and the physical time t (or u upon the Laplace transform) is a parameter. The span of the z coordinate $0 < z < L$ will influence the behavior of the system, while the dimensions of the transverse plane are not important for the effects we consider.

Our main story is now the nature and interactions of the topologically nontrivial excitations in the system (4). A task which is in a sense more basic, the analysis of the topologically trivial vacua of (4) and perturbative calculation of their stability, is not of our primary interest now, in part because this was largely accomplished by other methods in Refs. [31,32]. We nevertheless give a quick account in Appendix C; first, because some conclusions about the geometry of the patterns can be carried over to vortices, and second, to give another example of applying the field-theoretical formalism whose power we wish to demonstrate and popularize in this paper.

III. VORTICES AND MEAN FIELD THEORY OF VORTEX INTERACTIONS

A. The classification of topological solutions and the vortex Hamiltonian

Now we discuss the possible topological solitons in our system. Remember once again that they differ from dynamical

solitons such as those studied in Ref. [17] and references therein. In order to classify the topologically nontrivial solutions, consider first the symmetries of the Lagrangian (4). It describes a doublet of two-dimensional (2D) complex fields which interact solely through the phase-invariant total intensity $I = \Psi^\dagger \Psi$ (and the spatial derivative term $|\nabla \Psi|^2$), while in the kinetic term $\Psi^\dagger \sigma_3 \partial_z \Psi$ the two components have opposite signs of the "time" derivative, so this term cannot be reduced to a functional of I. The intensity I has the symmetry group SU(2) (the isometry group of the three-dimensional sphere in Euclidean space) and the kinetic term has the group SU(1,1) (the transformations which leave the combination $|F|^2 - |B|^2$ invariant, i.e., the isometry of the hyperboloid). The intersection of these two is the product $U(1)_F \otimes U(1)_B$: The forward- and backward-propagating doublet (F,B) has phases $\theta_{F,B}$ which can be transformed independently, as $\theta_{F,B} \mapsto \theta_{F,B} + \delta\theta_{F,B}$.

The classification of possible topological solitons is straightforward from the above discussion [52]. They can be characterized in terms of homotopy groups. We remind readers that the homotopy group π_n of the group G is the group of transformations which map the group manifold of G onto the n-dimensional sphere $\mathbb{S}_n$. In D-dimensional space, the group π_{D-1} therefore classifies what a field configuration looks like from far away (from infinity): It classifies the mappings from the manifold of the internal symmetry group of the system to the spherical "boundary shell" in physical space at infinity. Since the beams in our PR crystal effectively see a two-dimensional space (we regard z as time), we need the first homotopy group π_1 to classify the topological solitons. Since $\pi_1(U(1)) = \pi_1(\mathbb{S}_1) = \mathbb{Z}$ and $\pi_1(\mathbb{G} \otimes \mathbb{G}) = \pi_1(\mathbb{G}) \otimes \pi_1(\mathbb{G})$ for any group $\mathbb{G}$, the topological solutions are flavored vortices, and the topological charge is the pair of integers $\{Q_F, Q_B\}$.

Let us now derive the effective interaction Hamiltonian for the vortices and study the phase diagram. In principle, this story is well known: For a vortex at $\mathbf{r}_0$, in the polar coordinates (r,ϕ), we write $\Psi(\mathbf{r}) = \psi \exp(i\theta(\mathbf{r}))$ for $|\mathbf{r} - \mathbf{r}_0|/|\mathbf{r}_0| \ll 1$, and a vortex of charge Q has $\theta(\phi) = Q\phi/2\pi$. In general the phase has a regular and a singular part, $\nabla\Psi = \psi(\nabla\delta\theta + \nabla \times \zeta \mathbf{e}_z)$, where finally $\zeta = Q \ln|\mathbf{r} - \mathbf{r}_0|$. The difference in the CP beam system lies in the existence of two beam fields (flavors) *and* the nonconstant amplitude field $\psi_\pm(r)$, so the vortex looks like

$$\Psi_{0\pm}(\mathbf{r}) = \psi_{0\pm}(r) e^{i\delta\theta_\pm(\phi) + i\theta_{0\pm}(\phi)}. \tag{6}$$

When we insert this solution into the equations of motion (or, equivalently, the Lagrangian), it is just a matter of algebra to obtain the vortex Hamiltonian, analogous to the well-known one but with two components (flavors) and their interaction. We refer the reader to the Appendix D for the full derivation. The outcome is perhaps expected: We get the straightforward generalization of the familiar Coulomb gas picture for the XY model where all interactions of different flavors, F-F, B-B, and F-B, are allowed. In order to write the Hamiltonian (and further manipulations with it) in a concise way, it is handy to introduce shorthand notation $\vec{Q} \equiv (Q_+, Q_-)$, $\vec{Q}_1 \cdot \vec{Q}_2 \equiv Q_{1+}Q_{2+} + Q_{1-}Q_{2-}$, and $\vec{Q}_1 \times \vec{Q}_2 \equiv Q_{1+}Q_{2-} + Q_{1-}Q_{2+}$. For the self-interaction within a vortex $\vec{Q}_1$, we have $\vec{Q}_1 \cdot \vec{Q}_1 =$

$Q_{1+}^2 + Q_{1-}^2$ but $\vec{Q}_1 \times \vec{Q}_1 \equiv Q_{1+}Q_{1-}$ (i.e., there is a factor of 2 mismatch with the case of two different vortices). Now for vortices at locations $\mathbf{r}_i, i = 1, \ldots, N$ with charges $\{Q_{i+}, Q_{i-}\}$ we get

$$\mathcal{H}_{\text{vort}} = \sum_{i<j} (g \vec{Q}_i \cdot \vec{Q}_j + g' \vec{Q}_i \times \vec{Q}_j) \ln r_{ij}$$
$$+ \sum_i (g_0 \vec{Q}_i \cdot \vec{Q}_i + g_1 \vec{Q}_i \times \vec{Q}_i). \tag{7}$$

The meaning of the Hamiltonian (7) is obvious. The first term is the Coulomb interaction of vortices; notice that only like-flavored charges interact through this term (because the kinetic term $|\nabla\Psi|^2$ is homogenous quadratic). The second term is the forward-backward interaction, also with Coulomb-like (logarithmic) radial dependence. This interaction comes from the mixing of the F and B modes in the fourth term in Eq. (D2), and it is generated, as we commented in Appendix D, when the amplitude fluctuations $\delta\psi_\alpha(r)$, which couple linearly to the phase fluctuations, are integrated out. In a system without amplitude fluctuations, i.e., classical spin system, this term would not be generated. The third and fourth terms constitute the energy of the vortex core. The self-interaction constants g_0, g_1 are of course dependent on the vortex core size and behave roughly as $g \ln a/\epsilon, g' \ln a/\epsilon$, where ϵ is the UV cutoff. The final results will not depend on ϵ, as expected, since g_0, g_1 can be absorbed in the fugacity y (see the next subsection). Expressions for the coupling constants in terms of original parameters are given in (D11).

In three space dimensions, vortices necessitate the introduction of a gauge field [24] which, in multicomponent systems, also acquires the additional flavor index [28,53]. In our case, there is no emergent gauge field and the whole calculation is a rather basic exercise at the textbook level but the results are still interesting in the context of nonlinear optics and analogies to magnetic systems: They imply that the *phase* structure (vortex dynamics) can be spotted by looking at the *intensity* patterns (light intensity I or local magnetization $\mathcal{M}$; see the penultimate section).

B. The phase diagram

1. The mean-field theory for vortices

The phases of the system can be classified at the mean field level, following, e.g., Refs. [24,41]. In order to do that, one should construct the partition function, assuming that well-defined time-independent configuration space exists. We have already mentioned the question of equilibration and address it in detail in Appendix B. Knowing that the system reaches equilibrium (in some part of the parameter space), we can count the ways in which a system of vortices can be placed in the crystal—this is by definition the partition function $\mathcal{Z}$. First, the number of vortices N can be anything from 0 to infinity; second, the vortex charges can be arbitrary; and finally, the number of ways to place each vortex in the crystal is simply the total surface section of the crystal divided by the size of the vortex. Then, each vortex carries a Gibbs weight proportional to the energy, i.e., the vortex Hamiltonian (7) for a single

vortex.[1] Let us focus first on a single vortex. If the vortex core has linear dimension a and the crystal cross section linear dimension Λ, the vortex can be placed in any of the $(\Lambda/a)^2$ cells (and in the mean-field approach we suppose the vortex survives all the way along the crystal, from $z = 0$ to $z = L$, so there is no additional freedom of placing it along some subinterval of z). This gives

$$\mathcal{Z} = \sum_{Q_+,Q_-} \left(\frac{\Lambda}{a}\right)^2 e^{-L\mathcal{H}_1} = \sum_{Q_+,Q_-} e^{2\ln\frac{\Lambda}{a} - L(g\vec{Q}\cdot\vec{Q} + g'\vec{Q}\times\vec{Q})\ln\frac{\Lambda}{a}}.$$

$$(8)$$

Remember that $\mathcal{H}$ is energy density along the z axis, so it appears multiplied by L. The factor $\ln(\Lambda/a)$ in the second term of the exponent comes from the Coulomb potential of a single vortex (in a plane of size Λ). The exponent can be written as $-L\mathcal{F}^{(1)}$, with $\mathcal{F}^{(1)} = \mathcal{H}_1 - (1/L)S_1$, recovering the relation between the free energy $\mathcal{F}^{(1)}$ and entropy $S^{(1)}$ of a single vortex. The entropy comes from the number of ways to place a vortex of core size a in the plane of size $\Lambda \gg a$: $S \sim \ln(\Lambda/a)^2$. Suppose for now that elementary excitations have $|Q_\pm| \leqslant 1$, as higher values increase the energy but not the entropy, so they are unlikely (when only a single vortex is present). Now we can consider the case of single-charge vortices with possible charges $(1,0),(-1,0),(0,1),(0,-1)$, and the case of two-charge vortices where F and B charge may be of the same sign or opposite signs, $(1,1),(-1,-1),(1,-1),(-1,1)$:

$$\mathcal{F}_0^{(1)} = \left(g - \frac{2}{L}\right)\ln\frac{\Lambda}{a}, \quad \vec{Q} = (\pm1,0) \text{ or } \vec{Q} = (0,\pm1), \quad (9)$$

$$\mathcal{F}_1^{(1)} = \left(2g - g' - \frac{2}{L}\right)\ln\frac{\Lambda}{a}, \quad (Q_+,Q_-) = (\pm1,\mp1),$$

$$(10)$$

$$\mathcal{F}_2^{(1)} = \left(2g + g' - \frac{2}{L}\right)\ln\frac{\Lambda}{a}, \quad (Q_+,Q_-) = (\pm1,\pm1).$$

$$(11)$$

Now we identify four regimes, assuming that $g,g' > 0$:[2]

(1) For $L > 2/g$, a vortex always has positive free energy so vortices are unstable like in the low-temperature phase of the textbook Berezinsky-Kosterlitz-Thouless (BKT) system. This is the vortex-free phase where the phase $U(1)_F \otimes U(1)_B$ does not wind. This phase we logically call *vortex insulator* in analogy with the single-flavor case.

(2) For $2/g > L > 1/(g - g'/2)$, a double-flavor vortex always has positive free energy but single-flavor vortices are stable; in other words, there is proliferation of vortices of the form $\vec{Q} = (Q_+,0)$ or $\vec{Q} = (0,Q_-)$. This phase is like the conductor phase in a single-component XY model, and the

topological excitations exist for the reduced symmetry group, i.e., for a single $U(1)$. We thus call it *vortex conductor*; it is populated mainly by single-flavor vortices $(Q,0)$, $(0,Q)$.

(3) For $1/(g - g'/2) > L > 1/(g + g'/2)$, double-vortex formation is only optimal if the vortex has $Q_+ + Q_- = 0$, which corresponds to the topological excitations of the diagonal $U(1)_d$ symmetry subgroup, the reduction of the total phase symmetry to the special case $(\theta_F,\theta_B) \mapsto (\theta_F + \delta\theta, \theta_B - \delta\theta)$. In other words, vortices of the form $(Q_+,-Q_+)$ proliferate. Here, higher charge vortices may be more energetically favorable than unit-charge ones, contrary to the initial simplistic assumption, the reason being that the vortex core energy proportional to gQ_+^2 may be more than balanced out by the intravortex interaction proportional to $-g'Q_+^2$ (depending on the ratio of g and g'). This further means that there may be multiple ground states of equal energy (frustration). We thus call this case *frustrated vortex insulator* (FI); it is populated primarily with vortices of charge $(Q,-Q)$.

(4) For $1/(g + g'/2) > L$ vortex formation always reduces the free energy, no matter what the relation between Q_+ and Q_- is, and each phase can wind separately: $(\theta_F,\theta_B) \mapsto (\theta_F + \delta\theta_F, \theta_B + \delta\theta_B)$. Vortices of both flavors proliferate freely at no energy cost and for that reason we call this phase *vortex perfect conductor* (PC). We deliberately avoid the term superconductor to avoid the (wrong) association of this phase with the vortex lines and type I or type II superconductors familiar from the three-dimensional (3D) vortex systems: Remember there is no emergent gauge field for the vortices in two spatial dimensions, and we only have perfect conductivity in the sense of zero resistance for transporting the (topological) charge, but no superconductivity in the sense of breaking a gauge symmetry.

A more systematic mean-field calculation will give the phase diagram also for an arbitrary number of vortices. This is not so interesting as it already does not require much less work than the RG analysis, which is more rigorous and more accurate for this problem. For completeness, we give the multivortex mean-field calculation in Appendix E.

One might worry that the our whole approach approach misses the CP geometry of the problem, i.e., the fact that the Ψ_+ field has a source at $z = 0$ and the Ψ_- field at $z = L$. In Appendix F, we show that nothing is missed at the level of approximations taken in this paper, i.e., mean-field theory in this subsection and the lowest-order perturbative RG in the next one. Roughly speaking, it is because the sources are irrelevant in the RG sense—the bulk configuration dominates over the boundary terms. The appendix states this in much more precise language.

2. RG analysis

We have classified the symmetries and thus the phases of our system at the mean-field level. To describe quantitatively the borders between the phases and the phase diagram, we will perform the renormalization group (RG) analysis. Here we follow closely the calculation for conventional vortex systems [24]. We consider the fluctuation of the partition function $\delta\mathcal{Z}$ upon the formation of a virtual vortex pair at positions $\mathbf{r}_1,\mathbf{r}_2$ with charges $\vec{q},-\vec{q}$ (with $\mathbf{r}_1 + \mathbf{r}_2 = 2\mathbf{r}$ and $\mathbf{r}_1 - \mathbf{r}_2 = \mathbf{r}_{12}$), in the background of a vortex pair at positions

---

[1]Again, this is not generally true for out-of-equilibrium configurations but if the system reaches equilibrium, i.e., stable fixed point, this follows by usual statistical mechanics reasoning.

[2]One specificity of multicomponent vortices is that the coupling constants may be negative, as can be seen from (D11). In that case, the ordering of the four regimes (how they follow each other upon dialing L) changes but the overall structure remains.

$\mathbf{R}_1, \mathbf{R}_2$ (with $\mathbf{R}_1 + \mathbf{R}_2 = 2\mathbf{R}$ and $\mathbf{R}_1 - \mathbf{R}_2 = \mathbf{R}_{12}$) with charges $\vec{Q}_1, \vec{Q}_2$. This is a straightforward but lengthy calculation and we state just the main steps. First, it is easy to show that the creation of single-charge vortices is irrelevant for the RG flow so we disregard it. Also, we can replace the core self-interaction constants $g_{0,1}$ with the fugacity parameter defined as $y \equiv \exp\left[-\beta(g_0 + g_1) \ln \epsilon\right]$. Here we introduce the notation $\beta \equiv L$ in analogy with the inverse temperature β in standard statistical mechanics, in order to facilitate the comparison with the literature on vortices in spin systems, and also with antiferromagnetic systems in Sec. V.[3]

Now from the vortex Hamiltonian $\mathcal{H}_{\text{vort}}$ the fluctuation equals (at the quadratic order in y and r)

$$\frac{\delta\mathcal{Z}}{\mathcal{Z}} = 1 + \frac{y^4}{4} \sum_{q_\pm} \int dr_{12}\, r_{12}^3 \, e^{g\vec{q}\cdot\vec{q} + g'\vec{q}\times\vec{q}}$$
$$\times \left[\int dr\, r^2 (g\vec{Q}_1 \cdot \vec{q} + g'\vec{Q}_1 \times \vec{q}) \right.$$
$$\times \nabla \ln|\mathbf{R}_1 - \mathbf{r}| + (g\vec{Q}_2 \cdot \vec{q} + g'\vec{Q}_2 \times \vec{q})$$
$$\left. \times \nabla \ln|\mathbf{R}_2 - \mathbf{r}| \right]^2. \tag{12}$$

Notice that ∇ is taken with respect to $\mathbf{r}$. The above result is obtained by expanding the Coulomb potential in r_{12} (the separation between the virtual vortices being small because of their mutual interaction) and then expanding the whole partition function (i.e., the exponent in it) in y around the equilibrium value $\mathcal{Z}$. The term depending on the separation r_{12} is the mutual interaction energy of the virtual charges, and the subsequent term proportional to r^2 is the interaction of the virtual vortices with the external ones (the term linear in r cancels out due to isotropy). Then by partial integration and summation over $q_\pm \in \{1, -1\}$ we find

$$\frac{\delta\mathcal{Z}}{\mathcal{Z}} = 1 + y^4 [8\pi g^2 \vec{Q}_1 \cdot \vec{Q}_2 + 8\pi(g')^2 \vec{Q}_1 \cdot \vec{Q}_2$$
$$+ 16\pi g g' \vec{Q}_1 \times \vec{Q}_2] I_3 \ln R_{12}$$
$$+ y^4 [4\pi g(g + g')(\vec{Q}_1 \times \vec{Q}_1 + \vec{Q}_2 \times \vec{Q}_2)$$
$$\times I_1 + 8(g')^2 I_1] \ln \epsilon, \tag{13}$$

with $I_n = \int_{\epsilon a}^{\Lambda a} dr\, r^{n+g+g'}$. Now, by taking into account the definition of the fugacity y, rescaling $\Lambda \mapsto \Lambda(1 + \ell)$, performing the spatial integrals, and expanding over ℓ, we can equate the bare quantities g, g', y in (7) with their corrected values in $\mathcal{Z} + \delta\mathcal{Z}$ to obtain the RG flow equations:

$$\frac{\partial g}{\partial \ell} = -16\pi(g^2 + g'^2)y^4, \quad \frac{\partial g'}{\partial \ell} = -2\pi g g' y^4,$$
$$\frac{\partial y}{\partial \ell} = 2\pi(1 - g - g')y. \tag{14}$$

---

[3] Of course, the physical meaning of β in our system is very different: We have no thermodynamic temperature or thermal noise, and the third law of thermodynamics is not satisfied for the "temperature" $1/\beta = 1/L$. We merely use the β notation to emphasize the similarity between free energies of different systems, not as a complete physical analogy.

Now let us consider the fixed points of the flow equations. If one puts $g' = 0$, they look very much like the textbook XY model RG flow, except that the fugacity enters as y^4 instead of y^2 (simply because every vortex contributes two charges). They yield the same phases as the mean-field approach as it has to be, but now we can numerically integrate the flow equations to find exact phase borders. The fugacity y can flow to zero (meaning that the vortex creation is suppressed and the vortices tend to bind) or to infinity, meaning that vortices can exist at finite density. At $y = 0$, there is a fixed line $g + g' = 1$. This line is attracting for the half-plane $g + g' > 1$; otherwise, it is repelling. There are three more attraction regions when $g + g' < 1$. First, there is the point $y \to \infty, g = g' = 0$ which has no analog in single-component vortex systems. Then, there are two regions when $g \to \infty$ and $g' \to \pm\infty$ (and again $y \to \infty$). Of course, the large g, g' regime is strongly interacting and the perturbation theory eventually breaks down, so in reality the coupling constants grow to some finite values g_*, g'_* and g_{**}, g'_{**} rather than to infinities. The situation is now the following:

(1) The attraction region of the fixed line is the vortex insulator phase: The creation rate of the vortices is suppressed to zero.

(2) The zero-coupling fixed point attracts the trajectories in the vortex perfect conductor phase: Only the fugacity controls the vortices and arbitrary charge configurations can form. Numerical integration shows that this point also has a finite extent in the parameter space.

(3) In the attraction region of the fixed point with $g_* < 0$ and $g'_* > 0$ (formally they flow to $-\infty$ and $+\infty$, respectively), same-sign F and B charges attract each other and those with the opposite sign which repel each other. This is the frustrated insulator.

(4) The fixed point with $g_{**}, g'_{**} < 0$ (formally both flow to $-\infty$) corresponds to the conductor phase.

The RG flows in the g-g' plane are given in Fig. 2. Full RG calculation is given in Fig. 2(b); for comparison, we include also the mean-field phase diagram (following from the previous subsubsection and Appendix E) in Fig. 2(a). In the half-plane $g + g' > 1$ every point evolves toward a different, finite point (g, g') in the same half-plane. In the other half-plane we see the regions of points moving toward the origin or toward one of the two directions at infinity. The PC phase (the attraction region of the point $(0,0)$) could not be obtained from the mean field calculation (i.e., it corresponds to the single point at the origin at the mean field level).

It may be surprising that the coupling constants can be negative, with like charges repelling and opposite charges attracting each other. However, this is perfectly allowed in our system. In the usual XY model, the stiffness is proportional to the kinetic energy coefficient and thus has to be positive. Here, the coupling between the fluctuations of F and B beams introduces other contributions to g, g' and the resulting expressions (D11) give bare values of g, g' that can be negative, and the stability analysis of the RG flow clearly shows that for nonzero g', the flow can go toward negative values even if starting from a positive value in some parameter range. If we fix $g' = 0$, the flow equations reproduce the ones from the single-component XY model, and the phase diagram is reduced to just the $g' = 0$ line. If we additionally suppose that
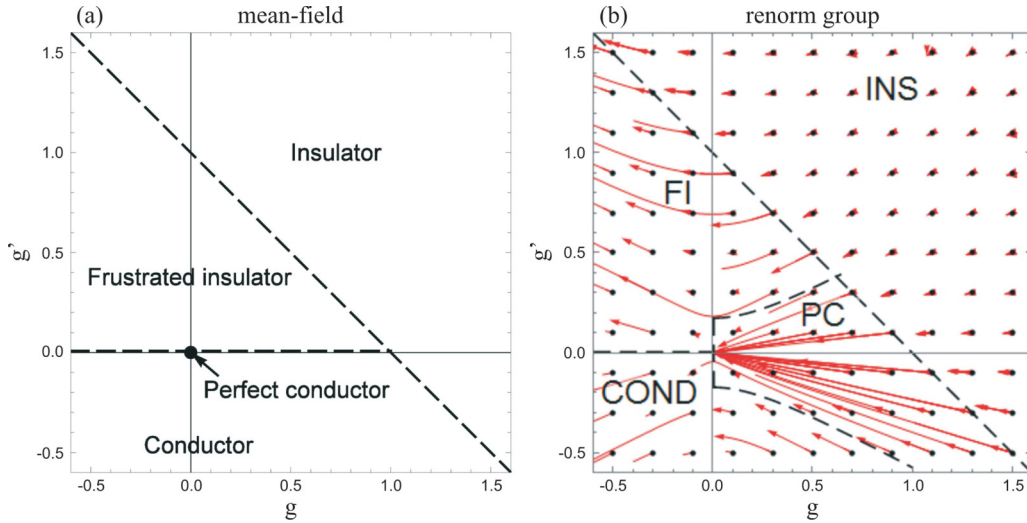
FIG. 2. Phase diagram for the clean system in the g-g' plane, at the mean-field level (a) and with RG flows (b). We show the flows for a grid of initial points, denoted by black dots; red lines are the flows. Four phases exist, whose boundaries are delineated by black dashed lines. In the mean-field calculation (a) all phase boundaries are analytical. In the RG calculation, the straight line $g + g' = 1$ is obtained analytically whereas the other phase boundaries can only be found by numerical integration of the flow equations (14). The flows going to infinity are the artifacts of the perturbative RG; they probably correspond to finite values which are beyond the scope of our analytical approach. Notice how the flows in the $g + g' > 1$ phase all terminate at different values.

the bare value of g is non-negative, than we are on the positive $g' = 0$ semiaxis in the phase diagram—here we see only two phases, insulator (no vortices, $g \to$ const.) and perfect conductor ($g \to 0$). However, for g' fixed to zero (that is, with a single flavor only), the perfect conductor reduces to the usual conductor phase of the single-component XY model—in other words, we reproduce the expected behavior.

Physically, it is preferable to give the phase diagram in terms of the quantities Γ, τ, I, I_x, L that appear in the initial equations of motion (1) and (2): The light intensities can be directly measured and controlled, whereas the relaxation time and the coupling cannot, but at least they have a clear physical interpretation. The relations between these and the effective Hamiltonian quantities y, g, g' are found upon integrating out the intensity fluctuations to obtain (7) and the explicit relations are stated in (D11). Making use of these we can easily plot the phase diagram in terms of the physical quantities for comparison with experiment. However, for the qualitative understanding we want to develop here, it is much more convenient to use g, g' as the phase structure is much simpler.

As an example, we plot the Γ-g' diagram in Fig. 3 (we have kept g' to keep the picture more informative; the Γ-L and Γ-I diagrams contain multiple disconnected regions for each phase). The noninteracting fixed point $g = g' = 0$ is now mapped to $\Gamma = 0$. The tricritical point where the PC, the FI, and the conductor phases meet is at $R = 1$. Therefore, the rule of thumb is that low couplings Γ produce stable vortices with conserved charges—the perfect vortex conductor. Increasing the coupling pumps the instability up, and the kind of instability (and the resulting phase) is determined by the relative strength of the photonic lattice compared to the propagating beams. Obviously, such considerations are only a rule of thumb and detailed structure of the diagram is more complex. This is one of the main motives of this study—blind numerical search for patterns without the theoretical approach

adopted here would require many runs of the numerics for a good understanding of different phases.

C. Geometry of patterns

Now we discuss what the intensity pattern $I(\mathbf{r})$ looks like in various phases, for various boundary conditions. This is very important as this is the only thing which can be easily measured in experiment—phases θ_α are not directly observable, while the intensity distribution is the direct outcome of the imaging of the crystal [31]. We shall consider three situations. The first is a single Gaussian beam on zero
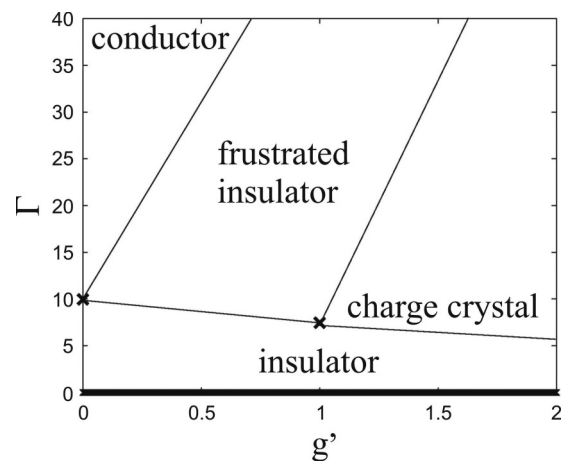

FIG. 3. Typical phase diagram for the system without disorder, in the Γ-g' plane. There are two discrete fixed points and the critical line at $\Gamma = 0$, which corresponds to the critical line $g + g' = 1$ in the previous figure. We also see two discrete fixed points, corresponding to $g_{*,**}, g'_{*,**}$. The advantage of physical parameters is that the location of these fixed points in the Γ-I plane can be calculated directly from the numerics (or measured from the experiment).

background ($I_x = 0$), with Gaussian initial intensity profile $|F(z = 0, \mathbf{r})|^2 = |B(z = L, \mathbf{r})|^2 = \mathcal{N} \exp(-r^2/2s^2)$ and possibly nonzero vortex charges: $\arg \Psi_{\pm}(\mathbf{r}) \sim \exp(Q_{F,B}\phi)$, with $\mathbf{r} = (r \cos \phi, r \sin \phi)$. The second case is a quadratic vortex lattice of F and B beams, so the initial beam intensity is $I_0 = \sum_{i,j} \exp[-(x - x_i)^2/2s_0^2 - (y - y_i)/2s_0^2]$, with $x_{i+1} - x_i = y_{i+1} - y_i \equiv b = $ const., the situation particularly relevant for analogies with condensed matter systems. In the third case, we have again a quadratic vortex lattice but now on top of the background photonic square lattice, which is either coincident or off phase (shifted for half a lattice spacing) with the beam lattice. The background intensity is thus of the form $I_x = \sum_{i,j} \exp[-(x - x_i)^2/2s^2 - (y - y_i)/2s^2]$.

First of all, it is important to notice that there are two kinds of instabilities that can arise in a vortex beam:[4]

(1) There is an instability which originates in the imbalance between the diffusion and self-focusing (crystal response) in favor of diffusion in *high-gradient regions*: If a pattern $I(x, y)$ has a large gradient ∇I, the kinetic term in the Lagrangian (4), i.e., the diffusion term in (1) is large and the crystal charge response is not fast enough to balance it as we travel along the z axis, so the intensity rapidly dissipates and the pattern changes. Obviously, the vortex core is a high-gradient region so we expect it to be vulnerable to this kind of instability. This is indeed the case: In the center of the vortex the intensity diminishes, a dark region forms, and the intensity moves toward the edges. We dub this the core or central instability (CI), and in the effective theory it can be understood as the decay of states with low fugacity y, i.e., high self-interaction constants g_0, g_1. This instability prevents the formation of vortices in the insulator phase, or limits it in the frustrated insulator and conductor phases.

(2) There is an instability stemming from the dominance of diffusion over self-focusing in *low-intensity regions of sufficient size and/or convenient geometry*. At low intensity, the charge response is nearly proportional to I [from Eq. (2)], so if I is small diffusion wins and the intensity dissipates. If there is sufficient inflow of intensity from more strongly illuminated regions, it may eventually balance the diffusion, but if the pattern has a long "boundary", i.e., outer region of low intensity, it will not happen and the pattern will dissipate out or reshape itself to reduce the low-intensity region. We call this case the edge instability (EI). For a vortex, it happens when the positive and negative vortex charges tend to redistribute due to Coulomb attraction and repulsion. In our field theory Hamiltonian (7), this instability dominates in the conductor and perfect conductor phases.

Let us first show how the CI and EI work for a single beam with nonzero vortex charge. In Fig. 4, we show the intensity patterns for a single vortex with charges (1,0) and (3,0) as the x-y cross sections (transverse profiles) in the middle of the
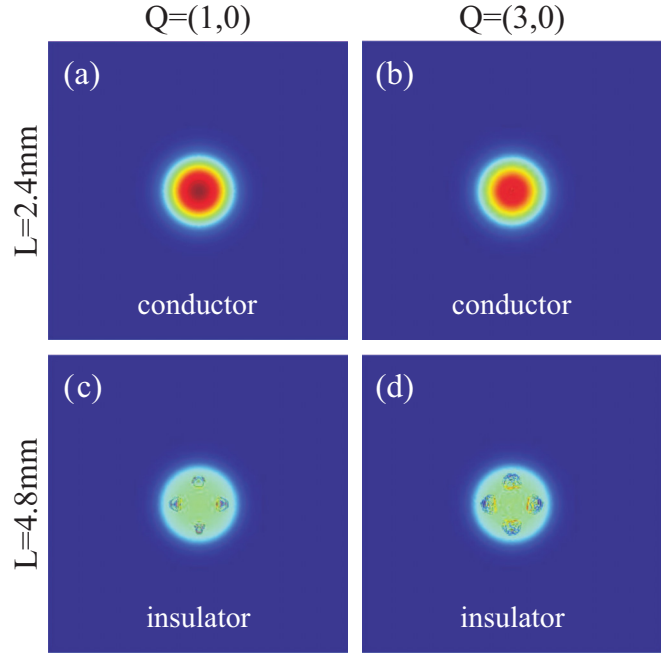

FIG. 4. Transverse profiles for a single Gaussian beam for two different propagation distances, $L = 2.4$ mm (top) and $L = 4.8$ mm (bottom), with vortex charges (1,0) [(a), (c)] and (3,0) [(b), (d)], at the back face of the crystal ($z = L$). The regime on top [(a), (b)] corresponds to the conductor phase, which has a single conserved vortex charge Q_F. This vortex charge conservation prevents significant instabilities; nevertheless, the multiquantum vortex (3,0) shows the onset of CI; notice the reduced intensity and incoherent distribution of the beam in the central region in the top right panel (the CI is expected to grow roughly as $Q_+^2 + Q_-^2$). The insulator phase only preserves the $F - B$ invariance but not the vortex charge, and in the absence of topological protection the vortices can annihilate into the vacuum. Here we see the EI taking over for both charges; four unstable regions appear near the boundary, violating the circular symmetry and dissipating away the intensity of the vortex. Parameter values: FWHM 40 μm, $\Gamma I_0 = 41$, $t = 10\tau$.

crystal, i.e., for $z = L/2$. The parameters chosen (Γ, I_0, R, L) correspond to the conductor phase (top) and the insulator phase (bottom). In top panels, for $Q_+^2 + Q_-^2 = 1$, the core energy is not so large and CI is almost invisible. For $Q_+^2 + Q_-^2 = 9$, we see the incoherence and the dissipation in the core region, signifying the CI. The conductor phase allows the proliferation of vortices but only those with $|Q_{\pm}| \leqslant 1$ are stable. In the bottom panels, both vortices have almost dissipated away due to EI, which starts from discrete poles near the boundary.[5] Indeed, the insulator phase has no free vortices, no matter what the charge. In Fig. 5, we see no instability even for a high-charge vortex in the perfect conductor phase (top), whereas the frustrated insulator phase (bottom) shows strong EI for the like-charged vortex (3,3) since this fixed point has $g_*' > 0$, but the $(3,-3)$ vortex is stable. Notice that we could not expect

---

[4]They are distinct from the bifurcations which happen also in topologically trivial beam patterns and lead to the instability which eventually destroys optical (nontopological) solitons. These instabilities have been analyzed in Appendix C and in more detail in Ref. [32], where the authors have found them to start from the edge of the beam and result in the classical "walk through the dictionary of patterns."

---

[5]As a rule, it follows the sequence (C9) found in Appendix C from the pole structure of the propagator, though some of the steps can be absent, e.g., for a single Gaussian vortex there is no $\mathbb{C}_2$ stage.
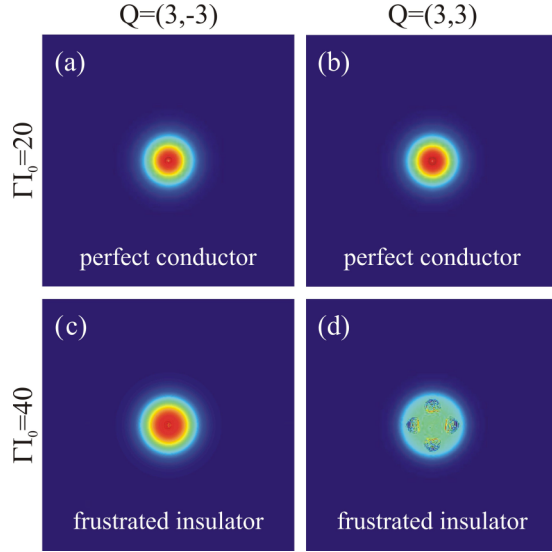
FIG. 5. Transverse profiles for a single Gaussian beam for two different coupling strengths, $\Gamma I_0 = 20$ (top) and $\Gamma I_0 = 40$ (bottom), with vortex charges $(3,-3)$ [(a), (c)] and $(3,3)$ [(b), (d)] at the back face of the crystal $(z = L)$. The regime on top corresponds to the perfect conductor phase, where the vortices of all charges freely proliferate—both vortices are reasonably stable. The bottom case is in the frustrated insulator phase—the forward-backward coupling makes the $(3,3)$ vortex unstable from EI while the $(3,-3)$ vortex survives. Parameter values: FWHM 40 μm, $L = 2$ mm, $t = 10\tau$.

CI for this case since the sum $Q_+^2 + Q_-^2 = 9$ is the same in both cases—if for $Q_- = -Q_+$ the vortex has no CI, then for $Q_- = Q_+$ it cannot have it either (since the value $Q_+^2 + Q_-^2$ is the same).

We have thus seen what patterns to expect from CI and EI and also what kind of stable vortices to expect in different phases: The perfect conductor phase allows free proliferation of vortices of any charge, the conductor phase allows only single-quantum vortices (or vortices with sufficiently low $Q_+^2 + Q_-^2$) while others dissipate from CI, the frustrated insulator supports the vortices with favorable charges (or favorable charge distribution in multiple-vortex systems) while others disintegrate from EI, and the insulator phase supports no vortices—they all dissipate from CI or EI, whichever settles first (depending on the vortex charges).

The case rich with analogies with condensed matter systems is the square vortex lattice on the background photonic square lattice, Fig. 6. Here we can also appreciate the transport processes. The photonic lattice is coincident with the beam lattice and equal in intensity, so $\Gamma(I_0 + I_x) = 2\Gamma I_0$. In the perfect conductor phase [Fig. 6(a)], the vortices are stable and coherent and keep the uniform lattice structure. In the conductor phase [Fig. 6(b)], the CI is visible but the lattice structure survives. The bottom panels show the nonconducting phases: frustrated insulator [Fig. 6(c)] and insulator [Fig. 6(d)]. The insulator loses both lattice periodicity and the Gaussian profile of the vortices but the frustrated insulator keeps the regular structure: From EI the intensity is *inverted* and the resulting lattice is *dual* to the original one [compare Fig. 6(c) to Fig. 6(a)]. The phase patterns $\theta_F(x,y; z = L/2)$
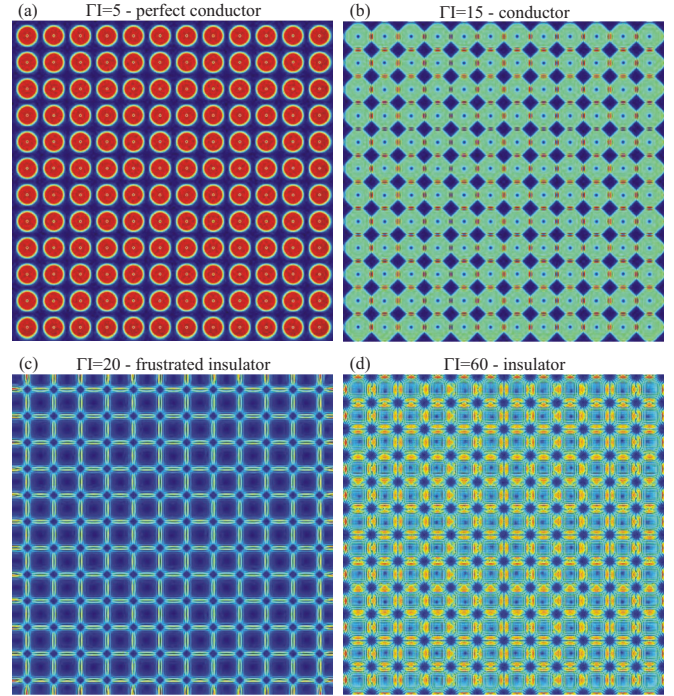

FIG. 6. Vortex lattice with Gaussian profile for $\Gamma I = 5$ [PC, panel (a)], $\Gamma I = 15$ [conductor, panel (b)], $\Gamma I = 20$ [FI, panel (c)], and $\Gamma I = 60$ [insulator, panel (d)]. The perfect conductor phase has a coherent vortex lattice and no instabilities. Conductor exhibits a deformation of the vortex lattice and the reduction of the full O(2) symmetry, starting from the *center*, whereas the FI exhibits the reduction of symmetry and the inversion of the lattice due to *edge* effects. Notice how both phases have reduced symmetry compared to PC but retain coherence. Only the insulator phase loses not only symmetry but also coherence; i.e., the intensity diffuses and the pattern is smeared out. Transverse size of the lattice is 512×512 in computational space; same lattice size, FWHM, and lattice spacing are used for all subsequent figures unless specified otherwise. Parameter values: $L = 4.8$ mm, $t = 10\tau$, FWHM 10 μm, and lattice spacing equal to FWHM.

and $\theta_F(x,z; y = 320\ \mu$m) for the perfect conductor (top) and the frustrated insulator phase (bottom) are shown in Fig. 7. Here we see the vortex charge transport mechanism in a PC: The vortices are connected in the sense that the phase θ_F is coherently traveling from one vortex to the next. In the FI phase, the phase is initially frozen along the z axis, until the transport starts at some $z \approx L/2$.

It may be instructive to take a closer look at the lattice dynamics of the most interesting phase: the frustrated insulator. In Fig. 8, we inspect square lattices on the photonic lattice background for several charges of the form $(Q_+ = 3, Q_-)$. The first row shows how the vortices lose stability and develop CI as the total square of the charge grows [from Fig. 8(a) to Fig. 8(c)]. Figures 8(d)–8(i) show how the g' coupling favors the opposite sign of Q_+ and Q_- and how the optimal configuration is found for $Q_- = -3$. This is easily seen by minimizing the free energy over Q_-: It leads to the conclusion that the forward-backward coupling favors the "antiferromagnetic" ordering in the sense that $Q_+ + Q_- = 0$.
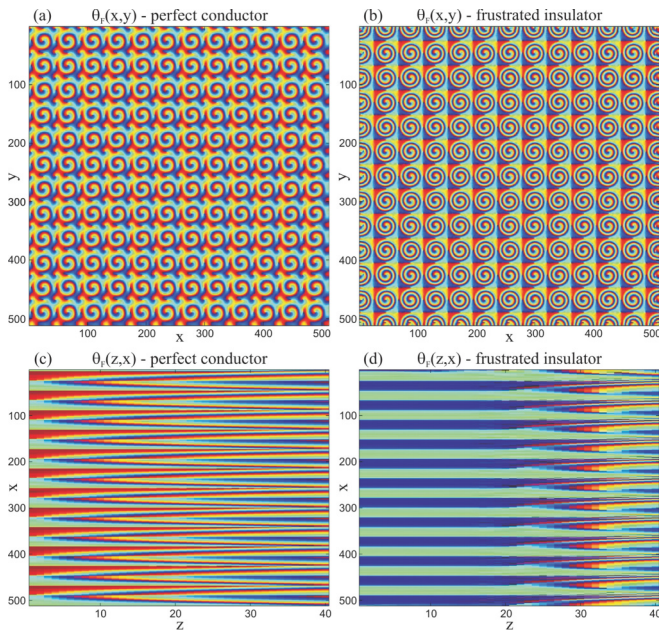
FIG. 7. Same system as in panels (a) and (c) from the previous figure (PC and FI phases) but now we plot the phase θ_F, as the transverse cross section $\theta_F(x,y; z = L/2)$ [(a), (b)] and as the longitudinal section along the PR crystal $\theta(x,z; y = 320 \ \mu m)$ [(c), (d)]. The perfect conductor phase has well-defined vortices in contact which allows the transport of the vortex charge through the lattice and shows as the periodical modulation of the phase along the z axis (vortex lines). The frustrated insulator keeps well-defined vorticity even though the intensity map undergoes inversion [Fig. 6(c)] with frozen phase along the z axis, so there is no vorticity transport until some $z \approx L/2 = 2.4$ mm, when the phase stripes develop into vortex lines. The unit on the x and y axis is 1 μm (1 in computational space) and on the z axis 0.12 mm (120 in computational space).

Finally, it is interesting to see how the FI phase at high intensities and coupling strengths contains a seed of translation symmetry breaking which will become important in the presence of disorder. In Figs. 9 and 10, we give intensity and phase transverse profiles across the PC-FI transition and deep into the FI phase at large couplings. The intensity maps show the familiar inverse square lattice but the phase maps show stripelike ordering, i.e., translation symmetry breaking along one direction in Figs. 10(c) and 10(d)—horizontal and vertical lines with a repeating constant value of the phase θ_F on all lattice cells along the line. This is a new instability, distinct from CI and EI. We cannot easily derive this instability from the perturbation theory in Appendix C as it is a collective phenomenon and cannot be understood from a single beam.

IV. THE SYSTEM WITH DISORDER

Consider now the same system in the presence of quenched disorder. This is a physically realistic situation: The disorder corresponds to the holes in the photonic lattice which are caused by the defects in the material. The defects are in fixed positions, i.e., they are quenched, whereas the beam is dynamical and can fluctuate. Now $I_x(\mathbf{r}) \to I_x(\mathbf{r}) + I_h(\mathbf{r})$; i.e.,
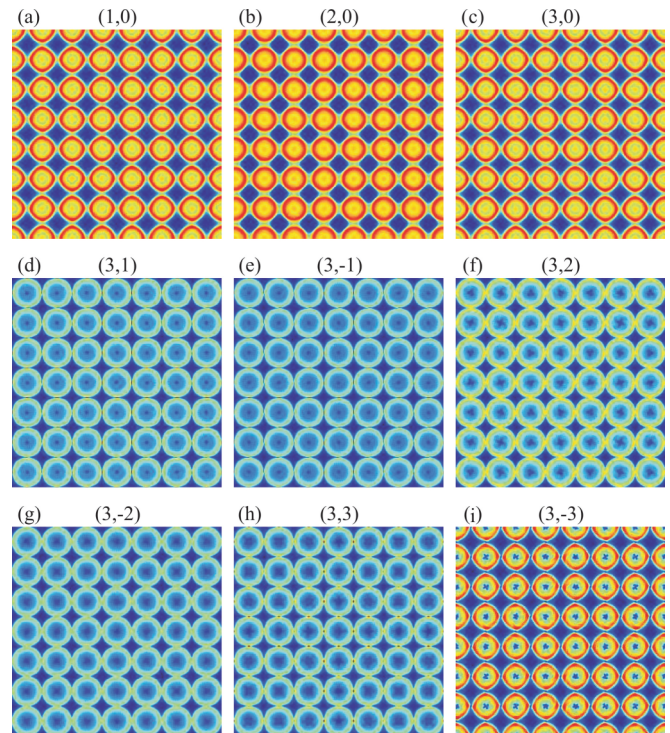

FIG. 8. Transverse profiles for vortex lattices with different charges in the FI phase. In the first row [(a)–(c)], we see how the CI gets stronger and stronger as the total vortex core energy grow (with the square of the total charge). The second and third rows show the growth of CI from $(3,0)$ to $(3,\pm3)$ (notice the increasingly reduced intensity in the center and the strong ringlike structure of the beams) but also the forward-backward interaction which favors the configurations $(3,-3),(3,-2),(3,-1)$ over $(3,3),(3,2),(3,1)$. In particular, the $(3,-3)$ lattice is the optimal configuration of all $(3,Q_-)$ configurations even though it has greater CI than say $(3,0)$ (notice the small dark regions in the center), because the $\sum_{ij} gg' Q_{i+} Q_{i-} \ln r_{ij}$ term minimizes the EI—notice there is no "spilling" of intensity from one vortex to the next. The parameters are $\Gamma I = 20, L = 2.5$ mm.

the quenched random part $I_h(\mathbf{r})$ is superimposed to the regular background (whose intensity is I_x). The disorder is given by some probability distribution, assuming no correlations between defects at different places. As in the disorder-free case, the lattice is static and "hard", i.e., does not backreact due to the presence of the beams. One should, however, bear in mind that the backreaction on the background lattice can sometimes be important as disregarding it violates the conservation of the angular momentum [37]. Disregarding the backreaction becomes exact when $I_x + I_h \gg |\Psi|^2$, i.e., when the background irradiation is much stronger than the propagating beams.

To treat the disorder, we use the well-known replica formalism [54]. For vortex-free configurations, typical experimental values of the parameters suggest that the influence of disorder is small [31,33,35]. However, the influence of disorder becomes dramatic when vortices are present. This is expected, since holes in the lattice can change the topology of the phase field $\theta_\pm$ (the phase now must wind around the holes). Our equations of motion are still given by the Lagrangian (4), but with $I_x \mapsto I_x + I_h$. In our analytical calculations, we assume
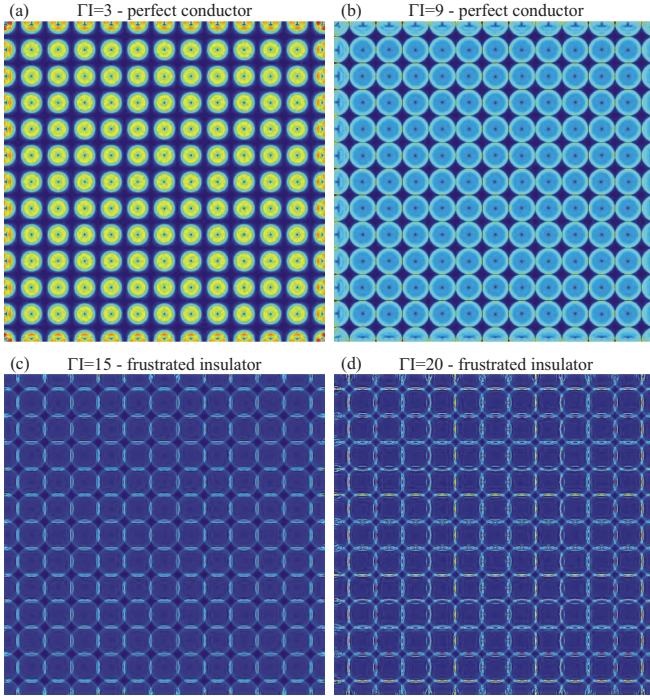
FIG. 9. Intensity maps for the quadratic vortex lattice with charges $(1,1)$, for increasing values of $\Gamma I = \Gamma(I_0 + I_x)$. The transition from the PC phase [(a), (b)] into the FI phase [(c), (d)] happens at about $\Gamma I \approx 12$. The edge instability sets in progressively, in accordance with what we saw in the previous figure, leading eventually to an inverse square lattice. Propagation length $L = 5$ mm.

that a defect in the photonic lattice changes the lattice intensity from I_x to $I_x + I_h$, with Gaussian distribution of "holes" in I_h, which translates to the approximately Gaussian distribution of the couplings g, g', g_0, g_1. In the numerics, however, we do a further simplification and model the defects in a discrete way; i.e., at a given spot either there is a lattice cell of intensity I_1 (with probability h), or there is not (the intensity is zero, with probability $1 - h$). This corresponds to $I_x = I_1/2$, $I_h = \pm I_1/2$ so the disorder is discrete. Due to the central limit theorem, we expect that the Gaussian analytics should be applicable to our numerics.

A. The replica formalism at the mean-field level

To study the system with quenched disorder in the photonic lattice, we need to perform the replica calculation of the free energy of the vortex Hamiltonian (7). We refer the reader to the literature [41,42] for an in-depth explanation of the replica trick. In short, one needs to average over the various realizations of the disorder *prior* to calculating the partition function, i.e., prior to averaging over the dynamical degrees of freedom (vortices in our case). This means that we need to perform the disorder average of the free energy, i.e., the logarithm of the original partition function $-\ln \mathcal{Z}$, and not the partition function $\mathcal{Z}$ itself. The final twist is the identity $\ln \mathcal{Z} = \lim_{n \to 0} (\mathcal{Z}^n - 1)/n$: We study the Hamiltonian consisting of n copies (replicas) of the original system and then *carefully*
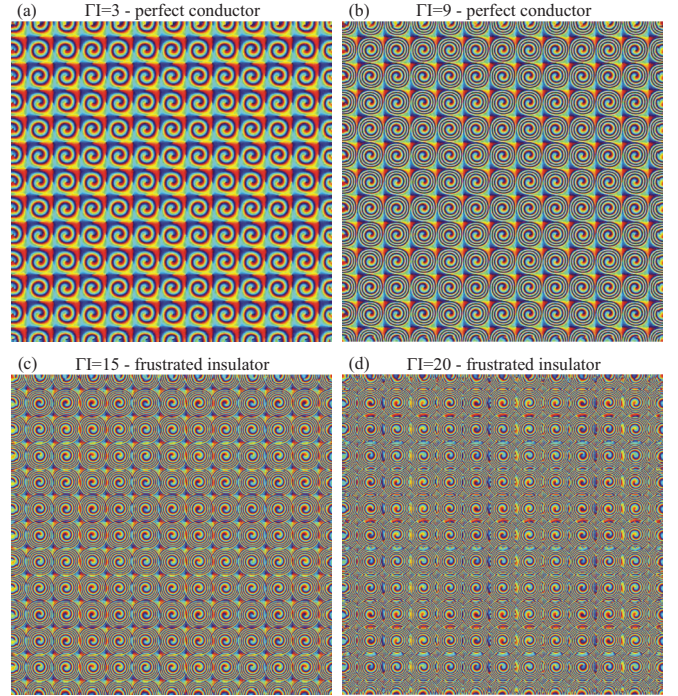

FIG. 10. Transverse phase maps for the F beam for the same cases as in Fig. 9. As the coupling strength ΓI grows toward very large values (d), the violation of translation symmetry becomes obvious: Notice the vertical and horizontal phase stripes. This instability gives rise to the charge density wave ordering in the presence of disorder.

take the $n \to 0$ limit.[6] The partition function of the replicated Hamiltonian reads

$$\mathcal{Z} = \lim_{n \to 0} \mathrm{Tr} \exp \left[-\sum_{\mu=1}^{n} \mathcal{H}_{\mathrm{vort}}(Q^{(\mu)}) \right], \qquad (15)$$

where $Q^{(\mu)}$ are the vortex charges in the μth replica of the system. In the original Hamiltonian (7), the disorder turns the interaction constants into quenched random quantities $g_{ij}, g'_{ij}, g_{0;ij}, g_{1;ij}$, so we can compactly write our interaction term as

$$\mathcal{H}_{\mathrm{vort}} = \sum_{ij} \sum_{\alpha\beta} Q_{i\alpha} J_{ij}^{\alpha\beta} Q_{j\beta} \qquad (16)$$

with $J_{ij}^{++} = J_{ij}^{--} = g_{ij}(1 - \delta_{ij})\ln r_{ij} + g_0\delta_{ij}$, $J_{ij}^{+-} = J_{ij}^{-+} = g'_{ij}(1 - \delta_{ij})\ln r_{ij} + g_1\delta_{ij}$. Now we again make the mean-field approximation for the long-ranged logarithmic interaction. Similar to the clean case, for $i \neq j$ we approximate $g\ln r_{ij} \sim g'\ln r_{ij} \sim \ln \Lambda$, knowing that $g, g' \sim 1$ and assuming that average intervortex distance is of the same order of magnitude as the system size Λ, and for the core energy we likewise get $g_0, g_1 \sim \ln a/\epsilon \sim -\ln \epsilon \sim \ln \Lambda$. The result is that all terms in $J_{ij}^{\alpha\beta}$, both for $i \neq j$ and $i = j$, are on average of the order $\ln \Lambda \gg 1$, and the mean-field approach is justified. We will sometimes denote the 2×2 matrices in the flavor space by hats (e.g., $\hat{J} = J^{\alpha\beta}$).

---

[6]Care is needed as the $n \to 0$ limit does not in general commute with the thermodynamic limit.

The final Hamiltonian (16) has the form of the random-coupling and random-field Ising-like model: Random couplings stem from the stochasticity of J_{ij} values and random field from the fact that $\langle J_{ij} \rangle \neq 0$ introduces terms linear in $Q_{i\alpha}$, i.e., an effective external field coupling to the "spins." We have arrived at this model through three steps of simplification: our microscopic model is a type of the XY-glass model (Cardy-Ostlund model [55]), a well-known toy model for disorder. At this stage, our model is similar to the work of Refs. [9,10], only with two components instead of one. Then we have written the effective vortex Hamiltonian with Coulomb-like interaction, disregarding the topologically trivial configurations. This is a rather extreme approximation but a necessary one as it is very complicated to consider the full model with vortices. Finally, we have approximated the logarithmic potential with a constant all-to-all vortex coupling. Such an approximation

(essentially the infinite dimension limit) is frequently taken and lies at the heart of the solvable Sherington-Kirkpatrick Ising random coupling model [41]. Our case differs from the Sherington-Kirkpatrick model as it (i) has also a random field, (ii) has two flavors, and (iii) has the Ising spins taking arbitrary integer values. From the random XY model it differs by (i) and (ii) above, and also by considering only vortices and no nontopological spin configurations. The additional phases we get in comparison to Refs. [9,10] and its generalization in Refs. [11,12,46] come from the interactions between the forward and backward flavors. But bearing in mind the drastic approximations we take, we stress that we cannot aspire to solve either the XY model or the resulting Ising-like model in any rigorous way (certainly not at the level of rigor of mathematical physics). We merely try to obtain a crude understanding.

The Gaussian distribution of defects reads $p(J_{ij}^{\alpha\beta}) = \exp\left[-(J_{ij}^{\alpha\beta} - J_0^{\alpha\beta})(\hat{\sigma}^{-2})_{\alpha\beta}(J_{ij}^{\alpha\beta} - J_0^{\alpha\beta})\right]$, where the second moments are contained in the matrix $\sigma_{\alpha\beta}$, with $\sigma_{+-} = \sigma_{-+}$. In this case, we get the replicated partition function

$$\bar{\mathcal{Z}}^n = \int \mathcal{D}[Q_{i\alpha}^{(\mu)}] \int \mathcal{D}[J_{ij}^{\alpha\beta}] \exp\left[-\frac{1}{2} \sum_{i,j=1}^{N} \sum_{\alpha,\beta} \left(J_{ij}^{\alpha\beta} - J_0^{\alpha\beta} \right) \sigma_{\alpha\beta}^{-2} \left(J_{ij}^{\alpha\beta} - J_0^{\alpha\beta} \right) - \sum_{\mu=1}^{n} \sum_{i,j=1}^{N} \sum_{\alpha,\beta} \beta J_{ij}^{\alpha\beta} Q_{i\alpha}^{(\mu)} Q_{j\beta}^{(\mu)} \right]. \quad (17)$$

We can now integrate out the couplings $J_{ij}^{\alpha\beta}$ in (17) and get

$$\bar{\mathcal{Z}}^n = \text{const.} \int \mathcal{D}[Q_{i\alpha}^{(\mu)}] \exp\left[\frac{1}{2}\beta^2 \sum_{\mu,\nu=1}^{n} \sum_{i,j=1}^{N} \sum_{\alpha,\beta} Q_{i\alpha}^{(\mu)} Q_{i\beta}^{(\nu)} (\hat{\sigma}^2)_{\alpha\beta} Q_{j\alpha}^{(\mu)} Q_{j\beta}^{(\nu)} - \beta \sum_{\mu=1}^{n} \sum_{i,j=1}^{N} \sum_{\alpha,\beta} J_0^{\alpha\beta} Q_{i\alpha}^{(\mu)} Q_{j\beta}^{(\mu)} \right]. \quad (18)$$

Integrating out the disorder has generated the nonlocal quartic term proportional to the elements of $\sigma_{\alpha\beta}^2$. The additional scale given by the average disorder concentration means we cannot scale out $\beta = L$ anymore, and it becomes an additional independent parameter. The partition function can be rewritten in the following way, usual in the spin-glass literature [42,54]. We can introduce the nonlocal order parameter fields

$$p_\alpha^{(\mu)} = \frac{1}{N}\sum_{i=1}^{N} Q_{i\alpha}^{(\mu)}, \quad q_{\alpha\beta}^{(\mu\nu)} = \frac{1}{N}\sum_{i,j=1}^{N} Q_{i\alpha}^{(\mu)} Q_{j\beta}^{(\nu)}, \quad (19)$$

which have the meaning of overlap between different metastable states. The rest is just algebra, although rather tedious: One rewrites the Hamiltonian in terms of new order parameters, and then one can solve the saddle-point equations for p_α and $q_{\alpha\beta}$, or do an RG analysis. The calculation is found in Appendix G.

The mean-field analysis yields six phases:

(1) One phase violates both the replica symmetry and the flavor symmetry, breaking it down to identity. We dub this phase *vortex charge density wave* (CDW), as it implies spatial modulation of the vortex charge, leading to nonzero net charge density $\sum_i Q_{i\alpha}^{(\mu)}$ in some parts of the system even if the boundary conditions are electrically neutral (the *total* net charge density must still be zero due to charge conservation). Vortices take their charges from $\mathbb{Z} \otimes \mathbb{Z}$.

(2) The second phase violates the replica symmetry in both flavors and reduces the flavor symmetry but does not break it down to identity. Instead, it reduces it to the diagonal subgroup

$U(1)_F \otimes U(1)_B \rightarrow U(1)_d$, so it has nonzero density of the vortex charge in a given replica $\sum_i Q_{i+}^{(\mu)} = -\sum_i Q_{i-}^{(\mu)}$. Again, the charge density is locally nonzero but now with an additional constraint resulting in frustration (multiple equivalent free energy minima). This is thus the dirty equivalent of the frustrated insulator phase and we dub it *vortex glass*, as it has long-range correlations (because of the logarithmic interactions between charged areas), does not break spatial symmetry, and exhibits frustration; its charges are from $\pi_1[U(1)_d] = \mathbb{Z}$.

(3) The remaining phases have no nonzero vortex charge density fluctuation and are similar to the phases in the clean system. Vortex perfect conductor violates the replica symmetry of all three fields q^{++}, q^{--}, q^{+-} and allows free proliferation of vortices with charges $(Q_+, Q_-) \in \mathbb{Z} \otimes \mathbb{Z}$.

(4) Frustrated vortex insulator preserves the replica symmetry of $q^{\pm\pm}$ but has nonzero value, with broken replica symmetry, of the mixed q^{+-} field, which gives $U(1)_d$ vortices, with charges $Q_+ = -Q_- \in \mathbb{Z}$.

(5) Vortex conductor preserves the replica symmetry of the mixed q^{+-} order parameter but violates it in $q^{\pm\pm}$, resulting in the proliferation of single-flavor vortices with $\mathbb{Z}$ charge.

(6) Vortex insulator fully preserves the replica symmetry, all order parameters are zero, and vortices cannot proliferate. RG analysis will show that insulator surivives only at zero disorder; otherwise it generically becomes CDW.

The phase diagram (given in Fig. 11 in the next subsection) now contains six phases (only five are visible for the parameters chosen in the figure): CDW, insulator, FI,
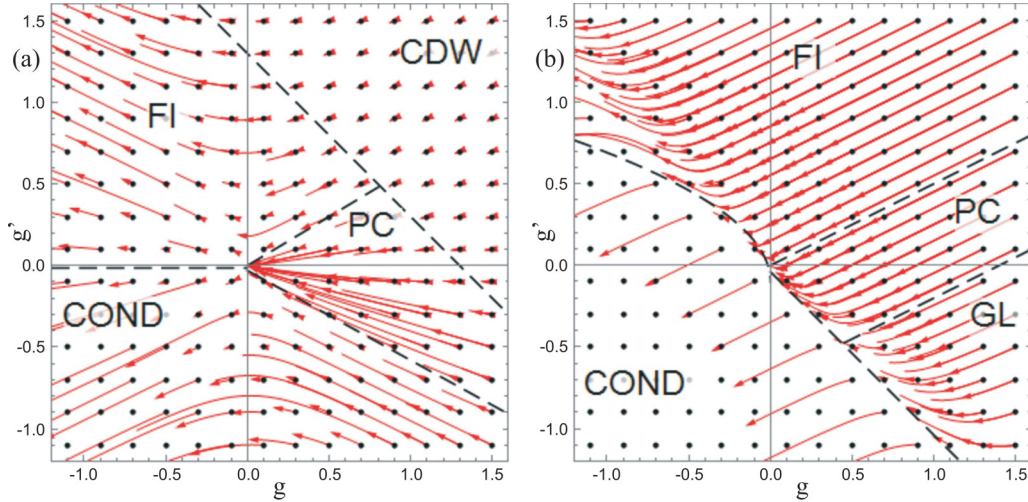
FIG. 11. Phase diagram for the system with lattice disorder in the g-g' plane together with RG flows, with red lines denoting the flows starting at the initial conditions denoted by black points. The dashed black lines are approximate phase boundaries from mean-field theory, for $\sigma^2 = 0.4$ (a) and $\sigma^2 = 1.2$ (b). In panel (a), the area where $g + g' + \beta^2\sigma^2 > 1$ is inhabited by the flows toward nonuniversal values of (g, g') which belong to the CDW phase and the opposite region is divided between the attraction regions of $(0,0)$, $(g_* \to \infty, g'_* \to \infty)$, and $(g_{**} \to \infty, g'_{**} \to -\infty)$—the familiar PC, FI, and conductor phases. In panel (b), for $\sigma^2 = 1.2$, the disorder becomes relevant in the glass phase (denoted by "GL"), whose RG flows end on the half-line of fixed points $g + g' + \beta^2\sigma^2 = 1, g' < 0$. For our parameter values, this line happens to pass almost through the origin; in general, this is not necessarily the case. The nondisordered phases (flowing to $\sigma^2 = 0$) FI, conductor, and PC have survived. Propagating length is $L = 3.0$ mm.

conductor, PC, and the glassy phase. The insulator phase is now of measure zero in the (g, g', σ^2) plane, existing only for the points at $\sigma^2 = 0$; for generic nonzero values we have a CDW. For simplicity, we have plotted the phase diagram for $\sigma_{++}^2 = \sigma_{--}^2 = \sigma_{+-}^2 \equiv \sigma^2$.

B. RG analysis and the phase diagram

To study the RG flow, we can start from the replicated partition function (18), inserting the definition of the couplings $J_{ij}^{\alpha\beta}$ and keeping the vortex charges $Q_{i\alpha}^{(\mu)}$ as the degrees of freedom (without introducing the quantities $p_\alpha^\mu, q_{\alpha\beta}^{(\mu\nu)}$). The basic idea is the same: We consider the fluctuation $\delta(\bar{\mathcal{Z}}^n)$ upon the creation of a vortex pair at $\mathbf{r}_{1,2}$ with charges $\vec{q}_1^{(\mu)}, -\vec{q}_2^{(\mu)}$, in the background of the vortices $\vec{Q}_{1,2}^{(\nu)}$ at positions $\mathbf{R}_{1,2}$. Likewise, we introduce the fugacity parameter $y^{(\mu)}$ to account for the vortex core energy. However, this problem is much harder than the clean problem and one has to resort to many approximations to perform the calculation. In its most general form, the problem is still open, in the sense that all known solutions suppose a certain form of replica symmetry breaking or truncate the RG equations [42]. The RG analysis is thus less useful in the disordered case but at least the numerical integration of the flow equations is supposed to give a more precise rendering of the phase diagram compared to the mean field theory. We again describe the calculation in Appendix G and jump to the results.

The fixed point of the flow equations lies either at infinite y or at $y = 0$ like in the clean case. This is again controlled by the the equation for $\partial y / \partial \ell$ but now depending on the combination $g + g' + \beta^2\sigma^2$ instead of $g + g'$ in the clean case (for simplicity, we consider the case where $\sigma_{\alpha\beta}^2$ are all equal). The following cases appear:

(1) When the fugacity flows toward infinity, we reproduce the phases and the fixed point values (g, g', σ^2) from the clean case: The PC flows toward $(0,0,0)$, the FI toward $(g_*, g'_*, 0)$, and the conductor toward $(g_*, g'_{**}, 0)$ with $g_* \to -\infty, g'_* \to -\infty, g'_{**} \to \infty$. Notice that all these phases flow to $\sigma^2 = 0$; i.e., disorder is irrelevant.

(2) When the fixed point lies at $y = 0$, one possibility is that all parameters (g, g', σ^2) flow toward some nonuniversal nonzero values. The attraction region of this point is the CDW phase: The disorder term stays finite as well as the couplings. In particular, the points on the half-plane $g + g' > 0, \sigma^2 = 0$ stay at $\sigma^2 = 0$ (with constant coupling values) and this is the insulator phase from the clean case. Notice that $\sigma^2 > 0$ now; i.e., disorder is relevant. For $\sigma^2 < 1$, this are the only fixed points when $y = 0$.

(3) However, for sufficiently strong disorder ($\sigma^2 > 1$), there is a new line of fixed points at $y = 0$ with a finite attraction region, corresponding to a new phase. For $\beta > 1$, the right-hand side of the second RG equation in (G19) has a zero at nonzero g' and there are trajectories flowing toward $(y, g, g', \sigma^2) = [0, g, g'(g), \sigma^2(g)]$ and not toward an arbitrary nonuniversal value of σ^2. This is precisely the glass phase, where disorder is again relevant. At the lowest order, the relation between g, g', σ^2 at the fixed point line is given by the relation $g + g' + \beta^2\sigma^2 = 1$.

Now we have made contact between the mean-field classification of phases and the fixed points and regions of the RG flow. The flows in the (g, g') plane are given in Fig. 11. The parameter space is four-dimensional so the phase structure is different at different disorder concentrations σ^2. In Fig. 11(a) for $\sigma^2 = 0.4$, the phase structure is similar to the clean case; we see the same four phases except that insulator (no stable vortices) is replaced by the CDW phase with localized vortices. In Fig. 11(b) for $\sigma^2 = 1.2$, the CDW phase is replaced by
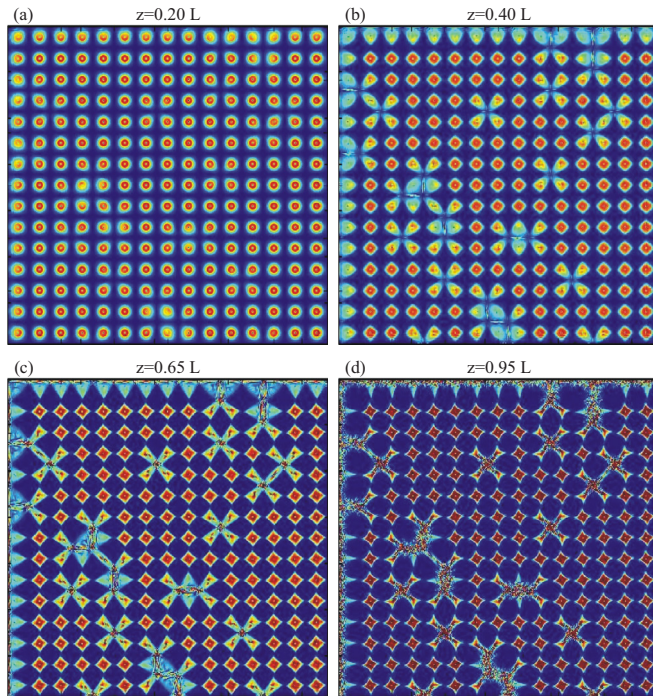
FIG. 12. Transverse profile for the PC phase in a Gaussian beam lattice on a background lattice, for four different propagation distances. The vortex charge is $(1,1)$, which is sufficiently low that the CI does not destroy the vortices. We see some CI-induced symmetry reduction from $O(2)$ to C_4 but the overall lattice structure is preserved. Parameter values are $\sigma^2 = 0.1, \Gamma I = 20, L = 2$ mm, FWHM for the CP beams is 9 μm and for the photonic lattice 6 μm.
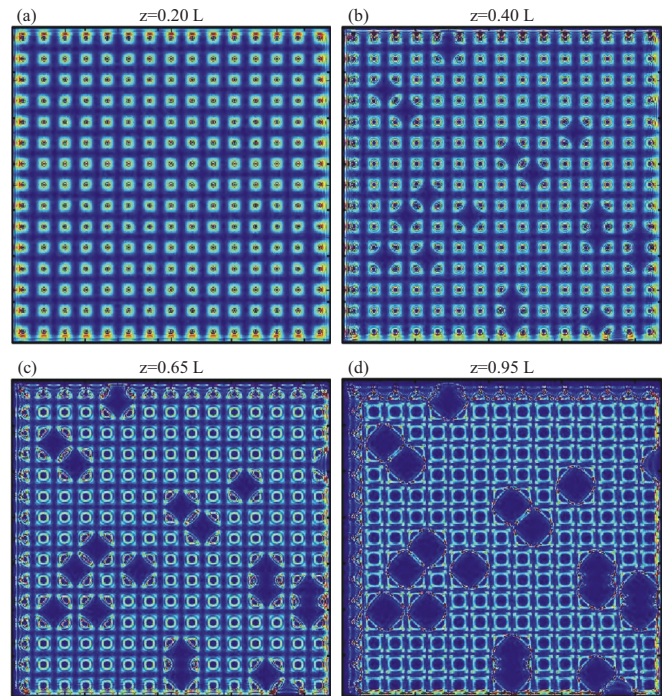

FIG. 13. Transverse profile for the FI phase, present in the same system as in Fig. 12 but for $\Gamma I = 40$. Now both the CI [low-intensity regions in the beam center in panels (a) and (b)] and the EI [lattice inversion in panels (c) and (d)] are present. The net result is the lattice inversion, and the vortex charge dissipates along the inverse lattice.

another disordered phase, the glasslike regime. Importantly, the glass phase does not cross the $g' = 0$ axis, meaning that a single-flavor system even with disorder could not support a glass. We thus conjecture that the transition at $\sigma^2 = 1$ is of first order, as the change is the structure of the (g, g') phase diagram is discontinuous, and we do not see how this could happen if the first derivative $\partial \mathcal{F}/\partial \rho_\pm$ (the derivative of the free energy with respect to vortex charge density) is continuous. However, we have not checked the order of this transition by explicit calculation. The phase structure is further seen in the $\sigma^2 - g'$ diagram, where we see the glass phase emerge at some value of the disorder. This is discussed further in the next section, where we study the equivalent antiferromagnetic system (with the same structure of the phase diagram, Fig. 16).

C. Geometry of patterns

The two previously considered mechanisms of instability— central instability and edge instability—remain active also in the presence of disorder. However, in the presence of disorder there is a third, inherently collective effect that we dub *domain instability* (DI). It follows from the fact that the self-focusing term ΓE grows with intensity I: More illuminated regions react faster [Eqs. (1) and (2)]. In the presence of background lattice, there will be regions of initially zero beam intensity I_0 where the regular lattice cells have some nonzero intensity I_x. Approximating $I = I_0 + I_x \approx I_x = $ const., our equations in the vicinity of the defect (hole) in the background lattice

becomes the Schrödinger equation in a step potential (equal to I_x in the regular parts of the photonic lattice, and equal to zero where a hole is found), so the z-dependent part of the solution is of the form $\sum_k e^{i\lambda_k z}$ and the eigenenergies along z are gapped by the inverse length: $\lambda_k > 1/L$. For small eigenenergies, the transmission coefficient is very low, whereas for large energies it approaches unity. Thus for $1/L$ large (i.e., there are few λ_k's which are larger than $1/L$), most of the intensity remains confined by the borders of the defect and the intensity does not spill but for small $1/L$ the beam profile is deformed by the "spilling" into the hole regions. For vortices, there is an additional Coulomb interaction in the x-y plane, meaning the effective potential is not piecewise constant anymore (even in the simplest approximation) but the qualitative conclusion remains: Large L brings global reshaping of the intensity profile.

The other phases are analogous to the ones in the clean case, though with a general trend that the presence of disorder decreases the stability of vortex patterns. The PC and FI phases are shown in Figs. 12 and 13. In this section, we only look at the lattices, as the notion of disorder is inapplicable for a single beam. Consider first the patterns in the PC phase (Fig. 12). Compared to the clean case [Fig. 6(a)], the symmetry is much reduced, from $O(2)$ to C_4, but the vortices are conserved and the original lattice structure (outside the holes) is clearly visible. The FI (Fig. 13) shows mainly EI (and to a smaller extent CI), which together lead to the lattice inversion. The rule of thumb for differentiating the conductor and PC on one side from the CDW and FI on the other side is precisely the presence of the lattice inversion. The absence of the charge transport is
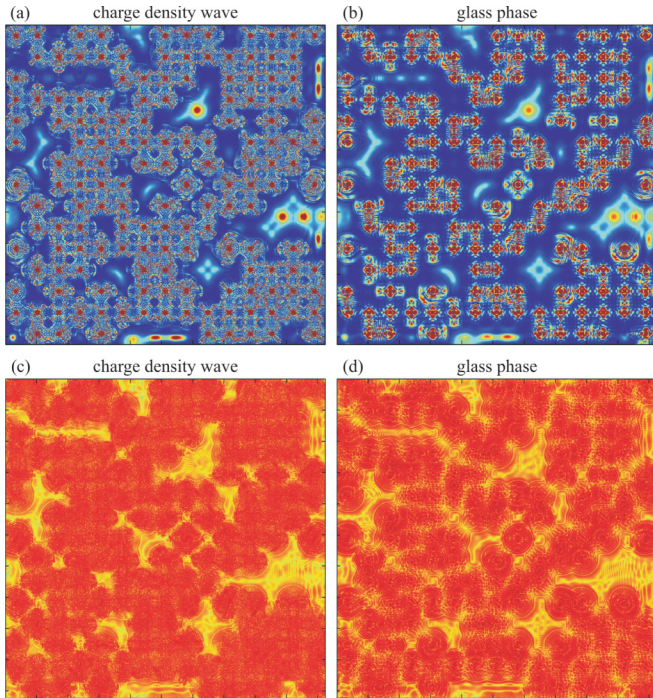
FIG. 14. Transverse profiles for the charge density wave [panels (a) and (c)] and the glass phase [panels (b) and (d)]: intensity maps (top) and vortex charge density maps (down). The telltale difference is that the CDW loses the regular lattice as the intensity "flows" between the regular and the defect regions and we see the DI at work. Glass, on the other hand, consists of domains with coherent (well-defined) vortices though with reduced symmetry (C_4) mostly due to EI. The charge density forms a connected network in the glass phase and transport is possible, whereas in a frustrated insulator the charge is stuck in isolated points.

best appreciated in the phase images: The charge pins to the defects and localizes toward the end of the crystal (i.e., for z near L). Only near the edges we see high vorticity, somewhat analogous to topological insulators, which only have nonzero conductivity along the edges of the system.

The CDW versus the glass phase is given in Fig. 14. The charge density wave [Figs. 14(a) and 14(c), $L = 240 \ \mu$m] exhibits the diffusion of intensity due to DI, and the vortex beams are in general asymmetric and not clearly delineated. In Figs. 14(b) and 14(d), where $L = 120 \ \mu$m with all other parameters the same, there is a clear border between defects and the regular parts of the lattice and the intensity is concentrated in the vortex cores. We give also the vortex charge density map in Figs. 14(c) and 14(d) in addition to the intensity maps in Figs. 14(a) and 14(b)] as the charge density shows why the CDW is insulating: Even though individual beams diffuse and smear out in *intensity*, the regions of nonzero vortex charge are disjoint and no global conduction can occur. Glass is divided into ordered domains in intensity but the vortex charges form a connected network which supports transport. This is analogous to the percolation transition in a disordered Ising model [56,57] and we may expect that the CDW-glass transition follows the same scaling laws near the critical point. However, we have not checked this explicitly and we leave it for further work.

V. THE CONDENSED MATTER ANALOGY: COLLINEAR DOPED HEISENBERG ANTIFERROMAGNET

The two-beam photorefractive system can serve as a good model for quantum magnetic systems. The most obvious connection is to multicomponent XY antiferromagnets (i.e., two-dimensional Heisenberg model): Planar spins are nothing but complex scalars, and the vortex Hamiltonian remains identical $(\pi_1[SO(2)] = \pi_1[U(1)] = \mathbb{Z})$. The nonlinearity in the spin system is different and usually much simpler, but that typically does not influence the phase diagram (the symmetry structure remains the same). Such connection is so obvious it does not require further explanations. Our point is that the CP beams in a PR crystal can also describe more general magnetic systems in the presence of topological solutions described by homotopy groups different from $\mathbb{Z}$. In particular, we want to point out to a connection with a two-sublattice antiferromagnetic system which has some time ago enjoyed considerable popularity as a possible description of magnetic ordering in numerous planar strongly coupled electron systems, including cuprate high-T_c superconductors [5,38,58]. This is the collinear doped antiferromagnet defined on two sublattices. When coupled to a charge density wave (speaking about the usual U(1) electromagnetic charge) and a superconducting order parameter, it becomes a toy model of cuprate materials (one variant is given in Ref. [58]). In the light of what we know today, the ability of this model to realistically describe the cuprate physics is quite questionable; but even so it is an interesting magnetic system on its own, and it was already found in Refs. [39,47] to exhibit a spin-glass phase, though in a slightly different variant (in particular, with spiral instead of collinear ordering).

Let us formulate the model. While the material is a lattice on the microscopic level, here we are talking about an effective field theory model. The order parameter is the staggered magnetization

$$M(\mathbf{r}) = \sum_{\alpha=1,2} \mathbf{M}_\alpha(\mathbf{r}) \cos(\mathbf{n} \cdot \mathbf{r}), \qquad (20)$$

where $\alpha \in \{1,2\}$ is the sublattice "flavor" index (analogous to the α index for the F and B beam in the previous sections)[7] and each component $\mathbf{M}_\alpha$ is a three-component spin, describing the internal, i.e., spin degree of freedom (we label the spin axes as X, Y, Z). The total spin is thus the sum of the spins of the two components, and $\mathbf{n}$ is the modulation vector. The modulation gives rows of alternating staggered magnetization in opposite directions as in Fig. 15(a). This stands in contrast with the spiral order, where the modulation vectors become $\mathbf{n}_\alpha$, i.e., differ for the two sublattices, and are themselves space dependent [39]. The ordered phase of the collinear system has the nonzero expectation value of the staggered magnetization along one direction, which can be chosen as the Z axis ("easy axis"), where the spin fluctuations about the easy axis remain massless, and the symmetry is broken from O(3) to O(3)/O(2). The spiral order, on the other hand, breaks the symmetry down to identity, as the order parameter is a dreibein [39].

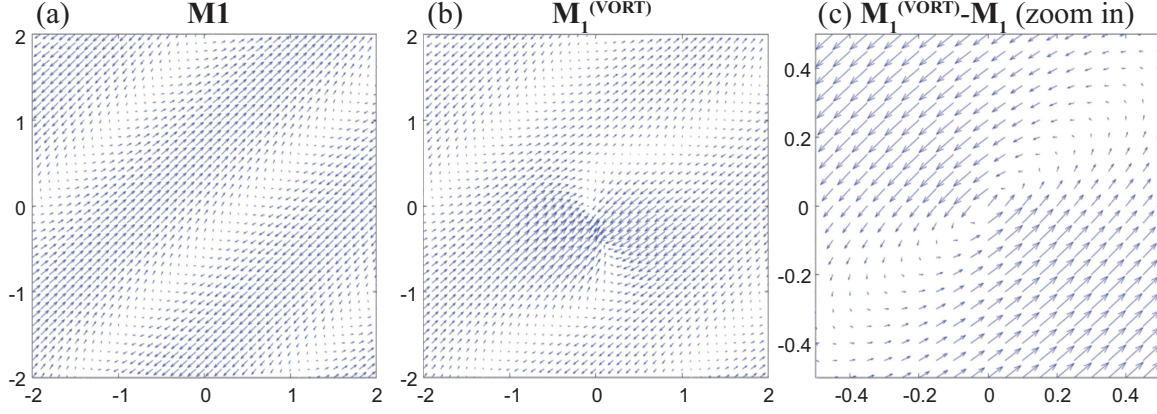[7]Sometimes we will denote the sublattices by $\pm$ instead of 1,2 for compactness of notation.

FIG. 15. Numerical realization of the spin pattern (staggered magnetization $\mathbf{M}_1$) in the collinear O(3) antiferromagnet. Magnetization is three dimensional and we give the projection in the XY plane, $\mathbf{M}_1 \cdot \mathbf{n}_{XY} \equiv M_\perp$. In panel (a), we show the characteristic collinear spin pattern in absence of vortices. In panel (b), we plot $\mathbf{M}_1^{(\text{vort})}$, a $\mathbb{Z}_2$-charged point vortex defect with $Q = 1$. In panel (c), we give an enlargement of the vortex from panel (b) shown as the difference $\mathbf{M}_1^{(\text{vort})} - \mathbf{M}_1$ to show more clearly the structure of the vortex—now the regular periodic pattern is absent and we appreciate the pointlike structure of the vortex. The parameters are $u = r = 1$ and $v = 0.5$.

The symmetry conditions (isotropy in absence of external magnetic field) determine the Hamiltonian up to fourth order, as discussed in Ref. [58]:

$$\mathcal{H}_{\text{af}} = \frac{1}{2g_M}\left[\left(\frac{1}{c_M}\partial_\tau \mathbf{M}_\alpha\right)^2 + |\nabla \mathbf{M}_\alpha|^2 + \frac{r}{2}|\mathbf{M}_\alpha|^2\right] + \frac{u_0}{2}|\mathbf{M}_\alpha|^4 - v_0(|\mathbf{M}_1|^2 + |\mathbf{M}_2|^2)^2. \quad (21)$$

The antiferromagnetic coupling is g_M, the spin stiffness is c_M, and the effective mass of spin wave excitations is r. The fourth-order coupling u_0 comes from the "soft" implementation of the constraint $|\mathbf{M}_\alpha| = 1$[8] and v_0 is the anisotropy between the two sublattices, justified by the microscopic physics [5,58]. The Hamiltonian can be transformed by rescaling τ and x, y, together with the couplings $u_0 \mapsto u$ and $v \mapsto v_0$ to set $g_M = c_M = 1$ so that the kinetic term becomes isotropic, giving

$$\mathcal{H}_{\text{af}} = \frac{1}{2}(\partial_\tau M)^2 + \frac{1}{2}|\nabla M|^2 + \frac{r}{2}|M|^2 + \frac{u}{2}(|M|^2)^2 - v|\mathbf{M}_1|^2|\mathbf{M}_2|^2, \quad (22)$$

where we have also rewritten the quartic terms for convenience. Without anisotropy, the energy of the system is a function of $|\mathbf{M}_1|^2 + |\mathbf{M}_2|^2$ only and the symmetry group is the full O(6). With $v \neq 0$, the symmetry is reduced to $O(3)_1 \otimes O(3)_2$: The internal spin symmetry in each sublattice remains unbroken but the spatial rotation symmetry between the layers is broken down to just the discrete flip. Compare this to the $U(1) \otimes U(1)$ symmetry in the PR system: There, it is the internal phase symmetry that remains unbroken.

---

[8]One could also enforce the constraint exactly, through the nonlinear σ model, as was done in Ref. [39]. While the leading term of the "vortex" Hamiltonian would remain the same in that case, the amplitude fluctuations have different dynamics which influences some terms of the Hamiltonian and thus its RG flow (though probably not the very existence of the glass phase).

A. $\mathbb{Z}_2$ vortices

Remember that topological solitons are classified by homotopy groups and that we work in a two-dimensional plane. The relevant group is again the first homotopy group, $\pi_1[O(3)] = \mathbb{Z}_2$. For simplicity, we will call these excitations "vortices," bearing in mind that the only possible charges are $Q_\alpha = \pm 1$ and not all integers. A realization of the vortex with $Q = 1$ is shown in Fig. 15(b). Since the spins are three-dimensional (the figure shows the projection in the XY plane), it becomes clear that vortex charge is only defined modulo 2; i.e., it makes no sense to talk about charges $|Q| > 1$. For example, winding around twice in the XY plane can be done along a closed line in the XYZ space which can be contracted to a point. That could not happen for the two-dimensional phase U(1) precisely because there is no extra dimension. In Fig. 15(b), the vortex is superimposed onto the regular configuration: It is recognizable as a contact point between two lines of alternating staggered magnetization. In Fig. 15(c) we have subtracted the regular part and only the vortexing spin pattern is shown: Here we see the vortex interpolates between two opposite spin orientations in two opposite directions in the plane.

Now let us derive the effective Hamiltonian of the vortices. For the $\mathbb{Z}_2$ vortex, a loop in real space is mapped onto a π arc in the internal space, so the vortex can be represented as

$$\mathbf{M}_\alpha(r, \phi) = \int d\phi' e^{\frac{i}{2}(\phi' - \phi)\hat{\ell}_3} \mathbf{m}_\alpha, \quad (23)$$

giving (the matrices $\ell_{1,2,3}$ represent the so(3) algebra)

$$\mathbf{M}_\alpha = \begin{pmatrix} \cos\phi & \mp\sin\phi & 0 \\ \pm\sin\phi & \cos\phi & 0 \\ 0 & 0 & 1 \end{pmatrix} \begin{pmatrix} m_{1\alpha} \\ m_{2\alpha} \\ m_{3\alpha} \end{pmatrix}, \quad (24)$$

where $\mathbf{m}_\alpha$ is the magnetization amplitude, analogous to the beam amplitude ψ_α in the optical system. The leading-order, noninteracting term in (22) gives the following for the energy of a single vortex of charge Q:

$$E_1 = 2\pi(|\mathbf{m}_X \times \mathbf{e}_Z|^2 + |\mathbf{m}_Y \times \mathbf{e}_Z|^2)\ln\Lambda = 2\pi|\mathbf{m}_{\perp\alpha}|^2 \ln\Lambda, \quad (25)$$

which is in fact independent of the sign of $\vec{Q}$ (as could be expected, as it is in general proportional to $\vec{Q} \cdot \vec{Q}$ which is a constant for parity vortices). The vortex singles out an easy axis (Z axis) around which the staggered magnetization winds (ϕ being the winding angle). This allows one to introduce $\mathbf{m}_{\alpha\perp} \equiv (m_{X\alpha}, m_{Y\alpha}, 0)$. A vortex pair with charges $\vec{Q}_i$ and $\vec{Q}_j$ has the binding energy

$$
\begin{aligned}
E_2 &= 2\pi \vec{Q}_i \cdot \vec{Q}_j (|\mathbf{m}_1 \times \mathbf{e}_Z|^2 + |\mathbf{m}_2 \times \mathbf{e}_Z|^2) \ln r_{ij} \\
&= 2\pi |\mathbf{m}_{\perp\alpha}|^2 \vec{Q}_i \cdot \vec{Q}_j \ln r_{ij}.
\end{aligned}
\tag{26}
$$

Now we should integrate out the amplitude fluctuations as we did in Appendix D for the CP beams. This again leads to the coupling between different flavors, giving a vortex Hamiltonian analogous to (7):

$$
\mathcal{H}_{\text{vort}} = \sum_{i<j} (g\vec{Q}_i \cdot \vec{Q}_j + g'\vec{Q}_i \times \vec{Q}_i) \ln r_{ij} + \sum_i \vec{\mu} \cdot \vec{Q}_i.
\tag{27}
$$

Two obvious differences with respect to the optical system are (i) the charges are now limited to the values ± 1, and (ii) there is a term linear in charge density, which acts as a chemical potential. The latter arises from the coupling of the *three-dimensional* spin waves (i.e., the topologically trivial excitations of the amplitude $\mathbf{m}_\alpha$) to the vortices. Remember that in the CP system, the amplitude fluctuations also couple to the vortices, but there is no third, Z axis of the order parameter so no linear term appears. The microscopic expressions for the effective parameters g, g', μ_α read

$$
g = m_\perp^2 + \frac{4r + 6um_\perp^2}{\left(2v + \frac{3}{2}um_\perp^2 + \frac{v}{2}m_\perp^2\right)\left(2r + \frac{3}{2}um_\perp^2 - \frac{v}{2}m_\perp^2\right)},
\tag{28}
$$

$$
g' = -\frac{4vm_\perp^2}{\left(2v + \frac{3}{2}um_\perp^2 + \frac{v}{2}m_\perp^2\right)\left(2r + \frac{3}{2}um_\perp^2 - \frac{v}{2}m_\perp^2\right)},
\tag{29}
$$

$$
\mu_\alpha = \frac{1}{2}m_\perp m_z,
\tag{30}
$$

assuming $m_{1\perp} = m_{2\perp} \equiv m_\perp$. Now the RG calculation is similar to the optical case but the nonzero chemical potential introduces two differences. First, there is obviously the additional term proportional to the total charge of the virtual pair of vortices, $\mu_\alpha(q_{1\alpha} + q_{2\alpha})$. Second, there is no charge conservation as the expectation value of the total vortex charge is now $\langle \vec{Q} \rangle = \partial \mathcal{F}/\partial\vec{\mu} \neq 0$. Thus we need to take into account not only the fluctuations with zero net charge (virtual vortex pairs with charges $\vec{q}_1 \equiv \vec{q}$ and $\vec{q}_2 \equiv -\vec{q}$) but also the situations with arbitrary pairs $\vec{q}_1, \vec{q}_2$.[9] This modifies the variation of the

---

[9]In the CP beam system, the total vortex charge can be nonzero if the boundary conditions at $z = 0, L$ have nonzero total vorticity. But there we had no *bulk* chemical potential so the total vorticity in the crystal could not change during the propagation along z. Here, we have a *bulk* term in the Hamiltonian which violates charge conservation.

partition function from (12) and (13) to

$$
\begin{aligned}
\frac{\delta \mathcal{Z}}{\mathcal{Z}} = 1 &+ \frac{y^4}{4}\sum_{\vec{q}_{1,2}}\int dr_{12}r_{12}^3 e^{-g\vec{q}_1\cdot\vec{q}_2 - g'\vec{q}_1\times\vec{q}_2 - \vec{\mu}\cdot\vec{q}'} \\
&\times \Bigg[\int dr r^2 (g\vec{Q}_1 \cdot \vec{q} + g'\vec{Q}_1 \times \vec{q})\nabla \ln |\delta\mathbf{R}_1| \\
&\quad + (g\vec{Q}_2 \cdot \vec{q} + g'\vec{Q}_2 \times \vec{q})\nabla \ln |\delta\mathbf{R}_2|\Bigg]^2 \\
&+ \frac{y^4}{4}\sum_{\vec{q}_{1,2}}\int dr_{12}r_{12}^3 e^{-g\vec{q}_1\cdot\vec{q}_2 - g'\vec{q}_1\times\vec{q}_2 - \vec{\mu}\cdot\vec{q}_1} \\
&\times \Bigg[\int dr r^2 (g\vec{Q}_1 \cdot \vec{q}_0 + g'\vec{Q}_1 \times \vec{q}_0)\ln |\delta\mathbf{R}_1| \\
&\quad + (g\vec{Q}_2 \cdot \vec{q}_0 + g'\vec{Q}_2 \times \vec{q}_0)\ln |\delta\mathbf{R}_2|\Bigg]^2,
\end{aligned}
$$

where we have introduced $2\vec{q} \equiv \vec{q}_1 - \vec{q}_2, \vec{q}_0 \equiv \vec{q}_1 + \vec{q}_2$ and $\delta\mathbf{R}_{1,2} \equiv \mathbf{R}_{1,2} - \mathbf{r}$. The mixed term which includes both $\vec{q}$ and $\vec{q}_0$ vanishes due to isotropy. By matching the terms in the resulting expression with the original Hamiltonian, we find the recursion relations:

$$
\frac{\partial g}{\partial \ell} = -16\pi y^4(g^2 + g'^2), \quad \frac{\partial g'}{\partial \ell} = -16\pi y^4 gg',
$$

$$
\frac{\partial \vec{\mu}}{\partial \ell} = 0, \quad \frac{\partial y}{\partial \ell} = (1 - g - g' - \mu_+ - \mu_-)y.
\tag{31}
$$

Crucially, the chemical potential does not run which could be guessed from dimensional analysis (it couples to dimensionless charge). This is the same system as (14) up to the trivial rescaling of the coupling constants and the shift of the critical line $g + g' = 1$ in the PR system to the line $g + g' + \mu_+ + \mu_- = 1$. It becomes obvious that the phase diagrams are equivalent and can be mapped onto each other.

B. Influence of disorder

The disorder in a doped antiferromagnet comes from electrically neutral metallic grains quenched in the bipartite lattice. Being metallic and neutral, they are naturally modeled as magnetic dipoles $\mathbf{X}$ quenched in the bipartite lattice. This picture stems from the microscopic considerations in Ref. [48]. We again assume the Gaussian distribution of the disorder as $p(X) \propto \exp(-|\mathbf{X}|^2/2\sigma_X^2)$. The disorder dipoles are one and the same for both sublattices, so $\mathbf{X}$ has no flavor (sublattice) index. The minimal coupling of the dipoles to the lattice spins $\partial_i \mapsto \partial_i - i\hat{\ell}_i X_i$ gives

$$
\mathcal{H}_{\text{af}} \mapsto \mathcal{H}_{\text{dis}} = \mathcal{H}_{\text{af}} + \nabla\mathbf{M}_\alpha \cdot (\mathbf{X} \times \mathbf{M}_\alpha) + M^2 X^2.
\tag{32}
$$

Now the replica calculation requires the multiplication of the M field into n copies and performing the Gaussian integral over the disorder. The initial distribution of the disorder $p(X)$ gives rise to two independent Gaussian distributions: for the couplings $J_{ij}^{\alpha\beta}$ with dispersion matrix $\sigma_{\alpha\beta}^2$ and for the chemical potential μ_i^α with the dispersion vector ξ_α^2. The resulting

Hamiltonian is

$$\mathcal{H}_{\text{dis}} = \sum_{\mu=0}^{n} \left(\frac{1}{2} \left| \partial_\tau \mathbf{M}_\alpha^{(\mu)} \right|^2 + \frac{1}{2} \left| \nabla \mathbf{M}_\alpha^{(\mu)} \right|^2 \right.$$
$$+ \frac{u}{2} \left| \mathbf{M}_\alpha^{(\mu)} \right|^2 - v \left| \mathbf{M}_1^{(\mu)} \right|^2 \left| \mathbf{M}_2^{(\mu)} \right|^2 \right)$$
$$+ \frac{\sigma^2}{4} \sum_{\mu,\nu=0}^{n} \left(\nabla \mathbf{M}_\alpha^{(\mu)} \times \mathbf{M}_\alpha^{(\mu)} \right) \cdot \left(\nabla \mathbf{M}_\alpha^{(\nu)} \times \mathbf{M}_\alpha^{(\nu)} \right), \quad (33)$$

where we have disregarded the subleading logarithmic term ($\sim \ln |\mathbf{M}_\alpha^{(\mu)}|$). Now making use of the representation (23) and plugging it in into (33) gives the disordered vortex Hamiltonian

$$\beta \mathcal{H}_{\text{vort}} = \sum_{\mu,\nu=1}^{n} \sum_{i,j=1}^{N} \left[\frac{\beta^2}{2} Q_{i\alpha}^{(\mu)} Q_{i\beta}^{(\nu)} Q_{j\alpha}^{(\mu)} Q_{j\beta}^{(\nu)} \right.$$
$$\left. - \beta Q_{i\alpha}^{(\mu)} J_0^{\alpha\beta} Q_{j\beta}^{(\mu)} + \beta^2 Q_{i\alpha}^{(\mu)} \xi^2 Q_{i\alpha}^{(\nu)} \right]$$
$$- \sum_{\mu=1}^{n} \sum_{i=1}^{N} \beta \xi^2 \mu_0^\alpha Q_{i\alpha}^{(\mu)}. \quad (34)$$

Of course, we could have arrived at the same effective action starting from the vortex Hamiltonian (27), taking the infinite-range approximation and identifying $J_{ij}^{\alpha\alpha} = g_{ij} \ln r_{ij}$ and similarly for other components of $J_{ij}^{\alpha\beta}$ as we demonstrated for the PR system. The final result has to be same at leading order.

The next step is to rewrite the Hamiltonian in terms of the order parameters $p_\alpha^{(\mu)}, q_{\alpha\beta}^{(\mu\nu)}$ defined in (19). Compared to the effective action for the photonic lattice with disorder in Eq. (G4), there are two extra terms in the resulting action S_{eff}: One is proportional to the dispersion ξ^2 and the other to the mean chemical potential $\vec{\mu}_0$. The former term just introduces the shift $J_0^{\alpha\beta} \mapsto J_0^{\alpha\beta} - \sigma^2/2\beta$ and the latter term, linear in the vortex charges and proportional to the chemical potential, introduces solutions with nonzero net vortex charge density. Looking back at the results of the saddle-point calculation in Eqs. (19) and (G14), this tells us that the relation between the phase diagrams is the following. The phases with no net vortex charge density—insulator, conductor, frustrated insulator, and perfect conductor—remain the same as in the PR system, since both the average coupling value $J_0^{\alpha\beta}$ (which gets shifted) and the term proportional to the chemical potential μ_α couple only to $\vec{p}^{(\mu)}$. For brevity, denote $J_0^{\pm\pm} \equiv J_0^{\pm}$ and notice that $J_0^{-+} = J_0^{+-}$. The structure of phases with nonzero $\vec{p}^{(\mu)}$ depends on the zeros of the saddle-point equation

$$J_0^\pm p^\pm + \left(\frac{J_0^{+-}}{\beta} - \frac{\beta}{2} \xi^\pm \right) p^\mp + (p^\pm)^{-1}$$
$$- \frac{\mu_0^\pm (\sigma^{\pm\pm})^2 + \mu_0^\mp \sigma_{+-}^2}{\beta} = 0, \quad (35)$$

analogous to (G13), where the one-step replica symmetry breaking implies $p_{(\mu)}^\pm = (p^\pm, \ldots, p^\pm)$. Now the equation is cubic and the structure of solutions is different from (G14). We could not find the solution in the closed form but it is clear that a pair of cubic equations will have either a

single solution (p^+, p^-) or nine combinations (p^+, p^-), not necessarily all different. Numerical analysis of (35) reveals only two inequivalent solutions, analogous to (G14), i.e., one of them has a single free energy minimum and the other one a pair of degenerate minima. Therefore, we again have two disordered solutions, one of which is glassy (frustrated).

Now we can write down also the RG equations for the effective action (34). In this calculation, we put $\xi_\alpha^2 = \sigma_{\alpha\beta}^2 \equiv \sigma^2$ for simplicity. Following the same logic as earlier, the equations are found to be[10]

$$\frac{\partial g}{\partial \ell} = -8\pi (g + g')^2 y^4 \cosh(2\beta^2 \sigma^2)$$
$$\times \cosh(2\beta^2 \sigma^2) - 8\pi (g - g')^2 y^4,$$
$$\frac{\partial g'}{\partial \ell} = -\pi (g + g')^2 y^4 \cosh(2\beta^2 \sigma^2)$$
$$\times \cosh(2\beta^2 \sigma^2) - \pi (g - g')^2 y^4,$$
$$\frac{\partial y}{\partial \ell} = 2\pi (1 - g - g' - \mu_+ - \mu_- - \beta^2 \sigma^2) y,$$
$$\frac{\partial \mu}{\partial \ell} = -8\pi \mu,$$
$$\frac{\partial \sigma^2}{\partial \ell} = -2\pi \beta^4 \sigma^4 y^4. \quad (36)$$

Like in the clean case, the chemical potential is irrelevant and the solutions for fixed point are the same as for the PR beams, including the spin-glass fixed point. We conclude that the phase structure of the optical system is repeated in strongly correlated doped antiferromagnets, which also exhibit the spin-glass phase and have the phase diagram sketched in Fig. 16. In this context, it is more interesting to plot the phase diagram in the $\sigma^2 - 1/g'$ plane, mimicking the $x - T$ phase diagram of quantum critical systems [38] (remember that the coupling constants g, g' behave roughly as inverse temperature in XY-like models). Bear in mind that all phases shown are about vortex dynamics; i.e., one should not compare Fig. 16 to the textbook phase diagram of high-temperature superconductors, which accounts also for the charge or stripe order and the superconducting order. All vortex phases would be located inside the pseudogap regime of the superconductor, where various exotic orders can coexist (assuming, of course, that our model is an adequate approximation of the magnetic order in a cuprate or similar material, which is a complex question). Crucially, the spin-glass phase (blue curves) flows toward *finite disorder* σ^2, whereas the remaining two phases end up at zero disorder, either at infinite $1/g'$ (PC, red flows) or at zero $1/g'$ (conductor, green flows). The RG flows in the conductor phase are almost invisible in the figure, as the flows are much slower than in the remaining two phases.

Discussion

Early papers which found and explored the spin-glass phase in a very similar model are Refs. [39,40,47,49]. The

---

[10] For the most general case of different and nonscalar $\sigma_{\alpha\beta}^2$ and ξ_α^2, the flow equations for them complicate significantly and we will not consider them.
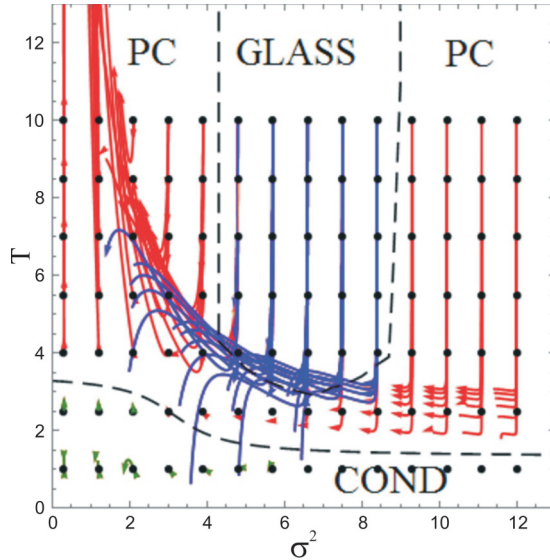
FIG. 16. The phase diagram of the two-sublattice-doped Heisenberg antiferromagnet model in the σ^2-T plane (we have rescaled $\sigma^2 \mapsto 12\sigma^2$). Since $T \sim 1/g'$, we can alternatively understand the vertical axis as $1/g'$. Black dashed curves are approximate phase boundaries. RG flows (starting from black dots) are colored differently according to the phase they belong to: spin glass (blue), PC (red), and conductor (green). At high temperatures, the vortex conductor becomes either a perfect vortex conductor or a spin glass. Spin glass (blue) is recognized by the fact that the RG equations flow to nonzero disorder at finite and large g' (low temperatures). The PC phase (red) flows toward zero disorder and zero coupling (infinite T), collapsing practically to a single trajectory. The flows for the conductor (green) end up at $T = \sigma^2 = 0$ but are not shown to scale in the figure. Parameter values are $u = r = 1$ with varying v so as to have $g = -0.5$ for all trajectories.

main difference is that the papers cited consider the spiral (noncollinear) spin order. These works are all inspired by the cuprate materials, the most celebrated brand of high-temperature superconductors. While Refs. [40,47] explore in detail the transport properties, we have no pretension either to provide a realistic model of cuprates or to explore in detail all the properties of the spin-glass phase. We are content to see that the PR system of $\mathbb{Z}$ vortices reproduces the phase structure of a certain kind of dirty Heisenberg antiferromagnets (with O(3) spins and $\mathbb{Z}_2$ vortices), besides the more obvious connection to systems which directly reproduce the $\mathbb{Z}$ vortices in multicomponent U(1) systems like multicomponent Bose-Einstein condensates and type-1.5 superconductors.

VI. CONCLUSIONS

We have investigated the light intensity patterns in a nonlinear optical system consisting of a pair of counterpropagating laser beams in a photorefractive crystal. We have studied this system as a strongly interacting field theory and have focused mostly on the formation and dynamics of vortices. The vortices show a remarkable collective behavior and their patterns are naturally classified in the framework of statistical field theory: The effective action shows several different

phases with appropriate order parameters, and the system is essentially an XY model with two flavors, i.e., two kinds of vortex charge, for the two beams. The interaction between the flavors is the central reason that the total energy of the Coulombic interactions between the vortices in general cannot be locally minimized at every point. In the presence of disorder, a phase with multiple free energy minima arises, where the absence of long-range order is complemented by the local islands of ordered vortex structure, and which resembles spin glasses.

The phase diagram is simple in terms of the effective parameters—vortex coupling constants—and quite complex when expressed in terms of the experimentally controllable quantities—the intensity of the laser beams, the intensity of the background photonic lattice, and the properties of the photorefractive crystal (the last is not controllable but can be estimated reasonably well [3]). The lesson is that the approach we adopt can save us from demanding numerical work if the space of original parameters is blindly explored. Our phase diagrams can serve as a starting point for guided numerical simulations, suggesting what phenomena one should specifically look for. So far the field-theoretical and statistical approach was not much used in nonlinear optics (important exceptions are Refs. [9–12,14,15,50,51,59,60]). We hope to stimulate work in this direction, which is promising also because of the potential of the photorefractive systems to serve as models of strongly correlated condensed matter systems. They make an excellent testing ground for various models because of the availability and relatively low cost of experiments.

In this work, we have focused on the relation of the photorefractive counterpropagating system to the model of an O(3) doped antiferromagnet with two sublattices. The authors of previous works on this model [40,47,48,58] were motivated mainly by the ubiquitous problem of understanding the pseudogap phase in cuprate superconductors. The applicability of the model to this particular problem is still an open question; it may well be that cuprate physics goes far beyond. Nevertheless, it is an important quantum magnetic system in its own right and serves as an illustration of how one can simulate condensed matter systems in photorefractive optics.

Another field where vortices are found as solutions of a nonlinear Schrödinger equation are cold atom systems and Bose-Einstein condensates [26]. Notice, however, that Bose-Einstein condensates in optical traps are usually (but not always; see Ref. [30]) three-dimensional systems with vortex lines (rather than XY-type systems with point vortices) and our formalism would be more complicated there: In three spatial dimensions, vortices give rise to emergent gauge fields. The multicomponent systems of this kind give rise to so-called type-1.5 superconductors [53], which are a natural goal of further study.

A more complete characterization of the glasslike phase is also left for further work. The reader will notice we have devoted very little attention to the correlation functions in various parameter regimes or the scaling properties of susceptibility, which should further corroborate the glassy character of the system. This is quite difficult in general but very exciting as it offers an opportunity to tune the parameters (e.g., disorder strength) freely in the optical system and study the glasslike phase and its dynamics.

APPENDIX A: NUMERICAL ALGORITHM

In order to solve numerically the system [(1) and (2)], we employ a variation on the method of Refs. [61,62]. The method does not make use of any analytical ansatz: It is an *ab initio* numerical procedure which integrates the equations of motion. The system has four independent variables: the transverse coordinates (x, y), the longitudinal coordinate (formal time) z, and the (physical) time t. That means we have essentially three nested loops: (i) At every z slice we integrate the transverse Laplacian and the interaction terms for the whole z axis, (ii) we advance the time t, and (iii) we repeat the whole procedure until reaching some time t_f, which certainly should be much longer than the relaxation time τ.

The important point is the very different natures of the initial and boundary conditions for various coordinates. The boundary conditions in the (x, y) plane, i.e., at the crystal edge are not crucial: We have either just one or a few Gaussian beams whose intensity drops exponentially away from the center and is practically zero at the crystal edge, or we have a large lattice consisting of many (of the order of 50–100) Gaussian beams so the edge effects only affect a small portion of the whole lattice. Therefore, imposing periodic boundary conditions (stemming naturally from the integration in Fourier space, see the next paragraph) are perfectly satisfying. Crucially, however, the CP geometry means that $F(t; z = 0; x, y) = F_0(x, y)$ and $B(t; z = L; x, y) = B_0(x, y)$ are given functions, fixed for all times. We thus have a two-point boundary value problem along z and have to iterate the z integration several times until we reach the right solution. Finally, the initial condition for the relaxation equation (2) is that the crystal is initially at equilibrium, meaning that $E(t = 0) = -I_x/(1 + I_x)$; specifically, for zero background lattice, $E(t = 0) = 0$.

The algorithm now has the following structure:

(1) The innermost loop integrates in the x-y plane. This is a Poison-type (elliptic) equation, thus we employ the operator-split method, integrating the Laplacian operator in the Fourier space and the interaction term (the EF and EB terms) in real space, in the second-order leapfrog scheme. Thus, at every time instant $t_i = i \Delta t$, we start from $z = 0$ where we set the condition $F(i \Delta t; z = 0; x, y) = F_0(x, y)$, divide the z axis into N steps of size $\Delta z = L/N$, and at every slice $z = j \Delta z$ perform the frog's leap: We do the fast Fourier transform (FFT) to turn the (x, y) dependence into (q_x, q_y) dependence,[11] then we advance the Laplacian for $\Delta z/2$ as $F(i \Delta t; j \Delta z; \mathbf{q}) \equiv \tilde{F}_{i,j}^{(0)} \mapsto \tilde{F}_{i,j}^{(1)} = \exp(-iq^2 \Delta z/2) \tilde{F}_{i,j}^{(0)}$, and then we do the inverse FFT and advance the interaction in real space as

---

$F_{i,j}^{(2)} = \exp[i \Gamma E(i \Delta t; j \Delta z; x, y)] F_{i,j}^{(1)}$. Finally we do the FFT again and advance the Laplacian for the remaining half-step, $\tilde{F}_{i,j+1} = \exp(-iq^2 \Delta z/2) \tilde{F}_{i,j}^{(2)}$. Once we reach $j = N$, the integration goes backward, along the same lines, updating now the B field [starting from $B_0(x, y)$], where all signs in the exponents of the above formulas are to be reversed. When we reach $z = 0$ again, we are done. In this loop, we use the field $E_{1,j}$ as already known for all j.

(2) The above loop will, in general, produce results inconsistent with the charge field $E_{i,j}$ because the equation for E couples F and B and we have ignored that by integrating the two fields one after the other instead of simultaneously. This is, of course, commonplace in two-point boundary value problems: Either only one boundary condition can be imposed exactly and the other is shot for or, as in our case, both are imposed exactly but at the cost of the solution being inconsistent with the equations, so we have to iterate the system to arrive at the correct solution everywhere. The second loop thus iterates the first loop A times, at each step updating the charge field as $E_{i,j}^{(a-1)} \mapsto E_{i,j}^{(a)} = E_{i-1,j} - \tau[E_{i,j}^{(a-1)} + I_{i,j}^{(a-1)}/(1 + I_{i,j}^{(a-1)})]/(1 + I_{i,j}^{(a-1)})$. The number of iterations A is not fixed: We stop iterations when the intensity pattern stabilizes, $\sum_j \sum_{x,y} (I_{i,j}^{(a)} - I_{i,j}^{(a-1)}) < \epsilon$, for some tolerance ϵ. Here, $I_{i,j}$ refers to total intensity, i.e., $|F|^2 + |B|^2 + I_x$.

(3) Finally, the outermost loop integrates in time t, from $t = 0$, with the initial condition $E(t = 0) = -I_x/(1 + I_x)$ given above. The integration time t_f is divided into $M = t_f/\Delta t$ intervals, and at the end of each step we update $(F_{i,j}, B_{i,j}, E_{i,j}) \mapsto (F_{i+1,j}, B_{i+1,j}, E_{i+1,j})$. Only the charge field is directly integrated (as written above), in the first-order, Euler scheme. The beam envelopes depend on time only parametrically, through $E(t)$, and they evolve by using an updated $E_{i,j}$ in the first two loops at every time step.

This procedure is very close to that in Ref. [61]; the main difference is that we use a second-order (leapfrog) scheme, while on the other hand our time integration is of the lowest, linear order instead of second order as in Ref. [61].

APPENDIX B: TIME-DEPENDENT PERTURBATION THEORY AND THE EXISTENCE OF EQUILIBRIUM CONFIGURATIONS

1. Stability analysis: fixed points and limit cycles

In this appendix, we consider the time evolution of the CP beams and show the existence of a stable equilibrium point with nonzero intensity. This means that the system reaches a stationary state for long times, justifying the basic assumption of the paper that one can study the vortex configurations within equilibrium statistical mechanics. Not all patterns are stable: Depending on the boundary conditions and parameter values, the system may or may not have a stable equilibrium, and nonequilibrium solutions in photorefractive optics are well known [37,50]. For our purposes, however, it is enough to identify the region of parameter space where the equilibrium exists; other cases are not the topic of this paper.

The time evolution of the beams Ψ_α and the charge field E in (k, q) space is obtained by differentiating Eqs. (1) with respect to time and plugging in $\partial E/\partial t$ from the relaxation

equation (2):

$$\frac{\partial \Psi_\alpha^\pm}{\partial t} = -\frac{\Gamma}{\tau} \frac{[(1+I)E+I]}{\alpha k - q^2 - \Gamma E} \Psi_\alpha^\pm,$$

$$\frac{\partial E}{\partial t} = -\frac{1}{\tau}[(1+I)E+I].$$

(B1)

This system has three equilibrium points. One is the 0 point,

$$(\Psi_+^\pm, \Psi_-^\pm, E) = \left(0, 0, -\frac{I_x}{1+I_x}\right),$$

and the remaining two are related by a discrete symmetry $\Psi_\pm \mapsto \Psi_\mp$, so we denote them as "$\pm$" points, with the "$+$" point being

$$(\Psi_+^\pm, \Psi_-^\pm, E) = \left(\sqrt{\frac{E(1+I_x)+I_x}{1+E}} e^{i\phi_+}, 0, E\right),$$

and the "$-$" point has instead $\Psi_+ = 0$ and $\Psi_- = \sqrt{(E(1+I_x)+I_x)/(1+E)} \exp(i\phi_-)$. Notice that the phase $\phi_\pm$ remains free to vary, so this solution supports vortices. The 0 point is the trivial vacuum, i.e., the zero-intensity configuration with only background lattice. The fluctuation equations about this point to quadratic order read

$$\partial_t X = -\Big[-f_+ X_1 X_5, -f_+ X_2 X_5, -f_- X_3 X_5, -f_- X_4 X_5,$$

$$-\frac{1}{1+I_x}\big(X_1^2 + X_2^2 + X_3^2 + X_4^2\big) - (1+I_x)X_5 \Big],$$

(B2)

where we have introduced the real variables $X_{1,3} = \mathrm{Re}\delta\Psi_\pm, X_{2,4} = \mathrm{Im}\delta\Psi_\pm, X_5 = \delta E$ and

$$f_\pm = \frac{\Gamma(1+I_x)^2}{\Gamma I_x \mp (1+I_x)(k \pm q^2)}.$$

(B3)

The system (B2) is degenerate at linear order; thus, we need a quadratic order expansion to analyze stability. The simplest approach is to construct a Lyapunov function for Eq. (B2). The function $V(X) = X^2$ is positive for and only for $X \neq 0$, and its derivative is

$$\frac{dV}{dt} = -2f_+\big(X_1^2 + X_2^2\big)X_5 - 2f_-\big(X_3^2 + X_4^2\big)X_5$$

$$-\frac{1}{1+I_x}\big(X_1^2 + X_2^2 + X_3^2 + X_4^2\big)X_5 - (1+I_5)X_5^2,$$

(B4)

which is strictly negative for X nonzero if $f_\pm > 0$ and $X_5 > 0$. However, we always have $X_5 > 0$ because dX_5/dt in the full relaxation equations (B1) has a strictly negative right-hand side and E grows monotonically from zero to $-I_x/(1+I_x)$, and at any finite t we have $E(t) - E(t=\infty) = X_5 > 0$. Thus the trivial equilibrium point is *locally* stable for $f_+ > 0, f_- > 0$, i.e., $k > q^2$. It is much harder to construct the Lyapunov function for the global equations (B1): In this case, there are no additional symmetries and the stability of higher dimensional systems is in general an extremely difficult topic. Thus there may well be regions far away from the 0 point which do not flow toward it.

The "$\pm$" pair is quite hard to study. All hope of expanding the system to second order and understanding the resulting complicated five-variable system is lost. This time, however, we can do a nontrivial first-order analysis as the system is nondegenerate and nicely reduces to the (X_1, X_5) subsystem. Rescaling $X_1 \mapsto (1+E_0)^{-3/4}[I_x + E_0(1+I_x)]^{1/2}$ and $t \mapsto t\{(1+E_0)/[I_x + E_0(1+I_x)]\}^{1/4}$, the equation of motion for the $\pm$ point reads

$$\partial_t \begin{pmatrix} X_1 \\ X_5 \end{pmatrix} = \begin{pmatrix} -\frac{a_\pm}{\Gamma E_0 + k + q^2} & -1 \\ 1 & -\frac{a_\pm}{\Gamma E_0 + k + q^2} \end{pmatrix} \begin{pmatrix} X_1 \\ X_5 \end{pmatrix}$$

$$+ O\big(X_1^2 + X_5^2; X_2, X_3, X_4\big),$$

(B5)

with $a_\pm$ being some (known) *positive* functions of Γ, E_0, I_x (independent of k, q). This is precisely the normal form for the Andronov-Hopf bifurcation [63], and the bifurcation point lies at $k = -\Gamma E_0 - q^2$. As a reminder, the bifurcation happens when the off-diagonal element in the linear term changes sign: The fixed point is stable when $a_\pm/(\Gamma E_0 + k + q^2)$ is positive. The sign of the nonlinear term determines the supercritical or subcritical nature of the bifurcation. A negative sign means the fixed point is stable everywhere before the bifurcation and is replaced by a stable limit cycle after the bifurcation (supercritical). A positive sign means the fixed point coexists with the stable limit cycle before the bifurcation and the (X_1, X_5) plane is divided among their attraction regions; after the bifurcation there is no stable solution at all (subcritical).[12]

In conclusion, stable $+$ equilibrium exists for $k > -\Gamma E_0 - q^2$ where E_0 is best found numerically. Exactly the same condition holds for the $-$ point. For $k < -\Gamma E_0 + q^2$, dynamics depends on the sign of the nonlinear term in (B5): For the positive sign, we expect periodically changing patterns. If the term is negative and the bifurcation is subcritical, various possibilities arise: The system may wander chaotically between the $+$ and the $-$ point, or it may end up in the attraction region of the 0 point and fall onto the trivial solution with zero intensity. Naively, the attraction regions of the two fixed points ($\pm$ and 0) are separated by the condition $-\Gamma E_0 - q^2 = q^2$, i.e., $q_c = \sqrt{-\Gamma E_0(\Gamma, \tau)/2}$, where we have emphasized that E_0 is in general nonuniversal. The actual boundary may be more complex, however, as our analysis is based on finite-order expansion around the fixed points, which is not valid far away from them.

The outcome is that the system generically has stable trivial and nontrivial (nonzero intensity) equilibria, in addition to time-dependent, periodic, or aperiodic solutions. Numerical integration gives a similar picture of the stability diagram in Fig. 17. Numerically we find that the stability limit is $k > \Gamma - q^2$, i.e., $E_0 \approx -1$. The region of applicability of our formalism lies in the top right corner of the diagram (nontrivial equilibrium), above $k \approx 1/L$. Formally, both k and q can be any real numbers. In practice, however, k is discrete and its minimal value is of the order $1/L$. The spatial momentum q

---

[12]One should not take the stability in the whole (X_1, X_5) plane in the supercritical case too seriously. We have expand the equations of motion in the vicinity of the fixed points and the expansion ceases to be valid far away from the origin.
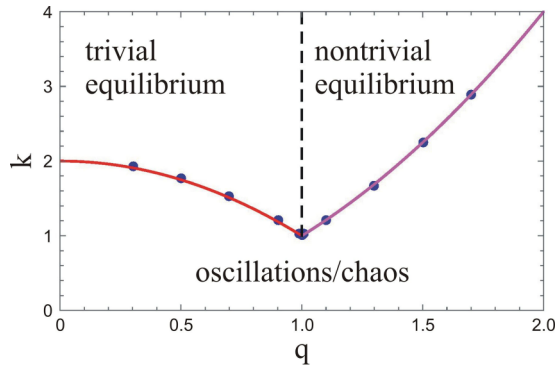
FIG. 17. Stability diagram in the q-k plane. The onset of instability for $k < k_c(q)$ is found numerically for a range of q values. The solid lines are the analytical prediction for the stability of the 0 point ($k_c = q^2$, magenta) and of the $+$ point ($k_c = \Gamma E_0 - q^2 \approx \Gamma - q^2$, red). The black dashed line at $q = q_c \approx 1$ separates the stability regions of the two points. The domain of applicability of our main results is the top left corner (nontrivial equilibrium), above $k > k_{\min} \sim 1/L$ and for not very large q values. Parameter values: $\Gamma = 2, I_x = 0$.

lies between the inverse of the transverse length of the crystal (which is typically an order of magnitude smaller than L, i.e., minimal q can be assumed equal to zero) and some typical small-scale cutoff which in our case is the vortex core size. We made no attempt to study the nonequilibrium behavior in detail or to delineate the boundary between the oscillatory and the chaotic regime since it is irrelevant for the main story of the paper.

From a practical viewpoint, the Γ-I_x plane can be divided into two regions. One of them has a single stable "$+$" or "$-$" equilibrium *or* a $+ \mapsto -$ limit cycle whose amplitude vanishes in the thermodynamic limit at all scales, i.e., for all $(k, \mathbf{q})$. This region can be legitimately described within the formalism of partition functions and equilibrium field theory. The second region flows toward the trivial fixed point and does not support vortices—this can also (trivially) be described by our formalism, as it always corresponds to the insulator regime, with no stable vortices. Thus the consistency check is that our method predicts no other phases in this region but insulator. In the third regime, long-term dynamics is either a limit cycle with amplitude of order unity or chaos. This regime was studied in detail in some earlier publications (e.g., Ref. [3] and references therein), and it cannot be reached within our present formalism.

2. Numerical checks

Now we complement the analytical considerations with numerical evidence that the phases described in the main text exist as long-term stable configurations. In Fig. 18, we show the time evolution of a vortex lattice in three different phases, where a visual inspection clearly suggests the system approaches equilibrium. In contrast, in Fig. 19 we see first a pattern that oscillates forever, i.e., follows a limit cycle [Fig. 19(a)], becomes incoherent [wandering chaotically over the unstable manifold, Fig. 19(b)], or dissipates away (reaching the 0-fixed point), in Fig. 19(c). The loss of stability corresponds to an Andronov-Hopf bifurcation, as found earlier for nonvortex patterns in Ref. [32].
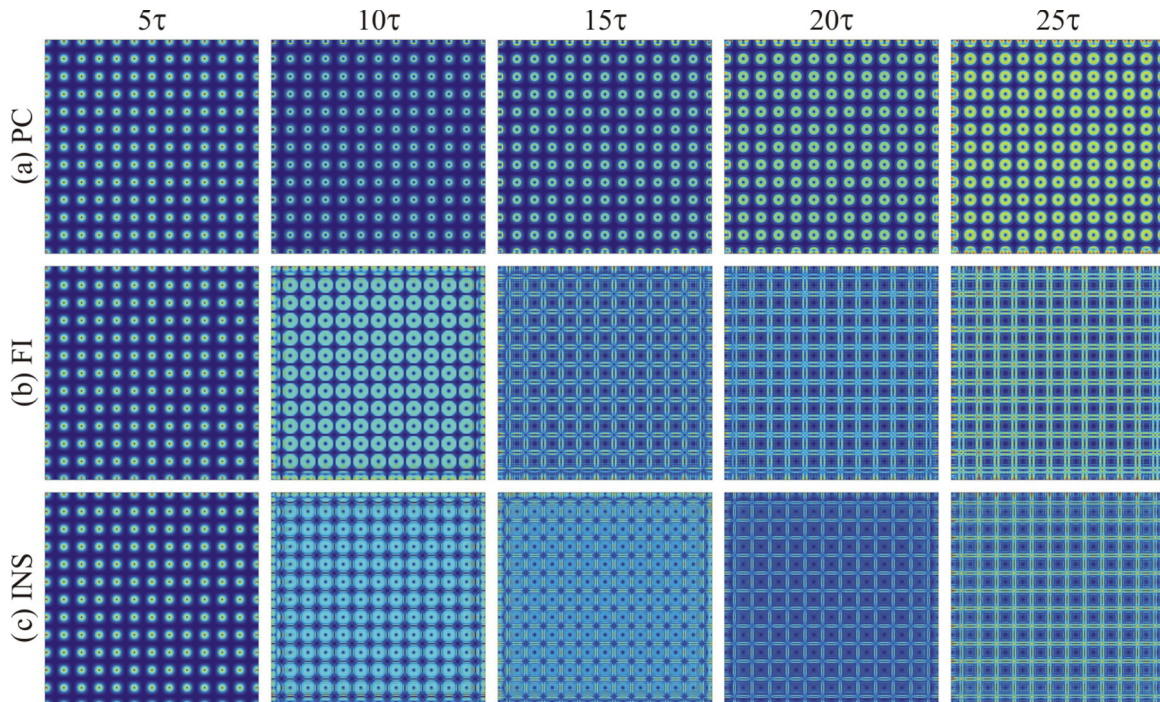

FIG. 18. Time evolution of patterns at five different times: (a) perfect conductor phase, (b) frustrated insulator phase, and (c) insulator phase. In all cases, the approach to equilibrium is obvious, and we expect that for long times a thermodynamic description is justified. The parameters are the same as in Fig. 6, for the corresponding phases.
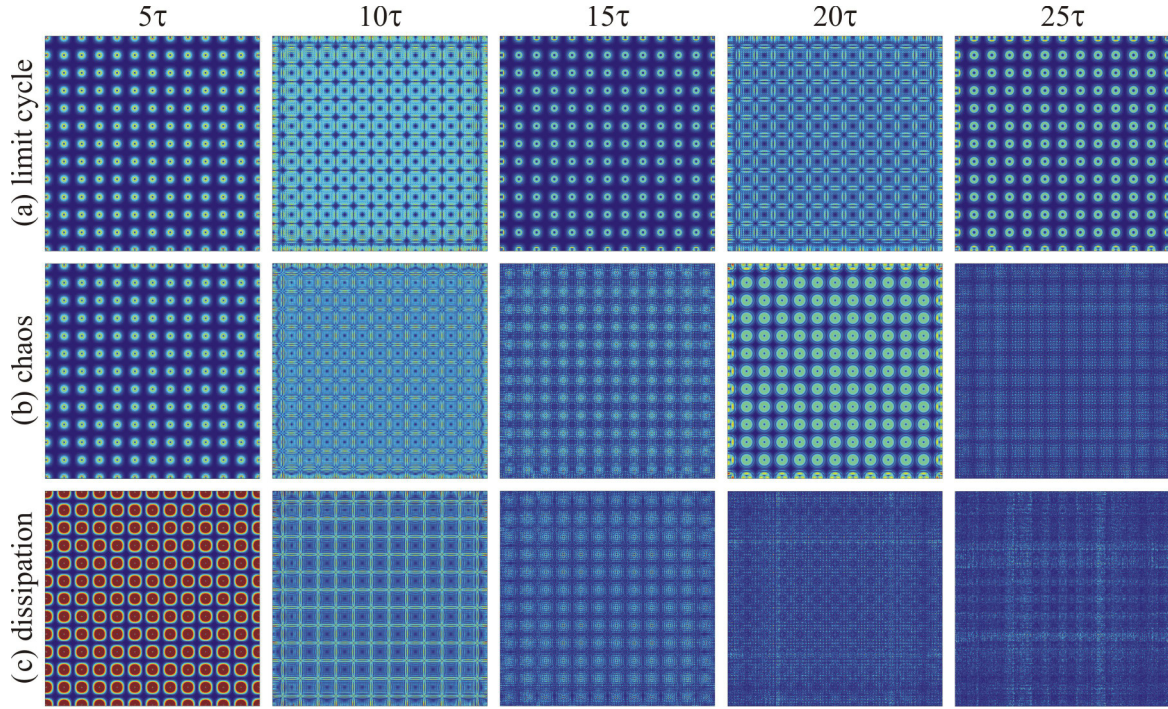
FIG. 19. Time evolution of nonequilibrium patterns. In panel (a), the limit cycle leads to permanent oscillatory behavior, in panel (b) wandering along the unstable manifold between the equilibrium points gives rise to chaos, and in panel (c) dissipation wins and dynamics dies out. The parameters are the same as in the previous figure, except that the length L is increased three times.

Dynamics can be most easily traced by looking at the numerically computed relaxation rate

$$\frac{1}{X}\frac{dX}{dt} = \frac{\sum_{x,y}|X(t_{j+1}x,y) - X(t_j;x,y)|^2}{\sum_{x,y}|X(t_j;x,y)|^2}, \quad \text{(B6)}$$
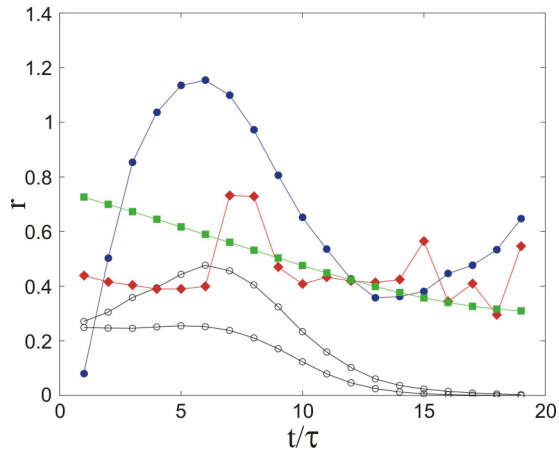
FIG. 20. Time evolution of the relaxation rate r for the various situations from Figs. 18 and 19, illustrating the relaxation to nontrivial (non-zero-intensity) equilibrium, i.e., "$\pm$"-fixed points [Figs. 18(a), 18(c), hollow black circles], limit cycle [Fig. 19(a), full blue circles], chaos [Fig. 19(b), full red romboids], and the relaxation to trivial (zero-intensity) equilibrium, i.e., 0 fixed point [Fig. 19(c), full green squares]. In the main text, we study the cases like the black curves, where time-independent stable configurations are seen. The symbols are data points from numerics and the lines are just to guide the eye.

which is expected to reach zero for a generical relaxation process, where in the vicinity of an asymptotically stable fixed point $X \sim X_{eq} + xe^{-rt}$ will be generically nonzero for a limit cycle or chaos and will asymptote to a constant for the 0 point, where $X_{eq} = 0$, so we get $(1/X)dX/dt \sim r$. Figure 20 summarizes these possibilities. The black curves, corresponding to Figs. 18(a) and 18(c), show the situation which is in the focus of this work—the approach toward static equilibrium. The blue curve shows the limit cycle leading to periodic oscillations. The green curve corresponds to the chaotic regime with aperiodic dynamics and no relaxation, as in Fig. 19(b). Finally, the red curve corresponding to the pattern which radiates away in Fig. 19(b) reaches a constant value of r. In conclusion, the system shows roughly four classes of dynamics: fixed point, limit cycle, chaos, and incoherence. Our work only covers the first of the four, but the bifurcation diagrams in the previous subsection give a good hint of the part of the parameter space which contains them, facilitating experimental or numerical verification.

APPENDIX C: PERTURBATION THEORY AND STABILITY ANALYSIS

In this appendix, we develop the perturbation theory of the photorefractive beam system starting from the Lagrangian (4). The perturbation theory yields the criterion for the stability of the intensity patterns as they propagate along the z axis. Formally, it is just the perturbative diagrammatic calculation of the propagator. This calculation explicitly excludes topologically nontrivial patterns and thus is somewhat peripheral for our main goal, understanding the vortex dynamics. But the general ways by which an envelope $\Psi_\pm$ can evolve along the z axis and

become unstable remain valid also for vortices. In particular, we will end up with a classification of geometrical symmetries of the intensity pattern $\Psi^{\dagger}\Psi$; the same symmetries are seen in vortex patterns and are an important guide for numerical and experimental work—how to recognize instabilities and also phases of the system.

Our system is strongly nonlinear, thus a naive perturbation theory about the trivial vacuum, i.e., constant beam intensity is out of question. The right way is to perturb about a nontrivial solution, which approximates a stable pattern. This means we treat the light intensity as constant in time z but nonconstant in space (x, y). This is the hallmark of spatial dynamical solitons: They propagate with a constant profile along the z axis and to a good approximation do not interact with each other and do not radiate [3]. We thus write $\Psi = \Psi_0 + \delta\Psi$, giving $\Psi^{\dagger}\Psi = I_0 + F_0(\delta\Psi_{+}^{\dagger} + \delta\Psi_{+}) + B_0(\delta\Psi_{-}^{\dagger} + \delta\Psi_{-}) + \delta\Psi^{\dagger}\delta\Psi + O(|\delta\Psi|^2)$ with $F_0^2 + B_0^2 = I_0$. The lowest-order Lagrangian for Ψ_0 now reads

$$\mathcal{L}_0 = \Psi_0^{\dagger}\Delta\Psi_0 + \Gamma I_0 - \Gamma(1 + \tau u + \tau E_0)$$
$$\times \ln(1 + \tau u + I_x + I_0), \qquad (C1)$$

which determines the shape of the solution $\Psi_0(x, y)$ in the first approximation. The dynamical term with $\partial_z\Psi$ drops out (it is proportional to the equation of motion for Ψ). Nontrivial propagation in time z is obtained from second-order expansion of the potential which is given in the next appendix in Eq. (D1) and we will not copy it here. Varying the quadratic expansion with respect to the fluctuation $\delta\Psi$ gives the linearized equation of motion for $\delta\Psi$:

$$[\pm i\sigma_3\partial_z - q^2 + \Gamma - (1 + \tau u + \tau E_0)]\delta\Psi^{\mp}$$
$$\mp \Gamma\frac{1 + \tau u + \tau E_0}{(1 + \tau u + I_x + I_0)^2}\delta\Psi^{\pm} = 0, \qquad (C2)$$

where $\delta\Psi^{+} \equiv \delta\Psi^{\dagger}, \delta\Psi^{-} \equiv \delta\Psi$. In homogenous spacetime (z, x, y), we can transform to momentum space in both transverse and longitudinal directions. In the transverse plane, we get $(x, y) \mapsto (q_x, q_y)$ and $\Delta \mapsto -q^2$. The longitudinal coordinate or time z transforms as $z \mapsto k_n$ where $k_n = \pi n/L$, so the time maps to discrete frequencies. The reason is, of course, that its domain is finite, corresponding to the crystal length L.

Now we can derive the bare propagator (Green's function) of the fluctuating dynamical field $\delta\Psi$ by inserting the appropriate source $S(z)$ on the right-hand side of Eq. (C2). Normally, the source in the equation for the Green's function is just the Dirac δ function but the counterpropagating nature of our beams imposes a two-sided source:

$$S(z) = \begin{pmatrix} \delta(z) & 0 \\ 0 & \delta(z - L) \end{pmatrix}. \qquad (C3)$$

With this source (also Fourier-transformed in z), Eq. (C2) gives the bare propagator $G_{\alpha\beta}^{(0)}$ for the fields $\delta\Psi_{\alpha\beta}^{\pm}$:

$$G_{\alpha\beta}^{(0)}(k_n, q) = [-ik_n S_{\alpha\gamma}(k_n) + A_{\alpha\delta}^* S_{\delta\gamma}(k_n) - B_{\alpha\delta}S_{\delta\gamma}(k_n)]$$
$$\times [-k_n^2 + A_{\gamma\delta}^* A_{\delta\beta} - B_{\gamma\delta}B_{\delta\beta}^* + [A^*, B]_{\gamma\beta}]^{-1}. \qquad (C4)$$

The auxiliary matrices A, B are defined as follows:

$$A_{\alpha\beta} = i\begin{pmatrix} P_0 + P_1 - q^2 & P_0 \\ -P_0 & -P_0 - P_1 + q^2 \end{pmatrix},$$
$$B_{\alpha\beta} = i\begin{pmatrix} P_0 & P_0 \\ -P_0 & -P_0 \end{pmatrix}, \qquad (C5)$$

where $P_1 = (1/4)I_0\Gamma(1 + \tau u + \tau E_0)/(1 + \tau u + I_x + I_0)^2$, $P_0 = \Gamma - \Gamma(1 + \tau u + \tau E_0)/(1 + \tau u + I_x + I_0)$, and $S(k_n) = \text{diag}(1, e^{ik_n L})$.

Now we have the basic ingredient of the perturbation theory: the bare propagator. The self-energy correction Σ of the propagator from the potential V_{eff} can be expanded in a power series over $\delta\Psi$, which gives an infinite tower of vertices. Simple combinatorial considerations give the expansion

$$\Sigma = \sum_{j_1, j_2, j_3 \in \mathbb{N}} \frac{(-1)^{j_1 + j_2 + j_3}(j_1 + j_2 + j_3 - 1)!}{j_1! j_2! j_3!}$$
$$\times \frac{\Gamma(1 + \tau u + \tau E_0)}{(1 + \tau u + I_0 + I_x)^{j_1 + j_2 + j_3 + 1}}(\Psi_0^{\dagger}\delta\Psi)^{j_1}$$
$$\times (\Psi_0\delta\Psi^{\dagger})^{j_2}(\delta\Psi_{\dagger}\delta\Psi)^{j_3}, \qquad (C6)$$

and the contraction over the internal indices of $\Psi^{\pm}, \delta\Psi^{\pm}$ is understood. Now we can formulate the diagrammatic rules. We have two kinds of propagators, $G^{(0)}$ and its Hermitian conjugate. The mean-field values $\Psi_0^{\pm}$ are external sources. The term of order (j_1, j_2, j_3) contains $j_1 + j_3$ propagator lines $G^{(0)}$ (j_1 of them ending with the source Ψ_0) and $j_2 + j_3$ lines $(G^{(0)})^{\dagger}$ (j_2 of them ending with a source $\Psi_0^{\dagger}$); altogether, there are $j \equiv j_1 + j_2 + 2j_3$ lines. The expansion has to be truncated at some j. Since the mass dimension of Ψ is 1, the (j_1, j_2, j_3) diagram has the scaling dimension $2 - 2(j_1 + j_2 + 2j_3) < 0$, so *all* diagrams are irrelevant in the IR. This means we can make a truncation at small j.[13] The leading terms are those where the order of the perturbation in $\delta\Psi^{\pm}$, which equals $j_1 + j_2 + 2j_3$, is the smallest. This gives two classes of diagrams, one with $j_1 = 1, j_2 = j_3 = 0$ and another with $j_2 = 0, j_1 = j_3 = 0$. They contain a single external source and introduce the wave-function renormalization, $G^{(0)} \mapsto ZG^{(0)}$, which does not influence the stability analysis. The four quadratic terms [with $(j_1, j_2, j_3) = (2, 0, 0), (0, 2, 0), (1, 1, 0), (0, 0, 1)$] introduce a mass operator. Only the terms $(1, 1, 0)$ and $(0, 0, 2)$ are trivial (noninteracting); the other two are interacting as they contain $(\delta\Psi^{\pm})^2$ and require the calculation of an internal loop, giving the dressed propagator

$$G_{\alpha\beta}^{-1}(k_n, q) = [G^{(0)}(k_n, q)]_{\alpha\beta}^{-1} + (m^2)_{\alpha\beta}, \qquad (C7)$$

where the mass squared is a *positive* matrix, because the corresponding coefficients in (C6) have positive signs [from the term $(-1)^{j_1 + j_2 + j_3}$ with $j_1 + j_2 + j_3 = 2$] and the integral of the bare propagator is also positive. Explicitly, it reads

$$(m^2)_{\alpha\beta} = \frac{\Gamma(1 + \tau u + \tau E_0)}{(1 + \tau u + I_0 + I_x)^2}\sum_{k_n}\int_0^{\infty}dq q G_{\alpha\beta}^{(0)}(k_n, q), \qquad (C8)$$

---

[13]We do not worry about the UV divergences: We have an effective field theory and the UV cutoff is physical and finite.
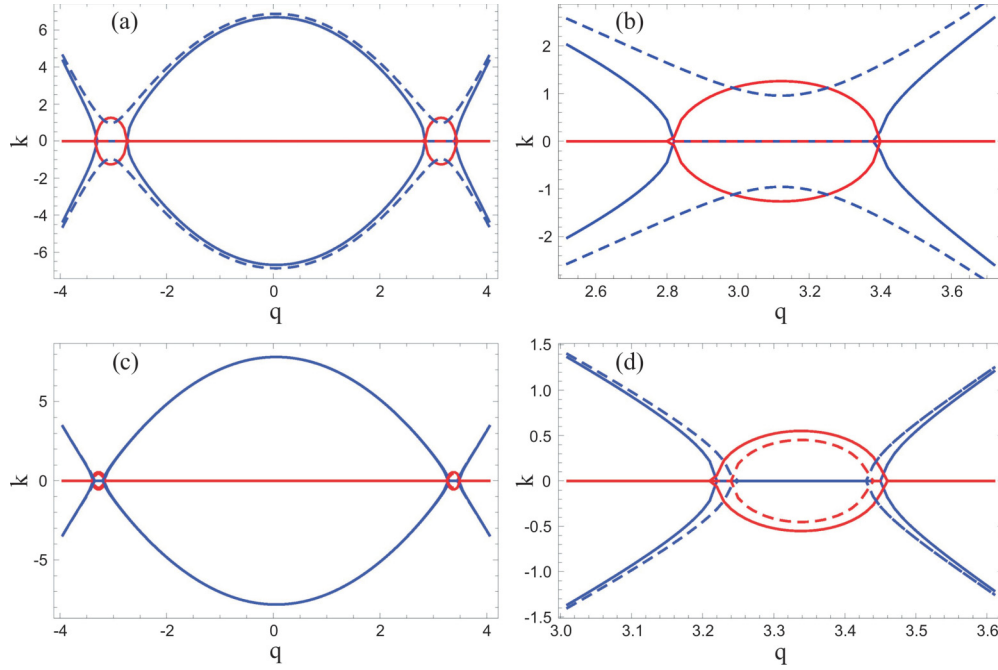
FIG. 21. Dispersion relation (position of the poles of the propagator) $k(q)$, where k is the continuous approximation of the discrete effective momentum $k_n = \pi n L$, for $I_x = 0$ [(a), (b)] and $I_x = 1$ [(c), (d)]. The plots (b) and (d) are enlargements of the plots (a) and (c). Blue lines denote $\mathrm{Re} k$ and red lines show $\mathrm{Im} k$. Notice that the propagator contains only k_n^2 and q^2, so the pole has two copies with opposite signs and is either real or pure imaginary. Dashed lines are the corrected relations, with dressed propagator instead of the bare one. In the top panels, the region of instability, with $\mathrm{Im} k_n \neq 0$, is cured by the nonlinear corrections, whereas in the bottom panels the instability remains. This generically happens at finite q and corresponds to the edge instability. Parameter values: $I_0 = 1$, $\Gamma = 15$, $L = 10$ mm.

where the discrete "frequency" k_n is summed in steps of π/L. Other than the mass renormalization, the dressed propagator has the same structure as the bare one. Now we will consider what this means for the stability of the patterns.

1. The pole structure, stability, and dispersion relations

Consider the poles of the propagator defined by the zeros of the eigenvalues of the matrix $G_{\alpha\beta}^{-1}(k_n,q)$. The stable solution corresponds to the situation where the perturbation $\delta\Psi_\pm$ dies out along z, so the stability of the solution is determined by the condition that the pole in q should have a nonpositive imaginary part, i.e., that a small perturbation decays. The denominator depends on k_n,q solely through k_n^2,q^2; it is linear in k_n^2 and quadratic in q^2. Therefore, each of the two eigenvalues $\lambda_\pm$ defines two pairs of opposite poles, $\pm q_{*+}, \pm q_{*-}, \pm q_{**+}, \pm q_{**-}$. Out of these, two pairs are positive for all parameter values, so no imaginary part can arise, and we have either two pairs of centrally symmetric imaginary poles, or one such pair, or none at all. We thus expect the sequence of symmetry-breaking transitions:

$$O(2) \longrightarrow \mathbb{C}_4 \longrightarrow \mathbb{C}_2. \tag{C9}$$

Full circular symmetry is expected when there is no instability. With a single pair of unstable eigenvalues, we expect a square-like pattern with $\mathbb{C}_4$ symmetry, and with two pairs only a single reflection symmetry axis remains, yielding the group $\mathbb{C}_2$. Only in the presence of disorder in the background lattice intensity pattern I_x can we expect the full breaking of the symmetry

group down to unity, but this is an *explicit* breaking and is not captured by this analysis.

The dispersion relation for a typical choice of parameter values is represented in Fig. 21, where we plot the location of the pole $k(q)$ in the continuous approximation (interpolating between the k_n values), with real parts of the pole in blue and imaginary in red. Since we have two pairs of opposite eigenvalues, the dispersion is P symmetric in x,y, and z (remember that time is really another spatial dimension), and any dispersion relation with a nonzero imaginary part will have a branch in the upper half-plane, i.e., an unstable branch. The only way out of instability is that the pole is purely real, i.e., infinitely sharp—this quasiparticle-like excitation signifies a solitonic solution. In Fig. 21, the dashed lines are drawn with the bare propagator $G^{(0)}$ and the full lines with the dressed propagator G, for the sets of parameter values. The perturbation always reduces the instability, i.e., the magnitude of the imaginary part of the poles—in Figs. 21(a) and 21(b) completely, resulting in zero imaginary part, and in Figs. 21(c) and 21(d) only partially. This reduction of instability likely explains the fact that linear stability analysis works extremely well for hyper-Gaussian beams (which have most power at small values of q), as found in Ref. [32].

The fact that the imaginary region always lies at finite q implies that the instability always starts at a finite scale, which corresponds to the behavior seen in the edge instability, which is shown, e.g., in Fig. 4. In order to understand the central instability, which starts from a single point, corresponding to $q \to \infty$, one needs to take into account also the higher order corrections from the potential (C6) which, as we discussed,
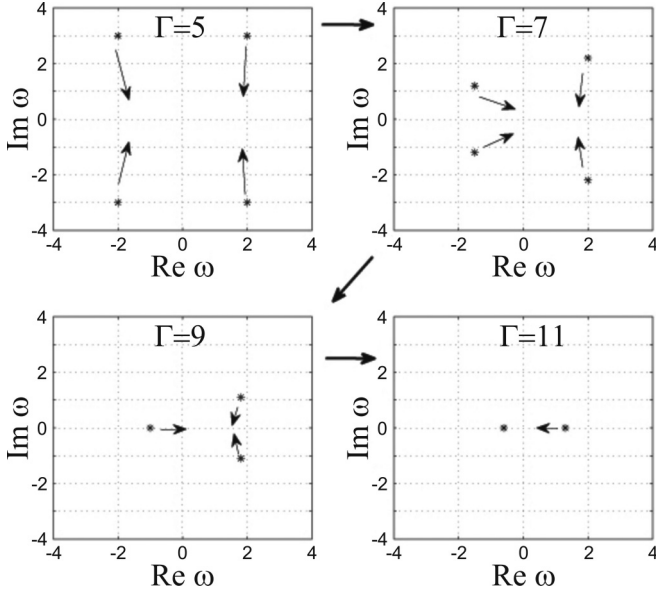
FIG. 22. The movement of the poles in the complex momentum plane in the case of central instability, for four different values of the PR coupling constant $\Gamma = 5, 7, 9, 11$. The complex momentum k is denoted by ω. Starting from the $\mathbb{C}_4$-symmetric situation with two pairs of complex-conjugate poles, we first break the symmetry down to $\mathbb{C}_2$ and eventually lose all geometric symmetry as the two pairs merge into two real poles. Parameter values $I_0 = I_x = 1, L = 10$ mm.

diverge at $q \to \infty$. While we always have a natural UV cutoff, it may happen that the corrections become large (though finite) before that UV scale is reached. We postpone a detailed account for the subsequent publication, and content ourselves to give only the diagram of the movement of the poles in the complex plane. Higher order terms bring q-dependent corrections and break the inversion symmetry, resulting in the evolution of poles, as in Fig. 22. The instability corresponds to the situations where at least one pole has a positive imaginary part, i.e., the first three situations in the figure. The last pattern, with no symmetry at all and two real poles, is stable (but not asymptotically stable, as there is no pole with nonzero negative imaginary part).

The analysis performed here is obviously incomplete, and we have contented ourselves merely to give a sketch of how the instabilities considered in the main text arise, as well as to formulate a perturbation scheme which allows one to study such phenomena. Further work along the lines of Refs. [20,32,36] is possible by making use of our formalism, and we plan to address this topic in the future.

APPENDIX D: DERIVATION OF THE VORTEX HAMILTONIAN FROM THE MICROSCOPIC LAGRANGIAN

Starting from the vortex solution (6), we want to obtain an effective Hamiltonian for the vortex-vortex interaction. The task is to separate the kinetic term of the winding phase (with $\nabla\theta_{0\pm} = \sum_i Q_\pm \ln |\mathbf{r} - \mathbf{r}_i|$) from (i) the intensity fluctuations $\delta\psi_\pm$ about some background value $\psi_{0\pm}$ and (ii) the nonvortex phase fluctuations ($\delta\theta_\pm$) in (6). The first task requires us

to integrate out the amplitude fluctuations in the quadratic approximation. We first write $\Psi = \Psi_0 + \delta\Psi$ and expand the Lagrangian to quadratic order:

$$
\begin{aligned}
\mathcal{L} &= \mathcal{L}_0 + \mathcal{L}_2, \\
\mathcal{L}_0 &= \frac{1}{2}\partial_r\psi_0^\dagger\partial_r\psi_0 + \frac{I_0}{2r^2}|\nabla\theta_{0\alpha}|^2, \\
\mathcal{L}_2 &= \frac{1}{2}\partial_r\delta\Psi_\alpha^\dagger\partial_r\delta\Psi_\alpha \\
&\quad + \frac{1}{2r^2}\delta\Psi_\alpha^\dagger|\nabla\theta_{0\alpha}|^2\delta\Psi_\alpha + V_{\text{eff}}(\delta\Psi_\pm),
\end{aligned}
$$

$$
\begin{aligned}
V_{\text{eff}}(\delta\Psi^\pm) &= -\Gamma\delta\Psi^\dagger\delta\Psi - \Gamma\frac{1 + \tau u + \tau E_0}{2(1 + \tau u + I_x + I_0)^2} \\
&\quad \times [(\Psi_0\delta\Psi^\dagger)^2 + (\Psi_0^\dagger\delta\Psi)^2 - 2(1 + \tau u + I_x + I_0) \\
&\quad \times \delta\Psi^\dagger\delta\Psi - (\Psi_0\sigma_2\delta\Psi^\dagger)(\Psi_0^\dagger\sigma_2\delta\Psi)].
\end{aligned} \tag{D1}
$$

The zeroth-order (nonfluctuating) term $\mathcal{L}_0$ determines the intensity $I_0 = \psi_0^\dagger\psi_0$ and produces the kinetic term for the vortex phase θ_α, which gives just two decoupled copies of the conventional XY vortex gas. The quadratic part $\mathcal{L}_2$ becomes quite involved when we separate the amplitude $\delta\psi$ and the phase $\delta\theta$. Inserting (6) into (D1), one gets a quadratic action for $\delta\psi_\alpha$ and $\delta\theta_\alpha$. The rest gives a coupled quadratic action for the amplitude and phase fluctuations. Altogether, the Lagrangian is

$$
\begin{aligned}
\mathcal{L} &= \frac{1}{2}(\delta\psi_+'^2 + \delta\psi_-'^2) + \frac{1}{2r^2}(\delta\psi_+^2 + \delta\psi_-^2)|\nabla\theta_\alpha|^2 \\
&\quad + \delta\psi_\alpha\hat{K}_{\alpha\beta}\delta\psi_\beta + (\delta\psi_\alpha^\dagger\psi_\alpha\nabla\theta_\alpha\nabla\delta\theta_\alpha + \text{H.c.}) + \cdots,
\end{aligned} \tag{D2}
$$

where $(\cdots)$ denote all terms of cubic or higher order in amplitude or phase fluctuations $\delta\psi_\alpha, \delta\theta_\alpha$, and we have left out the constant terms independent of all field values. Primes denote the derivatives with respect to r. The first term defines the intensity fluctuations through $\psi_\alpha(r)$, and the second term (transformed through partial integration) yields the aforementioned conventional Coulomb gas of vortices after inserting the vortex solution from (6) for θ_α. The third term has the meaning of stiffness or mass matrix for intensity fluctuations and the last term gives rise to the coupling between the flavors, upon integrating out $\delta\psi$. The matrix $\hat{K}$ is

$$
\begin{aligned}
\hat{K} &= \frac{1}{\left(b + \frac{3}{2}I_0\right)\left(b - \frac{1}{2}I_0\right)}\begin{pmatrix} b + \frac{I_0}{2} & I_0 \\ I_0 & b + \frac{I_0}{2} \end{pmatrix}, \\
b &= \Gamma\frac{1 + \tau E_0}{2(1 + \tau E_0)^2}(2 + 2I_x + 3I_0).
\end{aligned} \tag{D3}
$$

The action is quadratic in $\delta\psi$; therefore, we know how to integrate it out and obtain an effective action depending only on phase fluctuations. To do that, we need to solve the eigenvalue equation for $\delta\psi$ obtained from (D2), which reads

$$
\partial_{rr}\delta\psi_\alpha - K_{\alpha\beta}\delta\psi_\beta = \left(\frac{|\nabla\theta|^2}{2r^2} + \lambda_\pm\right)\delta\psi_\alpha, \tag{D4}
$$

and is solved by diagonalizing the system $\delta\psi_\alpha \mapsto \delta\chi_\alpha = U_{\alpha\beta}\delta\psi_\beta$ and reducing it to the Bessel equation:

$$\delta\chi_\pm(r) = \sqrt{r}\{C_\pm J_\nu[\sqrt{2(K_{11} \mp K_{12} - \lambda_\pm)}r]$$
$$+ D_\pm Y_\nu[\sqrt{2(K_{11} \mp K_{12} - \lambda_\pm)}r]\}, \quad \text{(D5)}$$

with $\nu = \sqrt{1/4 + |\nabla\theta|^2}$, where J_ν, Y_ν are Bessel functions of the first and second kinds, respectively. For well-defined behavior close to the vortex core (for $r \sim a$), we have $D_\pm = 0$, and $C_\pm$ are arbitrary as the equation is linear. The eigenvalues $\lambda_{n\pm}, n = 0, 1, \ldots$ are obtained by requiring that the fluctuation decays to zero at the crystal edge $r = \Lambda$:

$$\sqrt{2K_{11} \mp K_{12} - \lambda_{n\pm}}\Lambda = j_n(\nu), \quad \text{(D6)}$$

where j_n is the nth zero of the Bessel function J_ν. The values $\lambda_{n\pm}$ are impossible to express analytically in closed form; however, it is not necessary for our purposes as $\Lambda \gg a$. The functional determinant obtained after integrating out $\chi_\pm$ is now expressed in terms of the eigenvalues:

$$\mathcal{K}_{\alpha\beta} = \ln\left(\prod_n \lambda_{n\alpha}\lambda_{n\beta}\right)^{-1/2}$$
$$= -\frac{1}{2}\sum_n \ln\left(K'_\alpha + K'_\beta + \frac{2j_n(\nu)^2}{\Lambda^2}\right) \sim$$
$$- \frac{\Lambda}{2}(K'_\alpha + K'_\beta) + O\left(\frac{1}{\Lambda}\right), \quad \text{(D7)}$$

where $K'_\pm = 2K_{11} \mp K_{12}$. Now we are left with a solely phase-dependent quadratic Lagrangian:

$$\mathcal{L} = \psi_{0\alpha}\nabla\theta_\alpha\nabla\delta\theta_\alpha\hat{\mathcal{K}}_{\alpha\beta}\psi_{0\beta}\nabla\theta_\beta\nabla\delta\theta_\beta + \frac{I_0}{2r^2}|\nabla\theta_\alpha|^2. \quad \text{(D8)}$$

The final task is to integrate out the phase fluctuations, which is a trivial Gaussian integration, yielding

$$\mathcal{L} = \frac{I_0}{2r^2}|\nabla\theta_\alpha|^2 + I_0\nabla\theta_\alpha\mathcal{K}^{-1}_{\alpha\beta}\nabla\theta_\beta. \quad \text{(D9)}$$

The resulting Lagrangian now depends only on the vortexing phases θ_α. The first term is carried from the original Lagrangian, and it does not mix the flavors. But the second term, stemming from the fluctuations, has nonzero mixed $\pm$ cross terms. The quadratic derivative terms can be transformed by partial integration to the familiar Coulomb gas form of the XY model, with the same-flavor coupling which is already present in absence of fluctuations, *and* the coupling between the vortices of different flavors. Thus the existence of two beams together with the fact that amplitude and phase fluctuations do not decouple give us a richer system, with interaction between two vortex flavors. For future use, it is more convenient to look at the vortex Hamiltonian $\mathcal{H}_{\text{vort}}$—the difference from the Lagrangian lies just in the sign of the term V_{eff}. This finally yields the Hamiltonian [for Eq. (7), repeated here for convenience]:

$$\mathcal{H}_{\text{vort}} = \sum_{i<j}(g\vec{Q}_i \cdot \vec{Q}_j + g'\vec{Q}_i \times \vec{Q}_j)\ln r_{ij}$$
$$+ \sum_i (g_0\vec{Q}_i \cdot \vec{Q}_i + g_1\vec{Q}_i \times \vec{Q}_i), \quad \text{(D10)}$$

with $r_{ij} \equiv |\mathbf{r}_i - \mathbf{r}_j|$, and the indices $1 \leqslant i, j \leqslant N$ sum over all the vortices. The coupling constants g, g', g_0, g_1 are the result of integrating out the intensity fluctuations and in general are given by rather cumbersome (and not very illustrative) functions of Γ, I_0, τ. We give the expressions at leading order just for comparison with numerics:

$$g = I_0 + \frac{4b + 2I_0}{(2b + 3I_0)(2b - I_0)},$$
$$g' = \frac{4I_0}{(2b + 3I_0)(2b - I_0)},$$
$$b = \Gamma\frac{1 + \frac{\tau}{L} - \tau\frac{I_0+I_x}{1+I_0+I_x}}{2\left(1 + \frac{\tau}{L} - \tau\frac{I_0+I_x}{1+I_0+I_x}\right)^2}\left(2 + 2\frac{\tau}{L} + 2I_x + 3I_0\right).$$
$$\text{(D11)}$$

These expressions are used later to redraw the phase diagram in the space of physical parameters Γ, I_0, I_x, L.

APPENDIX E: MULTIVORTEX MEAN-FIELD THEORY

For a mean-field treatment of a system with multiple vortices, we start from the Hamiltonian (7) and introduce the order parameter fields in the following way. Denote the number of vortices with charge $(1,1)$ by ρ_{2+} and the number of vortices $(1,-1)$ by ρ_{2-}; due to charge conservation, this means we also have ρ_{2+} vortices of type $(-1,-1)$ and ρ_{2-} vortices with charge $(-1,1)$. The number of single-charge vortices of type $(1,0)$ and $(0,1)$ is denoted by ρ_{1+} and ρ_{1-}, respectively. Denote also $\rho_2 \equiv \rho_{2+} + \rho_{2-}$ and $\delta\rho_2 \equiv \rho_{2+} - \rho_{2-}$ (notice that $-\rho_2 \leqslant \delta\rho_2 \leqslant \rho_2$), and finally $\rho_1 \equiv \rho_{1+} + \rho_{1-}$. We insert this into the vortex Hamiltonian $\mathcal{H}_{\text{vort}}$ and assume that the long-ranged logarithmic interaction $\ln r_{ij}$ justifies the mean-field approximation: For $i \neq j$, we can approximate $\ln r_{ij} \sim \ln\Lambda$, assuming that average intervortex distance is of the same order of magnitude as the system size. For the core energy, we know that $g_0, g_1 \sim \ln(a/\epsilon) \sim -\ln\epsilon \sim \ln\Lambda$, where in the last equality we have assumed that the UV cutoff ϵ is of similar order of magnitude as the inverse of the IR cutoff $1/\Lambda$, which is natural.[14] Thus all terms are proportional to $L\ln\Lambda$ and we can write

$$\mathcal{F}_{\text{mf}} = \beta\ln\frac{\Lambda}{a}[2(g-1)\rho_2 + 2g'\delta\rho_2 + (g-1)\rho_1]$$
$$\equiv A\rho_2 + B\delta\rho_2 + \frac{B}{2}\rho_1. \quad \text{(E1)}$$

We use the notation $\beta \equiv L$ to emphasize the analogy with the free energy of spin vortices, where β is the inverse temperature. The analogy is purely formal as our system is not subject to thermal noise. Now the ground state is determined by minimizing the free energy, i.e., the effective action of the system. Notice that $\mathcal{F}_{\text{mf}}$ is linear in the fields $\rho_2, \delta\rho_2, \rho_1$ so the optimal configurations have either $\mathcal{F}_{\text{mf}} = 0$ or $\mathcal{F}_{\text{mf}} \to -\infty$, and the mean-field densities $\rho_{1,2}$ are either zero or arbitrary

---

[14]Nevertheless, this is clearly not a rigorous argument. Our mean-field calculation is somewhat sketchy and merely assumes that the long-range interactions can safely be modeled as a uniform vortex charge field.

(formally infinite). This is a well-known property of the 2D Coulomb gas and has to do with the fact that (assuming the cutoff dependence has been eliminated) this system is conformal invariant in the insulator phase, so all finite densities ρ are equivalent: There is no other scale to compare ρ to. Likewise, the prefactor β can be absorbed into the definition of the coupling constants g, g' and thus is not an independent parameter (this is well known also from the single-flavor case). Minimizing (E1) is an elementary exercise and we find again four regimes, corresponding to the four phases we guessed based on the single-vortex free energy $\mathcal{F}^{(1)}$:

(1) For $A > 0, A > |B|$, the minimum is reached for $\rho_2 = \delta\rho_2 = \rho_1 = 0$. In the ground state, there are no vortices at all—the system is a vortex insulator.

(2) For $B > 0, A + B < 0$, giving $g + g' < 1, g' > 0$, the free energy has its minimum for $\rho_2 > 0$ and $\delta\rho_2 = -\rho_2$ (notice that $-\rho_2 \leqslant \delta\rho_2 \leqslant \rho_2$). This means $\rho_{2+} = 0, \rho_{2-} > 0$, so opposite-charged vortices $(Q, -Q)$ proliferate, and the system is dominated by the interactions between the charges. This is the frustrated vortex insulator regime. Since $g' < 0$, the single-charge vortices (density ρ_1) are suppressed.

(3) For $B < 0, A + B < 0$, i.e., $g + g' < 1, g' < 0$, the minimum is reached for $\rho_2 = \delta\rho_2 > 0$, i.e., $\rho_{2-} = 0$, so the vortices (Q, Q) can proliferate. However, since $g' < 0$, there is also nonzero single-flavor density ρ_1 and the proliferation of vortices $(Q, 0)$ and $(0, Q)$ which generically dominate over two-flavor vortices. This is the conductor phase, with mostly single-flavor vortices (as in the standard XY model).

(4) The point $A = B = 0$ is special: Naively, from (E1), arbitrary nonzero $\rho_1, \rho_2, \delta\rho_2$ are allowed. Of course, higher order corrections will change, this but the energy cost of vortex formation will generically be smaller than in previous phases. This is the vortex perfect conductor phase. In the mean-field approach, it looks like a single point, but that will turn out to be an artifact of the mean-field approach: For small nonzero A, B the system still remains in this phase.

In terms of the original parameters g, g', one sees the insulator phase is given by $g + g' > 1$, and the conductor and the FI are separated by the line $g' = 0$. We can now sketch the phase diagram, which is given in Fig. 2(a), side by side with the more rigorous diagram obtained by the RG flow, in Sec. III B 2.

APPENDIX F: COUNTERPROPAGATING BOUNDARY CONDITIONS

In the derivation of the vortex Hamiltonian and its RG analysis, we have pulled under the rug the treatment of the CP boundary conditions: The effective Hamiltonian (and consequently the partition function and the phase diagram) depends solely on the bulk configuration, and nowhere can one see the fact that $\Psi_+(z = 0; \mathbf{r}, t)$ and $\Psi_-(z = L; \mathbf{r}, t)$ are fixed. Now we will explicitly show that these boundary conditions are irrelevant in the RG sense; i.e., they contribute additional, boundary terms to the effective Hamiltonian, but these terms do not change the fixed points to which the solution flows.

The full Hamiltonian with correct CP boundary conditions is obtained by adding the F source at $z = 0$ and the B source at $z = L$ to the Lagrangian $\mathcal{L}$ from (4) or, equivalently, to the equations of motion. The sources impose the conditions $F(z =$

$0; x, y; t) = F_0(x, y)$ and $B(z = L; x, y; t) = B_0(x, y)$ so they equal

$$J_+ = F_0(x, y)\delta(z), \quad J_- = B_0(x, y)\delta(z - L), \tag{F1}$$

and the full Lagrangian is

$$\begin{aligned}\mathcal{L}_{\mathrm{CP}} = \mathcal{L} + J_+\Psi_+ + J_-\Psi_- &\mapsto \mathcal{L} + F_0(x, y)\Psi_+(z; x, y; t) \\ &+ e^{ikz}B_0(x, y)\Psi_-(z; x, y; t).\end{aligned} \tag{F2}$$

Unlike the Dirac δ source (C3) for the Green's function, now the source has nontrivial dependence on transverse coordinates. Now we can insert the vortex solution (6) in both $\Psi_\pm$ and F_0, B_0 and repeat the steps from the subsequent derivation. The vortex charges in F_0 can be denoted by $\vec{P}_{i'}^{(+)} \equiv (P_{i'+}, 0)$ and $\vec{P}_{i'}^{(-)} \equiv (0, P_{i'-})$; by definition, the + component of B_0 as well as the − component of F_0 are zero and thus carry no vorticity. The primed indices refer to the vortices in the input beams, and the nonprimed, like before, to the bulk vortices. Notice the source term changes sign upon performing the Legendre transform, appearing as $-J_+\Psi_+ - J_-\Psi_-$ in the Hamiltonian.

Now we will check if the RG flow of the Hamiltonian with boundary terms is affected by the sources. In the notation introduced above, the total vortex Hamiltonian is

$$\begin{aligned}\mathcal{H}_{\mathrm{CP}} = &\sum_{i,j}(g\vec{Q}_i \cdot \vec{Q}_j + g'\vec{Q}_i \times \vec{Q}_j)\ln r_{ij} \\ &+ \sum_{i',j}\delta(z)P_{i'+}(gQ_{j+} + g'Q_{j-})\ln r_{i'j} \\ &+ \sum_{i,j'}\delta(z - L)P_{j'-}(gQ_{i-} + g'Q_{i+})\ln r_{ij'}.\end{aligned} \tag{F3}$$

Notice there is no source-source interaction: Same-flavor interaction cannot exist as $P_{i'-} = P_{j'+} = 0$, and cross-flavor interaction does not exist as J_+ and J_- exist at different z values, i.e., the cross term would be proportional to $\delta(z)\delta(z - L)$ and thus vanishes. The presence of sources breaks the spatial homogeneity, complicating the traces (integrals over the positions of virtual vortex-antivortex pairs), but does not change the main line of the calculation. The fluctuation of the partition function due to vortex pair creation is now

$$\begin{aligned}\frac{\delta\mathcal{Z}}{\mathcal{Z}} = 1 + \frac{y^4}{4}\sum_{\vec{q}}\int d^2r \\ \times \int d^2r_{12} e^{-C(\vec{q}, \mathbf{r}_1; -\vec{q}, \mathbf{r}_2) - \sum_{j'}[D_{j'}^+(\vec{q}, \mathbf{r}_1) - D_{j'}^-(\vec{q}, \mathbf{r}_2)]} \\ \times [e^{C(\vec{Q}_1, \mathbf{R}_1; \vec{q}, \mathbf{r}_1) + C(\vec{Q}_1, \mathbf{R}_1; -\vec{q}, \mathbf{r}_2) + C(\vec{Q}_2, \mathbf{R}_2; \vec{q}, \mathbf{r}_1) + C(\vec{Q}_2, \mathbf{R}_2; -\vec{q}, \mathbf{r}_2)} \\ - 1].\end{aligned} \tag{F4}$$

We have denoted $C(\vec{Q}_1, \mathbf{R}_1; \vec{Q}_2, \mathbf{R}) \equiv (g\vec{Q}_1 \cdot \vec{Q}_2 + g'\vec{Q}_1 \times \vec{Q}_2)\ln R_{12}$, and the coupling to the sources is encapsulated in the function

$$D_{j'}^\pm(\vec{q}, \mathbf{r}) \equiv \delta(z - z_\pm)(g_\pm\vec{q} \cdot \vec{P}_{j'} + g'_\pm\vec{q} \times \vec{P}_{j'})\ln|\mathbf{r} - \mathbf{r}_{j'\pm}|, \tag{F5}$$

with $z_+ = 0, z_- = L$. The coupling constants $g_\pm, g'_\pm$ are obtained from g, g' in (F4) by replacing

$$I_0 \mapsto \sqrt{I_0 I_\pm}, \tag{F6}$$

with $I_+ = |F_0|, I_- = |B_0|$. Now the exponential of the extra term with sources also needs to be expanded in r_{12}, as the combinations $2\mathbf{r} = \mathbf{r}_1 + \mathbf{r}_2, \mathbf{r}_{12} = \mathbf{r}_1 - \mathbf{r}_2$ do not decouple anymore and exact integration is impossible. After writing $D_{j'}^\pm(\vec{q}, \mathbf{r}_{1,2}) = D_{j'}^\pm(\vec{q}, \mathbf{r}) \pm \mathbf{r}_{12} \cdot \nabla D_{j'}^\pm(\vec{q}, \mathbf{r}) + \cdots$ and similarly for C, we notice first that the zeroth-order terms from $D_{j'\pm}$ cancel out: $D_{j'}^\pm(\vec{q}, \mathbf{r}) + D_{j'}^\pm(-\vec{q}, \mathbf{r}) = 0$. Then we get (at quadratic order in r_{12} in the integrand):

$$\frac{\delta \mathcal{Z}}{\mathcal{Z}} = 1 + \frac{y^4}{4} \sum_{j'} \int d^2 r \int d^2 r_{12} e^{-C(\vec{q}, \mathbf{r}_{12}; -\vec{q}, 0)}$$

$$\times \left\{ \mathbf{r}_{12} \cdot [\nabla C(\vec{Q}_1, \mathbf{R}; \vec{q}, \mathbf{r}) + \nabla C(\vec{Q}_2, \mathbf{R}; -\vec{q}, \mathbf{r})] \right.$$

$$+ \frac{r_{12}^2}{2} \left| \nabla C(\vec{Q}_1, \mathbf{R}; \vec{q}, \mathbf{r}) + \nabla C(\vec{Q}_2, \mathbf{R}; -\vec{q}, \mathbf{r}) \right|^2 \right\}$$

$$\times [\mathbf{r}_{12} \cdot [1 - \nabla D_{j'}^+(\vec{q}, \mathbf{r}) + \nabla D_{j'}^-(\vec{q}, \mathbf{r})]$$

$$+ \{\mathbf{r}_{12} \cdot [\nabla D_{j'}^+(\vec{q}, \mathbf{r}) + \nabla D_{j'}^-(\vec{q}, \mathbf{r})]\}^2] + \cdots$$

$$\equiv 1 + \frac{y^4}{4} [I_{10} + I_{20} - I_{11} + O(r_{12}^3)]. \tag{F7}$$

The integral I_{mn} is the term with the contribution of order r_{12}^m from the second line in the integrand and with the contribution of order r_{12}^n from the third line. The integrands in I_{mn} are thus of order $m + n$ in $\mathbf{r}_{12}$, m coming from the expansion of $D_{j'}^\pm$ and n from the expansion of C. By homogeneity, $I_{01} = 0$ and I_{02} is the same integral that appears in absence of sources, whose calculation was used in obtaining (13) and which gives the right-hand side of the RG flow (14). The remaining integral I_{11} is the new ingredient, and the only one which depends on the sources. Representing it as

$$I_{11} = \frac{\pi^2}{4} \sum_{j'} \sum_{\alpha = \pm} \sum_{\sigma = 1,2} \delta(z - z_\alpha)$$

$$\times (g_\alpha \vec{Q}_\sigma \cdot \vec{P}_{j'\alpha} + g'_\alpha \vec{Q}_\sigma \times \vec{P}_{j'\alpha})$$

$$\times \nabla \frac{1}{|\mathbf{R}_{12}|} \cdot \nabla \frac{1}{|\mathbf{r}_{j\alpha}|} \tilde{I}_{j'\alpha}, \tag{F8}$$

we compute the integral $\tilde{I}_{j'\alpha}$ in polar coordinates:

$$\tilde{I}_{j'\alpha} = \frac{1}{2} \int_0^{2\pi} d\theta_j \ln \left(r_{12}^2 - 2r_{12} r_{j'\alpha} \cos\theta_j + r_{j'\alpha}^2 \right) \Big|_{\Lambda_1}^{\Lambda_2}, \tag{F9}$$

where $\theta_{j'\alpha}$ is the angle between $\mathbf{r}_{j'\alpha}$ and $\mathbf{r}_{12}$. Assuming the RG scale changes as $\Lambda_1 = \Lambda, \Lambda_2 = \Lambda(1 + \ell)$, for small ℓ we can expand the integrand, getting

$$\tilde{I}_{j'\alpha} = \int_0^{2\pi} d\theta_{j'} \frac{\Lambda^2 - \Lambda r_{j'\alpha} \cos\theta_j}{\Lambda^2 - 2\Lambda r_{j'\alpha} \cos\theta_j + r_{j'\alpha}^2} \ell + O(\ell^2)$$

$$= 2\pi\ell + O(\ell^2). \tag{F10}$$

The complicated dependence on the positions of the sources disappears completely in the first order in ℓ.[15] Altogether, by comparing the outcome of (F7) to the original Hamiltonian (F3), we see that the renormalization of the bulk interaction between $\vec{Q}_1$ and $\vec{Q}_2$ is unaffected by the sources, given as before by the I_{02} term, and the source-bulk coupling renormalizes with a strictly negative shift (as $\tilde{I}_{j'\alpha} = 2\pi > 0$). The flow equations for g, g' couplings are unchanged, being the same as in (14). The bulk-to-boundary couplings $g_\pm, g'_\pm$ have the flow equations

$$\frac{\partial g_\pm}{\partial \ell} = -\pi^3 N\ell, \quad \frac{\partial g'_\pm}{\partial \ell} = -\frac{\pi^3}{2} N\ell, \tag{F11}$$

where $N = \sum_{j'} \sum_\alpha 1$ is the total vorticity of the sources. This obviously flows to $g_\pm, g'_\pm = 0$.

Intuitively, one may wonder how come such an important thing as the CP geometry has no bearing on the vortex dynamics; surely the behavior of a copropagating system would be expected to differ from a counterpropagating system. The answer is that the CP geometry does enter our calculations—the B beam has an extra minus sign in the equations of motion (1) (alternatively, in the Lagrangian in Eq. (4)); equivalently, the symmetry group of the effective potential in the Lagrangian is SU(1,1), not SU(2) as it would be for two copropagating beams. Finally, let us emphasize again that in the numerical simulations we directly solve the propagation equations (1) together with (2); i.e., we directly take into account the CP boundary conditions—no analytical approximations whatsoever are used in the numerics, and no use is made of the effective vortex Hamiltonian.

APPENDIX G: ORDER PARAMETERS AND RG ANALYSIS OF THE CP VORTICES IN THE PRESENCE OF DISORDER

1. Saddle-point solutions

We start by rewriting the replicated partition function $\bar{\mathcal{Z}}^n$ in terms of $p_\alpha, q_{\alpha\beta}$ and inserting the constraints which encapsulate their definition in Eq. (19):

$$1 \mapsto \int \mathcal{D}[\lambda_{(\mu)}^\alpha] \exp \left[\lambda_{(\mu)}^\alpha \left(p_\alpha^{(\mu)} - \frac{1}{N} \sum_{i=1}^N Q_{i\alpha}^{(\mu)} \right) \right], \tag{G1}$$

$$1 \mapsto \int \mathcal{D}[\lambda_{(\mu\nu)}^{\alpha\beta}] \exp \left[\lambda_{(\mu\nu)}^{\alpha\beta} \left(q_{\alpha\beta}^{(\mu\nu)} - \frac{1}{N} \sum_{i,j=1}^N Q_{i\alpha}^{(\mu)} Q_{j\beta}^{(\nu)} \right) \right]. \tag{G2}$$

We have five constraints, $\lambda_{(\mu\nu)}^{++}, \lambda_{(\mu\nu)}^{--}, \lambda_{(\mu\nu)}^{+-} = \lambda_{(\mu\nu)}^{-+}, \lambda_{(\mu)}^+, \lambda_{(\mu)}^-$, for the corresponding five order parameters in (19). We can denote

$$\hat{K} \equiv \begin{pmatrix} \lambda_{(\mu\nu)}^{++} & \lambda_{(\mu\nu)}^{+-} \\ \lambda_{(\mu\nu)}^{+-} & \lambda_{(\mu\nu)}^{--} \end{pmatrix}, \quad \vec{\lambda} \equiv \begin{pmatrix} \lambda_{(\mu)}^+ \\ \lambda_{(\mu)}^- \end{pmatrix}. \tag{G3}$$

We will also sometimes leave out the replica indices μ, ν to avoid cramming the notation too much. Now we can first integrate out the vortex degrees of freedom $Q_{i\alpha}^{(\mu)}$ from (18)

---

[15]The additional assumption is that $\Lambda > r_{j'\alpha}$ so the integrand contains no poles; this is clearly justified as Λ is the length cutoff.

to get the effective action

$$S_{\text{eff}} = -\frac{\beta^2}{4} \sum_{\mu,\nu=1}^{n} [\sigma_{++}^2 (q_{++}^{(\mu\nu)})^2 + 2\sigma_{+-}^2 (q_{+-}^{(\mu\nu)})^2 + \sigma_{--}^2 (q_{--}^{(\mu\nu)})^2] - \beta \sum_{\mu=1}^{n} [J_0^+ (p_+^{(\mu)})^2 + 2J_0^{+-} p_+^{(\mu)} p_-^{(\mu)} + J_0^- (p_-^{(\mu)})^2]$$

$$+ \frac{1}{2} \ln \det \hat{K} - \frac{1}{4} \vec{\lambda} \hat{K}^{-1} \vec{\lambda} - \sum_{\mu,\nu=1}^{n} (\lambda_{(\mu\nu)}^{++} q_{++}^{(\mu\nu)} + \lambda_{(\mu\nu)}^{+-} q_{+-}^{(\mu\nu)} + \lambda_{(\mu\nu)}^{--} q_{--}^{(\mu\nu)}) - \sum_{\mu=1}^{n} \vec{\lambda}_{(\mu)} \cdot \vec{p}^{(\mu)}. \tag{G4}$$

The saddle-point equations for the constraints give the constraints in terms of the expectation values $q^{(\mu\nu)}, p^{(\mu)}$. Luckily, the equation for $\vec{\lambda}$ is easy:

$$\frac{\partial S_{\text{eff}}}{\partial \vec{\lambda}} = \hat{K}^{-1} \vec{\lambda} - \vec{p} = 0, \tag{G5}$$

so we immediately solve $\vec{\lambda} = \hat{K} \vec{p}$. Now plugging this into the equations for the three remaining constraints yields

$$\frac{\partial S_{\text{eff}}}{\partial \lambda_{\pm\pm}} = \frac{1}{2} \frac{X \lambda_{\pm\pm}^{-1}}{X^2 - Y^2} - q_{\pm\pm} + \frac{1}{4}(p_\pm)^2 = 0, \tag{G6}$$

$$\frac{\partial S_{\text{eff}}}{\partial \lambda_{+-}} = \frac{Y \lambda_{+-}^{-1}}{X^2 - Y^2} - q_{+-} + \frac{1}{2} p_+ p_- = 0. \tag{G7}$$

We have denoted $X = \det \lambda_{++} = \det \lambda_{--}, Y = \det \lambda_{+-}$ (these have a well-defined limit for $n \to 0$). It is trivial to write $\lambda_{\pm\pm}, \lambda_{+-}$ from the above expressions, and we can feed the solutions for all the constraints into the effective action and then solve the saddle-point equations for the order parameters $p_\pm, q_{++}, q_{--}, q_{+-}$. Full equations are too complex to be solved, even approximately. We will simplify the problem with the following reasoning. The sums over single-replica order parameters generically scale as $\sum_\mu p_\pm^{(\mu)} \sim \sum_\mu (p_\pm^{(\mu)})^2 \sim n$, whereas the double-replica parameters have $\sum_{\mu,\nu} q_{\alpha\beta}^{(\mu\nu)} \sim n^2$. This means that in the limit $n \to 0$, the $p_\pm$ terms dominate over $q_{\alpha\beta}$ terms. Therefore, if $p_\pm \neq 0$ we can disregard the quantities $q_{\alpha\beta}$ or expand in a series over them, simplifying the equations significantly. Only if the replica symmetry breaking imposes $p_\pm = 0$ (not every replica-symmetry-breaking configuration does so) are the $q_{\alpha\beta}$ order parameters significant, and the saddle-point equations with $p_\pm = 0$ are again approachable.

Consider first the case $p_\pm = 0$. After some algebra, the effective action is now

$$S_{\text{eff}} = -\frac{\beta^2}{4} \sum_{\mu,\nu=1}^{n} [\sigma_{++}^2 (q_{(\mu\nu)}^{++})^2 + 2\sigma_{+-}^2 (q_{(\mu\nu)}^{+-})^2$$

$$+ \sigma_{--}^2 (q_{(\mu\nu)}^{++})^2] + \frac{1}{2} \ln(X^2 |q^{++}|^{-1} \cdot |q^{--}|^{-1}$$

$$- 4Y^2 |q^{+-}|^{-2}). \tag{G8}$$

Consider first the ansatz when the $q^{\pm\pm}$ fields are nonzero, whereas the mixed-flavor field q^{+-} is zero. In this case, the second term in (G8), coming from the determinant $\hat{K}$, simplifies further and we get the saddle-point equation

$$-\frac{\beta^2}{2} \sigma_{\pm\pm}^2 q^{\pm\pm} - \frac{1}{2}(q^{\pm\pm})^{-1} = 0, \tag{G9}$$

which is the same as for the infinite-range spin-glass Ising model [42,54]. One obvious solution is $q^{\pm\pm} = q^{+-} = 0$, the completely disordered system with no vortex proliferation—the familiar insulator phase. It is easy to check that this is indeed a minimum of the effective action S_{eff}. There is also a replica-symmetric but nontrivial solution

$$q_{(\mu\nu)}^{\pm\pm} = \mathcal{Q}_0^{\pm\pm} + (1 - \mathcal{Q}_0^{\pm\pm})\delta_{\mu\nu}, \tag{G10}$$

which yields the solution $\mathcal{Q}_0^{\pm\pm} = 1 - 1/(\beta\sigma^{\pm\pm})$. However, this solution is unstable and is not observable. A stable nontrivial solution is obtained if the replica symmetry is broken. The ansatz is well known from the spin-glass literature (e.g., Ref. [42]) and has a $\rho \times \rho$ matrix $\hat{Q}^{\pm\pm}$ on the block-diagonal and the constant zero elsewhere, with

$$\hat{Q}^{\pm\pm} = \mathcal{Q}_1^{\pm\pm} + (1 - \mathcal{Q}_1^{\pm\pm})\delta_{\mu\nu}, \mu,\nu = 1,\ldots,\rho. \tag{G11}$$

Equation (G9) suggests that $\mathcal{Q}_1^{\pm\pm} > 0$ for sufficiently large β, i.e., small L. However, no analytical solution for the elements $\mathcal{Q}_1^{\pm\pm}$ exists and they have to be solved for numerically, by plugging in the solution into the effective action and minimizing it. This is an easy task (for chosen values of the parameters and disorder statistics) but we will not do it here as we do not aim at quantitative accuracy anyway; we merely want to sketch the phase diagram. Now if the third field q^{+-} is nonzero, it satisfies the same equation as (G9) just with $\sigma_{++}^2 \mapsto 2\sigma_{+-}^2$. The three combinations of nonzero order parameters correspond to the three familiar phases: $q^{\pm\pm} \neq 0$ is the conductor, $q^{+-} \neq 0$ is the frustrated insulator, and $q^{\pm\pm}, q^{+-} \neq 0$ is the perfect conductor.

The solutions with $\vec{p} \neq 0$ yield new physics. In this case, we have at leading order $\lambda_{\pm\pm} = -2X/(X^2 - Y^2)(p^\pm)^{-2}, \lambda_{+-} = -2Y/(X^2 - Y^2)(p^+ p^-)^{-1}$, so the effective action is

$$S_{\text{eff}} = -\beta \sum_{\mu=1}^{n} [J_0^+ (p_{(\mu)}^+)^2 + 2J_0^{+-} p_{(\mu)}^+ p_{(\mu)}^- + J_0^- (p_{(\mu)}^-)^2]$$

$$- \ln p^+ p^- + O(|q^{\alpha\beta}|^2) + O\left(\frac{|q^{\alpha\beta}|}{|\vec{p}|^2}\right), \tag{G12}$$

giving the saddle-point equation

$$J_0^\pm p_{(\mu)}^\pm + \frac{J_0^{+-}}{\beta} p_{(\mu)}^\mp + (p_{(\mu)}^\pm)^{-1} = 0, \tag{G13}$$

which easily gives

$$p^\pm = s_1 \sqrt{\frac{1}{J_0^\pm + s_2 \frac{J_0^{+-}}{\beta} \sqrt{\frac{J_0^+}{J_0^-}}}}, \tag{G14}$$

with $s_{1,2} \in \{\pm 1\}$. The solution is the same for every μ and $p_{(\mu)}^\pm = (p^\pm, p^\pm, \ldots, p^\pm)$. Now, depending on the sign of the
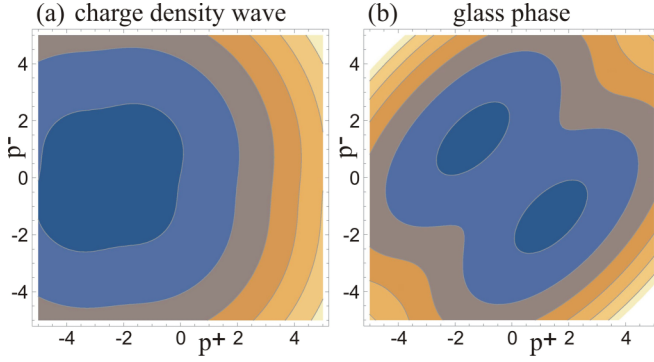
(a) charge density wave   (b)   glass phase

FIG. 23. Free energy (effective action $S_{\rm eff}^{(\mu)}$) in a given replica subsystem in a photonic lattice with quenched disorder, for the case when the order parameter $p^{\pm} = \sum_i Q_{i\pm}$ has a nonzero saddle-point solution for the action in a given subsystem (replica). Darker (blue) tones are lower values. The ground states of the system are the local minima. In panel (a) for $J^+ = -J^- = 1$, there is a single local minimum. In case (b), for $J^+ = -J^- = 1$, we see two distinct minima of equal height, for two different nonzero values of $p^{\pm}$. Such potential energy landscape fits the description of glassy systems.

determinant $J_0^+ J_0^- - (J_0^{+-})^2$, the solutions for different $s_{1,2}$

may be minima or saddle points. In either case, we have a phase with nonzero local charge density, which is the meaning of $\vec{p}$. If there are multiple minima, we call this phase vortex glass. The reader may argue that true glass should satisfy more stringent conditions and that our phase is not a true glass. Depending on the viewpoint this may well be accepted, and we use the term "glass phase" merely as shorter and more convenient than "phase with power-law correlation decay, no long-range order, and frustrated free energy landscape." The phase with a single minimum will be called charge density wave, as it has a unique ground-state configuration yielding macroscopically nonzero charge density; i.e., it has a true long-range order. On the other had, with multiple minima the replica-averaged charge density sums to zero. The landscape, i.e., the effective action of the system for given replica (μ) as a function of $p_{(\mu)}^{\pm}$, is given in Fig. 23 as the density map of the function $S_{\rm eff}(p^+, p^-)$ dependence for $J_0^+ = -J_0^- = 1$ (glass phase, A) and $J_0^+ = J_0^- = 1$ (charge density wave, B). We see that the glassy phase shows two inequivalent minima in each replica, with $s_1 = -s_2 = \pm 1$ in Eq. (G14), so the total action, the sum of actions of all replica subsystems, can have one and the same value for many configurations, the definition of a highly frustrated system, one of the reasons we dub this phase glass. The charge density wave only has a single minimum for $s_1 = s_2 = 1$.

2. RG flow equations

The starting Hamiltonian is the same as in (18). Now we will write it out more explicitly, keeping the distance-dependent parts:

$$\beta \mathcal{H}_{\rm eff} = \beta \sum_{\mu=1}^{n} \sum_{i,j} \left(\bar{g}_c \vec{Q}_i^{(\mu)} \cdot \vec{Q}_j^{(\mu)} + \bar{g}_c' \vec{Q}_i^{(\mu)} \times \vec{Q}_j^{(\mu)} \right) \ln r_{ij} - \frac{\beta^2}{2} \sum_{\mu,\nu=1}^{n} \sum_{i,j} Q_{i\alpha}^{(\mu)} Q_{i\beta}^{(\nu)} \sigma_{\alpha\beta}^2 Q_{j\alpha}^{(\mu)} Q_{j\beta}^{(\nu)}. \tag{G15}$$

We have denoted the elements of J_0 by $J_0^{++} = J_0^{--} = \bar{g}_c, J_0^{+-} = J_0^{-+} = \bar{g}_c'$ (the bars over the letter remind us that these are disorder-averaged values). The fluctuation of the partition function is completely analogous to the clean case, only it has the additional nonlocal quartic term. It can again be expanded over r_{12} as in (12) but the quartic term contains no small parameter for the power series expansion and has to be kept in the exponential form. Starting from the expression for the fluctuation analogous to the clean case (12), we get

$$\frac{\delta \mathcal{Z}}{\mathcal{Z}} = 1 + \frac{y^4}{4} \sum_{\vec{q}^{(\rho)}, \vec{q}^{(\sigma)}} e^{-\frac{\beta^2}{2}(\vec{q}^{(\rho)}, -\vec{q}^{(\sigma)}, \vec{q}^{(\rho)}, -\vec{q}^{(\sigma)}) + \frac{\beta^2}{2}(\vec{Q}^{(\mu)}, \vec{q}^{(\rho)}, \vec{Q}^{(\nu)}, \vec{q}^{(\sigma)})} \int dr_{12} r_{12}^3 e^{g \vec{q}^{(\rho)} \cdot \vec{q}^{(\rho)} + g' \vec{q}^{(\rho)} \times \vec{q}^{(\rho)}}$$

$$\times \left[\int dr r^2 \left(g \vec{Q}_1^{(\mu)} \cdot \vec{q}^{(\rho)} + g' \vec{Q}_1^{(\mu)} \times \vec{q}^{(\rho)} \right) \boldsymbol{\nabla} \ln |\mathbf{R}_1 - \mathbf{r}| + \left(g \vec{Q}_2^{(\mu)} \cdot \vec{q}^{(\rho)} + g' \vec{Q}_2^{(\mu)} \times \vec{q}^{(\rho)} \right) \boldsymbol{\nabla} \ln |\mathbf{R}_2 - \mathbf{r}| \right]^2. \tag{G16}$$

We have used the notation

$$(\vec{q}_1, \vec{q}_2, \vec{q}_3, \vec{q}_4) \equiv \sigma_{++}^2 q_{1+} q_{3+} q_{2+} q_{4+} + \sigma_{+-}^2 (q_{1+} q_{3-} q_{2+} q_{4-} + q_{1-} q_{3+} q_{2-} q_{4+}) + \sigma_{--}^2 q_{1-} q_{3-} q_{2-} q_{4-}. \tag{G17}$$

Now we trace out the fluctuations first by integrating over r and doing some simple algebra:

$$\frac{\delta \mathcal{Z}}{\mathcal{Z}} = \left[1 + 16 y^4 (g + g')^2 \cosh(\beta^2 \sigma_{++}^2 + \beta^2 \sigma_{+-}^2) \cosh(\beta^2 \sigma_{--}^2 + \beta^2 \sigma_{+-}^2) \left(\vec{Q}_1^{(\mu)} \cdot \vec{Q}_2^{(\nu)} + \vec{Q}_1^{(\mu)} \times \vec{Q}_2^{(\nu)} \right) \ln R_{12} \right]$$

$$\times \left[1 + 16 y^4 (g - g')^2 \cosh(\beta^2 \sigma_{++}^2 - \beta^2 \sigma_{+-}^2) \cosh(\beta^2 \sigma_{--}^2 - \beta^2 \sigma_{+-}^2) \left(\vec{Q}_1^{(\mu)} \cdot \vec{Q}_2^{(\nu)} - \vec{Q}_1^{(\mu)} \times \vec{Q}_2^{(\nu)} \right) \ln R_{12} \right]$$

$$\times \left[1 - 2\pi y^4 e^{-\frac{\beta^2}{2}(\sigma_{++}^2 (q_+^{(\mu)} q_+^{(\nu)})^2 + \sigma_{+-}^2 (q_+^{(\mu)} q_-^{(\nu)})^2 + \sigma_{+-}^2 (q_+^{(\mu)} q_-^{(\nu)}) + \sigma_{--}^2 (q_-^{(\mu)} q_-^{(\nu)})^2)} \int dr r^{1 - \beta(g \vec{q}^{(\mu)} \cdot \vec{q}^{(\mu)} + g' \vec{q}^{(\mu)} \times \vec{q}^{(\mu)})} \right]. \tag{G18}$$

The next step is the summation over all possible ± 1 charges of virtual vortices $\vec{q}^{(\mu)}, \vec{q}^{(\nu)}$ (the two replica indices mean two summations from 1 to n), which requires quite some algebra. The renormalized partition function $\bar{\mathcal{Z}}^n$ finally gives the RG flow

equations:

$$\frac{\partial g}{\partial \ell} = -8\pi(g+g')^2 y^4 \cosh(\beta^2\sigma_{++}^2 + \beta^2\sigma_{+-}^2)\cosh(\beta^2\sigma_{--}^2 + \beta^2\sigma_{+-}^2)$$
$$- 8\pi(g-g')^2 y^4 \cosh(\beta^2\sigma_{++}^2 - \beta^2\sigma_{+-}^2)\cosh(\beta^2\sigma_{--}^2 - \beta^2\sigma_{+-}^2),$$

$$\frac{\partial g'}{\partial \ell} = -\pi(g+g')^2 y^4 \cosh(\beta^2\sigma_{++}^2 + \beta^2\sigma_{+-}^2)\cosh(\beta^2\sigma_{--}^2 + \beta^2\sigma_{+-}^2)$$
$$- \pi(g-g')^2 y^4 \cosh(\beta^2\sigma_{++}^2 - \beta^2\sigma_{+-}^2)\cosh(\beta^2\sigma_{--}^2 - \beta^2\sigma_{+-}^2),$$

$$\frac{\partial y}{\partial \ell} = 2\pi\left[1 - g - g' - \frac{\beta^2}{4}(\sigma_{++}^2 + 2\sigma_{+-}^2 + \sigma_{--}^2)\right]y, \quad \frac{\partial \sigma_{\alpha\beta}^2}{\partial \ell} = -2\pi\beta^4\sigma_{\alpha\beta}^4 y^4. \tag{G19}$$

As discussed in the main text, the fixed point must lie either at $y = 0$ or $y \to \infty$, depending on the magnitude of $g + g' + \beta^2\sigma^2$. For $y \to 0$, three clean fixed points remain, which flow to zero disorder: These correspond to PC, FI, and conductor. The disordered fixed point also has $y \to 0$ but the disorder is nonzero: This is the CDW phase from the mean-field analysis, the dirty analog of the insulator. Finally, when $y \to \infty$ and nonzero σ^2 at the fixed point, we expect glassy behavior.

[1] M. Cross and P. Hohenberg, Pattern formation outside of equilibrium, Rev. Mod. Phys. **65**, 851 (1993).

[2] M. I. Rabinovich, A. B. Ezersky, and P. D. Weidman, *The Dynamics of Patterns* (World Scientific, Singapore, 2000).

[3] C. Denz, M. Schwab, and C. Weilnau, *Transverse Pattern Formation in Photorefractive Optics* (Springer, Berlin, 2003).

[4] L. I. Pismen, *Vortices in Nonlinear Fields* (Oxford University Press, London, 1999).

[5] A. Auerbach, *Interacting Electrons and Quantum Magnetism* (Springer, Berlin, 1994).

[6] E. Fradkin, *Field Theories of Condensed Matter Systems* (Addison-Wesley, Redwood City, CA, 1991).

[7] A. M. Tsvelik, *Quantum Field Theory in Condensed Matter Physics* (Cambridge University Press, Cambridge, UK, 2003).

[8] P. Cvitanović, R. Artuso, R. Mainieri, G. Tanner, and G. Vattay, ChaosBook.org version 15 [chaosbook.org].

[9] L. Leuzzi, C. Conti, V. Folli, L. Angelani, and G. Ruocco, Phase Diagram and Complexity of Mode-Locked Laser: From Order to Disorder, Phys. Rev. Lett. **102**, 083901 (2009).

[10] C. Conti and L. Leuzzi, Complexity of waves in nonlinear disordered media, Phys. Rev. B **83**, 134204 (2011).

[11] F. Antenucci, C. Conti, A. Crisanti, and L. Leuzzi, General Phase Diagram of Aultimodal Ordered and Disordered Lasers in Closed and Open Cavities, Phys. Rev. Lett. **114**, 043901 (2015).

[12] F. Antenucci, A. Crisanti, and L. Leuzzi, Complex spherical 2 + 4 spin glass: A model for nonlinear optics in random media, Phys. Rev. A **91**, 053816 (2015).

[13] N. Ghofraniha, I. Viola, F. Di Maria, G. Barbarella, G. Gigli, L. Leuzzi, and C. Conti, Experimental evidence of replica symmetry breaking in random lasers, Nat. Commun. **6**, 6058 (2015).

[14] M. C. Rechtsman, J. M. Zeuner, Y. Plotnik, Y. Lumer, D. Podolsky, F. Dreisow, S. Nolte, M. Segev, and A. Szameit, Photonic Floquet topological insulators, Nature (London) **496**, 196 (2013).

[15] Y. Plotnik, M. Rechtsman, D. Song, M. Heinrich, J. Zeuner, S. Nolte, Y. Lumer, N. Malkova, J. Xu, A. Szameit, Z. Chen, and M. Segev, Observation of unconventional egde states in "photonic graphene," Nat. Mater. **13**, 57 (2014).

[16] R. Rajaraman, *Solitons and Instantons* (North Holland, Amsterdam, 1989).

[17] M. S. Petrović, M. R. Belić, C. Denz, and Yu. S. Kivshar, Counterpropagating optical beams and solitons, Lasers Photon. Rev. **5**, 214 (2011).

[18] M. I. Rodas-Verde, H. Michinel, and Yu. S. Kivshar, Dynamics of vector solitons and vortices in two-dimensional photonic lattices, Opt. Lett. **31**, 607 (2006).

[19] T. J. Alexander, A. S. Desyatnikov, and Yu. S. Kivshar, Multivortex solitons in triangular photonic lattices, Opt. Lett. **32**, 1293 (2007).

[20] B. Terhalle, T. Richter, A. S. Desyatnikov, D. N. Neshev, W. Krolikowski, F. Kaiser, C. Denz, and Yu. S. Kivshar, Observation of Multivortex Solitons in Photonic Lattices, Phys. Rev. Lett **101**, 013903 (2008).

[21] D. Y. Tang, H. Zhang, L. M. Zhao, and X. Wu, Observation of High-Order Polarization-Locked Vector Solitons in a Fiber Laser, Phys. Rev. Lett. **101**, 153904 (2008).

[22] H. Zhang, D. Y. Tang, L. M. Zhao, and X. Wu, Dark pulse emission of a fiber laser, Phys. Rev. A **80**, 045803 (2009).

[23] V. L. Berezinsky, Destruction of long-range order in one-dimensional and two-dimensional systems having a continuous symmetry group. I Classical systems, Sov. Phys. JETP **32**, 493 (1971); J. Kosterlitz and D. Thouless, Ordering, metastability and phase transitions in two-dimensional systems, J. Phys. C **6**, 1181 (1973).

[24] H. Kleinert, *Superflow and Vortex Lines*, Vol. 1 of Gauge Fields in Condensed Matter (World Scientific, Singapore, 1989).

[25] P. W. Anderson, Two new vortex liquids, Nat. Phys. **3**, 160 (2007).

[26] A. L. Fetter, Rotating trapped Bose-Einstein condensates, Rev. Mod. Phys. **81**, 647 (2009).

[27] J. D. Sau and S. Sachdev, Mean-field theory of competing orders in metals with antiferromagnetic exchange interactions, Phys. Rev. B **89**, 075129 (2014).

[28] E. Babaev, J. Carlström, M. Silaev, and J. M. Speight, Type 1.5-superconductivity in multicomponent systems, Phys. C **533**, 20 (2017).

[29] M. Silaev and E. Babev, Microscopic derivation of two-component Ginzburg-Landau model and conditions of its applicability in two-band systems, Phys. Rev. B **85**, 134514 (2012).

[30] X. Ma, R. Driben, B. Malomed, T. Meoer, and S. Schumacher, Two-dimensional symbiotic solitons and vortices in binary

condensates with attractive cross-species interaction, Nat. Sci. Rep. **6**, 34847 (2016).

[31] M. Petrović, D. Jović, M. Belić, J. Schröder, P. Jander and C. Denz, Two Dimensional Counterpropagating Spatial Solitons in Photorefractive Crystals, Phys. Rev. Lett **95**, 053901 (2005).

[32] D. M. Jović, M. S. Petrović, and M. R. Belić, Counterpropagating pattern dynamics: From narrow to broad beams, Opt. Commun. **281**, 2291 (2008).

[33] M. S. Petrović, D. M. Jović, M. S. Belić, and S. Prvanović, Angular momentum transfer in optically induced photonic lattices, Phys. Rev. A **76**, 023820 (2007).

[34] M. Petrović, D. Träger, A. Strinić, M. Belić, J. Schröder, and C. Denz, Solitonic lattices in photorefractive crystals, Phys. Rev. E **68**, 055601(R) (2003).

[35] M. S. Petrović, Counterpropagating mutually incoherent vortex-induced rotating structures in optical photonic lattices, Opt. Exp. **14**, 9415 (2006).

[36] B. Terhalle, T. Richter, K. Law, D. Göries, P. Rose, T. Alexander, P. Kevrekidis, A. Desyatnikov, W. Krolikowski, F. Kaiser, C. Denz, and Yu. S. Kivshar, Observation of double-charge discrete vortex solitons in hexagonal photonic lattices, Phys. Rev. A **79**, 043821 (2009).

[37] D. M. Jović, S. Prvanović, R. D. Jovanović, and M. S. Petrović, Gaussian induced rotation in periodic photonic lattices, Opt. Lett. **32**, 1857 (2007).

[38] S. Sachdev, *Quantum Phase Transitions* (Cambridge University Press, Cambridge, UK, 1999).

[39] N. Hasselmann, A. H. C. Neto, and C. M. Smith, Spin-glass phase of cuprates, Phys. Rev. B **69**, 014424 (2003).

[40] V. Juričić, L. Benfatto, A. O. Caldeira, and C. Morais Smith, Dynamics of Topological Defects in a Spiral: A Scenario for the Spin-Glass Phase of Cuprates, Phys. Rev. Lett **92**, 137202 (2004).

[41] M. Mezard, G. Parisi, and M. A. Virasoro, *Spin Glass Theory and Beyond* (World Scientific, Singapore, 1987).

[42] T. Castellani and A. Cavagna, Spin-glass theory for pedestrians, J. Stat. Mech. (2005) P05012.

[43] A. Perret, Z. Ristivojevic, P. Le Doussal, G. Schehr, and K. Wiese, Super-Rough Glassy Phase of the Random Field XY Model in Two Dimensions, Phys. Rev. Lett. **109**, 157205 (2012).

[44] C. A. Bolle, V. Aksyuk, F. Pardo, P. L. Gammel, E. Zeldov, E. Bucher, R. Boie, D. J. Bishop, and D. R. Nelson, Observation of mesoscopic vortex physics using micromechanical oscillators, Nature (London) **399**, 43 (1999).

[45] S. Bogner, T. Emig, A. Taha, and C. Zeng, Test of replica theory: Thermodynamics of two-dimensional model systems with quenched disorder, Phys. Rev. B **69**, 104420 (2004).

[46] A. Crisanti and L. Leuzzi, Spherical $2 + p$ glass model: An analytically solvable model with a glass-to-glass transition, Phys. Rev. B **73**, 014412 (2006).

[47] V. Juričić, L. Benfatto, A. O. Caldeira, and C. Morais Smith, Dissipative dynamics of topological defects in frustrated Heisenberg spin systems, Phys. Rev. B **71**, 064421 (2005).

[48] L. Benfatto, M. Silva-Neto, V. Juričić, and C. Morais Smith, Derivation of the generalized nonlinear sigma model in the presence of the Dzyaloshinskii Moriya interaction, Phys. B (Amsterdam, Neth.) **378**, 449 (2006).

[49] V. Juričić, M. B. Silva-Neto, and C. Morais Smith, Lightly Doped as a Lifshitz Helimagnet, Phys. Rev. Lett. **96**, 077004 (2006).

[50] A. Gordon and B. Fisher, Phase transition theory of pulse formation in passively mode-locked lasers with dissipation and Kerr nonlinearity, Opt. Commun. **223**, 151 (2003).

[51] A. Gordon and B. Fischer, Phase Transition Theory of Many-Mode Ordering and Pulse Formation in Lasers, Phys. Rev. Lett **89**, 103901 (2002).

[52] N. D. Mermin, The topological theory of defects in ordered media, Rev. Mod. Phys. **51**, 591 (1979).

[53] M. Silaev and E. G. Babaev, Microscopic theory of type-1.5 superconductivity in multiband systems, Phys. Rev. B **84**, 094515 (2011).

[54] J. Cardy, *Scaling and Renormalization in Statistical Physics* (Cambridge University Press, Cambridge, UK, 1996).

[55] J. L. Cardy and S. Ostlund, Random symmetry-breaking fields and the XY model, Phys. Rev. B **25**, 6899 (1982).

[56] M. Castellana and G. Parisi, Non-perturbative effects in spin glasses, Nat. Sci. Rep. **5**, 8697 (2015).

[57] D. S. Fisher and D. A. Huse, Equilibrium behavior of the spin-glass ordered phase, Phys. Rev. B **38**, 386 (1988).

[58] J. Zaanen, Quantum phase transitions in cuprates: Stripes and antiferomagnetic supersolids, Phys. C (Amsterdam, Neth.) **317**, 217 (1999).

[59] O. Gat, A. Gordon, and B. Fischer, Solution of a statistical mechanics model for pulse formation in lasers, Phys. Rev. E **70**, 046108 (2004).

[60] R. Weill, A. Rosen, A. Gordon, O. Gat, and B. Fischer, Critical Behavior of Light in Mode-Locked Lasers, Phys. Rev. Lett **95**, 013903 (2005).

[61] O. Sandfuchs, F. Kaiser, and M. R. Belić, Dynamics of transverse waves and zigzag instabilities in photorefractive two-wave mixing with a feedback mirror, J. Opt. Soc. Am. B **18**, 505 (2001).

[62] O. Sandfuchs, F. Kaiser, and M. R. Belić, Self-organization and Fourier selection of optical patterns in a nonlinear photorefractive feedback system, Phys. Rev. A **64**, 063809 (2001).

[63] V. I. Arnol'd, V. S. Afraymovich, Yu. S. Il'yashenko, and L. P. Shil'nikov, *Bifurcation Theory and Catastrophe Theory* (Springer-Verlag, Berlin, 1994).

Spontaneous isotropy breaking for vortices in nonlinear left-handed metamaterials

Trivko Kukolj ⬤ *

*Scientific Computing Laboratory, Center for the Study of Complex Systems, Institute of Physics Belgrade, University of Belgrade, Serbia
and Department of Physics, Faculty of Sciences, University of Novi Sad, Trg Dositeja Obradovića 4, Novi Sad, Serbia*

Mihailo Čubrović ⬤ †

Scientific Computing Laboratory, Center for the Study of Complex Systems, Institute of Physics Belgrade, University of Belgrade, Serbia

We explore numerically and analytically the pattern formation and symmetry breaking of beams propagating through left-handed (negative) nonlinear metamaterials. When the input beam is a vortex with topological charge (winding number) Q, the initially circular (isotropic) beam acquires the symmetry of a polygon with Q, $2Q$, or $3Q$ sides, depending on the details of the response functions of the material. Within an effective field-theory model, this phenomenon turns out to be a case of spontaneous dynamical symmetry breaking described by a Landau-Ginzburg functional. Complex nonlinear dependence of the magnetic permittivity on the magnetic field of the beam plays a central role, as it introduces branch cuts in the mean-field solution, and permutations among different branches give rise to discrete symmetries of the patterns. By considering loop corrections in the effective Landau-Ginzburg field theory we obtain reasonably accurate predictions of the numerical results.

I. INTRODUCTION

The idea of a material with negative refraction index was first considered long before it could be realized in experiment, in the now famous paper by Veselago [1], in 1968. He considered a material with negative electric permeability ϵ *and* magnetic permittivity μ, and predicted a number of interesting properties in such systems, among them negative refraction. Only much later did it become possible to combine elements with negative ϵ and negative μ at a microscopic level, as a composite metamaterial. First experimental realizations were reported in [2,3]. Negativity, or left-handedness, is typically only achieved in a narrow frequency range, close to the resonant frequency of the conductive elements of the metamaterial. This was the original motivation for studying nonlinear effects in these systems. Nonlinearities can be strengthened by appropriate design at the microscopic level. The study of nonlinear phenomena in metamaterials started with [4]. This has become a broad and important field in metamaterials research [5]. Nonlinear phenomena like solitons [6,7], nonlinear surface waves [8], modulational instability [9,10], and ultrashort pulses [11] were observed. Other work in left-handed metamaterials relevant for our paper includes, among others, [12–20]. We have no intention of being exhaustive in this short review of the literature; we merely mention the results we have directly used or found particularly inspiring.

The focus of our paper is the dynamics of symmetry breaking in intensity patterns of electromagnetic waves propagating through a left-handed nonlinear metamaterial. Numerical solutions of the equations of motion reveal that circular

(usually Gaussian) input beams turn into polygonal patterns, with some discrete symmetry. This fits the textbook notion of symmetry breaking, more specifically dynamical symmetry breaking. The general theory of dynamical criticality is by now well developed [21] and has been applied to numerous systems [22]. In [22], a systematic theory of isotropy-breaking transition is presented, though mainly for periodic and quasiperiodic structures (convection in fluids, fluctuations in quasicrystals). The basic mechanism is that the system develops momentum eigenmodes of a fixed module but with multiple discrete directions on the sphere $|\mathbf{k}| = \mathrm{const}$ in momentum space. In nonlinear negative materials, the situation is complicated by the strong frequency dependence of the magnetic permittivity but the same basic logic remains. At a fundamental level, this situation can be understood from the viewpoint of a spatially nonuniform Landau-Ginzburg theory. Quantitative accuracy is, however, hard to achieve; this requires cumbersome perturbative calculations. Ultimately, numerical work is the best way to describe the patterns in detail; they look like polygons or, occasionally, necklaces, with C_{3Q}, C_{2Q}, or C_Q symmetry, depending on the parameter regime; here, Q is the topological charge of the beam, a property we will discuss in detail in the next paragraph. The paper [10] is very important in this context: it starts from the model derived in [9] and studies mainly necklace configurations, which consist of discrete beads (spots of high intensity) distributed more or less uniformly along a circle. The authors find the same C_{3Q} symmetry that we see. Our goal is to gain a detailed understanding of the phenomenon, and move beyond single beams toward collective behavior and interactions.

We have chosen to study this phenomenon on vortices, topologically nontrivial solutions where the phase of the

*trivko98@gmail.com
†mcubrovic@gmail.com

complex electric and magnetic field winds one or more times along a closed line encircling the vortex core. Vortices appear in many systems described by a complex field, i.e., a field with U(1) phase invariance [23,24]. In optics, this is just the complex beam envelope of the electric and magnetic field. The phase of any complex wave function or field can wind along some closed line around a defect, forming a vortex. Famously, vortices may coexist with the superconducting order [U(1) symmetry breaking] in type-II superconductors or they may exist only in the normal phase, upon destroying the superconductivity (type I). Pattern-forming systems like fluids and soft matter often have rich vortex dynamics [22]. Other examples of vortex matter in nature arise in liquid helium [25], Bose-Einstein condensates [26], and magnetic systems [27]. In two spatial dimensions, interactions among the vortices lead to a vortex unbinding phase transition of infinite order found by Berezinsky, Kosterlitz, and Thouless for the planar XY model [28]. We study a three-dimensional metamaterial but with an elongated geometry, so we treat it as a $2 + 1$-dimensional system (the x and y coordinates are spatial dimensions and the z direction has the formal role of time). We therefore have a similar situation to the XY model but with different equations of motion and different phenomena.

In addition to direct numerical and analytical study of the equations of motion, we also propose an effective field-theory Lagrangian which gives slightly different equations but captures the key properties of the system. The Lagrangian form makes it easier to understand some of the phenomenology we find in numerical simulations; the foundations of the symmetry breaking are obtained from this model in a natural way. Numerical work is done with original equations of motion, as they are directly grounded in the microscopic physics. The Lagrangian is just a phenomenological tool to facilitate the theoretical understanding. It is difficult (and perhaps impossible) to package the exact original equations in a Lagrangian form because the system is strongly nonlinear *and* dissipative. Dissipative systems can be encapsulated in a Lagrangian (our Lagrangian is also dissipative) but with some limitations, and there is certainly no general method to write down a Lagrangian for a broad class of dissipative systems.

The structure of the paper is the following. In the next section we describe the model of a nonlinear left-handed metamaterial, following closely the wave propagation equations used in previous research, e.g., in [4,6,7] and others, which correspond to a specific experimentally realizable metamaterial. We also formulate and motivate the field-theory model of the system. In the third section, we describe our numerical findings, above all the anisotropy of the intensity patterns. The fourth section offers the theoretical explanation for the patterns: first by a direct approximate solution of the propagation equations, and then also from field theory, which makes the physics of the symmetry breaking particularly clear. In the fifth section we briefly discuss how to check our predictions in experiment and how prominent the effects of symmetry breaking are compared to other possible instabilities in realistic metamaterials. The last section sums up the conclusions. We have included some long calculations in the Appendices.

II. WAVE EQUATIONS IN A NONLINEAR LEFT-HANDED METAMATERIAL

We adopt the model of [4,7] to describe a left-handed metamaterial with a nonlinear response. Microscopically, the material is realized as a lattice of split-ring resonators and wires. In the terahertz range, this is an experimentally well-studied system [3]. In [6], a detailed microscopic derivation is given, starting from the current transport equations in the resonator-wire system. The outcome is a nonlinearity similar to that postulated phenomenologically in [4]. We adopt essentially the same model, described by the electric permeability ϵ and the magnetic permittivity μ:

$$\epsilon(E, E^\dagger) \equiv \epsilon(|E|^2) = (\epsilon_{D0} + \alpha|E|^2)\left(1 - \frac{\omega_0^2}{\omega(\omega + \iota\gamma)}\right), \quad (1)$$

$$\mu(H, H^\dagger) \equiv \mu(|H|^2) = 1 + \frac{F\omega^2}{\omega_{0NL}^2(|H|^2) - \omega^2 + \iota\Gamma\omega}, \quad (2)$$

with $\alpha = 1$ or -1 for self-focusing or self-defocusing nonlinearity, respectively. Frequency is denoted by ω and ϵ_{D0} is the linear part of the permittivity. By F, γ, and Γ we denote the filling factor of the material and the electric and magnetic damping coefficients. Equations (1) and (2) allow us to model also the real (lossless) dielectric response by putting $\gamma = 0$. For the magnetic field, the permittivity will in general stay complex even for $\Gamma = 0$, as the nonlinear frequency of the resonator rings ω_{0NL} can always have a nonzero imaginary part. This frequency is related to the magnetic field through the relation ($X \equiv \omega_{0NL}/\omega_0$):

$$|H|^2 = \alpha A^2 \frac{(1 - X^2)[(X^2 - \Omega^2)^2 + \Omega^2\gamma^2]}{X^6}, \quad (3)$$

where $\Omega \equiv \omega/\omega_0$, ω_0 is the eigenfrequency of the rings, and A is a parameter which can be derived microscopically [4,6,7]; for our purposes, it can be treated just as a phenomenological parameter. This cubic equation yields three branches for ω_{0NL}^2. All these branches are physical and correspond to different possible nonlinear oscillations [7]. Now the equations of motion are just the Maxwell equations in a medium described by (1) and (2), in the approximation of slowly changing beam envelopes. We assume an elongated (cylindrical or parallelepipedal) slab of metamaterial, so we can employ the paraxial beam approximation (e.g., [29]). The beam is initially collimated along the longitudinal axis z and focuses or defocuses slowly in the transverse x-y plane due to the nonlinearity of the material. The electric and magnetic field $\hat{E}(t; x, y, z)$ and $\hat{H}(t; x, y, z)$ are directed along the z axis. From now on, the speed of light is put to unity, $c = 1$. All the steps in deriving the nonlinear Schrödinger-like equation are well known so we merely state the final result here, which is quite close to the equations used in [13] in $1 + 1$ dimension, or the equations found in [9–11]. Full derivation can be found in Appendix A. The equations of motion turn out to be

$$-\frac{\iota}{b}\partial_z E = \nabla_\perp^2 E + [\omega^2\epsilon(|E|^2)\mu(|H|^2) - k^2]E$$

$$- \frac{\nabla_\perp\mu(|H|^2)}{\mu(|H|^2)}\nabla_\perp E - \iota\frac{\partial_z\mu(|H|^2)}{2\mu(|H|^2)}E, \quad (4)$$

$$-\frac{\iota}{b}\partial_z H = \nabla_\perp^2 H + [\omega^2\epsilon(|E|^2)\mu(|H|^2) - k^2]H. \quad (5)$$

Here, $\boldsymbol{\nabla}_\perp \equiv (\partial_x, \partial_y)$ is the nabla operator in the transverse plane, k is the wave vector along the z direction, and b is the characteristic propagation length along the z axis. Equations of motion (4) and (5) together with the equations (1) and (3) for the permittivities contain the following five parameters: $\epsilon_{D0}, F, \Gamma, \gamma$, and ω_0. Realistic values for all the parameters are discussed in [7]. The natural length scale of the model is dominated by the $1/\omega_0$ scale. Dimensional analysis of the terms on the right-hand side of (4) determines the length scale b in (4) and (5) as $b \sim 1/\omega_0$. Both in analytical and in numerical calculations, we express the transverse coordinates (x, y) in millimeters but the longitudinal coordinate z is often stated in units of b. This is because the length scales of all patterns in the transverse plane are similar whereas the propagation lengths along z can vary by an order of magnitude as γ and Ω are varied, so it is more natural to express them in terms of the characteristic distance b.

A. field-theoretical model

For some theoretical considerations it is useful to formulate a Lagrangian (gradient) model which captures the essential features of the equations of motion (4) and (5). As it often happens in studies of complex nonlinear pattern-forming systems, we cannot easily write the original equations in such a form. Instead, we construct a field theory which yields equations of motion somewhat different from the original ones but which still give the same phenomenology, and are able to explain the results of numerical calculations with the equations (4) and (5).

Let us think what such a field theory would look like. The terms with the gradient of magnetic permittivity obviously introduce dissipation, which physically originates from the losses in the inductive rings of the metamaterial. In general, dissipative systems do not have a Lagrangian, although a number of generalized Lagrangian approaches exist for dissipative systems: either with more general functional forms of the Lagrangian, or with a dissipative function in addition to the Lagrangian, or with extra degrees of freedom [30,31]. We will take the first, most conventional of the three approaches: we will consider a conventional Lagrangian (no dissipative function, no extra degrees of freedom) which gives slightly generalized equations of motion compared to (4) and (5), with dissipative terms for both electric and magnetic fields coming from the complex terms in the effective potential. The effective action reads

$$
\begin{aligned}
\mathcal{L} &= \mathcal{L}_E + \mathcal{L}_H, \\
\mathcal{L}_E &= \frac{\iota}{2\mu(|H|^2)}(E\partial_z E^\dagger - E^\dagger \partial_z E) \\
&\quad + \frac{|\boldsymbol{\nabla}_\perp E|^2}{\mu(|H|^2)} + \frac{k^2|E|^2}{\mu(|H|^2)} - \omega^2 \epsilon(|E|^2)|E|^2, \\
\mathcal{L}_H &= \frac{\iota}{2\epsilon(|E|^2)}(H\partial_z H^\dagger - H^\dagger \partial_z H) \\
&\quad + \frac{|\boldsymbol{\nabla}_\perp H|^2}{\epsilon(|E|^2)} + \frac{k^2|H|^2}{\epsilon(|E|^2)} - \omega^2 \int_0^{HH^\dagger} dx\,\mu(x). \quad (6)
\end{aligned}
$$

The last term in $\mathcal{L}_E$ equals $-\omega^2 \int_0^{EE^\dagger} dx\,\epsilon(x)$, analogously to the corresponding term in $\mathcal{L}_H$, but since ϵ is polynomial in

$E^\dagger E$ the integral can be solved explicitly. Now (6) gives the equations of motion:

$$
\begin{aligned}
-\frac{\iota}{b}\partial_z E &= \boldsymbol{\nabla}_\perp^2 E + [\epsilon(|E|^2)\mu(|H|^2) - k^2]E \\
&\quad - \frac{\iota\partial_z\mu(|H|^2)}{\mu(|H|^2)}E - \frac{\boldsymbol{\nabla}_\perp\mu(|H|^2)}{\mu(|H|^2)}\boldsymbol{\nabla}_\perp E - \Phi_H, \quad (7)
\end{aligned}
$$

$$
\begin{aligned}
-\frac{\iota}{b}\partial_z H &= \boldsymbol{\nabla}_\perp^2 H + [\epsilon(|E|^2)\mu(|H|^2) - k^2]H \\
&\quad - \frac{\iota\partial_z\epsilon(|E|^2)}{\epsilon(|E|^2)}H - \frac{\boldsymbol{\nabla}_\perp\epsilon(|E|^2)}{\epsilon(|E|^2)}\boldsymbol{\nabla}_\perp H - \Phi_E, \quad (8)
\end{aligned}
$$

where $\Phi_{E,H}$ are related to the fluxes of the electric and magnetic field (prime denotes the derivative of ϵ and μ with respect to their arguments $E^\dagger E$ and $H^\dagger H$):

$$
\begin{aligned}
\Phi_H &= \frac{\epsilon'(|E|^2)}{\epsilon^2(|E|^2)}\bigg(\frac{\iota}{2}(H\partial_z H^\dagger - H^\dagger\partial_z H) \\
&\quad + |\boldsymbol{\nabla}_\perp H|^2 + k^2|H|^2\bigg), \quad (9)
\end{aligned}
$$

$$
\begin{aligned}
\Phi_E &= \frac{\mu'(|H|^2)}{\mu^2(|H|^2)}\bigg(\frac{\iota}{2}(E\partial_z E^\dagger - E^\dagger\partial_z E) \\
&\quad + |\boldsymbol{\nabla}_\perp E|^2 + k^2|E|^2\bigg). \quad (10)
\end{aligned}
$$

These are the extra terms compared to the physical equations (4) and (5).[1] Inserting $\partial_z E^\pm$ from the equations of motion (7) and (8) into the above we derive

$$
\Phi_E = \frac{\mu'}{\mu}\boldsymbol{\nabla}_\perp\bigg(\frac{E\boldsymbol{\nabla}_\perp E^\dagger - E^\dagger\boldsymbol{\nabla}_\perp E}{\mu}\bigg), \quad (11)
$$

and analogously for Φ_H, with $\epsilon \leftrightarrow \mu, E \leftrightarrow H$. This term is proportional to a total derivative, and is therefore related to the flux $(E\boldsymbol{\nabla}_\perp E^\dagger - E^\dagger\boldsymbol{\nabla}_\perp E)/\mu$. For slowly changing ϵ and μ, which is often the case in our system (i.e., for $\epsilon', \mu' \ll \epsilon, \mu$), this term is small, which partly justifies the choice (6) for the Lagrangian. But the ultimate justification, as it frequently happens, is that *a posteriori* we will find that this model is able to explain the features observed in the numerics. Therefore we will not try to interpret the term (11) in detail.

III. GEOMETRY AND STABILITY OF VORTICES

We will now sum up our numerical results which demonstrate the breaking of the circular symmetry of the vortex beams and their decay during the propagation. We always start from a Gaussian input beam with a topological charge Q, of the form $E(r, \phi; z = 0) = E_0 \times e^{-r^2/2\sigma^2}e^{iQ\phi}$ and analogously for the magnetic field, with amplitude H_0 but with the same vortex charge Q. Therefore, we always give an exact vortex as an input. The parameters of the model were chosen so that the permittivities ϵ and μ, given by (1) and (2), respectively, are of order unity. This serves to limit the dissipative effects, so that the propagation along the longitudinal direction can be clearly observed. Same phenomena are found for arbitrary values of

---

[1]The dissipative term proportional to $\boldsymbol{\nabla}_\perp H$ in (8) is also absent in the original equations, but that one is easy to interpret: we make both $\mathcal{L}_E$ and $\mathcal{L}_H$ complex, so both fields have dissipative dynamics.
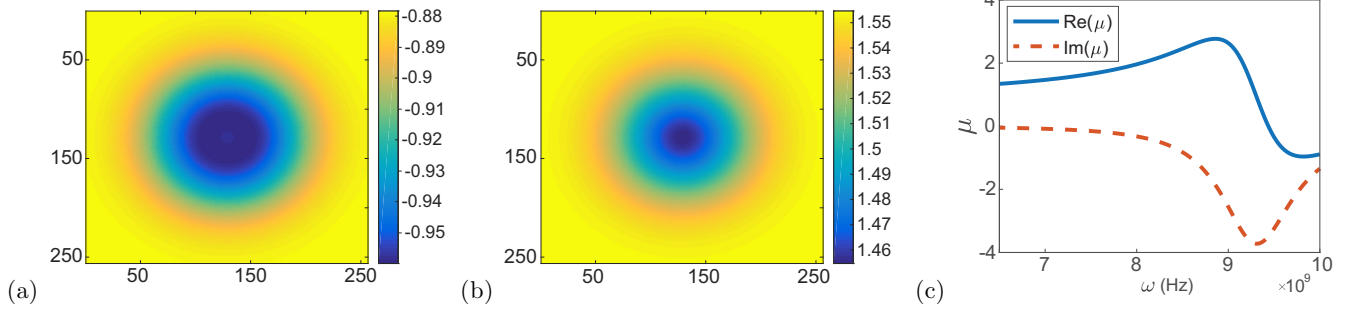
FIG. 1. The radial profile of μ for a left-handed medium (a) and a right-handed medium (b), for a vortex of charge $Q = 1$. The profiles are radially symmetric in accordance with the fact that μ depends strictly on the magnitude of the magnetic-field vector $|H|^2$. The real (blue) and imaginary (red) values of the complex permeability μ vs the frequency of the beam ω are displayed in (c). For frequencies higher than the eigenfrequency of the resonator rings ω_0, the real part of the permeability is negative, essentially yielding a left-handed medium. The figure is made for dissipative ϵ; for lossless ϵ the behavior is similar.

ϵ and μ but on a different length scale. We do not aim at a stamp-collecting exhaustive description of patterns for all possible parameter values, so we will focus on just a few relevant cases. We are mainly interested in left-handed materials ($\epsilon, \mu < 0$) and how they compare to right-handed ones, so for the dielectric constant we always choose the self-defocusing Kerr nonlinearity ($\alpha = -1$) with a linear part $\epsilon_{D0} = 12.8$, which has both a left-handed and a right-handed regime. To check the effects of dissipation, we either adopt $\gamma = 0$ in (1), i.e., the lossless case, or we tune γ so that $\omega_0^2/(\omega^2 + \iota\gamma\omega) = 1/2$. In other words, we impose either $\mathrm{Im}\epsilon = 0$ or $\mathrm{Im}\epsilon = \mathrm{Re}\epsilon$. This is for simplicity and to avoid probing a huge parameter space for all possible γ values; from now on we will call these cases simply lossless ϵ and dissipative ϵ. The filling factor is $F = 0.4$ and the magnetic dampening coefficient is $\Gamma = 10^9$ Hz; these values are kept fixed in all calculations. Numerical calculations are performed with an operator split algorithm described in detail in the Appendices of [32].

The nonlinear frequency of the oscillator rings is obtained as a solution to (3). Of the three branches of the solution, we take the one that yields a negative real value of μ for $\omega > \omega_0$ (Fig. 1). We have freely taken $\omega = 9.8 \times 10^9$ Hz to represent a left-handed medium, and $\omega = 7.0 \times 10^9$ Hz to represent a right-handed medium. The transverse profiles are displayed in Fig. 1. We see there is a well-defined left-handed regime.

Now we discuss the transverse intensity profile for different initial beam configurations, with vortex input beams as explained in the beginning. We observe the following features.

(1) Circular symmetry of the vortex input always breaks down to a discrete group.

(a) In a dissipative left-handed medium, the discrete symmetry group for a vortex of charge Q is C_{3Q}, before breaking down to simple C_2 axial symmetry at longer distances [Fig. 2(a)].

(b) In a dissipative right-handed medium, the discrete symmetry group for a vortex of charge Q is C_{2Q}, before breaking to C_Q and then to C_2 axial symmetry at longer distances [Fig. 2(b)].

(c) In a lossless left-handed medium, the discrete symmetry group for a vortex of charge Q is C_{3Q} for very short distances, before quickly breaking down to C_Q and finally C_2 [Fig. 2(c)].

(d) In a lossless right-handed medium, the discrete symmetry group for a vortex of charge Q is C_{2Q}, before breaking to simple C_2 axial symmetry at longer distances [Fig. 2(d)].

(2) Vortices decay approximately exponentially as they propagate along the longitudinal axis. Figure 4 shows the intensity of the beam across the z axis, for various regimes. At early z values, total intensity may behave nonmonotonically and nonuniversally but on longer scales it decays exponentially. For different charges, the intensity curves collapse to a unique exponential function at large z. As could be expected, lossless and dissipative cases differ somewhat and collapse to different curves.

The bottom line is that there is a vocabulary of patterns with C_Q, C_{2Q}, and C_{3Q} symmetries. One of them dominates in each case (left and right handed, dissipative and lossless) but at longer propagation distances the symmetry can change, before the intensity drops to near zero from dissipation. The final stadium of C_2 symmetry is only seen at very low intensities, so it might be practically unobservable in experiment; that is why we say the vocabulary only has three possible patterns, excluding C_2.

The findings above are further corroborated by Fig. 3, which shows the vortices with different charges $Q = 1, 2,$ and 3 in the same regime [dissipative left handed (a) and lossless left handed (b)]. As claimed above, the symmetry is C_{3Q} in panel (a), and (except at small z values) C_Q in panel (b). Finally, it is obvious that there is some mixing of patterns: the polygons are never exactly regular, so the groups C_n are certainly not exact symmetries; we use the C_n nomenclature merely for convenience.

One interesting phenomenon in Fig. 2(c) is that the pattern rotates along the z axis. This can be understood as excitation of multiple angular modes (of the form $e^{\iota l z}$ with various l numbers) as the beam travels along the sample. This is a well-known consequence of nonlinear terms [5,29] and typically depends on the relative strength of nonlinear mode interactions compared to energy density $|E|^2 + |H|^2$ and dissipation γ. We will not explore it in quantitative detail in this paper as it is only tangential to our main topic of radial symmetry breaking; as one can see, the structure remains the same; just the orientation changes.
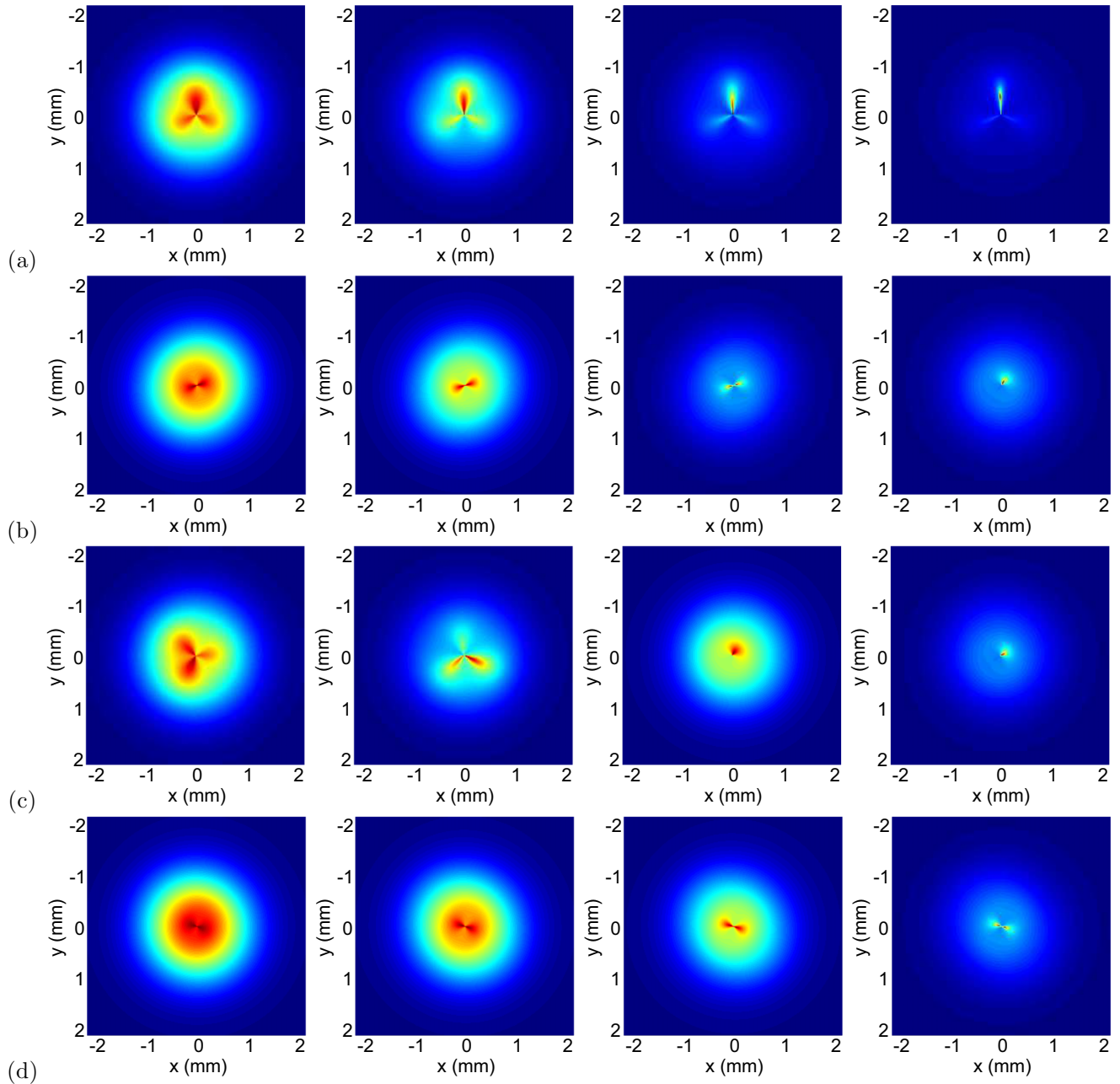
FIG. 2. The patterns for a $Q = 1$ vortex, in a left- and right-handed dissipative medium [(a) and (b), respectively], and in a left- and right-handed lossless medium [(c) and (d), respectively], at longitudinal slices $z = 2b, 4b, 6b,$ and $8b$, showing the $C_{3Q}, C_{2Q}, C_{3Q}/C_Q,$ and C_{2Q} regimes. The remaining parameters are defined in the text at the beginning of this section.

One might rightly worry that the initial conditions which contain a vortex in both electric and magnetic field are not very realistic, as in most materials the electric field dominates the optical response. Therefore, in experimental practice, one typically prepares a vortex in the electric field making use of phase masks or some other method, and the initial magnetic-field distribution is completely analytic. In Appendix B we repeat the calculations from Fig. 3 and show that the outcome is the same, including the vocabulary of patterns and their C_n shapes. Therefore, the E-H symmetric ansatz is merely a matter of convenience, and the realistic regime where $|H| \ll |E|$ is in fact covered by our paper.

Figure 4 shows that at long times the decay of intensity is universal for given dielectric dampening coefficient γ, which suggests the main mechanism of dissipation is in fact the radiative loss. This is because we deliberately chose ϵ and μ with small imaginary parts (for ϵ it can also be zero), so the losses in the medium are not so important when it comes to total energy (they are still important for being nonlinear and influencing the patterns). One important difference between the lossless medium (black and blue symbols in Fig. 4) and the dissipative medium (red, magenta) is that the former has a short interval of growing intensity, before reaching the universal regime of radiative decay. The physical reason is
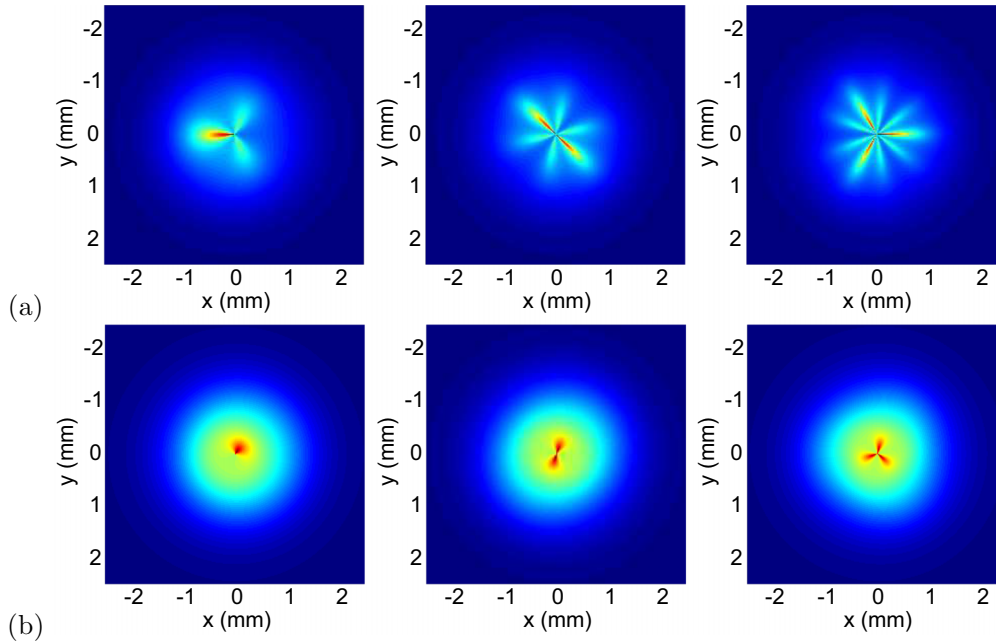
FIG. 3. The patterns for $Q = 1, 2,$ and 3 vortices (left to right), in a dissipative (a) and lossless (b) left-handed metamaterial. The behavior for three different charges confirms the previous conclusions for the type of symmetry encountered. All parameters except for the vortex charge are the same as for Fig. 2. The propagation distance is $z = 5b$ in (a) and $z = 8b$ in (b).

that the polarization, i.e., the rearrangement of charges in the self-defocusing metamaterial, reduces the overall electrostatic potential energy of the medium, and this energy becomes available to the beam, increasing its intensity. Clearly, once the radiative losses overcome the total potential energy available, the intensity decays. The growth is clearly a transient effect which cannot persist for long z intervals. A formal way to understand this is that the nonconservation of energy is encoded by the last term in (4), which can have a positive or

FIG. 4. Decay of the total intensity $I = \int dx \int dy (E^2 + H^2)$ in computational units for $Q = 1$ and 2, for a lossless (blue circles, black stars) and dissipative (red squares, magenta triangles) left-handed material. At early times the behavior is complicated and nonuniversal but at late times it collapses to an exponential curve. This is expected when loss through radiation dominates. The oscillatory features of the $Q = 2$ lossless case (black) are likely due to finite numerical resolution.

negative imaginary part depending on the sign of $\partial_z \mu / \mu$. At large values of z, we expect to enter a universal regime where this sign is constant, because the radiation loss dominates over nonlinearities and the exchange of energy between the beam and the medium; this is the universal decay regime in the figure.

IV. THE THEORY OF VORTEX EVOLUTION

The phenomenology described in the previous section can be understood on several levels. At the crudest level, we can introduce a variable-separation ansatz in the equations of motion and then linearize them in the amplitude (but not in the phase). This picture explains the C_{2Q} patterns, but not the C_{3Q} and C_Q regimes. It also does not explain the instabilities, that is, the changes and disappearance of patterns during the z propagation. For the full picture it is necessary to take into account the nonlinear effects through the loop corrections, i.e., to move perturbatively beyond the amplitude-linearized solution. A qualitative insight of the symmetry breaking can, however, be obtained also in a simpler and more elegant way, directly from the symmetry analysis of the model Lagrangian (6). Therefore, after finishing the amplitude-linearized analysis and the loop corrections from nonlinearity, we will obtain the same results from a unified mean-field treatment of the (nonlinear) model Lagrangian.

A note on terminology is in order. The solutions we find are not the textbook type of vortex with phase dependence solely of the type $e^{iQ\phi}$; rather, the dependence on the phase is more complicated, i.e., the phase is doing more than just the winding, but it is still true that the circulation of the phase around some point (the location of the vortex core) is an integer—the topological charge of the vortex. Such solutions are sometimes called spirals [22] whereas the term

"vortex" is reserved for the simple winding-phase solutions. We nevertheless stick to the widespread term "vortex" for any topologically charged solution under the fundamental group of the U(1) phase symmetry.

A. Amplitude-linearized solution

We will separate variables in the equations of motion (4) and (5) [or the Lagrangian equations (7) and (8), which do not differ from the original equations at the amplitude-linearized level] and then plug in the vortex ansatz. The vortex ansatz is a solution which has a winding phase Φ with some winding number Q, for a constant (averaged) value of the permittivity $\mu_c = $ const, because we ignore the nonlinear dependence of μ on $|H|$. The vortex solution of winding number (topological charge) Q in cylindrical coordinates (r, ϕ, z) can be separated into regular and vortex parts:

$$E = E_{\text{reg}} + E_{\text{vort}}. \tag{12}$$

We represent the vortex part as

$$E_{\text{vort}}(r, \phi, z) = Z_E(z) R_E(r) e^{\iota Q\phi - \iota \Phi(\phi)}, \tag{13}$$

and analogously for the magnetic field. Along the z axis we get $Z_E(z) = e^{\iota \lambda z}$ as expected, and the eigenvalue λ is arbitrary for now, i.e., it is determined by the boundary conditions along the z axis. Upon inserting (13) into (4), the equation separates into the angular part and the radial part. The former reads

$$\Phi'' - \iota(\Phi')^2 + 2\iota Q\Phi' + \iota l^2 = 0, \tag{14}$$

where l is the eigenvalue of the angular part. This is the crucial equation—the phase dynamics is nonlinear because μ is in general complex and the terms with $\nabla_\perp \mu$ contain nonlinear dependence on the phase. The equation is easily solved by first introducing $w \equiv \Phi'$ and then reducing it to quadratures. The outcome is

$$\Phi(\phi) = \cos(\sqrt{Q^2 + l^2}\phi + C_l). \tag{15}$$

In other words, we still stay with a winding solution but various winding numbers (equal to $\sqrt{Q^2 + l^2}$) are possible when multiple modes are excited. Clearly, only the solutions with integer windings are physical, otherwise they would not be single valued. The most general solution is thus a superposition of solutions $Z_E(\lambda, l; z)\Phi_E(\lambda, l; \phi)R_E(\lambda, l; r)$ with different l modes so as to result in a single-valued function. Now the radial part acquires the form

$$R_E'' + \frac{1}{r}R_E' + \left(\frac{\lambda}{r^2} - k^2 + \epsilon_{D0}\tilde{\omega}^2\right)R_E + \frac{\alpha\mu_c\tilde{\omega}^2}{E_c^2}R_E^3 = 0, \tag{16}$$

with $\tilde{\omega} \equiv \omega[1 - \omega_0^2/(\omega^2 + \iota\omega\gamma)]$. If we disregard the cubic term (amplitude-linearized approximation),[2] the well-known solution in terms of Bessel functions is obtained:

$$R_E(r) \approx c_E^{(1)}(\lambda, l)J_{Q_l}(ar) + c_E^{(2)}(\lambda, l)Y_{Q_l}(ar),$$

$$Q_l \equiv \sqrt{Q^2 + l^2}, \quad a \equiv \sqrt{\lambda - \epsilon_{D0}\mu_c\tilde{\omega}/\omega E_0^2 - k^2}. \tag{17}$$

---

[2]This is justified at least in some interval of z values, as the system is dissipative and loses power $\int (E^2 + H^2)$, so the amplitude progressively decreases along z.
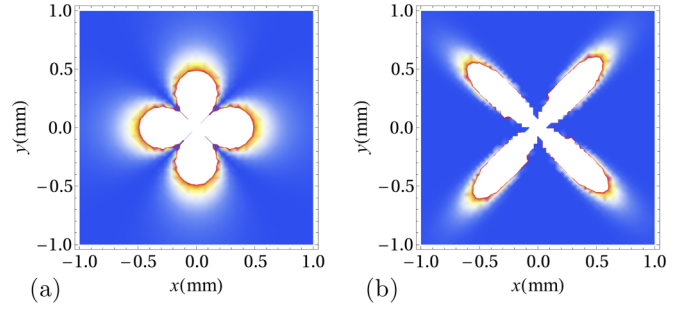
FIG. 5. Polygonal pattern $|E|^2$ for a vortex of charge $Q = 2$, for $k = 2$, $\epsilon_{D0} = 12.8$, and $\mu_c = 1.004$ (values of all parameters and constants in the main text), at radial slice $z = 1$, for a single vortex mode $l = 0$ (a), and for a linear combination of modes with $l = 0, 1$, and 2 decaying at infinity (b). The symmetry is $C_{2Q} = C_4$, which does not explain the C_Q and C_{3Q} regimes. Obviously, the crude picture of breaking the radial symmetry works but full explanation is lacking. It will come from the loop corrections.

Here, J and Y are the Bessel functions of first and second kind, respectively. Similar solutions $Z_H(z)$, $\Phi(\phi)$, and $R_H(r)$ are obtained for the magnetic field. The angular equation is identical for both fields: for this reason we have one solution Φ for both E and H. The eigenvalues λ and l and the values of the constants $c_{E,H}^{(1,2)}$ are determined by the boundary conditions. Obviously, (15) imposes the C_{2Q} symmetry, *if* $l = 0$. This simplest case is not necessarily the stable solution. We might have a sum over many l values. In principle, such sums may yield more complicated patterns, however we will see that when the physically reasonable boundary conditions are implemented (decay at infinity, single valuedness everywhere) one typically always has the robust C_{2Q} pattern. One important consequence of the fact that multiple l modes are possible is that due to nonlinear effects a new l mode can be created during the propagation along the z axis. We have already seen an example in Fig. 2(c). A quantitative analysis of this phenomenon requires a full nonlinear model and so can only be studied within the formalism of the next section.

This solution is not very satisfying but reproduces some of the features from the numerics, summarized at the start of the previous section: (1) the reduction of the full $O(2)$ symmetry down to a discrete symmetry C_n for some $n \in \mathbb{N}$, i.e., the polygonal form of the vortex, and (2) the value $n = 2Q$ is true in some but not in all situations. We show the solutions for a single angular mode from (15) and (17) in Fig. 5(a). In Fig. 5(b), we show a linear combination of angular modes with $l = 0, 1$, and 2, with the coefficients $c_{E,H}^{(1,2)}$ in (17) chosen so that the total intensity still decays sufficiently fast at infinity. The symmetry is still C_{2Q}. Apparently, the regimes with the C_Q and C_{3Q} symmetries require loop corrections from nonlinear μ to be taken into account.

B. Loop corrections

The origin of the breaking of radial symmetry is the fact that a discrete set of modes in Fourier space is selected. This is best seen from the Fourier transform of the solutions (15) and (17). We will calculate the propagator $G(\mathbf{u})$ at

constant z, i.e., the Fourier transform $\mathbf{r} \mapsto \mathbf{u}$ of the solution with a Dirac delta source. This source imposes the boundary condition $R_E(0) \to \infty$, $\int dr\, r \cos\phi R_E(r) = 1$, giving $c_E^{(1)} = 0$, $c_E^{(2)} = 2\pi/\Gamma(Q/2)$ in (17). Fourier transforming $(x, y) \mapsto (u_x, u_y)$ we get for a single mode (17), making use of the Bessel and Lommel integrals:

$$
\begin{aligned}
G_{E,H}(\mathbf{u}) = {} & \frac{2\pi}{\Gamma(Q/2)} \frac{e^{\iota Q(\pi/2+\phi)}}{au} \left(\frac{\sin[(u-a)\Lambda]}{u-a} - \frac{\cos[(u+a)\Lambda - \pi Q]}{u+a} \right) \\
& + \frac{2\pi}{\Gamma(Q/2)} \frac{e^{-\iota Q(\pi/2+\phi)}}{au} \left(\frac{\cos[(u-a)\Lambda + \pi Q]}{u-a} - \frac{\cos[(u+a)\Lambda]}{u+a} \right).
\end{aligned}
\tag{18}
$$

Here, Λ is the ultraviolet (UV) small-length and high-momentum cutoff, i.e., the Fourier transform is performed by integrating $\int_{1/\Lambda}^{\infty} dr \int_0^{2\pi} d\phi$. The cutoff has a clear physical meaning: $1/\Lambda$ is the size of the vortex core (where the vortex ansatz stops working because the gradient of the field becomes too high). We clearly do not get anything new by just Fourier transforming. The goal is to move beyond the amplitude-linearized approximation of the previous section by considering the effects of nonconstant permittivity μ instead of constant (averaged) μ_c. This calculation is essentially elementary but might be tedious and boring for readers who are not fond of perturbative field theory. Most of the integrations are in Appendix C. Even the rest of this subsection can be skipped until the the equation (22), where we discuss the final result.

Putting μ from (3) in place of μ_c requires the solutions for $\omega_{0\mathrm{NL}}$ in terms of the magnetic field. The solutions are readily found from the Cardan formulas (we do not give them explicitly as they are cumbersome and not very illustrative). But the form of the H dependence of $\omega_{0\mathrm{NL}}$ is seen already from the Viete formula:

$$
\left(\omega_{0\mathrm{NL}}^{(1)}\right)^2 + \left(\omega_{0\mathrm{NL}}^{(2)}\right)^2 + \left(\omega_{0\mathrm{NL}}^{(3)}\right)^2 = \frac{1 + 2\Omega^2}{1 + |H|^2/\alpha E_c^2},
\tag{19}
$$

so the solutions depend on $|H|^2$ only, with no higher powers of the magnetic field. Inserting this into $\mathcal{L}$, we get the nonlinear correction of the form

$$
\begin{aligned}
\delta\mathcal{L} = {} & g_{2,0,0} |\nabla_\perp E|^2 + g_{0,2,0} |E|^2 + g_{0,2,2} |E|^2 |H|^2 \\
& + g_{2,0,2} |\nabla_\perp E|^2 |H|^2.
\end{aligned}
\tag{20}
$$

We thus have two quartic interaction terms and two quadratic terms. We do not intend to calculate the loop corrections in full detail; it is not worth the effort as we only want to capture the symmetry, i.e., the form of the angular dependence. First of all, the quadratic corrections $g_{2,0,0}$ and $g_{0,2,0}$ trivially renormalize the parameters in the bare propagator and do not change its functional form. Lowest-order nontrivial loop corrections to the self-energy come from $g_{0,2,2}$ and $g_{2,0,2}$. The electric field receives the correction $G_E^{-1} \mapsto (G_E + \Sigma_E^{(1)} + \Sigma_E^{(2)})^{-1}$ with

$$
\Sigma_E^{(1)} = g_{0,2,2} \int d\mathbf{u}'\, G_H(\mathbf{u}') \approx g_{0,2,2} e^{3\iota Q/2} \sin(\pi Q) \ln\Lambda,
$$

$$
\Sigma_E^{(2)} = \frac{3}{2} g_{0,2,2} \int d\mathbf{u}' \int d\mathbf{u}''\, G_H(\mathbf{u}') G_H(\mathbf{u}'') G_E(\mathbf{u} - \mathbf{u}' - \mathbf{u}'')
$$

$$
\approx \mathrm{const} \times [a^{3/2} \cos(3Q\phi/2) - 2\iota Q^2 \ln a].
\tag{21}
$$

We will write all equations for E, because this field receives interesting corrections from the gradient of μ [Eqs. (4) and (7)]. The magnetic field does not couple to the permeability ϵ in the same way in the original equation (5), and in the Lagrangian form (8) it does but ϵ does not contain such strong (nonpolynomial) nonlinearities as μ. One- and two-loop corrections appear not only in the self-energy but also in the vertex operators. However, the vertex corrections only have a weak momentum dependence and consequently the coordinate dependence (geometric patterns) of the solution is not significantly affected by them. For that reason we will not discuss them in detail.

The correction $\Sigma_E^{(1)}$ is the Hartree correction with a single vacuum bubble which is not very interesting: it merely introduces an additional mass term and does not influence the momentum dependence and thus the geometry of the patterns. As could be expected from power counting, it is logarithmically divergent in the UV cutoff Λ. Of course, this is not a problem in an effective theory; we have already explained the physical meaning of Λ. The watermelon diagram $\Sigma_{E,H}^{(2)}$ is crucial: it is momentum dependent. Its calculation is found in Appendix C. An informal way to estimate its effect is the following: the leading contribution comes from the region where $\mathbf{u} \approx \mathbf{u}' - \mathbf{u}''$ because this is a pole of the self-energy correction. Then we are left with angular integrals only, and they reduce to integrals of products of three rational functions [for the three propagators in (21)] of the half angle—this gives rise to $3\phi/2$ in the argument of the cosine. Now the dressed propagator $(G_{E,H}^{-1} + \Sigma)^{-1}$ needs to be Fourier transformed back to real space. We will only do this approximately (it is likely impossible to do exactly in closed form). The outcome is

$$
\begin{aligned}
E_{\mathrm{vort}}(r, \phi, z) = {} & \frac{e^{(\iota\lambda - 2Q^2 \ln a)z} \cos(Q\phi)}{\sqrt{\kappa r}} \\
& \times \left[c_E^{(1)}(\lambda, l) \left(1 + \frac{(2\pi)^{3/2} g_{0,2,2}}{\Gamma(Q/2)^3} \cos(3Q\phi/2)\right) \right. \\
& \left. + c_E^{(2)}(\lambda, l) \left(1 + \frac{(2\pi)^{3/2} g_{0,2,2}}{\Gamma(Q/2)^3} \sin(3Q\phi/2)\right) \right].
\end{aligned}
\tag{22}
$$

No doubt the reader sees that the terms $\cos(3Q\phi/2)$ and $\sin(3Q\phi/2)$ give a pattern $|E_{\mathrm{vort}}|^2$ with $3Q$ branches, in addition to the $2Q$ polygons obtained from the term $\cos(Q\phi)$. The interference between the two patterns might (1) break the symmetry completely and (2) lead to C_Q

symmetry if the relative phase between the leading term and the corrections is approximately $2\pi/Q$. Both cases are seen in numerical work: C_{3Q} appears in all left-handed materials [Figs. 2(a) and 2(c)], and elements of C_Q symmetry are present in almost all cases at long propagation distances z [Figs. 2(a)–2(c) and 3].

The self-energy has an imaginary part [equivalently, the solution (22) exhibits exponential decay in z], meaning that these configurations are not stable—they are only seen up to some propagation distance z. The exact order (along z) and stability of each of the patterns depend on the details of the permeability ϵ. One important and universal lesson is, however, that the decay rate [the real part of the exponent in (22)] is proportional to Q^2, therefore the higher the value of $|Q|$ the faster it decays. This supports the general intuition that vortices with high winding numbers are not stable. But unlike the simplest case of the XY model or a superfluid where the stability only allows $Q = \pm 1$ we can in principle have arbitrarily high Q as we have seen also in the numerics; their lifetimes are smaller and smaller as Q grows, but still finite. The exponential decay itself is also confirmed by the numerics, as seen from Fig. 4.

C. Isotropy breaking: The look from the action

The basic mechanism leading to the symmetry breaking $O(2) \mapsto C_{3Q} \mapsto C_{2Q} \mapsto C_Q$ is seen already from the model Lagrangian (6). The symmetry breaking is essentially the consequence of the interplay of the nonlinear-sigma-model form of the kinetic term and the complex nonlinearity of the magnetic permittivity μ. Therefore, we can take a static approximation of the z dynamics, ignoring the z dependence; clearly, in that framework we can only obtain the vocabulary of patterns, not the relative stability of C_Q, C_{2Q}, and C_{3Q}.[3] The separation of variables remains a natural ansatz, and the vortex nature of the solution implies $E_{\text{vort}} = E_0(r)e^{\iota\Theta(\phi)}$ with $\oint d\phi\,\Theta(\phi) = 2\pi Q$ and analogously for the magnetic field. The Lagrangian (6) then becomes

$$\mathcal{L} = \frac{(E_0')^2 + \frac{(\Theta')^2}{r^2}E_0^2 + k^2 E_0^2}{\mu} + \frac{(H_0')^2 + \frac{(\Theta')^2}{r^2}H_0^2 + k^2 H_0^2}{\epsilon}. \quad (23)$$

The fact that μ contains $\omega_{0\text{NL}}^2(|H|^2)$, which is in turn the solution of the cubic equation, introduces a branch cut in H because of the cubic roots. This is the simplest explanation of the origin of the C_{3Q} symmetry. More quantitatively, the story follows exactly the Landau-Ginzburg paradigm: while the initial Lagrangian only depends on $|E|^2$ and $|H|^2$ and thus preserves isotropy, the saddle-point solution is given by the equation

$$\frac{\epsilon(\nabla_\perp^2 - H)E - \epsilon'\nabla_\perp E \cdot \nabla_\perp H}{\epsilon^2} + \frac{\mu'}{\mu^2}|H|^{-1/3} = 0, \quad (24)$$

where we have used that $\mu = \mu(\omega_{0\text{NL}}^2)$ and $\omega_{0\text{NL}}^2 = \omega_{0\text{NL}}^2(|H|^{2/3}, |H|^{4/3})$ (from the Cardan formulas). With the ansatz adopted above, the amplitude equation for $E_0(r)$ is the

nonlinear amplitude equation (16). The equation for the phase part Θ is more interesting. It reads

$$\frac{(\Theta')^2\left(1 - \frac{\epsilon'}{\epsilon}\frac{E_0}{H_0}\right) - k}{\epsilon} + \frac{2\mu'}{3\mu^2}|H|^{-1/3} = 0. \quad (25)$$

The cubic root carries a branch cut, and the last term really evaluates to $2\mu'/3\mu^2 \times H_0^{-1/3}e^{-\iota\Theta/3 + 2n\pi\iota/3}$ with $n = -1, 0,$ and 1. The solution Θ_0 which satisfies the phase winding condition is obtained in implicit form as

$$\iota(\Theta_0 + 2\pi n/3) = K_n \ln\left[\frac{k\left(1 - \frac{\epsilon'}{\epsilon}\frac{E_0}{H_0}\right)}{E_0^2 + H_0^2}\sec^2\left(\frac{Q}{2}\phi\right)\right],$$
$$(26)$$

where K_n is a constant determined by the amplitude solution and depending also on $n = -1, 0,$ and 1; its exact value is hard to find analytically as we do not know the solution to the amplitude equation in the nonlinear regime. But that is not crucial for our general argument. The point is that the system can choose a solution with any of the values $n = -1, 0,$ and 1; i.e., even though the equations of motion (and the Lagrangian) are isotropic, the solution is not. Each n branch behaves as $\approx 1/\cos^2(Q\phi/2)$, only they are rotated by $\pm 2\pi/3$ with respect to each other, and each of them has a C_Q symmetry. Put together, the three branches give C_{3Q} patterns. But all that holds if two of the cubic roots are complex. If all cubic roots are real, the phase remains single valued, and we only have C_Q symmetry, coming directly from (26) if we fix $n = 0$, i.e., if we only keep a single branch.[4]

What is the regime in which cubic roots are real and the symmetry is C_Q, as opposed to the complex roots and C_{3Q} patterns? The easiest way is to look at the cubic equation (3) for the magnetic permeability (and the nonlinear frequency $\omega_{0\text{NL}}$). For $\mu > 0$ (right-handed regime), the roots are all real and C_{3Q} patterns cannot occur. Indeed, the C_{3Q} phase is only present in Figs. 2(a) and 2(c), in left-handed media.

This approach is much more physical and elegant than the tour-de-force calculations of the previous two sections but it does not give explicit solutions for E and H; it only classifies the symmetries of the solution. This is why we we still needed the perturbative linear and two-loop analysis, to arrive at more quantitative results.

The saddle-point solution (26) is nonlinear, unlike the linearized solution found in the first subsection (15). It is not a vacuum in the usual field-theory sense, however, as it is not constant. We are dealing with dynamical criticality of the kind discussed in [21]. In the vicinity of this solution, the Lagrangian describes the fluctuations of amplitude δE and δH, and the fluctuations of phase $\delta\Phi$. Similar to the $O(3)$-type spin models [23] and multibeam optical systems [32], and unlike simple XY-type models, the phase and amplitude fluctuations mix. By analyzing the fluctuation equations, it should be possible to understand analytically also the transition from the left-handed to the right-handed regime as the parameters are varied, i.e., what are the instabilities that drive it. We will not

---

[3]We could take the ansatz $e^{\iota\lambda z}$ instead; it would merely modify $k^2 \mapsto k^2 - \lambda$.

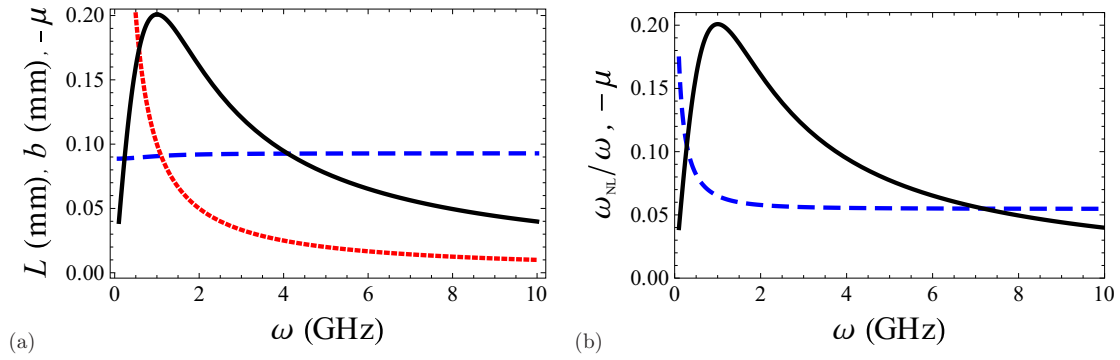[4]We use the fact that a cubic equation has either one or all three solutions real.

FIG. 6. (a) Frequency dependence of the typical propagation length scale for the dissipation of the vortex a^{2Q^2} (blue dashed line) and for the evolution of the symmetry-breaking C_n patterns (red dotted line). The symmetry breaking is detectable as long as the pattern evolution is faster than the dissipation, i.e., as long as the red curve is below the blue one. This is obviously the case for most of the frequency range. We also plot the frequency dependence of the negative permittivity $-\mu$ (black full line; because of the minus sign large positive values in the plot are really large negative values of μ). The left-handed regime is most prominent at intermediate frequencies, which are also inside the regime of the symmetry breaking. (b) Frequency dependence of the relative strength of nonlinear interactions ω_{0NL}/ω (blue dashed line) together with negative permittivity $-\mu$ as in (a) (black full line). Our calculations, based on a pair of nonlinear Schrödinger-like equations, are reliable as long as the nonlinearity is not too strong. This is again the case for all but very small frequencies, and again includes the left-handed regime.

attempt that here; it is a long subject that deserves separate work.

V. TOWARD EXPERIMENTAL VERIFICATION AND APPLICATIONS

We will now briefly discuss what an experimentalist can learn from our results and what to look for in practical work. Wave propagation through the metamaterial can be observed by measuring the transmission coefficients S_{ij}. From these coefficients, one can also reconstruct the electric-field intensity $|E|^2$, which can be directly compared to our intensity maps like Figs. 2 and 3 [33]. Another quantity which can be measured is the voltage waveform, which can be used to construct amplitude envelopes [34].

Therefore, the predicted symmetry breaking is in principle directly observable. But the question remains how widespread it will be for realistic values of the parameters. From a more applied viewpoint, this question is reversed: how to make a vortex transmission through a left-handed waveguide stable. In other words, how *not* to observe the symmetry breaking. It is true that the phenomenon disappears as soon as the vortex charge is zero, i.e., when the beam is not a vortex. However, the vortex patterns are likely important in applications. First, as a topologically protected object with conserved charge, a vortex is among the natural candidates for computational devices and information transmission (for the same reasons that solitons are also interesting in that regard: they are robust to noise, carry a discrete "quantum" number, i.e., charge, and are stable to small local perturbations). Second, in the presence of impurities in the sample, vortices can form in a nonlinear metamaterial from the initially nonvortexing beam [23].

Let us focus on the left-handed regime, which is the most interesting and the most relevant for applications. The first condition is therefore to be in the frequency regime with $\mu(\omega) < 0$. This can be checked directly from Eq. (2) as we did in Fig. 1(c). The second issue is that the symmetry breaking takes some finite time, i.e., some finite propagation length, which is of order b; as can be seen from Fig. 3 and

directly from Eqs. (4) and (5), this is the length scale over which the patterns change. On the other hand, the one-loop calculation (22) shows that the intensity decays with the rate $\sim a^{-2Q^2}$. As long as this is less than the characteristic length b, one will likely not see the symmetry breaking but just eventual dissipation of the beam. Therefore, these two scales should be compared for some reasonable parameter values. We show this in Fig. 6(a) for $F = 0.4$, $\epsilon_{D0} = 12.8$, $\gamma = 1$ GHz, and $\omega_0 = 10$ GHz. Apparently, the length scale of the C_n pattern development (red dotted line) is nearly always shorter than the dissipation scale (blue dashed line), so we expect that the effect predicted in the paper is readily seen in experiment, at least for $Q = \pm 1$. For larger vortex charges, the dissipation grows quickly and high Q values are probably not easily observed. Conversely, if the goal is to keep a stable radially symmetric vortex pattern, one should remain at small frequencies, although for $\omega \ll \omega_0$ the material is not strongly left handed, as can be seen from the $-\mu(\omega)$ dependence, also given in the figure.

There is still one remaining issue. Our theoretical approach, based on a pair of nonlinear Schrödinger-like equations, inherently disregards some effects. It describes a quasi-monochromatic wave without wave mixing or dissipation due to higher harmonic generation [5]. Such phenomena become significant for strong nonlinearities, so we should compare the nonlinearities in ϵ and μ to the typical energy (frequency) scale of the vortex. In Eqs. (1) and (2) the approximate ratios of the nonlinear to linear terms are given by $|E|^2/\epsilon_{D0}$ and $\omega_{0NL}/\omega_0 \sim (A/H)^{1/3}$. The first scale is frequency independent and solely depends on the beam intensity. The second scale depends on frequency and needs to be inspected more closely. In Fig. 6(b) we plot the nonlinearity ratio for the magnetic field for a range of frequencies ω, again together with the permittivity to make sure we are at the same time in the left-handed regime. The relative nonlinearity strength quickly saturates around a value $0.06 \ll 1$, so we are rather confident that our equations of motion still make sense.

Altogether, the conclusion is that the breaking of radial symmetry is observable by standard means (measuring the

transport coefficients and reconstructing the intensity map at the exit face of the metamaterial), as long as the frequency of the wave is not too low. This kind of instability kicks in at shorter propagation lengths [of order 0.1 mm in Fig. 6(a)] than the nonlinear diffraction effects studied for breathers in [35], suggesting that vortex signals are more fragile and less convenient for information transmission.

VI. DISCUSSION AND CONCLUSIONS

Our main result is contained already in the title—left-handedness and nonlinearity together create the breaking of the $O(2)$ symmetry down to a discrete group, with the pattern vocabulary consisting of the C_{3Q}, C_{2Q}, and C_Q patterns. In the right-handed system with the same nonlinearity the isotropy is broken again, but the pattern vocabulary only has C_{2Q} and C_Q stages. How exactly the patterns evolve into each other and through which instabilities is not universal, and it depends on the exact form of ϵ and μ. In our model, the ϵ dependence is mainly encapsulated in the dissipation γ: the left-handed nondissipative case is usually dominated by C_Q after a much shorter C_{3Q} phase, whereas the dissipative left-handed metamaterials most prominently show C_{3Q} patterns. For the right-handed materials, nondissipative and dissipative dynamics show mainly C_{2Q} and C_Q patterns, respectively.

A detailed account of the pattern dynamics was only possible through numerical work. But the vocabulary itself—the existence of symmetries C_{3Q}, C_{2Q}, and C_Q—we were able to understand analytically. The dynamic Landau-Ginzburg picture reveals this as a consequence of the cubic root non-linearity in the magnetic permittivity, *and* the fact that the cubic equation has either two complex roots in the left-handed regime or all three real roots in the right-handed regime, *and* the presence or absence of dissipation in the electric permeability. In the framework of our field theory model, the second derivative of the free energy (on-shell Lagrangian, Landau-Ginzburg functional) likely has a jump when the symmetry changes. This is a strong encouragement that the phenomena we observe here, and in general the walk through the pattern vocabulary, can be understood from the viewpoint of order and disorder transitions.

Similar phenomena were studied also in [15,18] and above all [10], where C_{3Q} necklaces were found, within a model of left-handed metamaterials given in [15] and similar to ours. Clearly, we have not exhausted this subject; more research is still needed to fully understand the transition between different symmetries and their instabilities. Vortices in meta-materials seem to be a promising arena, as in a metamaterial the nonlinearity and the frequency band where the material is left-handed can to some extent be tuned at will. Therefore, the phase diagram of collective vortex interactions can also be studied, and is an obvious topic for future work.

ACKNOWLEDGMENTS

APPENDIX A: DERIVATION OF THE EQUATIONS OF MOTION FROM THE MAXWELL EQUATIONS

Start from the definitions $\hat{D} = \epsilon\hat{E}$ and $\hat{B} = \mu\hat{H}$ and the Maxwell equations in the absence of external charges and currents ($\rho = \hat{j} = 0$):

$$\nabla \cdot \hat{D} = \rho = 0, \quad \nabla \cdot \hat{B} = 0, \quad \nabla \times \hat{E} = -\partial_t \hat{B},$$
$$\nabla \times \hat{H} = 4\pi \hat{j} + \partial_t \hat{D} = \partial_t \hat{D}. \tag{A1}$$

We make the following assumptions.

(1) We assume small gradients of the permittivities ϵ and μ, so their second and higher derivatives are disregarded. Since $\omega \propto k$, it means that mixed derivatives of the form $\partial_t \nabla \epsilon$ are also disregarded. In other words, the characteristic length scale l along the z axis on which ϵ and μ change is assumed to be large compared to the characteristic scale b of the changes in E and H.

(2) We assume that the time dependence is harmonic so $\partial_t = -\iota\omega$.

Acting on the last equation by $\nabla\times$ and making use of the identity $\nabla \times \nabla \times \hat{H} = -\nabla^2\hat{H} + \nabla(\nabla \cdot \hat{H})$, one gets for the left-hand side

$$\nabla \times \nabla \times \hat{H} = -\nabla^2\hat{H} + \nabla\left(\nabla \cdot \frac{\hat{B}}{\mu}\right)$$
$$= -\nabla^2\hat{H} + \nabla\left(\frac{1}{\mu}\nabla \cdot \hat{B}\right) - \nabla\left(\frac{\nabla\mu}{\mu^2} \cdot \hat{B}\right)$$
$$= -\nabla^2\hat{H} + \nabla\left(\frac{1}{\mu}\nabla \cdot \hat{B}\right) - \nabla \cdot \left(\frac{\nabla\mu}{\mu^2}\right)\hat{B}$$
$$- \frac{\nabla\mu}{\mu^2}\nabla \cdot \hat{B} = -\nabla^2\hat{H} + 0 + O(1/l^2) + 0$$
$$= -\nabla^2\hat{H}, \tag{A2}$$

where we used $\nabla \cdot \hat{B} = 0$ and disregarded the second derivative of μ. The right-hand side yields

$$\nabla \times \nabla \times \hat{H} = \nabla \times (\partial_t\hat{D}) = -\iota\omega\nabla \times \hat{D} = -\iota\omega\nabla \times (\epsilon\hat{E})$$
$$= -\iota\omega(\nabla\epsilon)\hat{E} - \iota\omega\epsilon\nabla \times \hat{E}$$
$$= -\iota\omega(\nabla\epsilon)\hat{E} - \omega^2\epsilon\mu\hat{H} = O(1/l^2) + \omega^2\epsilon\mu\hat{H}, \tag{A3}$$

so we obtain

$$\nabla^2\hat{H} + \omega^2\epsilon\mu\hat{H} = 0. \tag{A4}$$

For the $\hat{E}$ field we start from the third Maxwell equation, act by $\nabla\times$, and find for the left-hand side

$$\nabla \times \nabla \times \hat{E} = -\nabla^2\hat{E} + \nabla(\nabla \cdot \hat{E}) = -\nabla^2\hat{E} - \nabla\left(\nabla \cdot \frac{\hat{D}}{\epsilon}\right)$$
$$= \nabla^2\hat{E} - \nabla\left(\frac{1}{\epsilon}\nabla \cdot \hat{D}\right) + \nabla\left(\frac{\nabla\epsilon}{\epsilon^2}\right)\epsilon\hat{E}$$
$$+ \frac{\nabla\epsilon}{\epsilon^2}\nabla \cdot \hat{D} = -\nabla^2\hat{E} + 0 + O(1/l^2) + 0$$
$$= -\nabla^2\hat{E}, \tag{A5}$$

and for the right-hand side we get

$$\nabla \times \nabla \times \hat{E} = -\partial_t(\nabla \times \hat{B}) = -\partial_t(\nabla \times \hat{B})$$

$$= -\partial_t[\nabla \times (\mu\hat{H})] = -\partial_t[(\nabla\mu)\hat{H} + \mu\nabla \times \hat{H}]$$

$$= -(\partial_t\nabla\mu)\hat{H} - \nabla\mu \cdot \partial_t\hat{H} - \partial_t(\mu\partial_t\hat{D})$$

$$= O(1/l^2) - \frac{\nabla\mu}{\mu}\nabla\hat{E} + \omega^2\epsilon\mu\hat{E}, \qquad (A6)$$

so

$$\nabla^2\hat{E} + \omega^2\epsilon\mu\hat{E} - \frac{\nabla\mu}{\mu}\nabla\hat{E} = 0. \qquad (A7)$$

For our geometry we take the paraxial beam approximation, with the ansatz $\hat{E} = E(x,y)e^{\iota(kz-\omega t)}$, $\hat{H} = H(x,y)e^{\iota(kz-\omega t)}$, so the nabla acts as

$$\nabla\hat{E} = (\nabla_\perp E, \partial_z E + \iota kE)e^{\iota(kz-\omega t)}, \qquad (A8)$$

and the Laplacian operator acts as

$$\nabla^2\hat{E} = (\nabla_\perp^2 E + 2\iota k\partial_z E - k^2 E)e^{\iota(kz-\omega t)}, \qquad (A9)$$

and analogously for the magnetic field. Now to write the equations motion in the final form we rescale $E \to E \times 2kb$, $H \to H \times 2kb$, and $z \mapsto z \times 2kb$, where b is some characteristic length scale along the z axis, and divide the equations by bk^2 to obtain the equations (4) and (5), reprinted here for convenience:

$$-\frac{\iota}{b}\partial_z E = \nabla_\perp^2 E + [\omega^2\epsilon(|E|^2)\mu(|H|^2) - k^2]E$$

$$-\frac{\nabla_\perp\mu(|H|^2)}{\mu(|H|^2)}\nabla_\perp E - \iota\frac{\partial_z\mu(|H|^2)}{2\mu(|H|^2)}E, \qquad (A10)$$

$$-\frac{\iota}{b}\partial_z H = \nabla_\perp^2 H + [\omega^2\epsilon(|E|^2)\mu(|H|^2) - k^2]H. \qquad (A11)$$

For comparison to the equations given in [4,7,12], one needs (1) to rescale $H \mapsto \omega^2/c^2 H$ to get the term $-\gamma^2 H = -k^2/\omega^2$ in (A11) and (2) to absorb the factor $-k^2$ in (A10) in the definition of ϵ_{D0}. This is possible as ϵ and μ have a constant term (equal ϵ_{D0} and 1, respectively) so the product $\epsilon\mu$ also has a constant term proportional to ϵ_{D0}, and the contribution $k^2 E$ can be absorbed as $\epsilon_{D0} \mapsto \epsilon_{D0} - k^2$. We thus arrive at a system identical to that from [4], except for the extra terms for the propagation along the z axis.

APPENDIX B: CONFIGURATIONS WITH NO VORTICITY IN THE MAGNETIC FIELD

Here we show that our results stay valid also when only the electric field has vortex patterns whereas the magnetic field starts analytic everywhere. As we discuss in the main text, this situation is experimentally more relevant than the one assumed in most calculations in the paper (that both the

electric and the magnetic field have a vortex as they enter the material). The electric field is typically a few orders of magnitude more intense than the magnetic field, as seen in [4]. Therefore, one typically controls the electric field directly, imposing a given boundary condition at the front end of the material. Despite this fact, the magnetic field remains very important: the coupled equations of motion (4) and (5) require both E and H to be nonzero. Indeed, as explained in [4], the left handedness comes as a consequence of the hysteresis-type dependence of the magnetic permittivity on H. So while it is crucial that E and H are both nonzero, it is also true that the results should remain valid for $|H| \ll |E|$, and for the boundary condition that only has a vortex in E at the front of the metamaterial, not for H. With such boundary conditions and the same parameter values as before, Fig. 7 repeats the calculations of Fig. 3. Obviously, the symmetries remain the same and the similarity of the results for the two cases is striking. Obviously, the $|E|^2$ map is insensitive to the details of the initial magnetic-field pattern, as one expects from experiments and common wisdom in nonlinear optics. We are thus content that the numerically simplifying assumption of identical $z = 0$ boundary conditions for E and H does not put into question the findings of our paper.

APPENDIX C: THE CALCULATION OF THE SELF-ENERGY DIAGRAMS

We discuss here in some more detail the equations (21) from the main text. First we give the expressions for the couplings $g_{2,0,0}$, $g_{0,2,0}$, $g_{2,0,2}$, and $g_{0,2,2}$, which come from the expansion over the magnetic field H of the nonlinear dependence $\mu(H)$ in (20):

$$g_{2,0,0} = \frac{\alpha E_c^4\omega_0^2 - (\omega - \iota\Gamma)\omega\alpha E_c^8}{H_0 + \alpha E_c^4[\omega_0^2 - (\omega - \iota\Gamma)\omega\alpha E_c^2]}, \qquad (C1)$$

$$g_{0,2,0} = (k^2 - \lambda^2)g_{2,0,0}, \qquad (C2)$$

$$g_{2,0,2} = 2\alpha E_c^2 H_0 \frac{\omega_0^2 - (\omega - \iota\Gamma)\omega\alpha E_c^4}{\{H_0 + \alpha E_c^4[\omega_0^2 - (\omega - \iota\Gamma)\omega\alpha E_c^2]\}^2}, \qquad (C3)$$

$$g_{0,2,2} = (k^2 - \lambda^2)g_{2,0,2}. \qquad (C4)$$

For simplicity, we will treat the case when $\lambda = k$ and thus $g_{0,2,0} = g_{0,2,2} = 0$. This simplifies the calculations substantially while it does not change the symmetry of the solution. It is possible to evaluate the diagram $\Sigma^{(1)}$ exactly in terms of sine and cosine integrals Si and Ci. The angular integration is straightforward; the integration over u results in four combinations of the trigonometric integrals, for the four terms in (18). Three of the four integrals are finite and therefore they just shift the mass term. The third term of the propagator is logarithmically divergent:

$$\Sigma_3^{(1)} = \frac{4\pi\sin\pi Q}{Q\Gamma(Q/2)}e^{-3\iota\pi Q/2}\frac{1}{a^2}\{\gamma_E + \ln\Lambda + (-1)^Q a[\cos(a\Lambda)\text{Ci}(a\Lambda) + \sin(a\Lambda)\text{Si}(a\Lambda)]\}. \qquad (C5)$$

To judge the effect of this term, we should extract the mass squared r_m of the bare propagator, writing it out for small u:

$$G(\mathbf{u} \to 0) = \frac{2\pi}{\Gamma(Q/2)}\frac{1}{u(u^2 - a^2)}\{e^{\iota Q(\pi/2+\phi)}[\cos(a\Lambda - \pi Q) - \sin(a\Lambda)] + e^{-\iota Q(\pi/2+\phi)}[\cos(a\Lambda + \pi Q) - \cos(a\Lambda)]\}. \qquad (C6)$$
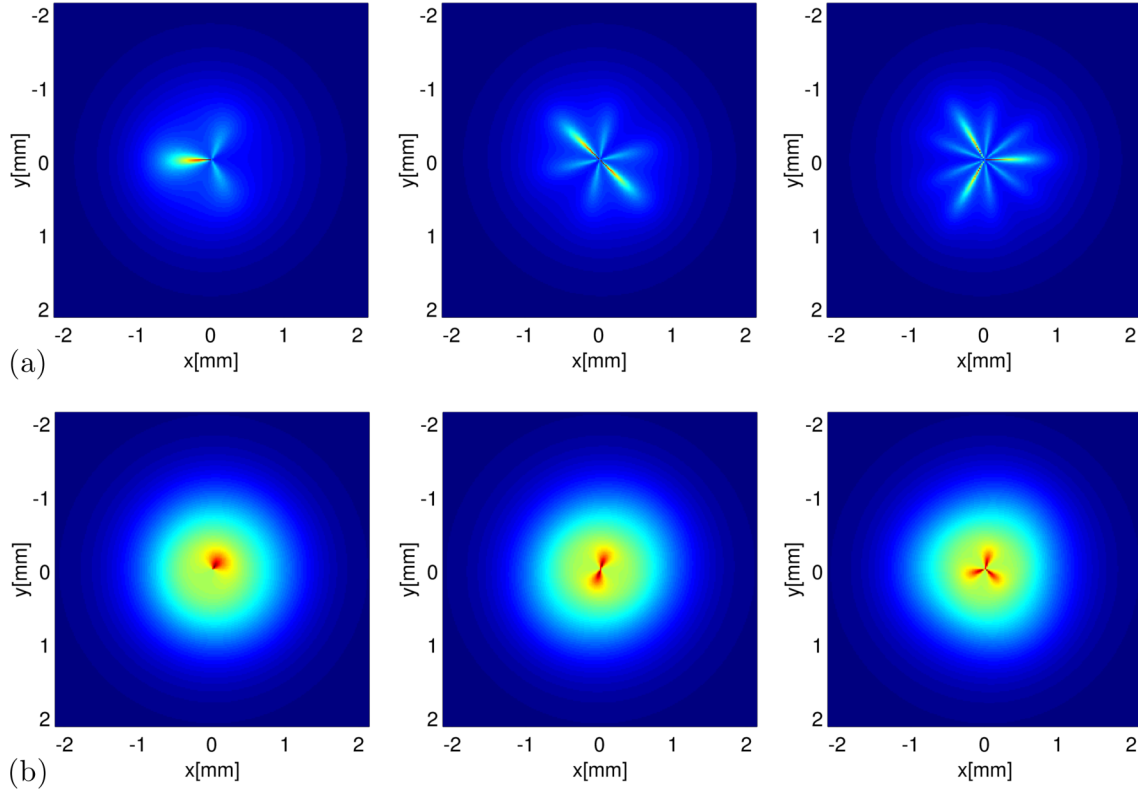
FIG. 7. The patterns for $Q = 1, 2,$ and 3 vortices (left to right), in a dissipative (a) and lossless (b) left-handed metamaterial. All parameters are the same as in Fig. 3 but the boundary condition at $z = 0$ is now a vortex for the electric field E and a homogenous background for H. The symmetries and the whole qualitative picture are the same as before, confirming that the predictions of the paper do not require preparing a vortex in magnetic field at the entry.

Since $G^{-1}(\mathbf{u} \to 0) \propto u = 0$, the bare propagator is massless. The one-loop correction $\Sigma^{(1)}$ therefore gives a cutoff-dependent mass $r_M \sim \ln \Lambda$, which could be absorbed in the overall normalization of the propagator. As we declared in the main text, the one-loop self-energy does not do much.

The crucial diagram $\Sigma^{(2)}$, the popular watermelon diagram, cannot be calculated exactly. It can be evaluated in the regime of small external momentum $\mathbf{u}$, i.e, when $u < u', u''$; more precisely, we can look at the regime when $u < u_0 < u', u''$ for some (arbitrary) scale u_0 and expand in a series in u/u_0. Let us denote such an entity by $\Sigma^{(2)}(\mathbf{u}; u_0)$: it contains enough information for our purposes: we are interested mainly in angular integrations which determine the symmetry, and these can be done exactly as they separate from the integrations over the module u in the small-u limit. For $\mathbf{u} = 0$ the watermelon diagram reads (with $\int \equiv \int_0^{2\pi} d\phi' \int_0^{2\pi} d\phi'' \int du' \int du''$)

$$\Sigma^{(2)} \approx \int \frac{G(\mathbf{u}')G(\mathbf{u}'')}{v}\{e^{\iota Q[\pi/2+(\phi-\phi'-\phi'')]}[\cos(a\Lambda - \pi Q) - \sin(a\Lambda)] + e^{-\iota Q[\pi/2+(\phi-\phi'-\phi'')]}[\cos(a\Lambda + \pi Q) - \cos(a\Lambda)]\},$$

$$v \equiv \sqrt{(u')^2 + (u'')^2 - 2u'u''\cos(\phi - \phi' - \phi'')}. \tag{C7}$$

One angular integration is performed by taking $\phi' \mapsto \phi' + \phi''$, which makes the ϕ'' integral completely trivial, and the ϕ' integral is evaluated in terms of the elliptic integrals E and K. The outcome is finite, hence it is observable (not only at the cutoff scale) and reads

$$\Sigma^{(2)}(0; u_0) = \left(\frac{2\pi)}{a\Gamma(Q/2)}\right)^3 e^{3\iota Q/2} \cos(3Q\phi/2)^2 \int du' \int du'' \frac{[(u')^2 - (u'')^2](u' + u'')E\left(-\frac{4u'u''}{(u'+u'')^2}\right)}{(u')^2(u'')^2[(u')^2 - a^2][(u'')^2 - a^2][(u')^2 - (u'')^2]}$$

$$= \frac{1}{4\pi}\left(\frac{2\pi}{a\Gamma(Q/2)}\right)^3 e^{3\iota Q/2} \cos(3Q\phi/2)^2(a^{3/2} - 1/\Lambda^{3/2}) + O(1/\Lambda^2). \tag{C8}$$

In particular, this means that a nontrivial mass term is acquired, of the order $a^{3/2}$. This mass is anisotropic, and the factor $\cos(3Q\pi/2)^2$ is all we need for the $3Q$ polygon. The leading correction in u/u_0 is in fact inessential for the symmetry, but it is

important as it contains a nonzero imaginary part, introducing a finite lifetime for such patterns. It reads

$$\Sigma^{(2)}(u; u_0) = \int \frac{G(\mathbf{u}')G(\mathbf{u}'')}{w} \{ e^{\iota Q[\pi/2 + (\phi' - \phi'')]}[\cos(a\Lambda - \pi Q) - \sin(a\Lambda)] + e^{-\iota Q[\pi/2 + (\phi' - \phi'')]}[\cos(a\Lambda + \pi Q) - \cos(a\Lambda)]\}$$

$$= \frac{1}{4\pi} \left(\frac{2\pi}{a\Gamma(Q/2)} \right)^3 e^{3\iota Q/2} \left(\frac{2\iota a^{3/2}}{\pi} \sin(3Q\phi/2) + \frac{2\Lambda^{3/2}}{\pi} \cos(3Q\phi/2) \right),$$

$$w \equiv \sqrt{(u')^2 + (u'')^2 - 2u'u''\cos(\phi' - \phi'') - 2u[u'\cos(\phi - \phi') + u''\cos(\phi - \phi'')]}. \tag{C9}$$

At leading order, this tedious expression behaves like $1/r^3$, falling off much quicker than the bare propagator (18), which goes as $1/\sqrt{r}$ (most obvious from the Bessel-function form of the real-space solution), suggesting that the shape of the vortex, which is mainly determined by long-distance behavior, is not much influenced by the finite-u correction to $\Sigma^{(2)}$.

---

[1] V. G. Veselago, The electrodynamics of substances with simultaneously negative values of epsilon and mu, Usp. Fiz. Nauk **92**, 517 (1967) (in Russian).

[2] R. A. Shelby, D. R. Smith, and S. Schultz, Experimental verification of a negative index of refraction, Science **292**, 77 (2001).

[3] T. J. Yen, W. J. Padilla, N. Fang, D. C. Vier, D. R. Smith, J. B. Pendry, D. N. Basov and D. Zhang Terahertz magnetic response from artificial materials, Science **303**, 1494 (2004).

[4] A. A. Zharov, I. V. Shadrivov and Y. S. Kivshar, Nonlinear Properties of Left-Handed Metamaterials, Phys. Rev. Lett. **91**, 037401 (2003).

[5] M. Lapine, I. V. Shadrivov and Y. S. Kivshar, Colloquium: Nonlinear metamaterials, Rev. Mod. Phys **86**, 1093 (2014); A. Baev, P. N. Prasad, H. Agren, M. Samoć and M. Wegener, Metaphotonics: An emerging field with opportunities and challenges, Phys. Rep. **594**, 1 (2015).

[6] I. V. Shadrivov, N. A. Zharova, A. A. Zharov and Y. S. Kivshar, Nonlinear transmission and spatiotemporal solitons in metamaterials with negative refraction, Optics Express **13**, 1291 (2005).

[7] I. V. Shadrivov and Y. S. Kivshar, Spatial solitons in nonlinear left-handed metamaterials, J. Opt. A: Pure Appl. Opt. **7**, S68 (2005).

[8] I. V. Shadrivov, A. A. Sukhorukov, Y. S. Kivshar, A. A. Zharov, A. D. Boardman and P. Egan, Nonlinear surface waves in left-handed materials, Phys. Rev. E **69**, 016617 (2004).

[9] S. Wen, Y. Wang, W. Su, Y. Xiang, X. Fu and D. Fan, Modulation instability in nonlinear negative-index material, Phys. Rev. E **73**, 036617 (2006).

[10] S. Z. Silahli, W. Walasik and N. M. Litchinitser, Modulation instability of structured-light beams in negative-index metamaterials, J. Opt. **18**, 054010 (2016).

[11] N. L. Tsitsas, N. Rompotis, I. Kourakis, P. G. Kevrekidis and D. J. Frantzeskakis, Higher-order effects and ultrashort solitons in left-handed metamaterials, Phys. Rev. E **79**, 037601 (2009).

[12] I. V. Shadrivov, A. A. Sukhorukov and Y. S. Kivshar, Guided modes in negative-refractive-index metamaterials, Phys. Rev. E **67**, 057602 (2003).

[13] A. Namdar, I. V. Shadrivov and Y. S. Kivshar, Backward Tamm states in left-handed metamaterials, App. Phys. Lett. **89**, 114104 (2006).

[14] H. Liu, J. Lei, G. Jiang, X. Guan L. Ji, and Z. Ma, Observation of tunable nonlinear effects in an analogue of superconducting composite right/left hand filter, Sci. Rep. **5**, 14846 (2015).

[15] L. Fan, Z. Chen, Y.-C. Deng, J. Ding, H. Ge, S.-Y. Zhang, Y.-T. Yang and H. Zhang, Nonlinear effects in a metamaterial with double negativity, App. Phys. Lett. **105**, 041904 (2014).

[16] A. O. Korotkevich, K. E. Rasmussen, G. Kovačič, V. Roytburd, A. I. Maimistov and I. R. Gabitov, Optical pulse dynamics in active metamaterials with positive and negative refractive index, J. Opt. Soc. Am. B **30**, 1077 (2013).

[17] M. Saha, A. K. Sarma, Modulation instability in nonlinear metamaterials induced by cubic-quintic nonlinearities and higher order dispersive effects, Opt. Commun. **291**, 321 (2005).

[18] Y. Shen, P. G. Kevrekidis, G. P. Veldes, D. J. Frantzeskakis, D. DiMarzio, X. Lan, and V. Radisic, From solitons to rogue waves in nonlinear left-handed metamaterials, Phys. Rev. E **95**, 032223 (2017).

[19] M. Liu, D. A. Powell, I. V. Shadrivov, M. Lapine and Y. S. Kivshar, Spontaneous chiral symmetry breaking in metamaterials, Nat. Comm. **5**, 4441 (2014).

[20] M. A. Gorlach, D. A. Dobrykh, A. P. Slobozhanyuk, P. A. Belov and M. Lapine, Nonlinear symmetry breaking in photometamaterials, Phys. Rev. B **97**, 115119 (2018).

[21] M. C. Cross and P. C. Hohenberg, Pattern formation outside of equilibrium, Rev. Mod. Phys. **65**, 851 (1993).

[22] M. I. Rabinovich, A. B. Ezersky, and P. D. Weidman, *The Dynamics of Patterns* (World Scientific, Singapore, 2000).

[23] L. I. Pismen, *Vortices in Nonlinear Fields* (Oxford University, London, 1999).

[24] H. Kleinert, *Gauge Fields in Condensed Matter Physics* (World Scientific, Singapore, 1989).

[25] P. W. Anderson, Two new vortex liquids, Nature Physics **3**, 160 (2007).

[26] A. L. Fetter, Rotating trapped Bose-Einstein condensates, Rev. Mod. Phys. **81**, 647 (2009).

[27] J. D. Sau and S. Sachdev, Mean-field theory of competing orders in metals with antiferromagnetic exchange interactions, Phys. Rev. B **89**, 075129 (2014).

[28] V. L. Berezinsky, Razrushenie dalnego poryadka v odnomernykh i dvumernykh sistemakh s neprerivnoy gruppoy simmetrii I. Klassichesskie sistemy, JETF **59**, 907 (1970) (in Russian); J. Kosterlitz and D. Thouless, Ordering, metastability and phase transitions in two-dimensional systems, J. Phys. C **6**, 1181 (1973).

[29] R. W. Boyd, *Nonlinear Optics* (Academic, New York, 2008).

[30] J. L. Cieslinski and T. Nikiciuk, A direct approach to the construction of standard and non-standard Lagrangians for dissipative-like dynamical systems with variable coefficients, J. Phys. A **43**, 175205 (2010).

[31] T. Shah, R. Chattopadhyay, K. Vaidya and S. Chakraborty, Conservative perturbation theory for nonconservative systems, Phys. Rev. E **92**, 062927 (2015).

[32] M. Čubrović and M. S. Petrović, Quantum criticality in photorefractive optics: Vortices in laser beams and antiferromagnets, Phys. Rev. A **96**, 053824 (2017).

[33] P. Alitalo, S. Maslovski and S. Tretyakov, Experimental verification of the key properties of a three-dimensional isotropic transmission-line superlens, J. Appl. Phys. **99**, 124910 (2006).

[34] A. B. Kozyrev and D. W. van der Weide, Trains of envelope solitons in nonlinear left-handed transmission line media, Appl. Phys. Lett. **91**, 254111 (2007).

[35] A. D. Boardman, N. King, R.-C. Mitchell-Thomas, V. N. Malnev, and Y. G. Rappoport, Gain control and diffraction-managed solitons in metamaterials, Metamaterials **2**, 145 (2008).

The bound on chaos for closed strings in Anti-de Sitter black hole backgrounds

Mihailo Čubrović

Scientific Computing Lab, Center for the Study of Complex Systems,
Institute of Physics Belgrade, University of Belgrade,
Pregrevica 118, 11080 Belgrade, Serbia

E-mail: mcubrovic@gmail.com

Abstract: We perform a systematic study of the maximum Lyapunov exponent values λ for the motion of classical closed strings in Anti-de Sitter black hole geometries with spherical, planar and hyperbolic horizons. Analytical estimates from the linearized variational equations together with numerical integrations predict the bulk Lyapunov exponent value as $\lambda \approx 2\pi T n$, where n is the winding number of the string. The celebrated bound on chaos stating that $\lambda \leq 2\pi T$ is thus systematically modified for winding strings in the bulk. Within gauge/string duality, such strings apparently correspond to complicated operators which either do not move on Regge trajectories, or move on subleading trajectories with an unusual slope. Depending on the energy scale, the out-of-time-ordered correlation functions of these operators may still obey the bound $2\pi T$, or they may violate it like the bulk exponent. We do not know exactly why the bound on chaos can be modified but the indication from the gauge/string dual viewpoint is that the correlation functions of the dual gauge operators never factorize and thus the original derivation of the bound on chaos does not apply.

Contents

1 Introduction

Sharp results like inequalities and no-go theorems are often the cornerstones of our understanding of physical phenomena. Besides being appealing and captivating, they are easy to test as they provide a sharp prediction on a certain quantity, and we can often learn a lot by understanding the cases when such bounds need to be generalized or abandoned. The upper bound on the Lyapunov exponent (the rate of the growth of chaos), derived in [1] inspired by hints found in several earlier works [2–7], is an example of such a result, which is related to the dynamics of nonstationary correlation functions and provides insight into the deep and important problem of thermalization and mixing in strongly coupled systems.

It is clear, as discussed also in the original paper [1], that there are cases when the bound does not apply: mainly systems in which the correlation functions do not factorize even at arbitrarily long times, and also systems without a clear separation of short timescales (or collision times) and long timescales (or scrambling times). A concrete example of bound violation was found in [8] for a semiclassical system with a conserved angular momentum (inspired by the Sachdev-Ye-Kitaev (SYK) model [9–12]) and in [13], again for a SYK-inspired system. In the former case, the reason is clear: the orbits that violate the bound are precisely those that cannot be treated semiclassically, so the violation just signals that the model used becomes inaccurate; in the latter case things are more complicated and the exact reason is not known. Finally, in [14] systematic higher-order quantum corrections to the bound are considered. The bound is in any case a very useful benchmark, which can tell us something on long-term dynamics of the system at hand, i.e. if some bound-violating mechanisms are at work or not.

Although the bound on chaos is mainly formulated for field theories in flat spacetime, it has an intimate connection to gravity: the prediction is that fields with gravity duals saturate the bound. This makes dynamics in asymptotically anti-de Sitter (AdS) space-times with a black hole particularly interesting: they have a field theory dual,[1] and black holes are conjectured to be the fastest scramblers in nature [2, 3], i.e., they minimize the time for the overlap between the initial and current state to drop by an order of magnitude. Some tests of the bound for the motion of particles in the backgrounds of AdS black holes and an additional external potential were already made [15]; the authors find that the bound is systematically modified for particles hovering at the horizon and interacting with *higher spin* external fields. When the external field becomes scalar, the exact bound by Maldacena, Shenker and Stanford is recovered (as shown also in [16]).

The idea of this paper is to study the bound on chaos in the context of *motion of strings in AdS black hole geometries*. Asymptotically AdS geometry is helpful not only because of the gauge/gravity duality, but also for another reason: AdS asymptotics provide a regulator, i.e., put the system in a box, making its dynamics more interesting (in asymptotically flat space, most orbits immediately escape to infinity with no opportunity to develop chaos). Now why consider strings instead of geodesics? Because geodesics are not the best way to probe the chaos generated by black holes: we know that geodesics in AdS-Schwarzschild, AdS-Reissner-Nordstrom and AdS-Kerr backgrounds (and also in all axially symmetric and static black hole geometries) are integrable, and yet, since the horizon in all these cases has a finite Hawking temperature, there should be some thermalization and chaos going on. The logical decision is therefore to go for string dynamics, which is practically always nonintegrable in the presence of a black hole. We look mainly at the Lyapunov exponents and how they depend on the Hawking temperature. We will see that the bound of [1] is surprisingly relevant here, even though the bound was formulated for *field theories* with a *classical gravity dual*, whereas we look at the *bulk* dynamics of *strings*, which go beyond the realm of Einstein gravity. At first glance, their Lyapunov exponents should not saturate (let alone violate) the bound; in fact, at first glance, it is not

---

[1]Of course, one should be careful when it comes to details; it is known that for some field contents in the bulk the boundary theory does not exist.

obvious at all how to relate the Lyapunov exponent of classical bulk orbits to the result [1], which defines the Lyapunov exponent in terms of the out-of-time ordered correlation functions (OTOC).[2] An important discovery in relation to this issue was made in [17], where the authors consider a holographically more realistic string (open string dual to a quark in Brownian motion in a heath bath), compute the Lyapunov exponent in dual field theory, and find that it exactly saturates the bound. However, their *world-sheet* theory, i.e., their induced metric itself looks somewhat like gravity on AdS$_2$; therefore, close connection to the Einstein gravity result is understandable. Our situation is different not only because the ring string configurations have worldsheet actions very different from Einstein gravity but also because we look mainly at the Lyapunov exponents of the bulk orbits.[3] We will eventually look also at the OTOC in dual field theory and find that the "quantum" Lyapunov exponents do not in general coincide with the classical bulk values. However, the subject of OTOC functions is more complicated as it requires one to consider the backreaction on the background, and studying the behavior of the ring string in such backreacted geometry is in general more difficult than for the open string od [17]. Therefore, we mostly leave the OTOC and quantum Lyapunov exponent for future work.

At this point we come to another question, distinct but certainly related to the chaos bound: the story of (non)integrability in various curved spacetimes. For point particles (i.e., motion on geodesics) it is usually not so difficult to check for integrability, and symmetries of the problem usually make the answer relatively easy. However, integrability in string theory remains a difficult topic. Most systematic work was done for top-down backgrounds, usually based on the differential Galois theory whose application for string integrability was pioneered in [19]. Systematic study for various top-down configurations was continued in [20–22]; [21] in particular provides the results for strings in a broad class of brane backgrounds, including Dp-brane, NS1 and NS5 brane configurations. The bottom line is that integrable systems are few and far apart, as could be expected. Certainly, AdS$_5 \times$ S^5 is an integrable geometry, as could be expected from its duality to the (integrable) supersymmetric Yang-Mills field theory. In fact, direct product of AdS space and a sphere is integrable in any dimension, which is obvious from the separability of the coordinates. But already a marginal deformation destroys integrability; a specific example was found analytically and numerically in [23], for the β-deformation of super-Yang-Mills and its top-down dual. More information can be found, e.g., in the review [24].

The first study of integrability in a black hole background was [25], where the nonintegrability of string motion in asymptotically flat Schwarzschild black hole background was shown. In [26] the first study for an AdS black hole background (AdS-Schwarzschild) was performed, putting the problem also in the context of AdS/CFT correspondence. In [27] the work on top-down backgrounds was started, considering the strings

---

[2]In addition, the scrambling concept of [2, 4–7] is more complex; it is about the equilibration of the black hole and its environment after something falls in. In other words, it necessarily includes the perturbation of the black hole itself. We do not take into account any backreaction so we cannot compute the scrambling time, only the Lyapunov exponent.

[3]Another example where the bound is modified (by a factor of 2) in a theory that goes beyond Einstein gravity is [18].

on the AdS$\times T^{1,1}$ geometry generated in a self-consistent top-down way. For the top-down AdS-Sasaki-Einstein background the nonintegrability was proven analytically [19]. Finally, AdS-soliton and AdS-Reissner-Nordstrom were also found to be nonintegrable in [28, 29]. So most well-known in AdS/CFT have nonintegrable string dynamics: AdS-Schwarzschild, AdS-Reissner-Nordstrom, AdS soliton and AdS-Sasaki-Einstein.[4] Other results on (non)integrability can be found in [30–33]; the list is not exhaustive.

Apart from the usual spherical static black holes (neutral and charged), we consider also non-spherical horizons with constant curvature. Among them are also the zero-curvature black branes, with infinite planar horizons, which are most popular in applied holography. But it is known that more general horizons can be embedded in AdS space (in general not in Minkowski space). Such black holes are usually called topological black holes, first constructed in [34–37] and generalized in [38]. The term topological is in fact partly misleading, as the backgrounds considered in some of the original papers [35] and also in our paper are not necessarily of higher topological genus: besides spherical and planar horizons, we mainly consider an infinite, topologically trivial hyperbolic horizon with constant negative curvature (pseudosphere).[5]

The reader might wonder how important the non-spherical black holes are from the physical viewpoint. In fact, as shown in the aforementioned references, they arise naturally in spaces with negative cosmological constant, i.e., in AdS spaces, for example in the collapse of dust [39], and the topological versions are easily obtained through suitable gluings (identifications of points on the orbit of some discrete subgroup of the total symmetry group) of the planar or pseudospherical horizon. Another mechanism is considered in [34], where topological black holes are pair-created from instanton solutions of the cosmological C-metric (describing a pair of black holes moving with uniform acceleration). More modern work on constant-curvature black holes and some generalizations can be found in [40–42], and AdS/CFT correspondence was applied to topological black holes in [43]. But our main motivation for considering non-spherical black holes is methodological, to maximally stretch the testing ground for the chaos bound and to gain insight into various chaos-generating mechanisms. In hindsight, we find that hyperbolic are roughly speaking most chaotic, because moving on a manifold of negative curvature provides an additional chaos-generating mechanism, in addition to the black hole.

The plan of the paper is the following. In the next section we write down the equations of motion for a closed string in static black hole background, inspect the system analytically and numerically and show that dynamics is generically non-integrable. In the third section we compute the Lyapunov exponents numerically and estimate them analytically, formulating a generalized bound in terms of the local temperature and the string winding number. The fourth section is a rather speculative attempt to put our results in the context of the dual field theory and the derivation of the original bound from [1]; we will also try to clarify the relation of the bulk classical Lyapunov exponent to the decay rates of OTOC functions in dual field theory. The last section sums up the conclusions.

---

[4]In [26, 29] it was shown that Reissner-Nordstrom black holes in asymptotically flat space are also nonintegrable.

[5]In fact, constant-curvature black holes would be a more suitable term than topological black holes.

2 String dynamics in static black hole backgrounds

A constant curvature black hole in $N + 1$ spacetime dimensions is a geometry of constant curvature with the metric [34–36]

$$ds^2 = -f(r)dt^2 + \frac{dr^2}{f(r)} + r^2 d\sigma_{N-1}^2$$

$$f(r) = r^2 + k - \frac{2m}{r^{N-2}} + \frac{q^2}{r^{2N-4}},\tag{2.1}$$

where $d\sigma_{N-1}^2$ is the horizon manifold, which has curvature k, and m and q define the mass and charge of the black hole. It is a vacuum solution of the Einstein equations with constant negative cosmological constant and thus interpolates to AdS space with radius 1. From now on let us stick to $N = 3$ unless specified otherwise. For $k = 1$ we have the familiar spherical black hole. For $k = 0$ we get the planar horizon (black brane) popular in AdS/CFT applications.[6] Finally, for $k = -1$ the horizon is an infinite hyperbolic sheet (pseudosphere), with the symmetry group $SO(2, 1)$.[7] Notice that k can always be rescaled together with the coordinates on σ_2 thus we only consider $k = -1, 0, 1$. The metric of the horizon surface takes the form

$$d\sigma_2^2 = d\phi_1^2 + \text{sink}^2\phi_1 d\phi_2^2,\tag{2.2}$$

with $\text{sink}(x) = \sin x$ for $k = 1$, $\text{sink}(x) = x$ for $k = 0$ and $\text{sink}(x) = \sinh(x)$ for $k = -1$.

A closed string with tension $1/\alpha'$ on the worldsheet (τ, σ) with target space X^μ and the metric $G_{\mu\nu}$ is described by the Polyakov action:

$$S = -\frac{1}{2\pi\alpha'} \int d\tau d\sigma \sqrt{-h} h^{ab} G_{\mu\nu}(X)\partial_a X^\mu \partial_b X^\nu + \epsilon^{ab} B_{\mu\nu}(X)\partial_a X^\mu \partial_b X^\mu.\tag{2.3}$$

In our black hole backgrounds we always have $B_{\mu\nu} = 0$ so we can pick the gauge $h^{ab} = \eta^{ab} = \text{diag}(-1, 1)$. This gives the Virasoro constraints

$$G_{\mu\nu}\left(\dot{X}^\mu \dot{X}^\nu + X'^\mu X'^\nu\right) = 0, \quad G_{\mu\nu}\dot{X}^\mu X'^\nu = 0,\tag{2.4}$$

where we introduce the notation $\dot{X} \equiv \partial_\tau X, X' \equiv \partial_\sigma X$. The first constraint is the Hamiltonian constraint $H = 0$. We consider closed strings, so $0 \leq \sigma \leq 2\pi$. From the second constraint the following ansatz is consistent (of course, it is not the only one possible):

$$\mathcal{T} = \mathcal{T}(\tau), \ R = R(\tau), \ \Phi_1 = \Phi_1(\tau), \ \Phi_2 = n\sigma.\tag{2.5}$$

We denote the (dynamical) target-space coordinates $X_\mu(\tau, \sigma)$ by capital letters $\mathcal{T}, R, \Phi_1, \Phi_2$, to differentiate them from the notation for spacetime coordinates t, r, ϕ_1, ϕ_2 in the metric (2.1). The form (2.5) was tried in most papers exploring the integrability and chaos

---

[6]With periodic identifications on σ_2 one gets instead a toroidal horizon.

[7]If we identify the points along the orbits of the little group of $SO(2, 1)$, we get a genus g surface with $g \leq 2$, and the horizon becomes compact and topologically nontrivial, hence the term topological black holes for this case.

of strings [19, 25–29]. It is not an arbitrary ansatz: the winding of Φ_2 follows from the equations of motion, i.e., from the fact that Φ_2 is a cyclic coordinate, leading to the solution $\ddot{\Phi}_2 = 0$. Since Φ_2 has trivial dynamics, from now on we will denote $\Phi \equiv \Phi_1$. The equations of motion follow from (2.3):

$$\partial_\tau \left(f \dot{\mathcal{T}} \right) = 0 \Rightarrow E \equiv f \dot{\mathcal{T}} = \text{const.} \tag{2.6}$$

$$\ddot{R} + \frac{f'}{2f}(E^2 - \dot{R}^2) + fR\left(\dot{\Phi}^2 - n^2 \text{sink}^2\Phi\right) = 0 \tag{2.7}$$

$$\ddot{\Phi} + \frac{2\dot{R}}{R}\dot{\Phi} + \frac{n^2}{2}\text{sink}(2\Phi) = 0. \tag{2.8}$$

Clearly, the stationarity of the metric yields the first integral E with the informal meaning of mechanical energy for the motion along the R and Φ coordinates (it is not the total energy in the strict sense). The system is more transparent in Hamiltonian form, with the canonical momenta $P_\mathcal{T} = -E = -f\dot{\mathcal{T}}, P_R = \dot{R}/f, P_\Phi = R^2\dot{\Phi}$:[8]

$$H = \frac{f}{2}P_R^2 + \frac{1}{2R^2}P_\Phi^2 + \frac{n^2}{2}R^2\text{sink}^2\Phi - \frac{E^2}{2f} = 0, \tag{2.9}$$

the second equality being the Virasoro constraint. We thus have a 2-degrees-of-freedom system (due to the integral of motion E, i.e., the cyclic coordinate $\mathcal{T}$), with a constraint, effectively giving a 1.5-degrees-of-freedom system, moving on a three-dimensional manifold in the phase space (R, P_R, Φ, P_Φ). Notice that the motion along a geodesic is obtained for $n = 0$; in this case, the system is trivially separable and becomes just motion in a central potential. For nonzero n, the Hamiltonian (2.9) is not separable and the system is nonintegrable.[9] On the other hand, for a point particle all constant-curvature black holes have a full set of integrals of motion leading to the integrability of geodesics: for the sphere, the additional integrals (besides E) are L^2 and L_z from SO(3), and for the pseudosphere these are K^2 and K_z from SO(2,1). For the planar black hole we obviously have $P_{x,y}$, the momenta, as the integrals of motion. Of course, if we consider compactified surfaces, the symmetries become discrete and do not yield integrals of motion anymore. Therefore, truly topological black holes are in general nonintegrable even for geodesics.[10]

---

[8]In this and the next section we put $\alpha' = 1/\pi$, as we only consider classical equations of motion, which are independent of α'. In section 4, when calculating the quantities of the dual gauge theory, we restore α' as it is related to the 't Hooft coupling, a physical quantity.

[9]One can prove within Picard-Vessiot theory that no canonical transformation exists that would yield a separable Hamiltonian, so the system is nonintegrable. We will not derive the proof here, as it is not very instructive; the nonintegrability of the spherical case was already proven in [26, 29], and the existence of nonzero Lyapunov exponents will *de facto* prove the nonintegrability for the other cases. One extra caveat is in order for the planar case. For $k = 0$ and $\text{sink}\Phi = \Phi$, the Hamiltonian is still not separable, and dynamics is nonintegrable. One could change variables in the metric (2.1) as $(\phi_1, \phi_2) \mapsto (\phi_1' = \phi_1 \cos\phi_2, \phi_2' = \phi_1 \sin\phi_2)$, and the string with the wrapping $\Phi_2' = n\sigma$ would provide an integrable system, with the separable Hamiltonian $H' = \frac{f}{2}P_R^2 + \frac{1}{2R^2}P_{\Phi'}^2 + \frac{n^2}{2}R^2 - \frac{E^2}{2f}$. But that is a *different* system from (2.9): even though a change of variables is clearly of no physical significance, the wrapping $\Phi_2' = n\sigma$ is physically different from $\Phi_2 = n\sigma$. Integrability clearly depends on the specific string configuration.

[10]For special, fine-tuned topologies and parameters, one finds integrable cases (even for string motion!) but these are special and fine-tuned; we will consider these cases elsewhere as they seem peripheral for our main story on the chaos bound.
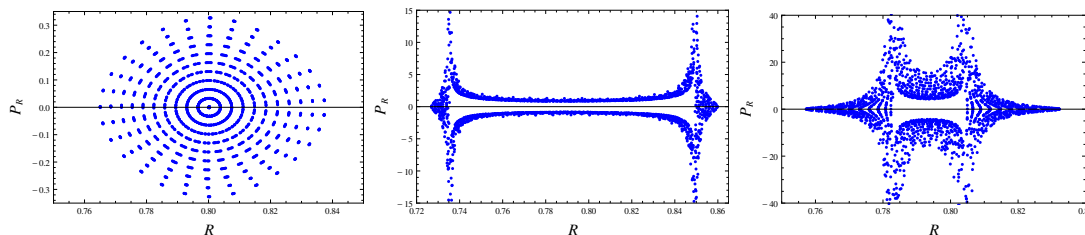
Figure 1. Poincare section (R, P_R) for orbits starting at the apparent horizon (removed for a distance of 10^{-4} from the event horizon), at increasing temperatures $T = 0.00, 0.05, 0.10$, for a planar black hole with $m = 1$ and charge parameter q determined by the temperature. The coordinate and momentum are in units of AdS radius.

2.1 Fixed points and near-horizon dynamics

For a better overall understanding of chaos in string motion, let us sketch the general trends in dynamics first. For spherical black holes, this job was largely done in [26, 29, 44] and for similar geometries also in [27, 28]. We will emphasize mainly the properties of near-horizon dynamics that we find important for the main story.

Typical situation can be grasped from figure 1, where the Poincare sections of orbits starting near the horizon are shown for increasing temperatures of the horizon, as well as figures 2 and 3 where we show typical orbits in the $x - y$ plane for different temperatures and initial conditions.

1. Higher temperatures generally increase chaos, with lower and lower numbers of periodic orbits (continuous lines in the Poincare section in figure 1) and increasing areas covered with chaotic (area-filling) orbits. This is also obvious from the figure 2.

2. Orbits closer to the horizon are more chaotic than those further away; this will be quantified by the analysis of the Lyapunov exponents. This is logical, since the equations of motion for strings in pure AdS space are integrable, and far away from the horizon the spacetime probed by the string becomes closer and closer to pure AdS. An example of this behavior is seen in figure 3(A).

3. The previous two trends justify the picture of the thermal horizon as the generator of chaos. However, for an extremal or near-extremal *hyperbolic* horizon there is a slight discrepancy — in this case, moving away from the horizon increases the chaos. In other words, there is yet another mechanism of chaos generation, independent of the temperature and not located precisely at the horizon, which is subleading and not very prominent, except when it is (almost) the only one, i.e., when the horizon is (near-)extremal. This is demonstrated in figure 3(B).

When we come to the consideration of the Lyapunov exponents, we will identify the horizon-induced scrambling and the chaotic scattering as the chaos-inducing mechanisms at work for $r \to r_h$ and for intermediate r, respectively.

Consider now the radial motion from the Hamiltonian (2.9). Radial motion exhibits an effective attractive potential $E^2/2f$ which diverges at the horizon. The Φ-dependent terms
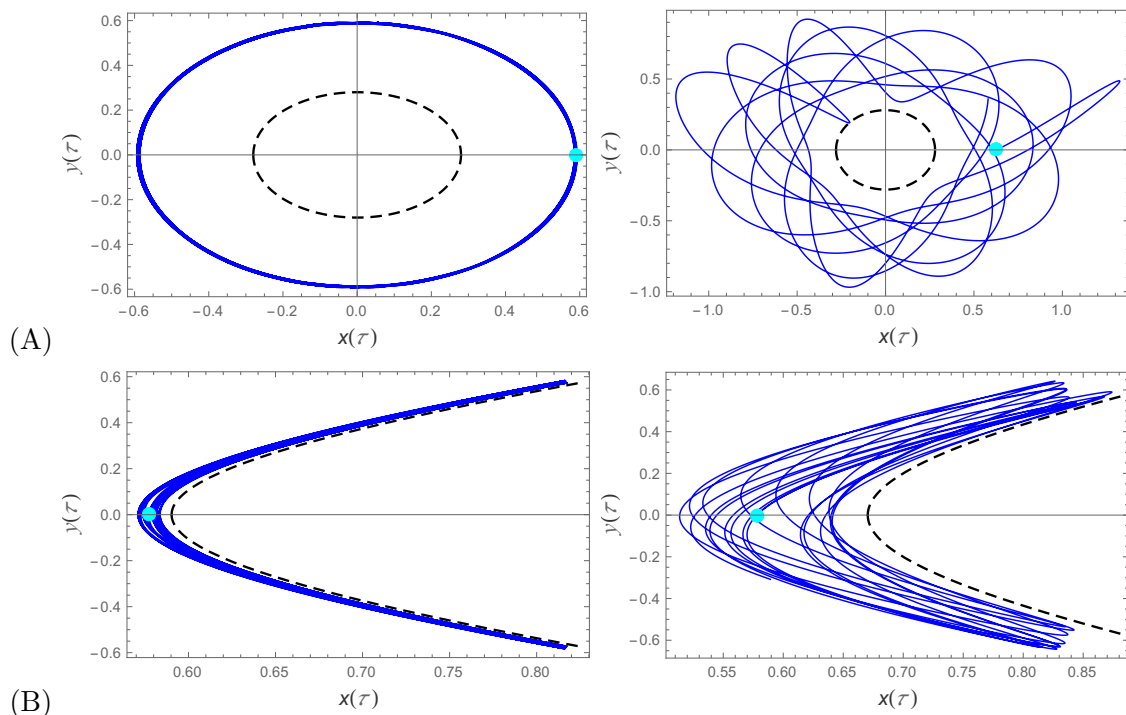
Figure 2. Thermal horizon as the generator of chaos. We show the orbits in the vicinity of the spherical (A) and hyperbolic (B) horizon, at $T = 0.01$ (left) and $T = 0.10$ (right); obviously, hot horizons generate more chaos than cold ones. The light blue dot is the initial condition of the orbit (the position of the point on the string with $\Phi = 0$ at $\tau = 0$).
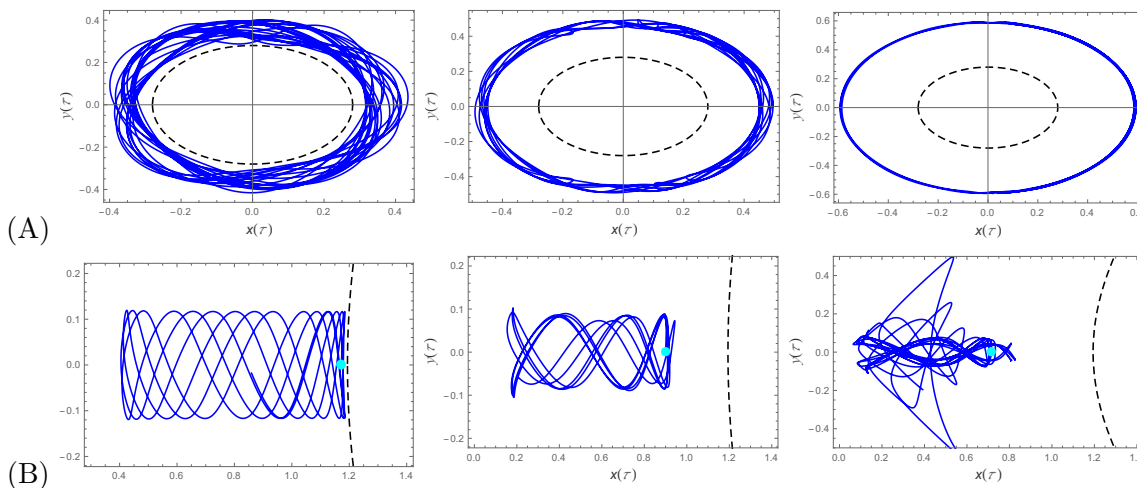
Figure 3. Thermal horizon and hyperbolic scattering as generators of chaos. In (A) and (B), we show the orbits in the vicinity of the spherical and hyperbolic horizon, respectively, at the small temperature $T = 0.01$ and starting at increasing distances from the horizon. In (A), the further from the horizon, the more regular the orbit becomes. But in the hyperbolic geometry (B), the thermally-generated chaos is negligible; instead, the orbit becomes chaotic as it explores larger and larger area of the hyperbolic manifold. Hence for hyperbolic horizons, an additional, non-thermal generator of chaos exists: it is the hyperbolic scattering. Light blue dots are again the initial positions of the string origin ($\Phi = 0$).

proportional to R^2 and $1/R^2$ are repulsive and balance out the gravitational attraction to some extent but they remain finite for all distances. For R large, the repulsion proportional to n^2 dominates so for large enough distances the string will escape to infinity. For intermediate distances more complex behavior is possible: the string might escape after some number of bounces from the black hole, or it might escape after completing some (non-periodic, in general) orbits around the black hole. The phase space has invariant planes given by $(R, P_R, \Phi, P_\Phi) = (R_0 + E\tau, E/f_0, N\pi, 0)$, with $R_0 = $ const. and $f_0 \equiv f(R_0)$ and N an integer. It is easy to verify this solution by first plugging in $\dot{\Phi} = 0$ into (2.8) to find Φ; eq. (2.7) and the constraint (2.9) then reduce to one and the same condition $\dot{R}^2 = E^2$. We discard the solution with the minus sign (with $R = R_0 - E\tau$) as R is bounded from below. Pictorially, this solution means that a string with a certain orientation just moves uniformly toward the black hole and falls in, or escapes to infinity at uniform speed, all the while keeping the same orientation. Besides, there is a trivial fixed point at infinity, $(R, P_R, \Phi, P_\Phi) = (\infty, 0, N\pi, 0)$, found also in [26, 29].

We are particularly interested if a string can hover at a fixed radial slice $R = r_0 = $ const.. Let us start from the spherical case. Inserting $R = r_0, \dot{R} = 0$ into eq. (2.8) leads to the solution in terms of the incomplete Jacobi sine integral sn (Jacobi elliptic function of the first kind, Jacobi E-function), and two integration constants to be determined. The other equation, (2.7), is a first-order relation for Φ acting as a constraint. Solving it gives a Jacobi elliptic function again, with one undetermined constant, and we can match the constants to obtain a consistent solution:

$$\sin \Phi(\tau) = \mathrm{sn}\left(\frac{E\sqrt{|f_0'|}}{\sqrt{2r_0}f_0}\tau, \frac{2n^2r_0f_0^2}{E^2|f_0'|}\right). \tag{2.10}$$

The value of r_0 is found from the need to satisfy also the Hamiltonian constraint. The constraint produces a Jacobi elliptic function with a different argument, and the matching to (2.10) reads

$$2f(r_0) + r_0f'(r_0) = 0. \tag{2.11}$$

This turns out to be a cubic equation independent of the black hole charge, as the terms proportional to q cancel out. It has one real solution, *which is never above the horizon.* The solution approaches the horizon as $f'(r_0)$, approaches zero, and $r = r_h$ is obviously a solution of (2.11) for $f'(r_h) = 0$. However, the $r \to r_h$ limit is subtle in the coordinates we use because some terms in equations of motion diverge, so we need to plug in $f(r) = 0$ from the beginning. Eqs. (2.6), (2.8) then imply $\dot{R} = E$, i.e., there is no solution at constant R except for $E = 0$. This is simply because the energy is infinitely red-shifted at the horizon, i.e., E scales with f (eq. (2.6)), thus indeed unless $\dot{\mathcal{T}} \to \infty$, which is unphysical, we need $E = 0$. Now solving eq. (2.7) gives the same solution as before, of the form $\mathrm{sn}(C_1\tau, C_2)$, with undetermined constants $C_{1,2}$, which are chosen so as to establish continuity with the solution (2.10). For an extremal horizon of the from $f \sim a(r - r_h^2) \equiv a\epsilon^2$, a smooth and finite limit is obtained by rescaling $E \mapsto E\epsilon^2$. Now expanding the sn function in ϵ produces simply a linear function at first order in ϵ:

$$\Phi(\tau) = E\tau/\sqrt{ar_0} + O\left(\epsilon^3\right). \tag{2.12}$$

Therefore, *a string can hover at the extremal horizon*, at strict zero temperature, when its motion (angular rotation) becomes a simple linear winding with a single frequency. Such an orbit is expected to be linearly stable, and in the next section we show it is also stable according to Lyapunov and thus has zero Lyapunov exponent. Finally, from (2.7) and (2.11) the radial velocity $\dot{R}$ in the vicinity of a non-extremal horizon behaves as:

$$\dot{R}^2 \approx E^2 + 4\pi T r_h (r - r_h)^2, \tag{2.13}$$

meaning that $\dot{R}$ grows quadratically as the distance from the horizon increases. This will allow us to consider near-horizon dynamics at not very high temperatures as happening at nearly constant radius: the string only slowly runs away.

For a hyperbolic horizon the calculation is similar, changing $\sin \mapsto \sinh$ in the solution (2.10). The constraint (2.11) is also unchanged (save for the sign of k in the redshift function), and the final conclusion is the same: the string can only balance at the zero temperature horizon (but now such a horizon need not be charged, as we mentioned previously). The zero temperature limit is the same linear function (2.12). For a planar horizon things are different. For $\dot{R} = 0$, we get simply harmonic motion $\Phi = C_1 \cos n\tau + C_2 \sin n\tau$, which is consistent with the constraint $H = 0$. But eq. (2.7) implies exponential motion instead, $D_1 \sinh n\tau + D_2 \cosh n\tau$. Obviously, there is no way to make these two forms consistent. Accordingly, no hovering on the horizon (nor at any other fixed radial slice) is possible for a planar black hole. But the same logic that lead to (2.13) now predicts oscillating behavior:

$$R(\tau) \approx E^2 + 4\pi T r_h (r - r_h)^2 \left(n^2 \cos^2 n\tau - \sin^2 n\tau \right). \tag{2.14}$$

Therefore, even though there are no orbits at all which stay at exactly constant R, we now have orbits which oscillate in the vicinity of the horizon forever. Averaging over long times now again allows us to talk of a string that probes some definite local temperature, determined by the average distance from the horizon.

The point of this (perhaps tedious and boring) qualitative analysis of possible orbits is the following. No orbits at fixed distance from the horizon are possible, *but* at low temperatures a string that starts near the horizon will spend a long time in the near-horizon area. Therefore, we can study the influence of the low-temperature horizon as the main chaos-generating mechanism by expanding the variational equations for the Lyapunov exponents in the vicinity of the horizon, This we shall do in the next section.

3 Lyapunov exponents and the bound on chaos

In general, Lyapunov exponents are defined as the coefficients λ of the asymptotic exponential divergence of initially close orbits; in other words, of the variation δX of a coordinate X:

$$\lambda \equiv \lim_{t \to \infty} \lim_{\delta X(0) \to 0} \frac{1}{t} \log \frac{|\delta X(t)|}{|\delta X(0)|}, \tag{3.1}$$

and the variation is expected to behave as $\delta X \sim \delta X(0) \exp(\lambda t)$ for t large and $\delta X(0)$ small enough in practice. This definition makes sense for classical systems; in quantum

mechanics, the linearity of the state vector evolution guarantees zero exponent but the intuition that initially small perturbations eventually grow large in a strongly coupled system remains when we look at appropriately defined correlation functions, like the OTOC used in [1]. We should first make the following point clear. In a classical nonlinear system, the presence of deterministic chaos leads to positive Lyapunov exponents even in absence of temperature or noise. Quantum mechanically, as we explained, the linearity of evolution means that exponential divergence is only possible in a thermal state, and this situation leads to the temperature bound on the Lyapunov exponents. This is easy to see upon restoring dimensionful constants, when the bound from [1] takes the form $\lambda \leq 2\pi k_B T/\hbar$, and indeed in a classical system where $\hbar \to 0$ no bound exists. In the context of our work, which effectively reduces to the classical Hamiltonian (2.9) which has no gravitational degrees of freedom, it is not *a priori* clear if one should expect any connection to the bound on chaos: instead of a QFT correlation function or its gravity dual, we have classical dynamics, and the Hawking temperature of the black hole is not the local temperature probed by the string. But we will soon see that analytical and numerical estimates of λ nevertheless have a form similar to the chaos bound of [1].

Before we proceed one final clarification is in order. One might worry that the Lyapunov exponents are gauge-dependent, as we consider equations of motion in terms of the worldsheet coordinate τ, and for different worldsheet coordinates the variational equations would be manifestly different; in other words, the definition (3.1) depends on the choice of the time coordinate (denoted schematically by t in (3.1)). Indeed, the value of λ clearly changes with coordinate transformations, however it has been proven that the *positivity* of the largest exponent (the indicator of chaos) is gauge-invariant; the proof was derived for classical general relativity [45] and carries over directly to the worldsheet coordinate transformations. This is all we need, because we will eventually express the τ-exponent in terms of proper time for an inertial observer, making use of the relation $\dot{\mathcal{T}} = -E/f$. This could fail if a coordinate change could translate an exponential solution into an oscillating one (because then λ drops to zero and it does not make sense to re-express it units of proper time); but since we know that cannot happen we are safe.

3.1 Variational equations and analytical estimates of Lyapunov exponents

3.1.1 Thermal horizon

Consider first a thermal black hole horizon at temperature T, with the redshift function behaving as $f = 4\pi T(r - r_h) + O\left((r - r_h)^2\right)$. Variational equations easily follow from (2.6)–(2.7):

$$\delta\ddot{R} - \frac{E^2}{(R - r_h)^2}\delta R - 4\pi T\left(\dot{\Phi}^2 - n^2\mathrm{sink}^2\Phi\right)\delta R - 8\pi T(R - 2r_h)R\dot{\Phi}\delta\dot{\Phi}$$
$$+4\pi n^2 TR\mathrm{sink}(2\Phi)\delta\Phi = 0 \qquad (3.2)$$

$$\delta\ddot{\Phi} + n^2\mathrm{sink}(2\Phi) + \frac{2}{r_h}\dot{\Phi}\delta\dot{R} = 0, \qquad (3.3)$$

with on-shell solutions $R(\tau), \Phi(\tau)$. This system looks hopeless, but it is not hard to extract the leading terms near the horizon which, as we explained, makes sense at low temperatures.

Therefore, we start from the solutions (2.10), (2.12), (2.14), adding a small correction $(r_0, \Phi(\tau)) \to (r_0 + \Delta R(\tau), \Phi(\tau) + \Delta \Phi(\tau))$. Then we expand in inverse powers of $r_0 - r_h$, and express the angular combinations $\dot{\Phi}^2 \pm \mathrm{sink}^2 \Phi$ making use of the constraint (2.9). When the dust settles, the leading-order equations simplify to:

$$\delta \ddot{R} - \left(16 \, (\pi T)^3 \, \frac{n^2}{E^2} (r_0 - r_h) - 32 \, (\pi T)^3 \, \frac{Cn}{E^2 \phi_0} \, (r_0 - r_h)^2 \right) \delta R = 0 \tag{3.4}$$

$$\delta \ddot{\Phi} + n^2 \langle \mathrm{cosk}^2(2\Phi) \rangle \delta \Phi = 0, \tag{3.5}$$

where $C = C(k, E)$ is a subleading (at low temperature) correction whose form differs for spherical, planar and hyperbolic horizons. From the above we read off that angular motion has zero Lyapunov exponent (the variational equation is oscillatory, because $\langle \mathrm{cosk}^2(2\Phi) \rangle \geq 0$) but the radial component has an exponent scaling as

$$\tilde{\lambda}(T) \sim 4\sqrt{(\pi T)^3 (r_0 - r_h)} \frac{n}{E} \left(1 - (r - r_h) \frac{C}{\phi_0 n} \right). \tag{3.6}$$

Now we have calculated the Lyapunov exponent in worldsheet time τ. The gauge-invariant quantity, natural also within the black hole scrambling paradigm, is the proper Lyapunov exponent λ, so that $1/\lambda$ is the proper Lyapunov time for an asymptotic observer. To relate $\tilde{\lambda}$ to λ, we remember first that the Poincare time t is related to the worldsheet time τ through (2.6) as $|dt| \sim E/f \times d\tau$. Then we obtain the proper time as $t_p = t\sqrt{-g_{00}} = t\sqrt{f}$, where near the thermal horizon we can write $f \approx 4\pi T(r - r_h)$. This gives[11]

$$\lambda(T) \sim 2\pi T n \left(1 - \epsilon \frac{C}{\phi_0 n} \right). \tag{3.7}$$

At leading order, we get the estimate $2\pi T n$, with the winding number n acting as correction to the original bound.

3.1.2 Away from the horizon

At intermediate radii we can do a similar linear stability analysis starting from $f \sim r^2 + k + A/r$ where A is computed by series expansion (with just the AdS term $r^2 + k$ in f, without the leading black hole contribution A/r, we would trivially have integral motion and zero λ; but this approximation applies at large, not at intermediate distances). In this case the equations of motion yield $R \sim \tau\sqrt{E^2 - 1}$, and the variational equations, after some algebra, take the form

$$\delta \ddot{R} - \frac{2}{R}(k + R^2)\delta \dot{\Phi} + E \left(\frac{3kR^2}{R^2 + k} + 1 \right) \delta R = 0. \tag{3.8}$$

One can show again that $\delta \dot{\Phi}$ is always bounded in absolute value, thus the third term determines the Lyapunov exponent. The exponent vanishes for $k > -1/3$ (because the equations becomes oscillatory) and for $k \leq -1/3$ we get

$$\lambda \sim \sqrt{-(3k + 1)E}. \tag{3.9}$$

---

[11]We introduce the notation $\epsilon \equiv r - r_h$.

Since the curvature only takes the values $-1, 0, 1$, the prediction (3.9) always holds for hyperbolic horizons. Notice that this same term (the third term in (3.8)) appears as subleading in the near-horizon expansion, so we can identify it with $C(k, E)$ and write (3.7) as $\lambda(T) \sim 2\pi T n \left(1 - \epsilon |(3k + 1)E| / (\phi_0 n)\right)$. This holds for any k, and we see that $C \leq 0$; thus the bound is only approached from below as it should be.

In absence of negative curvature, i.e., for $k > 0$, we have vanishing C at leading order in $1/R$ but subleading contributions still exist, so both the slight non-saturation of the limit $2\pi T n$ near-horizon (for small ϵ) and a parametrically small non-zero Lyapunov exponent at intermediate distances will likely appear, which we see also in the numerics. That the motion is chaotic on a pseudosphere (negative curvature) is of course no surprise; it is long known that both particles and waves have chaotic scattering dynamics on pseudospheres [46]. We dub this contribution the scattering contribution to the Lyapunov exponent, as opposed to the scrambling contribution. It is largely independent of temperature and largely determined by the geometry of the spacetime away from the horizon.

3.1.3 Extremal horizon

For an extremal horizon we replace f by $f \sim a(r - r_h)^2 = a\epsilon^2$, and plug in this form into the variational equations. Now the result is (for concreteness, for the spherical horizon)

$$\delta\ddot{R} - \left(\frac{a^2\epsilon^4 r_h^2 n^2}{2a\epsilon r_h - 2a\epsilon^2}\right)\delta R = 0 \tag{3.10}$$

$$\delta\ddot{\Phi} + n^2 \langle \cos k(2\Phi) \rangle \delta\Phi = 0, \tag{3.11}$$

leading to a vanishing exponent value:

$$\tilde{\lambda}(T) \sim \sqrt{ar_h/2}\, n\epsilon^{3/2} \to 0. \tag{3.12}$$

Obviously, this also means $\lambda = 0$ — there is no chaos at the extremal horizon. This is despite the fact that the string motion in this case is still nonintegrable, which is seen from the fact that no new symmetries or integrals of motion arise in the Hamiltonian in this case. The horizon scrambling is proportional to temperature and does not happen at $T = 0$, but the system is still nonintegrable and the chaos from other (scattering) origins is still present. In particular, the estimate (3.8)–(3.9) remains unchanged.

The estimates (3.7), (3.9), (3.12) are the central sharp results of the paper. We can understand the following physics from them:

1. At leading order, we reproduce (and saturate) the factor $2\pi T$ of the Maldacena-Shenker-Stanford bound, despite considering classical dynamics only.

2. The bound is however multiplied by the winding number n of the ring string. The spirit of the bound is thus preserved but an extra factor — the winding number — enters the story.

3. Taking into account also the scattering chaos described by (3.9), the results are in striking accordance with the idea of [2]: there are two contributions to chaos, one

proportional to the black hole temperature and solely determined by the scrambling on the horizon, with the universal factor $2\pi T$ expected from the concept of black holes as the fastest scramblers in nature, and another determined by the (slower) propagation of signals from the horizon toward the AdS boundary, which we call the scattering term, as it is determined also by dynamics at large distances.

4. For a particle ($n = 0$), we correctly get $\lambda = 0$, as the geodesics are integrable.

5. The temperature appearing in (3.7) is always the Hawking temperature of the black hole T.

In the next section, when we consider the AdS/CFT interpretation, we will try to shed some more light on where the modification of the bound $2\pi T \mapsto 2\pi T n$ comes from.

3.1.4 Lyapunov time versus event time

In the above derivations we have left one point unfinished. We have essentially assumed that $R(\tau) \approx \text{const.} = r$ and treated the difference $\epsilon = r - r_h$ as a fixed small parameter. This is only justified if the local Lyapunov time $1/\tilde{\lambda}$ is much shorter than the time to escape far away from r_h and the horizon, or to fall into the black hole. In other words, it is assumed that the Lyapunov time is much shorter than the "lifetime" of the string (let us call it event time t_E). Now we will show that this is indeed so. For the spherical black hole, upon averaging over the angle Φ, we are left with a one-dimensional system

$$\dot{R}^2 + R^2 f(R) \frac{E^2 f'(R)}{R f^2(R)} = E^2, \tag{3.13}$$

which predicts the event time as

$$t_E \sim \int_{r_0}^{r_h, \infty} \frac{dR}{\sqrt{|E - E f'(R) R f^2(R)|}} \approx \frac{\pi r_h}{\sqrt{2}} \frac{1}{\sqrt{4\pi T \epsilon n}} \approx \frac{\pi r_h}{\sqrt{2}} \times \frac{\tilde{\lambda}^{-1}}{\epsilon}. \tag{3.14}$$

In other words, the event times are roughly by a factor $1/\epsilon$ longer than Lyapunov times, therefore our estimate for λ should be valid. In (3.14), we have considered both the infalling orbits ending at r_h, and the escaping orbits going to infinity (for the latter, we really integrate to some $r_\infty > r_0$ and then expand over $1/r_\infty$). An orbit will be infalling or escaping depending on the sign of the combination under the square root, and to leading order both cases yield a time independent of r_0 (and the cutoff r_∞ for the escaping case). The hyperbolic case works exactly the same way, and in the planar case since $R(\tau)$ oscillates the event time is even longer (as there is no uniform inward or outward motion). For extremal horizons, there is no issue either as $r = r_h$ is now the fixed point.

3.1.5 Dimensionful constants

One might wonder what happens when dimensionful constants are restored in our results for the Lyapunov exponents like (3.7) or (3.9): the original chaos bound really states $\lambda \le 2\pi k_B T/\hbar$, and we have no $\hbar$ in our system so far. The resolution is simple: the role of $\hbar$ is played by the inverse string tension $2\pi\alpha'$, which is obvious from the standard form

of the string action (2.3); the classical string dynamics is obtained for $\alpha' \to 0$. Therefore, the dimensionful bound on chaos for our system reads $\lambda = 2\pi k_B T n / 2\pi\alpha' = k_B T n / \alpha'$. Another way to see that α' takes over the role of $\hbar$ in the field-theory derivation [1] is that the weight in computing the correlation functions for a quantum field is given by the factor $\exp\left(-1/\hbar \int \mathcal{L}\right)$, whereas for a string the amplitudes are computed with the weight $\exp\left(-1/2\pi\alpha' \int \mathcal{L}\right)$. In the next section, we will also look for the interpretation in the framework of dual field theory. In this context, α' is related to the number of degrees of freedom in the gauge dual of the string, just like the Newton's constant G_N is related to the square of the number of colors N^2 in the gauge dual of a pure gravity theory. But the issues of gauge/string correspondence deserve more attention and we treat them in detail in section 4.

3.2 Numerical checks

We will now inspect the results (3.7), (3.9), (3.12) numerically. Figure 4 tests the basic prediction for the horizon scrambling, $\lambda \approx 2\pi T n$ at low temperatures: both the n-dependence at fixed temperature (A), and the T-dependence at fixed n (B) are consistent with the analytical prediction. All calculations were done for the initial condition $\dot{R}(0) = 0$, and with energy E chosen to ensure a long period of hovering near the horizon. The temperatures are low enough that the scattering contribution is almost negligible. In figure 5 we look at the scattering term in more detail. First we demonstrate that at zero temperature, the orbits in non-hyperbolic geometries are regular (A): the scattering term vanishes at leading order, and the scrambling vanishes at $T = 0$. In the (B) panel, scattering in hyperbolic space at intermediate radial distances gives rise to chaos which is independent of the winding number, in accordance to (3.7). To further confirm the logic of (3.7), one can look also at the radial dependence of the Lyapunov exponent: at zero temperature, there is no chaos near-horizon (scrambling is proportional to T and thus equals zero; scattering only occurs at finite $r - r_h$), scattering yields a nonzero λ at intermediate distances and the approach to pure AdS at still larger distances brings it to zero again; at finite temperature, we start from $\lambda = 2\pi T n$ near-horizon, observe a growth due to scattering and fall to zero approaching pure AdS.

4 Toward a physical interpretation of the modified bound

4.1 Dual gauge theory interpretation

The ring string wrapped along the σ coordinate is a very intuitive geometry from the viewpoint of bulk dynamics. However it has no obvious interpretation in terms of the gauge/gravity duality, and the Hamiltonian (2.9) itself, while simple-looking, is rather featureless at first glance: essentially a forced nonlinear oscillator, it does not ring a bell on why to expect the systematic modification of the Maldacena-Shenker-Stanford bound and what the factor n means. Thus it makes sense to do two simple exercises: first, to estimate the energy and spin of the operators corresponding to (2.5) to understand if it has to do with some Regge trajectory; second, to consider some other string configurations, with a more straightforward connection to the operators in gauge theory. Of course, finite
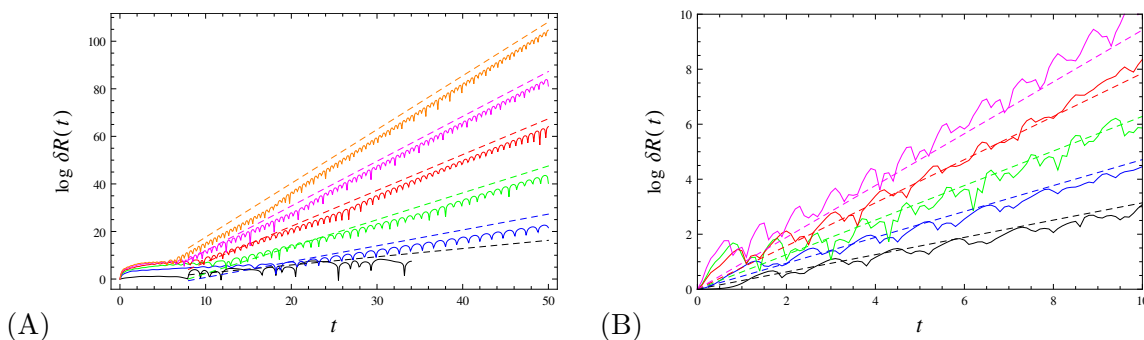
Figure 4. (A) Logarithm of the relative variation of the coordinate R, for a spherical AdS-Reissner-Nordstrom black hole, for a fixed temperature $T = 0.04$ and increasing winding numbers $n = 1, 2, 3, 4, 5, 6$ (black, blue, green, red, magenta, orange). Full lines are the numerical computational of the function $\log\left(\delta X\left(\tau\right)/\delta X\left(0\right)\right) = \lambda\tau$, so their slopes equal the Lyapunov exponents λ. Dashed lines show the analytically predicted bound $\log \delta X = 2\pi T n\tau + \log X_0$. Numerically computed variations almost saturate the bounds denoted by the dashed lines. The calculation for $n = 1$ is stopped earlier because in this case the orbit falls in into the black hole earlier than for higher n. (B) Same as (A) but for a hyperbolic AdS-Schwarzschild black hole, at fixed $n = 1$ and increasing temperature $T = 0.050, 0.075, 0.100, 0.125, 0.150$ (black, blue, green, red, magenta), again with analytically predicted bounds shown by the dashed lines. For the two highest temperatures (red, magenta) the computed slopes are slightly above the bound probably because the near-horizon approximation does not work perfectly well. The short-timescale oscillations superimposed on the linear growth, as well as the nonlinear regime before the linear growth starts in the panel (A) are both expected and typical features of the variation δR (Lyapunov exponents are defined asymptotically, for infinite times).

temperature horizons are crucial for our work on chaos, and saying *anything* precise about the gauge theory dual of a string in the black hole background is extremely difficult; we will only build some qualitative intuition on what our chaotic strings do in field theory, with no rigorous results at all.

Let us note in passing that the ring string configurations considered so far are almost insensitive to spacetime dimension. Even if we uplift from the four-dimensional spacetime described by (t, r, ϕ_1, ϕ_2) to a higher-dimensional spacetime $(t, r, \phi_1, \phi_2, \ldots \phi_{N-2})$, with the horizon being an $N - 2$-dimensional sphere/plane/pseudosphere, the form of the equations of motion does not change if we keep the same ring configuration, with $\Phi_1 = \Phi_1(\tau, \sigma), \Phi_2 = n\sigma, \Phi_3 = \text{const.}, \ldots \Phi_{N-2} = \text{const.}$ — this is a solution of the same eqs. (2.6)–(2.8) with the same constraint (2.9). The difference lies in the redshift function $f(r)$ which depends on dimensionality. This, however, does not change the main story. We can redo the calculation of the radial fixed point from the second section, to find a similar result — a string can oscillate or run away/fall slowly in the vicinity of a horizon, and the variational equations yield the same result for the Lyapunov exponent as before. It is really different embeddings, i.e., different Polyakov actions, that might yield different results.

4.1.1 Operators dual to a ring string?

We largely follow the strategy of [47] in calculating the energy and the spin of the string and relating them to the dual Yang-Mills theory. In fact, the ring string is quite close to
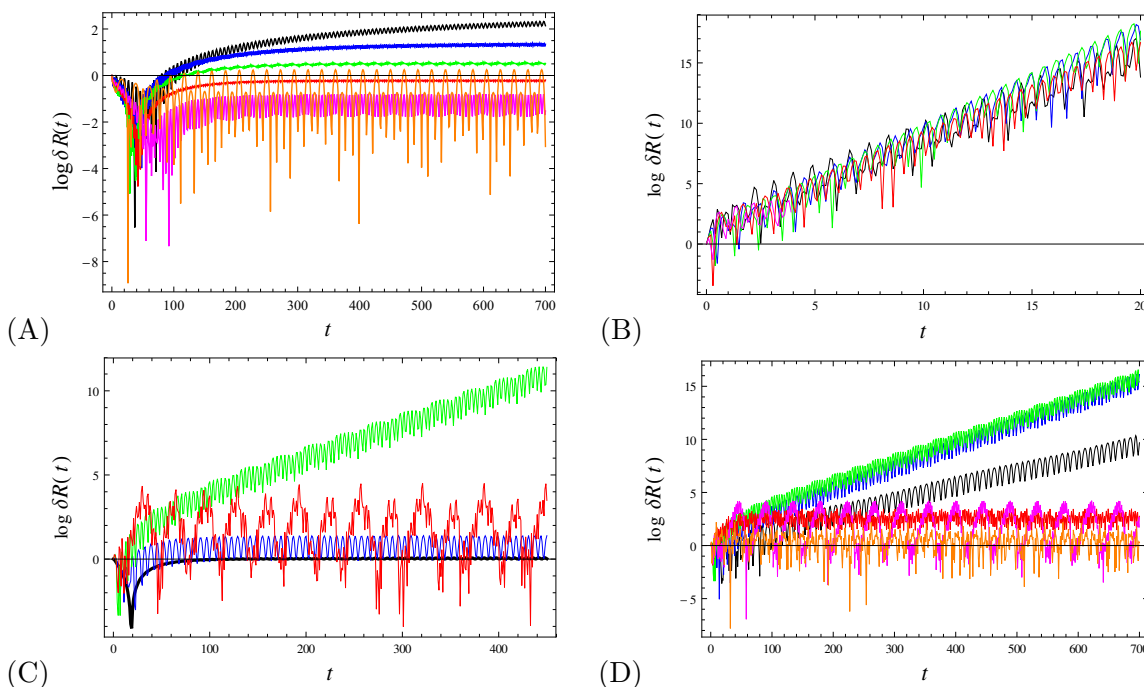
Figure 5. (A) Logarithm of the radial variation δR for near-horizon orbits with $n = 1, 2, 3, 4, 5, 6$ (black, blue, green, red, magenta, orange) in a planar extremal Reissner-Nordstrom geometry. All curved asymptote to a constant, i.e., (almost) zero slope, resulting in $\lambda \approx 0$. (B) Same as previous for an extremal hyperbolic black hole. Now the Lyapunov exponent is nonzero, and equal for all winding numbers: in absence of thermal scrambling, the chaos originates solely from scattering, which is independent of n. (C) The Lyapunov exponent in zero-temperature hyperbolic black hole background for $n = 1$ and $r = r_h, 1.1r_h, 1.2r_h, 1.3r_h$ (black, blue, green, red) starts at zero (no scrambling, no scattering), grows to a clear nonzero value for larger radii due to scattering, and again falls to zero for still larger distances, as the geometry approaches pure AdS (D) Lyapunov exponent in $T = 0.02$ hyperbolic black hole background for $n = 1$ and $r = r_h, 1.1r_h, 1.2r_h, 1.3r_h, 1.4rh, 1.5r_h$ (black, blue, green, red, magenta, orange) starts at the scrambling value (black), reaches its maximum when both scrambling and scattering are present (blue, green) and then falls to zero when AdS is approached (red, magenta, orange).

what the authors of [47] call the oscillating string, *except* that we allow one more angle to fluctuate independently (thus making the system nonintegrable) and, less crucially, that in [47] only the winding number $n = 1$ is considered.

Starting from the action for the ring string (2.3), we write down the expressions for energy and momentum:

$$\mathcal{E} = \frac{1}{2\pi\alpha'} \int d\tau \int d\sigma P_{\mathcal{T}} = \frac{E}{\alpha'} \int_{\phi_1}^{\phi_2} \frac{d\Phi}{\dot{\Phi}} \tag{4.1}$$

$$\mathcal{S} = \frac{1}{2\pi\alpha'} \int d\tau \int d\sigma P_{\Phi} = \frac{1}{\alpha'} \int_{\phi_1}^{\phi_2} \frac{d\Phi}{\dot{\Phi}} R^2(\Phi)\dot{\Phi}, \tag{4.2}$$

where the second worldsheet integral gives simply $\int d\sigma = 2\pi$ as R, Φ do not depend on σ, and we have expressed $d\tau = d\Phi/\dot{\Phi}$; finally, the canonical momentum is conserved, $P_{\mathcal{T}} = E$,

and in the expression for the spin we need to invert the solution $\Phi(\tau)$ into $\tau(\Phi)$ in order to obtain the function $R(\Phi)$. We are forced to approximate the integrals. Expressing $\dot{\Phi}$ from the Hamiltonian constraint (2.4), we can study the energy in two regimes: small amplitude $\phi_0 \ll \pi$ which translates to $E/T \ll 1$, and large amplitude $\phi_0 \sim \pi$, i.e., $E/T \sim 1$. For these two extreme cases, we get:

$$\mathcal{E} \approx \frac{4r_0\sqrt{f(r_0)}}{\alpha'}\phi_0 = \frac{4E}{\alpha'n}, \qquad \phi_0 \ll \pi \tag{4.3}$$

$$\mathcal{E} \approx \frac{\pi E}{\alpha'n}, \qquad\qquad\qquad \phi_0 \sim \pi \tag{4.4}$$

For the spin similar logic gives

$$\mathcal{S} \approx \frac{8r_0E}{\alpha'\sqrt{f(r_0)}}\phi_0 = \frac{8E^2}{\alpha'n}\frac{1}{f(r_0)} \approx \frac{8E^2}{\alpha'n}\frac{1}{4\pi T\epsilon}, \qquad \phi_0 \ll \pi \tag{4.5}$$

$$\mathcal{S} \approx \frac{4E^2}{\alpha'n}\sqrt{\frac{2f'(r_0)r_0}{f^3(r_0)}} \approx \frac{8E^2}{\alpha'n}\frac{\sqrt{2\pi}}{4\pi T\epsilon}, \qquad \phi_0 \sim \pi. \tag{4.6}$$

The bottom line is that in both extreme regimes (and then presumably also in the intermediate parameter range) we have $\mathcal{E} \propto E/\alpha'n$ and $\mathcal{S} \propto E^2/\alpha'nT\epsilon$; as before $\epsilon = r - r_h$ and it should be understood as a physical IR cutoff (formally, for $r \to r_h$ the spin at finite temperature diverges; but we know from section 2 that in fact no exact fixed point at constant r exists, and the average radial distance is always at some small but finite distance ϵ). Therefore, we have $\mathcal{E}^2 \propto \mathcal{S}/\alpha'nT\epsilon$.

The presence of temperature in the above calculation makes it hard to compare the slope to the familiar Regge trajectories. But in absence of the black hole, when $f(r) = 1$, we get

$$\mathcal{E} = 4E/\alpha'n, \ \mathcal{S} = 8E^2/\alpha'n \Rightarrow \mathcal{E}^2 = 2\mathcal{S}/\alpha'n. \tag{4.7}$$

For $n = 1$, this is precisely the leading Regge trajectory. For higher n the slope changes, and we get a different trajectory. Therefore, the canonical Lyapunov exponent value $\lambda = 2\pi T$ precisely corresponds to the leading Regge trajectory. We can tentatively conclude that the winding string at finite temperature describes complicated thermal mixing of large-dimension operators of different dimensions and spins, and these might well be sufficiently nonlocal that the OTOC never factorizes and the bound from [1] does not apply.

4.1.2 Planetoid string

In this subsection we consider so-called planetoid string configurations, also studied in [47] in the zero-temperature global AdS spacetime and shown to reproduce the leading Regge trajectory in gauge theory. This is again a closed string in the same black hole background (2.1) but now the solution is of the form[12]

$$\mathcal{T} = e\tau, \ R = R(\sigma), \ \Phi_1 = \Phi_1(\tau), \ \Phi_2 = \Phi_2(\sigma), \tag{4.8}$$

---

[12]The authors of [47] work mostly with the Nambu-Goto action but consider also the Polyakov formulation in the conformal gauge; we will stick to the Polyakov action from the beginning for notational uniformity with the previous section. For the same reason we keep the same coordinate system as in (2.1).

where the auxiliary field e is picked so as to satisfy the conformal gauge, and any additional coordinates $\Phi_3, \Phi_4, \ldots$ and $\Theta_1, \Theta_2, \ldots$ are fixed. The Lagrangian

$$L = -\frac{1}{2f}\left(R'\right)^2 - \frac{e^2}{2}f + \frac{R^2}{2}\left(-\dot{\Phi}_1^2 + \sin^2\Phi_1\,\Phi_2'^2\right) \tag{4.9}$$

has the invariant submanifold $\Phi_1 = \omega\tau, \Phi_2 = $ const. when the dynamics becomes effectively one-dimensional, the system is trivially integrable and, in absence of the black hole, it is possible to calculate exactly the energy and spin of the dual field theory operator. This is the integrable case studied in [47, 48], and allowing Φ_2 to depend on σ seems to be the only meaningful generalization, because it leads to another submanifold of integrable dynamics with $R = r_0 = $ const., $\Phi_2 = n\sigma$ and the pendulum solution for Φ_1:

$$\sin\Phi_1(\tau) = \operatorname{sn}\left(\ell\tau, -\frac{n^2}{\ell^2}\right), \tag{4.10}$$

where $\ell^2 = \dot{\Phi}_1^{\,2} - n^2\sin^2\Phi_1$ is the adiabatic invariant on this submanifold. With two integrable submanifolds, a generic orbit will wander between them and exhibit chaos. The variational equations can be analyzed in a similar fashion as in the previous section. Here, the chaotic degree of freedom is $\Phi_1(\tau)$, with the variational equation

$$\delta\ddot{\Phi}_1 - \Phi_2'^2\cos(2\Phi_1) = 0, \tag{4.11}$$

which in the near-horizon regime yields the Lyapunov exponent

$$\lambda = 2\pi T n, \tag{4.12}$$

in the vicinity of the submanifold (4.10). In the vicinity of the other solution ($\Phi_1 = \omega\tau, \Phi_2 = $ const.), we get $\lambda = 0$. Chaos only occurs in the vicinity of the winding string solution, and the winding number again jumps in front of the universal $2\pi T$ factor.

Now let us see if this kind of string reproduces a Regge trajectory. In the presence of the black hole the calculation results in very complicated special functions, but we are only interested in the leading scaling behavior of the function $\mathcal{E}^2(\mathcal{S})$. Repeating the calculations from (4.1)–(4.2), we first reproduce the results of [47] in the vicinity of the solution $\Phi_1 = \omega\tau$: for short strings, we get $\mathcal{E} \sim 2/\omega T, \mathcal{S} \sim 2/\omega^2 T^2$ and thus $\mathcal{E}^2 \propto 2\mathcal{S}$, precisely the result for the leading Regge trajectory. Now the Regge slope does not depend on the temperature (in the short string approximation!). This case, as we found, trivially satisfies the original chaos bound ($\lambda = 0$, hence for sure $\lambda < 2\pi T$). In the vicinity of the other solution, with $R = r_0$, things are different. Energy has the following behavior:

$$\mathcal{E} \sim \frac{8\pi}{\alpha'}\frac{T}{n}, \qquad \ell \ll 1 \tag{4.13}$$

$$\mathcal{E} \sim \frac{8\pi^2}{\alpha'}\frac{T}{\ell}, \qquad \ell \gg 1. \tag{4.14}$$

For the spin, the outcome is

$$\mathcal{S} \sim \frac{2r_0^2}{\alpha'}\frac{\ell}{n}, \qquad \ell \ll 1 \tag{4.15}$$

$$\mathcal{S} \sim \frac{2r_0^2}{\alpha'}, \qquad \ell \gg 1, \tag{4.16}$$

so in this case there is no Regge trajectory at all, i.e., no simple relation for $\mathcal{E}^2(\mathcal{S})$ because the scale r_0 and the quantity ℓ show up in the $\mathcal{E}^2(\mathcal{S})$ dependence even at zero temperature.

In conclusion, the strings that can violate the chaos bound have a strange Regge behavior in the gauge/string duality, in this case in a more extreme way than for the ring strings (even for $n = 1$ no Regge trajectory is observed). The strings which have $\lambda = 0$ and thus trivially satisfy the bound on the other hand obey the leading Regge trajectory.

4.2 The limits of quasiclassicality

One more thing needs to be taken into account when considering the modification of the chaos bound. Following [8], one can suspect that the violating cases are not self-consistent in the sense that they belong to the deep quantum regime when semiclassical equations (in our case for the string) cease to be valid and quantum effects kill the chaos. For a ring string this seems not to be the case. To check the consistency of the semiclassical limit, consider the energy-time uncertainty relation $\Delta\mathcal{E}\Delta t \geq 1$. The energy uncertainty is of the order of $E/\alpha' n$ as we found in (4.3)–(4.4), and the time uncertainty is precisely of the order of the Lyapunov time $1/2\pi Tn$; the uncertainty relation then gives $E \geq 2\pi Tn^2\alpha'$. On the other hand, we require that the spin $\mathcal{S}$ should be large in the classical regime: $\mathcal{S} \gg 1$. This implies $E^2 \gg 4\pi T\epsilon n\alpha'$ or, combining with the uncertainty relation, $Tn^3\alpha' \gg \epsilon$. Roughly speaking, we need to satisfy simultaneously $Tn^2 \leq 1/\alpha'$ and $Tn^3 \gg \epsilon/\alpha'$, which is perfectly possible: first, we need to have small enough α' (compared to Tn^2), as could be expected for the validity of the semiclassical regime; second, we need to have sufficiently large $n/\epsilon \gg 1$, which can be true even for $n = 1$ for small ϵ, and for sure is satisfied for sufficiently large n even for $\epsilon \sim 1$. In conclusion, there is a large window when the dynamics is well-described by the classical equations (and this window even grows when $n \gg 1$ and the violation of the chaos bound grows).

4.3 Ring string scattering amplitude and the relation to OTOC

So far our efforts to establish a field theory interpretation of a ring string in black hole background have not been very conclusive, which is not a surprise knowing how hard it is in general to establish a gauge/string correspondence in finite-temperature backgrounds and for complicated string geometries. Now we will try a more roundabout route and follow the logic of [4–6], constructing a gravity dual of the OTOC correlation function, which has a direct interpretation in field theory; it defines the correlation decay rate and the scrambling time of some boundary operator. In [17] this formalism was already applied to study the OTOC of field theory operators (heavy quarks) dual to an open string in BTZ black hole background, hanging from infinity to infinity through the horizon in eikonal approximation. That case has a clear interpretation: the endpoints of the string describe the Brownian motion of a heavy quark in a heath bath. As we already admitted, we do not have such a clear view of what our case means in field theory, but we can still construct the out-of-time ordered correlator corresponding to whatever complicated boundary operator our string describes.

We will be deliberately sketchy in describing the basic framework of the calculation as it is already given in great detail in [4–6]. The idea is to look at the correlation func-

tion $\langle\langle\hat{V}_{x_1}(t_1)\hat{W}_{x_2}(t_2)\hat{V}_{x_3}(t_3)\hat{W}_{x_4}(t_4)\rangle\rangle$ of some operators V, W at finite temperature (hence the expectation value $\langle\langle(\ldots)\rangle\rangle$ includes both quantum-mechanical and thermal ensemble averaging). The time moments need not be ordered; we are often interested in the case $\Re t_1 = \Re t_3 \equiv 0, \Re t_2 = \Re t_4 = t$.[13] This correlation function corresponds to the scattering amplitude between the in and out states of a perturbation sourced from the boundary. The propagation of the perturbation is described by the bulk-to-boundary propagators K. The perturbation has the highest energy at the horizon since the propagation in Schwarzschild time becomes a boost in Kruskal coordinates, and the pertubation, however small at the boundary, is boosted to high energy in the vicinity of the horizon. In the Kruskal coordinates defined the usual way:

$$U = -e^{\frac{t-r_*}{2r_h}}, \quad V = e^{\frac{t+r_*}{2r_h}}, \quad r_* = \int_r^\infty \frac{dr}{f(r)}, \tag{4.17}$$

the scattering amplitude becomes

$$D = \prod_{i=1}^4 \int d^2 p_i \int d^2 x_i K^*(p_3; x_3) K^*(p_4; x_4) K(p_1; x_1) K(p_2; x_2)_{\text{out}} \langle p_3^U, p_4^V; x_3, x_4 | p_1^U, p_2^V; x_1, x_2 \rangle_{\text{in}}. \tag{4.18}$$

The propagators are expressed in terms of the Kruskal momenta $p_i = (p_i^U, p_i^V)$ and the coordinates $x_i = (x_i^1, x_i^2)$ in the transverse directions. The in-state is defined by (p_3^U, x^3) at $U = 0$, and by (p_4^V, x^4) at $V = 0$, and analogously for the out-state. The form of the propagators is only known in the closed form for a BTZ black hole (in $2+1$ dimensions), but we are happy enough with the asymptotic form near the horizon. For simplicity, consider a scalar probe of zero bulk mass, i.e., the conformal dimension $\Delta = D$, and at zero black hole charge, i.e., for a Schwarzschild black hole. The propagator then behaves as ($\tilde{\omega} \equiv \omega/4\pi T$):

$$K(p^U, p^V) \sim \frac{\pi}{\sinh\left(\frac{\pi}{T}\right)} \frac{1 - e^{-\pi\tilde{\omega}}}{\Gamma(-\imath\tilde{\omega})\Gamma(\imath\tilde{\omega})} \frac{e^{-\imath\tilde{\omega}t}}{(p^U)^{1+\imath\tilde{\omega}} + (p^V)^{1-\imath\tilde{\omega}}} e^{\imath(p^U V + p^V U)}. \tag{4.19}$$

The task is thus to calculate the amplitude (4.18) with the propagators (4.19). In the eikonal approximation used in most of the literature so far, the problem boils down to evaluating the classical action at the solution. However, it is not trivial to justify the eikonal approximation for a ring string. Let us first suppose that the eikonal aproximation works and then we will see how things change if it doesn't.

4.3.1 Eikonal approximation

If the energy in the local frame near the horizon is high enough, then we have approximately $p_1^U \approx p_3^U \equiv p, p_2^V \approx p_4^V \equiv q$ so that $p_1^V \approx p_2^U \approx p_3^V \approx p_4^U \approx 0$, and for a short enough scattering event (again satisfied if the energy and thus the velocity is high enough) the coordinates are also roughly conserved, therefore the amplitude $\langle\text{out}|\text{in}\rangle$ is diagonal and can be written as a phase shift $\exp(\imath\delta)$. The point of the eikonal approximation is that the

---

[13]In the Schwinger-Keldysh finite-temperature formalism the time is complex, with the imaginary time axis compactified to the radius of the inverse temperature.

shift δ equals the classical action. The action of the ring configuration is

$$S = \frac{1}{2\pi\alpha'} \int d\tau \int d\sigma \left(\frac{R^2}{2} \left(\dot{\Phi}_1^2 - n^2 \sin^2 \Phi_1 \right) + \frac{\dot{R}^2}{2f} + \frac{f}{2} \dot{\mathcal{T}}^2 \right). \qquad (4.20)$$

We will consider again the string falling slowly in the vicinity of the horizon (see eqs. (2.10)–(2.14)) and put $\dot{R} \to 0, R(\tau) \approx r_0, r_0 - r_h \ll r_h$. Now we need to pass to the Kruskal coordinates and then introduce the new variables $\mathbb{T} = (V+U)/2, X = (V-U)/2$. In these coordinates the near-horizon geometry in the first approximation is Minkowskian and we can easily expand around it as required for the eikonal approximation. The action and the energy (to quartic order in the fluctuations) are now

$$S = \frac{1}{2\pi\alpha'} \int d\tau \int d\sigma \left[\frac{1}{2} \left(-\dot{\mathbb{T}}^2 + \dot{X}^2 + r_0^2 \dot{\Phi}^2 + r_0^2 n^2 \sin \Phi^2 \right) \left(1 + \frac{\mathbb{T}^2 - X^2}{2} \right) \right] \qquad (4.21)$$

$$\mathcal{E} = \frac{1}{2\pi\alpha'} \int d\tau \int d\sigma \frac{\dot{\mathbb{T}}}{(1 - \mathbb{T}^2 + X^2)^2}. \qquad (4.22)$$

As a sanity check, for $n = 0$ the fluctuations of the $(\mathbb{T}, X)$ variables in the action (4.21) are the same as in [17], although we use a different worldsheet parametrization. The dynamics of the angle Φ crucially depends on the winding number. One consequence is that the on-shell action is nontrivial already at quadratic order. For the solution (2.10) — the slowly-moving near-horizon string — we can assume $\dot{\mathbb{T}}, \dot{X} \ll \dot{\Phi}$, so the equations of motion yield as approximate on-shell solutions

$$\mathbb{T} = \mathbb{T}_0 e^{\imath n r_0 \tau / \sqrt{2}}, \quad X = X_0 e^{-\imath n r_0 \tau / \sqrt{2}}, \qquad (4.23)$$

so that, as the perturbation dies out, the string approaches the locus $\mathbb{T}_0 = 0 \Rightarrow U = -V \Rightarrow t \to \infty$. Inserting (4.23) into (4.21), we obtain, after regularizing the action:

$$S^{(0)} = \frac{n r_0}{2\alpha'} \mathbb{T}_0^2 + \dots \qquad (4.24)$$

$$\mathcal{E}^{(0)} = \frac{\sqrt{2}}{\alpha'} \mathbb{T}_0 + \dots. \qquad (4.25)$$

Therefore, $S^{(0)} = \left(\mathcal{E}^{(0)} \right)^2 \times n r_h \alpha' / 4$ (where we have plugged in $r_0 \approx r_h$): the action is proportional to the square of energy, which equals $\mathcal{E}^2 = pq$ in the center-of-mass frame. This is perfectly in line with the fast scrambling hypothesis. Plugging in $\delta = S^{(0)}$ into the amplitude in (4.18) and rescaling

$$T_{13} \equiv e^{2\pi T t_1} - e^{2\pi T t_3^*}, \qquad T_{24} \equiv e^{-2\pi T t_4^*} - e^{-2\pi T t_2} \qquad (4.26)$$

$$p^U = \frac{p}{\imath} \frac{1}{T_{13}}, \qquad p^V = \frac{q}{\imath} \frac{1}{T_{24}} \qquad (4.27)$$

we obtain:

$$D = N_\omega^4 \left(e^{2\pi T t_1} - e^{2\pi T t_3^*} \right)^2 \left(e^{-2\pi T t_4^*} - e^{-2\pi T t_2} \right)^2 \int \frac{dp}{p^2} \int \frac{dq}{q^2} e^{-p-q-\imath \frac{pq}{T_{13}T_{24}} \frac{\alpha' n r_h}{4}}, \qquad (4.28)$$

with N_ω containing the first two factors in (4.19) which only depend on ω and T. Introducing the change of variables $p = Q \sin \gamma, q = Q \cos \gamma$, we can reduce (4.28) to an exponential integral. With the usual contour choice for OTOC $\Im t_i = -\epsilon_i, \Re t_1 = \Re t_3 = 0, \Re t_2 = \Re t_4 = t$, we end up at leading order with

$$D \sim 1 + 2\imath \alpha' n r_h e^{2\pi T t} \Rightarrow \lambda_{\text{OTOC}} \sim 2\pi T, \; t_* \sim \frac{1}{2\pi T} \log \frac{1/\alpha'}{n r_h}. \tag{4.29}$$

Therefore, the Lyapunov time as defined by the OTOC in field theory precisely saturates the predicted bound $2\pi T$, and in the eikonal approximation is not influenced by the winding number n. On the other hand, the scrambling time t_* is multiplied by a factor of $\log(1/\alpha' n)$ (the horizon radius can be rescaled to an arbitrary value by rescaling the AdS radius, thus we can ignore the factor of r_h). The factor $1/\alpha'$ appears also in [17] and plays the role of a large parameter, analogous to the large N^2 factor in large-N field theories: the entropy of the string (the number of degrees of freedom to be scrambled) certainly grows with $1/\alpha'$. For a ring string, this factor is however divided by n, as the number of excitations is reduced by the implementation of the periodic winding boundary condition. Therefore, the winding of the ring string indeed speeds up the chaotic diffusion, by speeding up the scrambling. However, the faster scrambling is not seen in the timescale of local divergence which, unlike the classical Lyapunov exponent, remains equal to $2\pi T$; it is only seen in the timescale on which the perturbation permeates the whole system.

In conclusion, *the violation of the Maldacena-Shenker-Stanford limit for the bulk Lyapunov exponent in AdS space in the eikonal approximation likely corresponds to a decrease of scrambling time in dual field theory, originating from reduction in the number of degrees of freedom.*

4.3.2 Beyond the eikonal approximation: waves on the string

What is the reason to worry? Even if the scattering is still elastic and happens at high energies and momenta (therefore the overlap of the initial and final state is diagonal in the momenta), it might not be diagonal in the coordinates if the string ocillations are excited during the scattering. These excitations might be relevant for the outcome.[14] However, the quantum mechanics of the string in a non-stationary background is no easy matter and we plan to address it in a separate work. In short, one should write the amplitude (4.18) in the worldsheet theory and then evaluate it in a controlled diagrammatic expansion. For the black hole scrambling scenario, the leading-order stringy corrections are considered in [6]; the Regge (flat-space) limit is the pure gravity black hole scrambling with the Lyapunov exponent $2\pi T$ and scrambling time determined by the large N. We need to do the same for the string action (4.21) but, as we said, we can only give a rough sketch now.

---

[14]With an open string hanging from the boundary to the horizon as in [17] this is not the case, since it stretches along the radial direction and the scattering event — which is mostly limited to near-horizon dynamics because this is where the energy is boosted to the highest values — remains confined to a small segment of the string, whereas any oscillations propagate from end to end. However, a ring string near the horizon is *wholly in the near-horizon region all the time*, and the string excitations may happilly propagate along it when the perturbation reaches the area $UV \approx 0$.

The amplitude (4.18) is given by the worldsheet expectation value

$$\mathcal{A} = \prod_i \int d^2 z_i \langle \hat{V}(z_1, \bar{z}_1) \hat{W}(z_2, \bar{z}_2) \hat{V}(z_3, \bar{z}_3) \hat{W}(z_4, \bar{z}_4) \rangle \tag{4.30}$$

with the action (4.20), or (4.21) in the target-space coordinates $(\mathbb{T}, X)$ accommodated to the shock-wave perturbation. Here, we have introduced the usual complex worldsheet coordinates $z = \tau + \imath\sigma, \bar{z} = \tau - \imath\sigma$. We thus need to compute a closed string scattering amplitude for the tachyon of the Virasoro-Shapiro type, but with nontrivial target-space metric and consequently with the vertex operators more complicated than the usual plane-wave form. This requires some drastic approximations. We must first expand the non-Gaussian functional integral over the fields $\mathbb{T}(z, \bar{z})$, $X(z, \bar{z})$, $\Phi(z, \bar{z})$ perturbatively, and then we can follow [6] and [49] and use the operator-product expansion (OPE) to simplify the vertex operators and decouple the functional integral over the target-space coordinates from the worldsheet integration. First we can use the worldsheet reparametrization to fix as usual $z_1 = \infty$, $z_2 = z$, $z_3 = 1$, $z_4 = 0$. The most relevant regime is that of the highly boosted pertrubation near the horizon, with $|z| \sim 1/s$. At leading order in the expansion over $\mathbb{T}, X$, the action (4.21) decouples the Gaussian functional integral over the $(\mathbb{T}, X)$ coordinates from the pendulum dynamics of the Φ coordinate. We can just as easily use the (U, V) dynamics, with $1/2(\dot{\mathbb{T}}^2 - \dot{X}^2) \mapsto -2\dot{U}\dot{V}$; this is just a linear transformation and the functional integral remains Gaussian. The states in U and V coordinates are just the plane waves with $p_1 = p_3 = p, p_2 = p_4 = q$, but the Φ states are given by some nontrivial wavefunctions $\psi(\Phi)$. Alltogether we get

$$\mathcal{A} = \int d^2 z \int DU DV D\Phi \exp\left[-\frac{1}{2\pi\alpha'} \int d^2 z' \left(-2\dot{U}\dot{V} + r_h^2 \left(\dot{\Phi}^2 + n^2 \sin^2\Phi \right) \right) \right] \hat{V}_1 \hat{W}_2 \hat{V}_3 \hat{W}_4$$

$$\hat{V}_{1,3} = g(U_{1,3}) e^{\mp\imath p U_1} \psi^\mp(\Phi_{1,3}), \quad \hat{W}_{2,4} = g(V_{2,4}) e^{\mp\imath q V_{2,4}} \psi^\mp(\Phi_{2,4}), \tag{4.31}$$

where we denote by the index $i = 1, 2, 3, 4$ the coordinates depending on z_i and the coordinates in the worldsheet action in the first line depend on z' which is not explicitly written out to save space. The higher-order metric corrections in U and V give rise to the weak non-plane-wave dependence of the vertices on U and V, encapsulated in the functions g above. We will disregard them completely, in line with considering the decoupled approximation of the metric as written explicitly in the action in (4.31). The functional integral over U, V is easily performed but the Φ-integral is formidable. However, for small $|z|$, we can expand the ground state solution (2.10) in $z, \bar{z}$, which corresponds to the linearized oscillatory behavior and the functional integral becomes Gaussian: $\dot{\Phi}^2 + n^2 \sin^2\Phi \mapsto \dot{\Phi}^2 + n^2\Phi^2$. With the effective potential for the tachyon $V_{\text{eff}}(\Phi) = n^2\Phi^2$, the worldsheet propagator takes the form

$$G^\Phi(z, \bar{z}, z', \bar{z}') = K_0(n|z - z'|) \sim \log\frac{n|z - z'|^2}{2}. \tag{4.32}$$

For the plane wave states we take the ansatz $\psi(\Phi) = e^{\imath\ell\Phi}$, where $\ell = l - \imath\nu$, with $l \in \mathbb{Z}$ being the angular momentum and $0 < \nu \ll 1$ the correction from the interactions (fortunately we will not need the value of ν). The worldhseet propagator for the flat (U, V) coordinates

has the standard logarithmic form. Now we use the fact that $1/|z| \sim s = pq$ to expand the vertices for $\hat{W}_2$ and $\hat{W}_4$ in OPE. The OPE reads

$$: \hat{W}_2 \hat{W}_4 :\sim \exp \left(\imath q z \partial V_2 + \imath q \bar{z} \bar{\partial} V_2 \right) \exp \left(\imath \ell z \partial \Phi_2 + \imath \ell \bar{z} \bar{\partial} \Phi_2 \right) |z|^{-2 - \frac{2\pi\alpha'}{r_h^2} \left(\ell^2 - n^2/2 \right)}, \quad (4.33)$$

which follow from the action of the Laplace operator on the state $e^{\imath \ell \Phi}$. This finally gives

$$\mathcal{A} = \text{const.} \times \int d^2 z : \hat{W}_2 \hat{W}_4 : \exp \left(-\frac{\pi\alpha'}{2} pq \log |1 - z|^2 \right) \exp \left[\frac{\pi\alpha'}{r_h^2} \ell^2 \left(G^\Phi(z) + G^\Phi(1-z) \right) \right].$$
$$(4.34)$$

The above integral results in a complicated ratio of the $_1F_1$ hypergeometric functions and gamma functions. We still have three possible poles, as in the Virasoro-Shapiro amplitude. In the stringy regime at large pq, the dominant contribution must come from $\ell \sim l = 0$, for the other pole brings us back to the purely gravitational scattering, with $S \propto pq$, whereby the local scrambling rate remains insensitive to n, as we have shown in the eikonal approximation. The stringy pole yields the momentum-integrated amplitude

$$D \sim \int \frac{dp}{p^2} \int \frac{dq}{q^2} \exp \left[-p - q - \left(pq e^{-2\pi T t} \right)^{1 + \frac{\pi\alpha'}{r_h^2} n^2} \right] \sim 1 + \text{const.} \times e^{2\pi T \left(1 + \pi\alpha' n^2 \right)}$$

$$\lambda_{\text{OTOC}} \sim 2\pi T \left(1 + \pi\alpha' n^2 \right), \quad (4.35)$$

showing that the Lyapunov scale $2\pi T$ is modified (we again take $r_h = 1$ for simplicity). We conclude that *in the strong stringy regime the Lyapunov exponent in dual field theory behaves as $2\pi(1 + \pi\alpha' n^2)T$, differing from the expected chaos bound for nonzero winding numbers n.* Thus, if the classical gravity eikonal approximation does not hold, the modification of the bulk Lyapunov exponent also has an effect on the OTOC decay rate in field theory.

Once again, the above reasoning has several potential loopholes: (1) we completely disregard the higher-order terms in the metric, which couple that radial and transverse dynamics (2) we assume only small oscillations in Φ (3) we disregard the corrections to vertex operators (4) we disregard the corrections to the OPE coefficients. These issues remain for future work.

5 Discussion and conclusions

Our study has brought us to a sharp formal result with somewhat mystifying physical meaning. We have studied classical chaos in the motion of closed strings in black hole backgrounds, and we have arrived, analytically and numerically, at the estimate $\lambda = 2\pi T n$ for the Lyapunov exponent, with n being the winding number of the string. This is a correction by the factor of n of the celebrated chaos bound $\lambda \leq 2\pi T$. However, one should think twice before connecting these things. From the bulk perspective, what we have is different from classical gravity — it includes string degrees of freedom, and no gravity degrees of freedom. Therefore, the fast scrambler hypothesis that the black holes in Einstein gravity exactly saturate the bound is not expected to be relevant for our system

anyway, but the question remains why the bound is modified *upwards* instead of simply being unsaturated (in other words, we would simply expect to get $\lambda < 2\pi T$). The twist is that the Lyapunov exponent in the bulk is related to but in general *distinct* from the Lyapunov exponent in field theory, usually defined in terms of OTOC. Apparently, one just should not uncritically apply the chaos bound proven for the correlation function decay rates in flat-space quantum fields to worldsheet classical string dynamics.

Therefore, it might be that the field theory Lyapunov time does not violate the bound at all. The timescale of OTOC decay for a field theory dual to the fluctuating string is calculated in [17]: OTOC equals the expectation value of the scattering operator for bulk strings with appropriate boundary conditions. The field-theory Lyapunov time is then determined by the phase shift of the collision. In particular, [17] finds the saturated bound $\lambda = 2\pi T$ as following from the fact that the phase shift is proportional to the square of the center-of-mass energy. On the other hand, [6] predicts that the Lyapunov exponent is lower than the bound when stringy effects are considered. We have done first a completely classical calculation of OTOC and have found, expectedly perhaps, that the $2\pi T$ bound is exactly obeyed. Then we have followed the approximate scheme of [49] to include the one-loop closed string tachyon amplitude as the simplest (and hopefully representative enough?!) stringy process. For a ring string background, this gives an *increased* value for the field-theory Lyapunov rate, yielding some credit to the interpretation that complicated string configurations encode for strongly nonlocal operators, which might indeed violate the bound. But as we have explained, the approximations we took are rather drastic. We regard a more systematic study of loop effects in string chaos as one of the primary tasks for future work.

To gain some more feeling on the dual field theory, we have looked also at the Regge trajectories. In one configuration, the strings that violate the bound n times are precisely those whose Regge trajectory has the slope n times smaller than the leading one (and thus for $n = 1$ the original bound is obeyed and at the same time we are back to the leading Regge trajectory). In another configuration, the strings that violate the bound describe no Regge trajectory at all. However, it is *very* hard to say anything precise about the gauge theory operators at finite temperature. Deciphering which operators correspond to our strings is an important but very ambitious task; we can only dream of moving toward this goal in very small steps. What we found so far makes it probable that complicated, strongly non-local operators correspond to the bound-violating strings, so that (as explained in the original paper [1]) their OTOC cannot be factorized and the bound is not expected to hold.[15]

---

[15]In relation to the gauge/string duality it is useful to look also at the gauge theories with N_f flavors added, which corresponds to the geometry deformed by N_f additional D-branes in the bulk. In [50] it was found that the system becomes nonintegrable in the presence of the flavor branes (expectedly, as it becomes non-separable), but the Lyapunov exponent does not grow infinitely with the number of flavors, saturating instead when the number of colors N_c and the number of flavors become comparable. This is expected, as the D3-D7 brane background of [50] formally becomes separable again when $N_f/N_c \to \infty$ (although in fact this regime cannot be captured, the calculation of the background ceases to be valid in this case). In our case the winding number n is a property of the string solution, not geometry, and the Hamiltonian (2.9) seems to have no useful limit for $n \to \infty$, thus we do not expect the estimate $2\pi T n$ will saturate.

Preparing the final version of the paper, we have learned also of the work [52] where the n-point OTOCs are studied following closely the logic of [1] and the outcome is a factor of n enlargement, formally the same as our result. This is very interesting but, in the light of the previous paragraph, we have no proof that this result is directly related to ours. It certainly makes sense to investigate if the winding strings are obtained as some limit of the gravity dual for the n-point correlations functions. We know that n-point functions in AdS/CFT are a complicated business. The Witten diagrams include bulk propagators carrying higher spin fields that might in turn be obtained as string excitations. Just how far can one go in making all this precise we do not know for now.

In relation to [15, 16] one more clarifying remark should be given. In these works, particles in the vicinity of the horizon are found to exhibit chaos (either saturating the bound or violating it, depending on the spin of the background field). At first glance, this might look inconsistent with our finding that for $n = 0$, when the string degenerates to a particle, no chaos occurs; after all, we know that geodesic motion in the background of spherically symmetric black holes is integrable, having a full set of the integrals of motion. But in fact there is no problem, because in [15, 16] an additional external potential (scalar, vector, or higher-spin) is introduced that keeps the particle at the horizon, balancing out the gravitational attraction. Such a system is of course not integrable anymore, so the appearance of chaos is expected. The modification of the bound in the presence of higher-spin fields might have to do with the findings [51] that theories with higher-spin fields can only have gravity duals in very restricted situations (in particular, higher spin CFTs with a sparse spectrum and large central charge or, roughly speaking, massive higher spin fields, are problematic).

Another task on the to-do list, entirely doable although probably demanding in terms of calculations, is the (necessarily approximate) calculation of the black hole scattering matrix, i.e., the backreactrion of the black hole upon scattering or absorbing a string, along the lines of [7]. In this paper we have worked in the probe limit (no backreaction), whereas the true scrambling is really the relaxation time of the black hole (the time it needs to become hairless again), which cannot be read off solely from the Lyapunov time; this is the issue we also mentioned in the Introduction, that local measures of chaos like the Lyapunov exponent do not tell the whole story of scrambling. Maybe even a leading-order (tree-level) backreaction calculation can shed some light on this question.

Acknowledgments
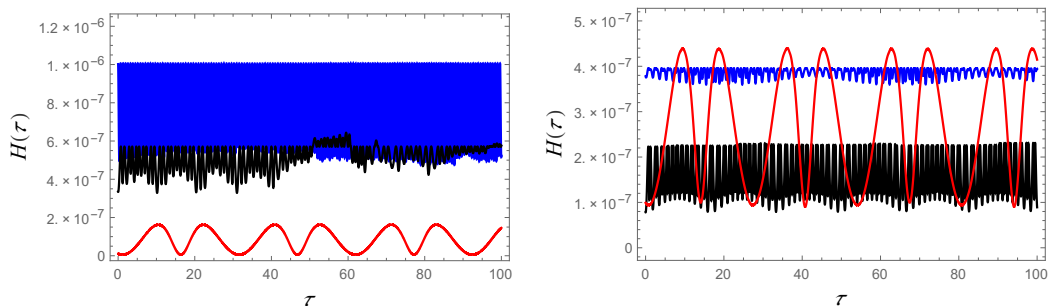
Figure 6. Check of the Hamiltonian constraint $H = 0$ during an integration for the spherical, planar and hyperbolic black hole (black, blue, red respectively), at temperature $T = 0.01$ (left) and $T = 0.10$ (right). The accuracy of the constraint is a good indicator of the overall integration accuracy, it is never above 10^{-6} and has no trend of growth but oscillates.

A Summary of the numerics

We feel it necessary to give a short account of the numerical methods used. The string equations of motion (2.6)–(2.8) present us with a system of two ordinary second-order differential equations with a constraint. This numerical calculation is not very difficult, and it would be trivial if it were not for two complicating factors. First, the constraint itself is the main complication; it is non-holonomic and cannot be easily eliminated. Second, the system is rather stiff, with $\dot{R}$ in particular varying for several orders of magnitude. We did the integration in the `Mathematica` package, using mostly the `NDSolve` routine, and controlling both the relative and the absolute error during the calculations. The constraint problem is solved serendipitously by ensuring that the initial conditions satisfy the constraint and then adjusting the required absolute and relative error tolerance so that the constraint remains satisfied. A priori, this is a rather unlikely way to succeed but we find it works in most cases. Only in a few integrations we needed to write a routine which shoots for the condition $H = 0$ at every timestep, using the `NDSolve` routine in the solver; the shooting itself we wrote using the tangent method which is handier for this problem than the built-in routines. The usual analytic way, making use of the Lagrange multipliers, seems completely unsuitable for numerical implementation in this problem. In figure 6 we show the evolution of the constraint for a few examples, demonstrating the stability of the integration. We have also checked that the functions $R(\tau), \Phi(\tau)$ converge toward definite values as the precision and accuracy (relative and absolute error per step) are varied.

Open Access. This article is distributed under the terms of the Creative Commons Attribution License ([CC-BY 4.0](https://creativecommons.org/licenses/by/4.0/)), which permits any use, distribution and reproduction in any medium, provided the original author(s) and source are credited.

References

[1] J. Maldacena, S.H. Shenker and D. Stanford, *A bound on chaos*, *JHEP* **08** (2016) 106 [arXiv:1503.01409] [INSPIRE].

[2] Y. Sekino and L. Susskind, *Fast scramblers*, *JHEP* **10** (2008) 065 [arXiv:0808.2096] [INSPIRE].

[3] N. Lashkari, D. Stanford, M. Hastings, T. Osborne and P. Hayden, *Towards the fast scrambling conjecture*, *JHEP* **04** (2013) 022 [arXiv:1111.6580] [ɪɴSPIRE].

[4] S.H. Shenker and D. Stanford, *Black holes and the butterfly effect*, *JHEP* **03** (2014) 067 [arXiv:1306.0622] [ɪɴSPIRE].

[5] D.A. Roberts, D. Stanford and L. Susskind, *Localized shocks*, *JHEP* **03** (2015) 051 [arXiv:1409.8180] [ɪɴSPIRE].

[6] S.H. Shenker and D. Stanford, *Stringy effects in scrambling*, *JHEP* **05** (2015) 132 [arXiv:1412.6087] [ɪɴSPIRE].

[7] J. Polchinski, *Black hole S matrix*, arXiv:1505.08108 [ɪɴSPIRE].

[8] T. Scaffidi and E. Altman, *Chaos in a classical limit of the Sachdev-Ye-Kitaev model*, *Phys. Rev.* **B 100** (2019) 155128 [arXiv:1711.04768] [ɪɴSPIRE].

[9] S. Sachdev and J. Ye, *Gapless spin fluid ground state in a random, quantum Heisenberg magnet*, *Phys. Rev. Lett.* **70** (1993) 3339 [cond-mat/9212030] [ɪɴSPIRE].

[10] O. Parcolet and A. Georges, *Non-Fermi liquid regime of a doped Mott insulator*, *Phys. Rev.* **B 59** (1998) 5341 [cond-mat/9806119].

[11] A. Kitaev, *A simple model of quantum holography (part 1)*, talk at *KITP*, April 7, 2015, http://online.kitp.ucsb.edu/online/entangled15/kitaev/.

[12] A. Kitaev, *A simple model of quantum holography (part 2)*, talk at *KITP*, May 27, 2015, http://online.kitp.ucsb.edu/online/entangled15/kitaev2/.

[13] E. Marcus and S. Vandoren, *A new class of SYK-like models with maximal chaos*, *JHEP* **01** (2019) 166 [arXiv:1808.01190] [ɪɴSPIRE].

[14] A.L. Fitzpatrick and J. Kaplan, *A quantum correction to chaos*, *JHEP* **05** (2016) 070 [arXiv:1601.06164] [ɪɴSPIRE].

[15] K. Hashimoto and N. Tanahashi, *Universality in chaos of particle motion near black hole horizon*, *Phys. Rev.* **D 95** (2017) 024007 [arXiv:1610.06070] [ɪɴSPIRE].

[16] S. Dalui, B.R. Majhi and P. Mishra, *Presence of horizon makes particle motion chaotic*, *Phys. Lett.* **B 788** (2019) 486 [arXiv:1803.06527] [ɪɴSPIRE].

[17] J. de Boer, E. Llabrés, J.F. Pedraza and D. Vegh, *Chaotic strings in AdS/CFT*, *Phys. Rev. Lett.* **120** (2018) 201604 [arXiv:1709.01052] [ɪɴSPIRE].

[18] J.R. David, S. Khetrapal and S.P. Kumar, *Local quenches and quantum chaos from perturbations*, *JHEP* **10** (2017) 156 [arXiv:1707.07166] [ɪɴSPIRE].

[19] P. Basu and L.A. Pando Zayas, *Analytic nonintegrability in string theory*, *Phys. Rev.* **D 84** (2011) 046006 [arXiv:1105.2540] [ɪɴSPIRE].

[20] A. Stepanchuk and A.A. Tseytlin, *On (non)integrability of classical strings in p-brane backgrounds*, *J. Phys.* **A 46** (2013) 125401 [arXiv:1211.3727] [ɪɴSPIRE].

[21] Y. Chervonyi and O. Lunin, *(Non)-integrability of geodesics in D-brane backgrounds*, *JHEP* **02** (2014) 061 [arXiv:1311.1521] [ɪɴSPIRE].

[22] C. Núñez, J.M. Penín, D. Roychowdhury and J. Van Gorsel, *The non-integrability of strings in massive type IIA and their holographic duals*, *JHEP* **06** (2018) 078 [arXiv:1802.04269] [ɪɴSPIRE].

[23] D. Giataganas, L.A. Pando Zayas and K. Zoubos, *On marginal deformations and non-integrability*, *JHEP* **01** (2014) 129 [arXiv:1311.3241] [ɪɴSPIRE].

[24] N. Beisert et al., *Review of AdS/CFT Integrability: An Overview, Lett. Math. Phys.* **99** (2012) 3 [arXiv:1012.3982] [INSPIRE].

[25] A.V. Frolov and A.L. Larsen, *Chaotic scattering and capture of strings by a black hole, Class. Quant. Grav.* **16** (1999) 3717 [gr-qc/9908039] [INSPIRE].

[26] L.A. Pando Zayas and C.A. Terrero-Escalante, *Chaos in the gauge/gravity correspondence, JHEP* **09** (2010) 094 [arXiv:1007.0277] [INSPIRE].

[27] P. Basu and L.A. Pando Zayas, *Chaos rules out integrability of strings on $AdS_5 \times T^{1,1}$, Phys. Lett.* **B 700** (2011) 243 [arXiv:1103.4107] [INSPIRE].

[28] P. Basu, D. Das and A. Ghosh, *Integrability lost: Chaotic dynamics of classical strings on a confining holographic background, Phys. Lett.* **B 699** (2011) 388 [arXiv:1103.4101] [INSPIRE].

[29] P. Basu, P. Chaturvedi and P. Samantray, *Chaotic dynamics of strings in charged black hole backgrounds, Phys. Rev.* **D 95** (2017) 066014 [arXiv:1607.04466] [INSPIRE].

[30] Y. Asano, D. Kawai, H. Kyono and K. Yoshida, *Chaotic strings in a near Penrose limit of $AdS_5 \times T^{1,1}$, JHEP* **08** (2015) 060 [arXiv:1505.07583] [INSPIRE].

[31] Y. Asano, H. Kyono and K. Yoshida, *Melnikov's method in string theory, JHEP* **09** (2016) 103 [arXiv:1607.07302] [INSPIRE].

[32] D. Giataganas and K. Sfetsos, *Non-integrability in non-relativistic theories, JHEP* **06** (2014) 018 [arXiv:1403.2703] [INSPIRE].

[33] T. Ishii, K. Murata and K. Yoshida, *Fate of chaotic strings in a confining geometry, Phys. Rev.* **D 95** (2017) 066019 [arXiv:1610.05833] [INSPIRE].

[34] R.B. Mann, *Pair production of topological anti-de Sitter black holes, Class. Quant. Grav.* **14** (1997) L109 [gr-qc/9607071] [INSPIRE].

[35] D.R. Brill, J. Louko and P. Peldan, *Thermodynamics of (3+1)-dimensional black holes with toroidal or higher genus horizons, Phys. Rev.* **D 56** (1997) 3600 [gr-qc/9705012] [INSPIRE].

[36] L. Vanzo, *Black holes with unusual topology, Phys. Rev.* **D 56** (1997) 6475 [gr-qc/9705004] [INSPIRE].

[37] D. Birmingham, *Topological black holes in anti-de Sitter space, Class. Quant. Grav.* **16** (1999) 1197 [hep-th/9808032] [INSPIRE].

[38] R.B. Mann, *Topological black holes — outside looking in, Annals Israel Phys. Soc.* **13** (1997) 311 [gr-qc/9709039] [INSPIRE].

[39] W.L. Smith and R.B. Mann, *Formation of topological black holes from gravitational collapse, Phys. Rev.* **D 56** (1997) 4942 [gr-qc/9703007] [INSPIRE].

[40] Y.C. Ong, *Hawking evaporation time scale of topological black Holes in anti-de Sitter spacetime, Nucl. Phys.* **B 903** (2016) 387 [arXiv:1507.07845] [INSPIRE].

[41] Y. Chen and E. Teo, *Black holes with bottle-shaped horizons, Phys. Rev.* **D 93** (2016) 124028 [arXiv:1604.07527] [INSPIRE].

[42] C.V. Johnson and F. Rosso, *Holographic heat engines, entanglement entropy and renormalization group flow, Class. Quant. Grav.* **36** (2019) 015019 [arXiv:1806.05170] [INSPIRE].

[43] R. Emparan, *AdS/CFT duals of topological black holes and the entropy of zero-energy states, JHEP* **06** (1999) 036 [hep-th/9906040] [INSPIRE].

[44] A.L. Larsen, *Chaotic string-capture by black hole*, *Class. Quant. Grav.* **11** (1994) 1201 [hep-th/9309086] [INSPIRE].

[45] A.E. Motter, *Relativistic chaos is coordinate invariant*, *Phys. Rev. Lett.* **91** (2003) 231101 [gr-qc/0305020] [INSPIRE].

[46] N.L. Balazs and A. Voros, *Chaos on the pseudosphere*, *Phys. Rept.* **143** (1986) 109 [INSPIRE].

[47] S.S. Gubser, I.R. Klebanov and A.M. Polyakov, *A semi-classical limit of the gauge/string correspondence*, *Nucl. Phys.* **B 636** (2002) 99 [hep-th/0204051] [INSPIRE].

[48] H.J. de Vega and I.L. Egusquiza, *Planetoid string solutions in* 3 + 1 *axissymmetric spaces*, *Phys. Rev.* **D 54** (1996) 7513 [hep-th/9607056] [INSPIRE].

[49] R.C. Brower, J. Polchinski, M.J. Strassler and C.-I. Tan, *The pomeron and gauge/string duality*, *JHEP* **12** (2007) 005 [hep-th/0603115] [INSPIRE].

[50] D. Giataganas and K. Zoubos, *Non-integrability and chaos with unquenched flavor*, *JHEP* **10** (2017) 042 [arXiv:1707.04033] [INSPIRE].

[51] E. Perlmutter, *Bounding the space of holographic CFTs with chaos*, *JHEP* **10** (2016) 069 [arXiv:1602.08272] [INSPIRE].

[52] P. Basu and K. Jaswin, *Higher point OTOCs and the bound on chaos*, arXiv:1809.05331 [INSPIRE].

Detecting few-body quantum chaos: out-of-time ordered correlators at saturation

Dragan Marković[a,b] **and Mihailo Čubrović**[b]

[a]*Department of Physics, University of Belgrade,*
Studentski Trg 12-16, 11000 Belgrade, Serbia

[b]*Center for the Study of Complex Systems, Institute of Physics Belgrade, University of Belgrade,*
Pregrevica 118, 11080 Belgrade, Serbia

E-mail: vokramnagard@gmail.com, cubrovic@ipb.ac.rs

ABSTRACT: We study numerically and analytically the time dependence and saturation of out-of-time ordered correlators (OTOC) in chaotic few-body quantum-mechanical systems: quantum Henon-Heiles system (weakly chaotic), BMN matrix quantum mechanics (strongly chaotic) and Gaussian random matrix ensembles. The growth pattern of quantum-mechanical OTOC is complex and nonuniversal, with no clear exponential regime at relevant timescales in any of the examples studied (which is not in contradiction to the exponential growth found in the literature for many-body systems, i.e. fields). On the other hand, the plateau (saturated) value of OTOC reached at long times decreases with temperature in a simple and universal way: $\exp(\mathrm{const.}/T^2)$ for strong chaos (including random matrices) and $\exp(\mathrm{const.}/T)$ for weak chaos. For small matrices and sufficiently complex operators, there is also another, high-temperature regime where the saturated OTOC grows with temperature. Therefore, the plateau OTOC value is a meaningful indicator of few-body quantum chaos. We also discuss some general consequences of our findings for the AdS/CFT duality.

Contents

1   Introduction

Recent years have seen a renewed interest in classical and quantum chaos in the context of high-energy physics, black holes and AdS/CFT, thanks to the relation of chaos to quantum information theory and the information problems of black holes. Sharp and reasonably rigorous results such as the celebrated MSS chaos bound [1] and its subsequent refinements [2, 3] establish a connection between chaos and the fundamental properties of gravity and black holes [4, 5]. Maximal chaos, with the Lyapunov exponent $\lambda = 2\pi T$ at temperature T, is reached for strongly coupled field theories in the large N limit, which have a classical gravity dual with a black hole. In [2] and other works it is explicitly shown how the Lyapunov exponent changes with finite N effects.

However, it has been pointed out many times, also in the pioneering MSS paper [1], that the multiple notions of quantum chaos in the literature mean different things. The out-of-time ordered correlation function (OTOC), given by the expectation value of the commutator of some operators A and B at times 0 and t:

$$C(t) \equiv \langle | \left[A(t), B(0) \right] |^2 \rangle, \tag{1.1}$$

is a natural quantity in quantum field theories, i.e. many-body systems, and defines the quantum Lyapunov exponent λ as the exponent of the time growth of OTOC. However, the classical limit of this exponent does not necessarily have much to do with the classical Lyapunov exponent λ_{class}, obtained by solving the variational equations [6–8]. The reason is the noncommutation of the three limits to be taken: the classical limit $\hbar \to 0$, the long-time limit $t \to \infty$, and the small initial variation limit $\delta x(0) \to 0$. The crucial insight of [7, 8] is that the mechanism of scrambling may be the chaotic dynamics, in which case λ_{class} is related though still not identical to the OTOC exponent (quantum Lyapunov exponent) λ, or it may originate in local instability (hyperbolicity), in which case even regular systems may have a nonzero λ exponent and likewise chaotic systems may have λ which is completely unrelated to the classical counterpart.

This mismatch between the classical and quantum Lyapunov exponent is just the tip of the iceberg. The problem is twofold: not only what is the relation between the quantum (OTOC) exponent and classical chaos, but also what is the relation between the quantum Lyapunov exponent λ and other indicators of quantum chaos such as, first and foremost, level statistics. The bread and butter of quantum chaos is the famous Dyson threefold way leading to the Wigner surmise, the level repulsion statistics determined solely by the time reversal properties of the Hamiltonian [10], which follows from the random matrix approximation of chaotic Hamiltonian operators [11]. It is no secret for several years already that the black hole quasinormal mode spectra follow the random matrix statistics [12], and the OTOC of a Gaussian unitary ensemble (GUE) has been computed analytically in terms of Bessel functions in [13, 14]; the outcome is close to the expected behavior of large-N field theories only at long timescales, longer than the scrambling time; at shorter timescales there are important differences. The authors of [13] have reached a deep conclusion in this respect: random matrices have no notion of locality as the correlation of any pair of eigenvalues is described by the same universal function. This is why the OTOC of a GUE system deviates from that of a local field theory at early times, when the perturbation in field theory has not had time to spread yet (i.e. when it is still localized). Therefore, the level repulsion does not imply the usual picture of the chaotic (exponential) OTOC behavior. However, we do not know yet how this correlates to the behavior of *few-body* or more precisely few-degrees-of-freedom quantum systems as opposed to the large-N field theories with a gravity dual. In few-body systems the notion of locality (and a classical gravity dual) does not exist anyway and the main problem found by [13] is irrelevant; at the same time, such systems are often very well described by random matrix statistics, i.e. Wigner-Dyson statistics [10]. In this paper we aim to understand the behavior of OTOC in such systems. Running a bit forward, we can say that the *growth* of OTOC is rather unremarkable: we find no universal trend, and little connection to level statistics. This confirms the results found for specific examples in [8, 15].

The relation of OTOC, level statistics and the classical Lyapunov exponent was studied for few-body systems (quantum mechanics) in [8, 15–18] and the picture is inconclusive. One can have a nonzero growth exponent in integrable systems,[1] whereas fast scrambling with

---

[1]This actually correlates with the classical variational equations in hyperbolic systems, which show exponential growth even in absence of chaos.

the exponent close to $2\pi T$ or at least growing linearly in T has not been found even in some clearly chaotic systems [8, 9]. Arguments for many-body systems such as spin chains even suggest that quantum-chaotic systems with Gaussian spectral statistics generically never show fast scrambling [19], but no claims of such generality have been tested or formulated for few-body quantum chaos.

Various indicators of chaos relevant also for small systems, and their relation to OTOC and scrambling were studied by [20–27] among others. In particular, in [26] some important insights can be found: even in small systems devoid of the locality notion, OTOC can be interpreted as a measure of delocalization of a state in phase space, and the oscillatory component of the OTOC dynamics has to do with the power spectrum of the system. This last insight provokes a more general question: can we learn something from the quasi-stationary regime of OTOC, where no systematic growth is present but only oscillations? In this paper we provide a partial answer from a detailed study of this saturated (asymptotic, plateau) OTOC regime: the magnitude of the OTOC average at the plateau has a simple temperature dependence, and apparently can differentiate between weak chaos (dominantly Poissonian level distribution with some admixture of the Wigner-Dyson statistics) and strong chaos (clear Wigner-Dyson level repulsion). We will demonstrate this on three representative systems: the quantum Henon-Heiles Hamiltonian, whose classical limit has mixed (regular/chaotic) phase space and thus we expect on average weak chaos, a simplified BMN matrix model (at small N) exhibiting strong chaos for most initial conditions, and Gaussian random matrices, the prototype of strong quantum chaos. The long-time limit of OTOC behaves in subtly different ways in each case.

Before we start, one caveat is in order (we will consider this issue in more detail later on): one might think that the saturated OTOC value is always trivially determined by the system size. We typically assume that the OTOC function C as defined in (1.1) behaves roughly as $C(t) \sim c/N^2 \times \exp(\lambda t)$ with c of order unity, so when $t \sim t_* \equiv \log N^2/\lambda$ the growth of $C(t)$ stops and OTOC approximately reaches unity (when appropriately normalized). But the twist is precisely that c is system-specific and in general poorly known. The leading N^2 behavior indeed determines the OTOC values for N large, but when N and c are comparable within an order of magnitude the effects of fluctuations and finite N corrections are significant. This is at the root of our observations in this work.

The plan of the paper is as follows. In section 2 we recapitulate and generalize some results on computing OTOC in quantum mechanics, and show how OTOC sensitively depends on both the Hamiltonian and the operators A, B from the definition (1.1). In section 3 we apply the general formalism to random matrix ensembles and show that the OTOC growth is a complicated and nonuniversal function but that its asymptotic value behaves in a rather simple way. Section 4 discusses the behavior of OTOC for deterministic quantum-chaotic Hamiltonians. Section 5 sums up the conclusions.

2 OTOC in quantum-mechanical systems

Consider a four-point time-disordered correlation function for a quantum-mechanical system in $0 + 1$ dimensions at temperature $T = 1/\beta$. Starting from the usual definition (1.1) as the

squared module of the commutator of the two operators A and B, we can write it out as

$$C(t) = \frac{1}{Z}\langle|\,[A(t),B(0)]\,|^2\rangle = \frac{1}{Z}\sum_n e^{-\beta E_n}\langle n||\,[A(t),B(0)]\,|^2|n\rangle, \qquad (2.1)$$

where the averaging is both thermal and quantum mechanical: $\langle\ldots\rangle = \mathrm{tr}\,e^{-\beta H}\langle\mathrm{vac}|\ldots|\mathrm{vac}\rangle$. We can pick a basis of states and express the above defining expression in terms of matrix elements of the operators (this closely follows the derivation in [8, 16]):

$$C(t) = \frac{1}{Z}\sum_{nm} e^{-\beta E_n}\langle n|\,[A(t),B(0)]\,|m\rangle\langle m|\,[A(t),B(0)]\,|n\rangle = \frac{1}{Z}\sum_{nm} e^{-\beta E_n}|c_{mn}(t)|^2, \quad (2.2)$$

where we have inserted the completeness relation $1 = \sum_m |m\rangle\langle m|$. For a single element $c_{mn}(t)$ one gets:

$$\begin{aligned}
c_{mn}(t) &= \langle n|\left[e^{\imath Ht}Ae^{-\imath Ht},B\right]|m\rangle = \\
&= \sum_k \left(\langle n|e^{\imath Ht}Ae^{-\imath Ht}|k\rangle\langle k|B|m\rangle - \langle n|B|k\rangle\langle k|e^{\imath Ht}Ae^{-\imath Ht}|m\rangle\right) = \\
&= \sum_k \left(\langle n|e^{\imath E_n t}Ae^{-\imath E_k t}|k\rangle\langle k|B|m\rangle - \langle n|B|k\rangle\langle k|e^{\imath E_k t}Ae^{-\imath E_m t}|m\rangle\right) = \\
&= \sum_k \left(a_{nk}b_{km}e^{-\imath E_{kn}t} - b_{nk}a_{km}e^{-\imath E_{mk}t}\right), \qquad (2.3)
\end{aligned}$$

where in the second line we have again inserted a completeness relation and in the third line we have used the fact that we work in the energy eigenbasis. The outcome is expressed in terms of the matrix elements a_{mn}, b_{mn} of the operators in the energy basis. In practice, it may or may not be possible to compute these analytically. Specifically, for $A = x, B = p$, we get the analogue of the classical Lyapunov exponent. From now on we call this the kinematic OTOC as it is directly related to the classical trajectory. Let us now see what general bounds can be put on (2.3) from the properties of quantum-mechanical Hamiltonians.

2.1 An upper bound on OTOC saturation

We begin with a very general and very formal result, which immediately makes it clear that in a generic quantum-mechanical system (integrable or nonintegrable) OTOC can be bounded from above by a quantity which solely depends on the energy spectrum of the Hamiltonian and the choice of the operators A and B. This upper bound remains valid no matter what is the time dependence of OTOC, even if it does not have a nonzero growth exponent at all (which is quite generic in quantum mechanics). Starting from the basic equations (2.2)–(2.3), let us denote $C_{nmk} = a_{nk}b_{km}$ i $D_{nmk} = -b_{nk}a_{km}$, and estimate a single coefficient $c_{mn}(t)$ in the sum. We clearly have

$$|c_{mn}(t)| = |\sum_k C_{nmk}e^{-iE_{kn}t} + D_{nmk}e^{-iE_{mk}t}| \le \sum_k |C_{nmk}e^{-iE_{kn}t} + D_{nmk}e^{-iE_{mk}t}| \Rightarrow$$

$$|c_{mn}(t)|^2 \le \left(\sum_k |C_{nmk}e^{-iE_{kn}t} + D_{nmk}e^{-iE_{mk}t}|\right)^2 \le \sum_k |C_{nmk}e^{-iE_{kn}t} + D_{nmk}e^{-iE_{mk}t}|^2 \le$$

$$\le \sum_k \left(|C_{nmk}|^2 + |D_{nmk}|^2 + 2|C_{nmk}||D_{nmk}|\cos\left(E_{mk} - E_{kn}\right)t\right), \qquad (2.4)$$

where N is the matrix size. In the second and third line we have used the inequality between the arithmetic and harmonic mean. Now we can bound the value of $C(t)$:

$$0 \le C(t) \le \frac{1}{Z} \sum_{nmk} e^{-\beta E_n} \left(|C_{nmk}|^2 + |D_{nmk}|^2 + 2|C_{nmk}||D_{nmk}| \cos\left(E_{mk} - E_{kn}\right) t \right) \quad (2.5)$$

This means that $C(t)$ is bounded at all times by an oscillatory function of time, whose frequencies are linear combinations of three eigenenergies ($E_{mk} - E_{kn} = E_m + E_n - 2E_k$). Such a combination is generically always nonzero for a chaotic system except when the energies coincide, e.g. $E_m = E_n = E_k$ (according to the non-resonance condition). Therefore, since OTOC is typically a non-decreasing function of time, the behavior of $C(t)$ for t large is roughly its maximum value and is likely close to the right-hand side in (2.5). This suggests that the OTOC dynamics after saturation likely consists of a very complex oscillatory pattern (with $\sim N^3$ frequencies if the Hilbert space has dimension N) superimposed on a plateau. The numerics will indeed confirm such behavior.

Another estimate, which is time-independent and relevant for our main result — the magnitude of the saturation (plateau) OTOC value, is obtained from the triangle and mean inequalities:

$$|c_{mn}(t)|^2 \le |\sum_k C_{nmk} e^{-iE_{kn}t}|^2 + |\sum_k D_{nmk} e^{-iE_{mk}t}|^2 \le |\sum_k C_{nmk}|^2 + |\sum_k D_{nmk}|^2 \Rightarrow$$

$$C(t) \le \frac{1}{Z} \sum_{nm} e^{-\beta E_n} \left(|(A \cdot B)_{nm}|^2 + |(B \cdot A)_{nm}|^2 \right) \le \frac{2}{Z} \sum_{nm} e^{-\beta E_n} |(A \cdot B)_{nm}|^2,$$

$$(2.6)$$

where we have used the obvious relations $\sum_k C_{mnk} = (A \cdot B)_{nm}$ and $\sum_k D_{nmk} = (B \cdot A)_{nm} = (A \cdot B)^*_{mn} = (A \cdot B)_{nm}$, assuming also the hermiticity of the operators. For some models (e.g. random matrices, Henon-Heiles), this sum can be estimated in a controlled way and provides an approximation for the plateau of OTOC. These estimates are obviously very simple and very weak (in the mathematical sense) but provide us with a framework into which we can insert specific A, B and H (the Hamiltonian with energies E_n) and perform back-of-the-envelope calculations which explain the numerical findings.

3 OTOC for random matrix ensembles

Random matrix theory [10, 11] provides a highly detailed and rigorous (within its starting assumptions) stochastic effective description of the few-body quantum chaos, and allows an analytic calculation of OTOC along the lines of (2.3). Let us focus on Gaussian orthohogonal ensembles of size $N \times N$, appropriate when there is full time reversal invariance. It is known [10] that the joint distribution all the elements of all eigenvectors is obtained simply from the statistical independence of the eigenvectors from each other and of the elements in each eigenvector (and the orthogonality of the eigenvectors):

$$P\left(\{c\}\right) = \left(\prod_{n=1}^{N} \delta \left(\sum_i (c_i^n)^2 - 1 \right) \right) \left(\prod_{n<m} \delta \left(\sum_i c_i^n c_i^m \right) \right), \quad (3.1)$$

where $i = 1 \ldots N$ is the component of the eigenvector and $1 \leq n, m \leq N$ count the eigenvectors themselves, i.e. the energy levels; so the n-th eigenvector $|n\rangle$ is represented by the column vector $\psi^{(n)}$ with the elements $(c_1^n, \ldots c_N^n)$. Special cases like the probability distribution for the p-tuple of elements of a single eigenvector are obtained from (3.1) by integrating out all the other elements [10]. We will also need the probability distribution of the energy levels $\{E\} = E_1, E_2, \ldots E_N$, the celebrated Wigner-Dyson distribution function [10]:

$$\mathcal{P}\left(\{E\}\right) = \text{const.} \times \prod_{n<m} |E_n - E_m|^b \exp\left(-\sum_k \frac{E_k^2}{\sigma^2}\right), \qquad (3.2)$$

where σ is the standard deviation, fixing the unit of energy, and $b = 1$, 2 or 4 for orthogonal, unitary and symplectic ensembles respectively. Most of our work is independent of the symmetry class, however our default class will be the Gaussian orthogonal ensemble (GOE) with $b = 1$ when not specified otherwise.

3.1 Estimate of the OTOC and its plateau

The idea is to use the results recapitulated in the previous section to find the ensemble expectation value of OTOC from the "master formulas" (2.2)–(2.3). Representing the eigenvectors and the operators as matrices in some (arbitrary) basis we can obviously write out

$$a_{nk} = \sum_{ij} \psi_i^{(n)} \psi_j^{(k)} A_{ij} \Rightarrow \langle a_{nk} \rangle = \int d^N \psi^{(n)} \int d^N \psi^{(k)} P\left(\psi^{(n)}, \psi^{(k)}\right) \psi_i^{(n)} \psi_j^{(k)} A_{ij}, \quad (3.3)$$

and similarly for b_{nk}. Inserting the above expression for the matrix elements into (2.3), multiplying $c_{mn}(t)$ by its complex conjugate taking into account the reality of the eigenvectors and relabelling the indices in the sums where convenient we find (denoting the average over the random matrix ensemble by $\langle C(t) \rangle$):

$$\langle C(t) \rangle = \int d^{N^2}\{c\} \int d^N\{E\} \mathcal{P}\left(\{E\}\right) P(\{c\}) \sum_{n,m} \sum_{k,k'} \sum_{i_{1,2}} \sum_{j_{1,2}} \sum_{i'_{1,2}} \sum_{j'_{1,2}} c_{j_1}^k c_{i_2}^k c_{j'_1}^{k'} c_{i'_2}^{k'} c_{i_1}^n c_{i'_1}^n c_{j_2}^m c_{j'_2}^m e^{-\beta E_n} \times$$

$$\times \left(A_{i_1 i_2} A_{i'_1 i'_2} B_{j_1 j_2} B_{j'_1 j'_2} e^{\imath(E_{k'} - E_k)t} + A_{i_2 j_2} A_{i'_2 j'_2} B_{i_1 j_1} B_{i'_1 j'_1} e^{\imath(E_k - E_{k'})t} - \right.$$

$$\left. - A_{i_2 j_2} A_{i'_1 i'_2} B_{i_1 j_1} B_{j'_1 j'_2} e^{\imath(E_k + E_{k'} - E_m - E_n)t} - A_{i_1 i_2} A_{i'_2 j'_2} B_{j_1 j_2} B_{i'_1 j'_1} e^{\imath(E_m + E_n - E_k - E_{k'})t} \right), \tag{3.4}$$

where $\{c\}$ determines the whole set of N^2 random elements $c_j^{(n)}$ with $j, n = 1 \ldots N$ and likewise $\{E_n\}$ is the whole set of eigenenergies. All the sums run from 1 to N. The integral over the eigenvector elements $\{c\}$ in (3.4) produces only an overall constant as these coefficients do not couple to the other quantities (in fact the integral $d^{N^2}\{c\}$ is a textbook Jeans integral, but we do not need its value as it only produces an N-dependent, T-independent constant). The remaining integral, over the eigenenergies, is again a sum of products of Jeans-type integrals but with an additional linear term $-\beta E$ in the exponent. Notice that the imaginary (sine) terms in (3.4) cancel out when the sum is performed; this

is a consequence of the module squared in $|c_{mn}|^2$, i.e. of the reality of OTOC. Now we see that (3.4) becomes a sum where each term is a product of factors of the form

$$p_i(E_i)e^{-E_i^2/4\sigma^2 - \beta E_i}\cos(sE_i t), \quad s \in \{0,1\},$$

where p_i is some polynomial and s may be zero or unity, i.e. some terms have this factor and some do not. Every such term is a Jeans-type integral. The number of terms in $\mathcal{P}(\{E\})$ equals the number of partitions of $N(N-1)b/2$, and the sums over the coefficients $\{c\}$ bring alltogether N^{12} terms. When everything is said and done (for details see appendix A), the final outcome, ignoring the multiplicative constant factors, reads:

$$\langle C(t) \rangle = \prod_{a=1}^{4} \sum_{\alpha_1^a, \ldots \alpha_N^a}^{\sum_j \alpha_j^a = N(N-1)b/2} \left[{}_1F_1\left(\frac{1+\alpha^a}{2}, \frac{1}{2}, \frac{\sigma^2}{4}(\beta-\imath t)^2\right) \right.$$
$$+ (\beta - \imath t){}_1F_1\left(\frac{2+\alpha^a}{2}, \frac{3}{2}, \frac{\sigma^2}{4}(\beta-\imath t)^2\right) + {}_1F_1\left(\frac{1+\alpha^a}{2}, \frac{1}{2}, \frac{\sigma^2}{4}(\beta+\imath t)^2\right)$$
$$\left. + (\beta + \imath t){}_1F_1\left(\frac{2+\alpha^a}{2}, \frac{3}{2}, \frac{\sigma^2}{4}(\beta+\imath t)^2\right) \right], \tag{3.5}$$

where ${}_1F_1$ is the confluent hypergeometric function. The sum runs over all partitions of $N(N-1)b/2$, and the product has four terms as each factor $|c_{mn}|^2$ has four matrix elements of A and B.

3.1.1 Kinematic OTOC

In order to move further we need to specify at least to some extent the operators A and B. We will consider (1) the kinematic OTOC, with $A = x$, $B = p$ (2) generic sparse operators, with $O(N)$ nonzero elements in the matrices a_{mn} and b_{mn}, and (3) dense operators A and B, with $O(N^2)$ nonzero elements, in particular the case when the operators A, B are themselves represented by Gaussian random matrices. Let us estimate OTOC for each case.

For the kinematic OTOC, $A_{ij} = x_i \delta_{ij}$ is diagonal and in the large-N limit B can be approximated as $B_{ij} \sim \delta_{ij}/x_i$. The Kronecker deltas reduce the number of terms in the sums over $\{c\}$ to N^4, the number of partitions $\sum_j \alpha_j = n$ can be approximated as $p(n) \sim \exp(\pi\sqrt{2n/3})/\sqrt{n}$, and the general expression (3.4) becomes[2]

$$\langle C(t) \rangle \sim e^{\pi\sqrt{\frac{b}{3}}N}N^3 e^{\frac{\sigma^2\beta^2}{4}}\left(W_0(\sigma\beta) + Q_1\left(\cos\frac{\sigma^2\beta t}{2}\right)W_1(\sigma\beta) + Q_2\left(\sin\frac{\sigma^2\beta t}{2}\right)W_2(\sigma\beta)\right), \tag{3.6}$$

where $W_{0,1,2}$ are polynomials in $\sigma\beta$ of degree $N(N-1)b/2 \sim N^2 b/2$, Q_1 is an even polynomial (with only even powers) of the same degree, and Q_2 is an odd polynomial of the same degree. Each coefficient in the polynomials $W_{0,1,2}$ comes from $\sim N^2$ terms (appendix A), therefore the size of the coefficients scales approximately with N^2. Eq. (3.6)

---

[2]One might be surprised by the unusual dependence on N. This happens because we have not normalized $C(t)$ by the product $\langle AA \rangle \langle AA \rangle$ as it is usually done. With appropriate normalization, $C(t)$ would of course be of order unity.

is a very complicated oscillating function as many terms are involved. But if we are only interested in the average value of $C(t)$ at long times, we may simply ignore the oscillations (which in the first approximation average out to some value of order unity) and write the estimate for the long-term, saturated or plateau OTOC value that we denote by C_∞:

$$C_\infty \sim \langle C(t \to \infty) \rangle \sim e^{\pi \sqrt{\frac{b}{3}} N} N^3 e^{\frac{\sigma^2 \beta^2}{4}} W_0 (\sigma \beta) \tag{3.7}$$

We deliberately do not write $\lim_{t \to \infty}$ in the above definition as the limit in the strict sense does not exist because of the oscillatory functions, and in addition our derivation is obviously nothing but a crude estimate. A similarly rough estimate of the temperature dependence of C_∞ can be obtained in the following way. For sufficiently large $\sigma \beta$, roughly $\sigma \beta / N^2 > 1$, the polynomial W_0 is dominated by the highest-degree term and we have, from (3.7):

$$C_\infty \sim (\sigma \beta)^{\frac{N^2 b}{2}} e^{\frac{\sigma^2 \beta^2}{4}} + \ldots \sim e^{\frac{\sigma^2}{4T^2}} + \ldots, \tag{3.8}$$

where in the second step we have assumed $\beta \gg 1$ so that the power-law prefactor $\beta^{N^2 b/2}$ becomes negligible compared to the exponential. We deliberately emphasize that there are other terms in the expansion $(\ldots)$, including also a constant term (from the zeroth-order term in W_0). This is important as it tells us that the scaling is in general of the form $C_\infty \approx \text{const.} + \exp(\sigma^2/4T^2)$, i.e. the temperature dependence is superimposed to a constant. This is also expected as the (appropriately normalized) saturated value C_∞ should always be of order unity, and the temperature dependence will only account for the relatively small differences between the plateau values of $C(t)$, as we will see later in figures 1 and 2.

On the other hand, for sufficiently small $\sigma \beta$, the polynomial W_0 can be estimated as a geometric sum of monomials in $-\sigma \beta N^2$ (remember the terms in W_0 have alternating signs):

$$C_\infty \sim \frac{e^{\frac{\sigma^2 \beta^2}{4}}}{1 + \sigma \beta N^2} \sim 1 - \sigma \beta N^2 + O\left(\beta^2\right). \tag{3.9}$$

We have now reached an important point: the plateau OTOC falls off exponentially with $1/T^2$ at low temperatures[3] and grows as a function of $1/T$ at high temperatures (we are not sure which function, as there are higher order terms in addition to the one written in (3.9), and there is no clearly dominant term like the exponential at large β), with the crossover temperature:[4]

$$T_c \sim \sigma N^2. \tag{3.10}$$

If we consider a pair of arbitrary sparse operators A and B, the whole above reasoning remains in place, except that the products of matrix elements such as $A_{i_1 i_2} A_{i'_1 i'_2} B_{j_1 j_2} B_{j'_1 j'_2}$ remain as arbitrary constants. Therefore we get the same qualitative behavior with two regimes and a crossover between them. The crossover temperature is very high for typical $N \gg 1$ (otherwise the random matrix formalism makes little sense) and finite σ (again, $\sigma \to 0$ makes little sense). In particular, in the $N \to \infty$ limit the crossover temperature becomes infinite and the only regime is the exponential decay.

---

[3]Actually, the falloff rate equals $\text{const.}/T^2$ with some system-specific constant, but for brevity we will denote it schematically as the $1/T^2$ regime throughout the paper.

[4]The crossover temperature is determined simply as $\beta_c \sigma N^2 = 1$, i.e. whether the terms in W_0 grow or decay at higher and higher order.

3.1.2 OTOC for dense and/or random operators

Now consider the case when the matrix elements in (3.5) are generically all nonzero (and for now nonrandom, i.e. we fix the operators and do not average over them). The large-t limit yields the expression

$$\langle C(t) \rangle \sim e^{\pi \sqrt{\frac{b}{3}}N} N^{11} e^{\sigma^2(\beta^2 - t^2)} \left[q_0(\sigma t) w_0(\sigma \beta) + q_1(\sigma t) w_1(\sigma \beta + \imath t, \sigma \beta - \imath t) \right], \quad (3.11)$$

where $q_{0,1}$ and w_0 are polynomials of degree $N(N-1)b/2 \sim N^2 b/2$, and w_1 is the polynomial of the same total degree of two variables, $\sigma\beta + \imath t$ and $\sigma\beta - \imath t$. The coefficients of $w_{0,1}$ are proportional to products of matrix elements $A_{i_1 j_1} B_{k_1 l_1} \ldots A_{i_8 j_8} B_{k_8 l_8}$, which are roughly proportional to $|A|^8 |B|^8$. The long-time limit yields

$$C_\infty \sim \frac{e^{\pi \sqrt{\frac{b}{3}}N}}{N^5} (|A||B|)^8 \, e^{\frac{\sigma^2 \beta^2}{4}} w_0(\sigma\beta) w_1(\sigma\beta, \sigma\beta), \quad (3.12)$$

but now a typical coefficient of the polynomials $w_{0,1}$ behaves as $N^2 (|A||B|)^8$. Therefore, the scaling in the low-temperature regime remains the same as (3.8): $C_\infty \sim \exp(\sigma^2/T^2)$. But the high-temperature regime yields

$$C_\infty \sim 1 - \sigma\beta N^2 (|A||B|)^8 + O\left(\beta^2\right), \quad (3.13)$$

therefore the crossover now happens at

$$T_c \sim \sigma N^2 (|A||B|)^8 \quad (3.14)$$

and therefore may be lower than the very high value (3.10), depending on the norm of the operators A and B.

Finally, if the operators A and B are both random Hermitian matrices (for concreteness, from the Gaussian unitary ensemble with the distribution function Π and the standard deviation ξ), we need to average also over the distribution functions for A and B and work with the double average $\langle\langle C(t) \rangle\rangle$:

$$\langle\langle C(t) \rangle\rangle \equiv \int d^N \{a\} \int d^N \{b\} \Pi(\{a\}) \Pi(\{b\}) \langle C(t) \rangle \sim \xi^{N^2} \langle C(t) \rangle. \quad (3.15)$$

This estimate is very crude, based simply on the fact that the distribution functions Π have $\sim N^2/2$ pairs of the form $(a_i - a_j)^2$. The important point is that the scaling from (3.13) that behaves essentially as $\sim \xi^{16}$ now becomes $\sim \xi^{N^2}$, therefore the crossover temperature is significantly reduced compared to (3.14) and behaves as $T_c \sim \sigma N^2 \lambda^{N^2}$. So for random operators the crossover may happen at temperatures that are not very high and thus can be clearly visible in the numerics and experiment.

3.2 Numerical checks

Now we demonstrate numerically that the crude estimates from the previous subsection indeed make sense and describe the characteristic behavior of OTOC. Our chief goal is to understand the behavior of C_∞, however it is instructive to start from the time dependence
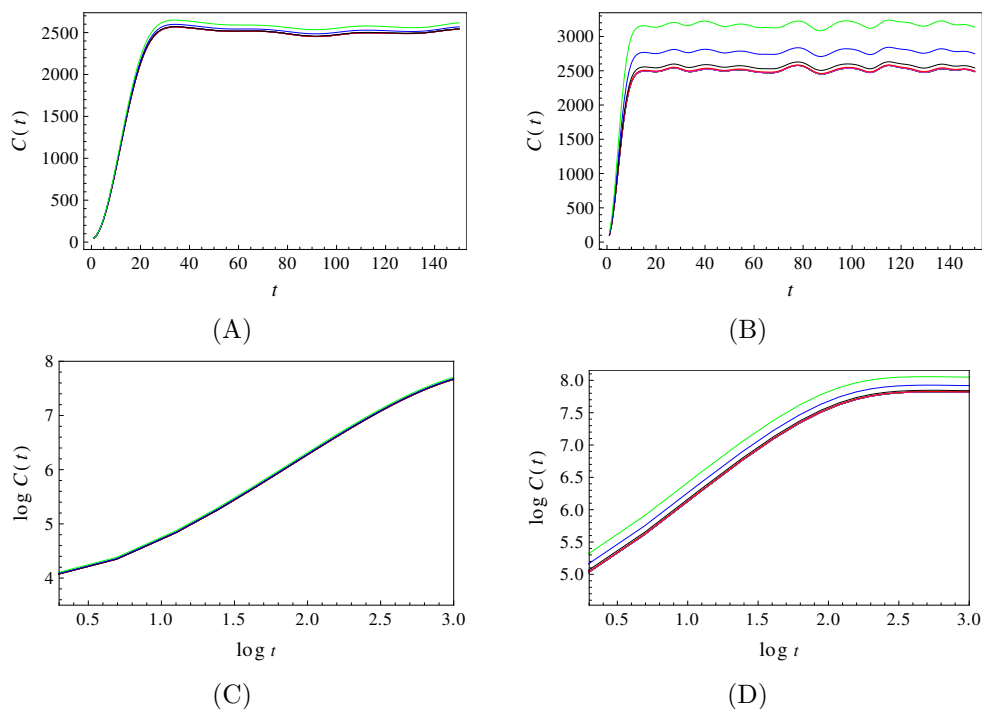
Figure 1. Numerically computed and averaged kinematic OTOC $C(t)$ for an ensemble of $l = 1000$ Gaussian orthogonal matrices of size $N = 20$ for the deviation $\sigma = 0.02$ (A, C) and $\sigma = 0.05$ (B, D), at temperatures 0.67 (black), 1.00 (blue), 1.25 (green), 2.50 (magenta), 5 (red). The plots (A, B) show the linear scale and the plots (C, D) the log-log scale. Crucially, the growth regime is not exponential and is actually closer to a power law. The growth ends on a plateau with superimposed oscillations. The plateaus differ slightly for different temperatures — the main effect we look at in this paper. Times is in units $1/\sigma$ in all plots.

of the kinematic OTOC (figure 1). We find the expected pattern of early growth followed by a plateau, however the growth is closer to a power law than to an exponential; this follows from the polynomial terms in (3.6), although the power law is not perfect either, as we see in the panels (A, C). This is in line with the prediction of [13], where the authors find

$$\langle C(t) \rangle \approx J_1^4(2t)/t^4 + t(t/2 - 1), \tag{3.16}$$

for a slightly different ensemble of random matrices (J_1 is the Bessel function of the first kind). This function is also neither an exponential nor a power law but at early times it is best approximated by a power law at leading order (at long times it falls off exponentially but the saturation is reached already prior to that epoch). In figure 2 we focus on the plateau behavior. It has the form of a constant function with superimposed aperiodic oscillations, and the differences of the plateau values are the subject of our theoretical predictions. These are relatively small and become important only when N is finite and not very large. In figure 2 we plot again the time dependence of the kinematic OTOC but now we focus on long timescales, to confirm that the plateau is indeed stable, and to show the very complex oscillation pattern superimposed on the plateau.
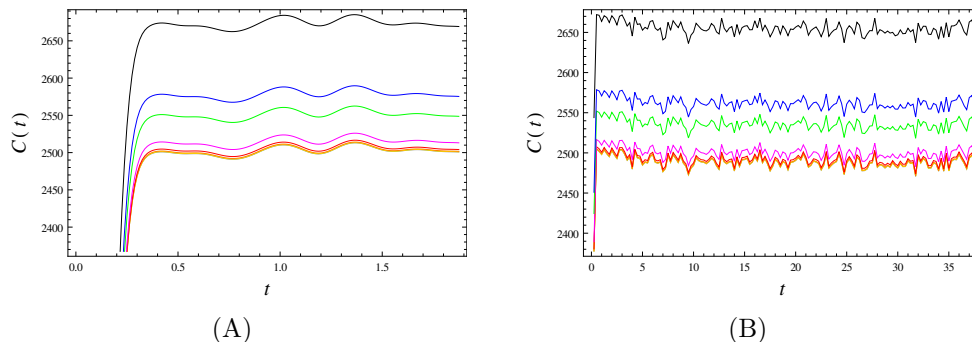
Figure 2. Numerically computed and averaged kinematic OTOC $C(t)$ for an ensemble of $l = 1000$ Gaussian orthogonal matrices of size $N = 60$ for the deviation $\sigma = 0.1$, at temperatures 0.67 (black), 1.00 (blue), 1.25 (green), 2.50 (magenta), 5 (red), 10 (orange), 20 (yellow) and 100 gray. In (B) we plot the same as in (A) but over a longer timescale, showing that the plateau remains stable for long times, i.e. represents true asymptotic behavior.
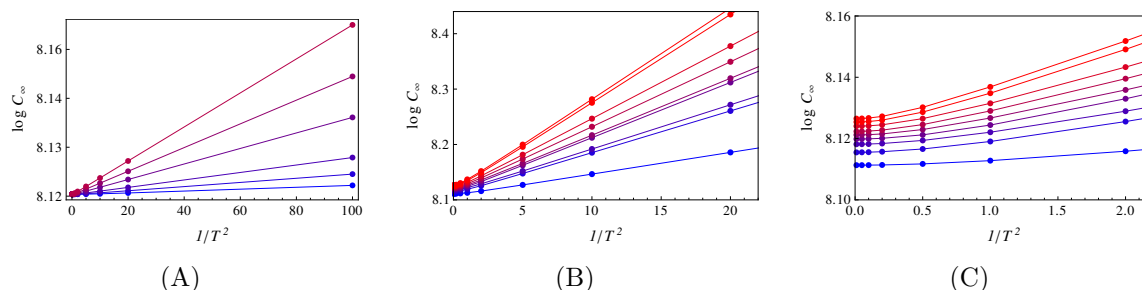
Figure 3. (A) The logarithm of the amplitude of the plateau C_∞ of the kinematic OTOC for the deviations $\sigma = 0.05, 0.1, 0.2, 0.4, 0.6, 0.8$ (blue to red) as a function of temperature for β values. The linear dependence is nearly perfect, in accordance with the predicted scaling $\log C_\infty \propto 1/T^2$. The matrix size is $N = 20$. (B) Same as (A) but for the deviation $\sigma = 0.4$ and varying matrix size $N = 10, 20, 40, 60, 80, 100$ and 120 (blue to red). In (C) we bring the zoom-in of the plot (B) for high temperatures. Appart from a slight deviation near $\beta = 0$, the behavior for larger matrices is still fully consistent with the analytical prediction. The solid lines are just to guide the eye.

Figure 3 confirms our main prediction for the low-temperature regime (again for the kinematic OTOC) — clear linear scaling of $\log C_\infty$ with $1/T^2$ in a broad range of temperatures. At small inverse temperatures there is some deviation from the linear scaling law but this we also expect. Looking now at the OTOC for a pair of random Hermitian operators in figure 4, we detect also the other regime at small enough temperatures — $\log C_\infty$ decays with the inverse temperature. This regime is likely present also in figure 3, but only at extremely high temperatures (which we have not computed in that figure).

4 OTOC for weakly and strongly chaotic Hamiltonians

For quasi-integrable few-degrees-of-freedom Hamiltonians one would naively expect that OTOC closely resembles the Lyapunov exponent, at least for high quantum numbers, approaching the classical regime. As we have already commented in the Introduction, it
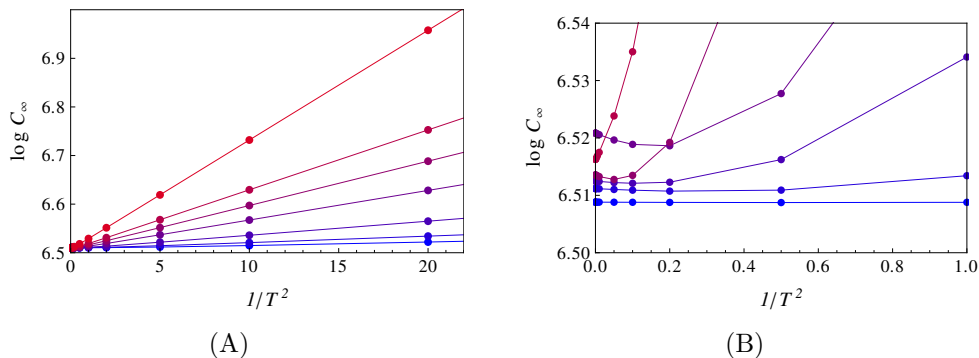
Figure 4. The saturated OTOC $C_\infty(T)$ of a pair of dense random operators A and B for the Gaussian orthogonal random Hamiltonian with $\sigma = 0.01, 0.05, 0.1, 0.2, 0.4, 0.6, 0.8$ (blue to red). In (A), looking at the full range of C_∞ values, it is obvious that the dominant regime is still the $\exp(c/T^2)$ scaling. However, focusing on the low-σ ensembles (B), we notice the high-temperature growing behavior of the OTOC plateau which is absent for sparse operators.

is known that this is not true in general [6, 8, 9, 16, 17] and that both chaotic systems with zero quantum Lyapunov exponent and regular systems with a nonzero exponent exist. We will now try to find some common denominator of OTOC dynamics in (deterministic) quantum-mechanical systems. It will quickly become clear from our general analysis of the master formula (2.3) that the function $C(t)$ is as complicated as for random matrices (indeed, even more so). But we will again construct an upper bound for the saturated OTOC value and arrive at a rough scaling estimate.

4.1 Weak chaos: perturbation theory

As an example of a quasi-integrable system (of the form $H = H_0 + \epsilon V$ where H_0 is integrable and the perturbation V makes it nonintegrable for $\epsilon \neq 0$) consider the Henon-Heiles Hamiltonian

$$H = \frac{1}{2}\left(p_x^2 + p_y^2\right) + \frac{1}{2}\left(\omega_x^2 x^2 + \omega_y^2 y^2\right) + \epsilon\left(x^2 y - \frac{1}{3}y^3\right), \tag{4.1}$$

a well-known paradigm for classical chaos with applications in galactic dynamics and condensed matter. For $\epsilon = 0$ it obviously reduces to a 2D linear harmonic oscillator and becomes integrable. As we know, nonintegrability does not always imply chaos; indeed, this is a typical system with mixed phase space, with both chaotic and regular orbits. Chaotic orbits proliferate only when the perturbation is larger than some finite ϵ_c; they are almost absent at low energies, numerous at intermediate energies and again absent at very high energies when the potential energy is negligible compared to the kinetic energy [28, 29]. For such a quasi-integrable system our idea is to apply elementary perturbation theory in the occupation number basis to estimate OTOC starting from (3.4). We will present the perturbation theory in a fully general way, for an arbitrary Hamiltonian $H_0 + \epsilon V$, and some of the conclusions will also turn out to be quite general. Only at the end we will show the quantitative results for the Henon-Heiles system (4.1).

Let us write the perturbative expression for OTOC. Replacing the initial basis states $|n\rangle$ with the first-order[5] perturbatively corrected states $|n + \delta n\rangle$ and introducing likewise the perturbative corrections δa_{mn}, δb_{mn} for the matrix elements of A and B, the equation (2.3) becomes

$$
\begin{aligned}
c_{mn}^{(1)} &= c_{mn} + \sum_k \left(\delta a_{mk} b_{kn} + a_{mk} \delta b_{kn} \right) e^{-\imath E_{km} t} - \sum_k \left(\delta b_{mk} a_{kn} + b_{mk} \delta a_{kn} \right) e^{-\imath E_{nk} t} = \\
&= c_{mn} + \sum_{kl} \left(\delta_{ml} a_{lk} b_{kn} + \delta_{kl}^* a_{lm}^* b_{kn} + \delta_{kl} b_{ln} a_{mk} + \delta_{nl}^* b_{lk}^* a_{mk} \right) e^{-\imath E_{km} t} + (a \leftrightarrow b) \, e^{-\imath E_{nk} t} = \\
&= c_{mn} + \left(\delta \cdot A \cdot B + A^\dagger \cdot \delta^\dagger \cdot B + A \cdot \delta \cdot B + A \cdot B^\dagger \cdot \delta^\dagger \right)_{mn} e^{-\imath E_{km} t} + (A \leftrightarrow B)_{mn} \, e^{-\imath E_{nk} t}.
\end{aligned}
\tag{4.2}
$$

Now we insert this result into (2.2) and apply the Cauchy-Schwarz-Bunyakovski inequality:

$$
\begin{aligned}
C^{(1)}(t) &= \frac{1}{Z} \sum_{mn} e^{-\beta E_n} |c_{mn}^{(1)}|^2 \leq \\
&\leq \frac{1}{Z} \sum_{mn} e^{-\beta E_n} \left(|c_{mn}|^2 + |\delta \cdot A \cdot B + A^\dagger \cdot \delta^\dagger \cdot B + A \cdot \delta \cdot B + A \cdot B^\dagger \cdot \delta^\dagger|_{mn}^2 + (A \leftrightarrow B) \right) = \\
&= C(t) + \frac{1}{Z} \left(4 \mathrm{Tr} \left(B^\dagger \cdot A^\dagger \cdot \delta^\dagger \cdot \tilde\rho^2 \cdot \delta \cdot A \cdot B \right) + 4 \mathrm{Tr} \left(B^\dagger \cdot \delta \cdot A \cdot \tilde\rho^2 \cdot A^\dagger \cdot \delta^\dagger \cdot B \right) \right) \leq \\
&\leq C_\infty + \frac{8}{Z} |\tilde\rho|^2 |A|^2 |B|^2 |\delta|^2 \equiv C_\infty + \delta C_\infty,
\end{aligned}
\tag{4.3}
$$

where $\tilde\rho \equiv \mathrm{diag}(\exp(-\beta E_n))$ is the non-normalized density matrix. In the above derivation, we have also used the definition of trace and the definition of thermal expectation values $\langle A \rangle \equiv \mathrm{Tr}\left(\rho \cdot A \right)$. The norm of a matrix is defined as usual by $|A|^2 \equiv \mathrm{Tr} A^\dagger A$. This estimate manifestly replaces $C(t)$ by its asymptotic (maximum) value, as we have replaced the terms containing the time-dependent phase factors by their time-independent norms.

In order to move further, notice first that $|\tilde\rho|^2 = \sum_n \exp(-2\beta E_n) = Z(2\beta)$ for a canonical ensemble with the diagonal density matrix that we consider here. This means, from (4.3), that the temperature dependence is encapsulated in the ratio $Z(2\beta)/Z(\beta)$. The prefactor will again differ between dense and sparse A, B and V. For sparse matrices, we can write $|A|^2 \sim N a^2$ whereas for dense matrices we have $|A|^2 \sim N^2 a^2$, assuming that all matrix elements have some characteristic magnitude a. Obviously, if this is not true the outcome will be more complicated, but it seems this does not influence the temperature dependence. For concreteness we assume sparse A and B. For sparse V with nonzero elements of order v concentrated near the diagonal (this is true for the Henon-Heiles Hamiltonian and in general for perturbations expressed as low-degree polynomials in coordinates and momenta), we can estimate $|\delta|^2 \sim N v^2 / \omega^2$. Here we assume an approximately equidistant spectrum of H_0 with frequency (neighboring level spacing) ω. This yields:

$$
C_\infty^{(1)} \sim C_\infty + \frac{Z(2\beta)}{Z(\beta)} N^3 a^2 b^2 \frac{v^2}{\omega^2}.
\tag{4.4}
$$

---

[5]The whole argument works the same way also for higher-order perturbation theory; we assume first order just for simplicity.
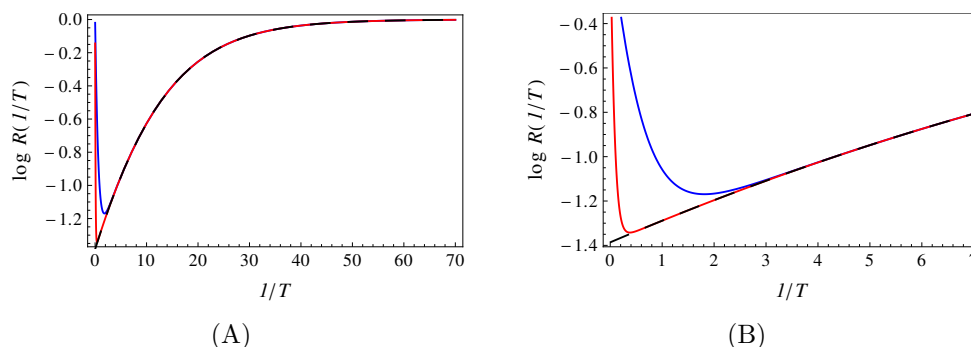
Figure 5. The thermal dependence factor of $\log C_\infty$ for weak perturbative chaotic systems, given by $Z(2\beta)/Z(\beta)$ with $\beta = 1/T$ the inverse temperature, here given for a 2D linear harmonic oscillator with the frequencies $\omega_x = \omega_y = 0.1$, with $N = 20$ levels (blue) and with $N = 150$ levels (red). We also plot the sum over $N = \infty$ levels (black). In (A) we zoom in at high β/low temperatures, and in (B) we focus on smaller β/larger T. The $N = 150$ plot is aready quite close to the monotonic $N = \infty$ dependence but at high temperatures there is always a region decaying with β, before the approximately linear $\log R(1/T)$ dependence sets in, just like in the numerical results. At very low temperatures the ratio saturates, as we see in the panel (A). This ensures that our estimate for the saturated OTOC has a finite limite at zero temperature. The overall scale is arbitrary as the R factor is always multiplied by various other factors.

For a dense perturbation V, the only factor that changes is $|\delta|$. Assuming again the utterly simple situation where all matrix elements of V are roughly equal v, we have $\delta_{mn} \sim v/E_{mn} \sim v/(\omega(m-n))$, which yields a series that can be summed analytically. However, we will not pursue this further as the temperature dependence is universal in all cases, given by the simple ratio of the partition functions:

$$ C_\infty \propto R(\beta) \equiv \frac{Z(2\beta)}{Z(\beta)} \to \frac{\sum_{j=1}^{N} e^{-2\beta\omega}}{\sum_{j=1}^{N} e^{-\beta\omega}} \to \frac{e^{\beta\omega}}{1 + e^{\beta\omega}}. \tag{4.5} $$

The first simplification holds when H_0 is a 1D harmonic oscillator, and the second one when $N \to \infty$. But the basic result (the ratio of partition functions) always holds. We are in fact more interested in the 2D harmonic oscillator, which is the integrable part of the Henon-Heiles Hamiltonian. For that case, we plot the sum (for finite N) in figure 5. Of course, the analysis of the function $R(\beta)$ is trivial — we plot it in the figure merely to emphasize the qualitative agreement with the numerics.

As a final remark, what we have found is the correction of the OTOC plateau δC_∞. There is still the unperturbed value of C_∞ for the integrable Hamiltonian H_0. We know that this can be nonzero and even quite large because of local instability [6, 7, 9]. We are mainly interested in the opposite situation, when the scrambling chiefly comes from chaos so that OTOC does not grow when $H = H_0$. In this case $C^{(1)} \approx \delta C_\infty$ and the temperature dependence is primarily determined by (4.4). In the next subsection we will look both at the Henon-Heiles system where this holds, and a perturbed inverse chaotic oscillator where H_0 is unstable.

4.2 Weak chaos: examples and numerics

As our main example we can now study the Henon-Heiles system of eq. (4.1). Starting from the nonperturbed Hamiltonian (2D harmonic oscillator), we will express the nonzero elements of $c_{mn}(t)$ exactly, i.e. we will not use the estimates (4.3) as the perturbation is quite simple and amenable to analytic treatment. Denoting a basis state by the quantum number $n = (n_x, n_y)$, we can write the amplitudes $c_{n_x n_y n'_x n'_y}$ as products of amplitudes of the two decoupled subsystems $c_{n_x n_y n'_x n'_y} = C_{n_x n'_x} C_{n_y n'_y}$, with

$$C_{n_x n_x} = -\imath n_x \omega_x \cos t$$
$$C_{n_x, n_x-2} = \frac{\imath}{2}\sqrt{n_x - 1}\left(\sqrt{n_x + 1}e^{-\imath\omega_x t} - \sqrt{n_x + 2}e^{\imath\omega_x t}\right)$$
$$C_{n_x, n_x+2} = \frac{\imath}{2}\sqrt{n_x + 1}\left(\sqrt{n_x - 1}e^{\imath\omega_x t} - \sqrt{n_x - 2}e^{-\imath\omega_x t}\right),$$

(4.6)

and all other elements are zero; for the y quantum numbers the coefficients are the same with $(n_x, \omega_x) \mapsto (n_y, \omega_y)$. For nonzero ϵ, the off-diagonal matrix elements can be represented exactly as

$$c_{n_x n'_x n_y n'_y}(t) = \epsilon \delta_{|n_x - n'_x| - 2}\delta_{|n_y - n'_y| - 1}\sqrt{m_x(m_x - 1)}\sqrt{m_y + 1}, \quad m_{x,y} \equiv \min(n_{x,y}, n'_{x,y}).$$

(4.7)

The state vectors are now easily calculated in textbook perturbation theory. We have compared the analytic calculation to the numerics and find that they agree within a relative error ≤ 0.04; therefore, one may safely use (4.6)–(4.7) in order to speed up the computations and avoid numerical diagonalization of large matrices.

The magnitude of the plateau value of $C(t)$, computed by long-time averaging similarly to the random matrix calculations in section 3, are given in figure 6. At large T values, C_∞ decays with $1/T$, at intermediate values it shows an exponential growth with $1/T$ just like $R(1/T)$ in figure 5, and as the temperature goes to zero it reaches a finite value. In figure 7 we consider a system with much reduced state space, with $N = 25$. We expect that for small N the existence of two regimes is more clearly visible, and that the crossover temperature is higher. This is indeed what happens, although the exact form of the function $C_\infty(1/T)$ is not very well described by the analytical result. As we have made many crude approximations, this is not surprising: our analytical result still explains the existence of two regimes and the crossover between them.[6] One unexpected finding is that the high-temperature regime is apparently universal for all perturbation strengths and scales as $C_\infty \propto \exp(-4\pi/T)$. This is probably specific for the Henon-Heiles system; we do not understand it at present.

It is instructive to look at the energy level statistics of the Henon-Heiles system for the same parameters that we have used for the OTOC calculation, in order to understand the relation of OTOC to chaos. In figure 8 we plot the histograms of the neighboring level

---

[6]One might regard such truncation of the state space as artificial and unphysical. It is clearly just a technical step in order to show the effect we seek for more clearly, however in principle it can be realized by introducing an additional external potential. In other contexts, e.g. finite spin systems, a finite Hilbert space is perfectly natural.
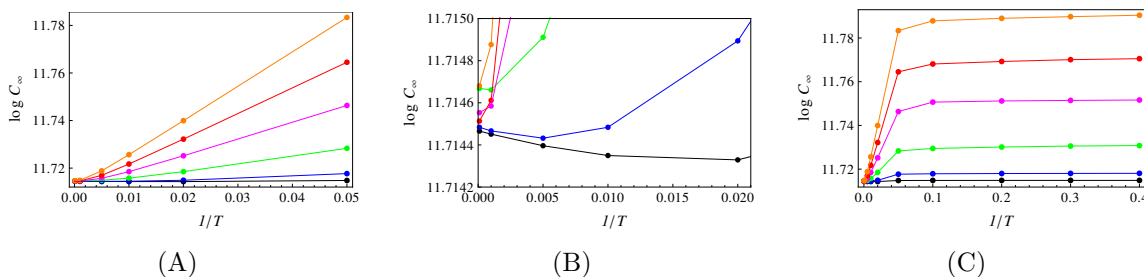
Figure 6. (A) The saturated kinematic OTOC value C_∞ for a range of inverse temperatures $\beta = 10^{-4}, 10^{-3}, 5 \times 10^{-3}, 0.01, 0.02, 0.05$ and a range of perturbation strengths $\epsilon = 1, 2, 5, 10, 15, 20$ (black, blue, green, magenta, red, orange). Here we see the scaling $C_\infty \propto \exp(c/T)$, with c growing with ϵ. In the (B) panel we zoom in the high-temperature region, to show that for $\epsilon \leq 5$ there is also the other regime where C_∞ grows with T. Since the number of points in this interval is small it is not easy to judge the form of T-dependence. In (C) we focus on the opposite regime, at very low temperature, showing that C_∞ saturates as $T \to 0$. This is again in accordance with the $\beta \to \infty$ limit of $Z(2\beta)/Z(\beta)$. The system is truncated to $N = 144$ levels.
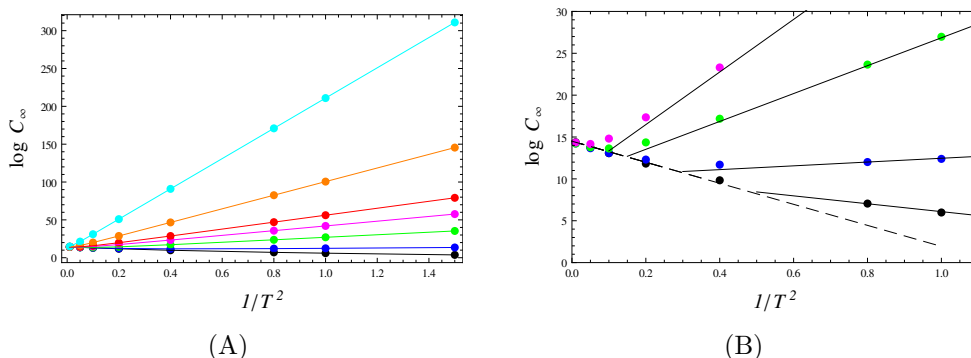
Figure 7. The saturated kinematic OTOC value $C_\infty(T)$ for the truncated Henon-Heiles model with $N = 25$ levels. The perturbation strength is $\epsilon = 0.1, 0.3, 0.5, 0.7, 0.9, 1.5, 3.0$ (black, blue, green, magenta, red, orange, cyan). Already in (A) we see that for $\epsilon \leq 0.5$ there is a finite crossover temperature T_c so that C_∞ grows wth temperature for $T > T_c$. Since T_c goes down when the Hilbert space is reduced, we can observe the high-temperature regime very clearly and see that it collapses to a universal law $C_\infty \sim \exp(-4\pi/T)$. This is seen in the panel (B) where we zoom in at the interesting region.

spacing. Even for large ϵ, the regular (Poisson) component is dominant over the chaotic (Wigner-Dyson) component. In other words, the classically mixed phase space, with the increasing chaotic component, is almost completely regular in the quantum regime; quantum chaos is "weaker", as is often found in the literature [33]. For us, the fact that the system is outside the Wigner-Dyson regime means that indeed the behavior of C_∞ is a good litmus test of quantum dynamics, behaving (at low temperatures) as $\exp(1/T^2)$ or $\exp(1/T)$ for strong or weak chaos respectively.[7] Indeed, we would not expect that a system which is well described by perturbation theory shows strong level repulsion.

---

[7]In fact, this is only true provided that the scrambling is chaos-related, i.e. that the integrable limit with $\epsilon = 0$ and $H = H_0$ does not scramble significantly. We will come to this issue in the next paragraph.
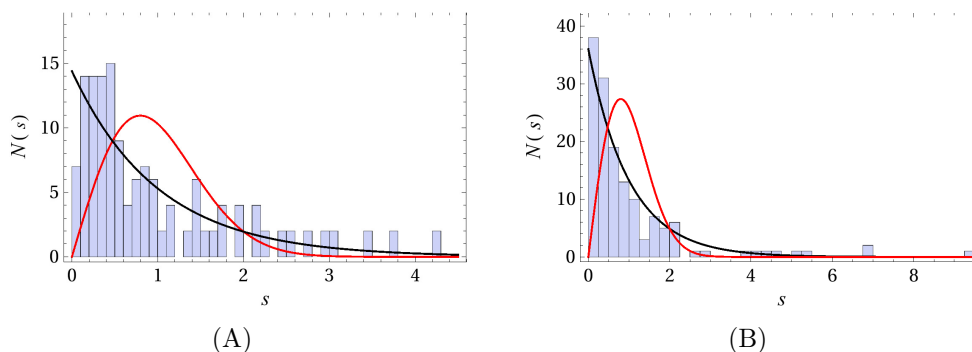
Figure 8. Distribution of neighboring energy level spacings $N(s)$ for the Henon-Heiles Hamiltonian with $\epsilon = 0.1$ (A) and $\epsilon = 1.5$ (B). In each plot we compare the level distribution to the Poisson law ($\exp(-s)$) and the Wigner-Dyson law for orthogonal matrices ($s\exp(-\pi s^2/4)$). The distribution is dominantly Poissonian even for large perturbations, although there is a small admixture of Wignerian statistics. The perturbative dynamics of the Henon-Heiles system is always weakly chaotic in quantum mechanics (despite being classically strongly chaotic for large enough ϵ).
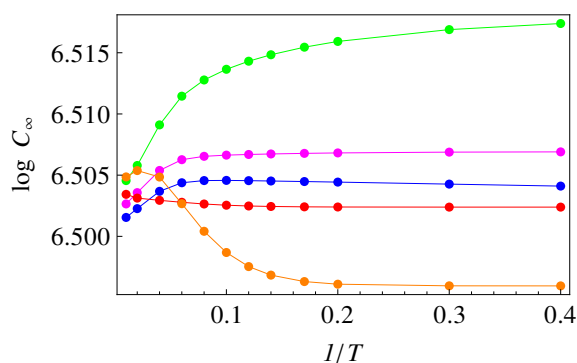
Figure 9. Temperature dependence of the asymptotic OTOC C_∞ for the inverse Henon-Heiles Hamiltonian, with $\omega_x^2 = 4\omega_y^2 = -1$, and perturbation strength $\epsilon = 0, 0.1, 0.5, 0.9, 1.5$ (blue, green, magenta, red, orange). The curves are more or less flat and without a clear trend, as the scrambling is rooted in local instability, not chaos.

Finally, it is instructive to look at the inverse Henon-Heiles system, with $(\omega_x^2, \omega_y^2) \mapsto (-\omega_x^2, -\omega_y^2)$, so that H_0 is the inverse harmonic oscillator. As already found in the literature, scrambling is significant already at $\epsilon = 0$, and this contribution dominates even at high ϵ, at all temperatures. In other words, neither the perturbation nor the temperature have a significant influence over C_∞. This is fully in accordance with the result (4.3) and the morale is that OTOC directly describes scrambling, and chaos only indirectly, through the scrambling, *if the scrambling originates mainly from chaos*; if not, OTOC is largely insensitive to chaos. Therefore, the temperature dependence of the OTOC value, derived from the assumptions about the dynamics (perturbative chaos or strong, random-matrix chaos) cannot be seen when there is a strong non-chaotic component to scrambling (figure 9).

4.3 Strong chaos: numerics and the return to random matrices

As a final stroke, we will now examine a strongly chaotic system which is also relevant for black hole scrambling and related problems in high energy physics. This is the bosonic sector of the D0 brane matrix model known as the BMN (Berenstein-Maldacena-Nastase) model [30], obtained as a deformation of the BFSS (Banks-Fischler-Shenker-Susskind) model [31] by a mass term and a Chern-Simons term. This model has been studied in detail in the context of non-perturbative string and M theory. It is known to describe the dynamics of M theory on pp-waves and is also related to the type IIA string theory at high energies; for details one can look at the original papers or the review [32]. Following [33–36], we focus solely on the bosonic sector which is enough to have strongly chaotic dynamics with equations of motion that are not too complicated. The quantum-mechanical Hamiltonian of the BMN bosonic sector reads:[8]

$$H = \text{Tr}\left(\frac{1}{2}\Pi^i\Pi^i - \frac{1}{4}\left[X^i, X^j\right]\left[X^i, X^j\right] + \frac{1}{2}\nu^2 X^a X^a + \frac{1}{8}\nu^2 X^\alpha X^\alpha + \imath\nu\varepsilon_{abc}X^a X^b X^c\right)$$
$$i \in \{1\ldots9\}, \quad a, b, c \in \{1, 2, 3\}, \quad \alpha \in \{4\ldots9\}, \tag{4.8}$$

where Π^i are the canonical momenta, X^i the canonical variables, ε_{abc} is the Levi-Civitta tensor, and $\nu^2 > 0$ is the mass deformation which also determines the size of the Chern-Simons deformation (the last term in (4.8)). Following [35], we will study the "mini-BMN" model with $X^\alpha = 0$, so we effectively only have three degrees of freedom. The matrices $X_{1,2,3}$ and $P_{1,2,3}$ are $N \times N$ matrices. For this example we have to abandon the master formulas for OTOC (2.2)–(2.3) as it is very difficult to find the quantities c_{mn} — for this we would have to perform exact diagonalization of the Hamiltonian (4.8). Instead, we follow [36] and write a truncated system of equations directly for the expectation values $\langle X^a \rangle$ and $\langle P^a \rangle$ and the two-point correlators $\langle X^a X^b \rangle$, $\langle \Pi^a X^b \rangle$ and $\langle \Pi^a \Pi^b \rangle$, where the expectation value is obtained through the trace over the density matrix: $\langle X^a \rangle \equiv \text{Tr}(\rho X^a)$. The equations read (for their derivation see [36]):

$$\partial_t \langle X^a \rangle = \frac{1}{N}\langle \Pi^a \rangle$$
$$\frac{1}{N}\partial_t \langle \Pi^a \rangle = \langle X^b \rangle\langle X^b \rangle\langle X^a \rangle - 2\langle X^b \rangle\langle X^a \rangle\langle X^b \rangle + \langle X^a \rangle\langle X^b \rangle\langle X^b \rangle + \nu^2\langle X^a \rangle + \imath\nu\varepsilon_{abc}\langle X^b \rangle\langle X^c \rangle +$$
$$+ \left(X^a\langle X^b X^b \rangle - \langle X^b X^b \rangle X^a + X^b\langle X^a X^b \rangle - \langle X^a X^b \rangle X^b + \imath\nu\varepsilon_{abc}\langle X^b X^c \rangle\right), \tag{4.9}$$

where the last line contains the leading quantum corrections: all possible terms with a single contraction of the classical equation of motion, and the summation over repeated indices is understood. The equations of motion for the two-point correlators are obtained again by writing the classical equations of motion for the bilinears $\Pi^a\Pi^b$, $\Pi^a X^b$ and $X^a X^b$

---

[8]Do not confuse with the classical action considered in [33, 35].
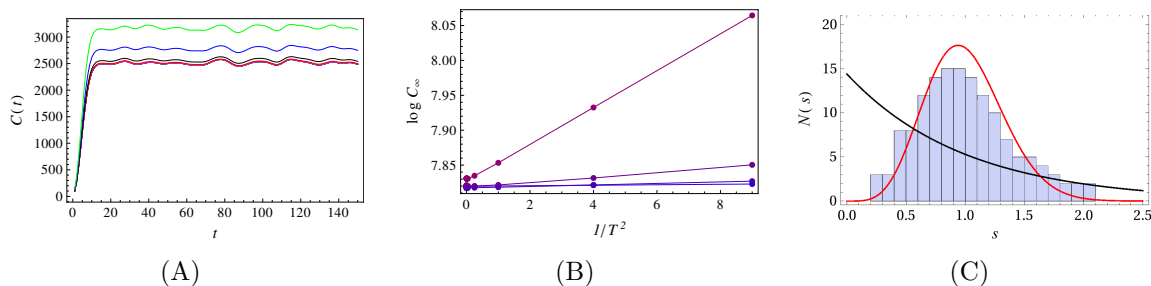
Figure 10. (A) Time dynamics $C(t)$ for the truncated quantum-mechanical mini-BMN model, with $\nu = 0.1, 0.3, 0.5, 1.0$ (red, black, blue, red), shows the expected pattern of growth followed by an oscillating plateau. (B) Temperature dependence of the saturated value $C_\infty(T)$ for the same values of ν (blue to red) has the same $\exp(1/T^2)$ scaling as the random matrix ensembles. The level spacing statistics, shown in (C) for $\nu = 0.5$, is indeed quite close to the Gaussian unitary ensemble (full red curve) and clearly at odds with the Poisson statistics (full black curve), confirming that this system is within the scope of our random matrix calculation.

and taking all possible single contractions in each term. This yields:

$$\partial_t \langle X^a X^b \rangle = \frac{1}{N} \left(\langle \Pi^a X^b \rangle + \langle X^a \Pi^b \rangle \right) \tag{4.10}$$

$$\partial_t \langle \Pi^a X^b \rangle = \frac{1}{N} \langle \Pi^a \Pi^b \rangle + N \langle X^a X^b \rangle \langle X^c X^c \rangle - N \langle X^c X^c \rangle \langle X^a X^b \rangle + N \langle X^b X^c \rangle \langle X^a X^c \rangle - \\ - N \langle X^a X^c \rangle \langle X^b X^c \rangle + \nu^2 \langle X^a X^b \rangle \tag{4.11}$$

$$\partial_t \langle \Pi^a \Pi^b \rangle = N \langle X^a X^b \rangle \langle X^c X^c \rangle - N \langle X^c X^c \rangle \langle X^a X^b \rangle + N \langle X^b X^c \rangle \langle X^a X^c \rangle - \\ - N \langle X^a X^c \rangle \langle X^b X^c \rangle + \nu^2 \langle X^a X^b \rangle + (a \leftrightarrow b) . \tag{4.12}$$

As explained in [36], this truncated system is obtained by assuming a Gaussian approximation for the wavefunctions. Therefore, we solve the truncated quantum dynamics of the mini-BMN model — essentially a toy model, but it will serve our purpose. Now that we have set the stage, we can express the kinematic OTOC as $C(t) = \langle X^a \Pi^b \rangle - \langle \Pi^a X^b \rangle$ and study its dynamics. The outcome is given in figure 10. We are essentially back to the random matrix regime of section 3 — there is a clear scaling $C_\infty \sim \exp(1/T^2)$ (we do not see the other regime, but again it may well be there for sufficiently high temperatures), and the level distribution is a near-perfect fit to the Wigner-Dyson curve. Therefore, if a Hamiltonian is strongly chaotic, then both the level distribution and the OTOC plateau are well described by the random matrix theory.

5 Discussion and conclusions

In this paper we have formulated a somewhat unexpected indicator of quantum chaos, useful mainly in few-body (few-degrees-of-freedom) systems. While OTOC has become the quintessential object in the studies of quantum chaos and information transport, characterized mainly by its growth rate — the (quantum) Lyapunov exponent, in our examples its growth pattern tends to be quite nonuniversal and "noisy" (in the sense that it depends sensitively on the system at hand and the operators we look at). Our analytic

treatment of OTOC dynamics is quite sketchy, however both analytical and numerical results strongly suggest there is no clear exponential growth. At first glance, one might think that this finding is completely at odds with the established wisdom, however this is not true. In the literature, exponential growth is mainly characteristic for systems with a classical gravity dual (and reaches its maximum when the dual contains a thermal black hole horizon). There are abundant examples of quantum chaotic systems which do not have an exponentially growing OTOC (we especially like [19] but there are many other published examples). The exponential growth follows, in the AdS/CFT picture, from the shock wave dynamics in a classical gravity background, and need not exist when the background is not classical or when the gravity dual does not exist at all. This is precisely what happens here: the Henon-Heiles Hamiltonian is certainly nothing like a strongly coupled large N field theory, while the truncated mini-BMN model comes closer (it is actually related to discretized Yang-Mills) but we tackle it at finite N and thus away from the fast scrambling dual. For random matrices, our findings for $C(t)$ are in line with the rigorous results of [13]. As pointed out in that work, the crucial difference between random matrices and strongly coupled field theories is that the former have no notion of locality neither in time nor in space. In our small systems, the spatial locality is irrelevant anyway but if the system is not sufficiently chaotic there will still be long-term temporal correlations in dynamics (this indeed gives rise to different scaling regimes for strong and weak chaos).

On the other hand, what we have found is that the long-time OTOC behavior, when it becomes essentially stationary, with a complex oscillation pattern, is surprisingly regular — behaving as $\exp(1/T^2)$ and $\exp(1/T)$ respectively in strong and weak chaos. This indicator seems to have a stronger connection to quantum chaos in the sense of level statistics than the Lyapunov exponent; in all examples we have studied the $\exp(1/T^2)$ regime and the Wigner-Dyson level distribution go hand in hand. At very high temperatures we detect also a different regime, when the OTOC plateau grows with temperature. This regime seems less universal, and we do not understand it very well. One might think that the plateau value should not carry any useful information; it is often laconically stated that OTOC reaches saturation when the initial perturbation has spread all over the system and that this saturation value is unity when OTOC is appropriately normalized. This is roughly true, however "spreading all over the system" is not a rigorous notion — depending on the system and the operators A, B in OTOC, the perturbation may never spread completely due to symmetry constraints, specific initial conditions, quasi-integrals of motion etc. Such factors are particularly important in finite systems (quantum mechanics as opposed to quantum field theory) that we study. Looking at the figures, one sees that differences in the asymptotic OTOC value C_∞ tend to be small, and C_∞ tends to be about the same to an order of magnitude in all cases. We conjecture that such differences would dwindle to zero in the field limit.

A simple intuitive explanation for the falloff of asymptotic OTOC with temperature is the following: we expect that higher temperatures lead to faster information spreading and quicker equilibration. Therefore, it is logical that the plateau value will be lower, so that the system needs less time to reach it, i.e. it needs less time to equilibrate.

We note in passing that we have confirmed that scrambling can originate from at least two distinct mechanisms: local instability and chaos, so in the former case the relation of OTOC to chaos is largeley lost. This is a known fact in many examples already [6, 7, 9, 16, 26] and we emphasize it here merely as a reminder to the reader that the OTOC-chaos connection is really a relation of three elements: OTOC-scrambling-chaos, and if the second link is missing no attempt should be made to understand chaotic dynamics from OTOC.

We conclude with some speculations. The OTOC plateau value, as we found, is a rather universal function of temperature, and it is essentially a finite-size fluctuation of the correlation function, when the system is small enough that the relative size of fluctuations does not go to zero. We may then look for universality and the connections to chaotic dynamics in other similar quantities, e.g. the average fluctuation of the expectation value of some operator during thermalization. Such a quantity remains nonzero also in AdS/CFT at large N, and may relate our results to the more familiar fast scrambling, strongly correlated holographic systems.

Acknowledgments

A   Detailed structure and calculation of OTOC for Gaussian orthogonal ensembles

In this appendix we consider the calculation of OTOC for random matrix systems in some more detail, and describe the detailed structure of the correlation function $C(t)$. Let us first denote, for the sake of brevity:

$$\sum_{\text{tot}} \equiv \sum_{n,m} \sum_{k,k'} \sum_{i_1,i_2} \sum_{j_1,j_2} \sum_{i_1',i_2'} \sum_{j_1',j_2'}, \quad \mathbf{C} \equiv c_{j_1}^k \dots c_{j_2'}^m.$$

Denote also the products of matrix elements of the operators A, B entering the expression (3.4) by $\chi_1, \chi_2, \chi_3, \chi_4$. Now the expression for $\langle C(t) \rangle$ can be written as:

$$\langle C(t) \rangle = \sum_{\text{tot}} \int P(\{c\}) d^{N^2}\{c\} \int \mathcal{P}(\{E\}) d^N E e^{-\beta E_n} \mathbf{C}$$
$$\times \left(\chi_1 e^{i(E_{k'} - E_k)t} + \dots + \chi_4 e^{i(E_m + E_n - E_{k'} - E_k)t} \right) \tag{A.1}$$

As we have noticed in the main text, the integral over $\mathbf{C}$ yields just a numerical constant. Let us therefore evaluate the energy integral $I_1 = \int d^N\{E\}\mathcal{P}(\{E\})e^{-\beta E_n}\chi_1 e^{i(E_{k'}-E_k)t}$. We have:

$$I_1 = \int \int \cdots \int dE_n \int dE_k \int dE_{k'} \mathcal{P}(\{E\}) e^{-\beta E_n} \times \chi_1 e^{i(E_{k'}-E_k)t}. \tag{A.2}$$

The absolute values of the differences can be written out in the obvious way:

$$\prod_{n<m}|E_n - E_m| = \sum_i (-1)^{\pi(i)} E_1^{\alpha_{1,i}} E_2^{\alpha_{2,i}} \dots E_N^{\alpha_{N,i}}, \tag{A.3}$$

where all $\alpha_{i,j}$ are some (positive) integer exponents and $\pi(i)$ is the appropriate sign factor 0 or 1. Therefore, I_1 can be reorganized as:

$$I_1 = \sum_j \chi_1 \prod_{i \neq n,k,k'} \int E_i^{\alpha_{i,j}} e^{-E_i^2} dE_i \int dE_n e^{-\beta E_n} e^{-E_n^2} \int dE_k e^{iE_{k'}t} e^{-E_{k'}^2} \int dE_k e^{-iE_k t} e^{-E_k^2}. \tag{A.4}$$

Note that the part $\prod_{n<m}|E_n - E_m|$, is not essential for the general behavior, since the singular integral $\int E_i^{\alpha_{i,j}} e^{-E_i^2} dE_i$ is either some constant (if α is even), or zero if α is odd. Otherwise for $i \neq j$

$$\int \prod_{l<i<l'} E_i e^{-E_j^2} dE_j = \text{const.} \times \prod_{l<i<l'} E_i. \tag{A.5}$$

Therefore, we only focus on calculating integrals of the form

$$\int dE_n \int dE_k \int dE_{k'} e^{-\beta E_n} \times e^{-E_n^2 - E_k^2 - E_{k'}^2} \chi_1 e^{i(E_{k'}-E_k)t}, \tag{A.6}$$

which yields the closed-form expression for the temperature dependence of I_1:

$$I_1 \sim \delta_{k,k'} e^{\beta^2/4} + \left(1 - \delta_{k,k'}\right) e^{\beta^2/4} e^{-t^2/2}., \tag{A.7}$$

where $\delta_{k,k'}$ is the Kronecker delta, reminding us that the main contribution comes from the terms with $E_k = E_{k'}$ which generically means $k = k'$. It is clear that a similar calculation holds for the other parts of $\langle C(t) \rangle$. This produces the temperature scaling found in the main text for random matrices, of the form $\langle C(t) \rangle \sim e^{1/4T^2}$. But the time dependence is more complicated. In order to see this, we look at the structure of the polynomial factors in I_1 in some more detail. We see immediately that $\langle C(t) \rangle$ will also have dependence on t^{2n}, β^n. Start from

$$\int E_i^{\alpha_i} e^{-iE_i t} e^{-E_i^2} dE_i = e^{-t^2/4} \int (u - it/2)^{\alpha_i} e^{-u^2} du, \tag{A.8}$$

where $E_i = u - it/2$. Let us look at two cases: α_i even and α_i odd. For any α_i the polynomial will have the form:

$$(u - it/2)^{\alpha_i} = \sum_{j=0}^{\alpha_i} \gamma_j u^j (it/2)^{\alpha_i - j}. \tag{A.9}$$

Assume first that α_i is even. This means that j and $\alpha_i - j$ are of same parity. For even j the Gaussian integral evaluates to some constant, but we will also have the prefactor of $(it/2)^{\alpha_i - j}$, for all even $j \leq \alpha_i$. The odd powers (j odd) will disappear because of the symmetric domain of integration. For α_i odd, j and $\alpha_i - j$ will be of different parity so again, only even j give a nonzero integral. In conclusion, the integral (A.6) with polynomial prefactors included will have the form:

$$\int E_i^{\alpha_i} e^{-iE_i t} e^{-E_i^2} dE_i = e^{-t^2/4} Q(t^{2n}), \tag{A.10}$$

where $Q(t^{2n})$ is a real polynomial depending on even powers of t, and $2n \leq \alpha_i$. Alternatively, for α_i odd, we get:

$$\int E_i^{\alpha_i} e^{-iE_i t} e^{-E_i^2} dE_i = \imath e^{-t^2/4} R(t^{2n+1}), \tag{A.11}$$

where $R(t^{2n+1})$ is a real polynomial depending on odd powers of t, and $2n + 1 \leq \alpha_i$. Analogous logic holds for the β dependence. Now we look back at I_1:

$$I_1 = \text{const.} \int E_n^{\alpha_n} dE_n \int E_k^{\alpha_k} dE_k \int E_{k'}^{\alpha_{k'}} dE_{k'} e^{-\beta E_n} \times e^{-E_n^2 - E_k^2 - E_{k'}^2} \chi_1 e^{i(E_{k'} - E_k)t}. \tag{A.12}$$

When we write out the products of energies, we have the following types of monomials in the resulting polynomial:

1. QQU

2. QRU

3. QQV

4. QRV,

with the prefactor $\delta_{k,k'} e^{-t^2/2} e^{\beta^2/4}$. Here, Q, R are polynomials of t and are U/V are polynomials of even/odd powers of β respectively. Note however that QR and RQ give the same structure after integration.

The other integral appearing when writing out the master formula for OTOC is

$$K_n = \int E_n^{\alpha_n} e^{-\beta E_n} e^{-iE_n t} e^{-E_n^2} dE_n. \tag{A.13}$$

According to the same logic as for I_1, it is not hard to get the equivalent form of K_n (leaving out the exponentially decaying terms):

$$K_n = e^{\beta^2/4} e^{\imath \beta t/2} \int \sum_j \gamma_j u^j (\beta/2 + it/2)^{\alpha_n - j} e^{-u^2} du. \tag{A.14}$$

Now we will use the fact that OTOC is a real function, as we can see also from the definition (2.2). Therefore, all imaginary parts must vanish. From this fact we reach a few important conclusions:

1. In the structure of I_1, the combination QR is impossible, thus we will only have polynomials of t with an even exponent, and no restriction for polynomials of β as it is a real integral, and no term has to vanish.

2. In the structure of K_n, when we have the factor $\cos(\beta t/2)$, only even powers of t and arbitrary powers of β can survive.

3. In the structure of K_n when we have the factor $\sin(\beta t/2)$, only odd powers of t and arbitrary powers of β can survive.

The conclusion of the above analysis gives us a rough idea of what the $\langle C(t) \rangle$ looks like:

$$\langle C(t) \rangle = e^{\frac{\beta^2}{4}} W_0(\sigma\beta) + e^{\frac{\beta^2}{4}} \left(\cos\left(\frac{\beta t}{2}\right) Q\left(t^{2n}\right) W_1(\sigma\beta) + \sin\left(\frac{\beta t}{2}\right) R\left(t^{2n+1}\right) W_2\left(\beta^n\right) \right),$$
(A.15)

where W_0, W_1, W_2 are arbitrary polynomials of β. This is the form found also in the main text, with the exception that in the main text we have rescaled the combination βt as $\beta t/\sigma^2$ in order to have a dimensionless expression.

A.1 The large matrix limit

In the limit $N \longrightarrow \infty$ we can say more on the structure of OTOC. We can first schematically rewrite (A.15) together with any exponentially suppressed corrections as

$$\langle C(t) \rangle = e^{\frac{\beta^2}{4}} Q\left(t^{2n}\right) W(\sigma\beta) \left(L_1 + L_2 e^{-t^2/2} \right).$$
(A.16)

Here we have first absorbed all time and β dependence of (A.15) into the functions Q and W respectively, and then we have included the exponentially suppressed correction coming from the $k \neq k'$ terms in the integrals I_1 and K_n. By L_1, L_2 we denote the constant (time- and temperature-independent) factors. In general one can write L_1 as

$$L_1 = \sum_{j=1}^{N} \sum_{i=0}^{j} c_i \binom{j}{i}$$
(A.17)

We can easily estimate the second sum. Namely,

$$\left(\sum_{i=0}^{j} c_i \binom{j}{i} \right)^2 \leq \left(\sum_{i=0}^{j} c_i^2 \right) \left(\sum_{i=0}^{j} \binom{j}{i}^2 \right),$$
(A.18)

by the Cauchy-Schwarz-Bunyakovski inequality. Next, the well known formula $\sum_{i=0}^{j} \binom{j}{i}^2 = \binom{2j}{j}$ yields

$$\sum_{i=0}^{j} c_i \binom{j}{i} \leq \text{const.} \times \sqrt{\binom{2j}{j}}.$$
(A.19)

To get rid of the binomial coefficient we will use the Stirling's formula and get

$$\sqrt{\binom{2j}{j}} = \sqrt{\frac{(2j)!}{j! j!}} \approx \sqrt{\frac{\sqrt{4\pi j}\frac{(2j)^{2j}}{e^{2j}}}{2\pi j \frac{(j^j)^2}{(e^j)^2}}} \approx \text{const.} \times \frac{2^j}{j^{1/4}}.$$
(A.20)

Finally we reach the result:

$$L_1 \approx \text{const.} \times \sum_{j=1}^{N} \frac{2^j}{j^{1/4}} \approx \text{const.} \times \frac{2^{N+1}}{N^{1/4}},$$
(A.21)

for $N \longrightarrow \infty$. Exactly the same logic goes for L_2.

In the large matrix limit it is possible to show explicitly what we know has to happen: OTOC reaches a plateau. Looking at (A.16), the condition to reach the plateau for times longer than some scale t_0 is

$$e^{\frac{-t^2}{2}} Q(t^{2n}) \left(L_1 + L_2 e^{-t^2/2} \right) = \text{const.} \quad t > t_0. \tag{A.22}$$

It is more convenient to look at the forms given in (A.15). First let us look at the condition $Q(t^{2n}) = \text{const.} \times e^{t^2/2}$. The exponential term can be represented as a series; equating it with $Q(t^{2n})$ we get

$$\sum_j \alpha_j t^{2j} = \text{const.} \times \sum_j \frac{t^{2j}}{2^j j!}, \tag{A.23}$$

thus, we need $\alpha_j \sim \frac{1}{2^j j!}$, which we know is the case from (A.9). For the second term the situation is similar:

$$\sum_j \beta_j t^{2j} = \text{const.} \times \sum_j \frac{t^{2j}}{j!}, \tag{A.24}$$

so we need to have $\beta_j \sim \frac{1}{j!}$; this is true by $\cos(\beta t/2) = Q(t^{2n})W(\beta^{2n})$ and $\sin(\beta t/2) = Q(t^{2n+1})W(\beta^{2n+1})$, since the terms in the Taylor expansions of the left-hand sides behave as $\sim \frac{1}{j!}$.

We can also look at the opposite limit in which $t \longrightarrow 0$. Let us rearrange (A.16):

$$\langle C(t) \rangle = L_1' Q(t^{2n}) e^{-t^2/2} + L_2' Q(t^{2n}) e^{-t^2}. \tag{A.25}$$

Now, simply using the definition of Q and expanding into a series we get:

$$\langle C(t) \rangle = L_1' \left(1 - \frac{t^2}{2} + o\left(t^4\right) \right) \left(q_o + q_1 t^2 \right) + L_2' \left(1 - t^2 + o\left(t^4\right) \right) \left(q_o + q_1 t^2 \right). \tag{A.26}$$

After some algebra we get:

$$\langle C(t) \rangle = Q_0 + Q_1 t^2 + Q_2 t^4 + o\left(t^4\right) = P(t). \tag{A.27}$$

We see now that OTOC behaves in a very simple way for early times; this expansion is also consistent with the result (3.16) of [13].

References

[1] J. Maldacena, S.H. Shenker and D. Stanford, *A bound on chaos*, *JHEP* **08** (2016) 106 [arXiv:1503.01409] [INSPIRE].

[2] S.H. Shenker and D. Stanford, *Stringy effects in scrambling*, *JHEP* **05** (2015) 132 [arXiv:1412.6087] [INSPIRE].

[3] S. Kundu, *Extremal chaos*, *JHEP* **01** (2022) 163 [arXiv:2109.08693] [INSPIRE].

[4] Y. Sekino and L. Susskind, *Fast Scramblers*, *JHEP* **10** (2008) 065 [arXiv:0808.2096] [inSPIRE].

[5] N. Lashkari, D. Stanford, M. Hastings, T. Osborne and P. Hayden, *Towards the Fast Scrambling Conjecture*, *JHEP* **04** (2013) 022 [arXiv:1111.6580] [inSPIRE].

[6] E.B. Rozenbaum, L.A. Bunimovich and V. Galitski, *Early-Time Exponential Instabilities in Nonchaotic Quantum Systems*, *Phys. Rev. Lett.* **125** (2020) 014101 [arXiv:1902.05466] [inSPIRE].

[7] T. Xu, T. Scaffidi and X. Cao, *Does scrambling equal chaos?*, *Phys. Rev. Lett.* **124** (2020) 140602 [arXiv:1912.11063] [inSPIRE].

[8] K. Hashimoto, K. Murata and R. Yoshii, *Out-of-time-order correlators in quantum mechanics*, *JHEP* **10** (2017) 138 [arXiv:1703.09435] [inSPIRE].

[9] K. Hashimoto, K.-B. Huh, K.-Y. Kim and R. Watanabe, *Exponential growth of out-of-time-order correlator without chaos: inverted harmonic oscillator*, *JHEP* **11** (2020) 068 [arXiv:2007.04746] [inSPIRE].

[10] F. Haake, S. Gnutzman and M. Kuś, *Quantum signatures of chaos*, Springer-Verlag, Berlin, Germany (2019).

[11] M.L. Mehta, *Random matrices*, Academic, New York, U.S.A. (2004).

[12] J.S. Cotler et al., *Black Holes and Random Matrices*, *JHEP* **05** (2017) 118 [*Erratum ibid.* **09** (2018) 002] [arXiv:1611.04650] [inSPIRE].

[13] J. Cotler, N. Hunter-Jones, J. Liu and B. Yoshida, *Chaos, Complexity, and Random Matrices*, *JHEP* **11** (2017) 048 [arXiv:1706.05400] [inSPIRE].

[14] J. Cotler and N. Hunter-Jones, *Spectral decoupling in many-body quantum chaos*, *JHEP* **12** (2020) 205 [arXiv:1911.02026] [inSPIRE].

[15] W. Kirkby, D.H.J. O'Dell and J. Mumford, *False signals of chaos from quantum probes*, arXiv:2108.09391 [inSPIRE].

[16] T. Akutagawa, K. Hashimoto, T. Sasaki and R. Watanabe, *Out-of-time-order correlator in coupled harmonic oscillators*, *JHEP* **08** (2020) 013 [arXiv:2004.04381] [inSPIRE].

[17] A. Bhattacharyya, W. Chemissany, S.S. Haque, J. Murugan and B. Yan, *The Multi-faceted Inverted Harmonic Oscillator: Chaos and Complexity*, *SciPost Phys. Core* **4** (2021) 002 [arXiv:2007.01232] [inSPIRE].

[18] W. Kłobus, P. Kurzyński, M. Kuś, W. Laskowski, R. Przybycień and K. Życzkowski, *Transition from order to chaos in reduced quantum dynamics*, *Phys. Rev. E* **105** (2022) 034201 [arXiv:2111.13477] [inSPIRE].

[19] B. Bertini, P. Kos and T. Prosen, *Exact Spectral Form Factor in a Minimal Model of Many-Body Quantum Chaos*, *Phys. Rev. Lett.* **121** (2018) 264101 [arXiv:1805.00931] [inSPIRE].

[20] S. Pappalardi, A. Russomanno, B. Žunkovič, F. Iemini, A. Silva and R. Fazio, *Scrambling and entanglement spreading in long-range spin chains*, *Phys. Rev. B* **98** (2018) 134303 [arXiv:1806.00022] [inSPIRE].

[21] K. Okuyama, *Spectral form factor and semi-circle law in the time direction*, *JHEP* **02** (2019) 161 [arXiv:1811.09988] [inSPIRE].

[22] Q. Hummel, B. Geiger, J.D. Urbina and K. Richter, *Reversible quantum information spreading in many-body systems near criticality*, *Phys. Rev. Lett.* **123** (2019) 160401 [`arXiv:1812.09237`] [InSPIRE].

[23] H. Goto and T. Kanao, *Chaos in coupled Kerr-nonlinear parametric oscillators*, *Phys. Rev. Res.* **3** (2021) 043196 [`arXiv:2110.04019`] [InSPIRE].

[24] N.D. Varikuti and V. Madhok, *Out-of-time ordered correlators in kicked coupled tops and the role of conserved quantities in information scrambling*, `arXiv:2201.05789` [InSPIRE].

[25] A.V. Kirkova, D. Porras and P.A. Ivanov, *Out-of-time-order correlator in the quantum Rabi model*, *Phys. Rev. A* **105** (2022) 032444 [`arXiv:2201.06340`] [InSPIRE].

[26] J.R.G. Alonso, N. Shammah, S. Ahmed, F. Nori and J. Dressel, *Diagnosing quantum chaos with out-of-time-ordered-correlator quasiprobability in the kicked-top model*, `arXiv:2201.08175` [InSPIRE].

[27] K. Hashimoto, K. Murata, N. Tanahashi and R. Watanabe, *A bound on energy dependence of chaos*, `arXiv:2112.11163` [InSPIRE].

[28] J. Aguirre, J.C. Vallejo and M.A.F. Sanjuán, *Wada basins and chaotic invariant sets in the Hénon-Heiles system*, *Phys. Rev. E* **64** (2001) 066208.

[29] H.E. Kandrup, C. Siopis, G. Contopoulos and R. Dvorak, *Diffusion and scaling in escapes from two-degree-of-freedom Hamiltonian systems*, *Chaos* **9** (1999) 381 [`astro-ph/9904046`] [InSPIRE].

[30] D.E. Berenstein, J.M. Maldacena and H.S. Nastase, *Strings in flat space and pp waves from $N = 4$ superYang-Mills*, *JHEP* **04** (2002) 013 [`hep-th/0202021`] [InSPIRE].

[31] T. Banks, W. Fischler, S.H. Shenker and L. Susskind, *M theory as a matrix model: A Conjecture*, *Phys. Rev. D* **55** (1997) 5112 [`hep-th/9610043`] [InSPIRE].

[32] K.L. Zarembo and Y.M. Makeenko, *An introduction to matrix superstring models*, *Phys. Usp.* **41** (1998) 1 [InSPIRE].

[33] Y. Asano, D. Kawai and K. Yoshida, *Chaos in the BMN matrix model*, *JHEP* **06** (2015) 191 [`arXiv:1503.04594`] [InSPIRE].

[34] G. Gur-Ari, M. Hanada and S.H. Shenker, *Chaos in Classical D0-Brane Mechanics*, *JHEP* **02** (2016) 091 [`arXiv:1512.00019`] [InSPIRE].

[35] X. Han and S.A. Hartnoll, *Deep Quantum Geometry of Matrices*, *Phys. Rev. X* **10** (2020) 011069 [`arXiv:1906.08781`] [InSPIRE].

[36] P.V. Buividovich, M. Hanada and A. Schäfer, *Quantum chaos, thermalization, and entanglement generation in real-time simulations of the Banks-Fischler-Shenker-Susskind matrix model*, *Phys. Rev. D* **99** (2019) 046011 [`arXiv:1810.03378`] [InSPIRE].

Replicas, averaging and factorization in the IIB matrix model

Mihailo Čubrović

Center for the Study of Complex Systems,
Institute of Physics Belgrade, University of Belgrade,
Pregrevica 118, 11080 Belgrade, Serbia

E-mail: cubrovic@ipb.ac.rs

ABSTRACT: We study the partition functions of multiple replicas (copies) of D-brane configurations in the type IIB (IKKT) matrix model. We consider the quenched regime, where small fluctuations of the matrices are superimposed onto the slow (quenched) dynamics of the background, so the partition function is an ensemble average over the background. Interacting D-branes always factorize in a simple way. On the other hand, the non-interacting BPS configurations may or may not factorize depending on the number of replicas, and their factorization mechanism is more involved as the corresponding saddle-point solutions (half-wormholes) break the replica symmetry. We argue that the simple factorization mechanism of interacting branes is actually more interesting as it carries the specific signatures of quantum gravity, which are absent from disordered field theories like the SYK model.

Contents

1 Introduction

The factorization problem in gravity and holography has come into the spotlight with
the discovery of replica wormholes, entanglement islands and the path they open toward
a possible solution of the black hole information paradox [1–3]. It also resonates with
the general growth of knowledge in quantum information and its relation to black holes,
scrambling [4–6] and quantum chaos [7, 8]. Stated simply, the puzzle lies in the fact that
the spacetime (Euclidean)[1] wormholes constructed in [1, 2], which are crucial to save the
Page curve and the unitarity of black hole evaporation, imply that the partition function

---

[1]Usually, the literature speaks of spacetime=Euclidean wormholes versus spatial=Lorentzian wormholes.
But to be precise, Euclidean vs. Lorentzian signature is just a matter of choice, the true difference is between
spatial wormholes which act as bridges of Kip Thorne style, and spacetime wormholes considered in this
paper and in most works on factorization and averaging, which affect also the time direction. Therefore,
even though the latter are usually considered in Euclidean time (also in this paper), one could also study
them in Lorentzian signature. But one should still bear in mind that Euclidean/Lorentzian wormholes is the
term often used in the literature, meaning really spacetime/ spatial wormholes.

of two copies (two replicas) of a gravitating system does not equal the square of a single-replica partition function: $Z_{1\text{grav}}^2 \neq Z_{2\text{grav}}$. But at least in asymptoticlly anti-de-Sitter (AdS) geometries this contradicts the field theory intuition that the partition function of two identical decoupled systems should always factorize: $Z_{1\text{CFT}}^2 = Z_{2\text{CFT}}$. The way out proposed in several works [9–13] is that holography performs some kind of averaging or coarse-graning so that the dual CFT partition function is really an expectation value over some distribution:

$$\langle Z_{1\text{CFT}} \rangle^2 \neq \langle Z_{2\text{CFT}} \rangle. \tag{1.1}$$

In this case, the nonfactorization ceases being a puzzle — of course there is no reason that expectation values factorize. The averaging could in principle be carried over disorder ("explicit") or it could really be some kind of self-averaging in a chaotic system, i.e. some kind of coarse-graning.

A prototypical framework for explicit averaging is the Sachdev-Ye-Kitaev (SYK) model, featuring a system of Majorana fermions with all-to-all coupling, the coupling strengths being a quenched random variable. In a certain regime, this system is dual to gravity in AdS_2 [14], making it perfect for studying the factorization problem. A simplified version — SYK model in a single time point — was analyzed in [12, 15] and the outcome is very pleasing: although the wormhole configurations (which couple different replicas) are non-factorizing, there are additional solutions, dubbed half-wormholes, which restore the factorization; half-wormholes depend strongly on the choice of microscopic couplings. A similar picture was found to hold also in other systems like tensor models, random matrices and the two-site SYK model [16–19]. In [20–22] the traversable spatial ("Lorentzian") wormholes have also been related to field theories averaged over the states or over the operators, starting, as could be expected, from thermofield-dynamics (TFD)-like states. Some recent generalizations are found in [23–26] and in particular in [27], where the authors find that nonlocally interacting bulk branes in 2D gravity provide a mechanism which restores factorization in absence of any explicit disorder.

Our goal is to understand these workings of (half)wormholes in systems with an ensemble average but directly in quantum gravity, not in a field theory like SYK or a matrix model. The puzzle is now the following: is the averaging an operation which is somehow "automatically" performed specifically by holography, or we can perform it in a gravitating system directly, without any reference to the dual field theory (or for gravitating systems which have no dual CFT at all)? We will take a quantum gravity model (specifically the IIB string theory matrix model) and construct wormholes and half-wormholes by averaging over suitably chosen "quenched" degrees of freedom, thus repeating the logic of [9, 12, 15–17, 28, 29] but directly in gravity. Therefore, we mainly aim to understand factorization as such, not specifically in the context of AdS/CFT. But we will also discuss how one can make contact with AdS/CFT, by introducing a non-flat background metric; this is merely a first step and a full-fledged application of our findings to holography will be a subject of future work.

The arena for our work on wormholes and factorization is the model by Ishibashi, Kawai, Kitazawa and Tsuchiya (IKKT), proposed and developed in [30–33]. Like other

matrix models of string and M theory (see [34, 35] for a review), it is potentially capable of providing a nonperturbative description of string theory, including D-branes and other deep quantum effects, which are beyond the scope of old-style perturbative string theory. On the other hand, as a matrix model, the IKKT system allows the explicit computation of observables and partition functions in a controlled way, and it has a lot in common with matrix models in field theory. In fact, in a certain limit the system we study can also be thought of as ten-dimensional Yang-Mills field theory with a quenched background field configuration [36, 37]. This makes our results relevant in principle also in the field theory context, and highlights that the formal workings of (non)factorization of partition functions are in a sense quite technical and independent of many physical details of the system.

Another important point is that the IKKT model is well-defined both in Lorentzian and Euclidean signature. While the latter is more convenient when studying the landscape of saddle-point solutions, as we can define a partition function in terms of the Euclidean action S_E in the usual way as $Z = \int \exp(-S_E)$, the former is more frequently studied in the literature, as the amplitude $\mathcal{A} = \int \exp(-\imath S_L)$ of the Lorentzian action S_L is always real; this is not the case for the partition function when the fermionic excitations are turned on. For example, the Lorentzian dynamics was argued to explain the effective 3+1-dimensionality of spacetime and other cosmologically relevant issues in [38–42]. We have opted for the Euclidean model so we can readily read off the free energy and determine which of the wormhole and half-wormhole solutions are thermodynamically preferred, but the reader should bear in mind that this is just a matter of convenience (see also the first footnote).

With some hindsight, we can say that a picture rather similar to the wormhole/half-wormhole story in SYK and similar models will emerge here. We have not found a single case where the factorization of $\langle Z^n \rangle$ is not restored already at leading order in perturbation theory for $n \geq 4$, although there are cases where the factorization is violated for $n = 2$. In some cases the factorization is trivial (when the averaged value $\langle Z^n \rangle$ is at leading order just the product of n copies of the leading-order estimate for $\langle Z \rangle$), and sometimes it is nontrivial, in the sense that it cannot be written in terms of $\langle Z \rangle$ contributions only. This distinction is interesting and depends on the geometry of the D-brane configuration. All of this is happening in (discretized) string theory, without any reference to holographic duality (although of course, one expects that the nonperturbative IKKT model implicitly knows about the duality).

As a final word of caution, one should bear in mind that more general wormhole configurations exist which are not necessarily all related to averaging, see, e.g. [44–47] and the recent insights of [48]. There is actually a very general geometric perspective on wormhole solutions, which works also in quantum mechanics (not only field theory), resting on the symplectic structure of the Hamiltonian dynamics [49]; this likewise suggests Euclidean wormholes to be more general than the averaging-induced configurations in this paper.

1.1 The sharp question

After all this talk, we are ready to formulate in a sharp way the main question of the paper — if the fluctuations of the D-brane solutions to the IKKT model factorize when averaged

over the background fields. Factorization means that n replicas of the system behave in the same way as n independent copies. In precise language, this says that the averaged partition functions satisfy $\langle Z^n \rangle \sim \langle Z \rangle^n$. A related concept is self-averaging. Self-averaging means that the expectation value of $\langle Z^n \rangle$ is "close" to a "typical" Z^n value for some generic realization of the quenched variables (brane matrices). In precise language, denoting the quenched variables by λ, self-averaging is formulated as

$$\langle Z^n(\lambda) \rangle \sim Z^n \left(\sqrt{\langle \lambda^2 \rangle} \right). \tag{1.2}$$

The above means simply that the average over all λ values produces the same result at leading order as the value for an average λ; the reason we take the square root of $\langle \lambda^2 \rangle$ and not simply $\langle \lambda \rangle$ is that the latter is often zero (λ will often have a symmetric distribution).

The outline of the paper is the following. In section 2 we sum up the essential physics of D-branes in the type IIB matrix model and define the quenched approximation, setting the stage for the main work. Sections 3 and 4 contain the core of the paper: we find saddle-point solutions of Z^n, $\langle Z^n \rangle$ and $\langle Z \rangle^n$ and discuss their factorization properties, first for a simple, single-D-string configuration and then for interacting D-strings. Section 5 sums up the conclusions. In appendix A we show that a technical simplification made in the paper (putting the background fermions to zero) does not lead to any qualitative changes in our results. In appendix B we demonstrate another important technical point (that the conclusions do not depend qualitatively on whether the eigenvalue distribution is Gaussian or uniform). Finally, in appendix C we discuss how the reasoning of this paper could be applied specifically to the factorization puzzle of holography, in asymptotically AdS backgrounds.

2 Setup: D-brane configurations in the IKKT model

Let us start from the action of the type IIB matrix model, as found by Ishibashi, Kawai, Kitazawa and Tsuchiya [30, 31] by discretizing the Schild action for IIB superstrings:

$$S = -\text{Tr} \left(\frac{1}{4} [X_\mu, X_\nu]^2 + \frac{1}{2} \bar{\Psi}_\alpha \Gamma^\mu [X_\mu, \Psi_\alpha] \right). \tag{2.1}$$

Here, $\mu = 1, \ldots 10$ are the spacetime (target space) dimensions and $\alpha = 1, \ldots 16$ counts the Majorana-Weyl fermions. The gamma matrices are then 16×16 matrices. Both the scalars and the spinors are $N \times N$ Hermitian matrices. The size N is also dynamic, corresponding to the auxiliary field g in the Schild action (see e.g. [34]). However, we will always work with fixed and large N, assuming as usual that the partition function is strongly dominated by a single saddle point at some N. For this reason there is no sum over N in the partition functions throughout the paper.

The equations of motion follow from (2.1):

$$[X^\mu, [X^\mu, X^\nu]] = 0, \quad [X^\mu, (\Gamma^\mu \Psi)_\alpha] = 0. \tag{2.2}$$

We work in the Euclidean signature, hence the spacetime metric is $\eta_{\mu\nu} = \text{diag}(1, \ldots 1)$ and we do not need to differentiate between up and down indices. The partition function is now

given in the usual way

$$Z = \sum_N \int D[X_\mu] \int D[\Psi_\alpha] \int D[\bar\Psi_\alpha] \exp(-S).$$ (2.3)

When only the bosonic degrees of freedom are excited, the above partition function is positive definite. If, however, the fermionic matrices Ψ are also nonzero, then their contribution to the path integral (the Pfaffian) is complex in Euclidean signature.[2] Therefore, we will need to be careful in interpreting the results when we turn on also the Ψ fields.

Now let us remember how D_p branes show up in the matrix model. What follows is a resume of the crucial aspects of brane solutions from [30, 34, 37]. Type IIB string theory admits D_p branes with p odd, starting from $p = -1$, i.e. D-instantons. Taking D-instantons as elementary degrees of freedom, we can write any configuration of size N as a superposition of N D-instantons at coordinates λ_j, $j = 1, \ldots N$. For a general D_p brane, the BPS condition and equations of motion from the action (2.1) lead to solutions $X_\mu = A_\mu$ for the bosonic part, with A_μ of the form:[3]

$$A_\mu = \left(\frac{L_1}{2\pi}q_1, \frac{L_2}{2\pi}k_1, \ldots \frac{L_{2i-1}}{2\pi}q_{(p+1)/2}, \frac{L_{2i}}{2\pi}k_{(p+1)/2}, 0 \ldots, 0\right), \quad [q_i, k_i] \equiv \omega_i I = \imath \frac{L_{2i-1}L_{2i}}{2\pi N^{2/(p+1)}} I.$$ (2.4)

Here q_i and k_i are random Hermitian matrices with the eigenvalues $\lambda_j^{(q_i)}$ and $\lambda_j^{(k_i)}$ (of course, $p + 1 \leq 10$), and L_μ ($\mu = 1 \ldots p+1$) are the compactification radii of the coordinates X_μ. The commutators ω_i have the meaning of $\hbar$, and $\omega_i \to 0$ corresponds to the classical limit — in this case q_i and k_i are just any commuting Hermitian matrices, describing the moduli of the theory. Multi-brane configurations are described by block-diagonal matrices q_i, k_i with M_p blocks of size $N \times N$ for M_p branes D_p. We will specialize to configurations of two D-strings as this suffices to discuss the factorization. The solution to the equations of motion (2.2) which corresponds to two strings at distance ℓ, with angle 2θ between the strings, reads [30]:

$$A_0 = \begin{pmatrix} q & 0 \\ 0 & q \end{pmatrix}, \quad A_1 = \begin{pmatrix} p\cos\theta & 0 \\ 0 & p\cos\theta \end{pmatrix}, \quad A_2 = \begin{pmatrix} \frac{\ell}{2} & 0 \\ 0 & -\frac{\ell}{2} \end{pmatrix}, \quad A_3 = \begin{pmatrix} -p\sin\theta & 0 \\ 0 & p\sin\theta \end{pmatrix}$$

$$A_4 = \ldots = A_{10} = 0, \quad [p, q] = \imath \frac{L^2}{2\pi N} I.$$ (2.5)

For $\theta = 0$ ($\theta = \pi$) we get two parallel (antiparallel) strings, and for $\ell = 0$ the strings cross. Parallel D-branes (including D-strings), with $\theta = 0$, are a special case: they are BPS states with zero on-shell action. This will be important as the properties and mechanisms of factorization differ between the BPS and the interacting case.

---

[2]This is not a problem by itself. Indeed, there lies the mechanism of the SO(10) symmetry breaking studied in [50, 51] in the context of the origin of the four-dimensionality of the spacetime.

[3]From now on, I always denotes the $N \times N$ unit matrix. If we need the unit matrix of a different size N', we will write it explicitly as $I_{N' \times N'}$.

2.1 The background-field regime and the quenched regime of the IKKT model

In the semiclassical regime one can study the fluctuations a_μ around the classical geometry described by matrices A_μ from (2.4) or (2.5):

$$X_\mu = A_\mu + a_\mu, \quad \Psi_\alpha = \psi_\alpha, \tag{2.6}$$

where we have taken into account that the background configuration of the fermions is $\Psi_\alpha = 0$. This spoils the supersymmetry and non-renormalization results, but does not change the essence of our conclusions; indeed, in the large N limit this is physically justified as the fermions are large-N suppressed anyway.[4] In appendix A we redo the main calculation of the paper in the presence of nonzero background Ψ_α and show that the outcome is essentially the same, though different in quantitative details of the solution. In the classical (commuting) regime, the matrices A_μ can be diagonalized simultaneously, their eigenvalues having the role of locations of D-instantons. In applications to D-brane dynamics and other nonperturbative string theory phenomena, as well as gravity and the dynamics of spacetime dimensions, the natural viewpoint is the background field approach, i.e. to integrate out the quantum fluctuations a_μ, ψ_α and study the effective semiclassical action for the diagonal matrices A_μ.

The opposite limit is the quenched IKKT model of [37], where the moduli A_μ are considered as fixed backgrounds and not integrated over. Now a_μ (and ψ_α, if turned on) are "dynamical" variables, and A_μ are quenched, so the partition function Z is tied to a specific realization of A_μ. This approach is natural if we want to study the quantum dynamics of perturbative string excitations in a given geometry. It can also be interpreted in the context of the Eguchi-Kawai finding [36] that the Lagrangian of the Yang-Mills gauge theory in the large N limit loses the derivative terms and reduces just to (2.1). In that context the dynamics of a_μ and ψ_α is basically the dynamics of a Yang-Mills system in the presence of quenched disorder.[5] In other words, *the fields A_μ play the same role as disorder in the SYK and similar models, describing on one hand a prototypical strongly interacting large N field theory and on the other hand string theory in deep nonperturbative regime.* This is our motivation to study the quenched IKKT model. Furthermore, AdS/CFT suggests that the background-field limit and the quenched limit show different aspects of the same physics — the Eguchi-Kawai system must have a dual description in terms of D-brane stacks. Therefore, the quenched IKKT model is a robust system of equations with several important physical aspects and should provide us an excellent testing ground for the factorization puzzle. From now on, we will denote the non-averaged quantities by ordinary letters, e.g. Z for the partition function, and the quantities averaged over the realizations

---

[4]Another way to say this is that the fermionic background can be put to zero in the semiclassical limit. Our general formalism is not limited to the semiclassical regime, but the physical picture does become simpler in that case, as we can interpret the matrix entries as spacetime coordinates of the constituent D-instantons making the D-brane. Such approximation is also exploited for similar reasons in some of the original IKKT papers [30, 32].

[5]The equivalence is not complete, as the quenched IKKT model contains zero modes, from the terms which couple a^μ and ψ_α; such terms do not exist in the large-N Yang-Mills theory. However, at leading — quadratic — order such terms vanish also in the quenched IKKT model (see eqs. (2.8)–(2.9)).

of the quenched variables A_μ will be denoted as expectation values, inside angular brackets, e.g. $\langle Z \rangle$.

Let us now write the IKKT action (2.1) in terms of the background field A_μ and the fluctuations a_μ, ψ_α, as in (2.6). The quadratic (S_2) and quartic (S_4) contributions in a_μ and ψ_α read:

$$S = S_2 + S_4 \tag{2.7}$$

$$S_2 = \text{Tr} \left[-\frac{1}{4} a_\mu \left(P^2 \delta_{\mu\nu} + 2F_{\mu\nu} \right) a_\nu + \bar{\psi}_\alpha \slashed{P} \psi_\alpha - \bar{c} P^2 c \right], \tag{2.8}$$

$$S_4 = \text{Tr} \left[\bar{\psi}_\alpha \slashed{a} \psi_\alpha - 2 \left(P_\mu a^\mu \right) \left(a^\nu a_\nu \right) - \frac{1}{2} \left[a^\mu, a^\nu \right] \left[a_\mu, a_\nu \right] \right], \tag{2.9}$$

where we have introduced the superoperators P_μ and $F_{\mu\nu}$, acting on matrices as

$$P_\mu \equiv [A_\mu, \cdot], \quad F_{\mu\nu} = [[A_\mu, A_\nu], \cdot], \quad P^2 = P_\mu P^\mu. \tag{2.10}$$

We will also sometimes use the matrix $f_{\mu\nu} \equiv [A_\mu, A_\nu]$. Finally, c in (2.8) is the ghost field arising from the Faddeev-Popov ghost action. BPS states have $f_{\mu\nu} = \text{const.} \times I$ with I being the unit matrix or, equivalently, $F_{\mu\nu} = 0$; in that case the on-shell action vanishes, one-loop quantum corrections are absent and the eigenvalues of A_μ remain uniformly distributed.

As we explained, for our purposes it is enough to focus on the bosonic sector and put the background fermionic matrices to zero: $\Psi_\alpha = 0$. This is always a consistent (if not fully generic) solution of the equations of motion, and it simplifies the calculations significantly. Bose-only backgrounds always give real action but they are obviously not protected by supersymmetry so even if $F_{\mu\nu} = 0$ there will be a logarithmic attraction of the eigenvalues as there is no fermionic sector to cancel the determinant from the bosonic path integral; however it remains (trivially) true that the solutions with $F_{\mu\nu} = 0$ describe a non-interacting configuration (in the Eguchi-Kawai picture, the field strength is zero). In general, even in zero fermionic background there are still nonzero fermionic fluctuations ψ_α. As a special case, we can turn off these too: $\psi_\alpha = 0$. In that case only the first term in (2.8) is nonzero, and in (2.9) the second and the third term remain nonzero. We will consider this special case as a warmup but will always include also the fermionic fluctuations ψ_α in the end.

3 Replicas and factorization for a single D-string

Now that we have set up the formal framework, we can explore the main question of the paper: how do the partition functions of D-branes in the quenched IKKT model factorize? From now on, we will specialize to D-strings as the whole story remains the same for higher-dimensional branes. In this section we give a detailed calculation for a single bosonic D-string, so the reader can get acquainted with the basic algorithm on the simplest example. Afterwards it will be straightforward to redo the calculation for the more interesting configurations of interacting strings.

3.1 Single copy — direct calculation

As we know [34], the background fields A_μ representing a D-brane are described by random Hermitian matrices p, q which, according to (2.4), satisfy the commutation relation (putting

$L_1 = L_2 \equiv L$):

$$[p, q] = \omega = \frac{L^2}{2\pi N}I. \tag{3.1}$$

This is a BPS state (although we do not see the supersymmetry when we put $\Psi_\alpha = 0$) with $f_{21} = -f_{12} = \omega$ and $F_{\mu\nu} = 0$. The eigenvalues λ_μ^i ($\mu = 1, 2$, $i = 1 \ldots N$) are distributed in the interval $-L \leq \lambda_i \leq L$. Unlike the typical choice in the IKKT model literature, where the compactification radii L_μ define the hard cutoffs of the distribution, we adopt — solely for computational reasons — a soft cutoff with the Gaussian distribution of eigenvalues (Gaussian Unitary Ensemble) for A_μ so the width of the Gaussian equals L_μ. Our choice is unusual but on one hand it is no less physical (indeed, a hard cutoff is more of an idealization than a continuous Gaussian tail) and on the other hand more convenient for calculations. However, we emphasize that nothing changes qualitatively even when we return to hard cutoffs — in appendix B we show this explicitly, redoing the calculations with hard cutoff regularization.

From (2.3) we now have the following form for the partition function in the non-averaged and in the averaged form, respectively:

$$Z = \int D[a_\mu]e^{-S(a_\mu; A_\mu)} \tag{3.2}$$

$$\langle Z \rangle = \int D[A_\mu] \int D[a_\mu]e^{-S(a_\mu; A_\mu)}\mathcal{P}(A_\mu) = \int D[a_\mu] \int d^{2N}\lambda_\mu^i e^{-S(a_\mu; \lambda_\mu^i) - \frac{1}{2L^2}\lambda_\mu^i \lambda^{\mu i}}. \tag{3.3}$$

In the second equality, we have expressed A_μ in terms of its eigenvalues λ_μ^i and likewise the Gaussian measure (regulator) $\mathcal{P}$ is written out explicitly in terms of the width of the distribution L, as $-\lambda_\mu \lambda^\mu / 2L^2$. Now we want to write out the action in (3.3) in terms of matrices $A_0 = p$ and $A_1 = q$. It is easiest to diagonalize the matrices and work in the eigenbases. Then we have $A_\mu = \text{diag}(\lambda_1^\mu, \ldots \lambda_N^\mu)$. The superoperators P_μ are now represented as[6]

$$P_1 = q \otimes I - I \otimes q, \quad (P_1)_{kl}^{ij} = q_{ik}\delta_{jl} - q_{jl}\delta_{ik}$$
$$P_2 = k \otimes I - I \otimes k, \quad (P_2)_{kl}^{ij} = k_{ik}\delta_{jl} - k_{jl}\delta_{ik}. \tag{3.4}$$

However, since the canonical momentum and the conjugate coordinate do not commute, we cannot assume both matrices to be diagonal at the same time, i.e. in the same basis. The above representation (3.4) takes each P_μ in its own eigenbasis. In order to give the reader a clearer intuitive grasp, we can list a few supermatrix elements, say for P_1:

$$(P_1)_{11} = \begin{pmatrix} 0 & p_{12} & \ldots & p_{1N} \\ p_{21} & p_{22} - p_{11} & \ldots & p_{2N} \\ \ldots & \ldots & \ldots & \ldots \\ p_{N1} & p_{N2} & \ldots & p_{NN} - p_{11} \end{pmatrix}$$
$$(P_1)_{12} = \text{diag}(-p_{12}, \ldots - p_{12}), \quad (P_1)_{1N} = \text{diag}(-p_{1N}, \ldots - p_{1N})$$

---

[6]Superoperators act on $N \times N$ matrices, hence they are strictly speaking the Kronecker products of two $N \times N$ matrices. For convenience, we write them simply as $N^2 \times N^2$ matrices.

$$\cdots$$

$$(P_1)_{21} = \mathrm{diag}(-p_{21}, \ldots - p_{21}), \quad (P_1)_{22} = \begin{pmatrix} p_{11} - p_{22} & p_{12} & \cdots & p_{1N} \\ p_{21} & 0 & \cdots & p_{2N} \\ \cdots & \cdots & \cdots & \cdots \\ p_{N1} & p_{N2} & \cdots & p_{NN} - p_{22} \end{pmatrix}$$

$$(P_1)_{N,N-1} = \mathrm{diag}(-p_{N,N-1}, \ldots - p_{N,N-1})$$

$$(P_1)_{NN} = \begin{pmatrix} p_{11} - p_{NN} & p_{12} & \cdots & p_{1N} \\ p_{21} & p_{22} - p_{NN} & \cdots & p_{2N} \\ \cdots & \cdots & \cdots & \cdots \\ p_{N1} & \cdots & p_{N,N-1} - p_{NN} & 0 \end{pmatrix}. \tag{3.5}$$

Averaging over the quenched variables now requires either adopting a single basis and transforming all P_μ but one (say P_1) from the form (3.4) to this fixed basis, or keeping each P_μ in its own eigenbasis — but then we have to divide the integral measure by the volume of the unitary matrices that transform each supermatrix to its eigenbasis. The latter is more convenient, and it gives rise to the eigenvalue attraction term. Plugging in the representation (3.4) into Z from (3.3) and taking into account the basis change we get

$$\langle Z \rangle = \int D[a_\mu] \int d^{2N} \lambda_{\mu i} \Pi_{i<j} (\lambda_{\mu i} - \lambda_{\mu j})^2 \exp \left[-\frac{1}{4} a_{\mu ij}^\dagger \left(\lambda_{\mu i}^2 + \lambda_{\mu j}^2 \right) a_{\mu kl} \delta_{jk} \delta_{il} - \frac{1}{2L^2} \lambda_{\mu i}^2 \right]$$

$$= \int D[a_\mu] e^{-W_1}, \quad W_1 = \frac{1}{2} \sum_\mu \log \det \left(\frac{I}{L_\mu^2} + 2 a_\mu^\dagger a_\mu - 2I \mathrm{Tr} a_\mu^\dagger a_\mu \right). \tag{3.6}$$

We have introduced the effective macroscopic action W_1 akin to the thermodynamic free energy. The first line in (3.6) is obtained by inserting the matrix representations for P into the general expression (3.3) taking into account the basic change (see e.g. [32]), and the final expression for W_1 in the second line comes from performing the Gaussian integral over λ_i^μ and the second-order expansion of the determinant in small $a^\dagger a$ and $1/L^{2N}$. Since the partition function is not a power-law function of a and $a^\dagger$, the series expansion has correlation functions $a^\dagger a \ldots a^\dagger a$ of arbitrarily high order. Their meaning is better grasped in the collective field formalism that we introduce in the next subsection.

3.2 Collective fields and replicas

3.2.1 Warmup: single partition function again

The time is ripe to introduce the collective fields. We follow the formalism of [12, 15, 17] and largely adopt the notation of [12]. The idea is the following: we define a bilinear operator g as being equal to the current $a^\dagger a$. We impose this equality as a constraint through the Dirac delta functional, and finally replace the $a^\dagger a$-dependent terms by the appropriate functionals

of the bilinear:[7]

$$\langle Z \rangle = \int D[a] \int D[g] \int d\lambda \exp\left[-\frac{1}{2}\mathrm{Tr}a^\dagger P^2 a - \frac{2\left(\mathrm{Tr}g - \mathrm{Tr}a^\dagger a\right)}{L^{2N-2}}\right]\delta\left(g - a^\dagger a\right)\mathcal{P}(\lambda)$$

$$= \int D[a] \int D[g] \int D[s] \int d\lambda \exp\left[-\frac{1}{2}\mathrm{Tr}a^\dagger P^2 a - \frac{2\left(\mathrm{Tr}g - \mathrm{Tr}a^\dagger a\right)}{L^{2N-2}} - \imath\mathrm{Tr}\left[s^\dagger\left(g - a^\dagger a\right)\right]\right]\mathcal{P}(\lambda)$$

$$= \int D[a] \int D[g] \int \frac{D[s]}{2^N \pi^{N^2}} \exp\left[-\frac{1}{2}\log\det\left(\frac{I}{L^2} + 2a^\dagger a - 2I\mathrm{Tr}a^\dagger a\right) - \frac{2\left(\mathrm{Tr}g - \mathrm{Tr}a^\dagger a\right)}{L^{2N-2}}\right.$$

$$\left. - \imath\mathrm{Tr}\left[s^\dagger\left(g - a^\dagger a\right)\right]\right] \sim \int D[g] \int \frac{D[s]}{2^N \pi^{N^2}} \exp\left[-\frac{1}{2}\log\det s - \imath\mathrm{Tr}s^\dagger g - \frac{2}{L^{2N-2}}\mathrm{Tr}g\right]. \quad (3.7)$$

In the first line, we have inserted into the effective action the term proportional to $\mathrm{Tr}g - \mathrm{Tr}a^\dagger a$ which, at leading order in $a^\dagger a$, equals zero on-shell, i.e. when the constraint $g = a^\dagger a$ is obeyed. In the second line, we have implemented the Dirac delta in the usual way, through the auxiliary field s, and in the third line we have averaged over the eigenvalues of the quenched coordinates λ. Notice how the inserted "zero term" precisely cancels all $a^\dagger, a$ dependence after averaging, which was of course the reason to introduce it in the first place. Again, this only holds at leading order in the a-fields and $1/L^N$. This is important — all our calculations are perturbative (unlike the simpler SYK quantum mechanics where the collective fields can be introduced in an exact way); for example, the last line in (3.7) holds at the order $O\left(\left(a^\dagger a\right)^4\right) + O(1/L^{4N})$. We will not write explicitly such higher-order remainders. Higher order terms could be taken into account perturbatively, by introducing additional collective fields and eventually closing the series by expressing the $l + 1$-st order terms in terms of the loop integrals over the l-th and lower order terms. We will do this explicitly for the $\langle Z^2 \rangle$ calculation, when it will be necessary to get anything nontrivial. For now, let us stay at the lowest order.

Now we can look for the saddle-point solutions of the effective action W_1 defined by the last line in (3.7) in the same way as in (3.6), through $W_1 \equiv -\log\langle Z \rangle$:

$$\frac{\partial W_1}{\partial g} = \frac{2}{L^{2N-2}}I + \imath s = 0, \qquad \frac{\partial W_1}{\partial s} = \imath g + \frac{1}{2}\left(s^{-1}\right)^T = 0$$

$$s = \frac{2\imath}{L^{2N-2}}I, \qquad\qquad g = \frac{L^{2N-2}}{4}I. \quad (3.8)$$

Here, I is the $N \times N$ unit matrix as usual. The solution (3.8) is unique.

The important conclusion is that the nonzero solution (3.8) consists of scalar matrices which scale as L^{2N-2}, and inserting them into W_1 yields

$$W_1|_{\text{on-shell}} \sim (N^2 - N)\log L + \frac{N}{2}\log 2. \quad (3.9)$$

Here and in the future we routinely disregard the contributions which go to zero when $N \to \infty$ or $L \to \infty$; we will only write them in a few special occasions when we want

---

[7]For the sake of brevity we leave out the spatial indices μ, ν etc. from now on. We will only write them when leaving them out could lead to confusion.

to emphasize that some part of the partition function contributes only negligible terms. One can check that the same value follows from the expression (3.6) after we solve the saddle-point equation for a_μ. We will compare this value with the on-shell value of the effective action for $\langle Z^2 \rangle$ to check for factorization. One final remark: there is always a sum over the spacetime coordinate μ (in general $\mu = 1, \ldots 2p$, in our case $\mu = 1, 2$), hence W_1 from (3.9) is really multipled by 2 ($2p$ for a general D_p brane). But we do not write this factor explicitly in order not to clutter the notation; our W_1 (and similar for the two- and four-replica actions W_2 and W_4 we are yet to compute) is really the effective action per spacetime dimension (and since we work in Euclidean signature all dimensions are equivalent).

3.2.2 Double and quadruple partition function

Now that we have the averaged partition function $\langle Z \rangle$ for a D-brane, our question is: does the replicated partition function $\langle Z^2 \rangle$ factorize? With two copies (replicas), the collective fields show their true meaning. The replicated partition function is[8]

$$Z^2 = \int D[a] \exp\left[-\text{Tr}\left(2\lambda^i \left(a_A^\dagger a_A\right)\lambda^i + \frac{I}{2L^2}\lambda_i^2\right)\right],\tag{3.10}$$

where now we have the left and right replicas, denoted by the indices $A, B, \ldots$ taking values L or R. The fun part is the averaged function $\langle Z^2 \rangle$:

$$\langle Z^2 \rangle = \int D[a] \int D[g] \int \frac{D[s]}{2\pi} \int d\lambda e^{-\frac{1}{2}\text{Tr}a_A^\dagger P^2 a_A} e^{-V(g_{AA})+V\left(a_A^\dagger a_A\right)} e^{-\imath\text{Tr}\left[s_{AA}^\dagger\left(g_{AA}-a_A^\dagger a_A\right)\right]} \mathcal{P}(\lambda)$$

$$= \int D[g] \int \frac{D[s]}{2^N \pi^{N^2}} \exp\left[-\imath\text{Tr}\left(s_{AA}^\dagger g_{AA}\right) - \frac{1}{2}\log\det s_{AA} - V\left(g_{AA}\right)\right] \equiv e^{-W_2}.\tag{3.11}$$

Analogously to what we did for $\langle Z \rangle$, the term with $-V\left(g_{AA}\right) + V\left(a_A^\dagger a_A\right)$ in the exponent is the multiplication by unity on-shell, and the s_{AA} auxiliary fields implement the Dirac delta functional. Up to fourth order, the interaction terms V read (from performing the Gaussian integration over λ_i and expanding the determinant):

$$V = V_2 + V_4$$
$$V_2 = \frac{2}{L^{2N-2}}\text{Tr}(g_{LL} + g_{RR})$$
$$V_4 = \frac{4}{L^{2N-4}}\text{Tr}^2(g_{LL} + g_{RR}) - \frac{4}{L^{2N-4}}\text{Tr}\left(g_{LL}^2 + g_{LL}g_{RR} + g_{RR}g_{LL} + g_{RR}^2\right).\tag{3.12}$$

Again, this is just the expansion of the averaged function $\langle Z^2 \rangle$ to fourth order in a_A, i.e. to second order in g_{AA}; the full expansion of the log det term is infinite. This is a consequence of the initial action S_{eff} being quadratic in the fields, so the effective actions W_n contain the log det term. If we had a linear coupling to the sources of the form Ja, we would get the

---

[8]In order to make the equations more compact we do not write out the replica indices in the measure of the integrals. Therefore, we write $\int D[g]$ for $\int D[g_{AA}]$, or $\int D[a]$ for $\int D[a_A]$ and similar. We still write the replica indices in the integrands (unlike the spatial indices $\mu, \nu \ldots$ which we usually leave out.)

by now familiar wormholes with collective fields g_{LR}, as in the SYK model in [11, 15, 17]. Now the saddle point equations from (3.12) are:

$$\frac{1}{2}\left(s_{AA}^{-1}\right)^T + \imath g_{AA} = 0 \;\Rightarrow\; s_{AA} = \frac{\imath}{2}\left(g_{AA}^T\right)^{-1} \tag{3.13}$$

$$\imath s_{AA} + \frac{2I}{L^{2N-2}} + \frac{8I}{L^{2N-4}}\mathrm{Tr}(g_{LL} + g_{RR}) - \frac{8}{L^{2N-4}}(g_{LL} + g_{RR})^T = 0. \tag{3.14}$$

While complicated at first glance, this system of equations has a high degree of symmetry. First, it is manifestly $L \leftrightarrow R$ invariant; second, it allows (though does not require) the maximally symmetric ansatz, where s and g are scalar matrices. Their matrix indices are $i, j \in \{1, \dots N\}$ (which we do not write explicitly) and $A, B \in \{L, R\}$. Therefore a scalar solution assumes (1) the $\mathrm{U}(N)$ group of the matrix model is fully preserved (which is logical in the large-N, random matrix regime that we study) and (2) full *replica symmetry* is preserved. The latter can be broken, and later on we will discuss this possibility in detail; but for now let us look at the replica-symmetric solution. We first insert s from (3.13) into (3.14) and then take the trace of both sides. Denoting $\mathrm{Tr}g_{LL} = \mathrm{Tr}g_{RR} \equiv t$, we find

$$t \sim -\frac{1}{16L^2} \pm \frac{L^{N-2}}{4\sqrt{2}\sqrt{N}}. \tag{3.15}$$

At leading order in large N and L, the two traces are symmetric, behaving as $\mathrm{Tr}g_{LL} = \mathrm{Tr}g_{RR} \sim \pm L^{N-2}/\sqrt{N}$. Still assuming maximal symmetry, this gives the following solution:

$$s = \pm\frac{2\imath}{t}I \otimes E, \;\; g = \pm t I \otimes E. \tag{3.16}$$

Here, E is the two-by-two unit matrix in the replica space; its indices are $A, B \in \{L, R\}$. From now on we use this Kronecker product notation for the collective fields with replica indices: a field g_{AA} can be written in the form $B \otimes C$, with B being an $N \times N$ matrix and C being an $n \times n$ matrix with n the number of replicas.

The solutions scale as L^{N-2} instead of L^{2N-2} for the single replica solution (3.8). This fact already suggests that the two-replica solution does not factorize. Inserting (3.16) into (3.12) we find (for either sign in (3.16)):

$$W_2|_{\text{on-shell}} \sim 2N^2 \log L + L^{2N}/2 \pm (2N)^{3/2}L^{N+2}. \tag{3.17}$$

Comparing to (3.9), we see that indeed *the two-replica solution does not factorize:* $\langle Z^2 \rangle \neq \langle Z \rangle^2$. The first term in (3.17) precisely equals $2W_1$,[9] but it is actually strongly subleading compared to the other two terms, which behave entirely differently, as L^N and L^{2N}. Therefore, we can spot a contribution equaling $2W_1$ but there is also a much larger contribution absent in W_1.

So the partition function $\langle Z^2 \rangle$ is not factorizing. Is it self-averaging? To check this, we can again follow [12] and compute the four-replica solution. Exploiting the definition of the

---

[9]Remember that all the solutions and on-shell action values are calculated for large N and L, meaning we disregard the terms which tend to zero as $N \to \infty$. Such higher-order corrections would likely spoil the exact ratio but this is expected.

non-averaged Z^2 from (3.11) we write:

$$Z^2 = \int \frac{D[s]}{2^N \pi^{N^2}} \chi(s;g) \Phi(s)$$

$$\chi(s;g) = \int D[g] \exp\left[-\imath \text{Tr}\left(s_{AA}^\dagger g_{AA}\right) - V\left(g_{AA}\right)\right]$$

$$\Phi(s) = \int D[a] \exp\left[\imath \text{Tr}\left(s_{AA}^\dagger a_A^\dagger a_A\right) - \frac{1}{2}\text{Tr} a_A^\dagger P^2 a_A + V\left(a_A^\dagger a_A\right)\right]. \tag{3.18}$$

Here we have separated the partition function into the non-averaging part $\chi(s;g)$ which just doubles when computing $\langle Z^4 \rangle$ as it is independent of a_A, and the part $\Phi(s)$ with a_A-dependent integrand which gets nontrivial additional correlations when Z^4 is averaged. Now the replica indices A, B can take values L, R, and A', B' take values L', R'. In addition to the two-replica fields, we now also have combinations of the form $LLR'R'$ and similar:[10]

$$\langle \Phi^2(s) \rangle = \int D[a_A] \int D[a_{A'}] \int d^N\lambda \mathcal{P}(\lambda_i)$$

$$\times \exp\left[\imath \text{Tr}\left(s_{AA}^\dagger a_A^\dagger a_A + s_{A'A'}^\dagger a_{A'}^\dagger a_{A'} - \frac{1}{2}a_A^\dagger P^2 a_A - \frac{1}{2}a_{A'}^\dagger P^2 a_{A'}\right) + V\left(a_A^\dagger a_A\right) + V\left(a_{A'}^\dagger a_{A'}\right)\right]$$

$$= \int D[a_A] \int D[a_{A'}] \exp\left[\imath \text{Tr}\left(s_{AA}^\dagger a_A^\dagger a_A + s_{A'A'}^\dagger a_{A'}^\dagger a_{A'}\right) + V\left(a_A^\dagger a_A\right) + V\left(a_{A'}^\dagger a_{A'}\right)\right]$$

$$\times \exp\left[-\frac{1}{2}\log\det\left(\frac{I}{L^2} + 2a_A^\dagger a_A + 2a_{A'}^\dagger a_{A'} - 2I\text{Tr}a_A^\dagger a_A - 2I\text{Tr}a_{A'}^\dagger a_{A'}\right)\right]. \tag{3.19}$$

The next step is to expand the argument of the logarithm, which results in the mixing of L, R and L', R'. Expanding to order four, we generate a new interaction potential, mixing all four replicas, and again resort to the trick of multiplying by unity and introducing the four-replica collective field $G_{AAB'B'}$, together with the Dirac delta constraint implemented by $S_{AA'BB'}$:

$$\langle \Phi^2(s) \rangle = \int D[a_A] \int D[a_{A'}] \int D[S] \int D[G]$$

$$\times \exp\text{Tr}\left[\imath s_{AA}^\dagger a_A^\dagger a_A + \imath s_{A'A'}^\dagger a_{A'}^\dagger a_{A'} + \imath S_{AAB'B'}^\dagger\left(a_A^\dagger a_A a_{B'}^\dagger a_{B'} - G_{AAB'B'}\right)\right]$$

$$\times \exp\left[V\left(a_A^\dagger a_A\right) + V\left(a_{A'}^\dagger a_{A'}\right) - \mathcal{V}\left(g_{AA}, g_{B'B'}; G_{AAB'B'}\right) + \mathcal{V}\left(a_A^\dagger a_A, a_{B'}^\dagger a_{B'}\right)\right]$$

$$= \int D[S] \int D[G] e^{-\tilde{W}_4}, \tag{3.20}$$

with the effective action that now depends also on the new collective fields $G_{AAB'B'} \equiv a_A^\dagger a_A a_{B'}^\dagger a_{B'}$. From (3.18), the total effective action is the sum of $\tilde{W}_4$ from the last equation and the non-averaging contribution from $\chi(s;g)$:

$$W_4 = \imath \text{Tr}\left(s_{AA}^\dagger g_{AA}\right) + V\left(g_{AA}\right) + \tilde{W}_4$$

$$\tilde{W}_4 = \frac{1}{2}\left(\log\det s_{AB} + \log\det s_{A'B'} + \log\det S_{AAB'B'}\right) - \imath \text{Tr}\left(S_{AAB'B'}^\dagger G_{AAB'B'}\right) + \mathcal{V}$$

$$\mathcal{V}\left(g_{AA}, g_{B'B'}; G_{AAB'B'}\right) = \frac{8}{L^{2N-4}}\text{Tr}g_{AA}\text{Tr}g_{B'B'} - \frac{4}{L^{2N-4}}\text{Tr}G_{AAB'B'}. \tag{3.21}$$

---

[10]In this equation, exceptionally, we write the indices in the integrand, e.g., $\int D[a_{A'}]$, in order to emphasize that we now have extra copies of the fields.

This is the main formal result of this section. We will now consider various saddle-point solutions of the effective action (3.21), and consider which of these may restore the factorization and which are self-averaging.

3.3 Half-wormholes

The effective action (3.21) is slightly more involved but the highest symetry solutions are still easy to find. The saddle-point equations read:

$$-\frac{1}{2}\left(g_{AA}^{-1}\right)^T + \frac{2I}{L^{2N-2}} + \frac{8I}{L^{2N-4}}\mathrm{Tr}(g_{LL}+g_{RR}) - \frac{8}{L^{2N-4}}(g_{LL}+g_{RR})^T - \frac{8I}{L^{2N-4}}\mathrm{Tr}g_{B'B'} = 0$$
$$\frac{1}{2}\left(S_{AAB'B'}^{-1}\right)^T + \imath G_{AAB'B'} = 0, \quad -\imath S_{AAB'B'} - \frac{4}{L^{2N-4}}I = 0. \tag{3.22}$$

Notice that the first and the second line are decoupled. The second line (the equations for S and G) is linear and the solution is unique and left-right symmetric in the replica space (invariant to $L \leftrightarrow R$ and $L' \leftrightarrow R'$). In the first line, we have already implemented the relation $\left(s_{AA}^{-1}\right)^T + 2\imath g_{AA} = 0$ which remains the same as in (3.13); that is why s_{AA} is already elliminated from (3.22). This equation is nonlinear and potentially has many solutions. If we again take the fully replica-symmetric ansatz, we can easily solve for the trace as in (3.13)–(3.14). When everything is said and done the outcome is

$$s = \pm\frac{2\imath}{t}I \otimes E, \ g = \pm tI \otimes E \tag{3.23}$$

$$S_{LLL'L'} = S_{LLR'R'} = S_{RRL'L'} = S_{RRR'R'} = \frac{4\imath}{L^{2N-4}}I \tag{3.24}$$

$$G_{LLL'L'} = G_{LLR'R'} = G_{RRL'L'} = G_{RRR'R'} = \frac{L^{2N-4}}{8}I. \tag{3.25}$$

$$W_4|_{\mathrm{on-shell}} \sim 4(N^2-N)\log L + 2N\log 2 - \sqrt{2N}/L^N. \tag{3.26}$$

The remaining components of S and G (those not listed in (3.25)) are zero. The first and second term in $W_4|_{\mathrm{on-shell}}$ come from S and G fields; the third term comes from s and g. Although the first term clearly dominates over the others, and the last term is negligible, we have deliberately written all three to emphasize the different contributions. We notice the following:

1. The solution for W_4 factorizes at leading order, as we have $W_4 \sim 4W_1$ on-shell (compare to (3.9)). What is more, it factorizes nontrivially, i.e. the expression for W_4 in (3.21) does not consist of four copies of W_1 (3.7). The leading contribution to (3.26) comes roughly from the $\log \det S$ term in (3.21) and involves fields of the form $a_L^\dagger a_L a_{L'}^\dagger a_{L'}$ and similar, whereas the dominant contribution to W_1 comes from the term $\log \det s$ with fields of the form $a_L^\dagger a_L$.

2. There is no simple "wormhole" contribution, mixing the left and right copy, i.e. no fields g_{LR}, only g_{LL} and g_{RR}. As we already said, this is so because there is no linear source coupling to a. However, since the fields $G_{AAB'B'}$ (or explicitly $G_{LLR'R'}$ and $G_{RRL'L'}$) are nonzero, this solution can be called half-wormhole (HWH) in analogy

with the terminology of [11], already accepted in [15, 17, 18, 21].[11] The half-wormhole thus dominates the action.

3. The local contribution in replica space, the one coming from g_{LL} and g_{RR} fields, is negligible compared to the HWH part. It is also non-factorizing; but as in other cases in the literature, the HWH restores factorization.

4. The solution is not self-averaging. To see this, we follow the criterion (1.2) and insert $\sqrt{\langle \lambda_\mu^2 \rangle} = L_\mu$ into Z as given in (3.3). Since now we deal with a free quadratic action (having fixed $\lambda_\mu \mapsto L_\mu$) the n-replica partition function is easily found for any n: $W_n = nN \log L$; specifically, for $n = 4$, we have $W_4 \sim 4N \log L$. This does not capture the leading term in (3.26).

We can confirm our findings numerically by computing the full action for a numerically generated ensemble of quenched matrices A_μ. In figure 1 we plot the numerical realization and the estimate (3.26) in blue and red respectively. We also plot the quadraple value of the single-replica action W_1 for comparison (black dashed). The analytical estimate is very good and the factorization near-perfect, as the black dashed curve almost falls on top of the blue and red one.

So while the action of the two-replica system W_2 does not factorize, the four-replica action W_4 has a HWH saddle point which restores factorization. In our view, the most interesting aspect of this is that the four-replica system *factorizes nontrivially*: the effective action (3.26) is dominated by nonlocal terms, half-wormholes; it does not merely consist of four copies of W_1. Since our system contains explicit quenched disorder, it is no big surprise that in general $\langle Z^2 \rangle \neq \langle Z \rangle^2$ (this is the same situation as for the SYK model). But the restoration of the factorization in the sense that $\langle Z^4 \rangle = \langle Z \rangle^4$ was not *a priori* expected, nor the fact that this happens already in the collective fields formalism at leading order (disregarding an infinite series of higher-order terms in $\langle Z^4 \rangle$). Even though we look directly at the (discretized) string theory action, which includes gravity, there is no obvious geometric interpretation of the half-wormhole. This is not much of a surprise as the IKKT model should capture the nonperturbative stringy effects, far beyond general relativity and geometry.

3.4 Fermionic contribution to D-string partition functions

Now we turn on also the fermionic fluctuations ψ_α (while still putting the background fermions Ψ_α to zero). In addition to the collective fields introduced earlier, we now need also the fermion bilinear $\gamma_{AB} = \bar{\psi}_A \psi_B$, with $A, B \in \{L, R\}$; in order to implement the constraint that defines γ_{AB} we also have to introduce another auxiliary field called σ_{AB} (analogous to s_{AA}). Actually, the fermionic part may be more familiar to the reader as fermionic collective fields were investigated in the literature in much detail, mainly in the

---

[11]In fact, the name is not a very fortunate one, as there is nothing "halved" here; it a product of replicas just like a wormhole, only of different replicas. A more descriptive term would be "higher-order wormholes" but we will not attempt to change an already established name.
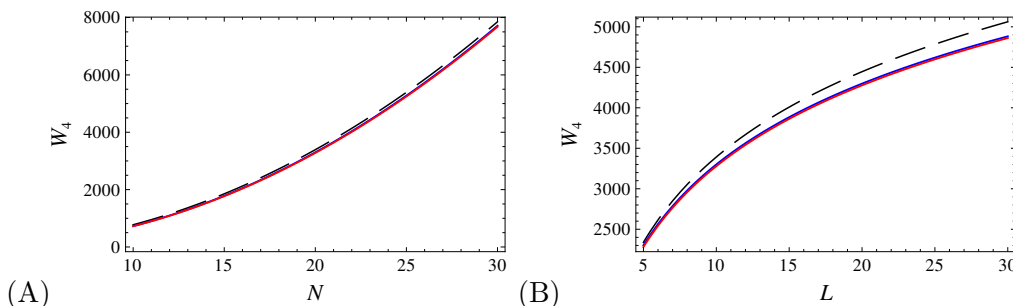
Figure 1. Effective action W_4 as a function of the matrix size N (A) and compactification radius L (B) from analytical (red) and numerical (blue) calculations; the curves almost coincide. For reference we also show the single-replica solution $4W_1$ (black dashed) which is nearly equal to W_4, confirming the factorizing property.

context of SYK model [12, 17, 20]. We can first write $\langle Z \rangle$:

$$
\begin{aligned}
\langle Z \rangle = & \int D[\psi] \int D[\bar{\psi}] \int D[a] \int D[g] \int D[\gamma] \int \frac{D[s]}{2^N \pi^{N^2}} \int \frac{D[\sigma]}{2^N \pi^{N^2}} \int d\lambda \\
& \times \exp \mathrm{Tr} \left(-\frac{1}{2} a P^2 a - \bar{\psi}_\alpha \not{P} \psi_\alpha \right) \\
& \times \exp \left[-\imath \mathrm{Tr} \left(s^\dagger \left(g - a^\dagger a \right) + \sigma^\dagger \left(\gamma - \frac{1}{N} \bar{\psi}_\alpha \psi_\alpha \right) \right) - V(g) + V(a^\dagger a) - \Gamma(\gamma) + \Gamma \left(\frac{1}{N} \bar{\psi}_\alpha \psi_\alpha \right) \right] \\
= & \int D[g] \int D[\gamma] \int \frac{D[s]}{2^N \pi^{N^2}} \int \frac{D[\sigma]}{2^N \pi^{N^2}} e^{-\imath \mathrm{Tr} \left(s^\dagger g + \sigma^\dagger \gamma \right) - V(g) - \Gamma(\gamma) + \mathrm{Tr} \left(\gamma s^{-1} \gamma \right) + \log \det \sigma}, \quad (3.27)
\end{aligned}
$$

where we have introduced the self-interaction potential $\Gamma(\gamma) = (L^2/4)\gamma^2$ for the collective fermionic fields analogously to $V(g)$ for the boson. At quadratic order $O(g^2 + \gamma^2)$ there is no interaction between the Bose and Fermi sectors. At the quartic level they couple, through the term $\gamma s^{-1} \gamma$ which comes from the term $\bar{\psi} \not{\phi} \psi$ in the original action. Defining the negative exponent in (3.27) as W_1, we will now compare W_1 to the four-replica effective action W_4. Let us first calculate W_1. The equations of motion read

$$
\begin{aligned}
& \frac{2}{L^{2N-2}} I + \imath s = 0, \ \imath g + \frac{1}{2} \left(s^{-1} \right)^T + \gamma s^{-2} \gamma = 0 \ \Rightarrow \ s = \frac{2\imath}{L^{2N-2}} I \otimes E, \ g = \frac{L^{2N-2}}{4} I \otimes E \\
& \imath \sigma + \frac{L^2}{2} \gamma - \frac{1}{4} \left(\gamma s^{-1} + s^{-1} \gamma \right) = 0, \ \imath \gamma + \left(\sigma^{-1} \right)^T = 0 \ \Rightarrow \ \sigma = \imath \frac{L^{N-1}}{\sqrt{2}} I, \ \gamma = \frac{\sqrt{2}}{L^{N-1}} I.
\end{aligned}
\tag{3.28}
$$

This yields the same solution for the bosonic fields g and s as before, since their coupling to the fermions (the last term in the first line of (3.28)) only contributes a correction which goes to zero for $L, N \to \infty$; in fact, the γ-s coupling does not influence the fermionic solution either at large L, N. The on-shell action is just the sum of the bosonic term (3.9) and the fermionic term from (3.28):

$$
W_1|_{\mathrm{on-shell}} = \left[(N^2 - N) \log L + \frac{N}{2} \log 2 \right] + \left[N \log L - \frac{N}{2} \log 2 \right] = N^2 \log L. \tag{3.29}
$$

Now we derive the four-replica action W_4. In order to do this, we need to write first the two-replica function. Just like for bosons, it separates into the averaging and non-averaging

part:

$$Z^2 = \int \frac{D[s]}{2^N \pi^{N^2}} \int \frac{D[\sigma]}{2^N \pi^{N^2}} \chi(s,\sigma;g,\gamma)\Phi(s,\sigma)$$

$$\chi(s,\sigma;g,\gamma) = \int D[g] \int D[\gamma] \exp\left[-\imath \mathrm{Tr}\left(s_{AA}^\dagger g_{AA} + \sigma_{AB}^\dagger \gamma_{AB}\right) - V\left(g_{AA}\right) - \Gamma(\gamma_{AB})\right]$$

$$\Phi(s,\sigma) = \int D[a] \int D[\psi_A] \int D[\bar{\psi}_A] \exp\left[\imath \mathrm{Tr}\left(s_{AA}^\dagger a_A^\dagger a_A\right) - \frac{1}{2}\mathrm{Tr} a_A^\dagger P^2 a_A + V\left(a_A^\dagger a_A\right)\right]$$

$$\times \exp\left[\imath \mathrm{Tr}\left(\sigma_{AA}^\dagger \frac{\bar{\psi}_A \psi_A}{N}\right) - \mathrm{Tr}\bar{\psi}_A \slashed{P}\psi_A + \Gamma\left(\frac{\bar{\psi}_A \psi_A}{N}\right) - \mathrm{Tr}\bar{\psi}_A \slashed{\phi}_A \psi_A\right]. \quad (3.30)$$

In order to test the factorization property we find $\langle \Phi^2 \rangle$ through the steps similar to those in eq. (3.19).

$$\langle \Phi^2(s) \rangle = \int D[a_A] \int D[a_{A'}] \int d\bar{\psi}_A \int d\psi_A \int d\bar{\psi}_{B'} \int d\psi_{B'} \int \frac{dS}{2^N \pi^{N^2}} \int dG$$

$$\times \exp\left[\imath \mathrm{Tr}\left(s_{AA}^\dagger a_A^\dagger a_A + s_{A'A'}^\dagger a_{A'}^\dagger a_{A'} + S_{AAB'B'}^\dagger a_A^\dagger a_A a_{B'}^\dagger a_{B'} + \sigma_{AA}^\dagger \frac{\bar{\psi}_A \psi_A}{N}\right)\right]$$

$$\times \exp\left[V\left(a_A^\dagger a_A\right) + V\left(a_{A'}^\dagger a_{A'}\right) + \mathcal{V}\left(a_A^\dagger a_A, a_{B'}^\dagger a_{B'}\right) + \Gamma\left(\frac{\bar{\psi}_A \psi_A}{N}\right) - \mathrm{Tr}\bar{\psi}_A \slashed{\phi}_A \psi_A\right]$$

$$\times \exp\left[-\imath \mathrm{Tr}\left(S_{AAB'B'}^\dagger G_{AAB'B'}\right) - \mathcal{V}\left(g_{AA}, g_{B'B'}; G_{AAB'B'}\right)\right] = \int \frac{dS}{2^N \pi^{N^2}} \int D[G] e^{-\tilde{W}_f}. \quad (3.31)$$

The final step is to integrate out the original fields. The bosonic integrals result in determinants and traces, as we have already seen, and the fermionic integrals are expressed in terms of Pfaffians, i.e. polynomials. Thanks to this the fermionic bilinear can contain any combination of L, L', R and R', giving rise to wormholes as we shall see. The effective action is finally:

$$W_f = \imath \mathrm{Tr}\left(s_{AA}^\dagger g_{AA} + \sigma_{AB}^\dagger \gamma_{AB}\right) + V + \tilde{W}_f$$

$$\tilde{W}_f = \frac{1}{2}\log\det\left(s_{AB}s_{A'B'}S_{AAB'B'}\right) - \imath \mathrm{Tr}\left(S_{AAB'B'}^\dagger G_{AAB'B'}\right) + \mathcal{V} + V_f$$

$$\mathcal{V}_f = \frac{L^2}{4}\mathrm{Tr}\left(\gamma_{AB'}^2\right) - \mathrm{Tr}\left(\gamma_{AA}s_{AA}^{-1}\gamma_{AA}\right) - \log\mathrm{Tr}\left(\sigma_{LR}\sigma_{L'R'} - \sigma_{LL'}\sigma_{RR'} + \sigma_{LR'}\sigma_{RL'}\right), \quad (3.32)$$

and the bosonic potentials V and $\mathcal{V}$ are given in (3.12) and (3.21) respectively. The saddle-point equations (3.22) now get additional terms and two additional equations from fermionic contributions:

$$\frac{1}{2}\left(s_{AA}^{-1}\right)^T + \imath g_{AA} + \gamma_{AA}s_{AA}^{-2}\gamma_{AA} = 0$$

$$\imath s_{AA} + \frac{2I}{L^{2N-2}} + \frac{8I}{L^{2N-4}}\mathrm{Tr}(g_{LL} + g_{RR}) - \frac{8}{L^{2N-4}}(g_{LL} + g_{RR})^T - \frac{8I}{L^{2N-4}}\mathrm{Tr} g_{B'B'} = 0$$

$$\frac{1}{2}\left(S_{AAB'B'}^{-1}\right)^T + \imath G_{AAB'B'} = 0, \quad -\imath S_{AAB'B'} - \frac{4}{L^{2N-4}}I = 0$$

$$\imath \sigma_{AB} + \frac{L^2}{2}\gamma_{AB} - \frac{1}{4}\{\gamma_{AB}, s_{AB}^{-1}\}\delta_{AB} = 0$$

$$\imath \gamma_{AB} - \sigma_{A'B'}\left(\sigma_{CD}\sigma_{C'D'} - \sigma_{CC'}\sigma_{DD'} + \sigma_{CD'}\sigma_{DC'}\right)^{-1} = 0. \quad (3.33)$$

This Bose-Fermi saddle-point system has a rich structure. We notice the following properties:

1. The collective field γ_{AB} can now couple different replicas already at the quadratic level. This is simply a consequence of the fact that fermions couple linearly to the quenched bosonic degrees of freedom A_μ. We would have obtained the same situation for the bosonic fields if we coupled them linearly to a source. The Pfaffian obtained upon integrating out ψ_α fields has a combinatorial structure which allows the breaking of replica symmetry, i.e. some σ_{AB} may be zero and some nonzero.

2. One solution is obtained by setting $\sigma_{LR} = \sigma_{L'R'} \equiv \sigma \neq 0$ while all other components are zero. This yields[12]

$$\sigma_{LR} = \sigma_{L'R'} = \frac{L^{N-1}}{\sqrt{2}}, \quad \gamma_{LR} = \gamma_{L'R'} = -\imath \frac{\sqrt{2}}{L^{N-1}}$$
$$W_4|_{\text{on-shell}} = 4N^2 \log L + 2N. \tag{3.34}$$

This is a wormhole (WH), coupling the L and R copies. The term $2N$ spoils the factorization (compare to (3.29)).

3. We can have $\sigma_{LR'} = \sigma_{RL'} \equiv \sigma \neq 0$ while the other components of σ_{AB} are zero. This is a half-wormhole. This solution reads

$$\sigma_{LR'} = \sigma_{RL'} = \frac{L^{N-1}}{\sqrt{2}}, \quad \gamma_{LR'} = \gamma_{RL'} = -\imath \frac{\sqrt{2}}{L^{N-1}}$$
$$W_4|_{\text{on-shell}} = 4N^2 \log L + N. \tag{3.35}$$

The effective action is lower than (3.34) by N so this solution is thermodynamically preferrable compared to the wormhole, and also the mismatch from factorization is smaller (N compared to $2N$).

4. The third possibility is $\sigma_{LL'} = \sigma_{RR'} \equiv \sigma$ as the only nonzero component. This solution acquires a minus sign in the logarithm of the Pfaffian (the last term in (3.32)) hence it has a nonzero phase:

$$\sigma_{LL'} = \sigma_{RR'} = \imath \frac{L^{N-1}}{\sqrt{2}}, \quad \gamma_{LL'} = \gamma_{RR'} = \frac{\sqrt{2}}{L^{N-1}}$$
$$W_4|_{\text{on-shell}} = 4N^2 \log L + \imath \pi. \tag{3.36}$$

This is a half-wormhole but inequivalent to the half-wormhole from the previous point; it breaks the phase symmetry and has lower (real part of) free energy than the previous solutions. Apart from the phase factor, it is a factorizing solution, as we have $\Re W_4 \sim 4N^2 \log L = 4W_1$.

---

[12]In all examples we consider, the solutions for the bosonic fields g, s, G, S do not change at leading order in the presence of fermions, hence we do not write the expressions for them again.

5. The last possibility is $\sigma_{LL} = \sigma_{RR} \equiv \sigma$ as the only nonzero component. This solution contributes to the last equation in (3.33) with the opposite sign, and thus leads to a different saddle point:

$$\sigma_{LL} = \sigma_{RR} = \frac{L^{N/2-2}}{2^{7/4}N^{1/4}}e^{-\imath\pi/4}, \ \gamma_{LL} = \gamma_{RR} = \frac{2^{7/4}N^{1/4}}{L^{N/2-2}}e^{-\imath\pi/4} \tag{3.37}$$

$$W_4|_{\text{on-shell}} = 4(N^2 + N/2)\log L + N - \frac{1}{4}e^{-\imath\pi/4}. \tag{3.38}$$

This saddle point would not exist for Majorana fermions (as in the SYK model) since for Majoranas $\bar{\psi} = \psi$ and thus $\gamma_{LL} = \langle\psi\psi\rangle = 0$. It is a strongly suppressed solution as its on-shell action is by $\sim 2N \log L$ larger than the real part of W_4 of all previous solutions (3.34), (3.35), (3.36).

This situation is more akin to the SYK and similar field theory models in the literature than the purely bosonic case — several competing solutions of the local (3.37), wormhole (3.34), and half-wormhole type (3.35), (3.36). There may be more general solutions with less symmetry than the ones we found analytically above. Such solutions are hard to find, and we did not explore them in detail. In figure 2 we plot the landscape of the real part of the action for varying σ_{LR} and $\sigma_{L'R}$ (fixing the remaining couplings). The outcome is invariant to the sign change of σ which was to be expected from the effective action. The trivial vacuum $\sigma_{LR} = \sigma_{L'R} = \sigma_{LR'} = 0$ is one solution, but we also have a nontrivial solution with all WH and HWH couplings nonzero. It seems however that the latter is never the global minimum, i.e. it is a false vacuum. So we fail to find any thermodynamically stable solutions other than (3.34)–(3.37), but we still have no proof that they never exist.

Looking at the on-shell actions (3.34)–(3.38), we see that the dominant (least-action) solution, the LL' HWH configuration, restores the factorization. It is true though that fermionic contributions are always subleading to the $4N^2 \log L$ term coming from the bosonic determinant, so one could also argue that the factorization is always roughly satisfied; but precisely the *dominant* fermionic saddle point, i.e. the true vacuum satisfies it also at the next order in L, N. This strongly suggests that the physical dynamics indeed tends to "know" about the factorization. The factorization remains nontrivial, as the same dominant term $\log \det S$ from the bosonic action still gives the main contribution. And — unlike the findings for the SYK model in [12] — *none of our solutions is self-averaging*. The total action for the fluctuations a_μ and ψ_α evaluated for $\lambda = L$ is easily found from (2.8) to be zero — the Bose and Fermi terms exactly cancel out each other, as it has to happen for a BPS configuration (the averaging over the quenched background A_μ spoils the supersymmetry and that is why the averaged on-shell actions we find are always nonzero; but expanding about fixed BPS solution for A_μ without averaging keeps the BPS property).

4 Replicas and factorization for a pair of interacting D-strings

We have found that for a single D-string the factorization of the partition function, broken for two replicas, is always re-established with four replicas essentially at the mean field level, and in a nontrivial way. A possible physical interpretation of this fact is simply
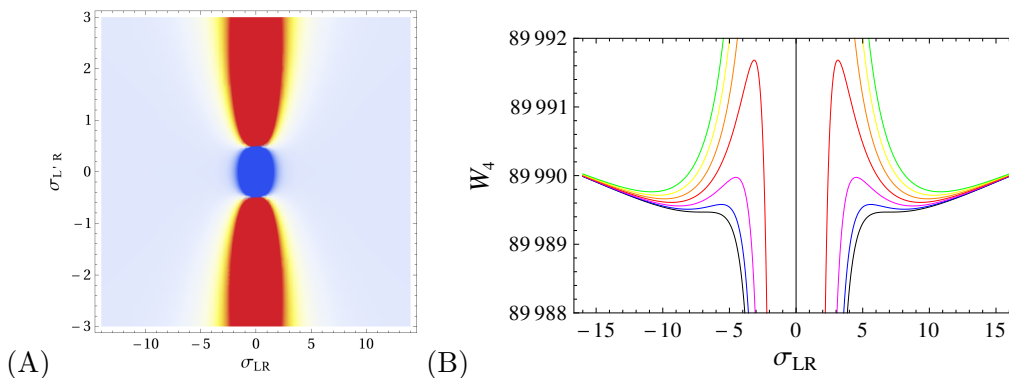
Figure 2. (A) Real part of the effective action W_4 as a function of the wormhole coupling σ_{LR} and the half-wormhole coupling $\sigma_{L'R}$, for $\sigma_{LL} = \sigma_{RR} = 0.3$ and $\sigma_{LL'} = \sigma_{RR'} = 0.5\imath$. The magnitude of W_4 is encoded by the color map, from blue (low) to red (high). The global minimum is the trivial solution $\sigma_{LR} = \sigma_{L'R} = 0$ (the blue area in the center). There is also a line of shallow local minima for nonzero WH and HWH couplings, which is easier to see along one-dimensional slices (B), where we plot $W_4(\sigma_{LR})$ for $\sigma_{L'R} = 0.1, 0.2, 0.3, 0.4, 0.5, 0.6, 0.7$ (black, blue, magenta, red, orange, yellow, green). But the true vacuum, in the presence of nonzero LL and LL' couplings, remains the one with no WH (LR) or additional HWH ($L'R$) contributions (there is already one HWH coupling LL').

that n noninteracting D-strings form an ergodic system, i.e. averaging the dynamics over all the strings (computing their partition function Z_n) is equivalent to averaging a single string over the quenched degrees of freedom (computing the partition function $\langle Z_1 \rangle$). A consequence of this is that *if we have a BPS configuration, the conclusion from the previous section cannot change: as long as $F_{\mu\nu} = 0$ there is no difference between n copies of a single D-brane and a stack of n parallel D-branes.* Notice this remains true also in absence of background fermions (for $\Psi_\alpha = 0$) since it only hinges on $F_{\mu\nu} = 0$.

Now we consider a pair of strings with angle 2θ between them — this is the solution given in (2.5). For nonzero angle, this solution is non-BPS, the interaction between the strings is nonzero as it has a nonzero component of $F_{\mu\nu}$. Following eq. (2.10) and [30], the superoperators are found to be:

$$P_0 = [q \otimes I_{2\times2}, \cdot] = \begin{pmatrix} I_{2\times2} \otimes \hat{Q} & 0 \\ 0 & I_{2\times2} \otimes \hat{Q} \end{pmatrix}$$

$$P_1 = \cos\theta \, [p \otimes I_{2\times2}, \cdot] = \cos\theta \begin{pmatrix} I_{2\times2} \otimes \hat{P} & 0 \\ 0 & I_{2\times2} \otimes \hat{P} \end{pmatrix}$$

$$P_2 = \frac{\ell}{2} \left[I_{N'\times N'} \otimes \sigma^3, \cdot \right] = \ell \begin{pmatrix} -\Pi_- \otimes I_{N'^2 \times N'^2} & 0 \\ 0 & \Pi_+ \otimes I_{N'^2 \times N'^2} \end{pmatrix}$$

$$P_3 = \sin\theta \left[p \otimes \sigma^3, \cdot \right] = 2\sin\theta \begin{pmatrix} -\Pi_- \otimes \hat{Q} & 0 \\ 0 & \Pi_+ \otimes \hat{Q} \end{pmatrix}$$

$$F_{03} = 2\omega \sin\theta \left[I_{N'\times N'} \otimes \sigma^3, \cdot \right] = 2\omega \sin\theta \begin{pmatrix} -\Pi_- \otimes I_{N'^2 \times N'^2} & 0 \\ 0 & \Pi_+ \otimes I_{N'^2 \times N'^2} \end{pmatrix}, \qquad (4.1)$$

and the other components are zero. For two strings, according to (2.5), the matrices A_μ

and a_μ have the two-by-two block structure, hence the superoperators in (4.1) have the four-by-four block structure. We have denoted $N' \equiv N/2$ and $\Pi_\pm \equiv (I_{2\times2} \pm \sigma^3)/2$. The superoperators $\hat{P} \equiv [p, \cdot]$ and $\hat{Q} \equiv [q, \cdot]$ are obtained by commuting with p and q and have the explicit form as given in (3.5). Now we follow the same path as in the previous section, so we will not repeat all the technical details. Unlike the previous section, we restore the spacetime indices and write e.g. $a_\mu^\dagger a_\mu$ and not $a^\dagger a$; this is because the different spacetime dimensions are not equivalent anymore as for a single string. The effective action reads

$$W_1 = \frac{1}{2} \log \det \left[\frac{I}{L^2} + \left(1 + \cos^2\theta\right) \left(a_\mu^\dagger a_\mu - I\mathrm{Tr}a_\mu^\dagger a_\mu\right) \right] + \frac{\ell^2}{2} \sin^2\theta \cdot \mathrm{Tr}a_\mu^\dagger K^2 a_\mu$$

$$+ 2\omega \sin\theta \mathrm{Tr}\left(a_0^\dagger K a_3 + a_3^\dagger K a_0\right), \quad K = \begin{pmatrix} -\Pi_- & 0 \\ 0 & \Pi_+ \end{pmatrix}. \tag{4.2}$$

Introducing the collective fields, expanding the log det term, and integrating out the original variables we get

$$W_1 = \mathrm{Tr}\left[\frac{2\left(1 + \cos^2\theta\right)}{L^{2N-2}} \left(g - a_\mu^\dagger a_\mu\right) + \frac{\ell^2}{2} \sin^2\theta \left(K^2 g - a_\mu^\dagger K^2 a_\mu\right) \right.$$

$$+ 2\omega \left(j - \sin\theta \left(a_0^\dagger K a_3 + a_3^\dagger K a_0\right)\right)$$

$$\left. + \imath s^\dagger \left(g - a_\mu^\dagger a_\mu\right) + \imath \zeta^\dagger \left(j - \sin\theta \left(a_0^\dagger K a_3 + a_3^\dagger K a_0\right)\right) \right]$$

$$= \frac{1}{2} \log \det s^2 \left(s^2 - \sin^2\theta K^2 \zeta^2\right)$$

$$+ \mathrm{Tr}\left[\frac{2\left(1 + \cos^2\theta\right)}{L^{2N-2}} g + \frac{\ell^2}{2} \sin^2\theta K^2 g + 2\omega j + \imath s^\dagger g + \imath \zeta^\dagger j \right]. \tag{4.3}$$

Here, j is the new current, equal (on-shell) to the bilinear originating from the string-string interaction, and ζ is the corresponding auxiliary field. The two-replica action (to quadratic order) is now

$$W_2 = \frac{1}{2} \log \det s_{AA}^2 \left(s_{AA}^2 - \sin^2\theta K^2 \zeta_{AA}^2\right) + V_2\left(g_{AA}\right) + \mathrm{Tr}\left[2\omega j_{AA} + \imath s_{AA}^\dagger g_{AA} + \imath \zeta_{AA}^\dagger j_{AA}\right]$$

$$V_2(g_{AA}) = \mathrm{Tr}\left[\frac{2\left(1 + \cos^2\theta\right)}{L^{2N-2}} g_{AA} + \frac{\ell^2}{2} \sin^2\theta K^2 g_{AA} \right]. \tag{4.4}$$

Finally, the four-replica solution yields

$$W_4 = \imath \mathrm{Tr}\left(s_{AA}^\dagger g_{AA} + \zeta_{AA}^\dagger j_{AA}\right) + V_2(g_{AA}) + 2\mathrm{Tr}\omega j_{AA} + \tilde{W}_4$$

$$\tilde{W}_4 = \frac{1}{2} \log \det \left[s_{AA}^2 \left(s_{AA}^2 - \sin^2\theta K^2 \zeta_{AA}^2\right) + (A \mapsto A') + S_{AAB'B'}^2 \left(S_{AAB'B'}^2 - \sin^2\theta K^2 \zeta_{AAB'B}^2\right) \right]$$

$$+ \mathcal{V}$$

$$\mathcal{V} = \frac{8}{L^{2N-4}} \mathrm{Tr}g_{AA}\mathrm{Tr}g_{B'B'} - \frac{4}{L^{2N-4}} \mathrm{Tr}G_{AAB'B'}. \tag{4.5}$$

The solutions to the saddle-point equations for $W_{1,2,4}$ depend crucially on whether the strings are parallel ($\theta = 0$) or not ($\theta \neq 0$). We will therefore consider each case separately. Parallel strings with $\theta = 0$ and thus $j = 0$ reduce to four times the result of the single-matrix calculation from the previous section; therefore we have $W_1|_{on-shell} = 4N^2 \log L$

(and analogously $W_4|_{on-shell} = 16N^2 \log L$).[13] This of course had to happen, as this case is BPS. The old conclusion thus remains, as we have anticipated at the beginning of this section: the partition functions factorize nontrivially.

For a non-BPS configuration the picture will actually turn out to be simpler. Let us first solve the saddle-point equations for W_1. The outcome is

$$s = \frac{2\imath}{L^{2N-2}} \left[(1 + \cos^2 \theta) I + \ell^2 \sin^2 \theta K^2 \right], \quad \zeta = 2\imath \omega I \tag{4.6}$$

$$j = \imath \frac{\sin^2 \theta K^2 \zeta}{K^2 \zeta^2 \sin^2 \theta - s^3} \Rightarrow j \sim \frac{1}{2\omega} I \tag{4.7}$$

$$0 = \frac{s^2 \left(2 + \imath g s - \sin^2 \theta K^2 \left(I + g s \right) \zeta^2 \right)}{s^3 - \sin^2 \theta K^2 s \zeta^2} \Rightarrow g \sim \frac{I}{2L^{2N-2}(1 + \cos \theta^2 + \ell^2 \sin^2 \theta K)} \tag{4.8}$$

This leads to the on-shell action (neglecting as usual the subleading terms):

$$W_1|_{\text{on-shell}} \sim 2N^2 \log L + N^2 \log(4Lc_1 c_2) + \ldots$$
$$c_1 = 1 + \cos \theta^2 + \ell^2 \sin^2 \theta, \quad c_2 = \omega \sin \theta. \tag{4.9}$$

It is easy to inspect W_1 and find that the leading contribution to the on-shell action value (4.9) comes from the term with $\log \det$ in (4.3). Now let us look at the two- and four-replica action. These lead to very cumbersome expressions which, however, do not present any principal difficulties so we do not write them out in full detail. The outcome reads

$$W_2|_{\text{on-shell}} \sim 4N^2 \log L + 2N^2 \log(4Lc_1 c_2) + \ldots$$
$$W_4|_{\text{on-shell}} \sim 8N^2 \log L + 4N^2 \log(4Lc_1 c_2) + \ldots \tag{4.10}$$

One can also check that nothing changes qualitatively when $\ell = 0$, i.e. when the strings intersect. The limit of parallel strings is subtler: taking the limit $\theta \to 0$ directly does not make sense as it gives a divergence in W_1; instead one should go back to the BPS solution (3.8) for the collective fields, which brings the old result $W_1|_{on-shell} = 4N^2 \log L$.

Obviously, from (4.10), the action always factorizes. But the interesting part is that the terms which contribute at (leading) order $N^2 \log L$ all come from the same term $\log \det (s^2 \ldots)$, obtained from the bosonic determinant upon integrating out the microscopic variables a_μ. Therefore, *interacting systems have partition functions which factorize trivially*. This is in contrast to the non-interacting (and specifically BPS) configurations where $\langle Z^4 \rangle$ factorizes nontrivially, from the sum of terms $\log \det s$ and $\log \det S$ (i.e., from both two-replica and four-replica couplings). An intuitive explanation would be the following: in BPS systems, the interactions (from gravity and from 2-form fields) precisely cancel out each other, but when multiple replicas are involved, there are combinations (like LR or $LLL'L'$) where this cancelation does not happen, so the structure of the effective action is different from that of a single replica (i.e. does not amount to four copies of a single replica). In the presence of interactions however, the dominant contribution to the free energy always comes from pairwise interactions: this is so for W_1, W_2, W_4 and for any W_n.

---

[13]The overall factor of four in these solutions compared to the solutions (3.9) and (3.26) comes from the fact that we now explicitly consider the four matrices A_μ, $\mu = 0 \ldots 3$; in section 3 we were working with a single matrix for simplicity.

4.1 Fermionic contributions

The fermionic contributions do not add anything fundamentally new to the picture, as they are subleading compared to the bosons. While the complete calculation is quite involved, it is easy to recognize the principle. Let us compute the fermionic contribution to the single-replica and two-replica actions. The fermionic contribution at leading order comes from the term $\bar{\psi}_\alpha \slashed{P} \psi_\alpha$ from (2.8). Using (4.1), integrating out the quenched degrees of freedom and then also the original fermionic fields ψ_α, we get the fermionic contribution in addition to the bosonic one from (4.2):

$$W_{1f} = \imath \sigma^\dagger \gamma + \frac{L^2}{4} \gamma (K \otimes I_{N^2 \times N^2}) \gamma - \text{Tr}(\gamma s^{-1} \gamma) - \log \det \left(\sigma - \frac{\ell}{2} \left(M \otimes I_{N^2 \times N^2} \right) \right)$$

$$M = I_{2 \times 2} \otimes \sigma_3 - \sigma_3 \otimes I_{2 \times 2}, \quad K = 2 I_{4 \times 4} + \ell \sin \theta M, \quad \gamma \sim \bar{\psi}_\alpha \psi_\alpha. \tag{4.11}$$

We remind that the matrices are now of size $2N \times 2N$, and therefore the superoperators are of size $4N^2 \times 4N^2$, so they are naturally regarded as block matrices of size 4×4 with each block of size $N^2 \times N^2$. That is why we have the four-by-four matrices in the expressions above. The contribution proportional to ℓ comes from the gap, i.e. the finite separation of the D-strings. To actually compute the saddle point solutions to (4.11) is not easy, but if we look at the doubled system:

$$W_{2f} = W_2 + \imath \text{Tr} \sigma^\dagger_{AB} \gamma_{AB} + \frac{L^2}{4} \gamma_{AB'} (K \otimes I_{N^2 \times N^2}) \gamma_{AB'} - \text{Tr} \left(\gamma_{AA} s^{-1}_{AA} \gamma_{AA} \right)$$

$$- \log \text{Tr} \left(\tilde{\sigma}_{LR} \tilde{\sigma}_{L'R'} - \tilde{\sigma}_{LL'} \tilde{\sigma}_{RR'} + \tilde{\sigma}_{L'R} \tilde{\sigma}_{LR'} \right),$$

$$\tilde{\sigma}_{AB'} \equiv \sigma_{AB'} - \frac{\ell}{2} M \otimes I_{N^2 \times N^2}, \tag{4.12}$$

with W_2 being the bosonic contribution from (4.10), we see that the only difference with respect to the parallel strings is the transformation $\sigma \mapsto \sigma - (\ell/2) M \otimes I_{N^2 \times N^2}$. However, the determinant (and the trace) of the matrix σ does not change under this transformation. This can be checked directly as M is a degenerate matrix, with two zero eigenvalues. Therefore, the solutions and the on-shell values of the effective action stay the same as before. We still have the multiple choices (3.34)–(3.38), where (3.36), the true vacuum, actually leads to nontrivial factorization, but they all contribute only subleading terms to the bosonic action. Therefore, even though the outcome is mixed (trivial factorization for bosons plus nontrivial for fermions), the picture at leading order remains the same, with or without fermionic contributions — the multi-replica solution factorizes trivially at leading order.

To wrap up, the leading order collective field description (i.e. a mean field description) reproduces the factorization of partition functions of fluctuating D_p-branes (the number of dimensions p plays no role here), nontrivially for BPS-stabilized branes and trivially for interacting branes. We will try to make a bigger picture out of this fact in the final section.

5 Discussion and conclusions

The main outcome of our adventure can be summarized in the following way: (1) the restoration of factorization with $n \geq 4$ replicas (2) the nonfactorization of the two-replica

system and the nontrivial factorization of the four-replica system for the noninteracting D-branes (3) the trivial factorization for any number of replicas in interacting D-brane systems (4) the absence of self-averaging. On one hand, the restoration of factorization is overall in line with the previous results from the literature for the SYK model [12, 15, 16, 23, 25] and the general expectation that our intuition should somehow survive so that the thermodynamic potentials of multiple independent copies of any system should just add up (i.e. the partition functions should just multiply). The points to ponder about are trivial vs. nontrivial factorization, the absence of self-averaging and above all the fact that we work with the IKKT model which is not a (fixed metric) field theory but is itself a quantum gravity system.

The absence of self-averaging, while in itself an important difference from the SYK and similar models, is maybe less surprising than it at first appears. Self-averaging means that the physics of the averaged model can be obtained as a small correction to a model with random fixed background (no matter which one!). That can only be true if the dynamics of the system is almost ergodic, i.e. if the system is strongly chaotic, perhaps only if it saturates the fast scrambling limit, like black holes and their dual field theories (such as the SYK model). Therefore, it is no surprise that self-averaging is never there for more general models. This has little to do with gravity in the IIB model; it only has to do with the fact that it is not (dual to) a black hole.[14] Thus we expect that a wide range of field theories will never be self-averaging (and the fact that our equations can be reinterpreted as the Eguchi-Kawai discretized Yang-Mills theory apparently corroborates that).

The trivial vs. nontrivial factorization is subtler. In the section 4 we have offered a somewhat handwaving explanation: the non-interacting nature of the BPS configurations is maintained by the precarious balance between different forces (in a single system), this balance is lost in multi-replica combinations and is only restored when the contributions from all combinations are included (this is the term $\log \det S_{AAB'B'}$). We have no proof that this will happen at all orders or for all BPS configurations. It is also not true that interacting systems necessarily have a trivial factorization. For example, the SYK model cannot in general be divided into mutually noninteracting subsystems, yet it factorizes nontrivially as found in [12, 23], in the sense that the factorization is restored roughly as $Z^2 \sim \text{WH} + \text{HWH}$, in other words *both* a wormhole and a half-wormhole contribute significantly. This is in contrast with our backgrounds, both BPS and non-BPS, where *only* half-wormholes contribute significantly and there is no WH+HWH solution. An additional caveat is the important insight of [23] that different collective field descriptions are possible, leading to different types of HWH solutions. It seems that the trivial factorization of interacting branes, with nonzero $F_{\mu\nu}$ terms, is really a consequence of the structure of interactions in the action of the IKKT model (eqs. (2.8)–(2.9)). It is an interesting task for future work to understand this better: is this a specific signature of theories with (quantum) gravity?

To answer that question, it would be useful to look at theories where we can directly construct interesting geometries, and interpret the disorder *geometrically*. This was done

---

[14]While the IKKT model should contain also the microscopic description of black holes, we don't know which background A_μ corresponds to that solution.

in [29], where a system of wrapped branes on complicated cycles within some compact manifold is represented as quiver quantum mechanics with a random superpotential. The basic strategy of our paper (modelling complicated solutions as effectively random, introducing the collective field formalism and then computing the effective action) is quite close to what was done in [29]. The authors find both replica-symmetric saddles and saddles which break the replica symmetry; the latter probably give rise to non-factorizing solutions whereas the former probably factorize.[15] In fact, as shown in [52], the same model in a different regime gives rise to ergodicity breaking already in classical dynamics, suggestive of glassy behavior. The appealing thing is that in this case the many local minima of the free energy have an obvious interpretation: these are geometries with multiple black holes, forming "molecules" [53] and a direct gravity analogue of structural glasses [54]. We hope to learn more about the factorization of leading saddles in such systems in our future work.

Speaking of (non)factorization, one technical point should be emphasized. We look mainly at averaged partition functions $\langle Z^n \rangle$ and find various saddle-point solutions to the effective actions obtained as $-\log\langle Z^n \rangle$. One could instead look directly at the average of the logarithm: $-\langle \log Z^n \rangle$. This latter variant is called the quenched free energy in the literature on disordered systems, whereas our effective actions W_n are called annealed free energies. The two differ precisely when the system is non-factorizing, and this criterion was used to explain the non-factorization due to replica wormholes in [47]. We use a slightly different criterion: direct comparison of annealed free energies for different numbers of replicas. For our purposes either of the two approaches (comparing $\log\langle Z^n \rangle$ to $\langle \log Z^n \rangle$ versus comparing $\log\langle Z^n \rangle$ among each other for different n) is suitable to check the factorization, although the difference between the two kinds of free energy is perhaps the more usual way in statistical physics.[16]

One might worry about the fact that we always disregard the terms which scale to zero as $L, N \to \infty$, i.e. the terms where L or N appears with a negative power. Indeed, we have not studied the behavior of such terms and there is no way to argue (except by performing additional calculations and checking explicitly) that these terms will obey the same factorization laws. However, even the starting ansatz for the background (with random Hermitian matrices) only makes sense for N large (otherwise we cannot speak of eigenvalue statistics), so the whole setup does not really address the regime of small N. Therefore, in the framework of our approach, the large-N results we find are sound.

In the context of very interesting findings of [27], one can also wonder if the D-branes of the IIB matrix model have a meaning analogous to the correlated bulk branes in 2D gravity models. In [27], such branes act as novel UV degrees of freedom which, when integrated out to arrive at an IR description, introduce nonlocalities in the gravity theory; in that paper it turns out that these nonlocalities save the factorization if tuned to a specific value. Essentially the same mechanism holds for our interacting D-branes — their interaction is also nonlocal and guarantees factorization for any number of replicas; when the (nonlocal) interaction is absent (in the BPS case), the factorization can be violated with $n = 2$ replicas,

---

[15]These are just our rough guesses; neither we nor [29] have explicitly checked the factorization of partition functions in this setup.

[16]We thank Souvik Banerjee for pointing out this issue.

and when restored it happens through a more complicated mechanism. We hope to reach a better understanding of this mechanism, and the relation to [27], in future work.

Finally, although we were motivated to look at (non)factorization by the puzzle arising from the replica wormholes in AdS/CFT (like most of the recent papers on the subject), this question is worth asking also on its own, as it is connected to dynamical and statistical properties of quantum gravity. Within our approach, we can in principle discuss also the matrix models of AdS geometries, with a CFT dual. One way would be to impose a background geometry along the lines of [55–57], by introducing a deformation of the action (2.1) to obtain matrices which satisfy the algebra of the generators of AdS isommetries. Another way is to consider a different matrix model, along the lines of [54, 58], which corresponds to D-particles in AdS. We discuss this briefly in appendix C, however a more complete treatment is again a task for future work.

Acknowledgments

A   Including the background fermions

Here we show that we do not lose anything by putting the background fermions to zero. Clearly this is a drastic change to the background as it destroys the supersymmetry and makes the on-shell action nonzero, but it should not strongly influence the factorization properties. The inclusion of background fermions merely shifts the action of the background to zero, but the background is frozen and not integrated over in the quenched regime. The dynamics and partition functions are determined by the fluctuations on top of the background, and these are not changed qualitatively when background fermions are included. Let us now show this explicitly, for a single degree of freedom (i.e., for noninteracting parallel D-strings). The outcome is that the fermionic fluctuations become even smaller (and for $\Psi = 0$, considered in the main text, they are already subleading to the bosonic ones), so our findings on factorization remain the same as those already found for bosonic fluctuations in sections 3 and 4.

Keeping nonzero Ψ and $\bar{\Psi}$, the action up to second order (we will not compute third- and fourth-order corrections) becomes:

$$S = S_1 + S_2 \tag{A.1}$$

$$S_1 = \mathrm{Tr}\left[\bar{\Psi}_\alpha \slashed{a} \Psi_\alpha + \bar{\Psi}_\alpha \slashed{P} \psi_\alpha + \bar{\psi}_\alpha \slashed{P} \Psi_\alpha\right] \tag{A.2}$$

$$S_2 = \mathrm{Tr}\left[-\frac{1}{4} a_\mu \left(P^2 \delta_{\mu\nu} + 2F_{\mu\nu}\right) a_\nu + \bar{\Psi}_\alpha \slashed{a} \psi_\alpha + \bar{\psi}_\alpha \slashed{a} \Psi_\alpha + \bar{\psi}_\alpha \slashed{P} \psi_\alpha\right]. \tag{A.3}$$

The steps analogous to eq. (3.27) leading to the effective action still consist of elementary Gaussian integrations, but we have a few extra terms. Comparing to the last line in (3.27), we have two extra terms in the action at second order:

$$W_1 = i\mathrm{Tr}\left(s^\dagger g + \sigma^\dagger \gamma\right) + V(g) + \Gamma(\gamma) - \mathrm{Tr}\left(\gamma s^{-1}\gamma\right) + \log\det\sigma + \frac{1}{4}\left(g\gamma + \gamma g\right) + \frac{1}{2}\left(\gamma\sigma^{-1} + \sigma^{-1}\gamma\right),$$

(A.4)

the last two terms being absent when $\Psi = 0$. The equations of motion for s are unchanged compared to (3.28) but the others change:

$$\frac{2}{L^{2N-2}}I + is + \frac{1}{2}\gamma = 0, \qquad ig + \frac{1}{2}\left(s^{-1}\right)^T + \gamma s^{-2}\gamma = 0$$

$$i\sigma + \frac{L^2}{2}\gamma - \frac{1}{4}\left(\gamma s^{-1} + s^{-1}\gamma\right) + \frac{1}{2}g + \frac{1}{2}\sigma^{-1} = 0$$

$$i\gamma + \left(\sigma^{-1}\right)^T - \left(\gamma\sigma^{-2} + \sigma^{-2}\gamma\right) = 0.$$

(A.5)

The relation between s and g is obviously unaffected, so we can express g in terms of s and insert in the remaining equations. The solution (ignoring the contributions which go to zero for large N and L) reads

$$s = \frac{4i}{L^{2N-2}}I \otimes E, \quad g = \frac{L^{2N-2}}{8}I \otimes E, \quad \sigma = -\frac{iL^{2N-4}}{8}I \otimes E, \quad \gamma = \frac{4}{L^{2N-2}}I \otimes E. \quad (A.6)$$

Inserting this into the action W_1, we find that both the first and the second extra term in the action are negligible since they scale as 1 and $1/L^{4N-4}$ respectively, the old fermionic terms are even more strongly subleading, and $\log\det\sigma$ doubles with respect to the on-shell value of W_1 found in eq. (3.8). The same doubling will occur also for a multiple-replica configuration, since the relation between σ and γ (the fourth equation in (3.33)) changes only trivially when we consider multiple copies of the system: all terms get the replica indices but there are no new terms — compare the mentioned equation in (3.33) and the third equation in (3.28).

One caveat remains: as mentioned in the main text, there is no guarantee that we have found all solutions. It is thus possible that solutions with less symmetry exist which change qualitatively in the presence of background fermions. Our numerical explorations (figure 2) suggest that this is unlikely, but clearly there is no rigorous proof.

B   Hard vs. soft cutoff for matrix eigenvalues

In this appendix we will rederive some of our results assuming the uniform distribution of the eigenvalues of the background matrices A_μ within some compactification interval: $-L_\mu \leq \lambda_i^\mu \leq L_\mu$. This is the usual picture in the IKKT model [30, 34].[17] From now on we again equate all compactification radii, so that $L_\mu \equiv L$. We will see that, apart from

---

[17]Sometimes in the literature the factor $L_\mu/\sqrt{2\pi N}$ is pulled in front of the matrices A_μ, so the eigenvalues are distributed between $\pm\sqrt{2\pi L_\mu}$ and the commutators between A_μ's are just i with no prefactors. We have adopted the conventions of [34] in this paper, where the eigenvalues are between $\pm L_\mu$ and the commutator acquires additional prefactors as in (2.5).

numerical factors of order unity, nothing changes compared to the Gaussian soft cutoff. The reason is essentially that we are looking at the quenched IKKT/large-N Yang-Mills model, expanding in small fluctuations a_μ, ψ_α and in large cutoff/compactification radius L; it is thanks to this quenched dynamics that the system is largely insensitive on the details of the eigenvalue distribution of the semiclassical background. If the matrices A_μ were annealed and not quenched, i.e. if we were to study the full dynamics of the background, this would not be true and we would have to be careful about the regulator. This point is explained in detail in [28] where the averaged theory depends crucially on the UV closure because in the setups of [28] both fast and slow degrees of freedom are dynamical.

Let us start from the defining expression for the single averaged partition function (3.3):

$$\langle Z \rangle = \int D[A_\mu] \int D[a_\mu] e^{-S(a_\mu; A_\mu)} \mathcal{P}(A_\mu) = \int D[a_\mu] \int_{-L_\mu}^{L_\mu} d^{2N} \lambda_\mu^i e^{-S(a_\mu; \lambda_\mu^i)}, \tag{B.1}$$

where we have now emphasized that the limits of integration for λ_μ^i are between $-L$ and L. Proceeding along the same lines as before, this yields the integral

$$\langle Z \rangle = \int D[a_\mu] \int_{-L}^{L} d^{2N} \lambda_{\mu i} \Pi_{i<j} (\lambda_{\mu i} - \lambda_{\mu j})^2 \exp\left[-\frac{1}{4} a_{\mu ij}^\dagger \left(\lambda_{\mu i}^2 + \lambda_{\mu j}^2\right) a_{\mu kl} \delta_{jk} \delta_{il}\right]$$

$$= \int D[a_\mu] e^{-W_1} \tag{B.2}$$

$$W_1 = \frac{1}{2} \sum_\mu \log \det \left(2 a_\mu^\dagger a_\mu - 2I \mathrm{Tr} a_\mu^\dagger a_\mu\right) - \log \mathrm{Erf} \left(L \sqrt{\frac{1}{2} \mathrm{Tr} a_\mu^\dagger a_\mu}\right). \tag{B.3}$$

The error function Erf in the result is quite difficult to work with (we understand the error function of a matrix and in general functions of matrices in the usual way). But when we expand in a_μ small just like we did in the last line of (3.6) the result simplifies:

$$W_1 = a_\mu^\dagger a_\mu - \frac{4}{3} I \mathrm{Tr} a_\mu^\dagger a_\mu + O\left(\left(a_\mu^\dagger a_\mu\right)^4\right) \mapsto \frac{1}{2} \log \det s + i \mathrm{Tr} s^\dagger g + \frac{2}{3L^{2N-2}} \mathrm{Tr} g. \tag{B.4}$$

In the above equation, we have first performed a straightforward series expansion of the effective action W_1 in (B.3), and then we have introduced the collective field $g = a_\mu^\dagger a_\mu$ just like with the Gaussian cutoff. As we see, the additional error function terms, when expanded to quadratic order, merely change the coefficients in front of some of the terms. From here it is already obvious that the whole logic will remain the same as before; we believe there is no reason to repeat all the calculations again, as the factorization does not depend on the numerical coefficients (if say the term $\mathrm{Tr} g$ has a different coefficient, the same coefficient will remain also in the two-replica term $\mathrm{Tr} g_{AA}$, and the same holds for the potentials $V(g_{AA})$).

Now we show the same result for the fermionic fluctuations. Starting from the basic expression (3.27) we can write

$$\langle Z \rangle = \int D[a_\mu] \int D[\bar{\psi}_\alpha] \int D[\psi_\alpha] \int_{-L}^{L} d^{2N} \lambda_{\mu i} \Pi_{i<j} (\lambda_{\mu i} - \lambda_{\mu j})^2 \exp\left[-\frac{1}{2} a_\mu^\dagger P^2 a_\mu - \frac{1}{2} \bar{\psi}_\alpha \slashed{P} \psi_\alpha\right]$$

$$= \int D[a_\mu] \int D[\bar{\psi}_\alpha] \int D[\psi_\alpha] e^{-W_1}$$

$$e^{-W_1} = \sqrt{\frac{\pi}{2 a_\mu^\dagger a_\mu}} e^{\frac{(\bar{\psi}_\alpha \psi_\alpha)^2}{2 a_\mu^\dagger a_\mu}} \left[\mathrm{Erf}\left(\frac{L a_\mu^\dagger a_\mu + \bar{\psi}_\alpha \psi_\alpha}{\sqrt{2 a_\mu^\dagger a_\mu}}\right) - \mathrm{Erf}\left(\frac{-L a_\mu^\dagger a_\mu + \bar{\psi}_\alpha \psi_\alpha}{\sqrt{2 a_\mu^\dagger a_\mu}}\right)\right], \tag{B.5}$$

where it is understood that expressions of the form $(\bar{\psi}_\alpha \psi_\alpha)^2/2a_\mu^\dagger a_\mu$ really mean $(2a_\mu^\dagger a_\mu)^{-1}(\bar{\psi}_\alpha \psi_\alpha)^2$, i.e. we divide by matrices the usual way, by multiplying by the matrix inverse. The result (B.5) is quite involved, but a series expansion again brings it to the form quite close to the Gaussian result (3.27):

$$W_1 = a_\mu^\dagger a_\mu - I \mathrm{Tr} a_\mu^\dagger a_\mu + \frac{L^2}{6}\left(\bar{\psi}_\alpha \psi_\alpha\right)^2 + O\left(\left(a_\mu^\dagger a_\mu\right)^4 + \left(\bar{\psi}_\alpha \psi_\alpha\right)^4\right) \Rightarrow$$

$$\Rightarrow W_1 = \imath \mathrm{Tr}\left(s^\dagger g + \sigma^\dagger \gamma\right) + V(g) + \Gamma(\gamma) + \log \det \sigma, \quad \Gamma(\gamma) = \frac{L^2}{6}\gamma^2, \qquad (B.6)$$

and $V = V_2 + V_4$ remains unchanged from (3.12). The only change with respect to the Gaussian eigenvalue statistics is the coefficient in $\Gamma(\gamma)$, being $L^2/6$ instead of $L^2/4$. Therefore, the story remains the same: while the on-shell values of the actions W_n will change, the (non)factorization properties will not, as the coefficient change in Γ affects equally the actions W_n with any number n of replicas.

C   Toward a holographic interpretation

So far, as we have mentioned in the Introduction, the connection of this work to AdS/CFT is only indirect, as the simple D-string configurations that we consider do not have an obvious CFT dual. We have also argued that it is nevertheless very relevant to know the factorization properties of theories with gravity, precisely in order to know if the restoration of factorization through half-wormholes despite the existence of non-factorizing wormhole saddles is a specific twist of holography or rather a generic phenomenon. But then again a realization of AdS replica wormholes, with a dual CFT, in the framework of IKKT model is clearly a worthy and exciting task. It is an open problem how to derive the holographic duality within the IKKT model, certainly deserving a separate work; here we just outline some ideas.

Recall first that the IIB matrix model at leading order coincides with the Eguchi-Kawai model of discretized 10-dimensional Yang-Mills theory [36]. Hence, there is a direct relation to a quantum field theory: all the partition functions we have calculated can be reinterpreted as field-theoretical partition functions of the Eguchi-Kawai system, and these should factorize for a set of non-interacting replicas.

The second thing to note is that the IKKT model, describing the type IIB string theory, should contain also the celebrated D3 brane background which gives rise to gravity on $\mathrm{AdS}_5 \times \mathbb{S}^5$, dual to the $\mathcal{N} = 4$ superconformal Yang-Mills. However, we do not know yet how to find such a solution explicitly in terms of matrices. A stack of parallel D3 branes is completely analogous to a pair of parallel strings that we consider, just with 4 matrices instead of 2. But the AdS geometry is not explicit in such a solution, as the starting action and its solutions (2.4) in terms of random Hermitian matrices still describe branes in flat space — the starting action already assumes a background, because the Schild action in the first place also describes strings on flat background. Therefore, we could in principle repeat the averaging over some set of fluctuating AdS configurations with our formalism but it is not known what this set should be.

For this reason, there is a much studied idea [55, 56] to impose a geometric symmetry by deforming the model so that the matrices satisfy the commutation relations of the corresponding isommetries. For example, [57] realizes the (Lorentzian) AdS$_2$ geometry by imposing the structure of SO$(2,1)$ algebra. In our (Euclidean) case, the group is SO$(1,2)$ and the deformed model reads:[18]

$$S = -\text{Tr}\left(\frac{1}{4}\left[X_\mu, X_\nu\right]^2 + cf_{\mu\nu\rho}\left[X_\mu, X_\nu\right]X_\rho\right), \tag{C.1}$$

where $f_{\mu\nu\rho}$ are the structure constants of SO$(1,2)$,[19] and c is the coupling constant. Classical equations of motion now read (putting again the background fermions to zero):

$$\left[X^\mu, \left[X_\mu, X_\nu\right]\right] + gf_{\nu\rho\sigma}\left[X_\rho, X_\sigma\right] = 0. \tag{C.2}$$

But the solution to this equation has to satisfy a nontrivial commutation relation, so it is more restricted than the IKKT brane solutions, where for $N \to \infty$ *any* commuting random matrices form a solution. Neverthless, for N large, the three commutation relations do not much reduce the space of solutions, and all but three eigenvalues can still be chosen at random from some interval (in other words, any reducible representation of $so(1,2)$, combined form arbitrary irreducible representations, is a solution). The fluctuating solutions of the form $X_\mu = A_\mu + a_\mu$ now yield the following structure of the quenched action up to second order, analogous to (2.8):

$$S_2 = \text{Tr}\Bigg[-\frac{1}{4}a_\mu\left(P^2\delta_{\mu\nu} + 2F_{\mu\nu}\right)a_\nu - \imath cf_{\mu\nu\rho}\Big(\left[a_\mu, A_\nu\right]A_\rho + \left[A_\mu, a_\nu\right]A_\rho + \left[A_\mu, A_\nu\right]a_\rho$$
$$+ \left[a_\mu, a_\nu\right]A_\rho + \left[a_\mu, A_\nu\right]a_\rho + \left[A_\mu, a_\nu\right]a_\rho\Big)\Bigg]. \tag{C.3}$$

We will not consider the third- and fourth-order terms. For the equations of motion (C.2), the superoperators are expressed as $P_\mu = A_\mu \otimes I + I \otimes A_\mu$ and $F_{\mu\nu} = -f_{\mu\nu\rho}A_\rho$. Making use of that and the antisymmetry of the structure constants, we arrive at the simplified action for the fluctuations:

$$S_2 = -\frac{1}{4}a_\mu\left[P^2\delta_{\mu\nu} + 2f_{\mu\nu\rho}\left(A_\rho - 8cP_\rho - 4c\Pi A_\rho\right)\right]a_\nu - 2cf_{\mu\nu\rho}P_\nu A_\rho a_\mu, \tag{C.4}$$

where $\Pi \equiv \sigma_3 \otimes I - I \otimes \sigma_3$. Here we will be somewhat sloppy: integrating over the background A_μ requires us to know the statistical properties of eigenvalues and traces of the $so(1,2)$ representations. These are known from the literature (see e.g. the references in [56]) but the calculation goes beyond the scope of this short appendix. For large N the central limit theorems suggest that it still makes sense to assume that the eigenvalues are only

---

[18]It is not entirely clear if the fermionic part should receive any deformations, but it is hard to think of any other meaningful term involving $\bar{\Psi}, \Psi$ which satisfies the necessary symmetries. In any case, in this appendix we will ignore the fermions completely, as we only want to provide a roadmap to a hologrpahic setup, not to perform a precise calculation.

[19]Although the commutator of classical solutions was denoted by $f_{\mu\nu}$, there can be no confusion as the structure constants have three indices instead of two, and in this appendix we will not make use of the commutators $f_{\mu\nu}$ anyway.

weakly correlated (which we approximate with totally uncorrelated), and limited by some cutoff function which we assume to be Gaussian, as we have shown in appendix B that the outcome is not sensitive to cutoff. In this case, paralleling the steps in the sections 3 and 4, we find the effective action for a single copy:

$$W_1 = \left(\frac{I}{2L^2} + 2a_\mu^\dagger a_\mu + 8c \left(a_\mu^\dagger + a_\mu \right) - 2I \mathrm{Tr} a_\mu^\dagger a_\mu \right) + \frac{1}{2L^2} \left(a_\mu^\dagger f_{\mu\nu\rho} \left(1 - 8c - 4c\Pi \right) a_\nu \right)^2 \mapsto$$

$$\mapsto W_1 + \imath s^\dagger s + \imath \zeta_{\mu\nu}^\dagger K_{\mu\nu}, \quad g \sim a_\mu^\dagger a_\mu, \ K_{\mu\nu} \sim a_\mu^\dagger a_\nu + a_\nu^\dagger a_\mu. \tag{C.5}$$

Therefore, because of the deformation, we have an additional set of collective fields $K_{\mu\nu}$ and the corresponding auxiliary fields $\zeta_{\mu\nu}$. Obviously, this is an interacting system, unlike the BPS parallel branes from section 3. Integrating out a_μ, we get the effective action in the form:

$$W_1 = \frac{3}{2} \log \det s^2 + \frac{3}{2} \log \det \zeta_{\mu\nu}^2 + 3\tilde{V}_2(g) - \frac{1 - 8c}{2L^2} \mathrm{Tr} K_{\mu\nu} + \imath s^\dagger g + \imath \zeta_{\mu\nu}^\dagger K_{\mu\nu}$$

$$\tilde{V}_2(g) = \frac{2 - 32c^2}{L^{2N-2}} g. \tag{C.6}$$

In a system with four replicas, we get a result of the form

$$W_4 = 6 \log \det s^2 + 6 \log \det \zeta_{\mu\nu}^2 + 3\tilde{V}_2(g_{AA}) + \tilde{W}_4 \left(s_{AA}, g_{AA}; \zeta_{AAB'B;\mu\nu}, K_{AAB'B';\mu\nu} \right)$$

$$- \frac{1 - 8c}{2L^2} \mathrm{Tr} K_{AA;\mu\nu} + \imath s_{AA}^\dagger g_{AA} + \imath \zeta_{AAB'B';\mu\nu}^\dagger K_{AAB'B';\mu\nu}. \tag{C.7}$$

We do not need detailed expressions for $\tilde{W}_4$ (although tedious, they are straightforward to find). The key point is that, just like the findings (4.9)–(4.10) for a pair of interacting D-strings, the term $\log \det s^2$ always dominates, with the solutions $g = 3\imath s^{-1}$ and $s = -(2 + 32c^2)/L^{2N-2}\imath I$. Finally, this yields

$$W_n \sim -6nN^2 \log L + 3nN \log(2 + 32c^2) + \dots, \tag{C.8}$$

hence we again have trivial factorization.

A big caveat is in order: the interpretation of this and similar models is different from D-branes in the IKKT model; the bosonic matrices X_μ are not branes but quantized (non-commuting) coordinates [55, 56]. Besides, we have not properly derived the eigenvalue distribution for the background. The connection to the IIB matrix model is thus rather indirect. In fact, the main limitation in applying this scheme directly to holographic setups lies in the general lack of knowledge on how to encode AdS/CFT (i.e., the corresponding AdS backgrounds) in the IKKT action; the general idea and the formalism itself remains applicable for any background.

As a side note, another possible connection of D-brane matrix models to AdS backgrounds is the quiver matrix model of [58] (see also the references therein), where D-particles in AdS are described by a supersymmetric matrix action in $0 + 1$ dimension, i.e. with a time derivative, hence only the static limit fits into our formalism. This setup is less directly related to the IKKT model, so we do not have a precise idea on what the meaningful background solutions would look like and what the averaging would give.

References

[1] A. Almheiri, T. Hartman, J. Maldacena, E. Shaghoulian and A. Tajdini, *Replica wormholes and the entropy of Hawking radiation*, *JHEP* **05** (2020) 013 [arXiv:1911.12333] [INSPIRE].

[2] G. Penington, S.H. Shenker, D. Stanford and Z. Yang, *Replica wormholes and the black hole interior*, *JHEP* **03** (2022) 205 [arXiv:1911.11977] [INSPIRE].

[3] A. Almheiri, T. Hartman, J. Maldacena, E. Shaghoulian and A. Tajdini, *The entropy of Hawking radiation*, *Rev. Mod. Phys.* **93** (2021) 035002 [arXiv:2006.06872] [INSPIRE].

[4] Y. Sekino and L. Susskind, *Fast scramblers*, *JHEP* **10** (2008) 065 [arXiv:0808.2096] [INSPIRE].

[5] S.H. Shenker and D. Stanford, *Stringy effects in scrambling*, *JHEP* **05** (2015) 132 [arXiv:1412.6087] [INSPIRE].

[6] J. Maldacena, S.H. Shenker and D. Stanford, *A bound on chaos*, *JHEP* **08** (2016) 106 [arXiv:1503.01409] [INSPIRE].

[7] F. Haake, *Quantum signatures of chaos*, Springer (2004).

[8] M.D. Mehta, *Random matrices*, Elsevier (2004).

[9] A. Altland and J. Sonner, *Late time physics of holographic quantum chaos*, *SciPost Phys.* **11** (2021) 034 [arXiv:2008.02271] [INSPIRE].

[10] A. Belin and J. de Boer, *Random statistics of OPE coefficients and Euclidean wormholes*, *Class. Quant. Grav.* **38** (2021) 164001 [arXiv:2006.05499] [INSPIRE].

[11] D. Stanford, *More quantum noise from wormholes*, arXiv:2008.08570 [INSPIRE].

[12] P. Saad, S.H. Shenker, D. Stanford and S. Yao, *Wormholes without averaging*, arXiv:2103.16754 [INSPIRE].

[13] P. Saad, S. Shenker and S. Yao, *Comments on wormholes and quantization*, arXiv:2107.13130 [INSPIRE].

[14] J. Maldacena and D. Stanford, *Comments on the Sachdev-Ye-Kitaev model*, *Phys. Rev. D* **94** (2016) 106002 [arXiv:1604.07818] [INSPIRE].

[15] B. Mukhametzhanov, *Half-wormhole in SYK with one time point*, *SciPost Phys.* **12** (2022) 029 [arXiv:2105.08207] [INSPIRE].

[16] B. Mukhametzhanov, *Factorization and complex couplings in SYK and in Matrix Models*, arXiv:2110.06221 [INSPIRE].

[17] S. Choudhury and K. Shirish, *Wormhole calculus without averaging from $O(N)^{q-1}$ tensor model*, *Phys. Rev. D* **105** (2022) 046002 [arXiv:2106.14886] [INSPIRE].

[18] A.M. García-García and V. Godet, *Half-wormholes in nearly AdS_2 holography*, *SciPost Phys.* **12** (2022) 135 [arXiv:2107.07720] [INSPIRE].

[19] A.M. García-García and V. Godet, *Euclidean wormhole in the Sachdev-Ye-Kitaev model*, *Phys. Rev. D* **103** (2021) 046014 [arXiv:2010.11633] [INSPIRE].

[20] T.-G. Zhou, L. Pan, Y. Chen, P. Zhang and H. Zhai, *Disconnecting a traversable wormhole: Universal quench dynamics in random spin models*, *Phys. Rev. Res.* **3** (2021) 022024 [arXiv:2009.00277] [INSPIRE].

[21] K. Goto, Y. Kusuki, K. Tamaoka and T. Ugajin, *Product of random states and spatial (half-)wormholes*, *JHEP* **10** (2021) 205 [arXiv:2108.08308] [INSPIRE].

[22] B. Freivogel, D. Nikolakopoulou and A.F. Rotundo, *Wormholes from averaging over states*, arXiv:2105.12771 [INSPIRE].

[23] K. Goto, K. Suzuki and T. Ugajin, *Factorizing wormholes in a partially disorder-averaged SYK model*, *JHEP* **09** (2022) 069 [arXiv:2111.11705] [INSPIRE].

[24] F.S. Nogueira, S. Banerjee, M. Dorband, R. Meyer, J.v.d. Brink and J. Erdmenger, *Geometric phases distinguish entangled states in wormhole quantum mechanics*, *Phys. Rev. D* **105** (2022) L081903 [arXiv:2109.06190] [INSPIRE].

[25] S. Banerjee, M. Dorband, J. Erdmenger, R. Meyer and A.-L. Weigel, *Berry phases, wormholes and factorization in AdS/CFT*, *JHEP* **08** (2022) 162 [arXiv:2202.11717] [INSPIRE].

[26] M. Berkooz, N. Brukner, S.F. Ross and M. Watanabe, *Going beyond ER=EPR in the SYK model*, *JHEP* **08** (2022) 051 [arXiv:2202.11381] [INSPIRE].

[27] A. Blommaert, L.V. Iliesiu and J. Kruthoff, *Gravity factorized*, arXiv:2111.07863 [INSPIRE].

[28] J.J. Heckman, A.P. Turner and X. Yu, *Disorder averaging and its UV discontents*, *Phys. Rev. D* **105** (2022) 086021 [arXiv:2111.06404] [INSPIRE].

[29] D. Anninos, T. Anous and F. Denef, *Disordered quivers and cold horizons*, *JHEP* **12** (2016) 071 [arXiv:1603.00453] [INSPIRE].

[30] N. Ishibashi, H. Kawai, Y. Kitazawa and A. Tsuchiya, *A large-N reduced model as superstring*, *Nucl. Phys. B* **498** (1997) 467 [hep-th/9612115] [INSPIRE].

[31] H. Aoki, S. Iso, H. Kawai, Y. Kitazawa and T. Tada, *Space-time structures from type IIB matrix model*, *Prog. Theor. Phys.* **99** (1998) 713 [hep-th/9802085] [INSPIRE].

[32] I. Chepelev, Y. Makeenko and K. Zarembo, *Properties of D-branes in matrix model of IIB superstring*, *Phys. Lett. B* **400** (1998) 40.

[33] H. Aoki, S. Iso, H. Kawai, Y. Kitazawa, A. Tsuchiya and T. Tada, *IIB matrix model*, *Prog. Theor. Phys. Suppl.* **134** (1999) 47 [hep-th/9908038] [INSPIRE].

[34] K.L. Zarembo and Yu. M. Makeenko, *Vvedenie v matrichnye modeli superstrun* (in Russian), *Usp. Fiz. Nauk* **168** (1998) 3.

[35] B. Ydri, *Review of M(atrix)-theory, type IIB matrix model and matrix string theory*, arXiv:1708.00734 [INSPIRE].

[36] T. Eguchi and H. Kawai, *Reduction of dynamical degrees of freedom in the large-N gauge theory*, *Phys. Rev. Lett.* **48** (1982) 1063 [INSPIRE].

[37] H. Kawai and M. Sato, *Perturbative Vacua from IIB Matrix Model*, *Phys. Lett. B* **659** (2008) 712 [arXiv:0708.1732] [INSPIRE].

[38] H. Kawai, S. Kawamoto, T. Kuroki, T. Matsuo and S. Shinohara, *Mean field approximation of IIB matrix model and emergence of four-dimensional space-time*, *Nucl. Phys. B* **647** (2002) 153 [hep-th/0204240] [INSPIRE].

[39] S.-W. Kim, J. Nishimura and A. Tsuchiya, *Expanding (3+1)-dimensional universe from a Lorentzian matrix model for superstring theory in (9+1)-dimensions*, *Phys. Rev. Lett.* **108** (2012) 011601 [arXiv:1108.1540] [INSPIRE].

[40] J. Nishimura and A. Tsuchiya, *Complex Langevin analysis of the space-time structure in the Lorentzian type IIB matrix model*, *JHEP* **06** (2019) 077 [arXiv:1904.05919] [INSPIRE].

[41] F.R. Klinkhamer, *On the emergence of an expanding universe from a Lorentzian matrix model*, *PTEP* **2020** (2019) 103 [arXiv:1912.12229] [INSPIRE].

[42] F.R. Klinkhamer, *A first look at the bosonic master-field equation of the IIB matrix model*, *Int. J. Mod. Phys. D* **30** (2021) 2150105 [arXiv:2105.05831] [INSPIRE].

[43] N. Kawahara and J. Nishimura, *The large N reduction in matrix quantum mechanics: A bridge between BFSS and IKKT*, *JHEP* **09** (2005) 040 [hep-th/0505178] [INSPIRE].

[44] J.M. Maldacena and L. Maoz, *Wormholes in AdS*, *JHEP* **02** (2004) 053 [hep-th/0401024] [INSPIRE].

[45] Y. Chen, V. Gorbenko and J. Maldacena, *Bra-ket wormholes in gravitationally prepared states*, *JHEP* **02** (2021) 009 [arXiv:2007.16091] [INSPIRE].

[46] D. Marolf and H. Maxfield, *Transcending the ensemble: baby universes, spacetime wormholes, and the order and disorder of black hole information*, *JHEP* **08** (2020) 044 [arXiv:2002.08950] [INSPIRE].

[47] N. Engelhardt, S. Fischetti and A. Maloney, *Free energy from replica wormholes*, *Phys. Rev. D* **103** (2021) 046021 [arXiv:2007.07444] [INSPIRE].

[48] J.-M. Schlenker and E. Witten, *No ensemble averaging below the black hole threshold*, *JHEP* **07** (2022) 143 [arXiv:2202.01372] [INSPIRE].

[49] H. Verlinde, *Wormholes in quantum mechanics*, arXiv:2105.02129 [INSPIRE].

[50] J. Nishimura and G. Vernizzi, *Spontaneous breakdown of Lorentz invariance in IIB matrix model*, *JHEP* **04** (2000) 015 [hep-th/0003223] [INSPIRE].

[51] J. Nishimura and G. Vernizzi, *Brane world generated dynamically from string type IIB matrices*, *Phys. Rev. Lett.* **85** (2000) 4664 [hep-th/0007022] [INSPIRE].

[52] D. Anninos, T. Anous, F. Denef, G. Konstantinidis and E. Shaghoulian, *Supergoop dynamics*, *JHEP* **03** (2013) 081 [arXiv:1205.1060] [INSPIRE].

[53] D. Anninos, T. Anous, P. de Lange and G. Konstantinidis, *Conformal quivers and melting molecules*, *JHEP* **03** (2015) 066 [arXiv:1310.7929] [INSPIRE].

[54] D. Anninos, T. Anous, F. Denef and L. Peeters, *Holographic vitrification*, *JHEP* **04** (2015) 027 [arXiv:1309.0146] [INSPIRE].

[55] H. Steinacker, *Emergent geometry and gravity from matrix models: an introduction*, *Class. Quant. Grav.* **27** (2010) 133001 [arXiv:1003.4134] [INSPIRE].

[56] H. Steinacker, *Non-commutative geometry and matrix models*, *PoS* **QGQGS2011** (2011) 004 [arXiv:1109.5521] [INSPIRE].

[57] D. Jurman and H. Steinacker, *2D fuzzy anti-de Sitter space from matrix models*, *JHEP* **01** (2014) 100 [arXiv:1309.1598] [INSPIRE].

[58] T. Anous and C. Cogburn, *Mini-BFSS matrix model in silico*, *Phys. Rev. D* **100** (2019) 066023 [arXiv:1701.07511] [INSPIRE].

Emerging Fermi liquids from regulated quantum electron stars

Nicolas Chagnet,[a] **Vladan Đukić,**[b,c] **Mihailo Čubrović**[b] **and Koenraad Schalm**[a]

[a]*Institute Lorentz for Theoretical Physics, Δ-ITP, Leiden University,*
Niels Bohrweg 2, Leiden, The Netherlands

[b]*Center for the Study of Complex Systems, Institute of Physics Belgrade,*
University of Belgrade, Pregrevica 118, 11080 Belgrade, Serbia

[c]*Department of Physics, University of Belgrade,*
Studentski Trg 12-16, 11000 Belgrade, Serbia

E-mail: chagnet@lorentz.leidenuniv.nl, vdjukicns@gmail.com,
cubrovic@ipb.ac.rs, kschalm@lorentz.leidenuniv.nl

ABSTRACT: We construct a fully quantum zero-temperature electron star in a soft-wall regulated anti-de-Sitter Einstein-Maxwell-Dirac theory that is thermodynamically stable compared to the Reissner-Nordström black hole. The soft wall only acts on the effective mass of the fermionic degrees of freedom, and allows for a controlled fully backreacted solution. The star is holographically dual to an RG flow where a gapped Fermi liquid starts to emerge from a UV CFT, but decouples again once the effective energy scale becomes lower than the gap of the fermionic degrees of freedom. The RG flow then returns to a non-trivial strongly coupled relativistic fixed point with a holographic dual. Our regulated quantum electron star is thus the fermionic analogue of the Horowitz-Roberts-Gubser-Rocha AdS-to-AdS domain wall solution for the holographic superconductor.

https://doi.org/10.1007/JHEP08(2022)222

Contents

1 Introduction

Strongly correlated electrons at finite density remain a deep and interesting puzzle, encountered in various quantum-many body systems, from condensed matter to heavy ion physics to astrophysics. Apart from some special cases, Fermi liquids are the only interacting fermionic systems at finite density where we have good control. A breakthrough was provided by the application of AdS/CFT to finite density large N-matrix fermionic systems. This allowed new strongly coupled IR fixed points characterized by an emergent Lifshitz scaling with dynamical critical exponent z to be discovered.[1] Though many of such results were found in bottom-up holographic models where only bosonic operators are tracked, there is reason to believe that any holographic finite density systems must also have microscopic fermionic degrees of freedom. Indeed a number of these holographically discovered fixed points have now been independently confirmed as Sachdev-Ye-Kitaev-like large N quantum spin-liquid fermionic ground states, where the additional microscopic description allows valuable extra insights into the workings of these novel states of matter.

---

[1] At finite N these fixed points may be not be true IR fixed points but intermediate scale attractors in the RG flow.

In holography these new ground states are qualitatively understood to arise as a deconfined phase of an underlying microscopic theory with the confined phase corresponding to a conventional Fermi liquid; see [1]. A dozen years ago this was a hotly debated topic and it was found that the prototypical deconfined state, characterized by the AdS$_2$, $z = \infty$ near horizon dynamics of AdS Reissner-Nordstrom (RN) black holes and an associated multitude N of non-Fermi-liquid Fermi surfaces [2–4] in the Thomas-Fermi limit of $N \to \infty$ indeed transitions at low temperatures to a charged Tolman-Oppenheimer-Volkov electron star [5–9]. These states are partially confined-partially deconfined in that they still have a finite z Lifshitz horizon; for a review and the transport responses of these states, see [10, 11].

However, away from the Thomas-Fermi limit a holographic description of a direct single Fermi-surface deconfined non-Fermi-liquid-to-confined Fermi-liquid $T = 0$ quantum phase transition has so far not yet been found. In the bulk, this problem corresponds to solving an Einstein-Maxwell-Dirac system in a self-consistent way, accounting for the backreaction of fermions on geometry, but keeping the number of Fermi surfaces finite or specifically keeping only one. The distinct puzzle here is that the signal of the putative instability towards confinement at low temperature — a log-oscillatory response in the single fermion spectral function [4] — occurs at a distinct point in parameter space from the one where the first stable Fermi surface is located (figure 1). In [12] an electron star model is introduced where N is finite but still very large; this hinted at a first order rather than a continuous transition. Approaching the question from the other side, a holographic description of confined single Fermi surface Fermi-liquid was constructed in [13] by enforcing confinement through a hard wall IR cut-off [13]. This confirmed that confinement-deconfinement is the correct viewpoint of the quantum phase transition, but did not yet include the gravitational backreaction. The most comprehensive study to date is the attempt at quantum electron star model of [14, 15] which regulates the system by putting it on a sphere and then tries to carefully remove this regularization procedure for a self-consistent solution of the Einstein-Maxwell-Dirac equations in the asymptotic AdS background.

The simple hard-wall solution of [13] already illustrates the fundamental problem. In the presence of an occupied Fermi surface the gravitational backreaction is uncontrolled, see [14, 15]. These subsequent papers then address this by a second cut-off for the backreaction, and then attempt to remove both cut-offs in a precarious balancing act. In the present paper we address this in a different way. We construct a fully gravitionally backreacted single-Fermi surface solution confined through a soft rather than a hard wall. From the gravitational point of view this soft wall determines the deep interior boundary conditions of the fermionic wave functions instead of the horizon geometry. As illustrated in detail in [14, 15] at the technical level the puzzle is that with the vanishing of the horizon (signalling deconfinement) at the quantum phase transition, not only must one find a new self-consistent (confining) IR geometry, but also an associated set of self-consistent boundary conditions for the fermion wave-function.

Because the confining boundary conditions suppress the fermion wave function in the IR, there is also no associated backreaction in the deep IR, which remains AdS. This confined regulated quantum electron star (rQES) is therefore the fermionic analogue of the Horowitz-Roberts-Gubser-Rocha AdS$_4$-to-AdS$_4$ groundstate/domain wall for holographic
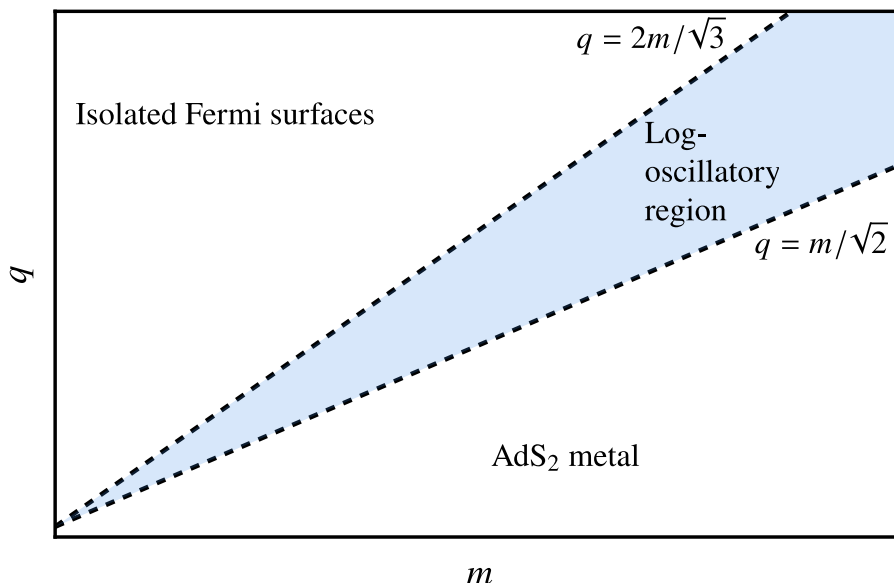
Figure 1. A schematic representation of the phase diagram of holographic fermions, where q and m are the charge and the mass (related to the scaling dimension in field theory $\Delta = 3/2 + m$) of the bulk fermion respectively. Along the line $q = m/\sqrt{2}$, determined by the Schwinger pair production threshold, the quantum phase transition ought to happen between the Reissner-Nordström black hole describing the strange metal phase and the quantum electron star solution (no black hole) corresponding to a metallic phase. However, this line is not identical to boundary of the regime where the Reissner-Nordström system supports stable Fermi surfaces as probed through the Reissner-Nordström spectral functions. The electron star (fluid) model requires taking the limit $q, m \to 0$ where both critical lines become indistinguishable. To understand the transition at finite q, m is the motivation for our approach. Adapted from [4].

superconductors [16, 17]. This solution (just like our soft wall confining electron star solution) describes a system that flows from a conformal pure AdS UV to an intermediate ordered holographic superconductor (Fermi liquid) state with a gap in the sense that below that gap it returns to the renormalized conformal theory and low energy excitations cannot disturb the ordered state. As is well-known the generic holographic superconductor ground state is not AdS$_4$-to-AdS$_4$ but of the Lifshitz type [18]. It is the technical difficulties described above that guided us to first construct this Horowitz-Roberts-Gubser-Rocha type solution. We leave the full Lifshitz quantum electron star for future work. One natural way to construct the latter is that, rather than trying to remove the soft-wall regulator, one can also make it dynamical, similar to the electron star study in [19].

We do confirm that within the class of non-dynamical soft-wall solutions this gapped confined holographic Fermi liquid is the thermodynamically preferred state over the deconfined Reissner-Nordström metallic state for appropriate charge and mass of the fermion. Because we are not yet able to remove the regulator we do not yet solve the puzzle of figure 1 directly.

The outline of the paper is the following. In section 2 we present the gravity setup and the regulated quantum electron star (rQES) solution. In section 3, we present the

properties of our rQES solution, i.e. the gapped confined Fermi liquid: we show it is the thermodynamically preferred solution in a certain range of parameters, and demonstrate the existence of the infinitely long-lived quasiparticle peaks in the spectrum of the boundary theory. In section 4, we present some considerations about removing the confining soft wall. Section 5 sums up the conclusions together with some musings on further directions of work and the physical meaning of our results.

2 A confined quantum electron star: set-up

The minimal bottom-up gravity dual of a strongly correlated electron system is the Einstein-Maxwell-Dirac system [2–4]. The new element of our setup is the phenomenological soft-wall-like regulator inspired by bottom-up AdS/QCD [20]. The regulator is a fixed non-dynamic scalar field, which neither backreacts on the metric itself nor does it feel the backreaction by the fermions. This is again in line with AdS/QCD models. Therefore, the geometry starts as pure AdS in the UV, in the interior it is influenced by the gauge and matter fields and deviates from AdS, and in far IR all matter fields are exponentially damped by the confining potential. However, in contrast to most hard/soft-wall models we will let the potential only damp the matter sector and not the gravitational sector. The action of the system is:

$$S = \int \mathrm{d}^4x \sqrt{-g} \left[\frac{L^2}{2\kappa^2} (R + 6) - \frac{L^2}{4} F_{\mu\nu} F^{\mu\nu} + L^3 \mathcal{L}_f[\Psi, \Phi] \right] \tag{2.1}$$

where κ is the gravitational coupling constant; and L is set to $L = 1$ in the remainder. The Dirac Lagrangian is:

$$\mathcal{L}_f = \bar\Psi \left[e^\mu_A \Gamma^A \left(\partial_\mu + \frac{1}{4} \omega^{BC}_\mu \Gamma_{BC} - iq A_\mu \right) - \left(m + \hat{M}\Phi \right) \right] \Psi \tag{2.2}$$

where $\bar\Psi = i\Psi^\dagger \Gamma^0$, e^μ_A is the vierbein, Γ^A are the gamma matrices in four dimensions, and ω^{AB}_μ is the spin connection. The regulator is fully encoded in an effective mass contribution $\hat{M}(z)\Phi(z)$ for the Dirac field, with $\Phi(z)$ a non-dynamical scalar field whose profile we shall choose later. Inspired by [21], we will consider two types of the confining potential:

$$\hat{M} = \begin{cases} -e^z_3 \Gamma^3, & \text{the potential preserves chirality}, \\ z\mathbb{1}_4, & \text{the potential breaks chirality}. \end{cases} \tag{2.3}$$

Here z, both as index and a variable, refers to the radial coordinate of the AdS space. We will assume a radially symmetric metric which is asymptotically AdS_{d+1} with $d = 3$, parametrized as:

$$\mathrm{d}s^2 = -\frac{f(z)h(z)}{z^2}\mathrm{d}t^2 + \frac{\mathrm{d}x_i\mathrm{d}x^i}{z^2} + \frac{\mathrm{d}z^2}{z^2 f(z)}. \tag{2.4}$$

The radial coordinate is defined for $z \geq 0$, where $z = 0$ is the location of AdS boundary (UV). Development of a horizon at finite z is in principle signified by the appearance of a zero of the function f: $f(z_H) = 0$. At zero temperature (the only case we consider), the space extends to infinity, $0 \leq z \leq \infty$.

Our choice to let the wall only confine the fermion-matter sector (together with the absence of backreaction by the confining scalar) implies that at finite chemical potential but zero bulk fermion density, the thermodynamically preferred solution is the regular charged (RN) black hole, though pure AdS with a constant electrostatic potential is also a solution.

For a certain value of the charge q of the fermion, it will be thermodynamically preferred to store all charge in an occupied bulk fermionic state, i.e. nonzero bulk density $n_c \equiv \langle \Psi^\dagger \Psi \rangle$, rather than a Reissner-Nordström black hole. Now the precise radial profile of the scalar $\Phi(z)$ becomes important. The original AdS/QCD papers used a quadratic scalar, behaving in the IR as $\Phi \sim z^2$ [22], which ensures confinement while still being smooth. Another form found in the literature is a profile which flattens out to a constant in the IR [23]. At the same time the UV completion of the scalar field has to ensure that its contribution to the Dirac equation decays quickly enough for small z to reproduce the equation of motion in pure AdS in the limit $z \to 0$. The forms that satisfy all the requirements and which we find numerically convenient are

$$
\begin{aligned}
\Phi(z) &= \lambda z^2, && \text{quadratic scalar} \\
\Phi(z) &= \lambda \frac{z^\alpha}{z_0^\alpha + z^\alpha}, && \text{flat scalar.}
\end{aligned}
\tag{2.5}
$$

The amplitude of the scalar (i.e. the measure of the "hardness" of the wall) is parametrized by λ, and z_0 is the scale at which the scalar begins to flatten (in the second, flat scalar model). The choice of α is merely that of computational convenience and we choose $\alpha = 4$. Similarly, we will consistently choose $z_0 = 2$ throughout the rest of this paper.

2.1 Einstein-Maxwell-Dirac equations

From the action we obtain the Maxwell equation and two convenient linear combinations of the tt and zz components of the Einstein equations. With the ansatz that only $A_t \neq 0$, and that all functions only depend on z, compatible with homogeneity and isotropy, they reduce to

$$
\begin{aligned}
A_t''(z) - \frac{h'(z)}{2h(z)} A_t'(z) &= \sqrt{h(z)}\, n(z)\,, \\
1 + \frac{z}{3} f'(z) - f(z) &= \frac{z^2}{3 f(z) h(z)} \rho(z) + \frac{z^4}{12 h(z)} A_t'(z)^2\,, \\
h'(z) &= -z h(z) p(z) - \frac{z}{f(z)^2} \rho(z)\,.
\end{aligned}
\tag{2.6}
$$

Compatible with the symmetries the current vanishes $J^i = 0$, the charge density J^0 is denoted as $J^0 = n(z)/\sqrt{-g} = z^4 n(z)/\sqrt{h(z)}$, and the stress tensor is parametrized as

$$
(T_f)_{\mu\nu} = \text{diag}(\rho(z), p_\perp(z), p_\perp(z), p(z)),
\tag{2.7}
$$

where $p_\perp(z)$ is the pressure in the transverse x, y directions.

The ii components of the Einstein equations are both equal to

$$
\begin{aligned}
&z h(z) \left[-z^3 A_t'(z)^2 + \left(3 z f'(z) - 4 f(z) \right) h'(z) + 2 z f(z) h''(z) \right] + \\
&+ 2 h(z)^2 \left[z \left(z f''(z) - 4 f'(z) - 2\beta z p_\perp(z) \right) + 6 f(z) - 6 \right] - z^2 f(z) h'(z)^2 = 0\,.
\end{aligned}
$$

They are not independent, however. Denoting the Einstein field equations as $E_{\mu\nu} \equiv G_{\mu\nu} - T_{\mu\nu}$ and the Maxwell equation as $E_M \equiv \nabla_\mu F^{\mu\nu} - J^\nu$, one can show that[2]

$$E_{xx} = \hat{L} \cdot E - \frac{1}{2z}\nabla_\mu T^{\mu\nu}\,, \tag{2.8}$$

where $\hat{L} \cdot E \equiv A_1 \partial_z E_{tt} + A_2 \partial_z E_{zz} + A_3 E_M + A_4 f'(z) E_{tt} + E_{zz}(A_5 f'(z) + A_6 h'(z) + A_7)$ is a linear combination of both $\{E_{tt}, E_{zz}, E_M\}$ and their derivatives and $T^{\mu\nu}$ is the total stress-energy tensor associated with the matter content of the theory. The stress-tensor is covariantly conserved if the matter sector is on-shell, i.e. obeys its equations of motion. Thus

$$E_{xx}^{\text{on-shell}} = \nabla_\mu T^{\mu\nu} = 0 \tag{2.9}$$

It is therefore sufficient to solve the three equations (2.6) together with the matter sector.

The charge, energy and pressure densities $n(z), \rho(z), p(z)$ are determined by the occupied fermionic states in the AdS bulk space. Importantly, we will compute them *solely from microscopic considerations*: we do *not* assume anything like a fluid limit or a specific form of the equation of state. We compute them from the Dirac Lagrangian, within the one-loop Hartree correction to the background. This is discussed in detail in the next subsection.

We will now proceed to derive the equation of motion for the Dirac field. From (2.2), the equation reads:

$$e_A^\mu \Gamma^A \left(\partial_\mu + \frac{1}{4}\omega_\mu^{BC}\Gamma_{BC} - iqA_\mu\right)\Psi = \left(m + \hat{M}(z)\Phi\right)\Psi\,. \tag{2.10}$$

It is known that the spin connection in this type of metric can be eliminated by rescaling the fermion [2, 24]:

$$\Psi = (-g^{zz}\det g_{\mu\nu})^{-\frac{1}{4}}\tilde{\psi} = \left(\frac{f(z)h(z)}{z^{2d}}\right)^{-\frac{1}{4}}\tilde{\psi} \equiv a(z)\tilde{\psi}. \tag{2.11}$$

In addition, it is convenient to eliminate any singular terms from the fermionic wavefunction. Since our solutions are smooth in the interior as we shall see, the only singularity is the branch cut in the UV behaving as z^m. We thus rescale one more time

$$\tilde{\psi} = z^m\psi \equiv b(z)\psi. \tag{2.12}$$

In most cases we will use the rescaled form and write the equations for ψ. So far this is all independent of the gamma matrix representation. In order to simplify the equations of motion, we now employ the representation

$$\Gamma^\mu = \begin{pmatrix} 0 & \gamma^\mu \\ \gamma^\mu & 0 \end{pmatrix}, \quad \Gamma^3 = \begin{pmatrix} 1 & 0 \\ 0 & -1 \end{pmatrix}, \tag{2.13}$$

with $\mu \in \{0, 1, 2\}$, $\gamma^0 = i\sigma^2, \gamma^1 = \sigma^1, \gamma^2 = \sigma^3$ and $\sigma^{1,2,3}$ are the usual Pauli matrices. Homogeneity and isotropy along the t, x, y directions allow us to take the energy ω and momentum $k \equiv k_x$ as good quantum numbers, so the Dirac bispinor is expressed as

$$\psi = e^{-i\omega t + ikx}\left(\psi_1(z), \chi_1(z), -i\chi_2(z), i\psi_2(z)\right)^T. \tag{2.14}$$

---

[2]This is essentially $\nabla_\mu G^{\mu\nu} = \nabla_\mu T^{\mu\nu}$.

As in [13, 24], this yields two (equivalent) decoupled systems for the two independent components, for $\psi_{1,2}$ and $\chi_{1,2}$, corresponding to the spin degeneracy of our system. We will focus on the ψ_i components for which the Dirac equation reads

$$
\left[\partial_z + \varepsilon_+ \Phi + \frac{m}{z}\left(1 - \frac{1}{\sqrt{f(z)}}\right)\right]\psi_1(z) - \left[\frac{k}{\sqrt{f(z)}} + \frac{\omega + qA_t}{f(z)\sqrt{h(z)}}\right]\psi_2(z) = 0
$$
$$
\left[\partial_z + \varepsilon_- \Phi + \frac{m}{z}\left(1 + \frac{1}{\sqrt{f(z)}}\right)\right]\psi_2(z) + \left[\frac{\omega + qA_t}{f(z)\sqrt{h(z)}} - \frac{k}{\sqrt{f(z)}}\right]\psi_1(z) = 0\,.
$$

(2.15)

where $\varepsilon_+ = \varepsilon_- = 1$ corresponds to the chiral-preserving potential and $\varepsilon_+ = -\varepsilon_- = -1/\sqrt{f(z)}$ corresponds to the chiral-breaking potential.

2.2 Fermion densities and backreaction

The fermionic densities and pressures are obtained microscopically, from the Dirac Lagrangian (2.2):

$$
\rho = \langle \Psi^\dagger e_0^t \Gamma^0 (-i\omega - iqA_t)\Psi\rangle\,,
$$
$$
n = -\langle \Psi^\dagger \Psi\rangle\,.
$$

(2.16)

The components of the pressure $p_\perp, p$ are likewise formally equal to

$$
p_\perp = \langle \bar{\Psi} i e_1^x k_x \Gamma^1 \Psi\rangle,
$$
$$
p = \langle \bar{\Psi} e_3^z \Gamma^3 \partial_z \Psi\rangle.
$$

(2.17)

The expectation value $\langle\ldots\rangle$ in (2.16)–(2.17) is the quantum-mechanical expectation value, i.e. one solves the Dirac equation with appropriate boundary conditions (see below) and sums over the quantum numbers in the appropriate range. The quantum numbers are the radial modes ℓ, and momenta k_x, k_y in the x, y-directions which determine the on-shell energy in terms of a dispersion relation $\omega = E_\ell(k)$. The role of the confining potential is essential here: it quantizes the radial number ℓ. Each discrete radial mode corresponds to a separate Fermi surface [2–4, 8, 9, 13]. As emphasized in the Introduction, we seek a state where only a single Fermi surface is occupied. This must be the lowest radial mode. Note that despite occupying a single mode, this mode still contains a thermodynamically large number of states counted by the x, y-momenta. Each radial mode is thus a fluid of fermions.

We will ignore the subtleties of the zero-point energy and the Dirac sea; in principle these are absorbed in a renormalization of the cosmological constant and the AdS radius; see however [14, 15] for a more detailed treatment. Then, in terms of the solutions to the Dirac equation, formally the expressions for the density are

$$
n(z) = \frac{2q}{z^3\sqrt{f(z)}}\,a(z)^2 b(z)^2 \sum_{k,\ell} \Theta(-E_\ell(k))\,\left(\psi_{1;\ell,k}^\dagger(z)\psi_{1;\ell,k}(z) + \psi_{2;\ell,k}^\dagger(z)\psi_{2;\ell,k}(z)\right)
$$

$$
\rho(z) = a(z)^2 b(z)^2 e_0^t(z)(-i\omega - iqA_t(z))\sum_{k,\ell}\Theta(-E_\ell(k))\left(\psi_{1;\ell,k}^\dagger(z)\psi_{1;\ell,k}(z) + \psi_{2;\ell,k}^\dagger(z)\psi_{2;\ell,k}(z)\right)
$$

$$
p(z) = a(z)^2 b(z)^2 e_3^z(z)\sum_{k,\ell}\Theta(-E_\ell(k))\left(\psi_{1;\ell,k}^\dagger \partial_z \psi_{2;\ell,k} - \psi_{2;\ell,k}^\dagger \partial_z \psi_{1;\ell,k}\right)
$$

(2.18)
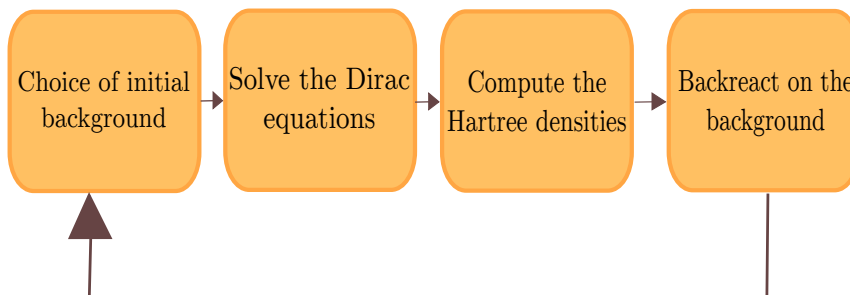
Figure 2. Iteration algorithm used to compute the rQES solution.

where the step-function $\Theta(x)$ selects the positive energy states. Note that due to the antisymmetry of the two spin components, the derivatives of the scaling factors $a(z), b(z)$ cancel out in the expression for p.

2.2.1 The self-consistent Hartree calculation

We solve the system (2.6), (2.15) in the one-loop Hartree approximation. As a reminder, the Hartree correction is the local single-particle diagram (vacuum bubble), ignoring anti-particles, i.e. ignoring the contribution from the Dirac sea. We do not take into account the Fock correction. In flat space, the Hartree correction is trivial [25]: in terms of the causal fermionic propagator G_R it equals $\lim_{t \to 0-} \int d\omega d^2 k\, G_R(\omega, k) e^{-i\omega t} = \delta\mu$,[3] merely renormalizing the chemical potential. In curved space however, the local chemical potential is $\mu_{\text{loc}}(z) = A_t(z)\sqrt{-g^{tt}(z)}$, with a nontrivial radial profile, thus the correction $\delta\mu(z)$ is also variable along z and therefore it can have nontrivial physical effects.

The Hartree approximation then proceeds by computing this one-loop Hartree correction self-consistently. One starts with an ansatz for the background, solves the Dirac equation in this background, computes the one-loop Hartree densities in the assumption that they are small, updates the background and iterates to convergence as in figure 2.

2.3 Boundary conditions on the Einstein-Maxwell sector

The Einstein-Maxwell equations (2.6) require four boundary conditions in total (two for $A_t(z)$ and one for each of the metric functions $f(z), h(z)$). The UV boundary conditions are

$$
\begin{aligned}
A_t(z_{\text{UV}}) &= \mu\,, & \text{the chemical potential.} \\
f(z_{\text{UV}}) &= h(z_{\text{UV}}) = 1\,, & \text{AdS}_4 \text{ asymptotics.}
\end{aligned}
\tag{2.19}
$$

The fourth boundary condition we impose is given by our demand that we seek a state where *all* the charge is contained in occupied fermionic states.[4] The confining potential ensures that the fermionic wavefunctions are localized at a finite value in the radial direction.

---

[3]The infinitesimal time separation $t \to 0-$ is really the point-splitting regularization, as the integral of G_R at coincident points in spacetime generally diverges; the sign of t is dictated by the contour choice for the retarded propagator [25].

[4]There could be interpolating solutions with both a charged horizon and a charge in occupied fermionic states. We will not seek for those here as the presence of the charged Reissner-Nordstrom like horizons should imply the continued presence of log-oscillatory instabilities.

Thus by construction the charge density will vanish in the deep AdS interior. From this follows that the fourth boundary condition is $\partial_z A_t(z_{IR}) = 0$. Formally $z_{IR} = \infty$; in our numerical computation it will be finite but large, and we have checked that our results do not depend on its value.

In practice, we solve the boundary value problem by shooting from the IR. We impose directly the condition $\partial_z A_t(z_{IR}) = 0$ as well as the condition $\partial_z f(z_{IR}) = 0$. The latter indirectly encodes our demand that we seek a $T = 0$ solution; recall that for a black hole solution $\partial_z f(z_{\text{horizon}}) \sim T$. Then we use the free value $A_t(z_{IR})$ and $h(z_{IR})$ to shoot for $A_t(z_{UV}) = \mu$, $h(z_{UV}) = 1$ at the boundary. From the equation of motion for $f(z)$ one obtains automatically that $f(z_{IR}) = 1$ once we fall on the right branch; for the same reason one can also use $f(z_{IR}) = 1$ as an IR boundary condition if one demands in addition that there is no energy density or electric field in the deep interior.

2.4 Boundary conditions for the fermions

The UV boundary conditions for the appropriate solutions to the Dirac equation are straightforward. Near the AdS boundary the rescaled field behaves as

$$
\begin{aligned}
\psi_1(z \to 0) &\sim A_\ell(\omega, k) \frac{\omega - k - \mu q}{2m - 1} z^{1-2m} + B_\ell(\omega, k) + \dots, \\
\psi_2(z \to 0) &\sim A_\ell(\omega, k)\, z^{-2m} + B_\ell(\omega, k) \frac{\omega + k - \mu q}{2m + 1} z + \dots.
\end{aligned}
\tag{2.20}
$$

On-shell solutions are normalizable, i.e. $A_\ell(\omega, k) = 0$. This agrees with the AdS/CFT dictionary, where a finite $A_\ell(\omega, k)$ would imply an external source for the fermions for a specific band ℓ and energy ω, k. Demanding normalizability $A_\ell(\omega, k) = 0$ instead, implicitly translates in a dispersion relation $\omega(k) = E_\ell(k)$.

The IR boundary conditions for the fermions require a more detailed discussion. Firstly, for the fermionic wavefunctions, the amplitude is set by normalization of each wavefunction to unity. For each radial mode ℓ this implies

$$
\int dz \sqrt{-g} |\psi_{i;\ell,k}(z)|^2 < \infty.
\tag{2.21}
$$

For finite temperature backgrounds this is usually not an issue as the horizon is parametrically at finite distance and finite IR boundary conditions, together with the UV-condition that the un-normalizable fall-off vanish, guarantees a finite integral. For the $T = 0$ background we consider here, the interior is parametrically at infinite distance and finiteness of the integral can only follow from bounded behavior of the wavefunction. Since the spin components are not independent, it is sufficient to demand $\psi_{1;\ell}(z \to \infty) \to 0$, i.e., the leading component should vanish in the interior.

It is well known in AdS/CFT that it is then the simultaneous requirement of a UV and an IR boundary condition that determines the spectrum of the small excitations. This spectrum can still be continuous or discrete; we address this directly below. Formally, however, the normalization together with two boundary conditions make the system overconstrained and one must search for accidental solutions. We again do so by shooting from the interior to search for parameters where the UV conditions are also satisfied.

The shooting condition we use is the ratio ψ_2/ψ_1, which still leaves the freedom to normalize the norm (2.21) to unity, and which we do after the solution is found.

2.4.1 Effective potentials and confinement

Pure $T = 0$ AdS — representing a deconfined phase of the strongly coupled boundary theory — has a continuum spectrum of normal modes computed in the way described above. The system must be considered in a different phase or have its IR dynamics modified by a confining potential to discretize the spectrum; this spectrum may still be ungapped or gapped. We will now demonstrate that the chiral-breaking soft-confining potential supports a discrete Fermi surface, i.e. a tower of bound states at discrete energies, for momenta up to some k_F, the Fermi momentum. The spectrum is also gapped. A convenient way to see the effect of this potential is to transform the Dirac equation to the Schrödinger form [4, 9, 10]:

$$\chi_{\text{Sch}}(z) = e^{\frac{1}{2} \int_0^z \mathrm{d}u \, \mathcal{P}(u)},$$

$$\left[\partial_z^2 - V(z)\right] \chi_{\text{Sch}}(z) = 0,$$

$$V(z) = \frac{1}{2}\mathcal{P}'(z) + \frac{1}{4}\mathcal{P}(z)^2 - \mathcal{Q}(z), \tag{2.22}$$

where the coupled equations (2.15) were decoupled into two second order equations, each taking the form

$$\psi''(z) + \mathcal{P}(z)\psi'(z) + \mathcal{Q}(z)\psi(z) = 0, \tag{2.23}$$

with the indices 1,2 on $\psi, \chi_{\text{Sch}}(z), V$ omitted.

In principle, the Schrödinger potential is itself a function of the background spacetime and electrostatic potential $f(z), h(z), A_t(z)$ and can be fully determined only by calculating numerically the full solution. However, we can give a qualitative estimate whether it is confining or not by studying its asymptotics. Since the bulk remains asymptotically AdS$_4$, we have $V(z \to 0) \sim \dfrac{1}{z^2}$. In pure AdS$_4$ the IR behavior would be $V_{\text{AdS-IR}}(z \to \infty) = -(\omega + \mu q)^2 + k^2 + m(m+1)/z^2 + \mathcal{O}(1/z^3)$ (figure 3).[5] This now gets modified by the confining potential due to the scalar $\Phi(z)$. Making the ansatz that the confining potential in the deep IR for $z \to \infty$ suppresses exponentially all sources in the Einstein and Maxwell equations for large z, i.e. the geometry in the deep IR is again an (emergent) AdS$_4$ geometry, the leading order IR behavior of the potential is then schematically

$$V_{\text{AdS-IR}} = V(z \to \infty) + (\varepsilon_- - \varepsilon_+)\left[-\frac{\phi'(z)}{2z} + \frac{\phi(z)(4m+2) + (\varepsilon_- - \varepsilon_+)\phi(z)^2}{4z^2} + \right] + \mathcal{O}(1/z^3). \tag{2.24}$$

Note that the chiral-preserving solution $\varepsilon_+ = \varepsilon_- = 1$ leads to a vanishing contribution and therefore does not lead to fermionic bound states. In contrast the chiral-breaking solution $\varepsilon_+ = -\varepsilon_- = -1/\sqrt{f(z)} = -1 + \mathcal{O}(1/z)$ in an AdS$_4$ IR does lead to a potentially bounding potential depending on the choice of $\Phi(z)$. For this reason, we will work solely with the chiral-breaking scalar field.

---

[5]We are interested in $k^2 < (\omega + \mu q)^2$ since the potential is otherwise confining even in AdS$_4$ with no regulator, as discussed in [26]. We will discuss this later.
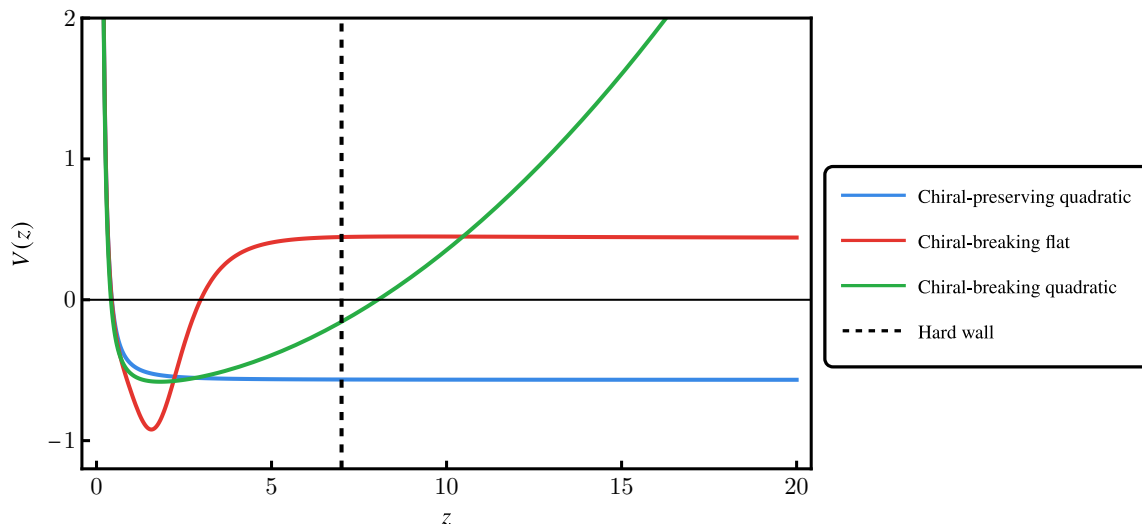
Figure 3. Comparison of the Schrödinger potentials for $\psi_1(z)$ for the two types of confining potential: chiral-breaking quadratic (green), chiral-breaking flat (red) and chiral-preserving quadratic (blue). The dashed black line indicates the truncation of spacetime which happens in the hard wall model of [13] at $z = 7$. Only the chiral-breaking potential and the hard wall allow for bound states. Parameters are $\{m, \mu q, k, \omega\} = \{0.1, 1.05, 0, -0.027\}$. The scalar parameters are $\lambda = 0.1$ for the two quadratic scalars and $\lambda = 1$ for the flat scalar.

Figure 3 shows the behavior of the Schrödinger potential for the various profiles of the scalar field and regulation schemes. With a chiral-breaking regulator, we indeed see that the infrared behavior of the potential is dominated by the large z behavior of each profile. The final choice of which scalar field profile to use is determined by the convergence of the iteration scheme. We numerically found the quadratic profile to be unstable while the flat profile leads to an emergent AdS$_4$ in the infrared. Specifically for the chiral-breaking confining potential with flat asymptotics the Schrödinger potential in the deep IR becomes

$$V(z \to z_{\rm IR})= - \omega_{\rm IR}^2 + \lambda_{\rm IR}^2 + k_{\rm IR}^2 + \mathcal{O}(1/z) \equiv V_{\rm IR} + \mathcal{O}(1/z)\,, \tag{2.25}$$

where we have used that $f(z), h(z), A_t(z)$ become constant in the emergent AdS$_4$ IR and we have defined $\omega_{\rm IR} \equiv \dfrac{\omega + q A_t(z_{\rm IR})}{f(z_{\rm IR})\sqrt{h(z_{\rm IR})}}$, $\lambda_{\rm IR} \equiv \dfrac{\lambda}{\sqrt{f(z_{\rm IR})}}$ and $k_{\rm IR} \equiv \dfrac{k}{\sqrt{f(z_{\rm IR})}}$.

In the IR limit, the Schrödinger equation becomes

$$\left[\partial_z^2 - V_{\rm IR}\right] \chi_{\rm Sch}(z) = 0\,, \tag{2.26}$$

which is solved by

$$\chi_{\rm Sch}(z) = \chi_{\rm Sch+}(z)e^{\sqrt{V_{\rm IR}}z} + \chi_{\rm Sch-}(z)e^{-\sqrt{V_{\rm IR}}z}\,. \tag{2.27}$$

We see from (2.27) that, for frequencies such that $V_{\rm IR} > 0$, the solutions have a growing and a decaying branch. The decaying branch clearly confines the wavefunction. This is the one we shall choose. This leads to the following IR form for our original Dirac fermion

components

$$\psi_{1,2}^{\mathrm{IR}}(z) = c_{1,2}^{\mathrm{IR}}(z)e^{-\sqrt{V_{\mathrm{IR}}}z}\,, \tag{2.28}$$

where the ratio of the coefficients is fixed by the Dirac equation (2.15):

$$\frac{\psi_2^{\mathrm{IR}}(z)}{\psi_1^{\mathrm{IR}}(z)} = \frac{c_2^{\mathrm{IR}}(z)}{c_1^{\mathrm{IR}}(z)} = \frac{1}{\omega_{\mathrm{IR}} + k_{\mathrm{IR}}}\left[\frac{m}{z}\left(\frac{1}{\sqrt{f_{\mathrm{IR}}}} - 1\right) + \sqrt{V_{\mathrm{IR}}} + \lambda_{\mathrm{IR}}\right] \tag{2.29}$$

and the normalization of the wavefunction to unity sets the remaining overall scale.

With these IR boundary conditions the equations (2.15) are solved by shooting from z_{IR} to z_{UV}.

The confinement imposed by both IR and UV boundary conditions leads to a discrete and gapped spectrum which defines a band structure (see figure 6 later). The fall-off of the wavefunction both at the AdS boundary and the interior also implies an absence of any backreaction in those regions. Once backreaction is included the resulting solutions will therefore be AdS_4-to-AdS_4 domain wall solutions, as we will show in the next section.

As a last remark, equation (2.25) gives us a simple way to view the effect of the chiral-breaking flat potential. As has been pointed out in [4, 26], in AdS_4 with constant electrostatic potential where $\lambda = 0$, the potential is deconfining for modes with $|\omega_{\mathrm{IR}}| > |k_{\mathrm{IR}}|$ and confining for modes such that $|\omega_{\mathrm{IR}}| < |k_{\mathrm{IR}}|$. The addition of a *flat* profile means that now modes with $|k_{\mathrm{IR}}| \leq |\omega_{\mathrm{IR}}| < \sqrt{k_{\mathrm{IR}}^2 + \lambda_{\mathrm{IR}}^2}$, which previously were not bound states, also become confined. This allows the existence of a window $\omega_-(k) < \omega < \omega_+(k)$, with $\omega_\pm(k) \equiv qA_t(z_{\mathrm{IR}}) \pm \sqrt{k_{\mathrm{IR}}^2 + \lambda_{\mathrm{IR}}^2}$ where a discrete set of (gapped) modes can be populated.

3 Regulated quantum electron star: thermodynamics and spectrum

Now that the problem is well-posed, we can follow the algorithm in figure 2 and construct a fully backreacted regulator-confined $T = 0$ quantum electron star. Choosing the chirality-breaking flat regulator the resulting solution is shown in figure 4. This is by construction an AdS_4-to-AdS_4 domain wall solution. Just like the analogous domain wall solutions for the holographic superconductor [16–18], it has a UV AdS_4 and an IR AdS_4 with the *same* radius but different effective speed of light. This can be checked by considering the diffeomorphism-invariant ratios $v_{\mathrm{IR}}/v_{\mathrm{UV}}$ and $L_{\mathrm{IR}}/L_{\mathrm{UV}}$ which are equal to

$$\frac{L_{\mathrm{IR}}}{L_{\mathrm{UV}}} = \sqrt{\frac{R(z \to z_{\mathrm{UV}})}{R(z \to z_{\mathrm{IR}})}} = 1\,, \quad \frac{v_{\mathrm{IR}}}{v_{\mathrm{UV}}} \equiv \frac{v(z \to z_{\mathrm{IR}})}{v(z \to z_{\mathrm{UV}})} = \sqrt{\frac{h(z \to z_{\mathrm{IR}})}{h(z \to z_{\mathrm{UV}})}} < 1 \text{ in our solution}\,. \tag{3.1}$$

Here $R(z)$ is the Ricci scalar and $v(z) = \sqrt{h(z)}$ is deduced from the null vector $\frac{\mathrm{d}}{\mathrm{d}t}X^\mu(z)$ where $X^\mu(z) \equiv \{t, 0, v(z)t, 0\}$ is a x-directed trajectory. Therefore, our solution obeys the c-theorem since the effective speed of light in the dual field theory is lower in the IR than in the UV, as discussed in detail in [17].

In accordance with our discussion in the Introduction, the chemical potential is chosen such that only the lowest radial mode of the fermionic wavefunction is occupied. The
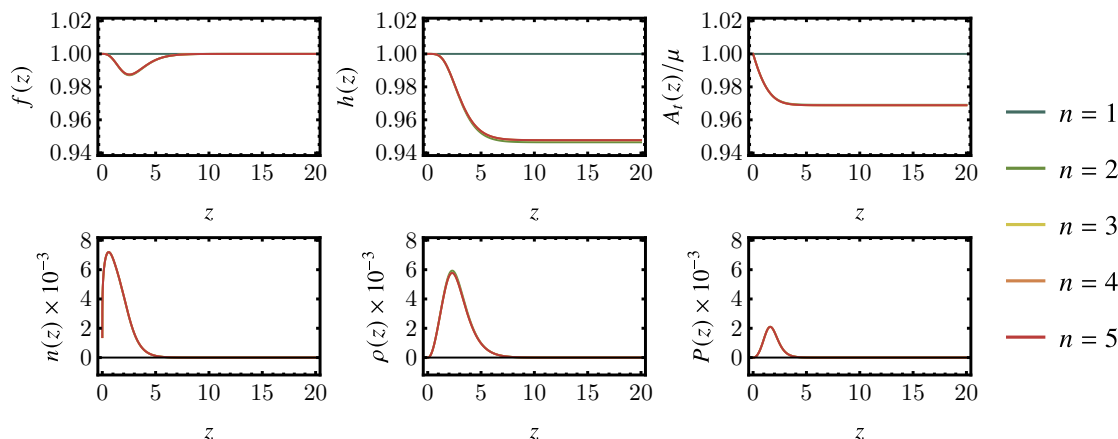
Figure 4. Iterative backreactions on the background fields $(f(z), h(z), A_t(z))$ and their associated currents $(n(z), \rho(z), P(z))$ with the same parameters as in figure 5. In total 5 iterations are performed, denoted by the color scale from green (first iteration) to red (last iteration). For these values $\{m, \mu q, \lambda\} = \{0.1, 0.9, 1\}$ only the first iteration differs significantly from the final solution, and the other curves are visually barely distinguishable from each other; for higher q convergence rapidly becomes slower.

associated matter content shows that a localized distribution of fermions in the mid-infrared region is characterized by a stable finite density of fermions with total charge $Q = -A_t'(z \to 0)$.

With the chirality-breaking flat potential the convergence is in fact quite fast at low density. The Hartree algorithm provides a discrete sequence of fields $(f^{(n)}, h^{(n)}, A_t^{(n)})$ as we iterate from $n = 1, 2, \ldots$. We can introduce a criterion for the convergence of the solution using the IR parameters used for shooting

$$\epsilon_n = \sqrt{f^{(n)}(z_{\mathrm{IR}})^2 + A_t^{(n)}(z_{\mathrm{IR}})^2 + h^{(n)}(z_{\mathrm{IR}})^2}\,. \tag{3.2}$$

Convergence is obtained if $(\Delta\epsilon)_n \equiv \epsilon_n - \epsilon_{n-1} \xrightarrow{n\to\infty} 0$. For a small occupation number/charge figure 5 shows that the solution already stabilizes after three iterations; for large occupation numbers the convergence rapidly becomes much slower. We have checked that the solution is not sensitive to the choice of the numerical cutoffs $\{z_{\mathrm{UV}}, z_{\mathrm{IR}}\}$.

3.1 Thermodynamics

For a large q/m ratio we expect that the quantum electron star at a given chemical potential μ is the thermodynamically preferred solution over the extremal Reissner-Nordström solution. In order to study the thermodynamics of the regulated quantum electron star, we need to compute its free energy. It consists of two parts. There is a direct saddle point contribution from the regularized Euclidean action:

$$S_E = \int \mathrm{d}^4x \sqrt{g_E} \left[\frac{1}{2\kappa^2} (R + 6) - \frac{1}{4}F^2 \right] + \oint_{z=\epsilon} \mathrm{d}^3x \sqrt{h}(-2K + 2\gamma)\,, \tag{3.3}$$

where g_E is the Euclidean metric, h is the induced metric on a hypersurface normal to a radial (z) slice, pointing outwards, K is the trace of the extrinsic curvature and $\gamma = 2$ is
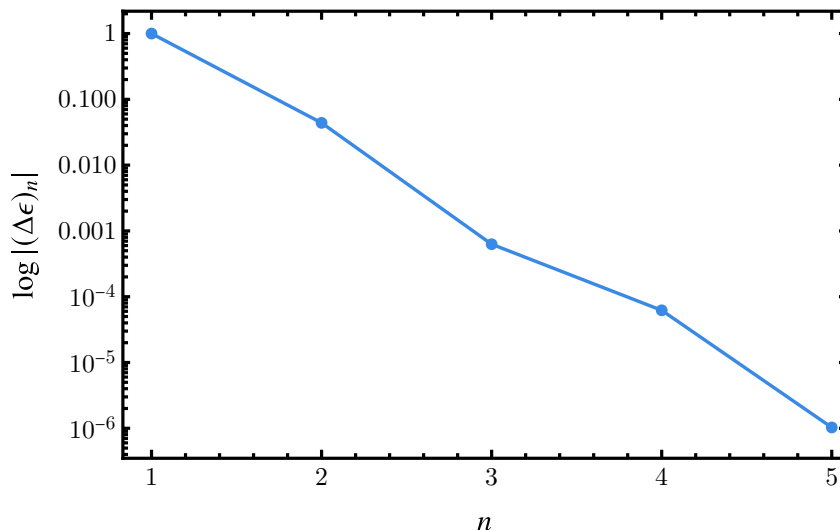
Figure 5. Convergence in terms of the logarithm of the difference in the IR between the n-th and $n + 1$-st iteration $\log |(\Delta\epsilon)_n|$ for a rQES with $\{m, \mu q, \lambda\} = \{0.1, 0.9, 1\}$. The convergence is exponentially fast and the agreement is very good already around the 3$^{\text{rd}}$ iteration.

required to make the AdS free energy vanish. The imaginary time at temperature T is compactified with the radius $\beta = 1/T$, the integral in the x–y plane produces the (infinite) volume Vol_2, and the radial integration is performed to some UV cutoff ϵ, yielding

$$S_E = \beta\text{Vol}_2 \int \mathrm{d}z \sqrt{g_E} \left[\frac{1}{2\kappa^2} (R + 6) - \frac{1}{4} F^2 \right] + \beta\text{Vol}_2 \sqrt{h(\epsilon)}(-2K(\epsilon) + 2\gamma). \quad (3.4)$$

This accounts for the contribution of the bosonic fields. The Dirac action vanishes on-shell and therefore does not contribute to this part. It does have a one-loop contribution to the free energy density

$$f \equiv \frac{S_E}{\beta\text{Vol}_2} + f_{\text{Dirac}}. \quad (3.5)$$

Here f_{Dirac} represents the fermionic contribution. Following [13, 24, 27, 28], at $T = 0$ we can simply sum the energies along the filled band of fermions (above the Dirac sea). This is the internal energy shifted by the chemical potential. For our normal modes, this leads to the expression

$$f_{\text{Dirac}} = \sum_\ell \int \frac{k\mathrm{d}k}{2\pi} \, \Theta(-E_\ell(k))\Theta(E_\ell(k) - \mu q)E_\ell(k) = \int \frac{k\mathrm{d}k}{2\pi} \, \Theta(-E_1(k))E_1(k)$$

where in the last line we have made explicit that we choose our chemical potential such that only states of the lowest electronic radial mode $E_{\ell=1}$ will be occupied. One must first choose the potential strength λ such that the Schrödinger potential supports at least one normalizable mode. At the same time, it is only these normalizable modes that can be populated. If there is only one band in the window of existence of normalizable modes $[\omega_-(k), \omega_+(k)]$, i.e.,$E_{\ell=1}(k) < \omega_+(k) < E_{\ell=2}(k)$, then increasing the chemical potential beyond that upper limit will not populate further normalizable modes. Our rQES is in this sense not plagued by the usual large-N Fermi surfaces artifact.
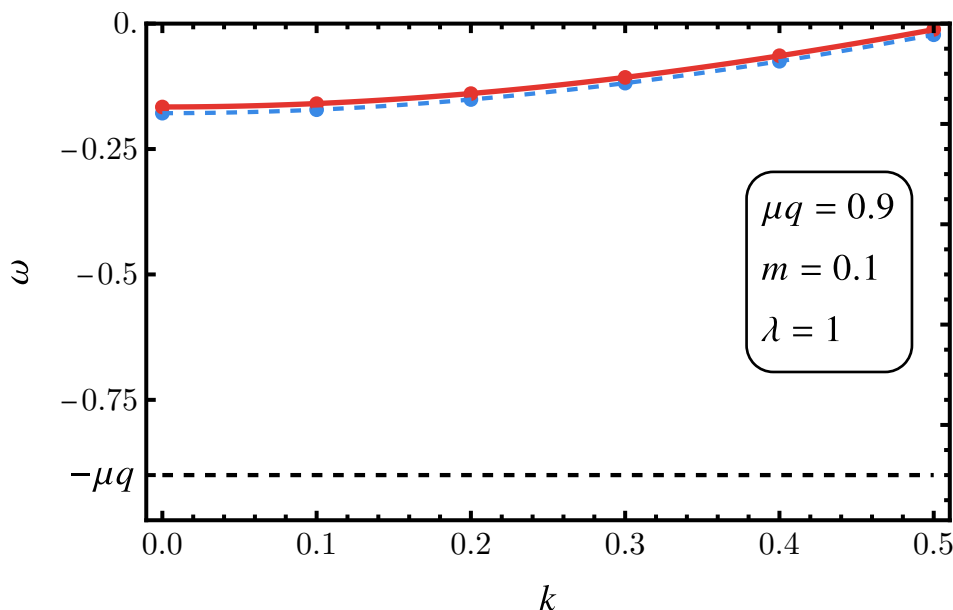
Figure 6. First electronic band for $\{m, \mu q, \lambda\} = \{0.1, 0.9, 1\}$, for the AdS$_4$ background with constant electrostatic potential (blue) and the backreacted solution (red). The lines are a fit to the form (3.6).

It is furthermore quite easy to show that both before and after accounting for backreaction the band structure follows a similar form as in pure AdS$_4$ [13]

$$E_\ell(k) = -E_0 + \sqrt{k^2 + k_0^2}\,, \tag{3.6}$$

where $k_F \equiv \sqrt{E_0^2 - k_0^2}$ and the parameters E_0, k_0 are most easily found by fitting from the numerical dispersion curves, as in figure 6.

Note that f_{Dirac} is negative semi-definite. This does not mean, however, that the occupied state is automatically thermodynamically preferred. The backreaction also changes the bosonic saddle point contribution compared to its original AdS$_4$ value $f(\text{AdS}_4) = 0$. Adding both contributions we compare to the RN free energy

$$f(\text{RN}) = -\frac{4 + z_h^2 \mu^2}{4 z_h^3} = -\frac{\mu^3}{6\sqrt{3}} \text{ at } T = 0\,. \tag{3.7}$$

Because the regulator does not act on the background sector, the Reissner-Nordström free energy is unaffected by it.

Figure 7 shows the free energy of the rQES as a function of the charge μq for a fixed mass m and confining potential strength λ. As q increases, the rQES grows, so we need to compute more and more modes. This becomes more and more time consuming. By constructing an interpolating curve based on low q rQES solutions (using the points until $\mu q \simeq 1.2$), we can estimate where the solution becomes thermodynamically preferred and verify this with a fewer number of large q datapoints ($\mu q = 1.4$ and $\mu q = 1.58$). We see that at $\mu q = \mu q_c \simeq 1.56$, the rQES becomes thermodynamically preferable over the RN background.
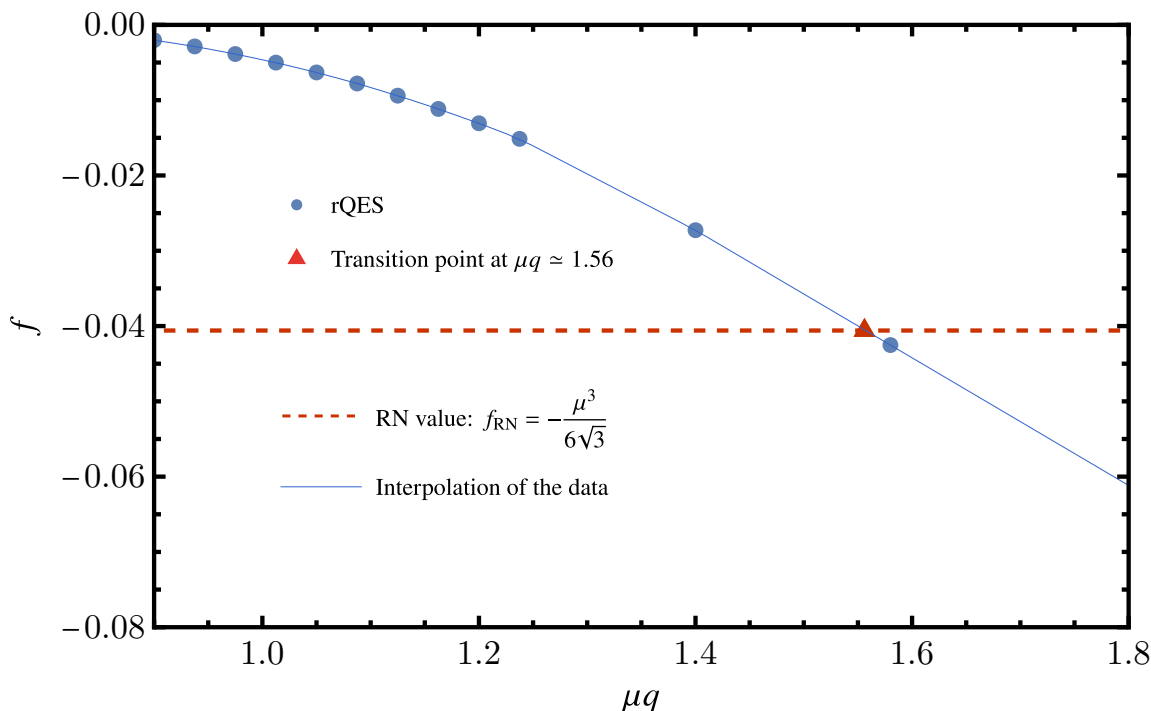
Figure 7. Plot of the free energy density for rQES at $\{\mu, m, \lambda\} = \{0.75, 0.1, 1\}$ as a function of the fermionic charge μq (blue dots) and the reference RN black hole free energy (red dashed line); the thin blue line and the red triangle are to guide the eye to the transition point. Since RN has no fermions its free energy curve is flat, i.e. does not depend on the fermion charge. The first-order phase transition from RN to rQES happens at the intersection of the two lines. Since the calculations for larger μq values are costly, we only compute two points for $\mu q > 1.5$ and interpolate.

In figure 8(a), we show that this transition point evolves linearly with the fermion mass m for fixed q and λ. Based on this finding, we can sketch a thermodynamic phase diagram for our model in figure 8(b). The critical charge satisfies an approximate relation $q_c(m; \lambda) \approx c_0(\lambda) + c_1(\lambda)\frac{m}{\mu}$ with c_0 and c_1 dependent on λ. It is tempting to compare this to the confounding phase diagram based on RN holography alone. For pure RN holography it is surmised [29] that the superradiant instability of the RN black hole toward an electron star (seen in the spectrum as log-periodic oscillations) sets in at $q = \sqrt{3}m$. This should correspond to the limit $\lambda \to 0$. As λ decreases we therefore expect the phase-boundary to pivot anti-clockwise. This comparison should be done with care, because the smaller λ becomes, the harder it is to observe bands that can be occupied — see the section on removing the regulator below. Another way to see this is that the effective Schrödinger potential in the extremal RN black hole for $\omega = k = 0$ (the onset of instability) has no linear term in m: $V_{\mathrm{RN}} \sim -4q^2 + 2m^2$. Hence we cannot extrapolate freely to $\lambda = 0$.

3.2 Spectrum of the rQES

To confirm our results, we consider the fermionic spectral function on rQES backgrounds. As a reminder, the spectral function is defined as the trace of the imaginary part of the retarded propagator: $A(\omega, k) = \operatorname{Im} \operatorname{Tr} G_R(\omega, k)$. In holography the type of propagator is defined by
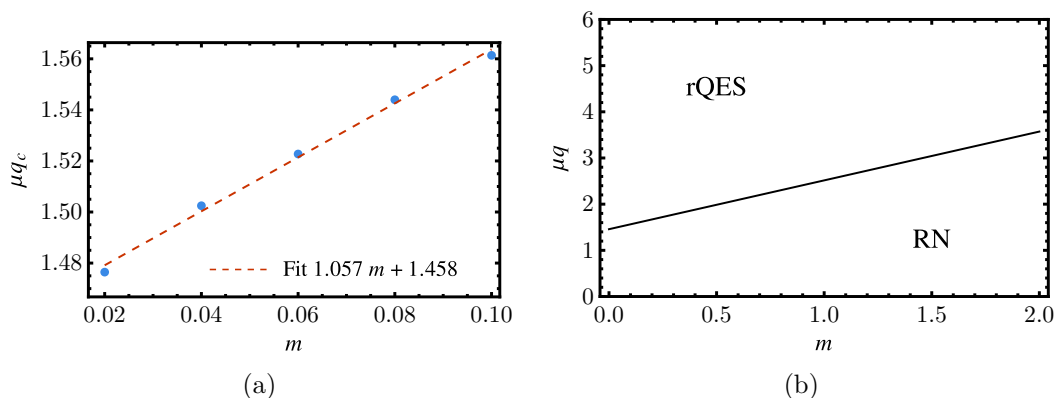
Figure 8. (a) Transition point μq_c as a function of m and its linear fit, for $\lambda = 1$. (b) Sketch of the phase diagram of the rQES. The black line indicates a first order transition between the regulated Reissner-Nordström and the rQES, occuring when their free energies cross.

the boundary conditions in the interior. Therefore the only difference with computing the normalizable Dirac solutions is the choice of appropriate boundary conditions.

Considering that we have an emergent AdS_4 geometry in the IR, we can use the known prescription for infalling boundary conditions in pure AdS, i.e. the presence of a Poincaré horizon [30]. Accounting for the confining potential, these are

$$
\psi_1(z \to \infty) = \begin{cases} e^{-z\sqrt{k_{\mathrm{IR}}^2}}, & \text{if} \quad \omega_{\mathrm{IR}}^2 < k_{\mathrm{IR}}^2 + \lambda_{\mathrm{IR}}^2, \\ e^{iz\sqrt{-k_{\mathrm{IR}}^2}}, & \text{if} \quad \mathrm{Re}[\omega_{\mathrm{IR}}] > \sqrt{k_{\mathrm{IR}}^2 + \lambda_{\mathrm{IR}}^2}, \\ e^{-iz\sqrt{-k_{\mathrm{IR}}^2}}, & \text{if} \quad \mathrm{Re}[\omega_{\mathrm{IR}}] < -\sqrt{k_{\mathrm{IR}}^2 + \lambda_{\mathrm{IR}}^2}, \end{cases} \tag{3.8}
$$

where $\omega_{\mathrm{IR}}, k_{\mathrm{IR}}, \lambda_{\mathrm{IR}}$ were defined by (2.25), $\boldsymbol{k}_{\mathrm{IR}} = \left(\omega_{\mathrm{IR}}, \sqrt{k_{\mathrm{IR}}^2 + \lambda_{\mathrm{IR}}^2}, 0\right)$ and $\boldsymbol{k}_{\mathrm{IR}}^2 = -\omega_{\mathrm{IR}}^2 + k_{\mathrm{IR}}^2 + \lambda_{\mathrm{IR}}^2 = V_{\mathrm{IR}}$. As we saw with the normal modes, the IR boundary condition for ψ_2 can be obtained using the Dirac equation and the boundary condition for ψ_1. After imposing these boundary conditions, the retarded propagator is then computed as

$$
G_R(\omega, k) = B/A = \lim_{z \to 0} z^{-2m} \frac{\psi_1(z)}{\psi_2(z)}, \tag{3.9}
$$

where A and B are the coefficients in the UV expansion of the spinor (2.20).

Inside the gap ($\omega_{\mathrm{IR}}^2 < k_{\mathrm{IR}}^2 + \lambda_{\mathrm{IR}}^2$) the IR boundary conditions are the same for the probe fermions as for the bulk normalizable modes – the wavefunction should fall off for $z \to \infty$, which yields $A = 0$ for the normal mode frequencies $\omega = E_\ell(k)$. Therefore, the propagator will present a pole along the bands of the background. Moreover, since the fermionic wavefunctions and thus also the Green's functions are real inside the domain where bound states exist, the spectral function will vanish there. Thus, we expect to see $\mathrm{Im}\, G_R(\omega, k) = 0$ for $\omega \in [\omega_-(k), \omega_+(k)]$, except when $\omega = E_\ell(k)$ where a pole should appear.

This general structure of the spectral function including the gap for $\omega_- \leq \omega \leq \omega_+$ can be seen in figure 9. The data here and in the remainder of this section is computed for $\{\mu, q, m, \lambda\} = \{3/4, 1.2, 1/10, 1\}$. Inside the gap (white area), the spectral weight of
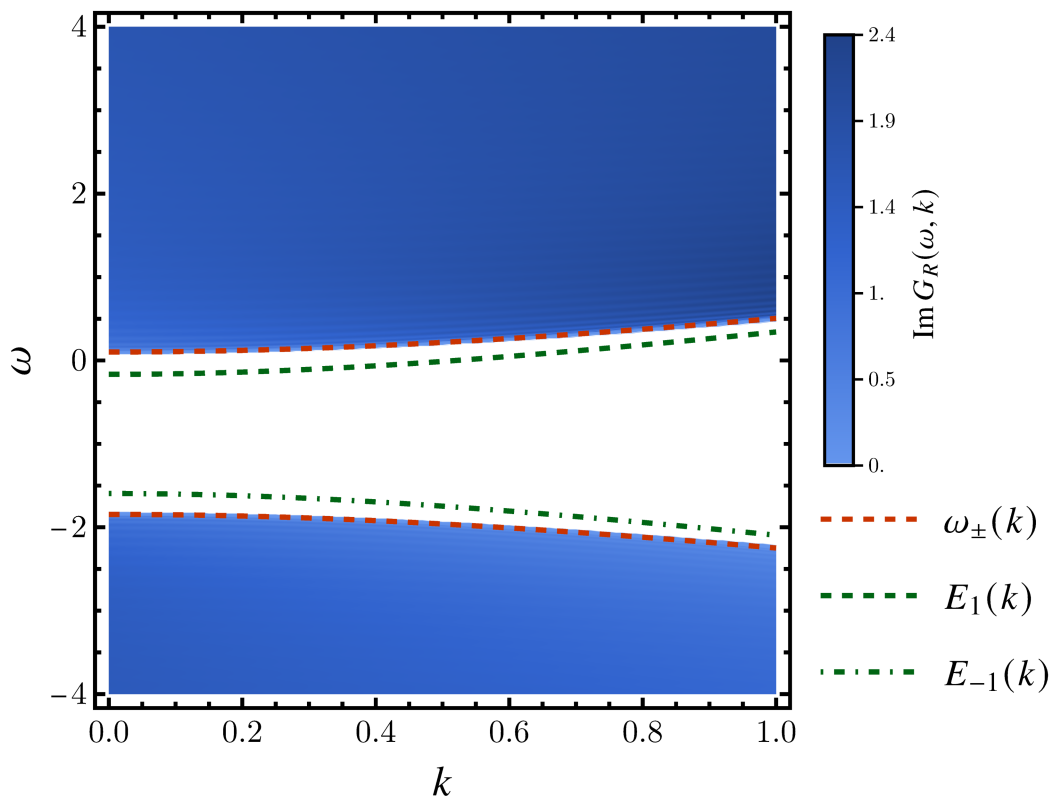
Figure 9. Spectral function $\operatorname{Im} G_R(\omega, k)$ for $\{m, \mu q, \lambda\} = \{0.1, 0.9, 1\}$. The gap appears in white and is well delimited by $\omega_\pm(k)$ (red dashed lines). The normal mode bands have been superimposed to show the infinitely long-lived modes, see figure 10. Outside the gap, there is no particle (normal mode) but a continuum shaped by the remnant of the UV conformal branch cuts. Since the regulator and the chemical potential explicitly break conformality, we do not reproduce the pure AdS Lorentz-invariant spectrum for any finite value of ω and k.

excitations is indeed zero to numerical accuracy except at the positions of the normal modes of the background fermions. The latter are computed directly from the solution of the background Dirac equation (green lines in figure 9), as they cannot be seen numerically in the spectral function because they are infinitely long-living modes which show in the spectrum as Dirac delta peaks. Being infinitely narrow on the real axis, they can only be detected in the complex-ω plane. Representing schematically the normal mode located at $\omega_\star$ by $\operatorname{Im} G(\omega = \operatorname{Re}(\omega)) = Z\delta(\omega - \omega_\star)$ where Z is the peak weight (wavefunction renormalization), we have, for complex ω:

$$\operatorname{Im} G_R(\omega, k) = -Z \frac{\operatorname{Im}\omega - \operatorname{Im}\omega_\star}{(\operatorname{Re}\omega - \operatorname{Re}\omega_\star)^2 + (\operatorname{Im}\omega - \operatorname{Im}\omega_\star)^2} \, . \tag{3.10}$$

When $\operatorname{Re}\omega = \operatorname{Re}\omega_\star$, this simplifies to

$$\operatorname{Im} G_R(\omega, k) = -\frac{Z}{\operatorname{Im}\omega - \operatorname{Im}\omega_\star} \, . \tag{3.11}$$

We check this picture against the numerics first in figure 10(A), where the absolute value of the spectral function in complex frequency plane shows the typical structure of a string of
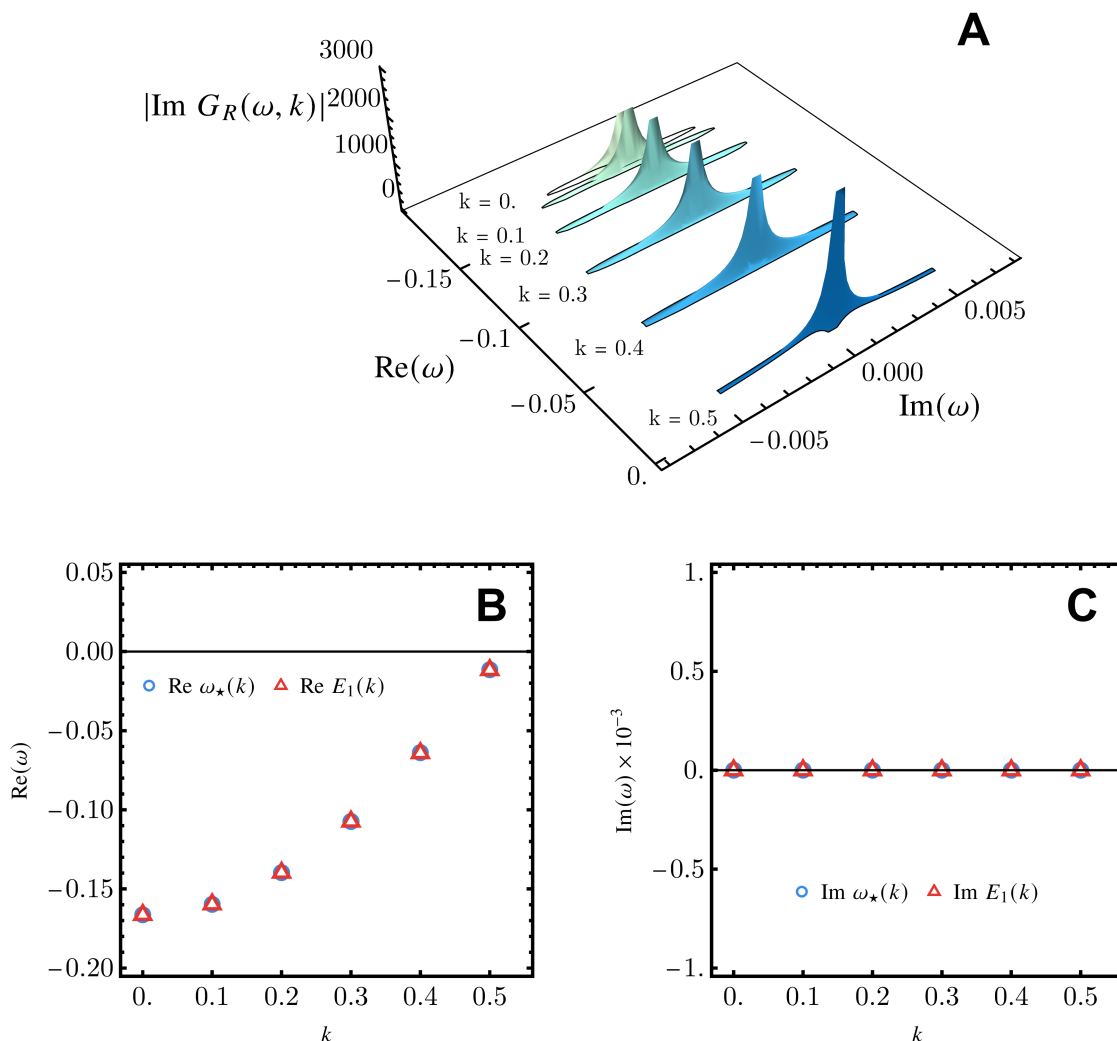
Figure 10. (A) Absolute value of the fermionic spectral function for different values of momentum. The plot is cropped for values below 100 to highlight the quasiparticle peaks. (B and C) Comparison of the poles in the spectrum (blue circles), identified in (A), to the first electron band of the background (red triangles). The real parts (B) of both sets agree perfectly; the imaginary parts (C) are both zero to high accuracy. All this data is computed for $\{m, \mu q, \lambda\} = \{0.1, 0.9, 1\}$.

poles (for various momentum values) lying on the real axis. The relation (3.11) is then used to identify the dispersion relation of the pole $\omega_\star(k)$ by fitting $\mathrm{Im}\, G_R(\omega, k)$. We find, with no big surprise, a perfect agreement with the normal mode excitations $E_1(k)$ corresponding to the first electron band, as seen in figure 10(C) and (D). A similar picture is found for the first hole band $E_{-1}(k)$ and this yields the spectrum inside the gap, plotted in figure 9.

In figure 11 we compare the spectral function at finite μ for our regulated quantum electron star (blue data points) to the fermionic spectral function in a pure AdS$_4$ background with finite chemical potential, either with (green line) and without (red line) regulation by the confining scalar. The comparison is given at $k = 0$ (left) and $k = 1$ (right). The Dirac
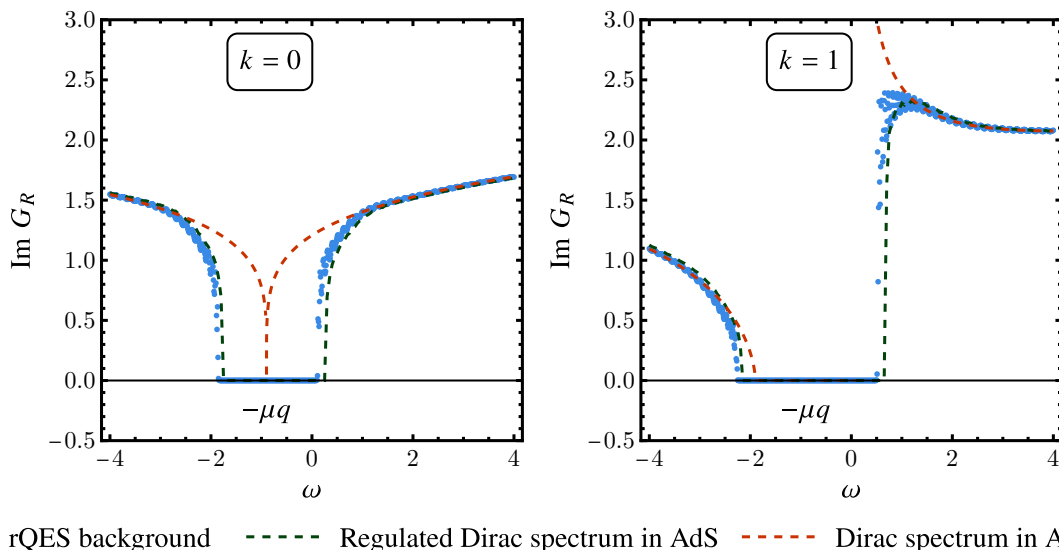
Figure 11. (Confined) Dirac spectral function (blue points) in the rQES background for $k = 0$ (left) and $k = 1$ (right), compared with the standard/unconfined (red dashed line) and regulated/confined (green dashed line) Dirac spectral function in AdS with finite electrostatic potential.

spectrum in AdS$_4$ is well-known [30]:

$$G_R(\omega, k) = \begin{cases} \dfrac{2}{\omega^2 - k^2} \dfrac{\Gamma(1/2 - m)}{\Gamma(1/2 + m)} \left[-\dfrac{i}{2} \left(\omega^2 - k^2 \right) \right]^{2m+1} \left[\omega \gamma^0 - k \gamma^1 \right] & \text{if } \omega > k, \\[3mm] \dfrac{2}{\omega^2 - k^2} \dfrac{\Gamma(1/2 - m)}{\Gamma(1/2 + m)} \left[\dfrac{i}{2} \left(\omega^2 - k^2 \right) \right]^{2m+1} \left[\omega \gamma^0 - k \gamma^1 \right] & \text{if } \omega < -k. \end{cases} \tag{3.12}$$

It has a conformal branch-cut at $\omega = k$ and a gap for $\omega^2 < k^2$. For AdS$_4$ with finite electrostatic potential, one merely needs to replace $\omega \to \omega + \mu q$ in the previous expression. Adding confining potential by turning on the chirality-breaking flat scalar widens the gap to $(\omega + \mu q)^2 < k^2 + \lambda^2$; in particular the gap is open also at $k = 0$. The rQES solution outside the gap exhibits qualitatively the same spectral function as that of the confined Dirac spectrum in pure AdS$_4$ but for renormalized IR values $\omega_{\text{IR}}, k_{\text{IR}}, \lambda_{\text{IR}}$ given in (2.25). It is important to emphasize that none of the modes in this continuum are normalizable and thus do not contribute when building the bulk rQES, even when μq is large enough that $\omega_+(k) < 0$. This is guaranteed by our choice of UV boundary conditions.

4 Towards a self-confining quantum electron star

4.1 Comparison to the holographic superconductor

By construction the confinement in our setup gives an AdS$_4$-to-AdS$_4$ solution. With the fully backreacted solution in hand we can also understand what the field theory dual describes. The confining regulator scale λ gaps the field theory fermion spectral function. Considering then the RG flow from the IR emergent conformal field theory towards the UV, this means that as one increases the energy scale it takes a finite distance for occupiable fermion states

to be encountered. This can also be seen in the band structure of figure 6. At this scale the theory deforms away from the strict conformal theory up to the scale μ beyond which it is no longer energetically favorable to occupy more states. The flow up the RG then continues towards the UV AdS$_4$ fixed point.

In the more usual flow from the UV to the IR this is not a natural RG trajectory. The generic IR will not be a non-trivial conformal field theory. Nevertheless, within holography such AdS$_4$-to-AdS$_4$ domain walls are well-known. Especially in the search for the holographic dual of the holographic superconductor ground state, Horowitz and Roberts and independently Gubser and Rocha have found AdS$_4$-to-AdS$_4$ domain walls (in some cases with logarithmic corrections) in a finite parameter range [16, 17]; the other solution found is the Lifshitz geometry. It was later understood that Lifshitz rather than an AdS$_4$ IR is the generic holographic superconductor ground state [17, 18], but this is only seen with the inclusion of a stabilizing quartic potential.

In detail of course the solutions are different. The Horowitz-Roberts-Gubser-Rocha holographic superconductor ground states do not need an additional confining scalar. They can also be obtained classically without the need for a one-loop Hartree mean field. This is due to the fact that the bosonic field already couples quadratically to the electrostatic potential A_t. A fermion only couples linearly, but its one-loop contribution can couple at all orders. This is why for fermionic systems one needs to go to one-loop.

4.2 Confinement in the rQES solution

Given that the Horowitz-Roberts-Gubser-Rocha AdS$_4$-to-AdS$_4$ solutions do not need a confining potential, and that the more generic holographic superconductor Lifshitz solutions are known, it is a natural question why we do not try to remove the soft-confining regulator alltogether. There was in fact a concerted effort to do so several years ago [5, 9, 12], culminating in the QES model of [14, 15]. The latter two articles show in detail how the presence of the gap and the discretized spectrum are crucial to construct any type of quantum fermionic backreacted solution, i.e. where one or a small finite number of radial modes are occupied. Any attempt to remove the confining potential results in a uncontrolled continuum spectrum.

It is precisely this insight that was the starting point for our confining potential. What we have furthermore shown, is that even then there are several severe technical hurdles to overcome to construct a converging fully backreacted confined quantum electron star solution. At the same time the general insight still holds. Our infrared boundary conditions crucially depend on the coupling to the scalar $\Phi(z)$ to extend the domain of existence of normalizable modes of AdS$_4$ all the way to $k = 0$. The parameter λ, as we previously noted, acts as a momentum shift in this domain such that a mode at $k = 0$ will behave as a mode at $k_{\text{eff}} = \lambda$ and therefore normalizable modes with $|\omega + \mu q| < \lambda$ will be found. These can be populated and will condense in the bulk. Turning off the potential, even slowly, will invariably lead to a lack of normalizable modes at the lowest momenta and will bring us back to a situation similar to that of AdS$_4$.

One sliver of hope would be that the domain wall solution itself, after convergence, can support a well in the Schrödinger potential such that a regulator is no longer necessary. We have therefore looked at this (figure 12) by comparing the Schrödinger potential for a $k = 0$,
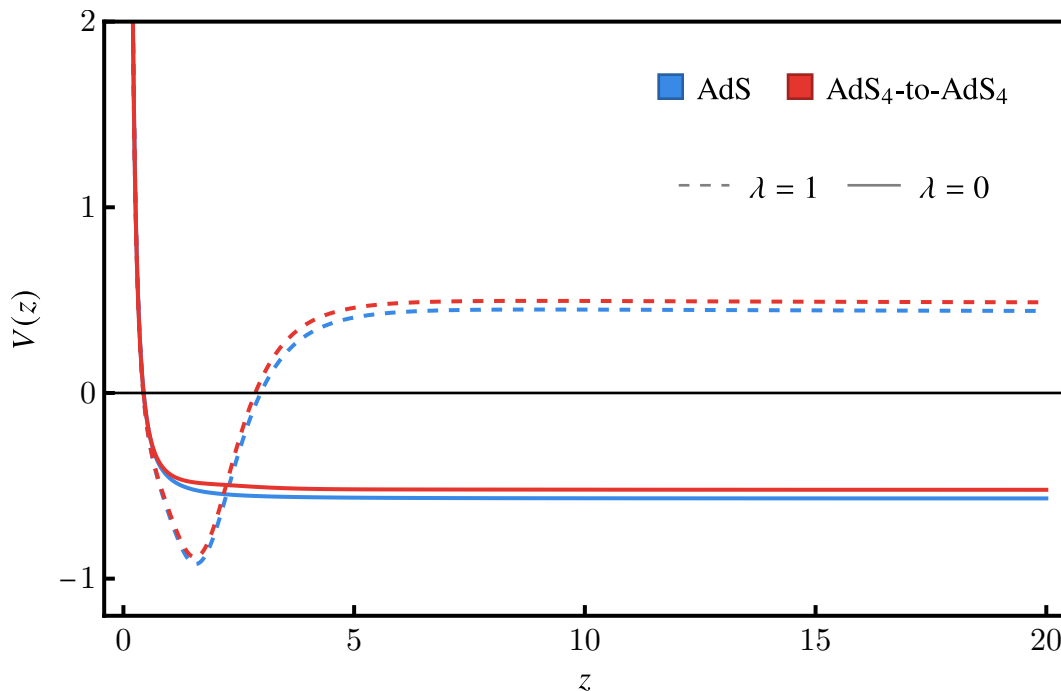
Figure 12. Comparison of the Schrödinger potential for the AdS$_4$ (blue) and AdS$_4$-to-AdS$_4$ (red) solutions with (dashed) and without (solid) regulator, for $\{m, \mu q, k, \omega\} = \{0.1, 1.05, 0, -0.027\}$.

$\omega = E_1(0)$ mode in the confined quantum electron star AdS$_4$-to-AdS$_4$ background with and without the confining potential. Without a potential, however, the AdS$_4$-to-AdS$_4$ quantum electron star domain wall solution is not confining. We do see that $V_{\mathrm{domain\,wall}}(z \to \infty) > V_{\mathrm{AdS}}$ which means the wedge of existence of normalizable modes is indeed wider in the domain wall solution than in the AdS$_4$ solution. Yet, the modes with sufficiently small momenta (including $k = 0$) are always outside the wedge.

This therefore leads us to believe a true QES would not *remove* the regulator but must *incorporate* it into the model, i.e. make the scalar field a dynamical dilaton which couples to the Dirac fermion and drives the geometry from one fixed point to another.

5   Discussion and conclusions

In this paper we have constructed a self-consistent model of a single band confined holographic Fermi liquid. The crucial technical problem, the infrared divergence brought about by the fermionic wavefunctions, is solved by controlling it by hand. We control the far infrared by the means of a scalar regulator, equivalent to a soft-confining potential. The confinement is drastic and 100%: our regulated quantum electron star is dual to a gas of infinitely-long living particles with zero self-energy. In the limit where we compute, it is a single-band Fermi-gas rather than a Fermi-liquid.[6] At higher energies, the spectrum switches to the featureless continuum inherited from the UV conformal field theory (though it is not conformally invariant due to the presence of the confining potential).

---

[6]This holds at zero temperature. At finite temperature a black hole horizon would form, causing inevitably some dissipation even in the presence of the confinement.

The regulated quantum electron star is the thermodynamically preferred solution over the Reissner-Nordström background for $\mu q/m > (\mu q/m)_{\text{critical}}$. The transition is first order, which means that the there is no continuous exchange of charge from the RN solution to the bulk Fermi sea. Instead all the charge is carried by the infinitesimally small rQES. This is somewhat different from the conundrum that we mention in the Introduction: the onset of a log-oscillatory signal in the spectral function signaling a putative instability and the presence of normalizable solutions. The first order transition is essentially unrelated to the RN horizon instability.

Although it is not yet clear how the rQES is related to the final state after the conjectured continuous quantum phase transition which destroys the Reissner-Nordström black hole horizon signalled by the log-oscillatory instability, we nevertheless feel it is a step in the right direction, bringing us closer to the full unregulated quantum electron star. The reasons are the following:

1. It is now much clearer what a healthy Fermi liquid should do on the gravity side: it should self-consistently form a geometry which yields such an effective potential for the Dirac fermion that it is just confined enough not to diverge in far IR but not so much that the bulk Fermi sea dies out in the far IR, failing to influence the low-energy physics.

2. We have inspected in some detail the spectrum and the phenomenology of the dual confined Fermi liquid. Although our confining bulk construction is somewhat more natural in holography — it just uses a non-dynamical rather than a dynamical scalar — than the hard-wall model [13], and it now allows us to compute the backreaction, qualitatively the field-theory side description is only marginally improved. Similar to the hard-wall model, the occupied fermions have vanishing self-energy. The main effect of the backreaction is to understand how this confined Fermi gas emerges in an RG-flow from the UV conformal field theory. In the likely event that an unregulated (confining) quantum electron star — supported for instance by a dynamical rather than a non-dynamical scalar (such as the fluid electron star in [19]) — has a Lifshitz IR rather than an AdS$_4$ IR, possible decay into the Lifshitz horizon could provide a finite lifetime and an honest Fermi liquid.

3. Unlike the global AdS radius regulator of [15] which cannot be easily sent to infinity, our scalar can at least in principle be made dynamical. That would be a perfectly natural holographic model, given the ubiquity of non-minimally coupled scalars in top-down holographic actions. Therefore, a very natural line of further research is to turn this construction into a fully dynamical Einstein-Maxwell-Dirac-scalar system, similar to the fluid approach of [19].

Apart from the natural next step — making the dilaton dynamic — a number of other directions of work open up. It would be useful to understand the relation of our work to the AdS/QCD studies, some of which employ a similar type of scalar (soft wall) to impose confinement. The role of the Fock correction (the one-loop exchange diagram) is also not clear yet, and may be important for a fully self-regulating solution and/or a finite self-energy. Finally, the most characteristic property of rQES — the domain-wall-type solution with

an infrared AdS$_4$, is analogous to the domain-wall holographic superconductor solutions of Horowitz-Roberts-Gubser-Rocha [16, 18, 31]. Based on those results and the macroscopic electron star with dynamical dilaton studied in [19], it strongly suggests that Lifshitz IR quantum electron stars must also exist.

Acknowledgments

References

[1] L. Huijse and S. Sachdev, *Fermi surfaces and gauge-gravity duality*, *Phys. Rev. D* **84** (2011) 026001 [arXiv:1104.5022] [ɪɴSPIRE].

[2] H. Liu, J. McGreevy and D. Vegh, *Non-Fermi liquids from holography*, *Phys. Rev. D* **83** (2011) 065029 [arXiv:0903.2477] [ɪɴSPIRE].

[3] M. Cubrovic, J. Zaanen and K. Schalm, *String Theory, Quantum Phase Transitions and the Emergent Fermi-Liquid*, *Science* **325** (2009) 439 [arXiv:0904.1993] [ɪɴSPIRE].

[4] T. Faulkner, H. Liu, J. McGreevy and D. Vegh, *Emergent quantum criticality, Fermi surfaces, and AdS$_2$*, *Phys. Rev. D* **83** (2011) 125002 [arXiv:0907.2694] [ɪɴSPIRE].

[5] S.A. Hartnoll and A. Tavanfar, *Electron stars for holographic metallic criticality*, *Phys. Rev. D* **83** (2011) 046003 [arXiv:1008.2828] [ɪɴSPIRE].

[6] V.G.M. Puletti, S. Nowling, L. Thorlacius and T. Zingg, *Holographic metals at finite temperature*, *JHEP* **01** (2011) 117 [arXiv:1011.6261] [ɪɴSPIRE].

[7] S.A. Hartnoll and P. Petrov, *Electron star birth: A continuous phase transition at nonzero density*, *Phys. Rev. Lett.* **106** (2011) 121601 [arXiv:1011.6469] [ɪɴSPIRE].

[8] S.A. Hartnoll, D.M. Hofman and D. Vegh, *Stellar spectroscopy: Fermions and holographic Lifshitz criticality*, *JHEP* **08** (2011) 096 [arXiv:1105.3197] [ɪɴSPIRE].

[9] M. Cubrovic, Y. Liu, K. Schalm, Y.-W. Sun and J. Zaanen, *Spectral probes of the holographic Fermi groundstate: dialing between the electron star and AdS Dirac hair*, *Phys. Rev. D* **84** (2011) 086002 [arXiv:1106.1798] [ɪɴSPIRE].

[10] J. Zaanen, Y. Liu, Y.-W. Sun and K. Schalm, *Holographic Duality in Condensed Matter Physics*, Cambridge University Press (2015) [DOI].

[11] S.A. Hartnoll, A. Lucas and S. Sachdev, *Holographic quantum matter*, arXiv:1612.07324 [INSPIRE].

[12] M.V. Medvedyeva, E. Gubankova, M. Čubrović, K. Schalm and J. Zaanen, *Quantum corrected phase diagram of holographic fermions*, *JHEP* **12** (2013) 025 [arXiv:1302.5149] [INSPIRE].

[13] S. Sachdev, *A model of a Fermi liquid using gauge-gravity duality*, *Phys. Rev. D* **84** (2011) 066009 [arXiv:1107.5321] [INSPIRE].

[14] A. Allais, J. McGreevy and S.J. Suh, *A quantum electron star*, *Phys. Rev. Lett.* **108** (2012) 231602 [arXiv:1202.5308] [INSPIRE].

[15] A. Allais and J. McGreevy, *How to construct a gravitating quantum electron star*, *Phys. Rev. D* **88** (2013) 066006 [arXiv:1306.6075] [INSPIRE].

[16] G.T. Horowitz and M.M. Roberts, *Zero Temperature Limit of Holographic Superconductors*, *JHEP* **11** (2009) 015 [arXiv:0908.3677] [INSPIRE].

[17] S.S. Gubser and F.D. Rocha, *The gravity dual to a quantum critical point with spontaneous symmetry breaking*, *Phys. Rev. Lett.* **102** (2009) 061601 [arXiv:0807.1737] [INSPIRE].

[18] S.S. Gubser and A. Nellore, *Ground states of holographic superconductors*, *Phys. Rev. D* **80** (2009) 105007 [arXiv:0908.1972] [INSPIRE].

[19] S.A. Hartnoll and L. Huijse, *Fractionalization of holographic Fermi surfaces*, *Class. Quant. Grav.* **29** (2012) 194001 [arXiv:1111.2606] [INSPIRE].

[20] C.P. Herzog, *A Holographic Prediction of the Deconfinement Temperature*, *Phys. Rev. Lett.* **98** (2007) 091601 [hep-th/0608151] [INSPIRE].

[21] G.F. de Teramond and S.J. Brodsky, *Excited Baryons in Holographic QCD*, *AIP Conf. Proc.* **1432** (2012) 168 [arXiv:1108.0965] [INSPIRE].

[22] A. Karch, E. Katz, D.T. Son and M.A. Stephanov, *Linear confinement and AdS/QCD*, *Phys. Rev. D* **74** (2006) 015005 [hep-ph/0602229] [INSPIRE].

[23] Z. Fang, D. Li and Y.-L. Wu, *IR-improved Soft-wall AdS/QCD Model for Baryons*, *Phys. Lett. B* **754** (2016) 343 [arXiv:1602.00379] [INSPIRE].

[24] N. Iizuka, N. Kundu, P. Narayan and S.P. Trivedi, *Holographic Fermi and Non-Fermi Liquids with Transitions in Dilaton Gravity*, *JHEP* **01** (2012) 094 [arXiv:1105.1162] [INSPIRE].

[25] L.D. Landau and E.M. Lifshitz, *Statistical Physics, Part 2: Theory of the Condensed State*, Fizmatlit (2004).

[26] S.S. Gubser, F.D. Rocha and P. Talavera, *Normalizable fermion modes in a holographic superconductor*, *JHEP* **10** (2010) 087 [arXiv:0911.3632] [INSPIRE].

[27] F. Denef, S.A. Hartnoll and S. Sachdev, *Quantum oscillations and black hole ringing*, *Phys. Rev. D* **80** (2009) 126016 [arXiv:0908.1788] [INSPIRE].

[28] K. Hashimoto and N. Iizuka, *A Comment on Holographic Luttinger Theorem*, *JHEP* **07** (2012) 064 [arXiv:1203.5388] [INSPIRE].

[29] N. Iqbal, H. Liu and M. Mezei, *Semi-local quantum liquids*, *JHEP* **04** (2012) 086 [arXiv:1105.4621] [INSPIRE].

[30] N. Iqbal and H. Liu, *Real-time response in AdS/CFT with application to spinors*, *Fortsch. Phys.* **57** (2009) 367 [arXiv:0903.2596] [INSPIRE].

[31] G. Horowitz, A. Lawrence and E. Silverstein, *Insightful D-branes*, *JHEP* **07** (2009) 057 [arXiv:0904.3922] [INSPIRE].

Correlation functions for open strings and chaos

Vladan Đukić [a,b] and Mihailo Čubrović [b]

[a]Faculty of Physics, University of Belgrade,
Studentski Trg 12-16, 11000 Belgrade, Serbia
[b]Center for the Study of Complex Systems, Institute of Physics Belgrade, University of Belgrade,
Pregrevica 118, 11080 Belgrade, Serbia

E-mail: djukic@ipb.ac.rs, cubrovic@ipb.ac.rs

Abstract: We study the holographic interpretation of the bulk instability, i.e. the bulk Lyapunov exponent in the motion of open classical bosonic strings in AdS black hole/brane/ string backgrounds. In the vicinity of homogeneous and isotropic horizons the bulk Lyapunov exponent saturates the MSS chaos bound but in fact has nothing to do with chaos as our string configurations live in an integrable sector. In the D1-D5-p black string background, the bulk Lyapunov exponent is deformed away from the MSS value both by the rotation (the infrared deformation) and the existence of an asymptotically flat region (the ultraviolet deformation). The dynamics is still integrable and has nothing to do with chaos (either in gravity or in field theory). Instead, the bulk Lyapunov scale captures the imaginary part of quasinormal mode frequencies. Therefore, the meaning of the bulk chaos is that it determines the thermal decay rate due to the coupling to the heat bath, i.e. the horizon.

Keywords: AdS-CFT Correspondence, Bosonic Strings, Black Holes, D-Branes

Contents

1 Introduction

Chaos in string theory has traversed the way from an arcane and little-noticed topic to a mainstream field, thanks to the ideas of fast scrambling and black holes as the fastest scramblers in nature [1], the Maldacena-Shenker-Stanford (MSS) maximum chaos bound for strongly coupled field theories with black hole duals [2] and the notion of out-of-time ordered correlators (OTOC) [3–5] and their applications in the physics of chaotic strongly coupled systems [6–8]. An important motor of the field is also the connection to recent progress on the black hole information problem [9–12] and the related puzzle of factorization [13–20]. In [21] it was demonstrated for the first time that the MSS scale characterizes also the time-disordered correlation functions on a string worldsheet, provided that the induced metric has a horizon and thus mimics black hole physics. The guiding idea through all these topics is of course the AdS/CFT duality, the unifying principle of many topics in string theory and gravity. Our primary interest thus lies in the dynamics in asymptotically AdS backgrounds.

Among the many questions which have opened up, there is one seemingly technical but in fact physically important subtlety. Several papers have reported the saturation of the bound $2\pi T$ for *bulk* orbits of particles [22, 23], or its slight modification/generalization for fields [22] and strings [24–30]; the systematic answer to the question of the bulk Lyapunov exponent is given in [31]. However, a very simple question arises: *why should there ever be*

an MSS-like bound for bulk Lyapunov exponents? The OTOC exponent and its MSS bound $\lambda = 2\pi T$ in principle have no simple relation to the classical bulk motion and its Lyapunov exponent: the former is a property of a time-dependent correlation function in dual CFT, determined by a 4-wave scattering amplitude in the bulk, and the latter is the solution of a bulk equation of motion, for a single orbit, with no scattering and thus no OTOC-like interpretation in the bulk. This relates to a more general question: what is the CFT dual of a bulk orbit (and its Lyapunov instability exponent)? Some important work was done on this issue [32–37], and the outcome is that a bulk particle is dual to a shock wave perturbation of the dual CFT. But many details are still missing; in particular, the answer cited above holds for a geodesic with both endpoints on the AdS boundary; it is less clear what the CFT dual is for an orbit not reaching the boundary.

Paradoxically, a string in the bulk, specifically an open string, is perhaps an easier case for study. It is long known that a static or dragging string, with one endpoint in the interior and the other on the boundary, is dual to a heavy quark in the quark-gluon plasma of the supersymmetric Yang-Mills gauge theory [38, 39]. Likewise, an open string with both endpoints on the boundary represents a quark-antiquark pair [40–44], and encodes information on the confinement mechanism. It is thus a convenient framework to pose our main question: *what is the meaning of the bulk Lyapunov exponent and what does it have to do with the MSS bound?*

In this work we give a partial answer to the question and demonstrate it by a number of case studies involving bosonic open strings in various backgrounds.[1] There is, in fact, no unique answer to the question of the CFT dual to a bulk Lyapunov exponent: just as various string configurations have various field theory duals (a quark, a bound pair of quarks, an EPR pair, an accelerating quark. . .), likewise the Lyapunov stability of these different solutions will have different meanings. Furthermore, on the string worldsheet there are two coordinates thus we have two Lyapunov exponents, with different CFT meanings.

We also find that the MSS form of the exponent is really a red herring: in the strict infinite-coupling, infinite-N limit and with maximal symmetry, $2\pi T$ becomes a natural scale which has to appear in all fluctuation equations. As soon as we decrease symmetry (e.g. by considering a D1-D5-p bound state in the bulk that breaks rotational invariance) or include stringy effects, the bulk exponent (as well as OTOC [5] and other CFT correlation functions) undergo corrections, and do not coincide anymore (neither among themselves nor with the MSS bound). Recent work on universal near-horizon symmetries [45, 46] has shone additional light on the issue, allowing us to view the MSS scale as the fundamental property of black hole horizons, so it can appear in any CFT correlator which is sensitive to temperature T, i.e. which probes the energy scales smaller than T. The puzzle of "why $2\pi T$ pops out everywhere" is thus a fake issue: it disappears as soon as leading corrections or broken symmetries are taken into account.

The sharpest finding of our analysis is that the bulk Lyapunov exponents of a probe string in fact reproduce the quasi-normal mode (QNM) spectrum of the black hole or black

---

[1]While the dynamics of a superstring would be an interesting problem to study, in this work we stick solely to the bosonic sector. This is enough to understand the principles, and also to model holographically the dynamics of a heavy quark in Yang-Mills plasma.

string background; in other words, they correspond to the thermal decay rate. Since this rate is also determined by the temperature times an $O(1)$ factor, we feel that this also provides an explanation for the origin of an MSS-like expression in bulk dynamics. It also clearly spells out that the relation of bulk instability scale to OTOC-ology and chaos in dual CFT is fake. In terms of the relation to QNM, our work is a stringy generalization of a similar result for geodesics [47, 48] and scalar waves [49, 50].

The plan of the paper is the following. In section 2 we study the simplest possible case: open string in AdS-Schwarzschild background, where the basic message already appears — the bulk Lyapunov exponent is $2\pi T$ but it is not related to chaos. In section 3 we demonstrate the same findings on more general background. In section 4 we address the dynamics of the string probe in the D1-D5-p and related backgrounds. Here we do a more detailed study, comparing the bulk variational equations to the retarded correlators dual to the string fluctuations, and finding that the bulk Lyapunov instability really described the quasinormal modes and hence the thermal decay rate in field theory. The final section sums up the conclusions.

2 Open string in AdS-Schwarzschild background

Our goal is to study the linear stability and fluctuations of classical solutions for the static open string stretching from the boundary to the horizon of an AdS black hole, the well-known simple holographic probe for a heavy quark in quark-gluon plasma.[2] Therefore, we write down the string action, derive the equations of motion and variational equations. Throughout the paper we consider only the bosonic sector of the string. Most of the time we will use the Polyakov action, but sometimes we will switch to the Nambu-Goto action, depending on the problem at hand.

2.1 Setup and radial fluctuations

Dynamics of a string in $D + 1$-dimensional AdS-Schwarzschild spacetime with the time coordinate t, radial coordinate r, transverse spatial coordinates x_i ($i = 1, \ldots D - 1$) and the horizon at r_h:

$$ds^2 \equiv G_{\mu\nu}(x)dx^\mu dx^\nu = r^2 \left(-h(r)dt^2 + d\vec{x}^2\right) + \frac{dr^2}{r^2 h(r)}, \quad h(r) = 1 - \left(\frac{r_h}{r}\right)^D, \qquad (2.1)$$

can be described by the Polyakov action for the string:

$$S_{\mathrm{P}} = -\frac{1}{2\pi\alpha'} \int d\tau d\sigma \; \eta^{\alpha\beta} \partial_\alpha X^\mu \partial_\beta X^\nu G_{\mu\nu}(X). \qquad (2.2)$$

Here and in the rest of the paper $\alpha, \beta, \cdots \in \{\tau, \sigma\}$ and $\mu, \nu, \cdots \in \{t, r, \vec{x}\}$ stand for worldsheet and spacetime indices respectively. Latin indices $i, j, \cdots$ count the transverse coordinates $x_1, \ldots x_{D-2}$. As we know [38], the equations of motion are consistent with the following ansatz:

$$t = t(\tau), \quad R = R(\sigma), \quad X_1 = X_1(\tau, \sigma), \quad X_j = X_j(\tau), \; j = 2, \ldots, D - 1, \qquad (2.3)$$

---

[2]In fact, to be precise, a heavy colored particle in super-Yang-Mills plasma.

describing a string stretching from the horizon at r_h to the boundary at $r = \infty$. It is easiest to impose the flat worldsheet metric and solve for the Virasoro constraints together with the equations of motion:

$$\ddot{t}(\tau) = 0, \quad \ddot{X}_j(\tau) = 0, \ j = 2, \ldots, D-1 \tag{2.4}$$

$$-2h^3(R)R^4(\sigma) - (R(\sigma)h'(R) + 2h(R)) \, R'^2(\sigma) + 2h(R)R(\sigma)R''(\sigma) +$$
$$+ h^2(R)R^4(\sigma) \left[-R(\sigma)h'(R) + 2 \left(X_1'^2(\tau,\sigma) + \dot{X}_1^2(\tau,\sigma) + \sum_{j=2}^{D-1} \dot{X}_j^2(\tau) \right) \right] = 0, \tag{2.5}$$

$$2R'(\sigma)X_1'(\tau,\sigma) + R(\sigma) \left(X_1''(\tau,\sigma) - \ddot{X}_1(\tau,\sigma) \right) = 0, \tag{2.6}$$

$$\frac{R'^2(\sigma)}{R^4(\sigma)} + h(R) \left(-h(R)\dot{t}^2(\tau) + X_1'^2(\tau,\sigma) + \dot{X}_1^2(\tau,\sigma) + \sum_{j=2}^{D-1} \dot{X}_j^2(\tau) \right) = 0, \tag{2.7}$$

$$X_1' \cdot \dot{X}_1 = 0. \tag{2.8}$$

The equations for $t, X_2, \ldots, X_{D-1}$ (2.4) are trivially satisfied when these are functions linear in τ, thus we can set $t = \tau$ and $X_j = $ const. Moreover, the second constraint (2.8) requires X_1 to depend on one variable only. For now we choose $X_1 = X_1(\sigma)$, i.e. the static open string/heavy quark (later on we will study both space- and time-dependent fluctuations). Now the remaining equation for $R(\sigma)$ (eq. (2.5)), together with the nontrivial Virasoro constraint (2.7), also decouples from $X_1(\sigma)$ and simplifies to the following form

$$4h^3(R)R^3(\sigma) + h^2(R)h'(R)R^4(\sigma) + h'(R)R'^2(\sigma) - 2h(R)R''(\sigma) = 0. \tag{2.9}$$

The same equation can be derived from the effective Lagrangian, obtained by first substituting the trivial solutions $t = \tau$ and $X_j = 0$, $\forall j \neq 1$ into the Polyakov Lagrangian, and then making use of the Virasoro constraint (2.7) to eliminate $X_1'^2$:

$$\mathcal{L}_{\text{eff}} = \frac{-h^2(R) - f(R)R'^2(\sigma) - h(R)X_1'^2(\sigma)}{\sqrt{f(R)}h(R)}. \tag{2.10}$$

This Lagrangian has the worldsheet energy as its integral of motion and is thus integrable, as we will argue more rigorously in the following section.

2.1.1 Variational equations and Lyapunov exponents

We will now write down the variational equation corresponding to the on-shell equation of motion (2.9). We will find that the solution to the variational equation is an exponential function, which defines the Lyapunov exponent the usual way. The unusual detail is the fact that both $R(\sigma)$ and its variation $\delta R(\sigma)$ depend on the *spatial* coordinate σ. Studying the spatial dependence of the worldsheet field and calling it dynamics as we do might be controversial; so is the term Lyapunov exponent for the growth exponent of the variation $\delta R(\sigma)$. The important difference between σ and τ dynamics is that the worldsheet time is unbounded and one can define asymptotic quantities as it is usually done for the Lyapunov exponent (defining it as the limit of small initial variation and long-time evolution

$\lambda = \lim_{t \to \infty} \lim_{\delta x(0) \to 0} \log\left(\delta x\left(t\right)\right)/t$, for some generic coordinate x). The extent of the σ coordinate is finite and there is no analogue to $\lim_t \to \infty$. Therefore, while we talk all the time of Lyapunov exponents, we really study what is often called finite-time Lyapunov indicator in the context of time evolution, i.e. the exponent defined locally rather than asymptotically. This is however often assumed as a matter of course: the bulk Lyapunov exponent (in time) computed, e.g. in [22, 26, 47], is also the finite-time quantity.

We are mainly interested in studying the variation near the horizon. To that end, we substitute $R(\sigma) \mapsto r_0 + \varepsilon \delta R(\sigma)$ into eq. (2.9), expand it in ε small to linear order, and finally take the limit $r_0 \to r_h$.[3] This yields the near-horizon variational equation:

$$\delta R'' - D^2 r_h^2 \delta R = 0. \tag{2.11}$$

The solution is thus $\delta R \propto e^{\pm 2\lambda_L \sigma}$ with a pair of Lyapunov exponents of equal magnitude and with opposite signs, as it has to happen in a Hamiltonian system. The exponent formally coincides with the MSS bound:

$$\lambda_L = \frac{Dr_h}{2} = 2\pi T. \tag{2.12}$$

The reason why we define the Lyapunov exponent with a factor of 2, i.e. through $\delta R \propto e^{\pm 2\lambda_L \sigma}$ instead of $\delta R \propto e^{\pm \lambda_L \sigma}$ is that the same expression appears also in the OTOC growth, and follows from the definition of OTOC on the thermal circle. Here, for bulk equations of motion, this argument is irrelevant (these are different quantities!) but we nevertheless want to stay consistent with the definition of the MSS bound as we want to compare the two situations.

We have shown that the exponent is $2\pi T$ regardless of the spacetime dimension or any other parameters save the temperature. While it is tempting to call this "maximal chaos in the bulk", we will soon show that this system is not chaotic at all. Therefore we should interpret λ_L not as a measure of chaos (neither in the bulk nor in CFT) but as some characteristic scale related to the near-horizon physics, that will likely correspond to relaxation time of some perturbations around a thermal horizon. Toward the end of the paper we will make this precise.

2.2 Integrability of the static open string

Here we prove that the simplest open string configuration — a static open string at the horizon of the AdS-Schwarzschild geometry — is integrable, unlike the motion of a closed winding string which is nonintegrable in the presence of a black hole [51, 52]. We emphasize that this does *not* imply integrability of the open string for generic boundary conditions.

We will preform the same type of analysis that is done in [51], exploiting the Kovacic algorithm [51, 53–56]. The algorithm can be described as follows: (1) find a family of solutions

---

[3]The order of limits is important because of the coordinate singularity at the horizon. If we immediately put $R(\sigma) \mapsto r_h + \varepsilon \delta R(\sigma)$ we end up with an equivalent variational equation which is however *nonlinear*: $\delta R'' - \delta R'^2/(2\delta R) - (D^2/2)r_h^2 \delta R = 0$; the nonlinearity stems from the vanishing of a term in the on-shell equation at the horizon, so that a linear expansion in ε yields an equation which is not necessarily linear in δR and its derivatives. If we try to expand the Lagrangian $\mathcal{L}_{\text{eff}}$ and then solve the equation which follows from the leading correction to $\mathcal{L}_{\text{eff}}$ (quadratic in ε), the coefficients of this equation diverge at $r = r_h$. Again, all of this is merely about the coordinate system we use; we could work in Kruskal-Szekeres coordinates and avoid the problem.

to the equations of motion defining an invariant plane in the parameter space (2) write down the normal variational equation (NVE) for the invariant plane (3) solve the NVE so obtained and check whether it is expressible in terms of Liouvillian functions; these are the elementary functions (powers, exponentials, trigonometric functions and their inverses), rational functions of such elementary functions, and their integrals.[4]

We want to show the integrability of the system described by the effective Lagrangian in eq. (2.10). One obvious invariant plane is the $R - X_1$ plane for a straight string solution:

$$R(\sigma) = r_h, \ X_1(\sigma) = \text{const.} \equiv X_c. \tag{2.13}$$

One can see that this plane is invariant simply by observing that the canonical momentum corresponding to the off-plane motion is zero: $p'_X = \partial\mathcal{L}_{\text{eff}}/\partial X_1 = 0$. The corresponding NVE along the X_1-direction is trivial: $\delta X''_1 = 0$, yielding the conclusion that the system is integrable. We have seen that the system nevertheless exhibits an exponential growth of the in-plane variation with a positive Lyapunov exponent in the near-horizon region. By itself this is not surprising: a local instability can lead to a growing mode even in a trivially integrable system, the simplest example being the inverse chaotic oscillator [57]. This is similar to findings of [31] where it is noted that horizons are really sources of instability in the bulk. Even integrable systems can display local instability in the vicinity of thermal horizons.

We need to make one thing clear. The integrability of the static open string Lagrangian (2.10) that we have demonstrated in no way conflicts the established nonintegrability of string motion in black hole and D-brane backgrounds proved in [51, 55]. The fact that a ring string in these backgrounds is nonintegrable, as found in the aforementioned references, is enough to prove the nonintegrability of string motion in these geometries in general, and this likely holds also for open strings with sufficiently complicated boundary conditions. On the other hand, the existence of special solutions and boundary conditions which are integrable (and therefore certainly nonchaotic) is perfectly possible also in a nonintegrable system.

3   Open string in other backgrounds

In order to further corroborate the universality of the result (2.12), we will repeat exactly the same analysis for two more backgrounds: (1) a general hyperscaling-violating metric and (2) a black Dp brane. The former is quite relevant for many holographic purposes, the latter does not in general have a holography dual (as its asymptotic geometry is in general not AdS) but it does appear as a sector in various backgrounds (and of course the AdS throat of the D3 brane provides the simplest and most famous top-down AdS/CFT construction). This endeavour might look like mere stamp collecting but it has a purpose: to show that the result is not special to AdSS metric and also to show (from the Dp case) that by itself it has nothing to do with holography or AdS asymptotics — it is all about thermal horizons.

---

[4]One can find the reasoning behind this algorithm in the literature. In brief, the existence of such a solution is equivalent to the solvability of the identity component G^0 of the Galois group; conversely, their nonexistence is equivalent to G^0 being not solvable, and hence non-Abelian. Non-Abelian nature of G^0 tells us that no complete system of integrals of motion in involution exists, therefore the system is nonintegrable.

3.1 General hyperscaling-violating background

In our first example we closely follow the idea of [31] and study bulk motion in a broad class of bulk geometries: hyperscaling-violating horizons at finite temperature, constructed in [58–61] as gravity duals of effective field-theories with scaling and long-range entanglement, thought to be ubiquitous in quantum-many body systems. In [31], it is shown that the bulk geodesics, i.e. particle orbits also have the $2\pi T$ Lyapunov exponent in a large part of the parameter space though not everywhere; here we show that static strings/holographic heavy quarks *always* yield $2\pi T$. The background metric reads

$$ds^2 = -r^{2\mathfrak{z}-\frac{2\theta}{D-2}}f(r)dt^2 + \frac{1}{f(r)r^{2+\frac{2\theta}{D-2}}}dr^2 + r^2 d\vec{x}^2, \quad f(r) = 1 - \left(\frac{r_h}{r}\right)^{D-2+\mathfrak{z}-\theta}, \tag{3.1}$$

and depends on two parameters, the Lifshitz exponent[5] $\mathfrak{z}$ that measures the anisotropy of space versus time scaling (so that Lorentz-invariant backgrounds correspond to $\mathfrak{z} = 1$) and the hyperscaling exponent θ which measures the deviation from the dimensional scalinig of free energy and roughly corresponds to long-range-entangled degrees of freedom. By definition, the temperature of the horizon at r_h is found as:

$$4\pi T = -\frac{g'_{tt}(r_h)}{\sqrt{g_{tt}(r_h)g_{rr}(r_h)}} = (D - 2 - \theta + \mathfrak{z})r_h^{\mathfrak{z}}. \tag{3.2}$$

We can easily redo the same analysis as for the AdSS configuration, keeping the same ansatz (2.3) and the equations of motion analogous to (2.4)–(2.8). When everything is said and done, we obtain the near-horizon variational equation

$$\delta R''(\sigma) - (D - 2 - \theta + \mathfrak{z})^2 r_h^{2\mathfrak{z}} \delta R(\sigma) = 0, \tag{3.3}$$

which, according to (3.2), implies again $\lambda_L = 2\pi T$ with the ansatz $\delta R \sim \exp(2\lambda_L \sigma)$.

3.2 Dp brane and related backgrounds

3.2.1 Extremal black Dp brane

Consider first the single Dp brane geometry in 10 spacetime dimensions. To the best of our knowledge no systematic work was done on string dynamics in brane backgrounds, except for the general proofs of nonintegrability in [51, 55] and of course the near-brane limit of the D3 brane when the asymptotics becomes AdS. The metric reads

$$ds^2 = \frac{\eta_{\mu\nu}dx^\mu dx^\nu}{f^2(r)} + f^2(r)\left(dr^2 + r^2 d\Omega_k\right), \quad \mu = 0, \dots p \tag{3.4}$$

$$f(r) = \left(1 + \frac{Q}{r^n}\right)^m, \quad n = 7 - p, k = 8 - p, m = \frac{1}{4}. \tag{3.5}$$

Here, r is the radial coordinate, x^μ are the directions on the brane, while $d\Omega_k$ is the k-sphere with coordinates $\Phi_1, \dots \Phi_k$. The string configuration we consider is completely analogous

---

[5]We denote the Lifshitz exponent by $\mathfrak{z}$ rather than the usual z, as z will be used for the radial coordinate $z = 1/r$. Likewise ζ is taken by another coordinate to be used in section 4.

to the static open string studied previously in AdS black hole backgrounds:

$$t = t(\tau), \quad X_1 = x_1, \quad \dots \quad X_p = x_p,$$
$$R = R(\sigma), \quad \Phi_1 = \phi_1, \quad \dots \quad \Phi_k = \phi_k \tag{3.6}$$

Therefore, our string configuration is only nontrivial in the directions transverse to the brane, and reduced to a point on the k-sphere (i.e., in longitudinal directions). In appendix A we show that more general ansätze are possible; but for our purposes, eq. (3.6) is perfectly sufficient. For the time direction we can again choose $t(\tau) = \tau$. We have one nontrivial Virasoro constraint which, upon plugging into the equation of motion, yields:

$$R'' + \frac{2f'(R)}{f(R)^5} - \frac{(R')^2 f'(R) \left(-f(R)^4 + QR^{p-7} + 1\right)}{f(R)^5} = 0. \tag{3.7}$$

We have some analytical control over the eq. (3.7) and its variational equation for small R, i.e. near the brane, when we expand $R(\sigma) = \epsilon + \delta R(\sigma)$. The variational equation then reads

$$\delta R'' - \epsilon^{5-p} \sqrt{\frac{(7-p)(6-p)}{2Q}} \delta R = 0, \tag{3.8}$$

where $R \sim \epsilon$, i.e. the small parameter is the distance from the brane; since this limit means $\epsilon \to 0$, the bulk Lyapunov exponent vanishes. We will see the opposite situation with black Dp branes, in the presence of a thermal horizon. The solution (3.8) is obviously only sensible for $p \leq 5$ but for $p > 5$ the same conclusion is reached, only the expansion in r large (ϵ small) is different.

3.2.2 Non-extremal black Dp brane

We will now consider a non-extremal black brane, the finite-temperature generalization of the extremal solution at temperature T:[6]

$$ds^2 = -h(r)\frac{dt^2}{f^2(r)} + \frac{d\vec{x}^2}{f(r)^2} + f^2(r)\left(\frac{dr^2}{h(r)} + r^2 d\Omega_k^2\right) \tag{3.9}$$

$$f(r) = \left(1 + \frac{Q}{r^n}\right)^m, \quad h(r) = 1 - \left(\frac{r_h}{r}\right)^4, \qquad n = 7-p, \ k = 8-p, \ m = \frac{1}{4} \tag{3.10}$$

$$\frac{1}{T} = \frac{4\pi f(r_h)}{\sqrt{h'(r_h)(h(r)/f^2(r))'|_{r=r_h}}} = \frac{4\pi r_h\sqrt{1 + Qr_h^{p-7}}}{p+1}. \tag{3.11}$$

In the limit $r_h \to 0$ (equivalently, $T = 0$) the black brane becomes the previously studied extremal black brane. The coordinates are the same as in the extremal solution (3.5). The $d\Omega_k$ sector is insensitive to temperature, which can be seen from the fact that its metric is independent of the redshift function h. The effect of the thermal horizon is thus seen solely

---

[6]For concreteness we again assume $p \leq 5$ but, just like for the extremal brane, the generalization for $p > 5$ is easy.

in the equation of motion for R (after plugging in the Virasoro constraint as usual):

$$R'' - \left[\frac{f'(R)\left(-f(R)^4 + QR^{p-7} + 1\right)}{f(R)^5} + \frac{h'(R)}{2h(R)} \right] R'^2 - \frac{h(R)\left(f(R)h'(R) - 4h(R)f'(R)\right)}{2f(R)^5} = 0.$$
(3.12)

Following the same logic as before, we find the near-horizon variational equation:

$$\delta R'' - \frac{(p+1)^2}{r_h^2 + Qr_h^{p-5}}\delta R = 0.$$
(3.13)

Looking for a solution of a form $\sim \exp(2\lambda_L \sigma)$ and using eq. (3.11), we find that $\lambda_L = 2\pi T$. The ubiquitous $2\pi T$ is present even if the metric is asymptotically flat, as thermal horizons generate instability, whatever the faraway asymptotics. The holographic meaning of this instability is theory-dependent, and in general does not exist when there is no AdS region.

3.2.3 From $\mathbf{AdS}_{p+2} \times \mathbb{S}^k$ throat to flat space

Following [51, 62, 63], we can consider a modification of the Dp brane geometry at zero or finite temperature to obtain a metric interpolating from an $\mathrm{AdS}_{p+2} \times \mathbb{S}^k$ throat (near-brane) to flat space in the far region; such solutions appear as solutions of supergravity and interpolate between different vacua. The expressions for the metric remain the same as before (eq. (3.5) at $T = 0$ or eq. (3.10) at $T > 0$) but the parameters are:

$$m = \frac{1}{n}, \quad p, n, k \text{ arbitrary.}$$
(3.14)

One can easily check that indeed for $Q \to 0$ or equivalently $r \to r_h$ (including the case $r_h = 0$ for the extremal brane) we obtain $\mathrm{AdS}_{p+2} \times \mathbb{S}^k$ and for $Q \to \infty$ or equivalently $r \to \infty$ we get flat space (in fact, its product with the k-sphere). We proceed along the same lines as before, hence we only give the end results. The variational equation reads

$$\delta R'' - \left(\frac{p+1}{r_h}\right)^2 \left(1 + Qr_h^{p-7}\right)^{\frac{4}{p-7}} \delta R = 0,$$
(3.15)

which yields once again $\lambda_L = 2\pi T$, computing the temperature by definition, similar as in eq. (3.11). Now we can however obtain an analytic solution also in the far region, which interpolates to $\mathbb{R} \times \mathbb{R}^{p+1} \times \mathbb{S}^k$. Writing $R(\sigma) = 1/\epsilon + \delta R(\sigma)$ with $\epsilon \to 0$, we get the variational equation

$$\delta R'' + 2(8-p)Q\epsilon^{9-p}\delta R = 0,$$
(3.16)

yielding $\lambda_L = 0$ as the coefficient of δR is positive (hence the dynamics is oscillatory rather than exponentially growing), and in addition it drops to zero as we reach infinity.

All these examples strongly suggest that the $2\pi T$ exponent (with the same value, but different meaning from the MSS bound for CFT chaos) for the unstable saddle point in bulk motion is present if and only if the geometry has a static thermal horizon, holographic or not. In the next section we will see that the presence of rotation changes the outcome. This will lead us to the general conclusion: that the bulk near-horizon Lyapunov exponent is universal for a given symmetry class of the metric. For maximally symmetric horizons (isotropic and static) the result is always $2\pi T$, which is argued in detail also in [46], on the basis of [45].

3.2.4 Numerical solutions

Although the equations we solve so far are quite elementary, it is always nice to have a numerical check too. Therefore, in this subsubsection we solve the equations of motion numerically; also, this is the only way to look at the string in whole space.[7] We will see explicitly that the system is integrable and yet that the variational equations have exponentially growing solutions.

We will look at the D3 black brane, The aim is thus to solve eq. (3.12) and its variational equation for $p = 3$.[8] In order to do so, it is more convenient to use the coordinate $z = 1/r$, so that the equation of motion for the new worldsheet field $Z(\sigma)$ becomes

$$Z'' - \frac{Z'^2}{Z} - \frac{h'(Z)Z'^2}{2h(Z)} - \frac{h^2(Z)Z^3}{f^4(Z)}\left(1 - Z\left(\frac{2f'(Z)}{f(Z)} + \frac{h'(Z)}{2h(Z)}\right)\right) = 0. \qquad (3.17)$$

We impose Dirichlet conditions at the brane and Neumann conditions at the other end (open strings should be attached to branes but they can float freely in the asymptotically flat outer region). Once we have the solutions $Z(\sigma)$ we substitute the solution into the variational equation:

$$
\delta Z'' - \frac{(2h(Z) + Zh'(Z))Z'}{Zh(Z)}\delta Z' + \frac{1}{2Z^2}\Bigg[\frac{Z'^2\left(2h^2(Z) + Z^2h'^2(Z) - h(Z)Z^2h''(Z)\right)}{h^2(Z)}
$$
$$
- \frac{20v^2h^2(Z)Z^6f'^2(Z)}{f^6(Z)} + \frac{4v^2h(Z)Z^5\left(3f'(Z)\left(2h(Z) + Zh'(Z)\right) + h(Z)Zf''(Z)\right)}{f^5(Z)}
$$
$$
- \frac{v^2Z^4\left(6h^2(Z) + Z^2h'^2(Z) + h(Z)Z\left(8h'(Z) + Zh''(Z)\right)\right)}{f^4(Z)}\Bigg]\delta Z = 0. \qquad (3.18)
$$

For δZ the meaningful boundary condition is the fixed (and small) difference between the on-shell trajectory and its clone at the brane ($\delta Z(\sigma = 0) = \epsilon$) and the Neumann condition at infinity (since the strings float freely so does the difference between to string profiles). The outcome is given in figure 1. Along with the radial profiles of the string for different temperatures, we plot the near-horizon values of the numerically computed Lyapunov exponent $\lambda_L^{(n)} = \log\left(\delta Z\left(\sigma_0\right)/\epsilon\right)/2$, where σ_0 is some near-brane cutoff (we want the Lyapunov exponent near the brane thus σ_0 should cut off the far-from-brane part).[9] The numerics is reasonably close to the analytic result, providing an additional confirmation.

4 Open string in D1-D5-p black string background

So far we have explored the bulk instability of open strings in black hole and black brane backgrounds and we have found the saturation of a fake MSS bound — fake as it is unrelated to chaos (the configuration we consider is even integrable, though a more involved setup likely

---

[7]Remember we have no analytic control at intermediate distances, far from both the brane/horizon and the infinity/AdS boundary (depending on the geometry).

[8]The value $p = 3$ is chosen as the D3 brane is particularly relevant for applications, having also the AdS throat, but the numerics works the same way for any p.

[9]Of course, we have checked that the results do not strongly depend on σ_0.
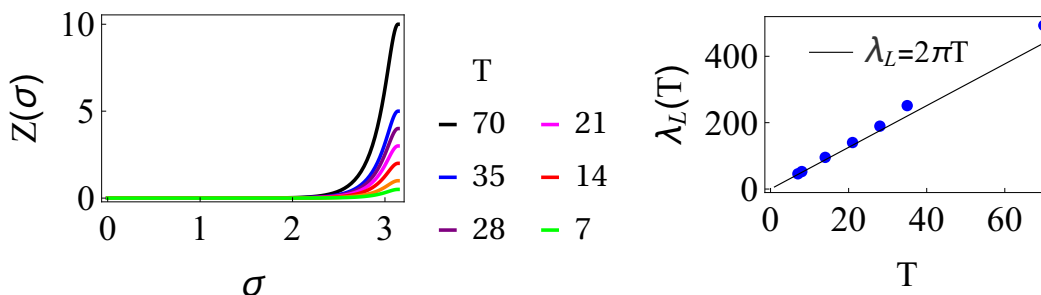
Figure 1. Radial profile $Z(\sigma)$ (A) and the numerical Lyapunov exponent $\lambda_L^{(n)} = \log\left(\delta Z\left(\sigma_0\right)/\epsilon\right)/2$ (B) for the static open string in thermal black brane background, for a range of temperatures T. We take $\sigma_0 = 0.2$ for the cutoff but values between 0.1 and 0.5 yield similar results. We compare the numerical result for the Lyapunov exponents to the analytic estimate (i.e., the chaos bound) and find reasonable agreement.

would not be such). Now we will interpret this finding and relate it to the thermal correlators and quasi-normal modes in a theory which is particularly interesting as we know something not only about the (super)gravity solution and the dual large-N field theory, but also about the microscopics: the D1-D5-p black string [64–69]. This setup is celebrated for being the first black hole solution in string theory for which the entropy was computed by counting the microscopic degrees of freedom, obtaining for a horizon area A the famous Bekenstein-Hawking result $S = A/4$ [65]. Another famous result is the calculation of the greybody factor in [64], the logical macroscopic extension of the entropy calculation. To remind, the greybody factor is obtained in [64] as the absorption cross section for a wavepacket in the black string background. In holographic setups, where the relevant near-horizon dynamics is dual to a two-dimensional CFT, the absorption cross section can be obtained from the imaginary part of the retarded Green's function.

Our idea here is twofold. First, we study the Lyapunov stability in D1-D5-p background — this will yield some surprises as the geometry has a global rotation with angular velocity Ω; so far we have only studied static geometries. Second, we will relate the Lyapunov exponent to the retarded propagator in dual field theory and pinpoint what it tells us about the meaning of bulk instability.

4.1 Holography of the D1-D5-p system: a reminder

The background describing the D1-D5-p black string reads

$$ds^2 = \frac{1}{\sqrt{f(r)}}\left(-dt^2 + dx_5^2 + \frac{r_0^2}{r^2}\left(\cosh\Sigma dt + \sinh\Sigma dx_5\right)^2\right) +$$
$$+ \sqrt{f(r)}\left(\frac{dr^2}{h(r)} + r^2\left(d\psi^2 + \sin^2\psi\left(d\theta^2 + \sin^2\theta d\phi^2\right)\right)\right), \tag{4.1}$$

$$f(r) = \left(1 + \frac{r_1^2}{r^2}\right)\left(1 + \frac{r_5^2}{r^2}\right), \quad h(r) = 1 - \frac{r_0^2}{r^2}. \tag{4.2}$$

As usual, t and r are the time and radial coordinate respectively, ψ, θ and ϕ are the angles on the 3-sphere, and x_i $(i = 1, \ldots 5)$ are the Cartesian coordinates in the plane. This is a classical

solution of ten-dimensional type IIB supergravity compactified on $T^5 \cong T^4 \times \mathbb{S}^1$ [64, 70]. It is charged under the Ramond-Ramond field of the corresponding theory; since D1 and D5 branes are magnetically dual to each other we get electric and magnetic charges that are related to the radii r_1 and r_5, respectively.[10] There is also an additional charge associated to the p-momentum along D1-brane, i.e. the Kaluza-Klein (KK) mode on $\mathbb{S}^1$, related to factors of $r_0^2 \cosh^2 \Sigma$ in the metric (4.1)–(4.2). In the dilute gas regime these three charges satisfy [64]:

$$r_0, r_0 \sinh \Sigma \ll r_1, r_5. \tag{4.3}$$

The solution is anisotropic and rotating for $\Sigma \neq 0$ as we see from the presence of non-vanishing tx_5-component in the metric (4.1), implying that we now have the left and right temperature:

$$T_L = \frac{r_0 e^\Sigma}{2\pi r_1 r_5}, \qquad T_R = \frac{r_0 e^{-\Sigma}}{2\pi r_1 r_5}. \tag{4.4}$$

We may further define the "average" (Hawking) temperature T as $1/T = (1/T_L + 1/T_R)/2$. This temperature and entropy are given by

$$\frac{1}{T} = \frac{2\pi r_1 r_5 \cosh \Sigma}{r_0}, \qquad S = \frac{2\pi^2 r_1 r_5 r_0 \cosh \Sigma}{4}. \tag{4.5}$$

We will need a few more features of this solution. The first is that in the extremal case ($T, S \propto r_0 = 0$), also known as the extremal D1-D5 bound state system, the near-horizon geometry becomes $\mathrm{AdS}_3 \times \mathbb{S}^3$. We can show this by performing the coordinate transformation $t \to t/\varepsilon L$, $r \to \varepsilon L r$, $x_5 \to x_5/\varepsilon L$ in the metric (4.1), where $L^2 = r_1 r_5$: in the limit $\varepsilon \to 0$ we recover the $\mathrm{AdS}_3 \times \mathbb{S}^3$ geometry

$$ds_{\mathrm{NHE}}^2 \approx \frac{r^2}{L^2}\left(-dt^2 + dx_5^2\right) + L^2 \frac{dr^2}{r^2} + L^2 d\Omega_3^2. \tag{4.6}$$

On the other hand in the near-extremal case ($r_0 \to 0$, $\Sigma \to \infty$), the p-momentum survives and we still have the full D1-D5-p system, with a near-horizon geometry of the rotating Banados-Teitelboim-Zanelli (BTZ) black hole:

$$ds_{\mathrm{NHNE}}^2 \approx \frac{r^2}{L^2}\left(-dt^2 + dx_5^2\right) + L^2 \frac{dr^2}{r^2 - r_0^2} + \frac{r_0^2}{L^2}\left(\cosh \Sigma dt + \sinh \Sigma dx_5\right)^2 + L^2 d\Omega_3^2. \tag{4.7}$$

The procedure to derive this is the same as in the extremal case, except that now we also need to take $r_0 \to \varepsilon L r_0$. In order to translate the metric (4.7) into the standard coordinates for BTZ black holes we have to perform an additional coordinate transformation:

$$r^2 = w^2 - w_-^2, \quad w_+ = r_0 \cosh \Sigma, \quad w_- = r_0 \sinh \Sigma. \tag{4.8}$$

For convenience we will write down the metric of the rotating BTZ in these coordinates:

$$ds_{\mathrm{BTZ}}^2 = -\frac{(w^2 - w_+^2)(w^2 - w_-^2)}{L^2 w^2}dt^2 + \frac{L^2 w^2 dw^2}{(w^2 - w_+^2)(w^2 - w_-^2)} + \frac{w^2}{L^2}\left(\frac{w_+ w_-}{w^2}dt + dx_5\right)^2. \tag{4.9}$$

The angular velocity is given by $\Omega = w_-/L w_+ = \tanh \Sigma / L$.

---

[10] One can think of these charges also as representing the number of copies in the stack of D1 branes compactified on $\mathbb{S}^1$ along the x_5 direction, and in the stack of D5 branes wrapping the whole $T^4 \times \mathbb{S}^1$ manifold.

From the above it is clear that the dual CFT lives in 1+1 spacetime dimension and encodes the physics of the $\mathrm{AdS}_3 \times \mathbb{S}^3$ sector: in the holographic regime the large-r flat asymptotics of the geometry (4.1) have to decouple. The classical gravity solution of course corresponds to the strongly coupled regime in CFT, however some direct comparisons were made (and count among the famous early tests of AdS/CFT) in the weakly-coupled regime where the CFT is approachable from field theory side [67, 69, 71, 72] and some basic results from gravity side (like thermodynamics) still hold for reasons of continuity. In this regime the CFT has an orbifold point [71, 72] which acts as UV deformation, driving the theory toward a weakly coupled regime. This is seen in gravity as the deformation of the metric away from the near-brane region (AdS_3 or BTZ). Therefore, we understand, at least to some extent, the UV physics and the meaning of the UV deformation of the theory.

4.2 Radial fluctuations

We consider a static open string in D1-D5-p background stretching from interior to the boundary just like in previous examples. In particular, we postulate the following string configuration

$$
\begin{aligned}
t(\tau, \sigma) &= \tau, & R(\tau, \sigma) &\equiv R(\sigma), \\
\Psi(\tau, \sigma) &\equiv \psi(\tau), & \Theta(\tau, \sigma) &\equiv \pi/2, & \Phi(\tau, \sigma) &\equiv \phi(\tau), & X_5(\tau, \sigma) &\equiv X_5(\sigma).
\end{aligned}
\tag{4.10}
$$

The τ-dependent degrees of freedom $\{\Psi, \Phi\}$ decouple. The remaining fields R and X_5 also decouple from each other, since we can combine the equation of motion for R with the nontrivial Virasoro constraint

$$
\frac{f(R) R'^2(\sigma)}{h(R)} + X_5'^2(\sigma) + \frac{r_0^2 \left(v^2 \cosh^2 \Sigma + \sinh^2 \Sigma X_5'^2(\sigma)\right)}{R^2(\sigma)} = 1
\tag{4.11}
$$

to obtain the following equation

$$
\begin{aligned}
2 f h^2 \left(-2 r_0^2 \cosh^2 \Sigma + R^2\right) &+ f' h^2 R \left(-r_0^2 \cosh^2 \Sigma + R^2\right) + \\
&+ f^2 R^2 \left(-\left(2h + R h'\right) R'^2 + 2 h R R''\right) = 0.
\end{aligned}
\tag{4.12}
$$

The effective Lagrangian for the coordinates R and X_5 takes the form

$$
\mathcal{L} = \frac{1}{\sqrt{f(R)}} \left[\left(-1 + \frac{r_0^2 \cosh^2 \Sigma}{R^2}\right) - \frac{f(R) R'^2}{h(R)} - \left(1 + \frac{r_0^2 \sinh^2 \Sigma}{R^2}\right) X_5'^2 \right],
\tag{4.13}
$$

and reproduces eq. (4.12) when combined with the Virasoro constraint (4.11).

We will assume that we are in the dilute gas regime, like in [64], defined by $r_0, r_0 \sinh \Sigma \ll r_1, r_5$. This boils down to the condition $T \ll 1/r_1, 1/r_5$. As usual, we can solve the equation analytically in two distinct regions: (1) near-horizon region $r \sim r_0, r_0 \sinh \Sigma \ll r_1, r_5$ and (2) far region $r_0, r_0 \sinh \Sigma \ll r \sim r_1, r_5$.

Expectedly, the system described by the Lagrangian (4.13) is integrable. Applying the NVE methods, we can choose the invariant plane to be $\{t = \tau, R = r_0, \Psi = 0, \Theta = \pi/2, \Phi = 0, X_5 = \text{const.}\}$. Since X_5 is a cyclic coordinate in (4.13), its conjugate momentum

is constant: $p'_{X_5} = \partial \mathcal{L}/\partial X_5 = 0$. Therefore, the $R - X_5$ plane is indeed invariant under the evolution of the system (along σ). The normal variational equation therefore corresponds to the variations in the X_5-direction, yielding $\delta X_5'' = 0$. Just like the open string dynamics on the Schwarzschild horizon, this system is integrable.[11] In both cases, the extra integrals of motion are simply the transverse momenta.

We solve the variational equation of the radial coordinate in (4.12) obtained by perturbing the horizon solution $R(\sigma) = r_0$ as $R \sim r_0 + \delta R(\sigma)$:

$$\delta R'' - \frac{2\mathfrak{a}^4}{r_0^6 f^2(r_0)}\delta R = 0, \tag{4.14}$$

$$\mathfrak{a}^4 \equiv r_0^2(r_1^2 + r_5^2) + 2r_1^2 r_5^2 + r_0^2 \left(2r_0^2 + r_1^2 + r_5^2\right)\cosh 2\Sigma \tag{4.15}$$

Plugging in the expression for f, we find the exponent of the asymptotic growth of the solution, determined as before by $\sim e^{2\lambda_L \sigma}$:

$$\lambda_L = \frac{r_0}{r_1 r_5}\sqrt{1 + \frac{r_0^2(r_1^2 + r_5^2)}{2r_1^2 r_5^2}\cosh(2\Sigma)}. \tag{4.16}$$

The above expression[12] can be written in terms of the temperatures (4.4)–(4.5) as:

$$\lambda_L = 2\pi T \cosh\Sigma \sqrt{1 + \pi^2\left(r_1^2 + r_2^2\right)\left(T_L^2 + T_R^2\right)} = 2\pi T \cosh\Sigma \left(1 + \frac{\pi^2}{2}\left(r_1^2 + r_5^2\right)\left(T_L^2 + T_R^2\right) + \dots\right). \tag{4.17}$$

The second equality (expansion in $r_0^2/\sqrt{r_1^2 + r_5^2}$) is the dilute-gas approximation. Importantly, the Lyapunov exponent *does not repeat the universal $2\pi T$ ("fake MSS") result*. It depends on r_1 and r_5 in addition to T, and its temperature dependence is a nonlinear function. But the leading term in the expansion has a simple form:

$$\lambda_L^{(0)} \approx \frac{r_0}{r_1 r_5} = 2\pi T \cosh\Sigma. \tag{4.18}$$

Therefore, *the Lyapunov exponent in the dilute-gas regime "comes close" to the static value but differs by a factor of* $\cosh\Sigma$ *which equals unity when $\Sigma = 0$, i.e. when there is no rotation.* In absence of rotation we return to the $2\pi T$ exponent in the dilute-gas regime.

We can translate our result into the standard variables for rotating BTZ solutions. Since in standard coordinates for BTZ black holes we have $\Omega = w_-/Lw_+$, using eq. (4.8) it follows that $L\Omega = \tanh\Sigma$. Therefore, using the identity $\cosh\Sigma = 1/\sqrt{1 - \tanh^2\Sigma}$, we get

$$\lambda_L^{(0)} = \frac{2\pi T}{\sqrt{1 - L^2\Omega^2}}, \quad L\Omega \in [0, 1). \tag{4.19}$$

We could express this result in terms of the left and right temperature $T_{L,R}$, making use of the relation $2/T = 1/T_L + 1/T_R \Rightarrow T = 2T_L T_R/(T_L + T_R)$. However, we do not get

---

[11]Again, a more general open string setup would not necessarily be integrable — one has to perform the Kovacic analysis for every boundary condition (i.e. effective Lagrangian) separately.

[12]One may worry whether this expression remains finite in the near-extremal limit where we take $\Sigma \to \infty$. We should pay attention to the fact that there is a factor of r_0 hiding inside the temperature T. In the near-extremal limit we also take a limit $r_0 \to 0$, while keeping $r_0 \cosh\Sigma$ fixed.

a particularly simple or more intuitive form than (4.19), which in fact nicely shows how a nonzero rotation rate Ω deforms us away from the universal $2\pi T$ scaling.

This result should be compared to the ones found in [73, 74], where chaos in dual CFT was studied by calculating the OTOC correlators of rotating BTZ black holes for a scalar field and for a probe string respectively. The calculation done in [73] obtains two different Lyapunov exponents $\lambda_L^\pm = 2\pi T/(1 \mp L\Omega)$ in the presence of rotation, one of which is above the MSS bound and the other one bellow it, presuming that $\Omega \neq 0$. Our result (4.19) turns out to be exactly equal to the geometric mean of $\{\lambda_L^+, \lambda_L^-\}$, implying that $\lambda_L^- < \lambda_L < \lambda_L^+$. Both results show that when an additional scale (angular velocity) appears there is no single "degenerate" exponent anymore, but different response functions receive different corrections.

We note in passing that our near-horizon analysis yields a single Lyapunov exponent, rather than a Lyapunov spectrum with two (in general different) exponents as one would expect in this background (and as [73] finds in the rotating BTZ case) — rotation breaks isotropy so the two directions normal to the invariant plane should be inequivalent. The reason that we nevertheless only see a single exponent could be that the quanta of p-momentum in D1-D5-p are only left-moving, thus we only see the Lyapunov exponent associated with the temperature of the left-moving modes.

The opposite limit when $r \gg r_0, r_0 \cosh \Sigma$ and $r \gg r_1, r_5$, is treated in the same way as the asymptotically flat limit of the interpolating geometry in subsubsection 3.2.3: we have noted that we can think of the six-dimensional black string as an interpolation between $\text{AdS}_3 \times \mathbb{S}^3$ and Minkowski spacetime. The far region corresponds to the latter, hence it must have zero Lyapunov exponent.

Unlike the examples from previous sections, we have now found some unexpected aspects of the bulk Lyapunov exponent: dependence on the rotation rate and the complex temperature dependence away from the dilute-gas limit.[13] Now we will relate it to the retarded propagator of a CFT quasiparticle interacting with the thermal ensemble,[14] the natural dual object to consider.

4.3 Transverse fluctuations

Now we want to study the retarded Green's function for transverse fluctuations, which describes thermal motion of quasiparticles in D1-D5 field theory, the more intuitive object to consider compared to the radial fluctuation. In this case, it is convenient to switch to the Nambu-Goto formalism and work in the static gauge. A similar calculation was already done in a slightly different setup [75], where the authors study the bulk dynamics of a fundamental string in an extremal and near-extremal Reissner-Nordström (RN) black hole background. Of course, the D1-D5 background will give very different physics.

---

[13]There is of course no rigorous reason for the bulk exponent to obey the MSS bound in all cases as it is a different object, and comparing to [73] we have seen that even though the OTOC exponent also changes in the presence of rotation the values are different. But still, the fact that (4.17)–(4.18) differ from the results like [73] suggests there is a difference in underlying physics.

[14]In the context of D1-D5 CFT it does not make much sense to talk about quarks as the symmetries of the theory differ from $\mathcal{N} = 4$ SYM.

The ansatz is now:

$$t(\tau,\sigma) = \tau \equiv t, \quad R(\tau,\sigma) = \sigma \equiv r,$$
$$\Psi(\tau,\sigma) \equiv \psi(t), \quad \Theta(\tau,\sigma) \equiv \pi/2, \quad \Phi(\tau,\sigma) \equiv \phi(t), \quad X_5(\tau,\sigma) \equiv X(t,r). \tag{4.20}$$

We expand $X(t,r)$ in Fourier modes

$$X(t,r) = \int \frac{d\omega}{2\pi} e^{-i\omega t} X_\omega(r), \tag{4.21}$$

and the relevant equation of motion obtained by varying the Nambu-Goto action reads

$$X_\omega''(r) + \left(\frac{r_0^2 \left(-3r^2 + r_0^2 + (r^2 - r_0^2)\cosh^2(2\Sigma) \right)}{r\left(r^2 - r_0^2\right)\left(-2r^2 + r_0^2 + r_0^2\cosh^2(2\Sigma)\right)} - \frac{f'(r)}{f(r)} + \frac{h'(r)}{2h(r)} \right) X_\omega'(r)$$
$$- \frac{2r^2\omega^2 f(r)}{\left(-2r^2 + r_0^2 + r_0^2\cosh^2(2\Sigma)\right)h(r)} X_\omega(r) = 0. \tag{4.22}$$

In the special case when there is no rotation $(\Sigma = 0)$ this equation simplifies to

$$X_\omega''(r) + \left(\frac{r_0^2}{r^3 h(r)} - \frac{f'(r)}{f(r)} + \frac{h'(r)}{2h(r)} \right) X_\omega'(r) + \frac{\omega^2 f(r)}{h^2(r)} X_\omega(r) = 0. \tag{4.23}$$

We will first solve the special case with no rotation; it will give us some useful prior intuition for the general case. Since the problem can be divided into two regions, we will again employ the matching procedure in order to gain some analytic control of the equation.

4.3.1 Static AdS: extremal case

Consider first the near-horizon region of the extremal black string, i.e. at temperature $T = 0$ on the field theory side. In this case the IR geometry is given by eqs. (4.6). The relevant equation of motion for string fluctuations along the x_5-direction in this regime is

$$X_\omega''(r) + \frac{4}{r} X_\omega'(r) + \left(\frac{L^2\omega}{r^2} \right)^2 X_\omega(r) = 0, \tag{4.24}$$

with general solutions of the form

$$X_\omega(r) = \mathcal{A}\left(1 - \frac{iL^2\omega}{r} \right) e^{\frac{iL^2\omega}{r}} + \mathcal{B}\frac{1}{2L^4\omega^2 r}\left(1 - \frac{ir}{L^2\omega} \right) e^{-\frac{iL^2\omega}{r}}. \tag{4.25}$$

Imposing the infalling boundary condition (appropriate for the retarded propagator) at the horizon requires $\mathcal{B} = 0$. Expanding this solution in the matching region $r_0 \ll r \ll L$, we get

$$X_\omega(r) = \mathcal{A}\left(1 + \frac{(L^2\omega)^2}{r^2} \right). \tag{4.26}$$

From this we can calculate the retarded Green's function at $T = 0$ in the IR region $r_0/r, \omega L \ll 1 \ll L/r$:

$$\mathcal{G}_R^{(T=0)} = L^4\omega^2 \Rightarrow \Im\mathcal{G}_R^{(T=0)} = 0. \tag{4.27}$$
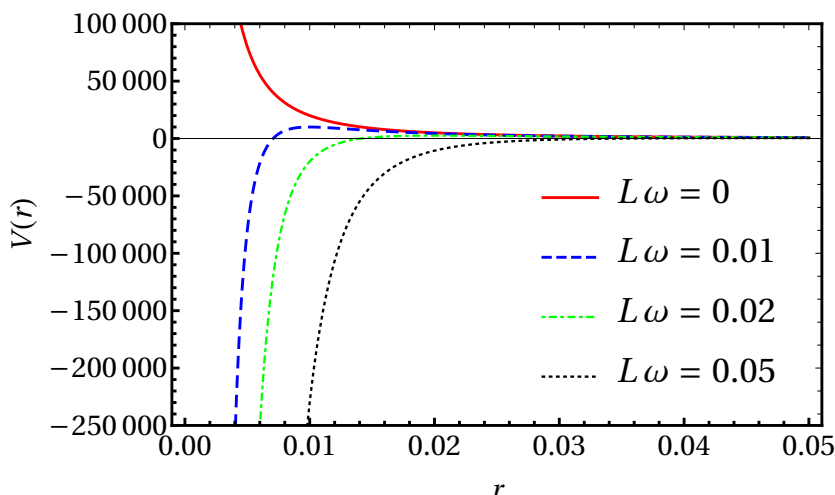
Figure 2. The effective Schrödinger potential (4.28) for the extremal D1-D5 geometry with $L = 1$, for four values of the frequency ω. The static case $\omega = 0$ (red full line) is qualitatively different because the potential is strongly repulsive: there is no absorption because plan waves coming from infinity are reflected away. For $\omega > 0$ (blue, green, black dotted lines) the potential is strongly attractive, diverging as $1/r^4$ at the origin $r = 0$. This again implies zero absorption cross section as there are no solutions behaving as plane waves at infinity.

Therefore, we get a vanishing absorption cross-section in the presence of the horizon, i.e. $\Im\mathcal{G}_R^{(T=0)} = 0$. So we need to understand why the extremal horizon does not absorb anything even though it is a horizon (with finite area and finite greybody factor). From the bulk viewpoint, one way to see the reason is to rewrite the fluctuation equation (4.24) in the Schrödinger form:

$$\partial_r^2 \widetilde{X}_\omega(r) - V_{\text{eff}}(r)\widetilde{X}_\omega(r) = 0, \quad V_{\text{eff}}(r) = \frac{2r^2 - L^4\omega^2}{r^4}. \tag{4.28}$$

The effective potential is shown in figure 2 for various values of ω. For $\omega = 0$ a zero imaginary part could be expected — for $\omega = 0$ the effective potential is positive and (quadratically) divergent at the horizon, thus there is no absorption, i.e. all incoming waves are reflected backward.

The nonstatic case $\omega \neq 0$ is qualitatively different — it has the expected negative divergence (infinite well) at the extremal horizon $r \to 0$, as we see from eq. (4.28) and figure 2. However, it is known that the scattering problem for attractive central potentials diverging as $1/r^s$ for $s > 2$ is not well-defined [76]: such potentials always lead to a wave "falling toward the center" and the solution to the Schrödinger equation in this case is always localized around zero — there is no absorption because the infalling plane wave at infinity is not a consistent boundary condition. We will see in the following section that we can infer this result for the retarded Green's function in the extremal case by considering the limit $\omega \ll T$ of the thermal correlator obtained in a near-extremal case.

4.3.2 Static BTZ: near-extremal case

At low but finite temperatures or equivalently in the near-extremal case we would be interested in the dynamics of the open string in the metric given by eq. (4.7). Therefore, we look for
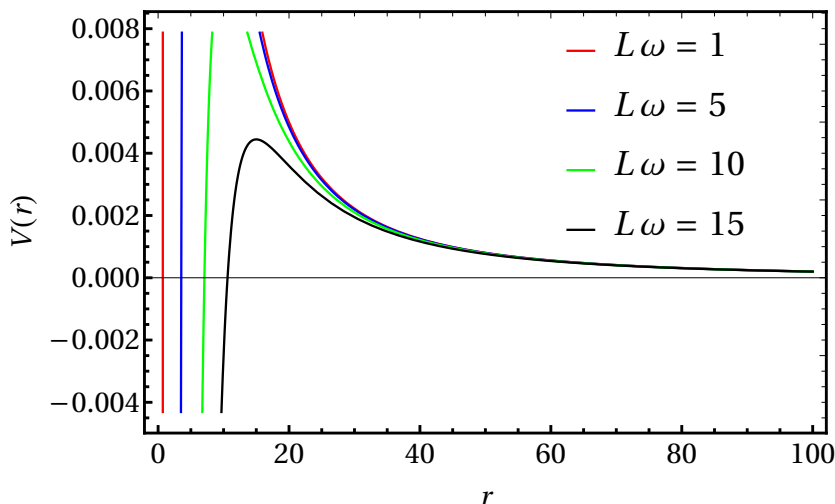
Figure 3. The effective Schrödinger potential (4.30) for a near-extremal D1-D5-p system with the parameters $r_0 = 0.1$, $L = 1$, for $L\omega = 1, 5, 10, 15$ (red, blue, green, black). Already from the expression in eq. (4.30) it is obvious that in the near-extremal case nothing special happens in the static limit $\omega = 0$. For all frequencies, the potential has the form typical of near-horizon effective potentials [68, 70], where a high but finite potential barrier is followed by the infinite well at the horizon $r = r_0$.

the solution of open string equations in BTZ×$\mathbb{S}^3$ geometry but (in this subsection) still with no rotation ($\Sigma = 0$). The relevant equation can be written in a compact form reminiscent of the relativistic wave equation in curved background:

$$\frac{h(r)}{r^4}\frac{d}{dr}\left(h(r)r^4\frac{dX_\omega(r)}{dr}\right) + \frac{L^4\omega^2}{r^4}X_\omega(r) = 0. \tag{4.29}$$

It is again instructive to look at the Schrödinger form of the equation, obtained by plugging in $X_\omega(r) = h^{-1/2}(r)r^{-2}\Psi(r)$ into eq. (4.29):

$$\left(\frac{d^2}{dr^2} - V_{\text{eff}}(r)\right)\Psi(r) = 0, \quad V_{\text{eff}}(r) = \frac{2r^2 - 3r_0^2 - L^4\omega^2}{\left(r^2 - r_0^2\right)^2}. \tag{4.30}$$

The second term inside the brackets is the effective Schrödinger potential, plotted in figure 3.

Proceeding further toward the analytic solution to eq. (4.29) it is convenient to transform the radial variable as

$$\zeta \equiv \frac{r_0^2}{r^2}. \tag{4.31}$$

In order to reduce eq. (4.29) to a hypergeometric differential equation,[15] we will make a further coordinate transformation $\zeta \mapsto 1 - \xi$. The equation now reads

$$X_\omega''(\xi) - \frac{1}{2\xi}\frac{2-\xi}{1-\xi}X_\omega'(\xi) + \frac{1}{\xi^2(1-\xi)}\left(\frac{L^2\omega}{2r_0}\right)^2 X_\omega(\xi) = 0. \tag{4.32}$$

---

[15]Since eq. (4.29) has three regular singular points at $r = 0$, r_0 and ∞, we can be sure that it can be written in the form of the hypergeometric differential equation.

We can solve this equation at the horizon $\xi = 0$, by making the substitution $y = -\log \xi$ in eq. (4.32). The solution at the horizon takes the form $X_\omega \sim e^{\pm i\alpha y} = \xi^{\pm i\alpha}$, with $\alpha = L^2 \omega / 2r_0$. The boundary condition at the horizon requires the outgoing modes to vanish, yielding

$$X_\omega(\xi) = \widetilde{\mathcal{A}} \, \xi^{-i\alpha}. \tag{4.33}$$

In order to get the full near-horizon solution, we plug the ansatz $X_\omega(\xi) = \xi^{-i\alpha} F(\xi)$ into eq. (4.32), yielding

$$\xi(1-\xi)\frac{d^2 F}{d\xi^2} + \left[1 - 2i\alpha - \left(1 - i\alpha - \frac{1}{2} - i\alpha\right)\xi\right]\frac{dF}{d\xi} - (-i\alpha)\left(-\frac{1}{2} - i\alpha\right)F(\xi) = 0. \tag{4.34}$$

We recognize eq. (4.34) as the hypergeometric equation with parameters

$$a = -i\alpha, \quad b = -\frac{1}{2} - i\alpha, \quad c = 1 - 2i\alpha. \tag{4.35}$$

The corresponding regular solution reads

$$F(\xi) = \widetilde{\mathcal{A}} \, {}_2F_1\left(a, b, c; \xi\right) + \widetilde{\mathcal{B}} \, \xi^{2i\alpha} \, {}_2F_1\left(a + 1 - c, b + 1 - c, 2 - c; \xi\right). \tag{4.36}$$

We impose the infalling boundary condition (4.33) at the horizon, implying that $\widetilde{\mathcal{B}} = 0$, thus the near-horizon solution becomes

$$X_\omega(\xi) = \widetilde{\mathcal{A}} \, \xi^{-i\alpha} \, {}_2F_1\left(a, b, c; \xi\right). \tag{4.37}$$

We can now use the following identity to express solution (4.37) in terms of functions depending on ζ, instead of $\xi = 1 - \zeta$:

$$
\begin{aligned}
{}_2F_1\left(a, b, c; \xi\right) &= \frac{\Gamma(c)\Gamma(c - a - b)}{\Gamma(c - a)\Gamma(c - b)} \, {}_2F_1\left(a, b, 1 + a + b - c; \zeta\right) + \\
&\quad + \frac{\Gamma(c)\Gamma(a + b - c)}{\Gamma(a)\Gamma(b)} \zeta^{c - a - b} \, {}_2F_1\left(c - a, c - b, 1 + c - a - b; \zeta\right).
\end{aligned} \tag{4.38}
$$

The matching region $r_0 \ll r$ corresponds to $\zeta \ll 1$, so we expand eq. (4.38) in small ζ:

$$
{}_2F_1\left(a, b, c; \xi\right) \approx \frac{\Gamma(c)\Gamma(c - a - b)}{\Gamma(c - a)\Gamma(c - b)} + \frac{\Gamma(c)\Gamma(a + b - c)}{\Gamma(a)\Gamma(b)} \zeta^{c - a - b}. \tag{4.39}
$$

We observe that the full solution in the matching region is of the form

$$X_\omega(r) \propto \widetilde{\mathcal{S}} \, r^{-d + \Delta} + \widetilde{\mathcal{F}} \, r^{-\Delta}, \quad d = \Delta = 3, \tag{4.40}$$

which allows us to read off the retarded Green's function as the ratio $\widetilde{\mathcal{F}}/\widetilde{\mathcal{S}}$:

$$\mathcal{G}_R^{(T)}(\omega) \propto \frac{\Gamma(c - a)\Gamma(c - b)}{\Gamma(a)\Gamma(b)} = \frac{\Gamma\left(1 - i\frac{\omega}{2\lambda_L}\right)\Gamma\left(\frac{3}{2} - i\frac{\omega}{2\lambda_L}\right)}{\Gamma\left(-i\frac{\omega}{2\lambda_L}\right)\Gamma\left(-\frac{1}{2} - i\frac{\omega}{2\lambda_L}\right)}. \tag{4.41}$$

We can take the imaginary part of (4.41) to get the absorption cross-section:

$$\sigma_{\text{abs}} = \Im\mathcal{G}_R^{(T)}(\omega) \propto \frac{\alpha}{4} + \alpha^3, \quad \alpha = \frac{\omega}{2\lambda_L}, \quad \lambda_L = 2\pi T. \tag{4.42}$$

This is the central result of our calculation — the IR propagator and the absorption cross section for a heavy quasiparticle excitation. Let us think what this result means:

1. The only energy scale in the Green's function is the temperature. This is in line with the problem of drift of a heavy quark through neutral $\mathcal{N} = 4$ super-Yang-Mills (SYM) plasma, dual to a dragging string in AdSS background [38, 39, 77] and many subsequent works in the same setup [78–82]: in this case the quasiparticle does not see the charges of the D1-D5-p system.[16] This can be ascribed to the fact that the additional charges of the D1-D5-p system are global and the quasiparticle is neutral with respect to them.

2. The form of the propagator (eq. (4.41)) could be expected from the BTZ asymptotics of the near-extremal geometry [83], as it has the form of conformal quantum mechanics, i.e. 0+1-dimensional CFT [84] (we know that in the near-horizon region of the BTZ geometry the transverse spatial coordinate decouples and the geometry becomes $\text{AdS}_2 \times \mathbb{S}$, so that AdS_2 gives the 0+1-dimensional CFT).

3. The imaginary part behaving as $\sim \omega + \omega^3$ suggests that in addition to the usual drag force $f \propto \dot{x}$ we also have a third-order term $\tilde{f} \propto dx^3/dt^3$. This is in fact expected — all odd-power terms[17] in velocity are allowed symmetry-wise and the leading-order holographic Green function already captures the first two terms.

4. This result could not be reproduced neither from the static limit ($\omega = 0$) nor from the extremal limit $T = 0$ — these two limits are singular, which is expected for the static limit but somewhat strange for the extremal limit.

As a sanity check we consider the high-frequency limit $\omega \gg T$ where one should recover the result for the extremal case.[18] In this limit we can compare our calculation to the pure CFT result for the two-point correlation function. We consider a two-point correlation function in a $2 + 1$-dimensional CFT for an operator with scaling dimension Δ: this behaves as $\langle \mathcal{O}_\Delta(t) \mathcal{O}_\Delta(0) \rangle \sim |t|^{-2\Delta}$, i.e. $\sim \omega^{2\Delta-d}$, where d is the spacetime dimensionality. For an operator with a scaling dimension $\Delta = 3$ living in $d = 3$ spacetime dimensions, one should indeed expect $\sim \omega^3$ power-law behavior of the thermal correlator in the high-frequency limit.

4.3.3 Rotating BTZ: near-extremal case

Now we study the rotating BTZ black hole. Compared to the static case, it is considerably more difficult for calculations. Conceptually, it is also distinct for having different left and right temperature. Now we cannot write an analytic solution in the whole throat, all the way to the AdS boundary (i.e., the throat of the D1-D5-p geometry, before the far-region flat asymptotics kick in), akin to eq. (4.37). Instead, we can only treat the near-horizon limit, when $r \to r_h$ or equivalently $\zeta \to 1$ (for ζ as defined in eq. (4.31)).

---

[16]At least, this is the case in our current setup with no drift; it would be interesting to check if this conclusion remains in force in presence of drift.

[17]Even-power terms (like $\dot{x}^2$) are not expected as their sign is independent of the sign of velocity, i.e. a proper drag force (opposing the motion) would have to look like $-\dot{x}^2 \text{sgn}\dot{x}$ but that implies the breaking of some discrete symmetry which we do not have.

[18]In this limit we consider wavelengths well below T^{-1} ($\omega^{-1} \ll T^{-1}$) that are insensitive to thermal fluctuations and thus resemble the behavior for the extremal background geometry.

The equation of motion for the transverse fluctuations (4.22) can be slightly rewritten as

$$\left(1 - \frac{r_0^2}{r^2}\right)\left(1 - \frac{r_0^2 + r_n^2}{r^2}\right)X_\omega''(r) + \frac{4}{r}\left[1 - \frac{3}{2}\left(1 - \frac{r_0^2}{3r^2}\right) - \frac{5}{4}\left(1 - \frac{2}{5}\frac{r_0^2}{r^2}\right)\right]X_\omega(r) + \frac{L^4\omega^2}{r^4}X_\omega(r) = 0.$$
(4.43)

Now we perform the same change of variables as before, $y = -\log\xi = -\log\left(1 - r_0^2/r^2\right)$, so that $y \to \infty$ at the horizon. Expanding the coefficients to order ξ^0 for ξ small or equivalently to order $1 = (e^{-y})^0$ for y large, we get the near-horizon limit of (4.43):

$$\left(1 + \frac{2r_n^2}{r_0^2} - e^y\frac{r_n^2}{r_0^2}\right)X_\omega''(r) + e^y\frac{r_n^2}{2r_0^2}X_\omega'(r) + \frac{L^4\omega}{4r_0^2}X_\omega(r) = 0.$$
(4.44)

The solution that satisfies the infalling boundary condition at the horizon is

$$X_\omega(y) \sim e^{i\delta y}\,{}_2F_1\left(i\delta, -\frac{1}{2} + i\delta, 1 + 2i\delta; \frac{e^y r_n^2}{r_0^2 + 2r_n^2}\right), \quad \delta = \frac{L^2\omega}{2\sqrt{r_0^2 + 2r_n^2}}.$$
(4.45)

Another way to understand the fact that in the presence of rotation the solution of this type cannot exist without imposing some approximations is that hypergeometric functions are the representations of $SL(2, \mathbb{R})$ which is broken by rotation.

In order to obtain the IR propagator (now we cannot obtain analytically the propagator for general ω values), we expand the above solution in the region far from the horizon, for $r \gg r_0$, that is for y small. Using the identity (4.39) this yields

$${}_2F_1\left(i\delta, -\frac{1}{2} + i\delta, 1 + 2i\delta; \frac{e^y r_n^2}{r_0^2 + 2r_n^2}\right) \sim \frac{\Gamma\left(\frac{3}{2}\right)\Gamma(1 + 2i\delta)}{\Gamma(1 + i\delta)\Gamma\left(\frac{3}{2} + i\delta\right)} + \frac{\Gamma(1 + 2i\delta)\Gamma\left(-\frac{3}{2}\right)}{\Gamma(i\delta)\Gamma\left(-\frac{1}{2} + i\delta\right)}\left(\frac{r_0}{r}\right)^3.$$
(4.46)

Identifying the leading term and subleading term as the source and response respectively we compute the retarded Green's function in the rotating case:

$$\mathcal{G}_R^{(T)}(\omega) \sim \frac{\Gamma(1 - i\delta)\Gamma\left(\frac{3}{2} - i\delta\right)}{\Gamma(-i\delta)\Gamma\left(-\frac{1}{2} - i\delta\right)}$$
(4.47)

It has the same form as the one that we have obtained in previous section in the absence of rotation (4.41), but with a different λ_L scale compared to eq. (4.18):

$$\lambda_L^{(\mathrm{mod})} = 2\pi T\cosh\Sigma\sqrt{1 + \frac{2r_n^2}{r_0^2}} = \lambda_L^{(0)}\sqrt{\cosh(2\Sigma)}, \quad \delta = \frac{\omega}{2\lambda_L^{(\mathrm{mod})}}.$$
(4.48)

We can interpret this as a modification of energy in the presence of a rotating horizon, i.e. the Lense-Thirring effect.

4.4 Quasinormal modes and their decay scale

So far, we have found that breaking a global symmetry in IR (introducing rotation) in general influences the bulk instability scale differently from the way it influences the exponent of the field-theory OTOC. We have likewise seen that UV deformations (full brane geometry

deforming the AdS throat) also change the instability scale away from $2\pi T$. It remains unclear however what exactly the bulk scale is from the CFT viewpoint, and to understand this we will relate the bulk instability exponent to the quasinormal mode frequencies. For simplicity we will consider the non-rotating case but all the results that we obtain still hold also in the presence of rotation with $\lambda_L \to \lambda_L^{(\mathrm{mod})}$.

Let us first remember that the poles in the retarded Green's function are related to transport properties of a thermal field theory. On the gravity side, they correspond to a spectrum of quasinormal modes [68, 70]. More specifically, the relaxation times in field theory are given by the imaginary part of the QNM spectrum in the bulk [85, 86]. Since our retarded Green's function (4.41) is singular at an infinite number of points in the complex plane, due to the presence of the gamma functions in the numerator, we can extract the whole QNM spectrum from it. Singular points are given by $c - a = -n$ or $c - b = -n$, for $n \in \mathbb{Z}^+$ (a set of non-negative integers), thus $\omega_n = -2i(n+1)\lambda_L$ or $\omega_n = -2i(n+3/2)\lambda_L$. The union of the two sets yields the following spectrum:

$$\omega_{\mathfrak{n}} = -2i(\mathfrak{n}+1)\lambda_L, \quad \mathfrak{n} = 0, \frac{1}{2}, 1, \frac{3}{2}, \cdots \tag{4.49}$$

or equivalently

$$\omega_{\mathfrak{m}} = -i(\mathfrak{m}+1)\lambda_L, \quad \mathfrak{m} = 1, 2, 3, \cdots . \tag{4.50}$$

We write the solution in these two obviously equivalent ways in order to facilitate the comparison with the literature.[19]

Another way to derive the QNM spectrum is by definition, as the eigenfrequencies of the equations of motion with infalling boundary conditions at the horizon and Dirichlet boundary conditions at the boundary. The latter require the solution at AdS boundary to vanish.[20] The equivalence of the two approaches should be obvious, since the same set of requirements that force the solution (4.39) to vanish at infinity also describes the poles of the retarded Green's function (4.41). This gives us a more intuitive picture of QNM: they tell us how a local near-horizon instability decays. Therefore, we can think of the inverse of the Lyapunov exponent λ_L^{-1} as some characteristic timescale for the decay of perturbations along the open string, that has nothing to do with chaos.

The result summarized in eqs. (4.49)–(4.50) is qualitatively the same as the one obtained in [85] for scalar perturbations in a nonrotating BTZ black hole background, except that the spectrum (4.50) also includes half-integer values of $\mathfrak{n}$ (which is simply due to different objects being considered: strings vs. scalar field). Similar scaling of the QNM spectrum with the Lyapunov exponent of some special orbit is known from two classic papers concerning *asymptotically planar* black holes:

---

[19]The form (4.50) is simpler and more natural but (4.49) has the same form as the scalar QNM solution [85] that we want to benchmark against.

[20]In this context we again ignore the asymptotically flat region of the D1-D5-p geometry and only consider its interior and AdS throat, just as we did when solving the string equations of motion. In an asymptotically Minkowski spacetime we would require outgoing boundary condition at infinity, very different from the situation in AdS. This will be important in what follows.

1. In [47], the imaginary part of the QNM frequencies is determined by the instability of geodesic motion, i.e. the Lyapunov exponent of a massless particle *on the photon sphere*, which acts as an unstable fixed point. This is obtained in the eikonal approximation when $\Re\omega \gg \Im\omega$.[21]

2. In the opposite, high-overtone or overdamped regime, when $\mathfrak{n} \gg 1$ and thus $\Re\omega \ll \Im\omega$, [50] find that $\Im\omega$ is proportional to the surface gravity at the horizon, which equals precisely $2\pi T$.

Our results are clearly obtained in the high-overtone regime since our Green's functions satisfy $\Im\mathcal{G}_R^{(T)} \gg \Re\mathcal{G}_R^{(T)}$. Therefore, our result essentially generalizes [50] for an open string in AdS. Yet, the coefficient itself is obtained as the Lyapunov exponent of an unstable fixed point, and in that sense generalizes also [47] from the eikonal (photon-sphere dominated) regime to the high-overtone (horizon-dominated) regime.

We have thus shown that both "easy" regimes ($l \gg 1$ and $\mathfrak{n} \gg 1$) can be understood from classical unstable saddle points, but of course the eikonal regime sees the scattering near the photon sphere while the overdamped regime (our case) sees the horizon. In this sense, earlier results on the universal $2\pi T$ exponent for geodesics and fields near-horizon [31], bringing the conclusion about the horizon as the "nest of chaos", are not in collision with the studies of the instability on the photon sphere [47, 87, 88] — only that they correspond to different regimes. It is somewhat surprising that for a special string configuration these results are obtained in asymptotically AdS backgrounds, as it is well known and discussed already in [47, 50] that for a geodesic the argument does not easily generalize to AdS asymptotics.

Finally, we should also comment on the field theory interpretation of the quasinormal modes spectrum that we have just found in the bulk. We already mentioned that an open string in the bulk stretched from the boundary to the thermal AdSS horizon corresponds to a heavy quark in thermal plasma of super-Yang-Mills quarks and gluons. Perturbations along the string describe thermal perturbations in the plasma. Similar holds in the D1-D5 CFT except that the elementary excitations now cannot be called quarks. We can summarize the findings above by noting that a Lyapunov exponent is really related to the QNM frequencies, which describe how local near-horizon instabilities on the string decay. Decay rates of those instabilities are given by the spectrum of quasinormal modes, so on the field theory side they describe how the thermal fluctuations in plasma die off. Thus, they predict the thermalization timescale in the dual CFT.

5 Discussion and conclusions

The initial motivation for this work was a rather technical question: what is the meaning of bulk chaos in particle and string motion in AdS spaces, and why it typically saturates the same universal chaos bound as OTOC in field theory. We were led to the study of open strings (rather than ring strings or particle geodesics) largely by reasons of calculational simplicity and direct CFT interpretation: a string with one end on the boundary and the

---

[21]Here $\Re\omega$ denotes the orbital frequency (oscillations) and $\Im\omega$ is the Lyapunov exponent for the unstable geodesic orbit (damping).

other in the interior describes the motion of a heavy quark in quark-gluon plasma. The holographic interpretation is less obvious for other string configurations, and for geodesics it corresponds to a rather special, high-conformal-dimension limit.

As usual, the chase is almost better than the catch. We have found a number of surprising properties of bulk dynamics, first and foremost the horizon as an unstable saddle point and the "fake nest of chaos" with local instability rate exactly equal to $2\pi T$ in the static case but different from it in the rotating black string geometry. But the holographic interpretation is equally interesting: the universal MSS-like exponent is a red herring, the artifact of the large-N limit in field theory, i.e. classical bulk dynamics, when temperature is the only scale, unless some additional symmetry is explicitly broken in IR. This happens in the D1-D5-p black string, where the rotation breaks the symmetry between left- and right-moving modes. Just like in [89], the rotating system deforms away from the universal $2\pi T$ exponent, and this shows directly in the correlation functions. We also note that away from the dilute gas approximation there are additional higher-order temperature corrections to the Lyapunov exponent — this is the effect of the UV deformation.

We have found the connection between the near-horizon Lyapunov exponent and the spectrum of quasinormal modes in the high-overtone regime. This gives us an important hint about the meaning of the bulk Lyapunov exponent: it is an instability scale associated to the decay of fluctuations along the string due to thermal dissipation, and has nothing to do with bulk chaos. This resembles two classic results on quasinormal modes of asymptotically flat black holes: in the eikonal regime the Lyapunov exponent on the photon sphere determines the quasinormal mode [47], whereas in the overdamped regime (our case) the imaginary part of the quasinormal mode equals the horizon surface gravity [50]. We have essentially shown that for near-horizon string orbits the bulk Lyapunov exponent equals the surface gravity (which generalizes even for a rotating horizon).

Motivated by this connection, one could try to extend some other known results on geodesic instabilities to the orbits of extended objects like strings. Of primary interest is the instability on the photon sphere which, apart from the well-known connection with quasinormal modes, holds the key to several other properties both in asymptotically flat and in global AdS spaces [90, 91]. However, our setup needs to be substantially modified to study the photon sphere, which arises as the locus of unstable saddle points for null geodesics *arriving from infinity*. An open string in our configuration does not even have a saddle point on the photon sphere, i.e. one cannot even define the Lyapunov exponent on the photon sphere unambiguously. Therefore, instead of having a static string, we would need to scatter an open string along a null geodesic. In that case one would expect the minimal allowed value for the impact parameter to be of order of the photon sphere size (analogous study for massless particles is performed in [48]). Such a setup is particularly suitable for the study of fuzzballs and microstate geometries, since they have no sharp length/energy scale analogous to a horizon [87, 92]. We would then be probing another branch of the QNMs spectrum, associated to stringy instabilities around the photon sphere.

One might find it surprising that our open string lives in an integrable sector. This is likely a consequence of the highly symmetric and simple boundary conditions for which we prove integrability: a static string at the horizon. It is known that a ring string is nonintegrable in thermal backgrounds, and also in generic Dp-brane backgrounds (although some very special cases can be integrable, even at finite temperature, see e.g. [93, 94]). A

more generic open string configuration is likely also nonintegrable. Essentially, since *different boundary conditions for string motion result in a different effective Lagrangian, the Liouville integrability has to be checked separately for every configuration*. While *physically* we like to think of "string motion in a given background", mathematically the system is integrable if the Euler-Lagrange equations satisfy certain conditions — and for a string the form of these equations depends on the string ansatz. Therefore, while a single example is enough to prove general nonintegrability, proving integrability in the most general case requires more powerful tools than the Kovacic algorithm. We do not do that: we merely focus on a single case which turns out to be integrable.

From our results it is clear that the study chaos and scrambling in gauge/string duality (i.e., beyond classical gravity) is a separate topic, not much touched upon in this work. Fluctuations of a static straight string stretched from boundary to boundary of a maximally extended (static and neutral) BTZ black hole are known to lead to the exact MSS value for the worldsheet OTOC [21]; for a dragging string, butterfly velocity also enters the picture, as the leading correction to the drag force [95]. Given the high symmetry of these systems, this is not surprising; when the symmetry is decreased or corrections added to the classical string solution the value will be modified but there is no reason to believe that the solutions and the OTOC exponents will be modified in the same way as the bulk exponents, i.e. quasinormal modes in our setup. Worldsheet scrambling for a rotating BTZ black hole was studied in [74] and indeed, while the OTOC exponent is modified from the MSS value, it is not the same as the bulk exponent that we find here. Of course, strings can also model spatiotemporal chaos if we allows both worldsheet coordinates to fluctuate as in [96].

Finally, the issue of gauge choice might be worth commenting. Our choice to work in the conformal gauge instead of static gauge most of the time is somewhat unusual. The static gauge equates the time and radial coordinate with the worldsheet coordinates τ and σ and thus immediately kills the unphysical (gauge-dependent) degrees of freedom. But the conformal gauge has several advantages for us: (*i*) it simplifies many calculations (*ii*) it allows us to look at the fluctuations along the holographic RG flow (the radial direction) (*iii*) it does not fully fix the reparametrization invariance on the worldsheet, leaving the $\mathrm{SL}(2,\mathbb{R})$ group of global coordinate transformations, but as argued in [45, 46, 97] this group provides a nice way to understand the appearance of a universal scale and its disappearance when we determine the boundary conditions for the transverse fluctuations that fully fix the gauge on the worldsheet. This approach was exploited in full depth in [97] to study quantum chaos, i.e. OTOC on the worldsheet of the open string.

5.1 Note added: quasi-normal modes, variational equations and the spectral form factor

At the end we want to comment on another connection between our calculation and the quasi-normal modes of the black hole (or black string) background. After finishing the first version of the paper we became aware of the work [98] where it is shown that the partition function and the spectral form factor of a holographic theory at finite temperature can be understood as a product over the QNM frequencies ω_{QNM} of the bulk black hole. Specifically, for a bosonic system at temperature T, one-loop partition function is found in [98] to be

$$Z = \mathrm{Tr}e^{-i\hat{\hat{K}}T} = \prod_{\omega_{\mathrm{QNM}}} \left(1 - e^{-i\omega_{\mathrm{QNM}}T}\right)^{-1}. \tag{5.1}$$

Here, $\hat{\tilde{K}}$ is the time-shift operator which acts as a boost near the horizon (where $g_{tt} \to 0$), in a complexified metric where the radial coordinate is shifted as $r \mapsto r - i\epsilon$. From (5.1), it is obvious that ω_{QNM} are just the eigenvalues of $\hat{\tilde{K}}$. But Lyapunov exponents are nothing but the eigenvalues of the Jacobian matrix of the equations of motion — in other words, they are the eigenvalues of the shift operator but now the shift is along the tangential directions in phase space. In a given background however, e.g. in a near-horizon region like the BTZ region of a near-extremal black string, one can choose the gauge so that the Jacobian *locally* (but not everywhere) coincides with the time-shift operator $\hat{K}$; the complexification to $\hat{\tilde{K}}$ then just imposes the analytic behavior at the horizon, as one normally does when computing correlation functions such as G_R from subsection 4.3.

The above discussion is obviously not rigorous. It would be interesting to formulate it in strict terms and see how much one can learn from such a viewpoint.

Acknowledgments

A   Slightly generalized ansatz for the Dp-brane background

Here we comment on the ansatz for the string configuration in Dp-brane backgrounds in subsection 3.2. We can have nontrivial dynamics of the string also on the k-sphere provided we impose some additional constraints which are necessary to preserve the separation of variables. For example, we can replace the ansatz from eq. (3.6) by

$$
\begin{aligned}
t &= t(\tau), & X_1 &= x_1, & \ldots & & X_{10-k} &= x_{10-k}, \\
R &= R(\sigma), & \Phi_1 &= \Phi_1(\tau), & \Phi_2 &= \Phi_2(\tau), & \Phi_3 &= \phi_3, & \ldots & & \Phi_k &= \phi_k
\end{aligned}
\tag{A.1}
$$

Choosing $t(\tau) = \tau$ as usual, we are left with a constraint (in addition to the Virasoro constraint) coming from the above ansatz, i.e. the assumption that R only depends on σ:

$$
\dot{\Phi}_1^2 + \sin \Phi_1^2 \dot{\Phi}_2^2 \equiv \ell^2,
\tag{A.2}
$$

where ℓ^2 is the conserved squared angular momentum on the k-sphere. The constraints decouple the dynamics of R from Φ^1 and Φ^2, so the equation of motion for R remains the same as eq. (3.7) and for Φ_1 we obtain:

$$
\ddot{\Phi}_1 + \left(\dot{\Phi}_1^2 - w^2 \right) \cot \Phi_1 = 0.
\tag{A.3}
$$

Therefore, it is possible to go for more general dynamics than in the main text, which might be of interest for some applications but is completely peripheral for our main interest in this paper.

References

[1] Y. Sekino and L. Susskind, *Fast Scramblers*, *JHEP* **10** (2008) 065 [arXiv:0808.2096] [ɪɴSPIRE].

[2] J. Maldacena, S.H. Shenker and D. Stanford, *A bound on chaos*, *JHEP* **08** (2016) 106 [arXiv:1503.01409] [ɪɴSPIRE].

[3] S.H. Shenker and D. Stanford, *Black holes and the butterfly effect*, *JHEP* **03** (2014) 067 [arXiv:1306.0622] [ɪɴSPIRE].

[4] D.A. Roberts, D. Stanford and L. Susskind, *Localized shocks*, *JHEP* **03** (2015) 051 [arXiv:1409.8180] [ɪɴSPIRE].

[5] S.H. Shenker and D. Stanford, *Stringy effects in scrambling*, *JHEP* **05** (2015) 132 [arXiv:1412.6087] [ɪɴSPIRE].

[6] J. Maldacena and D. Stanford, *Remarks on the Sachdev-Ye-Kitaev model*, *Phys. Rev. D* **94** (2016) 106002 [arXiv:1604.07818] [ɪɴSPIRE].

[7] E. Marcus and S. Vandoren, *A new class of SYK-like models with maximal chaos*, *JHEP* **01** (2019) 166 [arXiv:1808.01190] [ɪɴSPIRE].

[8] A.M. García-García, B. Loureiro, A. Romero-Bermúdez and M. Tezuka, *Chaotic-Integrable Transition in the Sachdev-Ye-Kitaev Model*, *Phys. Rev. Lett.* **120** (2018) 241603 [arXiv:1707.02197] [ɪɴSPIRE].

[9] N. Lashkari et al., *Towards the Fast Scrambling Conjecture*, *JHEP* **04** (2013) 022 [arXiv:1111.6580] [ɪɴSPIRE].

[10] A. Almheiri et al., *The entropy of Hawking radiation*, *Rev. Mod. Phys.* **93** (2021) 035002 [arXiv:2006.06872] [ɪɴSPIRE].

[11] G. Penington, S.H. Shenker, D. Stanford and Z. Yang, *Replica wormholes and the black hole interior*, *JHEP* **03** (2022) 205 [arXiv:1911.11977] [ɪɴSPIRE].

[12] A. Almheiri et al., *Replica Wormholes and the Entropy of Hawking Radiation*, *JHEP* **05** (2020) 013 [arXiv:1911.12333] [ɪɴSPIRE].

[13] D. Stanford, *More quantum noise from wormholes*, arXiv:2008.08570 [ɪɴSPIRE].

[14] P. Saad, S.H. Shenker, D. Stanford and S. Yao, *Wormholes without averaging*, arXiv:2103.16754 [ɪɴSPIRE].

[15] P. Saad, S. Shenker and S. Yao, *Comments on wormholes and factorization*, arXiv:2107.13130 [ɪɴSPIRE].

[16] J. Pollack, M. Rozali, J. Sully and D. Wakeham, *Eigenstate Thermalization and Disorder Averaging in Gravity*, *Phys. Rev. Lett.* **125** (2020) 021601 [arXiv:2002.02971] [ɪɴSPIRE].

[17] B. Mukhametzhanov, *Factorization and complex couplings in SYK and in Matrix Models*, *JHEP* **04** (2023) 122 [arXiv:2110.06221] [ɪɴSPIRE].

[18] F.S. Nogueira et al., *Geometric phases distinguish entangled states in wormhole quantum mechanics*, *Phys. Rev. D* **105** (2022) L081903 [arXiv:2109.06190] [ɪɴSPIRE].

[19] M. Čubrović, *Replicas, averaging and factorization in the IIB matrix model*, *JHEP* **09** (2022) 136 [arXiv:2203.10697] [INSPIRE].

[20] A. Blommaert, L.V. Iliesiu and J. Kruthoff, *Gravity factorized*, *JHEP* **09** (2022) 080 [arXiv:2111.07863] [INSPIRE].

[21] J. de Boer, E. Llabrés, J.F. Pedraza and D. Vegh, *Chaotic strings in AdS/CFT*, *Phys. Rev. Lett.* **120** (2018) 201604 [arXiv:1709.01052] [INSPIRE].

[22] K. Hashimoto and N. Tanahashi, *Universality in Chaos of Particle Motion near Black Hole Horizon*, *Phys. Rev. D* **95** (2017) 024007 [arXiv:1610.06070] [INSPIRE].

[23] S. Dalui and B.R. Majhi, *Near horizon local instability and quantum thermality*, *Phys. Rev. D* **102** (2020) 124047 [arXiv:2007.14312] [INSPIRE].

[24] C. Núñez, J.M. Penín, D. Roychowdhury and J. Van Gorsel, *The non-Integrability of Strings in Massive Type IIA and their Holographic duals*, *JHEP* **06** (2018) 078 [arXiv:1802.04269] [INSPIRE].

[25] C. Núñez, D. Roychowdhury and D.C. Thompson, *Integrability and non-integrability in $\mathcal{N} = 2$ SCFTs and their holographic backgrounds*, *JHEP* **07** (2018) 044 [arXiv:1804.08621] [INSPIRE].

[26] M. Čubrović, *The bound on chaos for closed strings in Anti-de Sitter black hole backgrounds*, *JHEP* **12** (2019) 150 [arXiv:1904.06295] [INSPIRE].

[27] D.-Z. Ma, D. Zhang, G. Fu and J.-P. Wu, *Chaotic dynamics of string around charged black brane with hyperscaling violation*, *JHEP* **01** (2020) 103 [arXiv:1911.09913] [INSPIRE].

[28] D. Roychowdhury, *Non-integrability for $\mathcal{N} = 1$ SCFTs in 5d*, *Phys. Rev. D* **104** (2021) 086010 [arXiv:2106.10646] [INSPIRE].

[29] C. Yu, D. Chen, B. Mu and Y. He, *Violating the chaos bound in five-dimensional, charged, rotating Einstein-Maxwell-Chern-Simons black holes*, *Nucl. Phys. B* **987** (2023) 116093 [INSPIRE].

[30] P. Dutta, K.L. Panigrahi and B. Singh, *Circular string in a black p-brane leading to chaos*, *JHEP* **10** (2023) 189 [arXiv:2307.12350] [INSPIRE].

[31] D. Giataganas, *Chaotic Motion near Black Hole and Cosmological Horizons*, *Fortsch. Phys.* **70** (2022) 2200001 [arXiv:2112.02081] [INSPIRE].

[32] T. Dray and G. 't Hooft, *The Gravitational Shock Wave of a Massless Particle*, *Nucl. Phys. B* **253** (1985) 173 [INSPIRE].

[33] T. Dray and G. 't Hooft, *The Effect of Spherical Shells of Matter on the Schwarzschild Black Hole*, *Commun. Math. Phys.* **99** (1985) 613 [INSPIRE].

[34] P. Kraus, F. Larsen and S.P. Trivedi, *The Coulomb branch of gauge theory from rotating branes*, *JHEP* **03** (1999) 003 [hep-th/9811120] [INSPIRE].

[35] V. Balasubramanian and S.F. Ross, *Holographic particle detection*, *Phys. Rev. D* **61** (2000) 044007 [hep-th/9906226] [INSPIRE].

[36] J. Louko, D. Marolf and S.F. Ross, *On geodesic propagators and black hole holography*, *Phys. Rev. D* **62** (2000) 044041 [hep-th/0002111] [INSPIRE].

[37] J.G. Russo, *Anomalous dimensions in gauge theories from rotating strings in $AdS_5 \times S^5$*, *JHEP* **06** (2002) 038 [hep-th/0205244] [INSPIRE].

[38] C.P. Herzog et al., *Energy loss of a heavy quark moving through $N = 4$ supersymmetric Yang-Mills plasma*, *JHEP* **07** (2006) 013 [hep-th/0605158] [INSPIRE].

[39] S.S. Gubser, *Drag force in AdS/CFT*, *Phys. Rev. D* **74** (2006) 126005 [`hep-th/0605182`] [INSPIRE].

[40] J.M. Maldacena, *Wilson loops in large N field theories*, *Phys. Rev. Lett.* **80** (1998) 4859 [`hep-th/9803002`] [INSPIRE].

[41] S.-J. Rey, S. Theisen and J.-T. Yee, *Wilson-Polyakov loop at finite temperature in large N gauge theory and anti-de Sitter supergravity*, *Nucl. Phys. B* **527** (1998) 171 [`hep-th/9803135`] [INSPIRE].

[42] A. Brandhuber, N. Itzhaki, J. Sonnenschein and S. Yankielowicz, *Wilson loops in the large N limit at finite temperature*, *Phys. Lett. B* **434** (1998) 36 [`hep-th/9803137`] [INSPIRE].

[43] S.-J. Rey and J.-T. Yee, *Macroscopic strings as heavy quarks in large N gauge theory and anti-de Sitter supergravity*, *Eur. Phys. J. C* **22** (2001) 379 [`hep-th/9803001`] [INSPIRE].

[44] K. Hashimoto, K. Murata and N. Tanahashi, *Chaos of Wilson Loop from String Motion near Black Hole Horizon*, *Phys. Rev. D* **98** (2018) 086007 [`arXiv:1803.06756`] [INSPIRE].

[45] H.W. Lin, J. Maldacena and Y. Zhao, *Symmetries Near the Horizon*, *JHEP* **08** (2019) 049 [`arXiv:1904.12820`] [INSPIRE].

[46] H.W. Lin and D. Stanford, *A symmetry algebra in double-scaled SYK*, *SciPost Phys.* **15** (2023) 234 [`arXiv:2307.15725`] [INSPIRE].

[47] V. Cardoso et al., *Geodesic stability, Lyapunov exponents and quasinormal modes*, *Phys. Rev. D* **79** (2009) 064016 [`arXiv:0812.1806`] [INSPIRE].

[48] M. Bianchi, A. Grillo and J.F. Morales, *Chaos at the rim of black hole and fuzzball shadows*, *JHEP* **05** (2020) 078 [`arXiv:2002.05574`] [INSPIRE].

[49] P. Hintz and A. Vasy, *Analysis of linear waves near the Cauchy horizon of cosmological black holes*, *J. Math. Phys.* **58** (2017) 081509 [`arXiv:1512.08004`] [INSPIRE].

[50] L. Motl and A. Neitzke, *Asymptotic black hole quasinormal frequencies*, *Adv. Theor. Math. Phys.* **7** (2003) 307 [`hep-th/0301173`] [INSPIRE].

[51] A. Stepanchuk and A.A. Tseytlin, *On (non)integrability of classical strings in p-brane backgrounds*, *J. Phys. A* **46** (2013) 125401 [`arXiv:1211.3727`] [INSPIRE].

[52] L.A. Pando Zayas and C.A. Terrero-Escalante, *Chaos in the Gauge/Gravity Correspondence*, *JHEP* **09** (2010) 094 [`arXiv:1007.0277`] [INSPIRE].

[53] V.E. Korepin, N.M. Bogoliubov and A.G. Izergin, *Quantum Inverse Scattering Method and Correlation Functions*, Cambridge University Press, Cambridge (1993) [`DOI:10.1017/CBO9780511628832`] [INSPIRE].

[54] J. Ruiz, *Differential Galois Theory and Non-Integrability of Hamiltonian Systems*, Springer Basel (1999) [`DOI:10.1007/978-3-0348-8718-2`].

[55] Y. Chervonyi and O. Lunin, *(Non)-Integrability of Geodesics in D-brane Backgrounds*, *JHEP* **02** (2014) 061 [`arXiv:1311.1521`] [INSPIRE].

[56] P. Basu and L.A. Pando Zayas, *Analytic Non-integrability in String Theory*, *Phys. Rev. D* **84** (2011) 046006 [`arXiv:1105.2540`] [INSPIRE].

[57] K. Hashimoto, K.-B. Huh, K.-Y. Kim and R. Watanabe, *Exponential growth of out-of-time-order correlator without chaos: inverted harmonic oscillator*, *JHEP* **11** (2020) 068 [`arXiv:2007.04746`] [INSPIRE].

[58] K. Goldstein, S. Kachru, S. Prakash and S.P. Trivedi, *Holography of Charged Dilaton Black Holes*, *JHEP* **08** (2010) 078 [arXiv:0911.3586] [INSPIRE].

[59] C. Charmousis et al., *Effective Holographic Theories for low-temperature condensed matter systems*, *JHEP* **11** (2010) 151 [arXiv:1005.4690] [INSPIRE].

[60] B. Gouteraux and E. Kiritsis, *Generalized Holographic Quantum Criticality at Finite Density*, *JHEP* **12** (2011) 036 [arXiv:1107.2116] [INSPIRE].

[61] B. Gouteraux and E. Kiritsis, *Quantum critical lines in holographic phases with (un)broken symmetry*, *JHEP* **04** (2013) 053 [arXiv:1212.2625] [INSPIRE].

[62] G.W. Gibbons and P.K. Townsend, *Vacuum interpolation in supergravity via super p-branes*, *Phys. Rev. Lett.* **71** (1993) 3754 [hep-th/9307049] [INSPIRE].

[63] H.J. Boonstra, B. Peeters and K. Skenderis, *Duality and asymptotic geometries*, *Phys. Lett. B* **411** (1997) 59 [hep-th/9706192] [INSPIRE].

[64] J.M. Maldacena and A. Strominger, *Black hole grey body factors and d-brane spectroscopy*, *Phys. Rev. D* **55** (1997) 861 [hep-th/9609026] [INSPIRE].

[65] A. Strominger and C. Vafa, *Microscopic origin of the Bekenstein-Hawking entropy*, *Phys. Lett. B* **379** (1996) 99 [hep-th/9601029] [INSPIRE].

[66] J.M. Maldacena, *The large N limit of superconformal field theories and supergravity*, *Adv. Theor. Math. Phys.* **2** (1998) 231 [hep-th/9711200] [INSPIRE].

[67] N. Seiberg and E. Witten, *The D1/D5 system and singular CFT*, *JHEP* **04** (1999) 017 [hep-th/9903224] [INSPIRE].

[68] O. Aharony et al., *Large N field theories, string theory and gravity*, *Phys. Rept.* **323** (2000) 183 [hep-th/9905111] [INSPIRE].

[69] O. Lunin and S.D. Mathur, *A toy black hole S-matrix in the D1-D5 CFT*, *JHEP* **02** (2013) 083 [arXiv:1211.5830] [INSPIRE].

[70] E. Kiritsis, *String theory in a nutshell*, Princeton University Press, U.S.A. (2019) [DOI:10.2307/j.ctvcm4hd1].

[71] O. Lunin and S.D. Mathur, *Correlation functions for M^N/S_N orbifolds*, *Commun. Math. Phys.* **219** (2001) 399 [hep-th/0006196] [INSPIRE].

[72] O. Lunin and S.D. Mathur, *Three point functions for M^N/S_N orbifolds with $N = 4$ supersymmetry*, *Commun. Math. Phys.* **227** (2002) 385 [hep-th/0103169] [INSPIRE].

[73] V. Jahnke, K.-Y. Kim and J. Yoon, *On the Chaos Bound in Rotating Black Holes*, *JHEP* **05** (2019) 037 [arXiv:1903.09086] [INSPIRE].

[74] A. Banerjee, A. Kundu and R.R. Poojary, *Rotating black holes in AdS spacetime, extremality, and chaos*, *Phys. Rev. D* **102** (2020) 106013 [arXiv:1912.12996] [INSPIRE].

[75] P. Banerjee, *Holographic Brownian motion at finite density*, *Phys. Rev. D* **94** (2016) 126008 [arXiv:1512.05853] [INSPIRE].

[76] L.D. Landau and E.M. Lifshits, *Quantum Mechanics: Non-Relativistic Theory*, Butterworth-Heinemann, Oxford (1991) [INSPIRE].

[77] S.S. Gubser, *Momentum fluctuations of heavy quarks in the gauge-string duality*, *Nucl. Phys. B* **790** (2008) 175 [hep-th/0612143] [INSPIRE].

[78] D. Giataganas and H. Soltanpanahi, *Universal Properties of the Langevin Diffusion Coefficients*, *Phys. Rev. D* **89** (2014) 026011 [arXiv:1310.6725] [INSPIRE].

[79] D. Giataganas, *Stochastic Motion of Heavy Quarks in Holography: A Theory-Independent Treatment*, *PoS* **CORFU2017** (2018) 032 [`arXiv:1805.09011`] [ɪɴSPIRE].

[80] J. Casalderrey-Solana and D. Teaney, *Transverse Momentum Broadening of a Fast Quark in a N = 4 Yang Mills Plasma*, *JHEP* **04** (2007) 039 [`hep-th/0701123`] [ɪɴSPIRE].

[81] J. Casalderrey-Solana, K.-Y. Kim and D. Teaney, *Stochastic String Motion Above and Below the World Sheet Horizon*, *JHEP* **12** (2009) 066 [`arXiv:0908.1470`] [ɪɴSPIRE].

[82] A.N. Atmaja, J. de Boer and M. Shigemori, *Holographic Brownian Motion and Time Scales in Strongly Coupled Plasmas*, *Nucl. Phys. B* **880** (2014) 23 [`arXiv:1002.2429`] [ɪɴSPIRE].

[83] M. Blake, R.A. Davison and D. Vegh, *Horizon constraints on holographic Green's functions*, *JHEP* **01** (2020) 077 [`arXiv:1904.12883`] [ɪɴSPIRE].

[84] T. Faulkner, H. Liu, J. McGreevy and D. Vegh, *Emergent quantum criticality, Fermi surfaces, and AdS₂*, *Phys. Rev. D* **83** (2011) 125002 [`arXiv:0907.2694`] [ɪɴSPIRE].

[85] V. Cardoso and J.P.S. Lemos, *Scalar, electromagnetic and Weyl perturbations of BTZ black holes: Quasinormal modes*, *Phys. Rev. D* **63** (2001) 124015 [`gr-qc/0101052`] [ɪɴSPIRE].

[86] E. Berti, V. Cardoso and A.O. Starinets, *Quasinormal modes of black holes and black branes*, *Class. Quant. Grav.* **26** (2009) 163001 [`arXiv:0905.2975`] [ɪɴSPIRE].

[87] M. Bianchi, D. Consoli, A. Grillo and J.F. Morales, *Light rings of five-dimensional geometries*, *JHEP* **03** (2021) 210 [`arXiv:2011.04344`] [ɪɴSPIRE].

[88] M. Bianchi, M. Firrotta, J. Sonnenschein and D. Weissman, *Measure for Chaotic Scattering Amplitudes*, *Phys. Rev. Lett.* **129** (2022) 261601 [`arXiv:2207.13112`] [ɪɴSPIRE].

[89] B. Craps, S. Khetrapal and C. Rabideau, *Chaos in CFT dual to rotating BTZ*, *JHEP* **11** (2021) 105 [`arXiv:2107.13874`] [ɪɴSPIRE].

[90] K. Hashimoto, K. Sugiura, K. Sugiyama and T. Yoda, *Photon sphere and quasinormal modes in AdS/CFT*, *JHEP* **10** (2023) 149 [`arXiv:2307.00237`] [ɪɴSPIRE].

[91] M. Riojas and H.-Y. Sun, *The Photon Sphere and the AdS/CFT Correspondence*, [`arXiv:2307.06415`] [ɪɴSPIRE].

[92] M. Bianchi and G. Di Russo, *Turning black holes and D-branes inside out of their photon spheres*, *Phys. Rev. D* **105** (2022) 126007 [`arXiv:2110.09579`] [ɪɴSPIRE].

[93] D. Roychowdhury, *Analytic integrability for holographic duals with $J\overline{T}$ deformations*, *JHEP* **09** (2020) 053 [`arXiv:2005.04457`] [ɪɴSPIRE].

[94] J. Pal, S. Roychowdhury, A. Lala and D. Roychowdhury, *Integrability and non-integrability for marginal deformations of 4d $\mathcal{N} = 2$ SCFTs*, *JHEP* **10** (2023) 173 [`arXiv:2307.12079`] [ɪɴSPIRE].

[95] D.S. Ageev, *Chaotic nature of holographic QCD*, *Phys. Rev. D* **104** (2021) 126013 [`arXiv:2105.04589`] [ɪɴSPIRE].

[96] T. Ishii, R. Kitaku, K. Murata and C.-M. Yoo, *Turbulence on open string worldsheets under non-integrable boundary conditions*, *JHEP* **02** (2024) 149 [`arXiv:2310.19317`] [ɪɴSPIRE].

[97] S. Giombi, S. Komatsu and B. Offertaler, *Chaos and the reparametrization mode on the AdS₂ string*, *JHEP* **09** (2023) 023 [`arXiv:2212.14842`] [ɪɴSPIRE].

[98] Y. Chen, V. Ivo and J. Maldacena, *Comments on the double cone wormhole*, [`arXiv:2310.11617`] [ɪɴSPIRE].

Weak chaos and mixed dynamics in the string S-matrix

Nikola Savić [iD] [a,b] **and Mihailo Čubrović** [iD] [b]

[a]*Université Paris-Saclay, CNRS, CEA, Institut de Physique Théorique,*
 91191 Gif-sur-Yvette, France
[b]*Institute of Physics Belgrade, University of Belgrade,*
 Pregrevica 118, 11080 Belgrade, Serbia

 E-mail: nikola.savic@ipht.fr, cubrovic@ipb.ac.rs

ABSTRACT: We investigate chaotic dynamics in tree-level S-matrices describing the scattering of tachyons, photons and gravitons on highly excited open and closed bosonic strings, motivated by the string/black hole complementarity. The eigenphase spacing distribution and other indicators of quantum chaotic scattering suggest that the dynamics is only weakly chaotic, consisting of both regular/Poisson and chaotic/Wigner-Dyson processes. Only for special values of momenta and (for photon scattering) scattering angles do we find strong chaos of random matrix type. These special values correspond to a crossover between two regimes of scattering, dominated by short versus long partitions of the total occupation number of the highly excited string; they also maximize the information entropy of the S-matrix. The lack of strong chaos suggests that perturbative dynamics of highly excited strings can never describe the universal properties and maximal chaos of black hole horizons.

Contents

1   Introduction

Chaos and dynamical phenomena have turned out to provide a fundamental insight into the structure and information content of black holes and gravity in general. Since the discovery of the black hole scrambling concept [1, 2], chaos bound and OTOC-ology [3, 4] and on the other hand the questions of factorization and microscopic statistics stemming from the replica wormhole proposal in the context of the information paradox [5–7], it is becoming clear that nonlinear dynamics is an integral part of high-energy theory, as many questions in gravity and string theory are naturally formulated in terms of scrambling, thermalization and microscopic chaos.

The time is now ripe to move beyond semiclassical horizons and black holes in general relativity. The same questions of scrambling, universal timescales and the like can be asked also for stringy black hole solutions [8] or for solutions proposed to replace black holes by horizonless stringy objects (microstate geometries and fuzzballs) [9]. With stringy corrections, things become much more difficult and less universal. One possible approach is the string/black hole (string/BH) complementarity paradigm [10–12]: a highly excited string should look like a black hole in the weak coupling regime.

The idea of string/BH complementarity stems from the fact that at sufficiently high occupation numbers, the Schwarzschild radius of the HES becomes smaller than the string scale, hence the string should collapse into a black hole. To remind, the mass of a string M_s and the mass of a black hole M_{BH} in $d+1$ spacetime dimension are

$$M_{\mathrm{BH}} \sim \frac{r_s^{d-2}}{G}, \ M_s \sim \frac{N}{\alpha'}, \tag{1.1}$$

where α' is the string tension, G is the Newton's constant and N the occupation number (level). At the string/BH transition, we expect the string length scale to be $\ell_s = \sqrt{\alpha'} \sim r_s$; then a string of mass M_s can become a black hole of mass $M_{\mathrm{BH}} = M_s \equiv M$. Equating the mass and length scales and taking into account that $G \sim g^2 \alpha'$ where g is the string coupling, we find the condition for the black hole description of the string:

$$Ng^4 \sim (\alpha')^{d-3} \Rightarrow g_c \propto N^{-1/4}(\alpha')^{\frac{d-3}{4}}. \tag{1.2}$$

Therefore, when the total occupation number N is large the string will approximately describe a black hole already at small g, i.e. in the perturbative regime. This is the motivation behind the recent works on the scattering amplitudes of highly excited strings (HES). By HES we mean simply a string with $N \gg 1$, and scattering amplitudes of the form $\mathrm{HES} \to \mathrm{HES} + \mathrm{A}$ or $\mathrm{HES} + \mathrm{A} \to \mathrm{HES} + \mathrm{B}$ provide a stringy equivalent to the scrambling perspective for black holes, where we scatter a field on an AdS black hole, obtaining a time-disordered correlation function as a probe of chaos [13–15]. In [16] a general framework for computing the HES scattering amplitudes was formulated, based on the Del Giudice-Di Vecchia-Fubini (DDF) formalism [17–20]. The idea is to obtain the HES in a controlled way, by adding photonic excitations to a tachyon (vacuum of the bosonic string). In [21–24] the poles and zeros of the resulting amplitudes are studied within the framework of random matrix theory (RMT), also making use of a novel chaos indicator, the ratio of eigenvalue spacings, discussed in [25, 26].

We are thus dealing with (possibly chaotic) quantum scattering. The reader is perhaps better acquainted with the study of quantum chaos in closed systems, i.e. the study of quantum Hamiltonians [27], where strong chaos is successfully described by the RMT approach [28]. To remind, quantum chaotic Hamiltonians of sufficiently large size approach Gaussian random matrices in their behavior, and can be described by the Gaussian ensemble statistics. In particular, the eigenvalue (i.e., eigenenergy) spacings obey the celebrated Wigner-Dyson distribution, and the system is chaotic in the RMT sense if the eigenvalue spacing histogram is well fit by the Wigner-Dyson curve.

A scattering problem is inherently different. Instead of a Hamiltonian, we deal with scattering amplitudes and the S-matrix which describes the probability amplitudes of all possible scattering outcomes. A difference of principle is that the scattered object ends up "at infinity", i.e. the system is not closed in the usual sense. For classical scattering, this means that exit curves behave in a sense like attractors in dissipative chaos, i.e. they tell us where the orbits end up when $t \to \infty$. A measure of chaos is then the very complex (usually fractal) dependence of the final state (e.g. scattering angle) on the initial conditions. Therefore, we might expect a similar fractal behavior for the dependence of amplitudes on the scattering angle. This approach was used in [23]. Another approach is to look at the spacings of special points in the amplitudes and to test if these satisfy the RMT statistics, analogously to the eigenenergy spacings in Hamiltonian systems; this approach was taken in [21, 22, 24, 26, 29]. The outcome of these works is very interesting and has uncovered several important ideas, e.g. the emergence of thermalization in [24] but concerning the chaos itself it is inconclusive: while there are clear signs of chaos some indicators, e.g. the spacing ratios in [26] deviate significantly from the RMT predictions, and the angular dependence of the amplitudes, while complex, is not fractal [23].

In this work we continue the exploration of chaos in HES scattering but attempt a more systematic approach, studying directly the S-matrix rather than individual amplitudes. We also introduce a novel element of "geometric" chaos which arises when we look at non-scalar scatterers, i.e. the process HES + photon instead of HES + tachyon. For the S-matrix a rigorous generalization of the RMT approach exists [30, 31]: the role of eigenenergies is taken by the eigenphases, i.e. the phases of the (complex) eigenvalues of the S-matrix. Now the eigenphase spacings are expected to obey the Wigner-Dyson distribution. It will turn out that the study of the S-matrix as a whole reveals some additional surprises: we find clear signs of chaos only for special values of the angles and/or momenta, and the underlying mechanism is the competition between different ("short" and "long") partitions of the total occupation number N. This "combinatorial" approach to chaos will also reveal the existence of quasi-invariant states, which necessarily spoil the chaos — in other words, despite finding strong chaos at special points in parameter space, we argue that there is always a regular component. All of the above holds for bosonic strings: we do not consider superstrings in this work so from now on it is understood that "string" means bosonic string.

Recently the work [32] has appeared which also studies the properties of the S-matrix and likewise sees a crossover between "short" and "long" partitions as dominant in the scattering (though their terminology is different). There is therefore some overlap of our work and [32] but our results are mostly complementary: in [32] the influence of the polarization of the DDF photons is studied, typicality of states is probed and in addition important indications of eigenstate thermalization are found, whereas we study in more detail the dynamics itself and introduce the photon (instead of tachyon) scattering. We warmly recommend the reader to study [32] in addition to our paper.

With some hindsight, we can say that our results indicate that HES scattering is never uniformly chaotic and therefore does not directly provide a look at black holes in the stringy regime; the naive hope that the string/BH complementarity can be seen directly in the HES S-matrix is thus invalid. But this conclusion is also useful for future work, and the HES S-matrix is in itself worth studying, as it shows some novel phenomena of quantum chaotic scattering.

The plan of the paper is the following. In section 2 we briefly recapitulate the construction of the HES in the DDF formalism and the calculation of the HES-tachyon amplitude; then we compute the HES-photon amplitude which was never studied so far. In section 3 we introduce the tools and ideas for studying the S-matrix dynamics: eigenphase statistics and the combinatorics of partitions/states. Section 4 brings the results of the analysis described in section 3, and in section 5 we discuss the implications of our findings and directions of further work.

2 Highly excited strings and their scattering amplitudes

In this section we set the stage: we construct the highly excited string states and then write the tree-level scattering amplitude for a few simple $2 \to 2$ processes, scattering a tachyon t or a photon γ off a HES:

$$\text{HES} + \text{t} \longrightarrow \text{HES}' + \text{t}' \tag{2.1}$$

$$\text{HES} + \gamma \longrightarrow \text{HES}' + \gamma'. \tag{2.2}$$

For open strings we closely follow the formalism of [16, 19] and specifically the calculations of [23]. For closed strings we construct the amplitude exploiting the KLT relations [33–35] and check the result by direct integration on the worldsheet. The KLT duality applied to eqs. (2.1) and (2.2) will yield the processes with closed HES (cHES) and tachyon or graviton respectively:

$$\text{cHES} + \text{t} \longrightarrow \text{cHES}' + \text{t}' \tag{2.3}$$

$$\text{cHES} + \text{g} \longrightarrow \text{cHES}' + \text{g}'. \tag{2.4}$$

In the rest of the paper we do not differentiate between open and closed HES in notation, i.e. we use HES (rather than cHES) for both cases, as the open/closed nature of the string will always be stated explicitly. Of course, we do differentiate between a photon γ and a graviton g as the two have different spins. We will thus always call the process in eq. (2.2) the HES-photon scattering and the process in eq. (2.4) will be called the HES-graviton scattering.

2.1 Open HES - tachyon amplitudes

The HES represents the state with a large number of excitations $\{n_k\}$, or equivalently with a high level $N = \sum_{k=1}^{\infty} n_k$, where k labels the modes and n_k is the occupation number of the k-th mode. Following the DDF formalism [17, 19, 20], a convenient way to think of the HES state is as a state created in a process in which the tachyon absorbs J photons (we will call them DDF photons) with momenta q_a and polarizations λ_a $(a = 1, \ldots J)$, one by one, as in figure 1. In the lightcone quantization the general HES state then has the form [19]:

$$|\text{HES}\rangle \propto \xi^{i_1 \cdots i_J} P \left(\partial X, (\partial X)^2, \ldots (\partial X)^N \right)_{i_1 \ldots i_J} |0, p\rangle \tag{2.5}$$

where $\xi^{i_1 \cdots i_J}$ is the polarization tensor, P is a polynomial of degree N over the derivatives of the string coordinates X^μ and $|0, p\rangle$ is the tachyon state (ground state of the bosonic string) with momentum p. Hence, the physical process in eq. (2.1) can be described by writing it formally as

$$\text{tachyon}(1) + (\text{tachyon}\,(2) + J \text{ photons}) \longrightarrow \text{tachyon}(1') + (\text{tachyon}\,(2') + J' \text{ photons})\,, \tag{2.6}$$

and then picking out the poles so that the (tachyon $+ J$ photons) part of the amplitude creates an intermediate on-shell HES state, as shown schematically in figure 1.

For this procedure to correctly describe the absorption of J photons by the tachyon one by one, it is necessary to remove the terms which couple the photons to each other. These are proportional to $\lambda_a \cdot \lambda_b$, so we must take the polarizations of different photons to be orthogonal to each other. For the sake of simplicity, we achieve this by making two special choices, again following [23]:[1]

1. We take all photons to have the same polarization $\lambda_a \equiv \lambda$ such that $\lambda \cdot \lambda = 0$.

2. The momenta of DDF photons are taken to be equal to $q_a = -N_a q$ $(a = 1, \ldots J)$ where N_a is a positive integer. Now q must satisfy the condition $q \cdot \lambda = 0$ (this essentially states that all polarizations are transverse, as they have to be for photons).

---

[1]These special choices essentially limit the polarization tensor $\xi^{i_1 \cdots i_J}$ to a subset of all possible values. We have not explored more general choices; a more detailed discussion of the influence of the DDF photon polarization can be found in [32].
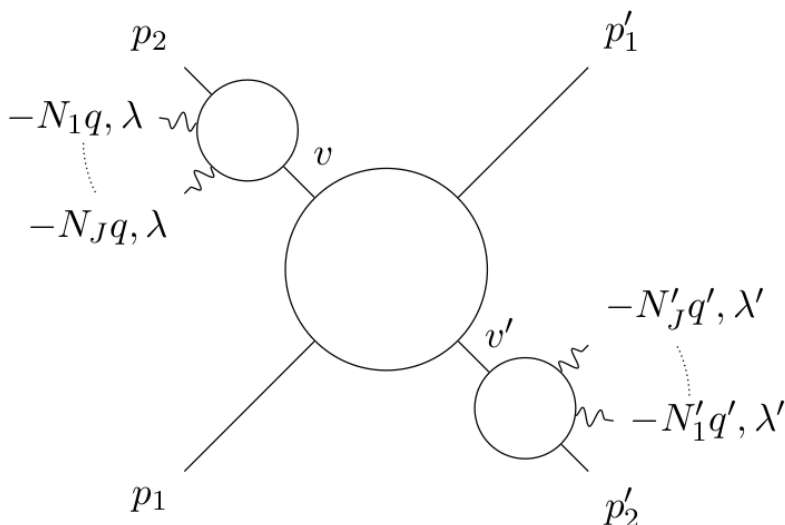
Figure 1. String amplitude for the HES-tachyon scattering process (2.1). The tachyon labeled by its momentum p_2 absorbs J photons with momenta and polarizations $\{-N_k q, \lambda\}$ which (after picking out appropriate poles) results in a HES state labeled by v (similarly for the HES'). The two HES states interact with tachyons labeled by p_1 and p_1'. Adapted from [23].

For the HES' state, on the right-hand side of eq. (2.1), we similarly take $\lambda' \cdot \lambda' = 0$ and $q_b' = -N_b' q'$. To find the tree-level amplitude we use the tachyon vertex operator $V_t(z, p) =:$ $e^{ipX(z)}:$, then we employ a computational trick to replace the photon vertex operators $V_p(z, p)$ by $: e^{i\zeta\partial X + ikX} :$ and keep only the part linear in the polarization ζ.

When the HES state is constructed as described above, we can express the tree-level amplitude as the path integral over the product of the vertex operators:

$$\mathcal{A} = \int \frac{\mathcal{D}X e^{-S_P}}{\mathrm{Vol}\,(\mathrm{SL}\,(2,\mathbb{R}))} \int \prod_i dw_i V_t(w_i, p_i) \prod_{a=1}^{J} dz_a V_p(z_a, -N_a q, \lambda) \prod_{b=1}^{J'} dz_b' V_p(z_b', -N_b' q, \lambda) \quad (2.7)$$

where $i \in \{1, 2, 1', 2'\}$ runs over the tachyons (1 and 1' are physical tachyons and 2 and 2' are DDF tachyons), $a \in \{1, \ldots, J\}$ runs over the photons in HES, $b \in \{1, \ldots, J'\}$ runs over the photons in HES' and the integration variables z and w run over the worldsheet. The action in the path integral is the usual Polyakov action $S_P = -\frac{1}{4\pi\alpha'} \int_z dz (\partial X)^2$. For open string calculations we set $\alpha' = \frac{1}{2}$, while for closed strings in subsection 2.3 we take $\alpha' = 2$. Next, still following [23], we make two more special choices to further simplify calculations:

1. The polarizations of DDF photons in HES and HES' satisfy $\lambda' \propto \lambda$.

2. The momenta of DDF photons in HES and HES' satisfy $q' \propto q$.[2]

---

[2]This choice was introduced in [20] and put to use also in [36, 37].

Using the above simplifications and performing the contractions we obtain:

$$\mathcal{A} = \frac{1}{\text{Vol}\,(\text{SL}\,(2,\mathbb{R}))} \int_{-\infty}^{\infty} \prod_i dw_i \int_{-\infty}^{\infty} \prod_{a=1}^{J} dz_a \int_{-\infty}^{\infty} \prod_{b=1}^{J'} dz_b' \times$$

$$\times \prod_{i<j} |w_i - w_j|^{p_i \cdot p_j} \prod_{a,i} |z_a - w_i|^{-\alpha_i} \sum_i \frac{-p_i \cdot \lambda}{w_i - z_a} \prod_{b,j} |z_b' - w_j|^{-\beta_j} \sum_j \frac{-p_j \cdot \lambda'}{w_j - z_b'}, \quad (2.8)$$

where we have expanded the integrand to linear order in photon polarizations, and introduced $\alpha_i \equiv N_a p_i \cdot q$ and $\beta_j \equiv N_b' p_j \cdot q'$. Exploiting the residual $\text{SL}(2,\mathbb{R})$ gauge invariance of the worldsheet to fix three out of four w_i values, we end up with six channels of the amplitude, labeled in terms of the Mandelstam variables s, t, u defined the usual way:[3]

$$\mathcal{A} = \mathcal{A}_{st} + \mathcal{A}_{tu} + \mathcal{A}_{us} + \mathcal{A}_{ts} + \mathcal{A}_{ut} + \mathcal{A}_{su}. \quad (2.9)$$

It is enough to state in full the expression for one channel; the others are then obtained by simple permutations of the momenta.[4] We give the expression for the st channel:

$$\mathcal{A}_{st} = \mathcal{A}|_{w_1'=-\infty, w_2=0, w_1=w, w_2'=1} =$$

$$= \int_0^1 dw \, w^{p_1 \cdot p_2} (1-w)^{p_1 \cdot p_2'} \prod_{a=1}^{J} Z_a^{212'}(\alpha, p, \lambda; w) \prod_{b=1}^{J'} Z_b^{212'}(\beta, p, \lambda'; w), \quad (2.10)$$

where the integrals Z_a^{ijk} are defined in [23] as

$$Z_a^{ijk}(\alpha, p, \lambda; w) \equiv Z_a(\alpha_i, \alpha_j, \alpha_k, p, \lambda; w) \equiv \quad (2.11)$$

$$\equiv \int_{-\infty}^{\infty} dz_a |z_a|^{-\alpha_i} |z_a - w|^{-\alpha_j} |z_a - 1|^{-\alpha_k} \left(\frac{-p_i \cdot \lambda}{-z_a} + \frac{-p_j \cdot \lambda}{w - z_a} + \frac{-p_k \cdot \lambda}{1 - z_a} \right).$$

The other channels are now related to the st channel in the following way:

$$\mathcal{A}_{tu} = \mathcal{A}|_{w_2=-\infty, w_2'=0, w_1=w, w_1'=1} = \mathcal{A}_{st}|_{2 \to 2', 2' \to 1'}, \quad (2.12)$$

$$\mathcal{A}_{us} = \mathcal{A}|_{w_2'=-\infty, w_1'=0, w_1=w, w_2=1} = \mathcal{A}_{st}|_{2 \to 1', 2' \to 2}, \quad (2.13)$$

$$\mathcal{A}_{ts} = \mathcal{A}_{st}|_{2 \longleftrightarrow 2'}, \quad (2.14)$$

$$\mathcal{A}_{ut} = \mathcal{A}_{tu}|_{2' \longleftrightarrow 1'}, \quad (2.15)$$

$$\mathcal{A}_{su} = \mathcal{A}_{us}|_{1' \longleftrightarrow 2}. \quad (2.16)$$

The on-shell condition needed to create HES and HES' is that after the first $j \leq J$ photons have been absorbed, the mass of the intermediate state is $M_j = 2(\sum_{a \leq j} N_a - 1)$. Having

---

[3]The definition is given in the description of kinematics, in eq. (2.27). At this place we do not need the definition of Mandelstam variables, we just want to emphasize that, depending on the permutations of the insertion points on the worldsheet, we get six different channels; for this reason we only give the definitions of s, t, u later in the text, when we have defined all the momenta.

[4]We write the amplitude without Chan-Patton factors so it reduces to the sum of the six cyclic orderings; equivalently, one can imagine Chan-Patton factors of an Abelian U(1) group which reduce to just an overall multiplication of the sum. It would be interesting to consider nontrivial Chan-Patton factors as additional group structure could well further reduce chaos and divide the S-matrix into symmetry sectors. But at the present level of understanding this would be a superfluous complication.

in mind that the total momentum of this intermediate state is $p_2 - \sum_{a \leq j} q$, and using the on-shell condition for tachyons $-p_2^2 = -2$, we obtain:

$$\alpha_2 \to N_a, \beta_2' \to N_b' \tag{2.17}$$

where the second condition comes from HES'. The Z_a^{ijk} integrals can be written in terms of regularized hypergeometric functions $_2\tilde{F}_1(a,b;c;z) \equiv {_2F_1}(a,b;c;z)/\Gamma(c)$. The coefficients of their Taylor expansions are then expressed in terms of gamma functions. This calculation is thoroughly described in [23], the result for the st channel being

$$\mathcal{A}_{st} = \sum_{i_a \in \{2,2'\}} \sum_{j_b \in \{2,2'\}} \sum_{k_a=1}^{N_a} \sum_{l_b=1}^{N_b'} \left(\prod_a^J (p_{i_a} \cdot \lambda) c_{k_a}^{(i_a)} \right) \left(\prod_b^{J'} (p_{j_b} \cdot \lambda') d_{l_b}^{(j_b)} \right) B\left(-1 - \frac{s}{2} + k, -1 - \frac{t}{2} + l\right), \tag{2.18}$$

where $l \equiv \sum_b^{J'} l_b$, $k \equiv \sum_a^J k_a$, the coefficients c and d are defined as:

$$c_k^{(2)} = c_k(\alpha_2 + 1, \alpha_1 + 1, \alpha_2'), \tag{2.19}$$

$$c_k^{(2')} = -c_{k-1}(\alpha_2, \alpha_1, \alpha_2' + 1), \tag{2.20}$$

$$d_l^{(2)} = -c_{l-1}(\beta_2', \beta_1, \beta_2 + 1), \tag{2.21}$$

$$d_l^{(2')} = c_l(\beta_2' + 1, \beta_1 + 1, \beta_2), \tag{2.22}$$

using the function:

$$c_k(\alpha_2, \alpha_1, \alpha_2') = (-1)^{\alpha_2 + k - 1} \frac{\pi}{\sin(\pi \alpha_2)} \frac{\Gamma(\alpha_2 - k + \alpha_1 - 1)\Gamma(\alpha_2' + k)}{\Gamma(\alpha_1)\Gamma(\alpha_2')\Gamma(\alpha_2 - k)\Gamma(k + 1)}, \tag{2.23}$$

and finally the beta function is defined as usual: $B(x,y) \equiv \Gamma(x)\Gamma(y)/\Gamma(x+y)$.

Because of the condition (2.17), the coefficients c and d from eqs. (2.19)–(2.22) diverge as we can see from the factor $\pi/\sin(\pi\alpha_2)$ in eq. (2.23). This divergence is just the expected behavior of the amplitude when one of the internal momenta in the diagram goes on-shell. In order to extract the amplitude of the HES + t $\longrightarrow$ HES' + t' process we thus have to regularize the amplitude. To achieve this we simply omit the divergent factor $\pi/\sin(\pi\alpha_2)$ in the definition (2.23), resulting in a finite expression for the amplitude (except of course for special choices of kinematic variables).[5]

For a generic partition $\sum_{a=1}^J N_a = N$ the number of operations needed to compute the amplitude (2.18) increases rapidly with the partition lengths J and J' due to the increase of the number of sums over k_a and l_b. In addition, the number of states with fixed level N grows exponentially in $\sqrt{N}$. These two effects make the calculation of the S-matrix in the whole subspace of fixed N and fixed kinematic variables computationally demanding, heavily limiting the maximum value of N we can work with and requiring the use of a cluster for larger values of N.

---

[5]This procedure is essentially the same as the one in quantum field theory where one would remove the divergence by multiplying the amplitude by the inverse propagator of the internal on-shell particle.

2.1.1 Kinematics

A look at the expression (2.18) for $\mathcal{A}_{st}$ tells that the kinematics is highly non-unique: there are many momenta and polarizations involved and we have many parameters to choose. We have made no attempt to consider their influence in full detail. We have varied the momenta and the scattering angles (one at a time) over some representative intervals; with some hindsight, we can say that for tachyon scattering only the magnitude of the incoming momentum is crucial. As noted above, p_1 and p'_1 are the momenta of the on-shell tachyons while HES is created from the tachyon with momentum p_2 and a set of J photons with momenta $\{-N_a q\}$ whose polarizations are all equal to λ (similarly for the HES' we have $p'_2, J', \{N'_b\}, q'$ and λ'). The on-shell conditions and the momentum conservation equation now read:

$$p_1^2 = p_2^2 = (p'_1)^2 = (p'_2)^2 = 2, \quad q^2 = q'^2 = 0 \tag{2.24}$$

$$p_1 + (p_2 - Nq) + p'_1 + (p'_2 - Nq') = 0. \tag{2.25}$$

The total mass of HES (and HES') is given by the total occupation number $M = 2(N-1) = 2(N'-1)$, while J and J' represent the total spin of HES and HES' respectively because the photons have identical polarizations. We choose to work in the center-of-mass frame and, as we already mentioned, for simplicity we take the polarizations and photon momenta to satisfy $\lambda = -\lambda'$, $\lambda \cdot \lambda = 0$ and $q' \propto q$. In order to satisfy these conditions we parametrize momenta and polarizations in the following way:

$$q = \frac{1}{\sqrt{2(N-1)+p^2-p\cos\theta}}(-1,0,0,1)^T$$

$$q' = \frac{1}{\sqrt{2(N-1)+p^2-p\cos\theta'}}(1,0,0,-1)^T$$

$$p_1 = \left(\sqrt{p^2-2}, p\sin\theta, 0, p\cos\theta\right)^T$$

$$p'_1 = -\left(\sqrt{p^2-2}, p\sin\theta'\cos\phi', p\sin\theta'\sin\phi', p\cos\theta'\right)^T$$

$$p_2 = \left(\sqrt{2N-2+p^2} - \frac{N}{\sqrt{2N-2+p^2-p\cos\theta}}, -p\sin\theta, 0, -p\cos\theta + \frac{N}{\sqrt{2N-2+p^2-p\cos\theta}}\right)^T$$

$$p'_2 = \left(-\sqrt{2N'-2+p^2} + \frac{N'}{\sqrt{2N'-2+p^2-p\cos\theta'}}, p\sin\theta'\cos\phi', p\sin\theta'\sin\phi',\right.$$

$$\left. p\cos\theta' - \frac{N}{\sqrt{2N-2+p^2-p\cos\theta'}}\right)^T$$

$$\lambda = \frac{1}{\sqrt{2}}(0,1,i,0)^T. \tag{2.26}$$

Defining the Mandelstam variables in terms of momenta:

$$s = -(p_1+p_2-Nq)^2, \quad t = -(p_1+p'_2-N'q')^2, \quad u = -(p_1+p'_1)^2, \tag{2.27}$$

we obtain $p_2 \cdot q = p'_2 \cdot q' = 1$ as required by the on-shell conditions (2.17). Furthermore, the only imaginary contribution to $\mathcal{A}_{st}$ comes from the $(p \cdot \lambda)$ factors which we calculate to

be $p_2' \cdot \lambda' = -\frac{p \sin \theta'}{\sqrt{2}} e^{i\phi'}$. Hence for $\phi' = 0$ the amplitudes calculated from eq. (2.18) will be real. For the collinear kinematics, that is $\theta, \theta' \in \{0, \pi\}$, the amplitude vanishes as can be seen from the fact that λ is orthogonal to all momenta.

From the above, the amplitude is fully characterized by the module of the momentum p, scattering angles θ, θ' and ϕ', and by the partitions of the levels N_a and N_b'. The amplitudes then define the elements of the S-matrix for fixed kinematics $(p, \theta, \theta', \phi')$ in the basis of different partitions of the level N.

2.2 Open HES-photon amplitudes

It will turn out crucial to check also the dynamics of a spinful (non-scalar) state scattering on the HES — some novel aspects of transient chaos will only show up for initial states with spin. We thus consider the HES-photon scattering process (2.2).[6] The DDF construction of HES states proceeds exactly the same way as before, with the same assumptions and conditions on the momenta q, q' and polarizations λ, λ' of DDF photons and the momenta p_2, p_2' of DDF tachyons. The sole difference lies in the states $1, 1'$ which now describe photons with vertex operators V_γ, momenta p_1, p_1' satisfying $p_1^2 = (p_1')^2 = 0$ and polarizations $\xi_1 \equiv \xi, \xi_{1'} \equiv \xi'$ satisfying the gauge invariance condition $\xi \cdot p_1 = \xi' \cdot p_1' = 0$. The amplitude is now

$$\mathcal{A}^\gamma = \frac{1}{\text{Vol}(\text{SL}(2,\mathbb{R}))} \int \mathcal{D}X e^{-S_P} \int \prod_i dw_i V_t(w_i, p_i) \int \prod_K dw_K V_\gamma(w_K, p_K) \times$$

$$\times \prod_{a=1}^{J} dz_a V_p(z_a, -N_a q, \lambda) \prod_{b=1}^{J'} dz_b' V_p(z_b', -N_b' q, \lambda), \tag{2.28}$$

where now $i, j \in \{2, 2'\}$ are DDF tachyons, $K, L \in \{1, 1'\}$ are the physical photons, and the rest of the notation is the same as in eq. (2.7). Writing out the insertions of the vertex operators, we can write the amlitude as

$$\mathcal{A}^\gamma = \frac{1}{\text{Vol}(\text{SL}(2,\mathbb{R}))} \int_{-\infty}^{\infty} \prod_i dw_i \prod_K dw_K \int_{-\infty}^{\infty} \prod_{a=1}^{J} dz_a \int_{-\infty}^{\infty} \prod_{b=1}^{J'} dz_b' \, \mathfrak{a}_I \mathfrak{a}_{II} \mathfrak{a}_{III}, \tag{2.29}$$

where the factors $\mathfrak{a}_{I,II,III}$ denote the tachyon-tachyon, tachyon-photon and photon-photon terms respectively:

$$\mathfrak{a}_I = \prod_{i<j} |w_i - w_j|^{p_i \cdot p_j}$$

$$\mathfrak{a}_{II} = \prod_{i,K} |w_i - w_K|^{p_i \cdot p_K} \sum_i \frac{-p_i \cdot \xi_K}{w_i - w_K} \prod_{i,a} |z_a - w_i|^{-\alpha_i} \sum_i \frac{-p_i \cdot \lambda}{w_i - z_a} \prod_{j,b} |z_b' - w_j|^{-\beta_j} \sum_j \frac{-p_j \cdot \lambda'}{w_j - z_b'}$$

$$\mathfrak{a}_{III} = \prod_{K,a} |z_a - w_K|^{-\alpha_K} \prod_{L,b} |z_b' - w_L|^{-\beta_L} \prod_{K<L} |w_K - w_L|^{p_K \cdot p_L} \times \exp\left[\sum_{K<L} \frac{\xi_K \cdot \xi_L}{2w_{KL}^2} + \right. \tag{2.30}$$

$$\left. \times \sum_{K,a} \left(\frac{-p_a \cdot \xi_K + p_K \cdot \lambda}{w_K - z_a} + \frac{\xi_K \cdot \lambda}{2|w_K - z_a|^2} \right) + \sum_{L,b} \left(\frac{-p_b \cdot \xi_L + p_L \cdot \lambda'}{w_L - z_b'} + \frac{\xi_L \cdot \lambda'}{2|w_L - z_b|^2} \right) \right].$$

---

[6] As we have mentioned, the HES-graviton process is obtained by applying the KLT relations to the HES-photon process.

Here α_i, α_K, β_j, β_L have the same meaning as before (taking into account the definition of i, j, K, L above), and it is understood as usual that we only take the terms in the expansion of the exponent which are linear in every single polarization. The integrals in eq. (2.29) can again be expressed in terms of the same functions Z_a^{ijk} from eq. (2.12), and different permutations of the insertion points on the worldsheet again produce the sum of contributions for various permutations as in eqs. (2.9), (2.12)–(2.16). But now the photon-photon interaction terms, encapsulated in $\mathfrak{a}_{\mathrm{III}}$ from eq. (2.30) cannot in general be avoided: we cannot in general impose the additional conditions on the physical photons $1, 1'$ akin to those for DDF photons as we would not have enough equations to satisfy the momentum conservation. Therefore, many additional terms will appear in the expression for each channel. We again give the expression for $\mathcal{A}_{st}$, understanding that the others are obtained by permutations of the indices $1, 2, 1', 2'$:

$$
\mathcal{A}_{st}^\gamma = \mathcal{A}|_{w_1'=-\infty, w_2=0, w_1=w, w_2'=1} = \int_0^1 dw\, w^{p_1 \cdot p_2}(1-w)^{p_1 \cdot p_2'} \times
$$

$$
\times \Bigg[\left(\frac{p_2 \cdot \xi_1}{w} + \frac{p_2' \cdot \xi_1}{1-w} \right) \prod_{a=1}^{J} Z_a^{212'}(\alpha, p, \lambda; w) \prod_{b=1}^{J'} Z_b^{212'}(\beta, p, \lambda'; w) +
$$

$$
+ (q \cdot \xi_1 - p_1 \cdot \lambda) \prod_{a=1}^{J} Z_a^{212'}(\alpha, p, \lambda; w; -1) \prod_{b=1}^{J'} Z_b^{212'}(\beta, p, \lambda'; w) +
$$

$$
+ (q' \cdot \xi_1 - p_1 \cdot \lambda') \prod_{a=1}^{J} Z_a^{212'}(\alpha, p, \lambda; w) \prod_{b=1}^{J'} Z_b^{212'}(\beta, p, \lambda'; w; -1) +
$$

$$
+ (\xi_1 \cdot \lambda) \prod_{a=1}^{J} Z_a^{212'}(\alpha, p, \lambda; w; -2) \prod_{b=1}^{J'} Z_b^{212'}(\beta, p, \lambda'; w) +
$$

$$
+ (\xi_1 \cdot \lambda') \prod_{a=1}^{J} Z_a^{212'}(\alpha, p, \lambda; w) \prod_{b=1}^{J'} Z_b^{212'}(\beta, p, \lambda'; w; -2) \Bigg]. \tag{2.31}
$$

Here we introduce the notation $Z_a^{212'}(\alpha, p, \lambda; w; -\sigma)$ with σ a positive integer. This is defined as

$$
Z_a^{iKj}(\alpha, p, \lambda; w; -\sigma) \equiv Z_a(\alpha_i - \sigma, \alpha_K, \alpha_j, p, \lambda; w) + Z_a(\alpha_i, \alpha_K, \alpha_j - \sigma, p, \lambda; w). \tag{2.32}
$$

In other words, the argument $-\sigma$ means we sum over the values of the original Z_a^{iKj} as defined in eq. (2.12) with the arguments α_i, α_j being reduced by σ one at a time. Notice that we do not include the function with $\alpha_K - \sigma$ in the sum in (2.32), i.e. we only reduce the α's corresponding to DDF tachyons, not physical photons. The outcome is that the photon amplitude $\mathcal{A}_{st}^\gamma$ consists of the same building blocks as the tachyon amplitude $\mathcal{A}_{st}$ given in eqs. (2.10), (2.18) but with different coefficients and arguments of the gamma and beta functions. Writing out in full the expression (2.31) we obtain:

$$
\mathcal{A}_{st}^\gamma = \sum_{i_a \in \{2, 2'\}} \sum_{K_b \in \{2, 2'\}} \sum_{k_a=1}^{N_a} \sum_{l_b=1}^{N_b'} \left(\mathfrak{b}_0 + \mathfrak{b}_{-1} + \mathfrak{b}_{-1}' + \mathfrak{b}_{-2} + \mathfrak{b}_{-2}' \right). \tag{2.33}
$$

Note that the terms $\mathfrak{b}_{0,-1,-2}$ and $\mathfrak{b}'_{-1,-2}$ are not related in any simple way to $\mathfrak{a}_{\text{I,II,III}}$ from eqs. (2.30). They are defined as:

$$\mathfrak{b}_0 = \left(\prod_a^J (p_{i_a}\cdot\lambda)c_{k_a}^{(i_a)}\right)\left(\prod_b^{J'}(p_{K_b}\cdot\lambda')d_{l_b}^{(K_b)}\right)\left[(p_{i_a}\cdot\xi_{K_b})B\left(-2-\frac{s}{2}+k,-1-\frac{t}{2}+l\right)+\right.$$

$$\left.+(p_{i_a}\cdot\xi_{K_b})B\left(-1-\frac{s}{2}+k,-2-\frac{t}{2}+l\right)\right] \tag{2.34}$$

$$\mathfrak{b}_{-1} = (q\cdot\xi_{K_b}-p_{i_a}\cdot\lambda)\left[\left(\prod_a^J (p_{i_a}\cdot\lambda)\bar{c}_{k_a}^{('i_a)}\right)\left(\prod_b^{J'}(p_{K_b}\cdot\lambda')d_{l_b}^{(K_b)}\right)B\left(-1-\frac{s}{2}+k,-2-\frac{t}{2}+l\right)+\right.$$

$$\left.+\left(\prod_a^J (p_{i_a}\cdot\lambda)\bar{c}_{k_a}^{('''i_a)}\right)\left(\prod_b^{J'}(p_{K_b}\cdot\lambda')d_{l_b}^{(K_b)}\right)B\left(-2-\frac{s}{2}+k,-1-\frac{t}{2}+l\right)\right] \tag{2.35}$$

$$\mathfrak{b}'_{-1} = (q'\cdot\xi_{K_b}-p_{i_a}\cdot\lambda')\left(\prod_a^J (p_{i_a}\cdot\lambda)c_{k_a}^{(i_a)}\right)\left(\prod_b^{J'}(p_{K_b}\cdot\lambda')\bar{d}_{l_b}^{(''K_b)}\right)B\left(-1-\frac{s}{2}+k,-1-\frac{t}{2}+l\right) \tag{2.36}$$

$$\mathfrak{b}_{-2} = (\xi_{K_b}\cdot\lambda)\left[\left(\prod_a^J (p_{i_a}\cdot\lambda)\bar{\bar{c}}_{k_a}^{('i_a)}\right)\left(\prod_b^{J'}(p_{K_b}\cdot\lambda')d_{l_b}^{(K_b)}\right)B\left(-1-\frac{s}{2}+k,-3-\frac{t}{2}+l\right)+\right.$$

$$\left.+\left(\prod_a^J (p_{i_a}\cdot\lambda)\bar{\bar{c}}_{k_a}^{('''i_a)}\right)\left(\prod_b^{J'}(p_{K_b}\cdot\lambda')d_{l_b}^{(K_b)}\right)B\left(-3-\frac{s}{2}+k,-1-\frac{t}{2}+l\right)\right] \tag{2.37}$$

$$\mathfrak{b}'_{-2} = (\xi_{K_b}\cdot\lambda')\left(\prod_a^J (p_{i_a}\cdot\lambda)c_{k_a}^{(i_a)}\right)\left(\prod_b^{J'}(p_{K_b}\cdot\lambda')\bar{\bar{d}}_{l_b}^{(''K_b)}\right)B\left(-2-\frac{s}{2}+k,-2-\frac{t}{2}+l\right). \tag{2.38}$$

The coefficients $c_k^{(i)}$, $d_l^{(K)}$ and the function $c_k(\alpha_i,\alpha_K,\alpha_j)$ have the same meaning as in eqs. (2.19)–(2.23). The newly introduced coefficients are defined as:

$$\bar{c}_k^{('2)} = c_k(\alpha_2,\alpha_1+1,\alpha'_2), \qquad\qquad \bar{c}_k^{('''2)} = c_k(\alpha_2+1,\alpha_1+1,\alpha'_2-1), \tag{2.39}$$

$$\bar{c}_k^{('2')} = -c_{k-1}(\alpha_2-1,\alpha_1,\alpha'_2+1), \qquad \bar{c}_k^{('''2')} = -c_{k-1}(\alpha_2,\alpha_1,\alpha'_2), \tag{2.40}$$

$$\bar{d}_l^{('' 2)} = -c_{l-1}(\beta'_2,\beta_1-1,\beta_2+1), \tag{2.41}$$

$$\bar{d}_l^{('' 2')} = c_l(\beta'_2+1,\beta_1,\beta_2) \tag{2.42}$$

and analogously for the two-bar coefficients:

$$\bar{\bar{c}}_k^{('2)} = c_k(\alpha_2-1,\alpha_1+1,\alpha'_2), \qquad\qquad \bar{\bar{c}}_k^{('''2)} = c_k(\alpha_2+1,\alpha_1+1,\alpha'_2-2), \tag{2.43}$$

$$\bar{\bar{c}}_k^{('2')} = -c_{k-1}(\alpha_2-2,\alpha_1,\alpha'_2+1), \qquad \bar{\bar{c}}_k^{('''2')} = -c_{k-1}(\alpha_2,\alpha_1,\alpha'_2-1), \tag{2.44}$$

$$\bar{\bar{d}}_l^{('' 2)} = -c_{l-1}(\beta'_2,\beta_1-2,\beta_2+1), \tag{2.45}$$

$$\bar{\bar{d}}_l^{('' 2')} = c_l(\beta'_2+1,\beta_1-1,\beta_2). \tag{2.46}$$

In other words, the number of bars (one or two) corresponds to the value of σ in the function $Z_a^{iKj}(\alpha,p,\lambda;w;-\sigma)$ in eq. (2.32), and the additional superscript $'$, $''$ or $'''$ means we should subtract σ from the first, second or third argument of the function $c_k(\alpha_i,\alpha_K,\alpha_j)$ from eq. (2.23).

Finally, we should define the kinematics. We minimally modify the setup for the HES-tachyon process in the subsubsection 2.1.1. Energy and momentum conservation now read

$$p_2^2 = (p_2')^2 = 2, \quad p_1^2 = (p_1')^2 = q^2 = q'^2 = 0 \tag{2.47}$$

$$p_1 + (p_2 - Nq) + p_1' + (p_2' - Nq') = 0. \tag{2.48}$$

The momenta and polarizations of the physical photons are now given by

$$p_1 = (p, p\sin\theta, 0, p\cos\theta)^T$$
$$p_1' = -(p, p\sin\theta'\cos\phi', p\sin\theta'\sin\phi', p\cos\theta')^T \tag{2.49}$$
$$\xi_1 \equiv \xi = (0, \cos\theta, 0, -\sin\theta)^T$$
$$\xi_1' \equiv \xi' = (0, -\cos\theta', 0, \sin\theta'\cos\phi'), \tag{2.50}$$

whereas all the other momenta are the same as for the HES-tachyon scattering, as given in eq. (2.50). The simplifications which eliminate the interaction terms among the DDF photons are still in place. For the physical photons they are absent (indeed, it seems the number of free parameters is insufficient to require $\xi' \propto \xi$ after implementing the conservation laws) therefore we indeed have photon-photon terms in the amplitudes as we found in eqs. (2.30)–(2.38).

2.3 Closed string amplitudes

In the previous section we have described the HES-tachyon scattering for open (bosonic) HES. This process already shows interesting physics as we will see, however to make closer contact with black holes or with the results on classical string scattering in the literature [38–40], we should also consider closed string amplitudes. This can be achieved in a similar way as for the open case, making use of the DDF operators. But at tree level we can circumvent this calculation by employing the celebrated KLT relations [33–35]. To remind, the idea behind the KLT relations is that a closed string amplitude can be constructed from two open string amplitudes coupled by a momentum-dependent kernel.[7] Schematically, an M-point closed string amplitude $\mathcal{A}_{\text{closed}}^M$ is given by:

$$\mathcal{A}_{\text{closed}}^M \propto \sum_{P,P'} \mathcal{A}(P)_{\text{open}}^M \bar{\mathcal{A}}(P')_{\text{open}}^M e^{iF(P,P')} \tag{2.51}$$

where P and P' denote the permutations of the M external legs, $\mathcal{A}(P)_{\text{open}}^M$ is the ordered M-point open string amplitude and F is a phase determined by the kinematics. In the case of interest for us, that is for the four-leg $(2 \to 2)$ scattering, the KLT relation becomes particularly simple:

$$\zeta_{\mu_1\dots\mu_4,\nu_1\dots\nu_4}\mathcal{A}_{\text{closed}}^{\mu_1\dots\mu_4,\nu_1\dots\nu_4} = -\pi\sin(\pi p_2\cdot p_1')\xi_{\mu_1\dots\mu_4}\mathcal{A}_{\text{open}}^{\mu_1\dots\mu_4}(s,t)\xi'_{\nu_1\dots\nu_4}\mathcal{A}'^{\nu_1\dots\nu_4}_{\text{open}}(t,u). \tag{2.52}$$

This enables us to construct the closed string S-matrix as a direct product of the st and tu contributions to the open string S-matrix. If we consider fixed kinematics and vary the partitions, the direct product structure changes the dimensions of the S-matrix from

---

[7]The connection between open and closed tree-level amplitudes can be seen from the fact that the closed string propagator can be constructed by joining the two open string propagators.

$p(N) \times p(N)$ for open to $p(N)^2 \times p(N)^2$ for closed strings, which is a big enhancement in size having in mind the fast growth of the number of partitions $p(N)$ with N. In this way we obtain the closed HES-tachyon and the closed HES-graviton processes of eqs. (2.3), (2.4) from the open HES processes of eqs. (2.1), (2.2) respectively.

For our main interest — inspecting the eigenphase statistics and chaos of the S-matrix — the KLT method may be potentially risky as it yields the closed string amplitudes in the uncorrelated basis, i.e. the closed string states are expressed in terms of direct products of open-string states $|\vec{n}\rangle \otimes |\vec{\tilde{m}}\rangle$ projected to the subspace satisfying $N = \tilde{N}$, i.e. $\sum_a n_a = \sum_b \tilde{m}_b$. In this basis the symmetry between the left- and right-moving modes is not manifest so even and odd states under this symmetry are dumped together. It is known that expressing the Hamiltonian/S-matrix in a basis which is not adapted to the symmetries of the system can invalidate the results in the sense that Wigner-Dyson statistics does not show up even if the system is in fact RMT chaotic. We have thus checked our results for small occupation numbers $N \le 6$ against numerically computed S-matrices in the even and odd sector separately (obtained by performing the worldsheet integrals via a grid method). We find no discrepancy between the resulting eigenphase statistics, however for larger N we were unable to perform this test as the numerical integration becomes unfeasible. Nevertheless, we consistently find equal or stronger chaos for closed than for open HES, meaning that there is no artifical reduction of chaos because the spectrum unfolding is not performed.[8]

3 The structure of the S-matrix

Our basic object is the S-matrix for the processes (2.1)–(2.2) involving two HES states and the two tachyons or two photons. Because of the complexity of the expressions for the amplitudes, in particular the photon amplitude $\mathcal{A}^\gamma$, the computation time grows rapidly, limiting the laptop calculations to $N \le 12$.[9] We first calculate the amplitudes for fixed kinematics and all possible partitions specifying the two HES states and from these we obtain the S-matrix on the subspace of fixed kinematics (which we call simply the S-matrix).

3.1 The partition basis

The S-matrix is characterized by its eigenvalues and eigenvectors. Being unitary, it has eigenvalues on the unit circle, and of particular relevance for the RMT statistics are the eigenphases, i.e. the phases of the eigenvalues. The natural basis for the analysis of eigenvectors at HES level N is the basis of partitions $\{\mathcal{P}\}$, i.e. the sets of K numbers $\{n_1, \ldots n_K\}$ with

---

[8]According to [25], testing the spacing ratios instead of spacings themselves is also helpful in such situations the ratios r and R are less sensitive to folding/unfolding of the spectrum, and in our case again they give similar results as the Wigner-Dyson fits themselves.

[9]In [16, 21, 24, 26] much larger N values were considered, however the calculations in these papers were performed for the three-leg and four-leg processes including one HES state rather than two (IN and OUT) as in our case, and only for a subset of amplitudes, not for the whole S-matrix. In [23] the $2 \to 2$ process was considered as in our eq. (2.1) but again only for individual amplitudes, considering $N \le 27$. Essentially, calculating individual amplitudes instead of the S-matrix allows one to go to much higher levels. In [32], where the whole S-matrix was calculated, the calculations was limited to modest values of N just as in our case.

$\sum_{k=1}^{K} n_k = N$ and K the highest nonzero occupation number. The dimension of the Hilbert space is the total number of partitions of N denoted by $p(N)$.[10]

We define the *partition length* $|\mathcal{P}|$ as the *total number of nonzero occupation numbers* n_k in the partition (obviously between 1 and $\min(N, K)$):[11]

$$\forall \, \mathcal{P} = \{n_1, \dots n_K\} \text{ with } \sum_{k=1}^{K} n_k = N, \; K = \max j|_{n_j > 0}: \quad |\mathcal{P}| \equiv \sum_j \Theta(n_j). \quad (3.1)$$

In the above $\Theta(n_j)$ is the Heaviside unit step: $\Theta(n_j) = 1$ for $n_j > 0$ and $\Theta(n_j) = 0$ otherwise. Now we can order all possible partitions according to partition lengths $|\mathcal{P}|$, from 1 (the shortest partitions, of length 1) to N (the longest partitions, of length N); when several partitions have the same length their relative order is chosen arbitrarily. A more widespread way to characterize the size of the partition is the partition rank, defined as $m(\mathcal{P}_N) = \max n_j|_{n_j > 0} - |\mathcal{P}|$. While the rank lies between $-(N-1)$ and $N-1$, the length is between 1 and N and is thus more convenient for our purposes as we will also consider the logarithms of the lengths.

A general eigenvector of the S-matrix is some linear combination of various partitions $\sum_{j=1}^{p(N)} c_j |\mathcal{P}_j\rangle$. We will argue that the distribution of the coefficients c_j as a function of j is a useful quantity when analyzing the scattering, in particular the relative contribution (i.e. the absolute value of the coefficients $|c_j|$) of short versus long partitions.

3.2 Tests of the RMT statistics

Once we have the eigenvalues (and eigenvectors), we can apply the textbook tests of quantum chaos by comparing the eigenvalue statistics with the predictions for Gaussian random ensembles. As we mentioned in the Introduction, the RMT theory of chaotic scattering essentially replaces the eigenvalue spacings of the Hamiltonian in a closed system by the eigenphase spacings of the scattering matrix [31]. To remind, eigenphase spacing is the difference between the phases of two neighboring eigenvalues:

$$s_n \equiv \frac{\arg \lambda_{n+1} - \arg \lambda_n}{\bar{s}}, \quad (3.2)$$

where $\bar{s}$ is the average value of the spacings for the whole S-matrix, and λ_n are the eigenvalues ordered according to their phases, i.e. $\arg \lambda_1 > \arg \lambda_2 > \dots > \arg \lambda_{p(\mathcal{N})}$ (or $\lambda_{p(\mathcal{N})^2}$ for the closed string). Therefore, *if the scattering is chaotic in the RMT sense*, then the distribution of normalized spacings s obeys the Wigner-Dyson distribution:

$$P_\beta(s) = A_\beta s^\beta e^{-B_\beta s^2}, \quad (3.3)$$

---

[10]As we know, this number grows exponentially as $p(N) \sim \exp\left(\sqrt{N}\right)$.

[11]One might be confused that we denote partition elements, i.e. occupation numbers by n_k whereas the DDF photon momenta were previously denoted by $N_k q$, where again N_k are the elements of the partition. The reason is that $n_k = N_k$ only for *open* strings. A closed string in the state $|n_k, \tilde{n}_k\rangle$ will have a different momentum, i.e. different N_k even though the partition elements are the same. For this reason we keep the notation separate.

where $\beta = 1, 2, 4$ for orthogonal (GOE), unitary (GUE) or symplectic (GSE) ensemble, respectively, and the constants A_β and B_β read

$$A_1 = \frac{\pi}{2}, \qquad\qquad B_1 = \frac{\pi}{4} \qquad\qquad (3.4)$$

$$A_2 = \frac{8}{\pi}, \qquad\qquad B_2 = \frac{4}{\pi} \qquad\qquad (3.5)$$

$$A_4 = \left(\frac{64}{9\pi}\right)^3, \qquad\qquad B_4 = \frac{64}{9\pi}. \qquad\qquad (3.6)$$

$$(3.7)$$

As we know, the three classes are determined by the properties under the time-reversal symmetry [27] — GOE describes time-reversal-invariant systems with "conventional time reversal operator", squaring to 1; GSE describes time-reversal-invariant systems with Krammers degeneracy where time reversal squares to -1; GUE describes systems which break time-reversal invariance. Our process is time-reversal invariant and the strings are bosonic hence there cannot be any Krammers degeneracy. We thus expect the GOE statistics, with $\beta = 1$. For purposes of checking the Wigner-Dyson statistics however we have tried fits with different β values and we have also tried fitting the eigenphase spacing distribution with β as a free fitting parameter. Finally, a regular scattering process can be written as a collection of independent channels, leading to the Poisson distribution of eigenphase spacings: $P_0(s) = \exp(-s)$. The crucial physical difference between the two is that the Wigner-Dyson distribution encapsulates eigenstate repulsion - one always has $P_\beta(s = 0) = 0$ and there is no clustering. The Poisson distribution, on the contrary, always has $P_0(s = 0) = 1$ and always leads to clustering of levels.

We will find that our S-matrices are typically not Gaussian random and certainly not Poissonian, but can — in the simplest picture — be thought of as being generated from a mixed ensemble with both Gaussian random matrices and integrable matrices. Therefore, it will make sense to consider the distribution

$$P_c(s) \equiv w_P P_0(s) + (1 - w_P) P_\beta(s). \qquad\qquad (3.8)$$

Importantly, while both the Wigner-Dyson and the Poison form follow from rigorous derivations, the above linear combination is purely phenomenological — there is no guarantee that a system with mixed (regular-chaotic) dynamics will indeed have eq. (3.8) for the eigenphase spacing distribution. We will use the size of w_P, i.e. the relative contribution of the Poisson contribution, as a rough indicator of non-chaoticity but it is not simply related to any physical quantity.

One important caveat concerning the Wigner-Dyson test is that the eigenstates with additional discrete symmetries that do not commute with time reversal can introduce novel behavior, leading to the Altland-Zirnbauer tenfold way instead of the Dyson threefold way [41]. In our case however there are no obvious additional symmetries that behave nontrivially under time reversal, so the threefold way of eqs. (3.4)–(3.6) remains valid.

Another measure of chaos which is perhaps more robust is the eigenspacing *ratio*, which considers the ratio of the spacings between two neighboring pairs of eigenphases, i.e. between

two neighboring spacings:

$$r_n \equiv \frac{s_n}{s_{n-1}} = \frac{\arg \lambda_{n+1} - \arg \lambda_n}{\arg \lambda_n - \arg \lambda_{n-1}}. \tag{3.9}$$

Another possibility is to consider normalized ratios, defined as $R_n = \min(r_n, 1/r_n)$. This chaos diagnostic was proposed in [42] and applied to field-theoretical systems in [43] and finally to HES scattering amplitudes in [24, 26]. Its appeal lies in the fact that the normalization cancels out hence this quantity is more robust to numerical fluctuations; in addition, it is argued in [26] to be less sensitive to the mixing of states with different symmetries. One can study the distributions $P(r)$, $P(R)$ or just the mean values $\langle r \rangle$, $\langle R \rangle$; the latter we find more useful as it gives robust and concise information within just a single number.

A few words about the calculations are in order. For smaller excitation numbers $N \leq 12$ it is easy to compute the S-matrix on a laptop in Wolfram Mathematica. For larger N we perform the calculations on a cluster, and in addition we use approximate interpolation formulas for beta and gamma functions to speed up the calculation, sacrificing some accuracy. Still, when computing the whole S-matrix, we cannot go further than $N \approx 30$. This is an inherent difficulty when working with the S-matrix instead of just the amplitudes: the matrix becomes huge.

Now we are ready to study the properties considered in this section — the structure of the S-matrix and its eigenvectors, and the eigenvalue statistics — for the S-matrices of the HES-tachyon, HES-photon and HES-graviton scattering.

4 S-matrix analysis of HES scattering processes

In this section we present numerical results on the S-matrix involving the HES states for the setting described in the previous section. We start with the open string and then move to discuss the physically more relevant closed string. Afterwards we provide some *a posteriori* analytic arguments explaining the numerical findings.

4.1 The HES-tachyon S-matrix

4.1.1 The eigenphase statistics

The first test that gives an idea on the degree of chaos in the S-matrix is the fit of the Wigner-Dyson distribution to the histogram of eigenphase spacings. Computing the S-matrix, diagonalizing it and producing the histogram of the differences of the eigenphases normalized by the mean of this difference, we typically obtain a picture such as figure 2. We give the fit for both open and closed strings (panels (A) and (B) respectively), with the expected GOE ensemble value $\beta = 1$, and with the GUE ensemble with $\beta = 2$; we do not give the fit with $\beta = 4$ as this case gives far worse fit quality (and is physically untenable in a bosonic system). The agreement with the RMT statistics is not impressive: in some cases (mainly $p = 16.1$ for open strings and $p = 4.1, 8.1$ for closed strings) the agreement is decent but far from perfect. For other momenta, in particular for large momenta in the closed HES case, the disagreement is drastic. Indeed, at large momenta many eigenvalues coalesce and the spacings cluster at $s = 0$.
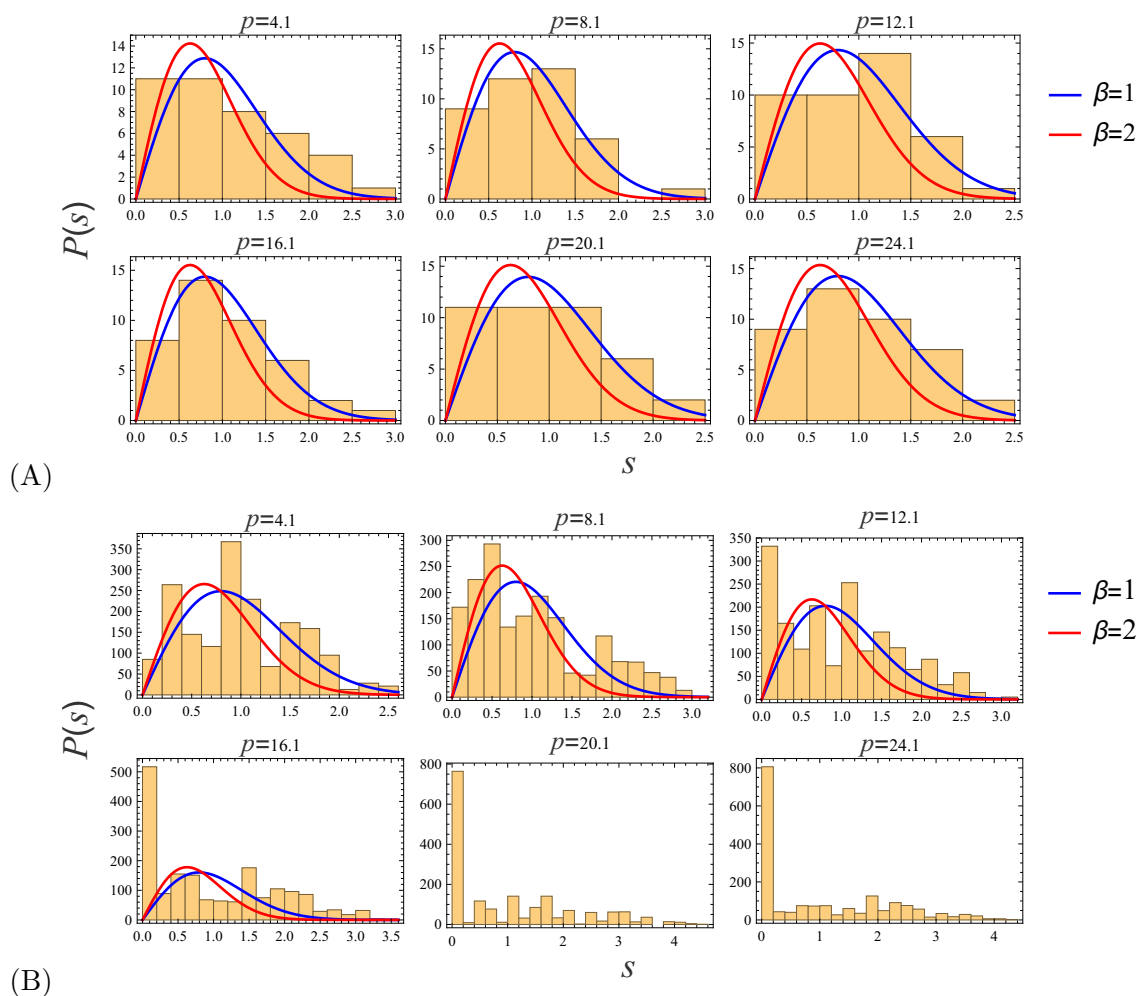
Figure 2. Normalized eigenphase spacing distribution for six momentum values $p = 4.1, 8.1, 12.1, 16.1, 20.1, 24.1$, with $N = 10$, $\theta = 0.23$, $\theta' = 0.5$ and $\phi' = 0.7$, for open (A) and closed (B) HES. The blue and red lines represent the best fits to the Wigner-Dyson distribution (eq. (3.3)) with $\beta = 1$ (eq. (3.4)) and $\beta = 2$ (eq. (3.5)) respectively; the former corresponds to GOE, expected from the time-reversal symmetry and the latter to GUE, for time-reversal-breaking systems. While the overall shape of the distribution is close to the Wigner-Dyson function for intermediate momenta (roughly $p = 16.1$ in (A) and $p = 8.1$ in (B)), the presence of near-zero spacings clearly excludes pure RMT statistics. For the closed string there is strong clustering of levels at large momentum values; for that reason we do not give the fit to Wigner-Dyson distributions for the closed string for $p = 20.1$ and $p = 24.1$.

The natural conclusion is that dynamics is mixed, consisting of contributions from both Poisson and Wigner-Dyson distribution. Of course, for $N = 10$, the value used in figure 2, the set of spacings available for an open string is rather small, so the outcome may well be influenced by finite-size fluctuations. But the closed string already has a much larger S-matrix (of size $p(N)^2 \times p(N)^2$ instead of $p(N) \times p(N)$) and significant finite-size effects seem unlikely.

The hypothesis of two-component dynamics (regular and chaotic) is checked by fitting the combination of the two distribution functions (eq. (3.8)). The relevant quantity now is w_P, the contribution of the Poisson distribution, which is expected to be minimal when
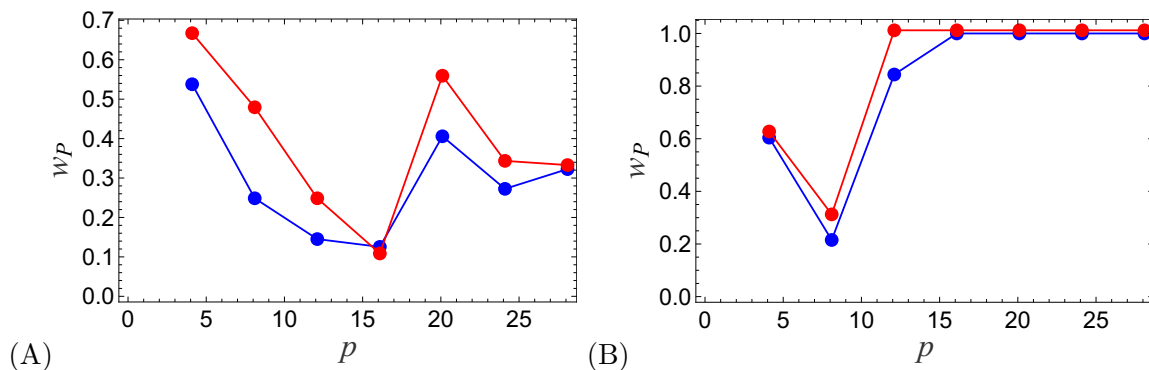
Figure 3. The relative contribution of the Poisson distribution w_P when fitting the Poisson-Wigner-Dyson combination to the histogram of eigenphase spacings as a function of momentum, for the same values of momenta and angles as in figure 2, for open (A) and closed (B) string. The smallest regular component, i.e. the smallest Poisson ratio w_P ($0 \leq w_P \leq 1$) is found for $p \approx 16.1$ (A) and $p \approx 8.1$ (B), roughly the same values which yield the nicest fit to the Wigner-Dyson distribution in figure 2. For large momenta we again see that the closed string becomes completely regular, with strong clustering of eigenphases. We fit the Poisson+Wigner-Dyson distribution both with $\beta = 1$ (blue) and $\beta = 2$ (red). The GOE value $\beta = 1$ gives somewhat better plots as we expect. The full lines are just to guide the eye.

chaos is the strongest. Its dependence on the momentum p is given in figure 3. Here and in most other figures throughout the paper we perform the fit both with $\beta = 1$ and $\beta = 2$ but in general the former value, corresponding to GOE and time-reversal invariance agrees better with the data as it should be.

Another way to characterize the proximity to the RMT-like chaotic behavior is the average spacing ratio $\langle r \rangle$ defined in eq. (3.9), or its normalized variant $\langle R \rangle$. We find it particularly convenient when studying the behavior of the S-matrix for increasing excitation number N. We have tentatively found that the scattering shows clear signs of chaos only for certain values of momentum, which we dub the crossover momentum p_c for reasons that will soon become clear. Now we fix this value ($p_c = 8.1$ for the open string and $p_c = 16.1$ for the closed string) and vary the total excitation number N (figure 4). Computing $\langle r \rangle$ (A) and $\langle R \rangle$ (B) for each N value at $p = p_c$ we find that already for $N \gtrsim 9$ the values are very close to the predicted outcome for the time-reversal-invariant GOE random matrix ensemble (black dashed line in figure 4). This suggests that indeed in a small interval of momenta around p_c the S-matrix shows clear signs of chaos which stay stable for large N (in accordance with the string/black hole complementarity and the fast scrambling of black holes, if there is strong chaos then indeed it has to remain strong (or become stronger and stronger) as N grows). Still, a more refined measure such as the fit to the Wigner-Dyson distribution or its combination with the Poisson distribution (figures 2, 3) reveals that even at p_c some non-chaoticity remains. Therefore, rather than a sharp strongly chaotic point it is a smeared crossover region where chaos becomes strong but still non-uniform. Now we will try to understand the nature of this crossover.
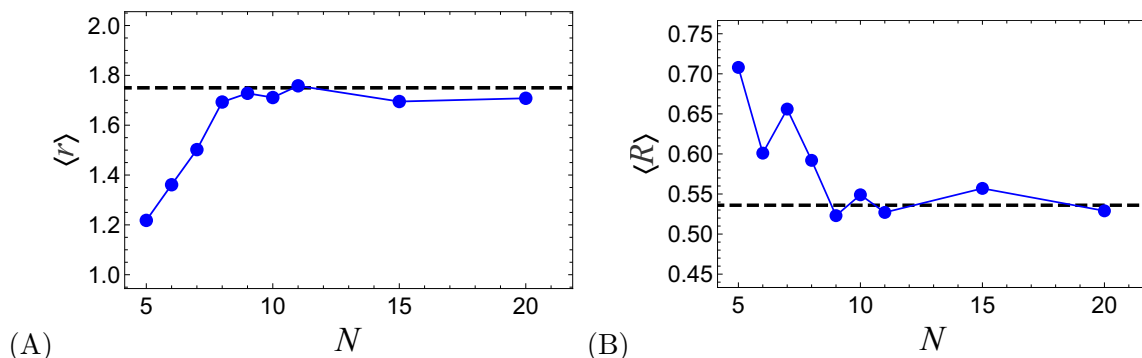
Figure 4. The non-normalized (A) and normalized (B) average spacing ratio at the crossover momentum $p_c = 16.1$ for the closed HES-tachyon scattering at different excitation levels N of the HES; the kinematic parameters are the same as in figures 2 and 4. For growing N the spacing ratios stay firmly around the values $\langle r \rangle = 1.75$ (A) and $\langle R \rangle = 0.536$ (B) predicted for the GOE random matrix dynamics (black dashed reference lines). The spacing ratio indicates stronger chaos at $p \approx p_c$ than the fits to the Wigner-Dyson distribution, which even around p_c show visible discrepancies.

4.1.2 The crossover

We now invoke the partition basis described in the subsection 3.1 and the notion of partition length from eq. (3.1). Finding the coordinates $c_k^{(n)}$ ($1 \leq k \leq p(N)$ for open HES and $1 \leq k \leq p(N)^2$ for closed HES) of the n-th S-matrix eigenvector $|n\rangle$ in the partition basis, we can speak of the relative contribution of short vs. long partitions to the eigenvector (large $c_k^{(n)}$ for small/large k implies dominant contribution of short/long partitions). One detail is still arbitrary: the ordering of the eigenvectors themselves, i.e. the number $n = 1, \ldots p(N)$ ($n = 1, \ldots p(N)^2$ for closed strings) in $c_k^{(n)}$ as defined above. We opt to order the eigenvectors according to the absolute value of the real part of their eigenvalues: thus $|1\rangle$ is the "leading" eigenvector, which contributes most to the OUT state after the scattering, and $|p(N)\rangle$ ($|p(N)^2\rangle$ for closed strings) is the "least important" eigenvector, which contributes the least.

In figure 5, we plot the set of coordinates $c_k^{(n)}$ for three eigenvectors, for a number of S-matrices with different momenta and fixed angles θ, θ' and ϕ'. We find that short partitions dominantly contribute to the leading eigenvector (the one with the largest eigenvalue) at small momenta p, while for large momenta long partitions dominate. The crossover from the domination of short partitions to the domination of long partitions happens just around the momentum where chaos is maximal, which we have denoted by p_c in the previous subsection: at $p \approx p_c$ partitions of all lengths contribute equally. We find that p_c slightly decreases with increasing ϕ' but overall is almost insensitive to the kinematics (for the tachyonic case that we consider here).

The fact that at large energies (and momenta) long partitions dominantly contribute to the dynamics is also seen from the plot of absolute values of the S-matrix elements in figure 6 (remember the rows of the matrix are nothing but the eigenvectors in the partition basis): the largest matrix element migrates from upper left corner (processes scattering short states into short states) to upper right corner (short-to-long processes) to bottom right corner

(long-to-long processes).[12] This can be roughly understood in a simple way: for $p \ll p_c$ there is not enough energy to activate most modes so only a few modes contribute (and they must have large occupation numbers n_k in order to have the total excitation number N); for $p \gg p_c$ the kinetic energy is much larger than the interaction energy scale thus all the modes are excited (and they must have mostly small occupation numbers so as not to overshoot the total occupation N). For $p \sim p_c$ these two factors balance each other and the dominant eigenvectors consist of partitions of all lengths.

Now why is the chaos clearly visible precisely around these crossover momenta p_c? For small energies only a few states effectively participate in the scattering dynamics hence it cannot be very complex. As we increase the energy more and more modes are activated providing more channels for the interaction, forming a complex structure through which chaotic behavior may develop. But at very high energies there is "less time" for the interaction to occur, the strings just "fly away from each other", which results in the suppression of the chaotic behavior.[13]

We further support the above reasoning by calculating the Shannon information entropy associated with the S-matrix. As we know, the Shannon entropy is defined as $\mathcal{S} = \sum_j p_j \log p_j$ for some classical probabilistic system with probability p_j assigned to each state j. The usual quantum-mechanical analogue is the von Neumann entropy, defined in terms of the density matrix ρ as $\mathrm{Tr}\,\rho \log \rho$. Since we have a quanutm scattering process, one should in principle speak of von Neumann rather than Shannon entropy. However, we work with the S-matrix and do not have the density matrix so defining the von Neumann entropy the canonical way would be tricky. We can introduce a phenomenological measure of entropy or complexity for a single amplitude from the IN state $|\vec{n}\rangle$ to the OUT state $|\vec{m}\rangle$ simply as:

$$C\left(|\vec{n}\rangle \to |\vec{m}\rangle\right) = \mathrm{Re}\,\left[\mathcal{A}_{|\vec{n}\rangle \to |\vec{m}\rangle} \log \mathcal{A}_{|\vec{n}\rangle \to |\vec{m}\rangle}\right]. \tag{4.1}$$

Taking the real part is necessary as amplitudes are in general neither real nor positive. For the whole scattering matrix, the natural choice is to sum the definition (4.1) for all amplitudes, or equivalently to take the trace of the expression over the whole S-matrix. But in the eigenbasis the S-matrix becomes diagonal, with elements $\mathcal{N} \exp(i\phi_k)$, where ϕ_k is the eigenphase of the state k and $\mathcal{N}$ is some overall normalization constant, which is irrelevant for our purposes. Therefore we can write

$$C(S) = \mathrm{Re}\,\mathrm{Tr}\,S \log S = -\sum_k \phi_k \sin \phi_k, \tag{4.2}$$

where the sum goes from $k = 1$ to $k = p(N)$ for open strings and from $k = 1$ to $k = p(N)^2$ for closed strings.[14] As the S-matrix becomes chaotic, we expect the information entropy to

---

[12]This was also seen and discussed in the recent paper [32].

[13]This situation is analogous to classical scattering, where likewise at low energies the skeleton of periodic orbits (which defines the symbolic dynamics) is quite simple as most orbits see just a near-harmonic potential well, at high energies most orbits barely feel the scattering potential and continue to infinity almost undisturbed, and at intermediate energies the competition between the bounded and unbounded dynamics generates sensitivity to initial conditions and chaos.

[14]For $N \to \infty$ the index of the state becomes continuous and we get the differential entropy, the well-known generalization of the Shannon entropy for continuous distributions. This limit is important for the string/BH complementarity but we leave it for further work.
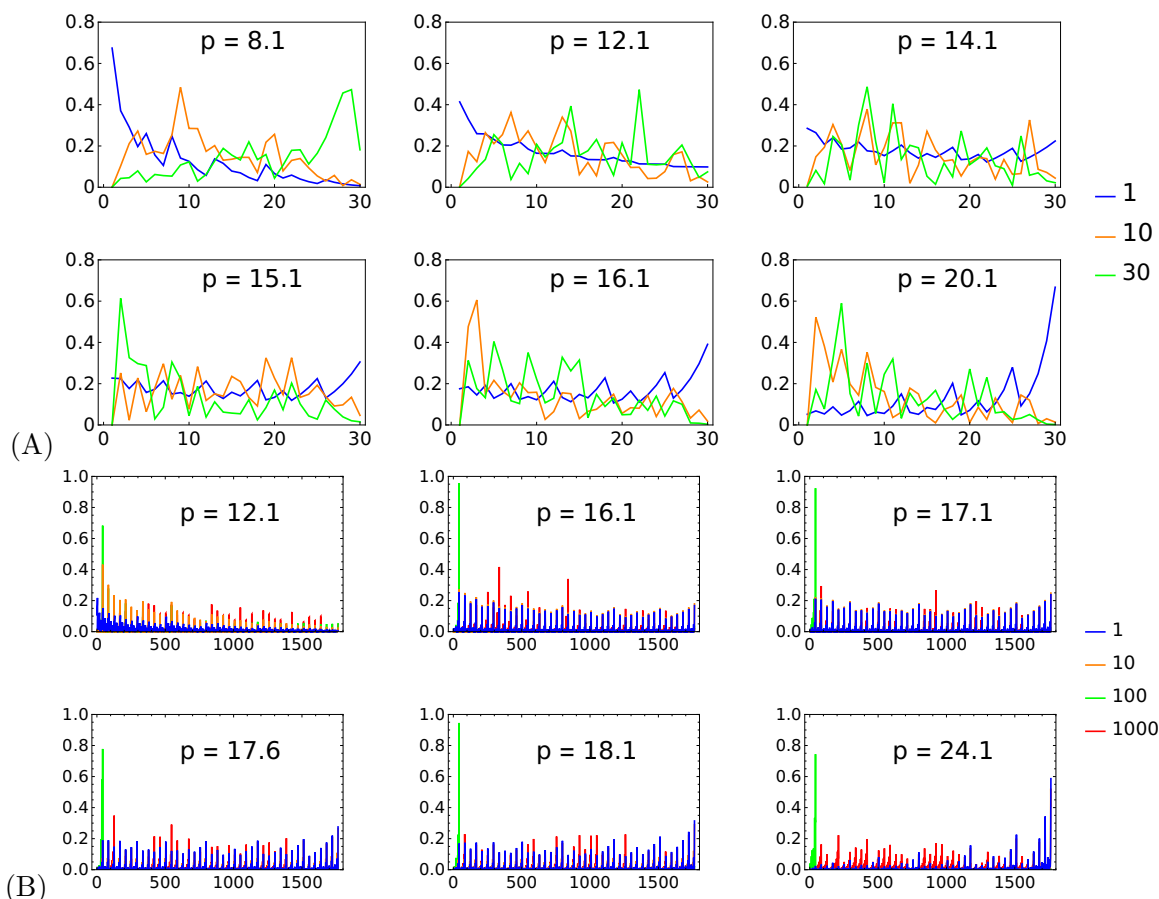
Figure 5. Coefficients of the S-matrix eigenvector $|n\rangle$ in the partition basis, for the leading eigenvector and a few smaller eigenvectors, denoted by colored lines (see the plot legends). The partitions are enumerated from shortest (of the form $(0,\ldots 0, N, 0,\ldots 0)$) to longest (of the form $(1,\ldots 1)$). The leading eigenstate $n = 1$ (blue line — corresponding to the largest eigenvalue, which dominates the final state of the scattering process) consists mainly of short partitions for small momenta, becomes approximately equipartitioned for intermediate momenta which we identify with the crossover scale p_c, and consists mainly of long partitions for high momenta. The eigenstates with $n = 10$ and $n = 30$ behave in a more or less complementary way (i.e. long partitions dominate for $p < p_c$ and short partitions for $p > p_c$), although for them the trends are less clear. Six momentum values are considered ($p = 8.1, 12.1, 14.1, 15.1, 16.1, 20.1$ in (A), for open strings, and $p = 12.1, 16.1, 17.1, 17.6, 18.1, 24.1$ in (B), for closed strings), with $N = 9$, $\theta = 0.23$, $\theta' = 0.30$, $\phi' = 0.70$ (A) vs. $N = 10$, $\theta = 0.20$, $\theta' = 0.30$ and $\phi' = 0.20$ (B). The crossovers in general happen at different momenta for open and closed strings; here we have $p_c \approx 15.1$ for open HES (A) and $p_c \approx 17.5$ for closed HES (B).

increase, reflecting the increase in the complexity of dynamics. In fact, it is likely possible to calculate $C(S)$ in a closed form for a Gaussian random matrix ensemble but so far we have not found an expression in terms of elementary functions. Still, figure 7 suggests that $C(S)$ is indeed a useful measure as it becomes maximal at about the same value where the spacing analysis and the eigenvector structure from figure 5(B) show the crossover and strong chaos.
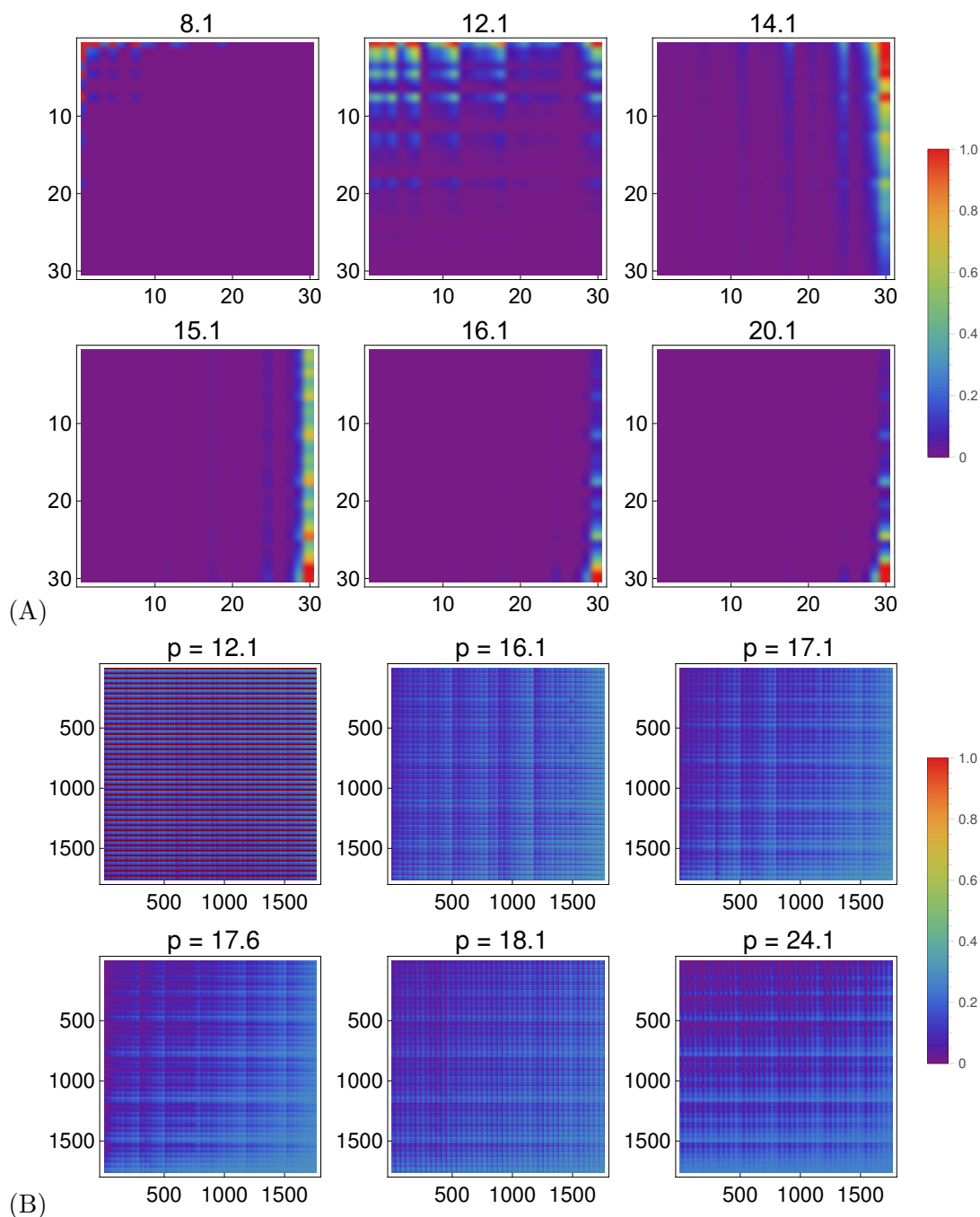
Figure 6. The S-matrices in the partition basis for open (A) and closed (B) HES scattering, for the same kinematics as in figure 5, the color code showing the module of the (generically complex) matrix elements. For the open string the S-matrix and consequently the interval of the values of its elements is much smaller hence it is convenient to use a linear color scale (normalized to the unit interval). For the closed string the S-matrix is much larger and the magnitude of its elements varies by several orders of magnitude hence we use the logarithmic color scale (again normalized to the unit interval). In accordance with figure 5, the dominant processes for $p < p_c \approx 15$ involve short partitions with few occupied levels and large occupation numbers (upper left corner), whereas for $p > p_c$ the opposite is true and the lower left corner of the S-matrix is dominant.
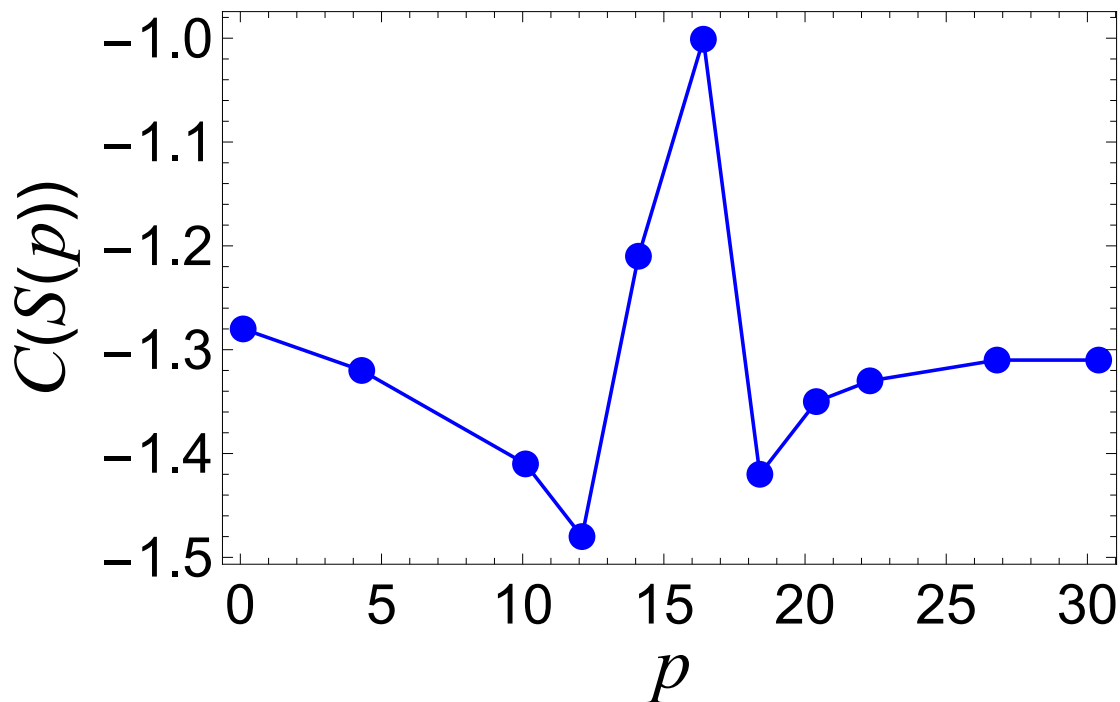
Figure 7. Shannon entropy $C(S(p))$ in computational units as a function of momentum p for the same kinematics as in figure 5(B). We observe a peak in the entropy at the crossover momentum $p_c \approx 17.5$. The line is just to guide the eye.

4.1.3 Quasi-invariant states

Returning again to the structure of the S-matrix akin to plots in figure 6, it is possible to detect the regular structure that spoils the Wigner-Dyson statistics at all momenta (to some extent even at p_c). For this it is necessary to plot different channels separately as they can behave very differently. In figure 8 we plot the *st* and *tu* parts of the open string amplitude. In the *tu* matrix we see clear structures — stripes, while in the *st* part we do not see any obvious regularities. Of course, the stripe structure of the *tu* channel induces similar structure in the complete S-matrix (though less sharp as it combines with the featureless structures of the other channels).

These quasi-invariant states are very intriguing for several reasons: (1) they provide a specific mechanism which precludes the canonical random matrix behavior of the HES S-matrix — we need to understand them if we want to know why the HES approach can seemingly never peep into the black hole regime (2) they are a natural generalization of the scar states which have drawn a lot of attention in quantum chaos studies in recent years but here we find quasi-invariant states *generically*, not for fine-tuned initial conditions as is usually the case for scars[15] (3) analyzing the structure of the amplitudes starting from the expressions (2.18)–(2.23) for the tachyon or (2.33)–(2.46) for the photon it might be possible

---

[15]In the context of our calculation of first-quantized string dynamics, we may see something like quantum-mechanical scars introduced in [44], rather than the scars in quantum many-body systems such as those in [45–47].
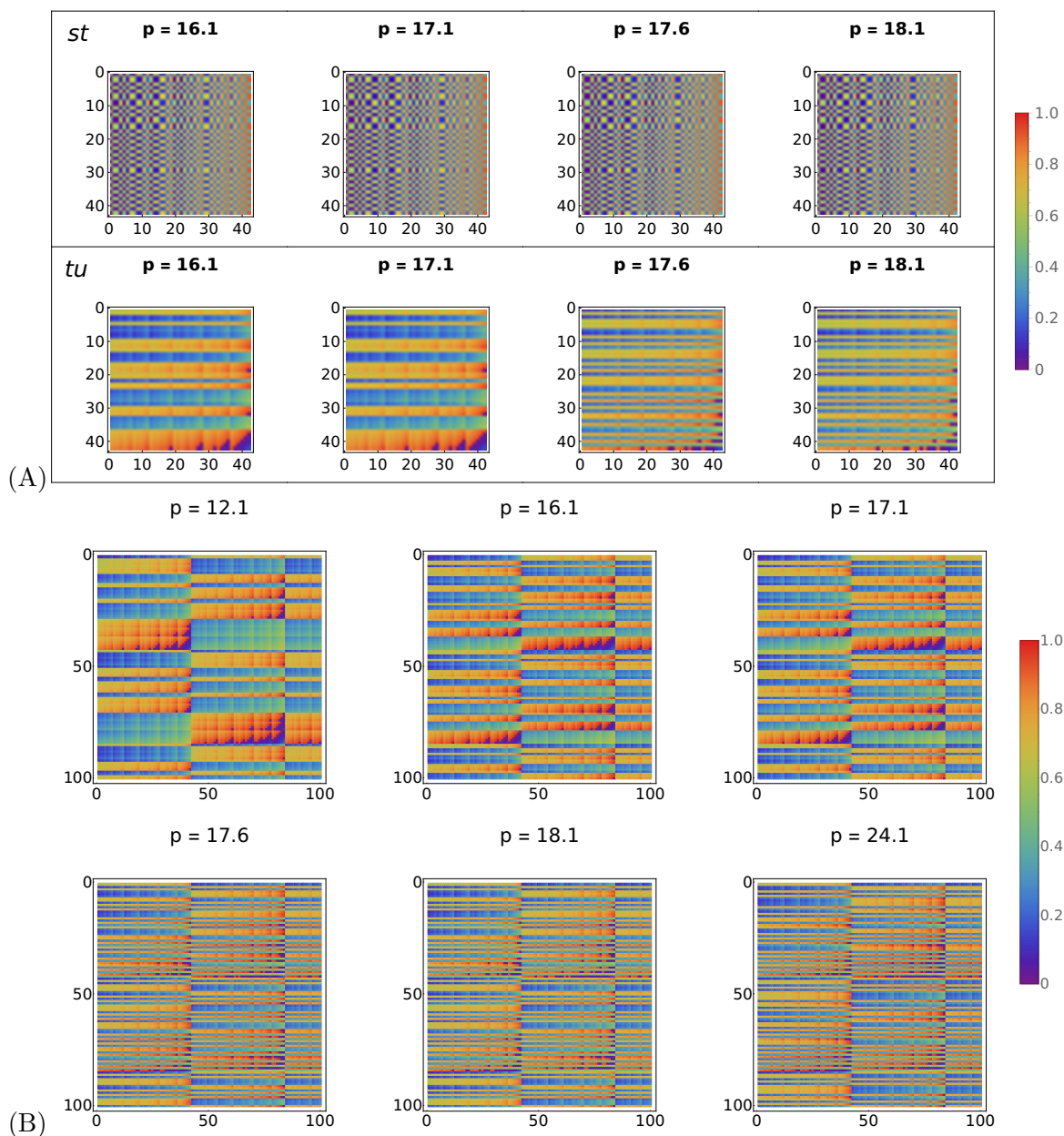
Figure 8. Channels $\mathcal{A}_{st}$ and $\mathcal{A}_{tu}$ of the open string (A) and the closed string (B) amplitude in the partition basis for the same kinematics as in figure 5, the color code showing the phases of the elements, normalized to the $[0, 1]$ interval. The tu part shows stripes (i.e., sets of partitions with lengths confined to some fixed interval), whose number increases at the crossover. The phase structure of the st part is on the other hand more or less featureless. In (B) only a part of the S-matrix is shown in order to zoom-in into the stripe structure; the rest of the S-matrix behaves in a similar manner.

to understand the quasi-invariant states analytically in future work. For now we can only give some general hints as to their appearance, which we do in the discussion in section 5.
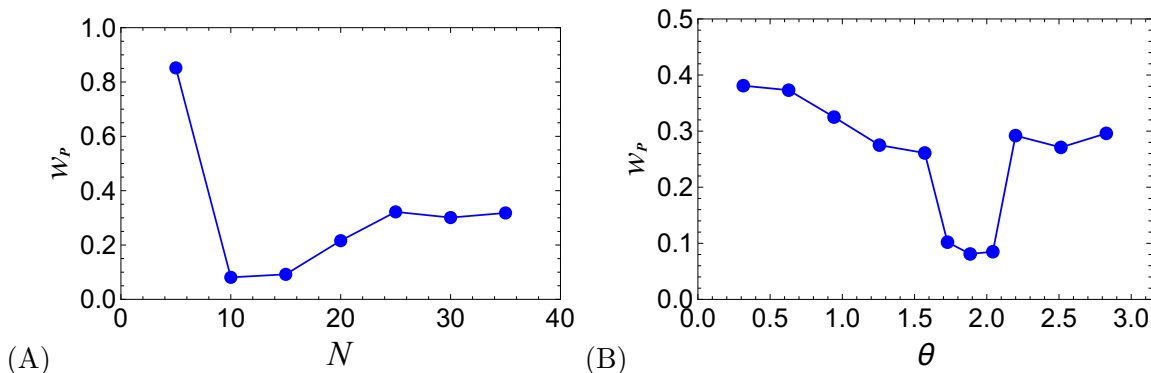
Figure 9. The contribution of the Poisson distribution to the fit of the level spacing histogram of the HES-graviton S-matrix, as a function of N for $\theta = 0.70$ (A), and as a function of θ for $N = 10$ (B), in both cases for $p = 10.1$, $\theta' = 0.25$, $\phi' = 0.70$. There is obviously a relatively narrow interval of angles where the eigenphase spacing distribution is almost of the RMT type, but this is not the case for all values of N. For large N values, when HES becomes really highly excited, the chaos is actually weaker. The fit is for $\beta = 1$, and the solid lines are just to guide the eye.

4.2 The HES-photon and HES-graviton S-matrices

For the HES-photon scattering (eq. (2.2)) and its closed-string equivalent, the HES-graviton scattering (eq. (2.4)) we can perform a similar analysis as for the HES-tachyon scattering discussed in the previous subsection. The overall phenomenology is similar, with two differences:

1. Dependence of dynamics on the momentum p and the angles θ and θ' is now much stronger and more complicated, so that in some cases there is more than one value of momentum where chaos becomes strong, but it only does so when the values of the angles are also inside the chaotic window.

2. The strong chaos found for special p and θ values is mainly there for finite N values and does not in general persist for growing N.

The above findings can be seen from figure 9. There is now a narrow interval in the angle θ where the Poisson contribution w_P becomes very low but this is only the case for $N = 10$ and $N = 15$, otherwise the dynamics is again highly mixed. This suggests that the mechanisms of chaos at work here are not relevant for the black hole scrambling and the string/black hole complementarity picture: otherwise the chaos could only become stronger for growing N. Therefore, unlike the tachyon case considered in figure 4, where indeed the strong chaos at $p \approx p_c$ persists for growing N, here it is a finite-N phenomenon.

The momentum dependence of the chaos indicators $\langle r \rangle$ and w_P can be seen in figure 10. Now we have several crossover values p_c where the main contribution to the eigenvectors goes back and forth between short and long partitions. In this example four p_c values exhibit clear signs of chaos. We note in passing that for mixed/weakly chaotic cases the $\langle r \rangle$ values are now above the GOE value 1.75 whereas for the tachyon they are below. We do not know the significance of this. For reference we also give a few plots of the eigenphase spacing distribution in figure 11, for two crossover momenta ($p = 1.3, 1.9$) and two other momenta ($p = 1.0, 1.6$), where we can directly observe an increased fit quality by the Wigner-Dyson
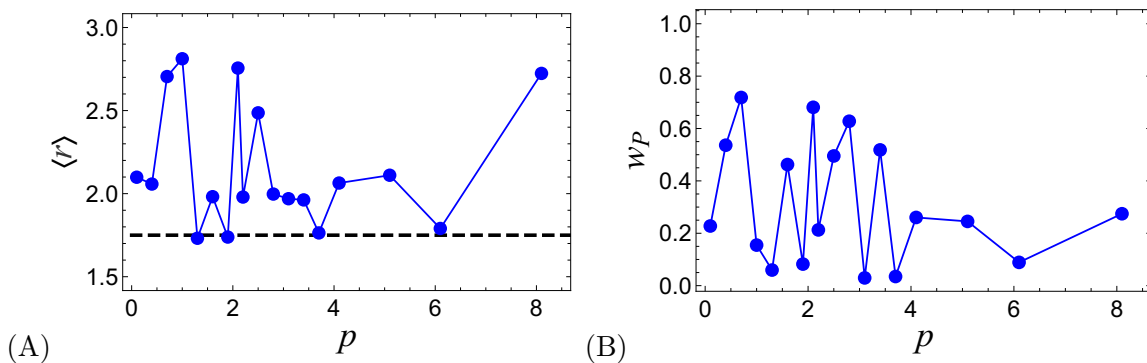
Figure 10. Mean level spacing ratio $\langle r \rangle$ (A) and the Poisson contribution to the eigenphase spacing histogram w_P for a HES-photon process with $N = 9$, $\theta = 0.23$, $\theta' = 0.5$, $\phi' = 0.7$, and a range of momenta p. Now we have several chaotic momenta instead of just one, roughly at $p_c = 1.3, 1.9, 3.7, 6.1$. Both measures of chaos ($\langle r \rangle$ and w_P) roughly agree in indicating chaotic dynamics at these points. The fit is for $\beta = 1$ in the Wigner-Dyson distirbution.
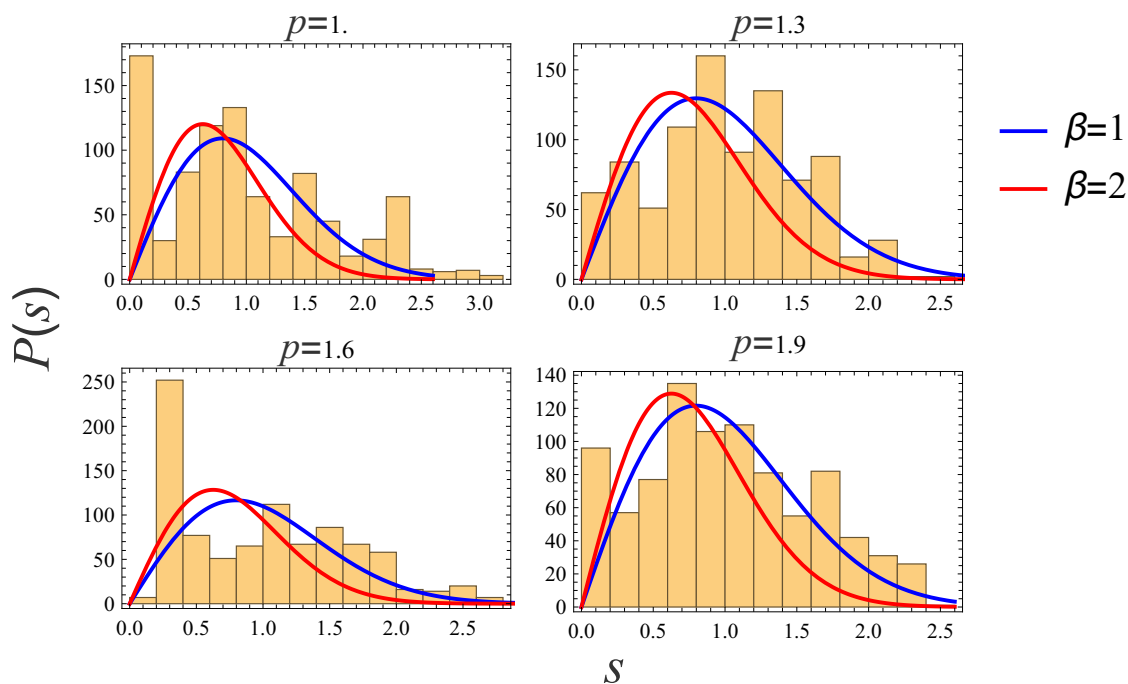
Figure 11. Eigenphase spacing distribution for the same kinematics as in figure 10 for four momentum values $p = 1.0, 1.3, 1.6, 1.9$. The points $p = 1.3$ and $p = 1.9$ provide a better fit to the Wigner-Dyson distribution with $\beta = 1/\beta = 2$ (blue/red line) than the other two, in accordance with the other chaos indicators ($\langle r \rangle$ and w_P).

distribution with $\beta = 1$ for the $p = p_c$ momenta. Here again we perform the Wigner-Dyson fit also for $\beta = 2$ in addition to $\beta = 1$ for comparison, but the fit is again better for $\beta = 1$.

In conclusion, the scattering of spinful states (such as the photon) provides a more complex phenomenology: strong chaos is still limited to special values of parameters, not only momenta but also the angles and the occupation number. In this sense one could argue

that this case is even less chaotic than the tachyonic case as chaos does not persist for infinite N. On the other hand, highly erratic dependence on p and θ is more in accordance with the classical chaotic scattering where precisely the high sensitivity of the scattering outcome on the initial conditions encapsulates chaos [48, 49]. In fact, [50] has found precisely such behavior also for the HES-tachyon process but for individual amplitudes only (here we have shown it does not hold for the S-matrix as a whole, where just a single p value is special). The result we have is akin to the classical scattering of the ring string off a black hole, studied e.g. in [38–40] and numerous later works.

5 Discussion and conclusions

The S-matrices paint a complex picture of HES dynamics. The dynamics varies from mostly regular, with strong eigenphase clustering, to mostly chaotic, in good agreement with the usual RMT measures of chaos. There is no simple characterization of chaos as a function of kinematics or the occupation number N, and spinful vs. scalar incoming state also influences the outcome. This variation is in itself our first conclusion: the dynamics is strongly non-uniform and no signs of black hole universality are seen.

The first important idea is that of a crossover at special momentum p_c between two mostly regular regimes in the HES-tachyon scattering: only when all the HES states are excited in the scattering process the chaos dominates in the eigenphase statistics. For scattering of photons and gravitons the picture is more complicated, and several values of special/chaotic momenta and angles can be found. To some extent this is expected: only a non-scalar state can exhibit strong dependence on the angles and geometry of the scattering process. But more important is the very idea of the crossover. First, it tells us how the chaos arises: it arises through the exponentially large number of excited states, a factor which makes up for the simplicity of the Polyakov action for the scattering and the Veneziano- and Virasoro-type amplitudes.[16]

The second important idea is that of quasi-invariant states. They provide a clear reason why chaos can never become uniform: as long as there are many IN states which give almost the same OUT state there will be a strong clustering of eigenphases and no uniform eigenphase repulsion. We plan to understand these states better in future work.

Both the crossover (mentioned also in [32]) and the quasi-invariant states could not be seen from amplitudes alone, they are properties of the whole S-matrix. Therefore it is important to move away from the study of individual amplitudes toward the study of the whole S-matrix. Yet, this is computationally demanding. Indeed, one possible weakness of this work is that we are forced to study relatively small N values (roughly around 10) when working on a laptop, and even on a cluster we cannot move beyond $N \approx 30$ and that with an approximate evaluation of the gamma and beta functions. Therefore, one might worry that we simply do not look at sufficiently high N to make our strings truly highly excited. Could it be that in fact chaos will become uniform and black-hole-like when going for much higher excitation numbers?

---

[16]Indeed, one may wonder how is it possible to see any chaos when the action is quadratic. The answer lies in the fact that the Polyakov action has an additional constraint and, as we mentioned, in the fact that we have an exponentially large number of amplitudes in the S-matrix, where each amplitude behaves as an infinite sum of field-theoretical amplitudes.

We cannot provide a definite answer but we have some reasons to conjecture that the answer is negative. First, we reach a seemingly constant ratio of regular to chaotic (Poisson to Wigner-Dyson) eigenphase populations: it is possible but not very likely that this constant ratio will suddenly drop at some N. Also, when studying individual amplitudes the authors of [26] have gone for much higher N (over 10^5 in some cases) and they still do not see the statistics collapse onto the RMT predictions. Finally, existing results on the eigenvalue distribution of beta-Wishart matrices [51, 52] provide a path toward an analytic proof that quasi-invariant states are present for S-matrices of arbitrarily large size. We plan to follow this path in further work on the subject.

All of the above shows that HES scattering is very different from black hole scrambling: in the latter, there are universal time and space scales encapsulated in the chaos bounds for the Lyapunov exponent and the butterfly velocity. These rest essentially on the existence of a (semi)classical horizon with an infinite redshift, thus any infalling wave behaves as a shock wave and leads to a universal response. It seems that, despite the string/BH complementarity, a perturbative tree-level string calculation just cannot describe the transition to a black hole. One reason might be that we work in flat space background. This poses another important task for the future: will we get different results if we allow at least for weak gravity, taking it into account through perturbative vertex corrections? This question is in principle approachable and is another task for the future. Finally, one may try to model the dynamics at the transition point, which was studied in a number of recent works [53–55].

Acknowledgments

References

[1] Y. Sekino and L. Susskind, *Fast scramblers*, *JHEP* **10** (2008) 065 [arXiv:0808.2096] [INSPIRE].

[2] N. Lashkari et al., *Towards the fast scrambling conjecture*, *JHEP* **04** (2013) 022 [arXiv:1111.6580] [INSPIRE].

[3] J. Maldacena, S.H. Shenker and D. Stanford, *A bound on chaos*, *JHEP* **08** (2016) 106 [arXiv:1503.01409] [INSPIRE].

[4] J. Polchinski, *Chaos in the black hole S-matrix*, arXiv:1505.08108 [INSPIRE].

[5] A. Almheiri et al., *Replica wormholes and the entropy of Hawking radiation*, *JHEP* **05** (2020) 013 [arXiv:1911.12333] [INSPIRE].

[6] G. Penington, S.H. Shenker, D. Stanford and Z. Yang, *Replica wormholes and the black hole interior*, *JHEP* **03** (2022) 205 [arXiv:1911.11977] [INSPIRE].

[7] A. Almheiri et al., *The entropy of Hawking radiation*, *Rev. Mod. Phys.* **93** (2021) 035002 [arXiv:2006.06872] [INSPIRE].

[8] J.R. David, G. Mandal and S.R. Wadia, *Microscopic formulation of black holes in string theory*, *Phys. Rept.* **369** (2002) 549 [hep-th/0203048] [INSPIRE].

[9] I. Bena, E.J. Martinec, S.D. Mathur and N.P. Warner, *Fuzzballs and microstate geometries: black-hole structure in string theory*, arXiv:2204.13113 [INSPIRE].

[10] L. Susskind, *Some speculations about black hole entropy in string theory*, hep-th/9309145 [INSPIRE].

[11] G.T. Horowitz and J. Polchinski, *A correspondence principle for black holes and strings*, *Phys. Rev. D* **55** (1997) 6189 [hep-th/9612146] [INSPIRE].

[12] G.T. Horowitz and J. Polchinski, *Selfgravitating fundamental strings*, *Phys. Rev. D* **57** (1998) 2557 [hep-th/9707170] [INSPIRE].

[13] S.H. Shenker and D. Stanford, *Black holes and the butterfly effect*, *JHEP* **03** (2014) 067 [arXiv:1306.0622] [INSPIRE].

[14] D.A. Roberts, D. Stanford and L. Susskind, *Localized shocks*, *JHEP* **03** (2015) 051 [arXiv:1409.8180] [INSPIRE].

[15] S.H. Shenker and D. Stanford, *Stringy effects in scrambling*, *JHEP* **05** (2015) 132 [arXiv:1412.6087] [INSPIRE].

[16] D.J. Gross and V. Rosenhaus, *Chaotic scattering of highly excited strings*, *JHEP* **05** (2021) 048 [arXiv:2103.15301] [INSPIRE].

[17] E. Del Giudice, P. Di Vecchia and S. Fubini, *General properties of the dual resonance model*, *Annals Phys.* **70** (1972) 378 [INSPIRE].

[18] M. Hindmarsh and D. Skliros, *Covariant closed string coherent states*, *Phys. Rev. Lett.* **106** (2011) 081602 [arXiv:1006.2559] [INSPIRE].

[19] D. Skliros and M. Hindmarsh, *String vertex operators and cosmic strings*, *Phys. Rev. D* **84** (2011) 126001 [arXiv:1107.0730] [INSPIRE].

[20] M. Bianchi and M. Firrotta, *DDF operators, open string coherent states and their scattering amplitudes*, *Nucl. Phys. B* **952** (2020) 114943 [arXiv:1902.07016] [INSPIRE].

[21] V. Rosenhaus, *Chaos in a many-string scattering amplitude*, *Phys. Rev. Lett.* **129** (2022) 031601 [arXiv:2112.10269] [INSPIRE].

[22] M. Firrotta and V. Rosenhaus, *Photon emission from an excited string*, *JHEP* **09** (2022) 211 [arXiv:2207.01641] [INSPIRE].

[23] K. Hashimoto, Y. Matsuo and T. Yoda, *Transient chaos analysis of string scattering*, *JHEP* **11** (2022) 147 [arXiv:2208.08380] [INSPIRE].

[24] M. Firrotta, *The chaotic emergence of thermalization in highly excited string decays*, *JHEP* **04** (2023) 052 [arXiv:2301.04069] [INSPIRE].

[25] M. Bianchi, M. Firrotta, J. Sonnenschein and D. Weissman, *Measure for chaotic scattering amplitudes*, *Phys. Rev. Lett.* **129** (2022) 261601 [arXiv:2207.13112] [INSPIRE].

[26] M. Bianchi, M. Firrotta, J. Sonnenschein and D. Weissman, *Measuring chaos in string scattering processes*, *Phys. Rev. D* **108** (2023) 066006 [arXiv:2303.17233] [iNSPIRE].

[27] F. Haake, *Quantum signatures of chaos*, in *Quantum coherence in mesoscopic systems*, Springer, Boston, MA, U.S.A. (1991), p. 583–595 [DOI:10.1007/978-1-4899-3698-1_38].

[28] M.L. Mehta, *Random matrices*, third edition, (2004).

[29] V. Rosenhaus, *Chaos in the quantum field theory S-matrix*, *Phys. Rev. Lett.* **127** (2021) 021601 [arXiv:2003.07381] [iNSPIRE].

[30] E. Doron and U. Smilansky, *Semiclassical quantization of chaotic billiards: a scattering theory approach*, *Nonlinearity* **5** (1992) 1055.

[31] R. Blümel, B. Dietz, C. Jung and U. Smilansky, *On the transition to chaotic scattering*, *J. Phys. A* **25** (1992) 1483.

[32] D. Das, S. Mandal and A. Sarkar, *Chaotic and thermal aspects in the* $|HES\rangle$ *S-matrix*, arXiv:2312.02127 [iNSPIRE].

[33] H. Kawai, D.C. Lewellen and S.-H.H. Tye, *A relation between tree amplitudes of closed and open strings*, *Nucl. Phys. B* **269** (1986) 1 [iNSPIRE].

[34] T. Sondergaard, *Perturbative gravity and gauge theory relations: a review*, *Adv. High Energy Phys.* **2012** (2012) 726030 [arXiv:1106.0033] [iNSPIRE].

[35] S. Stieberger and T.R. Taylor, *Closed string amplitudes as single-valued open string amplitudes*, *Nucl. Phys. B* **881** (2014) 269 [arXiv:1401.1218] [iNSPIRE].

[36] A. Addazi, M. Bianchi, M. Firrotta and A. Marcianò, *String memories... Lost and regained*, *Nucl. Phys. B* **965** (2021) 115356 [arXiv:2008.02206] [iNSPIRE].

[37] A. Aldi, M. Bianchi and M. Firrotta, *String memories... Openly retold*, *Phys. Lett. B* **813** (2021) 136037 [arXiv:2010.04082] [iNSPIRE].

[38] A.V. Frolov and A.L. Larsen, *Chaotic scattering and capture of strings by black hole*, *Class. Quant. Grav.* **16** (1999) 3717 [gr-qc/9908039] [iNSPIRE].

[39] L.A. Pando Zayas and C.A. Terrero-Escalante, *Chaos in the gauge/gravity correspondence*, *JHEP* **09** (2010) 094 [arXiv:1007.0277] [iNSPIRE].

[40] P. Basu, P. Chaturvedi and P. Samantray, *Chaotic dynamics of strings in charged black hole backgrounds*, *Phys. Rev. D* **95** (2017) 066014 [arXiv:1607.04466] [iNSPIRE].

[41] A. Altland and M.R. Zirnbauer, *Nonstandard symmetry classes in mesoscopic normal-superconducting hybrid structures*, *Phys. Rev. B* **55** (1997) 1142 [cond-mat/9602137] [iNSPIRE].

[42] V. Oganesyan and D.A. Huse, *Localization of interacting fermions at high temperature*, *Phys. Rev. B* **75** (2007) 155111 [iNSPIRE].

[43] M. Srdinšek, T. Prosen and S. Sotiriadis, *Signatures of chaos in nonintegrable models of quantum field theories*, *Phys. Rev. Lett.* **126** (2021) 121602 [arXiv:2012.08505] [iNSPIRE].

[44] E.J. Heller, *Bound-state eigenfunctions of classically chaotic Hamiltonian systems: scars of periodic orbits*, *Phys. Rev. Lett.* **53** (1984) 1515 [iNSPIRE].

[45] S. Moudgalya, B.A. Bernevig and N. Regnault, *Quantum many-body scars and Hilbert space fragmentation: a review of exact results*, *Rept. Prog. Phys.* **85** (2022) 086501 [arXiv:2109.00548] [iNSPIRE].

[46] D. Liska, V. Gritsev, W. Vleeshouwers and J. Minář, *Holographic quantum scars*, *SciPost Phys.* **15** (2023) 106 [`arXiv:2212.05962`] [ɪɴSPIRE].

[47] A. Milekhin and N. Sukhov, *All holographic systems have scar states*, `arXiv:2307.11348` [ɪɴSPIRE].

[48] E. Ott and T. Tél, *Chaotic scattering: an introduction*, *Chaos* **3** (1993) 417.

[49] E. Ott, *Chaos in dynamical systems*, second edition, Cambridge University Press, Cambridge, U.K. (2002).

[50] K. Hashimoto and N. Tanahashi, *Universality in chaos of particle motion near black hole horizon*, *Phys. Rev. D* **95** (2017) 024007 [`arXiv:1610.06070`] [ɪɴSPIRE].

[51] A. Dubbs, A. Edelman, P. Koev and P. Venkataramana, *The Beta-Wishart ensemble*, *J. Math. Phys.* **54** (2013) 083507 [`arXiv:1305.3561`]

[52] L. Luo, J. Wang, L. Zhang and S. Zhang, *The differential entropy of the joint distribution of eigenvalues of random density matrices*, *Entropy* **18** (2016) 342.

[53] Y. Chen, V. Gorbenko and J. Maldacena, *Bra-ket wormholes in gravitationally prepared states*, *JHEP* **02** (2021) 009 [`arXiv:2007.16091`] [ɪɴSPIRE].

[54] Y. Chen, J. Maldacena and E. Witten, *On the black hole/string transition*, *JHEP* **01** (2023) 103 [`arXiv:2109.08563`] [ɪɴSPIRE].

[55] Y. Chen and J. Maldacena, *String scale black holes at large D*, *JHEP* **01** (2022) 095 [`arXiv:2106.02169`] [ɪɴSPIRE].

Photoemission "experiments" on holographic lattices

Filip Herček[1,3], Vladan Gecin[2,3] and Mihailo Čubrović[3⋆]

1 Department of Physics, University of Novi Sad,
Trg Dositeja Obradovića 4, 21000 Novi Sad, Serbia
2 Department of Physics, University of Belgrade,
Studentski Trg 12-16, 11000 Belgrade, Serbia
3 Center for the Study of Complex Systems,
Institute of Physics Belgrade, University of Belgrade,
Pregrevica 118, 11080 Belgrade, Serbia

⋆ cubrovic@ipb.ac.rs

Abstract

We construct a 2D holographic ionic lattice with hyperscaling-violating infrared geometry and study single-electron spectral functions ("ARPES photoemission curves") on this background. The spectra typically show a three-peak structure, where the central peak undergoes a crossover from a sharp but not Fermi-liquid-like quasiparticle to a wide incoherent maximum, and the broad side peaks resemble the Hubbard bands. These findings are partially explained by a perturbative near-horizon analysis of the bulk Dirac equation. Comparing the holographic Green functions in imaginary frequency with the Green functions of the Hubbard model obtained from quantum Monte Carlo, we find that the holographic model provides a very good fit to the Hubbard Green function. However, the information loss when transposing the holographic Green functions to imaginary frequencies implies that a deeper connection to Hubbard-like models remains questionable.

Contents

1   Introduction

Holography has established itself as a natural point of view in the subject of strongly correlated electron systems – the strong/weak duality translates the problem into tractable perturbative calculations in general relativity, and the relation of bulk physics to the renormalization group flow establishes a novel framework where many phenomena can be naturally expressed and understood [1–3]. Paradoxically, it is likewise indisputable that the field of AdS/cond-mat is still in its infancy in many respects. For example, controlled (top-down) constructions are few and quite complicated, thus we are mainly condemned to phenomenological, bottom-up models without explicit knowledge of the field theory Hamiltonian. Another issue is that the ultraviolet (UV) CFT puts rather strong constraints on physics at short distances, often quite unphysical in the context of condensed matter. Finally, the treatment of electrons on crystalline lattices – the bread and butter of condensed matter physics – is numerically demanding and has not yet become common among holographers. Here we aim to reduce this gap by constructing a holographic lattice with infrared (IR) geometry appropriate for a range of phases from normal to strange metals, and studying in detail the spectral functions (measured by angle-resolved photoemission spectroscopy (ARPES) in real life) of probe fermions on these backgrounds.

Spectral functions of probe bulk fermions on holographic lattices have been studied in some detail by now. The basic idea of true lattice models is to introduce a periodically modulated chemical potential (through the appropriate boundary condition for the bulk gauge

field), yielding a lattice of finite "hardness" in continuous space, akin to cold atoms in a periodic potential (or indeed the potential of a real-world crystal) and unlike the idealized lattice models like the Hubbard or $t-J$ model where the space itself is discrete. A perturbative analytical approach was pioneered in [4] and the full numerical solution (although for conductivity, not fermionic spectra) in [5, 6]. Afterwards, a wealth of research was performed. Limiting ourselves to the works on fermionic spectral functions, let us mention the exploration of the lattice Fermi surface in [7], the effects of striped phases on the fermionic spectra in [8–10], and the weakening and destruction of the Fermi surface due to anisotropy and nonlinear effects in [11, 12].

Some alternatives to the modulation of the chemical potential, known in the literature as the "ionic lattice", which requires solving numerically a system of nonlinear partial differential equations (PDE), are the Q-lattice which breaks translation invariance without actually introducing a lattice [13, 14] (see also [15]), the helical lattice in the Bianchi-VII background [16, 17] and the linear axion model [18]. We do not treat such approaches: the Q-lattice (despite the name!) and the linear axion are not really lattices and their Fermi surfaces do not live in Brillouin zones, whereas the Bianchi-VII geometry is a very special solution. We did however try out a number of approximations to the ionic lattice which go under the name of semiholography. The simplest, original idea [19] is to consider a free fermion on the lattice, coupled linearly to the probe bulk fermion whose propagator therefore acts as a self-energy in the propagator of the semiholographic theory. More elaborate setups are proposed in [20]. We have also solved the averaged equations of motion (essentially a multipole expansion of the lattice potential) as a convenient way to obtain a quick glance at the system or to perform large scans over the parameter space. It turns out that the spectra do not crucially depend on the approximation taken. Quite unexpectedly, even semiholography provides a decent quick and dirty way to compute the spectrum.

Running a bit forward, we will find that the lattice physics can be understood to a good extent by combining the near-horizon analysis of the spectral functions in homogeneous space [21–26] and the perturbative lattice calculations within the weak binding framework [4]. This is however only true for relatively weak lattices, where the amplitude of the chemical potential $\delta\mu$ is no larger than the mean μ_0, i.e. $\delta\mu/\mu_0 \leq 1$. We are pretty much in the dark in the opposite, strong lattice regime. We realize the lattice in the hyperscaling-violating background of [27], a special case of the "effective holographic theories" or "holographic scaling atlas" framework of [28–31]. In homogeneous space, [27] shows that one can tune the parameters to have either a quasiparticle pole dressed in quantum-critical fluctuations, or just a quantum-critical continuum. On the lattice, the two regimes mix as different lattice momenta can belong to the first or the second regime. We will see that this provides an inhomogeneous and anisotorpic multi-peak structure of the spectral function (with quasiparticles, bands and wide bumps), which is not unlike the known phenomenology in real-world lattice models [32] and materials [33].

An important motivation and an additional challenge of this paper is the physics of the Hubbard model, the ubiquitous paradigm of non-Fermi liquids and strange metals, quite amenable to computational work at high temperatures and in certain approximations, yet still extremely rich, complex and unsolvable in the most general case (especially difficult at low temperatures), not the least because of the fermion sign problem [32, 34, 35]. No doubt the microscopy of this model has very little to do with the effective holographic theories – but the qualitative features of the spectrum are quite robust, and the general phenomenology as elucidated in [36–40] might be related to holographic physics.

Quantum Monte Carlo methods (specifically CTINT [41, 42]) provide us with high-quality Green functions of the Hubbard model at relatively high temperatures. We have directly

compared them to the holographic Green functions.[1] Therefore, a secondary goal of the paper is to find a holographic background (from the family of hyperscaling-violating geometries [27–29, 31]) which provides a good description of the correlation functions in the Hubbard model; one could then use the power of holography to study the low-temperature regime and other properties which are hard to access directly. It will turn out that we need one or two additional ingredients to model the Hubbard physics in AdS/CFT: regularization of the spectrum provided by a dynamical UV source, necessary to satisfy the ARPES sum rule [43], and perhaps the dipole coupling of the probe fermion (introduced first in [44, 45]) which makes the gaps in the spectrum more pronounced; we come close to the Hubbard model also without it but it does improve the fit. We emphasize however that the general phenomenology of holographic lattices and their spectra is important and interesting also in its own right: it yields a crossover from the quasiparticle regime to the strange metallic regime, and it will allow us to understand the effects of umklapp in the strong coupling regime.

The reader might be unhappy with the large number of figures and the emphasis on phenomenology as opposed to few equations and little analytical understanding. We certainly hope to gain a deeper view of our numerical findings, but in the present stage even a phenomenological exploration of the system is useful, hence the formulation "photoemission experiments" in the title, in conscious homage to [46].

The composition of the paper is the following. In section 2 we give the basic framework of our model: the Einstein-Maxwell-dilaton (EMD) system with hyperscaling violation and the ionic lattice; we describe the lattice solution in the bulk and list the relevant tunable parameters. Section 3 brings the Dirac equation, discussing the dipole term and the dynamical cutoff. Section 4 discusses in detail the properties of the spectral functions, the appearance of Hubbard-like bands and quasiparticles, and offers a tentative explanation for some phenomena through a perturbative analytic treatment. In Section 5, we explore how far the analogy to the Hubbard model can go by fitting our results (in imaginary frequency) to the quantum Monte Carlo results for the Hubbard Hamiltonian. In Section 6 we conclude the paper trying to find deeper implications of our results, in particular how fundamental the relation to the Hubbard model is and what to do next.

2 Holographic ionic lattice with hyperscaling violation

2.1 Action and geometry

The broad idea of the holographic setup is that a strange metal can be understood as a (not necessarily Fermi-liquid-like!) quasiparticle coupled to a bath of quantum critical excitations. This viewpoint (different in details and with a different choice of the holographic model) was pursued e.g. in [47] and formulated particularly clearly in the context of charge transport in [48]. To that end, we adopt from [27] a specific realization of the effective holographic theory of quantum critical phases of [29–31]. The holographic dual of this system is a theory with gravity, gauge and matter fields in AdS_4. Its action has the structure $S = S_{\text{bulk}} + S_{\text{bnd}}$, the sum of the bulk action and the boundary action. The boundary action contains the Gibbons-Hawking-York term and the regulator terms ($A_\mu \partial_\nu n^\nu A^\mu$ and Φ^2) for the gauge and dilaton field respectively. We do not use S_{bnd} explicitly (because we do not compute correlation functions of the EMD fields nor the thermodynamic quantities). The bulk action reads (in the $(-, +, +, +)$

---

[1]An important twist is that quantum Monte Carlo yields the Green function in imaginary (Matsubara) frequency, so we need to transform the holographic functions into imaginary frequencies too. Although this direction is easy – it is way harder to perform "analytical continuation" from imaginary to real frequencies – it will turn out nevertheless that comparing the Green functions in Matsubara frequencies destroys a lot of information and creates great difficulties.

convention that we use everywhere throughout the paper):

$$S = \int d^4x \sqrt{-g} \left[R - (\nabla \Phi)^2 - Z(\Phi) F_{\mu\nu} F^{\mu\nu} + V(\Phi) \right].$$ (1)

Here, $F_{\mu\nu}$ is the electromagnetic field strength tensor and the potentials of the dilaton Z and V depend on some scaling exponents α and δ:[2]

$$Z(\Phi) = \frac{1}{2} \left(1 + \cosh(2\alpha\Phi) \right), \quad V(\Phi) = 6 + V_0 \left(1 - \cosh(2\delta\Phi) \right).$$ (2)

The important feature is that Z and V run as $\exp(2\alpha\Phi)$ and $\exp(2\delta\Phi)$ respectively in the IR and reduce to unity and 6 respectively in the UV of AdS_4 (we will show shortly that $\phi \to 0$ at the boundary). For all calculations in the paper we choose $V_0 = -0.5$. The charged black brane sources the gauge field of the form $A = A_t dt$. Ionic square lattice solutions are obtained by introducing a boundary source for the gauge field with the periodicity of a square lattice with period $1/2\pi Q$. For such solutions a numerically convenient choice of coordinates, suggested in [9, 10], is $(t, x, y, \tilde{z})$ where the AdS boundary is at $\tilde{z} = 1$ and the horizon is at $\tilde{z} = 0$. We denote by r the usual radial coordinate which equals ∞ at the AdS boundary and some positive r_h at the horizon, and its inverse is $z = 1/r$. The relation between the three radial coordinates is

$$\frac{r_h}{r} = \frac{z}{z_h} = 1 - \tilde{z}^2.$$ (3)

The r coordinate will be convenient for analytical considerations near the horizon but the optimal coordinate choice for the numerical solution of EMD equations is $\tilde{z}$; the z coordinate will be convenient when discussing the calculation of the spectral functions and their UV cutoff. The electrostatic potential at the AdS boundary for the square lattice with period $1/2\pi Q$ now reads

$$A_t(x, y, \tilde{z} = 1) = \mu(x, y) \equiv \mu_0 + \delta\mu \cos(2Q\pi x) \cos(2Q\pi y).$$ (4)

With this boundary condition the solution becomes inhomogeneous and the metric $g_{\mu\nu}$ as well as the gauge and matter fields A_t and Φ depend on $x, y, \tilde{z}$ in the whole space. The most general form of the metric consistent with the symmetries of the square lattice is:

$$ds^2 = \frac{r_h^2}{(1-\tilde{z}^2)^2} \left[-f(\tilde{z}) q_{tt}(x, y, \tilde{z}) dt^2 + q_{xx}(x, y, \tilde{z}) \left(dx^2 + dy^2 \right) + 2q_{xy}(x, y, \tilde{z}) dx dy \right.$$
$$\left. + 2q_{x\tilde{z}}(x, y, \tilde{z})(dx + dy) d\tilde{z} + \frac{4\tilde{z}^2 q_{\tilde{z}\tilde{z}}(x, y, \tilde{z})}{r_h^2 f(\tilde{z})} d\tilde{z}^2 \right],$$ (5)

where $f(\tilde{z})$ is the redshift function (to be determined in the next subsection from the IR analysis) and $q_{tt}, q_{xx}, q_{xy}, q_{x\tilde{z}}, q_{\tilde{z}\tilde{z}}$ parametrize the inhomogeneous metric. Obviously f could be absorbed into q_{tt} and $q_{\tilde{z}\tilde{z}}$ but it is useful to keep it in order to understand the IR asymptotics. The gauge field is $A = A_t(x, y, \tilde{z}) dt$ so the electric field strengths E_x, E_y, E_z are all nonzero, and the dilaton is $\Phi = \Phi(x, y, \tilde{z})$.

2.1.1 IR asymptotics

In absence of lattice, this geometry was studied in detail in [27] and represents a case of hyperscaling-violating Lifshitz-scaling geometries [29–31] of the holographic "scaling atlas" [49]. With the lattice, it is extremely difficult to say anything about the IR geometry. It is

---

[2]These exponents determine the familiar Lifshitz exponent ζ and the hyperscaling-violation exponent θ, discussed in many holographic publications, e.g. [29–31].

known that an "explicit", i.e. not spontaneously generated lattice is always irrelevant in far IR at sufficiently low temperatures; the study of holographic Mott insulators [8] has also found that only the spontaneously generated lattice survives at the horizon. However, for any specific bulk action, the question is how low the temperature should be, and how far from the boundary (i.e., how close to the extremal horizon) the lattice dies out. If the lattice dies out only slowly as we approach the horizon at relatively small (though nonzero) temperature, then we have no good idea what IR ansatz to take.[3] Assuming a "weak" lattice in the sense that the amplitude is no larger than the mean of the chemical potential:

$$\frac{\delta\mu}{\mu_0} \leq 1 \,, \tag{6}$$

it makes sense to perform a perturbative expansion in $\delta\mu/\mu_0$ about a homogeneous scaling solution. The IR region is best described in the r coordinate, hence we start from the IR ansatz

$$ds^2_{\text{IR}} = -f(r)Q_{tt}(x,y,r)dt^2 + Q_{xx}(x,y,r)\big(dx^2 + dy^2\big) + 2Q_{xy}(x,y,r)dxdy$$
$$+ 2Q_{xr}(x,y,r)(dx+dy)dr + \frac{Q_{rr}(x,y,r)}{f(r)}dr^2 \,. \tag{7}$$

The redshift function f in (7) is the same as in (5), only in (5) we have expressed it in terms of $\tilde{z}$ rather than r. The other metric functions ($Q_{\mu\nu}$ vs. $q_{\mu\nu}$) differ in the two metrics and *a priori* have nothing to do with each other. The expansion around a scaling solution reads[4]

$$Q_{tt}(x,y,r \to 0) = r^{2\gamma}\mathcal{S}_{tt} \,, \quad Q_{xx}(x,y,r \to 0) = r^{2\beta}\mathcal{S}_{xx} \,, \quad Q_{rr}(x,y,r \to 0) = r^{-2\gamma}\mathcal{S}_{rr} \,,$$
$$Q_{xy}(x,y,r \to 0) = r^{2\nu}\mathcal{S}_{xy} \,, \quad Q_{xr}(x,y,r \to 0) = r^{2\lambda}\mathcal{S}_{xr} \,, \tag{8}$$
$$A_t(x,y,r \to 0) = r^{2\xi}f(r)\mathcal{S}_a \,, \quad \Phi(x,y,r \to 0) = 2\eta \log r \mathcal{S}_\Phi \,,$$

where the series $\mathcal{S}_{\text{field}}$ for any of the fields $Q_{tt}, Q_{xx}, Q_{xy}, Q_{xr}, Q_{rr}, A_t, \Phi$ has the form

$$\mathcal{S}_{\text{field}} = C^{(0)}_{\text{field}} + \sum_{n=1}^{\infty} r^n \bigg[C^{(n)}_{\text{field}} + D^{(n)}_{\text{field}} \cos(2Q\pi x)\cos(2Q\pi y) + E^{(n)}_{\text{field}} \cos(2Q\pi x)\sin(2Q\pi y)$$
$$+ F^{(n)}_{\text{field}} \sin(2Q\pi x)\cos(2Q\pi y) + G^{(n)}_{\text{field}} \sin(2Q\pi x)\sin(2Q\pi y) \bigg] \,. \tag{9}$$

In other words, the leading-order scaling IR solution acquires both homogeneous and inhomogeneous corrections.

Among the zeroth-order terms $C^{(0)}_{\text{field}}$ in (9), we must have $C^{(0)}_{xy} = C^{(0)}_{xr} = 0$ as the off-diagonal metric terms are always zero (in the appropriate gauge) in the homogeneous limit. Picking the appropriate gauge we may always put $C^{(0)}_{xx} = 1$ and also $C^{(0)}_{tt} = 1/C^{(0)}_{rr}$. Also, $C^{(0)}_\Phi = 1$ because any non-unit value could be absorbed in η. Now equating the scaling exponents in the leading terms in each equation of the EMD system yields

$$\beta = \frac{(\alpha+\delta)^2}{4+(\alpha+\delta)^2} \,, \quad \gamma = 1 - \frac{2\delta(\alpha+\delta)}{4+(\alpha+\delta)^2} \,, \quad \eta = -\frac{2(\alpha+\delta)}{4+(\alpha+\delta)^2} \,,$$
$$\xi = \alpha\sqrt{\beta(1-\beta)} + \beta + \frac{5}{4} \,, \tag{10}$$

$$f(\tilde{z}) = 1 - \left(\frac{r_h}{r}\right)^{2\beta+2\gamma-1} \,, \quad T = \frac{C^{(0)}_{tt}(2\beta+2\gamma-1)}{4\pi} r_h^{2\gamma-1} \,. \tag{11}$$

---

[3]We thank Aristomenis Donos and Koenraad Schalm for their remarks on this issue.

[4]In principle we should be expanding starting from $r = r_h$ not $r = 0$ at any finite temperature, however we assume that the temperature is not very high and r_h is reasonably small. Only in this case does it make sense to assume that an approximate scaling solution still exists, as argued also in [27].

This is just the homogeneous solution studied in [27] in slightly different notation. In order to have a smooth horizon the condition $2\gamma - 1 > 0$ has to be satisfied. We thus specialize to the domain $\delta > 0, \alpha < \alpha_0 < 0$ where α_0 is a negative constant which can be expressed from α, δ as in [27]. The coefficients of the first and higher order corrections can be obtained perturbatively in the usual way, equating with zero the prefactors of the terms in the small r expansion of the equations of motion. We list the coefficients of a few leading terms in Appendix A. The important point is that all coefficients are zero at first order, and only at second order there is an inhomogeneous branch of the solution. Since the leading (and even the first subleading) term for all functions is homogeneous, we conclude that indeed the ionic lattice is irrelevant in IR. But this result is clearly perturbative as it hinges on expanding over the oscillatory part, hence it may be unjustified for strong lattices, with $\delta\mu/\mu_0$ large. Since we do not consider strong lattices in this paper, we adopt this solution as the IR boundary condition. The numerical solution is found to be convergent and consistent with these boundary conditions, further strengthening the result.

We are now ready to state the boundary conditions for the numerics. We expect no Maxwell hair at the horizon, so we impose Dirichlet boundary conditions for A_t, which should drop to zero, in accordance with (8). The behavior of the dilaton is also determined by (8): at the horizon it approaches some constant value which at leading (scaling) order equals $2\eta \log r_h$. This is not enough for stable numerics, so we have included also the subleading corrections as stated in (8) and Appendix A. The boundary condition is given by this IR expansion. In fact, in $\tilde{z}$ coordinate the outcome is very simple: the dilaton is smooth at the horizon and has zero derivative, i.e. in computational coordinates we have Neumann conditions.

Finally, the metric functions should all be smooth (the simple zero at the horizon is taken care of by the redshift function f), so we impose Neumann boundary conditions, requiring their derivatives to be zero, again with the falloff in accordance with the IR expansion.

2.1.2 UV asymptotics

The UV asymptotics are straightforward to obtain by expanding the equations of motion in the vicinity of $\tilde{z} = 1$:

$$q_{ii}(x, y, \tilde{z} \to 1) = 1 + \mathcal{C}_{ii}^{(2)}(1 - \tilde{z}^2)^2 + \dots,$$
$$q_{ij}(x, y, \tilde{z} \to 1) = \mathcal{C}_{ij}^{(2)}(1 - \tilde{z}^2)^2 + \dots,$$
$$A_t(x, y, \tilde{z} \to 1) = \mu(x, y) + a(x, y)(1 - \tilde{z}^2) + \dots,$$
$$\Phi(x, y, \tilde{z} \to 1) = (1 - \tilde{z}^2)^{\Delta_-}(1 + \mathcal{C}_{\Phi}^{(1)}(1 - \tilde{z}^2) + \mathcal{C}_{\Phi}^{(2)}(1 - \tilde{z}^2)^2 + \dots),$$
$$\Delta_- = \frac{3}{2} - \sqrt{\frac{9}{4} - 4\delta^2 V_0}, \tag{12}$$

where in the first equation the index i can be t, x or $\tilde{z}$ and in the second equation ij is either xy or $x\tilde{z}$, and the leading term μ in the expansion of the gauge field is the inhomogeneous chemical potential.[5] We do not list here the (cumbersome) explicit expressions for the series coefficients as finding them poses no principal problems and goes along the same lines as in [9–11]. The UV boundary conditions are the following: for the metric functions we need Dirichlet conditions to ensure the AdS asymptotics; for the scalar potential A_t we likewise impose the Dirichlet condition with the boundary value (4). The boundary condition for the dilaton amounts to setting the leading term (proportional to the source) to unity, so that we do not have a spontaneous formation of the scalar condensate, therefore it is again of Dirichlet

---

[5]Note that the next term, $a(x, y)$, is not the charge density as the presence of the lattice makes the boundary integrals obtained in the on-shell action more complicated.

type; the effective mass squared of the dilaton field is $-4\delta^2 V_0$, from the form of the potential V in (2).

The equations of motion are the standard EMD equations, altogether 7 in number – 5 independent components of Einstein equations, one Maxwell equation and one dilaton equation. This matches the 7 independent fields taking into account the C_4 symmetry of the square – $q_{tt}, q_{xx} = q_{yy}, q_{\tilde{z}\tilde{z}}, q_{xy}, q_{x\tilde{z}} = q_{y\tilde{z}}$, plus A_t and Φ. We do not give the equations in human-readable form as the expressions are huge (we keep them as Wolfram Mathematica files). In the next section we give a phenomenological overview of the numerics and the solutions obtained.

2.2 Square ionic lattice – the solution

We solve the equations of motion numerically, with the boundary conditions determined by the coefficients in the expansions (8-12). The resulting system of nonlinear PDEs is integrated by a collocation pseudospectral algorithm on Gauss-Lobatto grid along the radial direction $\tilde{z}$ and on Fourier grid along the transverse directions x, y. Our code is mainly based on [50,51]. In Appendix B we give some more details on the integrator and some test examples. The production runs were performed on a lattice $2N \times 2N \times 2N$ with $N = 16$ but in the Appendix we have checked the convergence of the solution for varying lattice sizes from $N = 6$ to $N = 16$.

Typical solutions for the bulk are given in Figs. 1 and 2 for the matter and gauge fields and in Fig. 3 for components of the metric. The top panel of Fig. 1 shows that indeed the lattice is irrelevant: both fields modulate in UV but in IR the oscillations die out completely. The UV oscillations are of the same form $\cos(2Q\pi x)\cos(2Q\pi y)$ for both A_t and Φ, as we see in the bottom panel. Fig. 2 demonstrates that the scaling solution indeed survives in IR: both fields agree nicely with the analytical predictions for the scaling laws obtained in Eqs. (9-10). The figure is produced for a low temperature $T/Q = 0.1$ so the horizon radius is quite small; for higher temperatures the scaling is not as clear (expectedly, because the relevant scale is then $(r - r_h)/r_h$ rather than r/r_h). Finally, Fig. 3 confirms that the AdS asymptotics are preserved (no oscillations in UV) and that in deep IR the lattice also dies out.

All calculations in Section 4 are performed in this way, with the fully self-consistent PDE solver for the holographic ionic lattice. For mass runs needed for the comparison to the Hubbard model, we have also used approximate methods: averaged equations (multipole expansion) and semiholography (in the narrow sense, introduced in [19] and exploited e.g. in [52]) to gain a first guess at the solution; afterwards we have always confirmed the result through a full lattice calculation. The next two sections are devoted mainly to the full lattice calculation of the spectrum from the probe Dirac equation. In Appendix C we describe the other methods, which we all call semiholographic in the broad sense that one does not solve the full system of equations for the background.

3 Dirac equation for the probe fermion

3.1 The action and the equation of motion

We now come to the computation of the spectral functions. This is perhaps the "cleanest" way of doing bottom-up holography, as the outcome directly determines the density of states and the excitation spectrum of the electron in a given background. This calculation is well-established, both without [21, 22, 24, 25] and with a lattice [7–12]. The basic holographic dictionary entry stemming from the Gubser-Polyakov-Klebanov-Witten prescription [53,54] relates the two-point propagator of the strongly coupled CFT electron to the probe Dirac fermion in AdS. Being a probe, it does not backreact on the other fields and propagates in the fixed
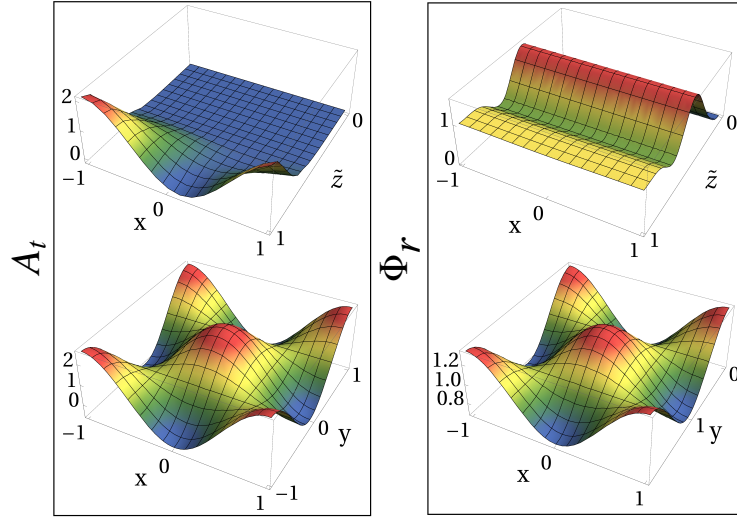
Figure 1: Numerically computed electrostatic field (left) and rescaled dilaton $\Phi_r \equiv \Phi/(1 - \tilde{z}^2)$ (right), along an $x - \tilde{z}$ slice at $y = 0.5$ (top) and along an $x - y$ slice at the AdS boundary $\tilde{z} = 1$ (bottom). Both fields oscillate at the boundary but the oscillation amplitudes rapidly diminish toward the horizon because the ionic lattice is irrelevant in IR. Unlike the rescaled dilaton Φ_r, the physical dilaton Φ does not oscillate at the boundary because the factor $1 - \tilde{z}^2$ kills the oscillations at $\tilde{z} = 1$. The scaling exponents are $(\alpha, \delta) = (-1.5, 1)$ at temperature $T = 0.1$, for $\mu_0 = 1$, $\delta\mu/\mu_0 = 1$ and $Q = 1/2$.

background found in Section 2 for given parameters (α, δ). The probe fermion has charge q, mass m and dipole momentum κ (more on it later). The action again has the bulk and boundary term: $S_f = S_{f\,\text{bulk}} + S_{f\,\text{bnd}}$. The bulk action reads:

$$S_{f\,\text{bulk}} = i \int d^4x \sqrt{-g}\, \bar{\Psi} \left[\frac{1}{2} \left(\overleftarrow{\slashed{D}} + \overrightarrow{\slashed{D}} \right) - m - \frac{i}{2} \kappa \Gamma^{ab} e_a^\mu e_b^\nu F_{\mu\nu} \right] \Psi. \tag{13}$$

Here, Ψ is the Dirac bispinor, $\slashed{D}$ is the covariant derivative determined by the spin connection $\omega_{ab\mu}$ and the gauge field A_μ, and the last term is the coupling of the electron dipole momentum κ with the field strength $F_{\mu\nu}$. Explicitly the covariant derivative reads

$$\slashed{D} = \Gamma^a e_a^\mu \left(\partial_\mu + \frac{1}{4} \omega_{bc\mu} \Gamma^{bc} - iq A_\mu \right). \tag{14}$$

The indices $a, b, c \in \{t, x, y, z\}$ denote the local flat coordinates and $\Gamma^{ab} \equiv \left[\Gamma^a, \Gamma^b \right]/2$. The expressions for the vielbein e_a^μ are quite cumbersome and we list them only as functions of a general metric $g_{\mu\nu}$ with nonzero components $g_{tt}, g_{xx} = g_{yy}, g_{rr}, g_{xy}, g_{xr}$. Inserting all the metric functions in their explicit form would result in expressions which are too cumbersome
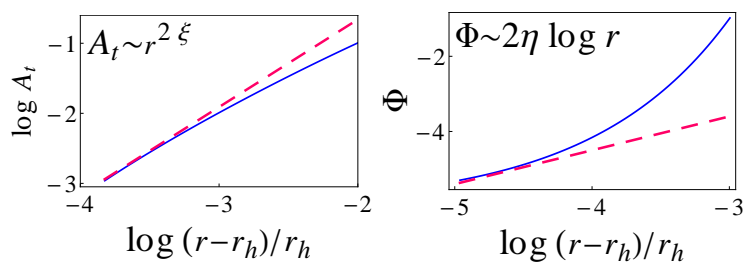
Figure 2: Far-IR scaling of the gauge field A_t (left) and the dilaton Φ (right), as a function of the radial coordinate r (related to $\tilde{z}$ as stated in Eq. (3)), for $(\alpha, \delta) = (-1.5, 1)$ at temperature $T = 0.1$, $\mu_0 = 1$, $\delta\mu/\mu_0 = 1$ and $Q = 1/2$. Full blue curves denote the numerical solution at $x = y = 0.5$ while the red dashed lines are the analytical scaling predictions from (9). Near the horizon the solutions are reasonably close to the scaling ansatz; further away they diverge. For higher temperatures the scaling is less and less prominent.

and not very illustrative:

$$e_t = \sqrt{-g_{tt}}\partial_t, \quad e_x = \sqrt{g_{xx} - g_{xy}}\partial_x + \sqrt{g_{xy}}\partial_r, \quad e_y = \sqrt{g_{xx} - g_{xy}}\partial_y + \sqrt{g_{xy}}\partial_r,$$
$$e_z = a_1\partial_x + a_2\partial_y + (a_3 + \sqrt{g_{rr}})\partial_r,$$
$$a_1 = g_{xr}\frac{\sqrt{g_{xx} - g_{xy}}}{g_{xx} - g_{xy}} + \frac{\sqrt{g_{xy}\left(-2g_{xr}^2 + g_{rr}\left(g_{xx} + g_{xy}\right)\right)}}{g_{xx} + g_{xy}},$$
$$a_2 = \sqrt{g_{xy}},$$
$$a_3 = \frac{2g_{xr}\sqrt{g_{xy}} - \sqrt{g_{rr}}\left(g_{xx} + g_{xy}\right) - \sqrt{g_{xx} + g_{xy}}\sqrt{-2g_{xr}^2 + g_{rr}\left(g_{xx} + g_{xy}\right)}}{g_{xx} + g_{xy}}. \tag{15}$$

To specify the boundary conditions the bulk action $S_{f\,\text{bulk}}$ in (13) needs to be supplemented by a boundary action $S_{f\,\text{bnd}}$. This action encapsulates the choice of standard or alternative quantization and any additional sources on the boundary. We adopt the usual maximally symmetric boundary action of [55, 56] but add the coupling to an external source $\mathcal{D}$ (which may break the Lorentz invariance or some other symmetry):

$$S_{f\,\text{bnd}} = \oint_{\tilde{z}=1-\epsilon} d^3x \sqrt{-h}\left[s\frac{i}{2}\bar{\Psi}_+(t,x,y,\tilde{z})\Psi_+(t,x,y,\tilde{z}) + \bar{\Psi}_-(t,x,y,\tilde{z})i\mathcal{D}\Psi_-(t,x,y,\tilde{z})\right],$$
$$s = -1, \quad \Psi_\pm = \frac{1}{2}\left(1 \pm \Gamma^z\right)\Psi, \tag{16}$$

where $\epsilon \to 0$ is the UV cutoff (computing the action at distance ϵ away from the boundary) and $\mathcal{D}$ is any sufficiently well-behaving function which can be interpreted as the external source of Ψ (in the simplest interpretation it is a kinetic term on the boundary and contains derivatives with respect to t, x, y). The sign in front of the first term, denoted by $s = \mp1$, corresponds to standard/alternative quantization [57]. For now we choose the sign $s = -1$, for the standard quantization, but eventually we will invert the propagator to work in the alternative one. This is equivalent to having a negative fermion mass $-1/2 < m \leq 0$, so we have the conformal dimension given by the usual formula:

$$\Delta = \frac{3}{2} + m. \tag{17}$$

We discuss the choice and physical meaning of $\mathcal{D}$ in subsection 3.3; we will first finish the derivation of the expression for the field theory propagator.
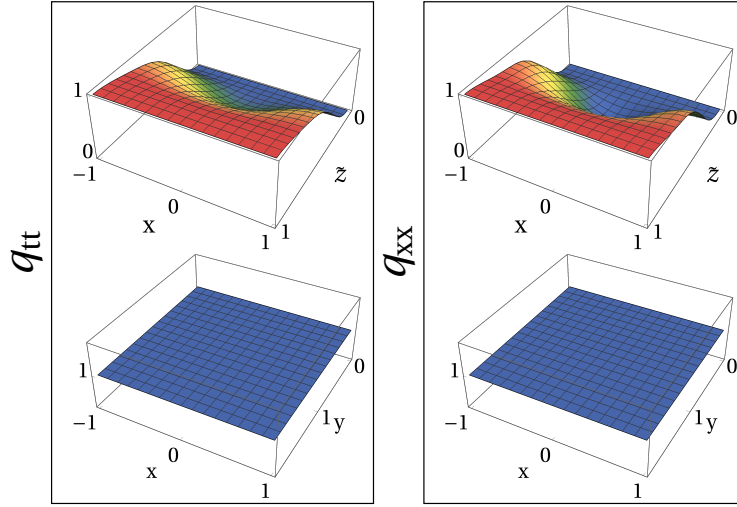
Figure 3: Numerically computed metric components q_{tt} (left) and q_{xx} (right), along an $x-\tilde{z}$ slice at $y = 0.5$ (top) and along an $x-y$ slice at the AdS boundary $\tilde{z} = 1$ (bottom), for the same parameter values as the previous two figures ($(\alpha, \delta) = (-1.5, 1)$, $T = 0.1$, $\mu_0 = 1$, $\delta\mu/\mu_0 = 1$, $Q = 1/2$). The top panels show that the metric becomes homogeneous both for $\tilde{z} = 0$ (there is no lattice in IR) and for $\tilde{z} = 1$ (the UV asymptotics is pure AdS). In the bottom row we show explicitly that the functions $q_{tt}(x, y; \tilde{z} = 1)$, $q_{xx}(x, y; \tilde{z} = 1)$ are flat and equal unity, which provides a sanity check on the numerics. The oscillatory nature of the solution is thus only seen at intermediate $\tilde{z}$ scales.

As usual, we can Fourier-transform the wavefunction from time t to frequency ω. On the other hand, the momentum in the periodic lattice background is only defined up to a Brillouin zone, as determined by the Bloch theorem [9–11]. Therefore, instead of a Fourier transform to the plane wave basis we expand the wavefunction over the Bloch states (plane waves modulated by periodic functions). The periodicity of the Bloch states is fixed by the umklapp vector K, so we have the following expansion for Ψ:

$$
\begin{aligned}
\Psi(t, x, y, \tilde{z}) &= \int \frac{d\omega}{2\pi} \int \frac{d^2\mathbf{k}}{(2\pi)^2} \psi_{\omega\mathbf{k}}(x, y, \tilde{z}) e^{-i\omega t + ik_x x + ik_y y} \\
&= \int \frac{d\omega}{2\pi} \int \frac{d^2\mathbf{k}}{(2\pi)^2} \sum_{n_x=-\infty}^{\infty} \sum_{n_y=-\infty}^{\infty} \psi_{\omega\mathbf{k}}^{(n_x, n_y)}(\tilde{z}) e^{-i\omega t + i(k_x + n_x K)x + i(k_y + n_y K)y} ,
\end{aligned}
\tag{18}
$$

where the Bloch momentum $\mathbf{k} = (k_x, k_y)$ is in the first Brillouin zone: $k_{x,y} \in (-K/2, K/2)$, $n_{x,y}$ are the numbers of the Brillouin zones, and the $\pm$ components of the bispinor are defined analogously to $\Psi_\pm$ in (16):

$$
\begin{aligned}
\psi_{\omega\mathbf{k}}^{(n_x, n_y)}(\tilde{z}) &= \begin{pmatrix} \psi_{\omega\mathbf{k}+}^{(n_x, n_y)}(\tilde{z}) \\ \psi_{\omega\mathbf{k}-}^{(n_x, n_y)}(\tilde{z}) \end{pmatrix}, \\
\psi_{\omega\mathbf{k}}(x, y, \tilde{z}) &= \begin{pmatrix} \psi_{\omega\mathbf{k}+}(x, y, \tilde{z}) \\ \psi_{\omega\mathbf{k}-}(x, y, \tilde{z}) \end{pmatrix} = \sum_{n_x=-\infty}^{\infty} \sum_{n_y=-\infty}^{\infty} \begin{pmatrix} \psi_{\omega\mathbf{k}+}^{(n_x, n_y)}(\tilde{z}) \\ \psi_{\omega\mathbf{k}-}^{(n_x, n_y)}(\tilde{z}) \end{pmatrix} e^{in_x K x + i n_y K y} .
\end{aligned}
\tag{19}
$$

The period K is related to Q as $K = 2\pi Q$. As we see, the wavefunction (and thus the Green function) on the lattice has an infinity of contributions from different Brillouin zones n_x, n_y. We now have all the ingredients for the Dirac equation. At this point we adopt the following

representation of gamma matrices:

$$\Gamma^{\mathrm{t}} = \begin{pmatrix} i\sigma^1 & 0 \\ 0 & i\sigma^1 \end{pmatrix}, \quad \Gamma^{\mathrm{x}} = \begin{pmatrix} -\sigma^2 & 0 \\ 0 & \sigma^2 \end{pmatrix}, \quad \Gamma^{\mathrm{y}} = \begin{pmatrix} 0 & \sigma^2 \\ \sigma^2 & 0 \end{pmatrix}, \quad \Gamma^{\mathrm{z}} = \begin{pmatrix} -\sigma^3 & 0 \\ 0 & -\sigma^3 \end{pmatrix}, \quad (20)$$

we write the two spinors $\psi_{\omega\mathbf{k}\pm}$ as

$$\psi_{\omega\mathbf{k}\pm}(x,y,\tilde{z}) = \begin{pmatrix} a_{\omega\mathbf{k}\pm}(x,y,\tilde{z}) \\ b_{\omega\mathbf{k}\pm}(x,y,\tilde{z}) \end{pmatrix}, \tag{21}$$

and obtain

$$\left(\partial_{\tilde{z}} + \Omega_{\tilde{z}} + \frac{2m\tilde{z}}{1-\tilde{z}^2}\sqrt{\frac{q_{zz}}{f}}\right) a_{\omega\mathbf{k}\pm} + \left(-\Omega_t \pm \Omega_x - \kappa\mathcal{K}\partial_{\tilde{z}}A_t\right) b_{\omega\mathbf{k}\pm} - \Omega_y b_{\omega\mathbf{k}\mp} = 0,$$

$$\left(\partial_{\tilde{z}} - \Omega_{\tilde{z}} - \frac{2m\tilde{z}}{1-\tilde{z}^2}\sqrt{\frac{q_{zz}}{f}}\right) b_{\omega\mathbf{k}\pm} + \left(\Omega_t \pm \Omega_x - \kappa\mathcal{K}\partial_{\tilde{z}}A_t\right) a_{\omega\mathbf{k}\pm} - \Omega_y a_{\omega\mathbf{k}\mp} = 0, \tag{22}$$

$$\Omega_t = \Omega_t(x,y,\tilde{z};\omega), \quad \Omega_{x,y} = \Omega_{x,y}(x,y,\tilde{z};\mathbf{k}), \quad \Omega_{\tilde{z}} = \Omega_{\tilde{z}}(x,y,\tilde{z};\mathbf{k}), \quad \mathcal{K} = \mathcal{K}(x,y,\tilde{z}).$$

We again refrain from writing out in full the (very cumbersome) expressions for the Ω and $\mathcal{K}$ terms which contain also the spin connection; they would not contribute to physical understanding anyway. The result is a linear (partial) differential equation, and thus presents no problems with numerical convergence. At the end of Appendix B we discuss some practicalities concerning the numerical implementation and solution of (22).

So far we have not discussed the dipole coupling term. As we know, the dipole couples to the field strength $F_{\mu\nu}$. This term was proposed in [44] and further explored in [14,45,58–61] and other works. Its action is to simulate a gap in the spectrum. Roughly speaking, it does so by shifting the effective momentum vector $\mathbf{k}$ so that, depending on the dipole strength κ and the position of the Fermi momentum k_F, the quasiparticle is "skipped" and we only have low-intensity incoherent background in some interval of momenta. More elaborate explanations are found in [45,61]: the authors show that the gap arises from the zero-pole duality between the Green functions in standard and alternative quantization. Since the dipole term mixes the leading and subleading mode at the boundary (see later in Eq. (24)), a pole can appear in the denominator of the propagator, i.e. in the self-energy, producing zeros in the spectrum. This is quite in line with the real-world Mott physics where likewise the self-energy diverges, however in order to really understand the relation to Mottness[6] one should certainly put the system on the lattice. We have done so, and we will comment both on the phenomenology of nonzero κ systems and on possible relations to the Mott phase of the Hubbard model.

3.2 Boundary conditions and the Green function

It is well known how to obtain the retarded real-time Green function on the CFT side from the bulk solutions with infalling boundary condition on the horizon.[7] Near-horizon expansion of the equation (22) in the background (7) in the Bloch wave representation (18) yields schematically:[8]

$$\begin{pmatrix} \psi_{\omega\mathbf{k}+}(x,y,r \to r_h) \\ \psi_{\omega\mathbf{k}-}(x,y,r \to r_h) \end{pmatrix} = (r - r_h)^{-\frac{i\omega}{2\pi T}}\left[\begin{pmatrix} \psi^{(0)}_{\omega\mathbf{k}+}(x,y) \\ -i\psi^{(0)}_{\omega\mathbf{k}+}(x,y) \end{pmatrix} + \begin{pmatrix} \psi^{(1)}_{\omega\mathbf{k}+}(x,y) \\ i\psi^{(1)}_{\omega\mathbf{k}+}(x,y) \end{pmatrix}(r - r_h) + \dots\right]. \tag{23}$$

---

[6]There are different views and definitions on what exactly defines Mottness. We understand it mainly as the presence of a gap due to "traffic jam" from the interactions, which is seen as the shift of the spectral weight from high to low frequencies when the doping changes.

[7]Since we are always at finite temperature, the notion of infalling solution is unambiguous. For the analytical near-horizon expansion we use the r coordinate instead of $\tilde{z}$.

[8]Although we have earlier denoted the number of the Brillouin zone by upper indices and now we use the upper indices to count the order of the terms in near-horizon expansion, we believe this will not cause confusion: previously we had a pair of numbers (n_x, n_y) and now just a single number; besides, we have already emphasized that solely the case $n_x = n_y = 0$ is considered throughout the paper.

Therefore, we have one independent spinor at the horizon at both leading ($\Psi_+^{(0)}$) and subleading ($\Psi_+^{(1)}$) order, as it should be. The coefficients $\psi_{\omega\mathbf{k}+}^{(0)}, \psi_{\omega\mathbf{k}+}^{(1)}$ can be determined from the near-horizon expansion of the Dirac equation, providing the Dirichlet boundary condition in the IR. We discuss the IR limit of the Dirac equation in more detail in the next section in order to learn about the scaling of the spectral function and self-energy. For now it suffices to say that (23) provides the IR boundary conditions.

Near the AdS boundary the behavior is universal (for the sake of brevity we do not write explicitly the ω and $\mathbf{k}$ dependence of the UV coefficients $A_\pm, B_\pm$ and the propagators):

$$\begin{pmatrix} \psi_{\omega\mathbf{k}+}(x, y, \tilde{z} \to 1) \\ \psi_{\omega\mathbf{k}-}(x, y, \tilde{z} \to 1) \end{pmatrix} = \begin{pmatrix} B_+(x, y) \\ 0 \end{pmatrix} \left(1 - \tilde{z}^2\right)^{3/2+m} + \begin{pmatrix} 0 \\ A_-(x, y) \end{pmatrix} \left(1 - \tilde{z}^2\right)^{3/2-m} + \dots \quad (24)$$

Inserting the near-boundary expansion into the boundary action (16)[9] we get

$$S_{f\,\text{bnd}} \sim \epsilon^{-3} \left[\frac{1}{2} \bar{B}_+(x, y) A_-(x, y) + \bar{A}_-(x, y) i \mathcal{D} A_-(x, y) \right]. \quad (25)$$

It remains to determine the Green function from this action.

3.2.1 The Green function and its regularization

The holographic dictionary [1] and more specifically the prescriptions of [20, 23, 43, 55, 56], define the Green function in the following way. Since A_- and B_+ are both finite at the boundary for $|m| < 1/2$ (the m values that we compute), there are two possible choices for G_R in field theory, known as the standard and alternative quantization. In the standard quantization, the propagator in absence of the source $\mathcal{D}$ is defined by the ratio of the subleading and the leading branch. In the alternative quantization, the propagator is the inverse of the standard-quantization propagator, i.e. the ratio of the leading and the subleading branch. More precisely, we have:[10]

$$G_R^{\text{std}}|_{\mathcal{D}=0} = i\epsilon^{-2m} B_+ \sigma^1 A_-^{-1}, \quad G_R^{\text{alt}}|_{\mathcal{D}=0} = \left(G_R^{\text{std}}|_{\mathcal{D}=0}\right)^{-1} = -i\epsilon^{2m} A_- \sigma^1 B_+^{-1}. \quad (26)$$

In the presence of the source, the above expression for the standard quantization generalizes in a straightforward way, taking the second variation of the total action (25) with respect to A_-:

$$G_R^{\text{std}} = i\epsilon^{-2m} B_+ \sigma^1 A_-^{-1} + i\epsilon^{-1} \mathcal{D} = G_R^{\text{std}}|_{\mathcal{D}=0} + i\epsilon^{-1}\mathcal{D}. \quad (27)$$

In order to get the Green function in the alternative quantization we keep the relation $G_R^{\text{alt}} = \left(G_R^{\text{std}}\right)^{-1}$ also in the presence of the source, getting from (27):

$$G_R^{\text{alt}} = \left(\left(G_R^{\text{alt}}|_{\mathcal{D}=0}\right)^{-1} + i\epsilon^{-1}\mathcal{D}\right)^{-1}. \quad (28)$$

This prescription is also in accordance with the regularization in [43] and its interpretation in [20]. The term ϵ^{-2m} in (26) is merely the dimensional regulator coming from the scaling of the boundary fermionic operator, and the ϵ^{-1} term in front of $\mathcal{D}$ corresponds to the canonical dimension of the operator $\mathcal{D}$. Here we see the role of the boundary operator $\mathcal{D}$ in the expression for the Green function. Such a nontrivial "source" was first proposed already in [56] and used in [43] to regulate the ω-dependence in order to satisfy the ARPES sum rule. We use it for precisely the same purpose, though we will motivate it in a slightly different way in the

---

[9]The bulk action vanishes on-shell as it is proportional to the Dirac equation.

[10]We write G_R, for the retarded Green function, as this is the one that we compute in this paper; but in fact the expressions for the Green function in terms of boundary values of the bulk fermion are independent of the contour prescription.

next subsection. From now on we will write just G_R instead of G_R^{alt} as we only calculate the alternative quantization.

The last stroke is to implement the above procedure for an inhomogeneous system, where the wavefunction depends on x, y as in (24). In principle, everything could be done just like in Eqs. (26-28), and the result would be a local Green function (depending on the coordinates x, y). But that is not appropriate for a photoemission "experiment": ARPES uses photons in plane wave states, thus we want the Fourier transform of the local propagator to the momentum space. This procedure is discussed in [7, 9–11]. We start from the expansion of $\psi_{\omega \mathbf{k}\pm}(x, y, \tilde{z})$ in terms of $\psi_{\omega \mathbf{k}\pm}^{(n_x, n_y)}(\tilde{z})$ and consequently the expansion of $a_{\omega \mathbf{k}\pm}, b_{\omega \mathbf{k}\pm}$ as

$$
\begin{pmatrix} a_{\omega \mathbf{k}\pm}(x, y, \tilde{z}) \\ b_{\omega \mathbf{k}\pm}(x, y, \tilde{z}) \end{pmatrix} = \sum_{n_x=-\mathcal{N}}^{\mathcal{N}} \sum_{n_y=-\mathcal{N}}^{\mathcal{N}} \begin{pmatrix} a_{\omega \mathbf{k}\pm}^{(n_x, n_y)}(\tilde{z}) \\ b_{\omega \mathbf{k}\pm}^{(n_x, n_y)}(\tilde{z}) \end{pmatrix} e^{in_x K_x + in_y K_y} , \tag{29}
$$

where now $a_{\mathbf{k}\pm}^{(n_x, n_y)}$ and $b_{\mathbf{k}\pm}^{(n_x, n_y)}$ only depend on $\tilde{z}$, with ω and $\mathbf{k}$ having the role of parameters, so these functions satisfy ordinary differential equations, obtained by plugging (29) into (22). We have now truncated the formally infinite expansion in (n_x, n_y) by a finite zone number $\mathcal{N}$. The next step is to expand the UV coefficients $A_\pm, B_\pm$ from (24) analogously to the expansion (29) and to insert them into the Green function in the alternative quantization from (26), getting:[11]

$$
A_\sigma^{(n_x, n_y)}(\omega, \mathbf{k}) = i\epsilon^{-2m} \sum_{\sigma'=\pm} \sum_{n_x=-\mathcal{N}}^{\mathcal{N}} \sum_{n_y=-\mathcal{N}}^{\mathcal{N}} G_{n_x, n_y}^{n_x', n_y'}(\omega, \mathbf{k}) B_{\sigma'}^{(n_x', n_y')}(\omega, \mathbf{k}) . \tag{30}
$$

The Green function thus becomes a matrix with both spinor and Brillouin zone indices. Computing the full matrix for a 2D lattice would be a huge computational job. But the off-diagonal terms (with $n_x' \neq n_x, n_y' \neq n_y$) are usually suppressed, at least for the weak lattice regime defined in Eq. (6); for strong lattices this approximation is of questionable validity. Since we stay in the weak lattice regime, we follow all previous works on ARPES spectra on lattices [7, 9–12] and disregard all off-diagonal terms, putting $(n_x', n_y') = (n_x, n_y)$ in (30) and eliminating the sum over the zone numbers.[12] One might worry that this is a basis-dependent notion but, as pointed out in [9], taking the trace when computing the spectral function eliminates the basis dependence as the trace is an invariant. The source is a plane wave, as in real ARPES experiments, therefore $A_-^{(n_x, n_y)} = 0$ for any $n_x \neq 0$ or $n_y \neq 0$ is the boundary condition for the Dirac equation (the normalization is arbitrary). We then extract the components $B_\pm^{(n_x, n_y)}$ with the cutoff $\mathcal{N} = 2$ and sum them. This yields directly the values of the diagonal terms in G_R. Once G_R is computed in this approximation, the spectral function is obtained as the trace of its imaginary part: $A(\omega, \mathbf{k}) = -\mathrm{Im\,Tr}\, G_R(\omega, \mathbf{k})/\pi$.

We are now ready to state the algorithm for computing the holographic Green function:

1. For chosen parameters (scaling exponents) (α, δ), calculate the background (metric, gauge field, dilaton) by solving numerically the EMD system of equations defined by the action (1).

2. With this background as the input, calculate the wavefunction of the probe fermion by solving numerically the Dirac equation defined by the bulk action (13) and the boundary action (16).

---

[11]For the wavefunctions we have written the ω and $\mathbf{k}$ dependence in the subscript, as the wavefunctions are really functions of coordinates. But for the coefficients of the UV expansion, which do not depend on any coordinate, it is natural to write $\omega, \mathbf{k}$ as function arguments.

[12]Actually, since earlier works on ARPES spectra considered unidirectional lattices, they only had to deal with a single n.

3. From this wavefunction (specifically its behavior at $\tilde{z} \to 1$) as the input, determine the Green function G_R as given in (28).

3.3 A detour – boundary sources and their holographic interpretation

A holographic action may incorporate some boundary source $\mathcal{D}$ as long as it does not violate the action principle and the AdS/CFT dictionary. Such a term is usually interpreted in the semiholographic sense, i.e. as some (typically weakly interacting or free) theory coupled to the strongly interacting holographic system. In [20, 43] the ARPES sum rule was enforced by coupling the holographic fermion to a free fermion of zero mass (with $\mathcal{D}$ being just the kinetic term). We could employ exactly the same recipe to arrive at normalizable spectral functions, however we prefer to choose a slightly different route for two reasons (1) to facilitate the comparison to the Hubbard model later in the paper, we want a faster decay at large ω (2) it is handy to have the source term which at least in principle can itself be obtained from holography. In that case, the source $\mathcal{D}$ is effectively another holographic system (in a different, "auxiliary" AdS space) coupled to the main model only through the boundary coupling.

This subsection is something of a detour – it addresses a technicality which is mainly important for the comparison to the Hubbard model and otherwise not really crucial; it defines a cutoff which (being just a cutoff) could also be introduced by hand; and it is more technical and less related to condensed matter applications than most of the paper. It can thus be skipped on first reading. Now we give a very quick derivation of the cutoff (very quick because the steps and the model itself are long known and we merely employ them in a novel context).

We propose to employ a soft wall model which introduces a dilaton-like scalar φ coupled to the auxiliary fermion χ. Such models have been widely studied in the context of AdS/QCD. In analogy with [62] (although there are many other papers with similar models), we start from the action[13]

$$S_{\mathcal{D}} = i \int d^4 x \sqrt{-g} \, \bar{\chi} \left[\frac{1}{2} \left(\overleftarrow{\slashed{D}} + \overrightarrow{\slashed{D}} \right) - M - \Gamma^0 \Gamma^1 \Gamma^2 \varphi \right] \chi \, . \tag{31}$$

The dilaton φ and the fermion χ are both considered in the probe limit, so the metric of the auxiliary system remains pure AdS. Following [62], we adopt the quadratic dilaton profile $\varphi = \varphi_0 z^2$; we use z as the radial coordinate so the boundary is at $z = 0$ and the interior is at z large. The Dirac equation for χ, written as $\chi = (x_+, x_-, y_+, y_-)$ is now

$$\left(\partial_z \pm \frac{M + \varphi_0 z^2}{z} \right) x_\pm \mp (\omega \mp k_x) x_\mp = 0 \, , \tag{32}$$

and the equation for $y_\pm$ is obtained from the above one by putting $(k_x \mapsto -k_x, \varphi_0 \to -\varphi_0)$. This can be solved analytically in terms of the Tricomi confluent hypergeometric functions $U(a, b, x)$:

$$\chi_\pm(\omega, k, z) = e^{\pm \varphi_0 z^2 / 2} z^{\pm M} U \left(\frac{\omega^2 - k^2}{4\varphi_0}, \frac{1}{2} \pm M, \mp \varphi_0 z^2 \right) . \tag{33}$$

Following the usual recipe – expanding the solutions near $z = 0$ and taking the ratio of the two independent branches of the solution, the propagator of the auxiliary fermion is

$$G_\chi = \mathcal{D} = \frac{\Gamma\left(\frac{\omega^2 - k^2}{4\varphi_0} \right)}{\Gamma\left(\frac{\omega^2 - k^2}{4\varphi_0} + \frac{1}{2} - M \right)} \, , \tag{34}$$

---

[13]The reader might protest that this form of coupling to the dilaton violates the Lorentz invariance. This is true but it is unavoidable: a cutoff in energy only cannot be Lorentz-invariant. On the other hand, a cutoff in both energy and momenta would not be justified, as the momentum is automatically regulated on the lattice. We have employed a similar regulator in a very different context (quantum electron stars) in [63].

with Γ being the usual gamma function. Notice that there is no chemical potential and of course no lattice in auxiliary AdS (the latter fact allows us to assume $k_y = 0$). The function $\mathcal{D}$ has a fast growth with ω for large and positive M. Inserting it into Eq. (28), we see that this in turn means a fast decay of the "physical" (as opposed to auxiliary) Green function G_R. Essentially, $\mathcal{D}$ acts like a regulator, with little influence at low energies but rapidly suppressing the spectral weight for ω large.

Of course, one can also adopt a pragmatic viewpoint and simply introduce a regulator by hand. For the purposes of this paper this is equally valid, however the viewpoint of this subsection may be of interest on its own; it is essentially the implementation of the idea from [64] to couple multiple AdS spaces in order to obtain a model with several different scales.

4 Fermionic spectral functions

We come now to the core of the paper, analyzing the spectral functions of our system as a function of frequency. From now on all dimensionful quantities in the paper are stated in units of the wavevector Q as defined in Eq. (4).

4.1 General phenomenology and the "phase diagram"

Let us first return to the homogeneous Fermi and non-Fermi liquids of [27]. The near-horizon analysis in that paper shows that the crucial parameter is the combination

$$\beta + \gamma = 1 + \frac{\alpha^2 - \delta^2}{4 + (\alpha + \delta)^2}, \tag{35}$$

where α and δ are the exponents of the dilaton potentials in (2) and β, γ are the IR scaling exponents of (10). For $\beta + \gamma > 1$, the imaginary part of the self-energy Σ (obtained by solving the near-horizon effective Schrödinger equation as in [23]) is exponentially small near the Fermi surface $\omega \to 0$ and the quasiparticle pole is stable and long-living. For $\beta + \gamma < 1$, similar analysis in [27] shows that $\mathrm{Im}\Sigma$ is always of order unity, hence there is no sharp quasiparticle. Properties at finite frequencies and of course the lattice effects cannot be described by this simple reasoning, but the above serves to show that we should expect at least two regimes, with and without a sharp quasiparticle peak. Since the combination $\beta + \gamma$ can be varied even with one of the fundamental exponents α, δ fixed, we choose $\delta = 1$ throughout the whole paper and vary α, as well as the fermion dimension Δ (defined in (17)) which characterizes the fermionic operator in field theory (not the background). For $\delta = 1$, the critical value $\beta + \gamma = 1$ is reached for $\alpha = -1$:[14]

$$\delta = 1 \Rightarrow \beta + \gamma = 1 + \frac{\alpha^2 - 1}{4 + (\alpha + 1)^2}, \tag{36}$$

so we will use the notation $\beta + \gamma > 1$ and $\alpha < -1$ interchangeably. Therefore, all our "phase diagrams" will be $\alpha - \Delta$ diagrams, keeping the fixed value of δ. We put "phase diagram" under quotation marks as we have not checked the free energy and there is no reason to believe that any sharp phase transition happens (indeed, Δ cannot influence thermodynamic phases at all as it is a probe parameter).

From now on we work on the lattice with $\delta\mu/\mu_0 = 0.5$ unless specified otherwise and express all quantities in units of μ_0. Numerical results (soon to be shown in detail) show two key phenomena (at least for some (α, Δ)) values: quasiparticle peaks and broad bumps at

---

[14]Remember that $\alpha < 0$.
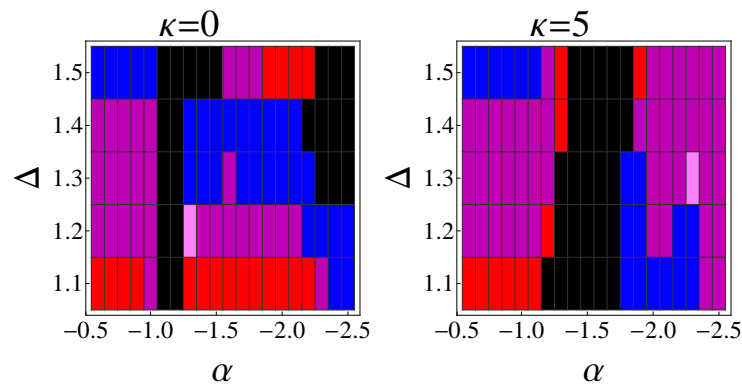
Figure 4: Presence of a coherent quasiparticle (QP) or a gap between the central peak and the Hubbard bands, as a function of the background exponent α and the conformal dimension of the probe fermion Δ, for no dipole coupling (left) and for strong dipole coupling (right): black – no QP and no gap, blue – QP only, red – gap only, violet – QP and the gap. Speaking very roughly, the violet regions correspond to Mott-like and Hubbard-like physics, where a more or less coherent central QP peak is surrounded by but well-separated from intermediate-frequency bands. The clear and deep local minima of the fit to quantum Monte Carlo solutions of the Hubbard lattice, denoted by light pink fields, are both located within the violet (QP+bands) regions. We will refer to this last feature again in Section 5 when discussing the Hubbard fit.

finite energy (to the left and to the right from $\omega = 0$). These finite-frequency maxima are separated from the central maximum around $\omega = 0$ by soft gaps; we call them (Hubbard-like) bands but one should bear in mind that the actual physics might be very different from the bands in the Hubbard Hamiltonian (running a bit forward, it still has to do with umklapp but in detail it is certainly different from Hubbard bands). The key property of the bands is precisely the soft gap (usually the spectral weight does not drop exactly to zero) separating them from the low-frequency part. In Fig. 4 we map the areas with a quasiparticle and/or a gap between the central peak and at least one of the bands (upper or lower). The central peak may be a quasiparticle or just a broad maximum, and the criterion for the gap is that there is a point (or an interval) at finite ω where the spectral weight $A(\omega, \mathbf{k})$ is exponentially low compared to the ratio of the peak maximum to the "background" value of the spectral function. For a Fermi liquid, this ratio grows roughly as T^2 so this essentially means that the gap has to be exponentially suppressed in inverse temperature (squared); for a non-Fermi liquid, it is harder to estimate the temperature scaling but it still makes sense to require that the gap be exponentially small in peak height.[15]

The general structure of different "phases" is seen in Fig. 5, containing the numerical EDCs for three backgrounds ($\alpha = -0.6, -1.1, -2.5$), each for a range of conformal dimensions and for now with $\kappa = 0$. As we have predicted, the gaped spectrum for $\alpha = -0.6$ (left panel) develops a sharp quasiparticle peak for increasing Δ, whereas the gapless spectrum of $\alpha = -2.5$ loses a coherent quasiparticle as Δ grows (right panel). In the central panel we show the case

---

[15]At this place we should comment on how we differentiate between quasiparticles and finite-width peaks ("bumps"). The ultimate criterion (in absence of good analytic insight) is to compute the spectral function, in the bottom half of the complex ω plane – then one can directly see the pole and differentiate it from a branch cut. However, such a calculation was too demanding for our present work (it requires a large number of points and the convergence becomes progressively worse as we increase the magnitude of the imaginary part of ω). Therefore, we have simply scanned the peak in real ω with increasing resolution, and decided we have the quasiparticle if the peak width is at most $O(1)$ times the temperature T. This is not quite satisfying but is apparently the only choice in absence of firm analytic results.
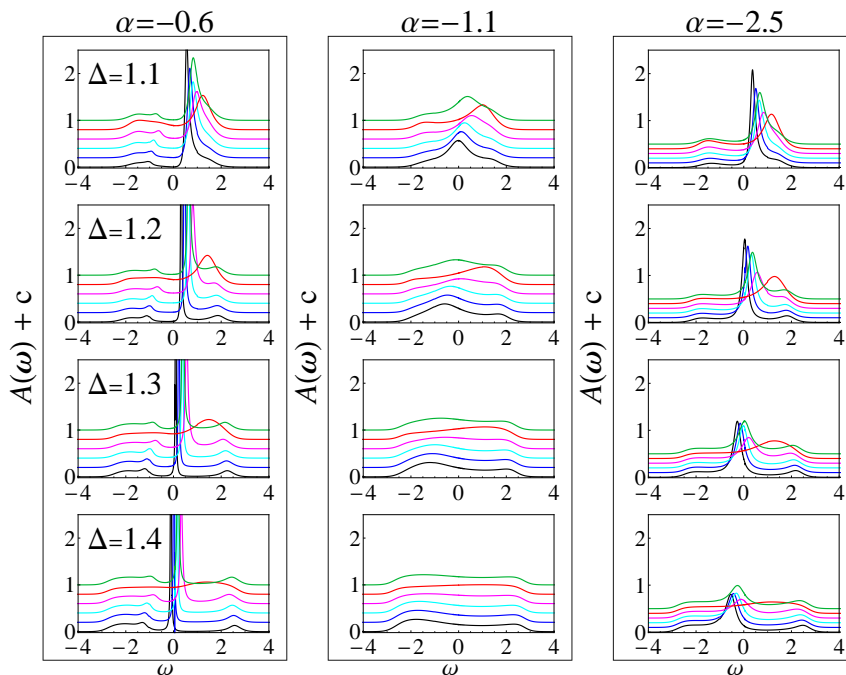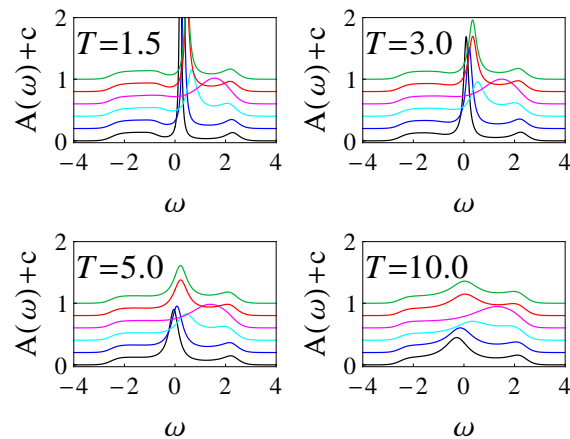
Figure 5: Energy spectra for six standard momentum values, taken along the high-symmetry path ΓXMΓ ((0,0) black, $(\pi/2, 0)$ blue, $(\pi, 0)$ cyan, $(\pi, \pi/2)$ magenta, (π, π) red, $(\pi/2, \pi/2)$ green), for three different backgrounds with $\alpha = -0.6, -1.1, -2.5$, each for four conformal dimensions. In the first case, the sharp peak and the gap between the peak and the bands are both present; in the second case, the spectrum only has a broad and featureless maximum, and in the third there is again a quasiparticle but without a clear gap separating it from the bands. We shift the spectral curves by a constant c for each subsequent momentum value for easier viewing.

with a featureless spectrum of $\alpha = -1.1$. Notice that the peak is in general asymmetric so the quasiparticle is not of Fermi liquid type.[16] In this and subsequent figures we give the EDCs for six momenta placed along the ΓXMΓ (high-symmetry) path for the square lattice: $(0,0)$, $(\pi/2, 0)$, $(\pi, 0)$, $(\pi, \pi/2)$, (π, π) and $(\pi/2, \pi/2)$; we call this the standard momentum set.

Temperature dependence of the EDCs is shown in Fig. 6 for the standard set of momenta and in Fig. 7 in the full $\omega - \mathbf{k}$ plane. The quasiparticle melts away upon heating the system, but we know that just had to happen. More interesting is the fact that the bands (soft bumps away from $\omega = 0$) also become almost indistinguishable for $T = 10$. This scale is higher than in the Hubbard model, where $T \sim 1$ is already a high-temperature regime, whereas here such regime only kicks in an order of magnitude later. We will have more to say on this matter when directly comparing to the Hubbard model (EDC actually converges toward a Gaussian at high T). In conclusion, the generic square lattice hyperscaling-violating model shows some essential features of Hubbard-Mott physics *in its single-particle spectra* (we do not know yet about transport and multi-particle operators): non-Fermi liquid (anomalously-

---

[16]In general, it is the asymmetry of momentum distribution curves (MDCs) that provides a litmus test for non-Fermi liquids, not the asymmetry of EDCs. However, it is known [26,27] that in the context of EMD models of our type Fermi liquid behavior always goes hand-in-hand with symmetric EDCs. In fact, this is known to be true in absence of lattice, but our weak binding analysis in subsection 4.2 extends this also to weak lattices. In Appendix D we show examples of MDCs which are indeed asymmetric, providing stronger evidence for the existence of the non-Fermi liquid phase. Finally, the asymmetry of the EDC peak only makes sense sufficiently near the Fermi surface; further away, the quasiparticle loses coherence anyway and we can say very little about its expected shape.

Figure 6: The EDC curves for six standard momentum values along the high-symmetry path ($(0,0)$ black, $(\pi/2, 0)$ blue, $(\pi, 0)$ cyan, $(\pi, \pi/2)$ magenta, (π, π) red, $(\pi/2, \pi/2)$ green), for a range of high temperatures, for $\mu_0 = 2.5, \alpha = -1.8, \Delta = 1.3$. As could be expected, the quasiparticle melts away and both the upper and lower band merge with the remnants of the quasiparticle. It can be shown (Section 5) that the high-temperature limit is just a single broad Gaussian peak.

scaling) quasiparticles which can be long- or short-living and Hubbard-like bands. Now we will explore the influence of dipole coupling on the system.

A robust feature seen in the first (lowest T) panel in Fig. 7, present also in single EDCs in Fig. 5 but perhaps not so obvious is that the quasiparticle changes intensity and sharpness as we move along the high-symmetry path in the momentum cell: around (π, π) there is a drastic weakening of the quasiparticle. This feature is robust and stays there for different resolutions and parameters. In subsection 4.2 we will show that this is a consequence of umklapp in the self-energy and thus should be regarded as a generic feature of hyperscaling-violating systems on a lattice. It remains to see if this behavior can be related to real-world systems.

4.1.1 Dipole coupling and Mott-like physics

In absence of lattice the dipole coupling opens a gap at low frequencies, destroying the quasiparticle and leading to a Mott-like spectrum, as we already commented from the results of [14, 44, 45, 59–61]. But that mechanism crucially depends on shifting the effective momentum *and* on the zero-pole duality in the spectrum. While the latter remains true on the lattice, the former mechanism will likely work in a different way. Indeed, the mixing of modes from different Brillouin zones shifts the gap to *finite* frequencies – the net result being not a Mott gap around $\omega = 0$ but a gap separating the low-energy peak from higher enegies. If we already have a soft gap there (when $\kappa = 0$), the result is a rather hard gap. This generally brings the spectrum closer to the Hubbard-Mott physics, but in some cases, in absence of quasiparticle, the hard gap actually hinders the transfer of the spectral weight from the central peak to the bands, killing the quasiparticle (Fig. 8).

What we said above holds for lower values of the dipole coupling κ. For stronger couplings, the gap both hardens and *broadens* and for some α values eventually encompasses also the Fermi surface, i.e. the zero of energy. In this regime (Fig. 9) we approach a Mott insulator, eliminating the central broad peak that we had in the non-quasiparticle regime at low κ (though the peak may still be present for some momenta, thus the system is not yet fully insulating). In Fig. 10 we show the action of κ also in a full $(\omega, \mathbf{k})$ density plot of the spectrum – we see both the hardening of the gap and the sharpening of the central peak. Crucially, the
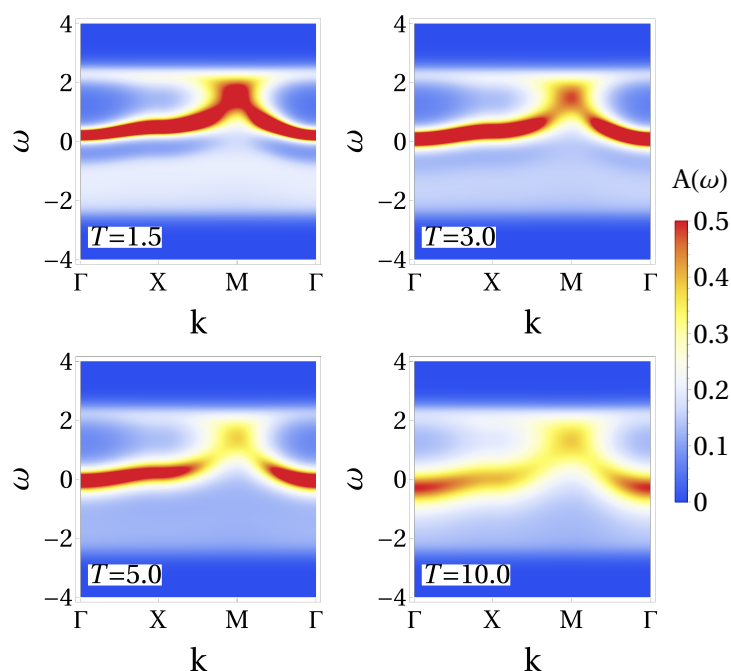
Figure 7: Same as in Fig. 6 but here with full $\omega - \mathbf{k}$ dispersion plots, to better appreciate the evolution of the spectrum with temperature.

weakening of the quasiparticle near (π, π) is less prominent and the central peak is in general less momentum-dependent: this brings the system more in line with the conventional wisdom (but takes away an interesting feature which is physical and might have its place in nature).

Having explored in the main the dependence of the spectrum on proxy interactions (α, Δ, κ), let us look how the spectrum reacts to doping (chemical potential). In Fig. 11 we increase the chemical potential, shifting the maximum of the spectral weight from $\omega < 0$ (black) to $\omega \approx 0$ corresponding to a Fermi surface of a metal (blue) to $\omega > 0$ (red), for two backgrounds and for zero or nonzero dipole coupling. This is maybe the best (although still shaky) argument toward the interpretation of κ as a source of Mottness on the holographic lattice.[17] In absence of dipole coupling, increased doping (chemical potential) just pushes the system toward a quasiparticle regime (left panel); this may also happen for nonzero coupling (central panel) but in the appropriate place in the (α, Δ) diagram we witness just a prominent lower band and a much smaller upper band with no quasiparticle, a possible signature of Mottness (right panel). Finally, we note that other bulk mechanisms (probe fermion self-interactions) have also been proposed as a source of Mottness [65]; we have not explored them in this work.

4.2 Perturbative analysis and matching for the holographic lattice

In this subsection we will write down the weak binding perturbation theory in the two limits (UV and IR) for the bulk Dirac equation in the hyperscaling-violating background. Essentially, we follow the approach of Hong Liu and coworkers in [23] but now in a periodic potential. A similar calculation was done in great detail in [4] for 1D probe lattice superimposed on the Reissner-Nordstrom background. We follow essentially the same logic. On one hand, our task is more difficult as the lattice is 2D and the geometry is much more complicated; on the other hand, since the lattice is a subleading (irrelevant) perturbation in the IR, the IR equations are

---

[17]In absence of lattice, as we mentioned, the situation is simpler and earlier works present a rather complete picture on how this works.
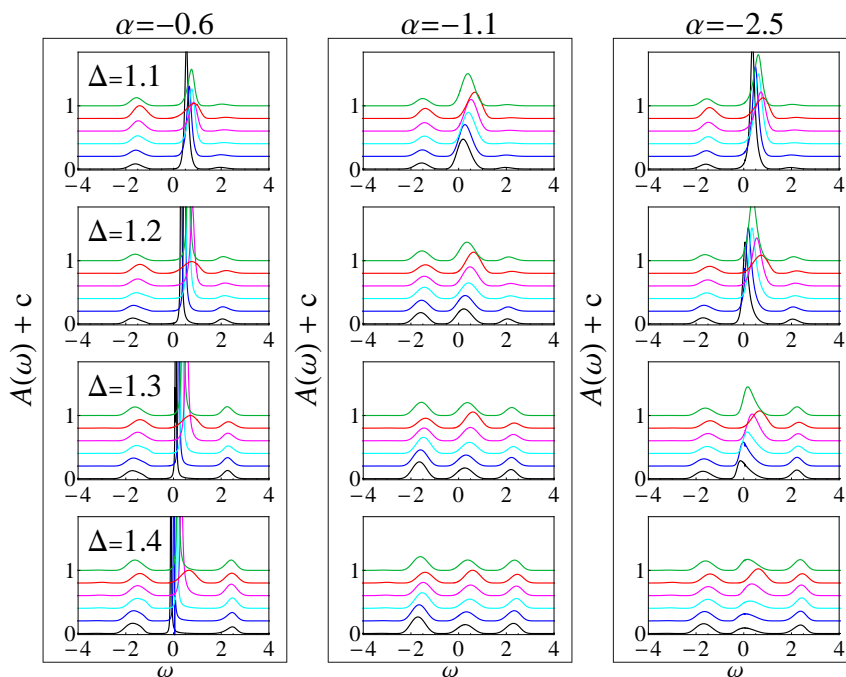
Figure 8: Energy spectra for the same (standard) momenta, scaling exponents and conformal dimensions as in Fig. 5 but with a nonzero dipole coupling $\kappa = 1.5$. The main effect of not very large κ is to harden the gap between the central peak/quasiparticle and the bands. This is reminiscent of Hubbard and similar microscopic models, and can be explained as a combination of momentum shift introduced by κ and the nonmonotonic ω dependence of the umklapp terms in the self-energy (see subsection 4.2).

somewhat simplified (though we still have the mixing of different Brillouin zones). We set the dipole coupling to zero in this subsection.

The basic idea is simply to expand the coefficients of the Dirac equation (22) in the (x, y)-dependent perturbation (proportional to $\delta\mu/\mu_0$ as a small parameter) and then to transform to the basis of Bloch states. We keep the notation from (18,19,21) with the additional convention that we write $\mathbf{n}$ for (n_x, n_y). The components of the Dirac bispinor (22) are then written as

$$\psi^{(\mathbf{n})} \equiv \left(a_+^{(\mathbf{n})}, b_+^{(\mathbf{n})}, a_-^{(\mathbf{n})}, b_-^{(\mathbf{n})} \right), \tag{37}$$

so for example $a_+^{(\mathbf{n})}$ stands for $a_+(\mathbf{k} + 2\pi\mathbf{n}Q)$ with $\mathbf{k}$ from the first Brillouin zone.

Let us start from the AdS boundary and use the coordinate r, related to $\tilde{z}$ as in (3). From the expansion (12), we know that the metric functions $q_{\mu\nu}$ and the dilaton are constant up to second order in $1/r$ (the boundary is at $r = \infty$). Of course, the modulation of the chemical potential is relevant and present already at leading order. For a weak lattice as in Eq. (6), we can expand the coefficients of the Dirac equation both in $1/r$ (UV expansion) and in $\delta\mu/\mu_0$ (weak binding expansion); the fermionic wavefunction is likewise expanded in $\delta\mu/\mu_0$.
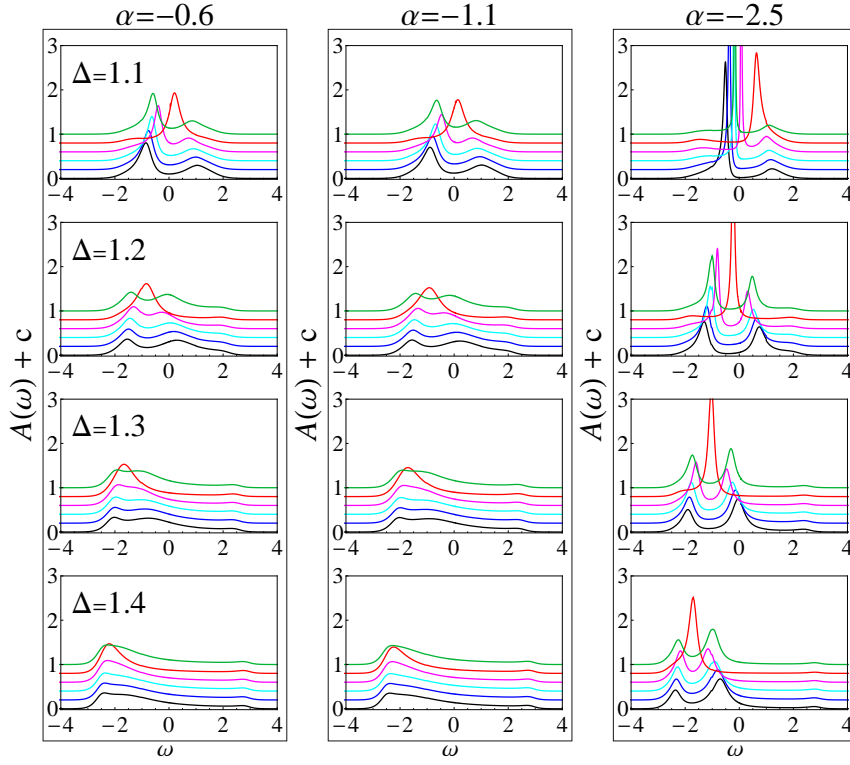
Figure 9: Energy spectra for the same (standard) momenta, scaling exponents and conformal dimensions as in Fig. 5 but with a strong dipole coupling $\kappa = 5$. Here the effect is different and more drastic than for $\kappa = 1.5$ in Fig. 8: the suppression of the spectral weight now encompasses also the Fermi surface and its vicinity (the region around $\omega = 0$), so the quasiparticle either disappears or splits into two. In this regime the dipole coupling overrides the umklapp and opens a broad gap.

The expansions for A_t and ψ read:

$$A_t^{(\mathbf{n})}(r) = \bar{A}_t^{(\mathbf{n})}(r) + \delta A_t^{(\mathbf{n})}(r), \tag{38}$$

$$\bar{A}_t^{(\mathbf{n})}(r) = \mu_0 \delta_{\mathbf{n}} \left(1 - \frac{1}{r} + \ldots \right), \tag{39}$$

$$\delta A_t^{(\mathbf{n})} = \left(\frac{\delta\mu}{\mu_0} \right) \frac{\mu_0}{4} \delta_{|n_x|-1} \delta_{|n_y|-1} \left(1 - \frac{1}{r} + \ldots \right), \tag{40}$$

$$\psi^{(\mathbf{n})}(\mathbf{k}, r) = \psi_{(0)}^{(\mathbf{n})} + \left(\frac{\delta\mu}{\mu_0} \right) \psi_{(1)}^{(\mathbf{n})} + \left(\frac{\delta\mu}{\mu_0} \right)^2 \psi_{(2)}^{(\mathbf{n})} + \ldots \tag{41}$$

Of course, $\delta_{\mathbf{n}}$ stands for the product of Kronecker deltas $\delta_{n_x} \delta_{n_y}$. The UV Dirac equation at leading order in $\delta\mu/\mu_0$ includes the zero- and first-order terms, so it can be solved hierarchically by obtaining $\psi_{(0)}^{(\mathbf{n})}$ first (this is just the homogeneous solution at the boundary) and plugging it in the first-order equation to obtain $\psi_{(1)}^{(\mathbf{n})}$:

$$\left(\partial_r + \frac{m}{r} \right) a_{\pm(1)}^{(\mathbf{n})} - \frac{\omega \mp k_x + q\bar{A}_t}{r^2} b_{\pm(1)}^{(\mathbf{n})} - \frac{k_y}{r^2} b_{\mp(1)}^{(\mathbf{n})} = \frac{q\delta\mu}{4r^2} \sum_{\mathbf{n}'} b_{\pm(0)}^{(\mathbf{n}')},$$

$$\left(\partial_r - \frac{m}{r} \right) b_{\pm(1)}^{(\mathbf{n})} + \frac{\omega \pm k_x + q\bar{A}_t}{r^2} a_{\pm(1)}^{(\mathbf{n})} - \frac{k_y}{r^2} a_{\mp(1)}^{(\mathbf{n})} = \frac{q\delta\mu}{4r^2} \sum_{\mathbf{n}'} a_{\pm(0)}^{(\mathbf{n}')}, \tag{42}$$

where $\mathbf{n}' \in \{(n_x + 1, n_y + 1), (n_x + 1, n_x - 1), (n_x - 1, n_x + 1), (n_x - 1, n_y - 1)\}$.
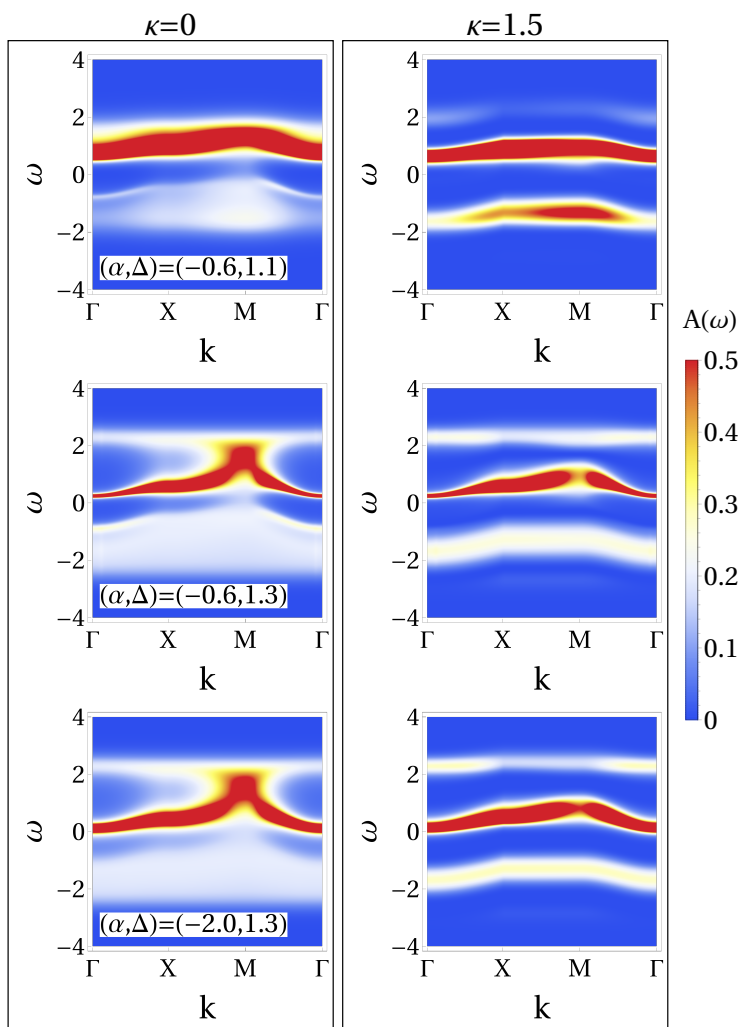
Figure 10: A set of density plots comparing the $\kappa = 0$ and $\kappa = 1.5$ spectra for a range of (α, Δ) values. From first to last row the central peak evolves from a wide bump to a sharp peak, and the role of the dipole coupling (second column) is to keep the side bands well-defined and separated from the center. The weakening of the quasiparticle near the M point is less prominent with nonzero dipole coupling.

The right-hand side of the above equation, i.e. the source terms are the terms which mix different zones. After solving for $\psi_{(1)}^{(\mathbf{n})}$ we can analogously obtain the next approximation and so forth, mixing the modes from more and more zones (in Eq. (42) we have only written the first equation of the infinite hierarchy). Since the mixing of different zones only appears in the sources, the solution to any order has the same form as in Eq. (24). This was already noticed in [4] – the UV side is easy to write down.

The IR region is subtler. Despite the fact that the leading periodic corrections only appear in the second order expansion of the bulk fields, in the Dirac equation they show up at leading order already, because its coefficients mix various terms from the scaling ansatz (8) for the background. Expanding in $r - r_h$ and $\delta\mu/\mu_0$, we end up with an equation of the same form as (42), with higher order terms mixing different modes, but the coefficients and the radial dependence are more complicated. For later use it is convenient to rewrite the equation in the Schrödinger form:

$$\left(\hat{I}_{4\times 4}\partial_r^2 + \hat{M}_1\partial_r + \hat{M}_0\right)\psi_{(1)}^{(\mathbf{n})} = \mathcal{S}_{(0)}^{(\mathbf{n})}. \tag{43}$$
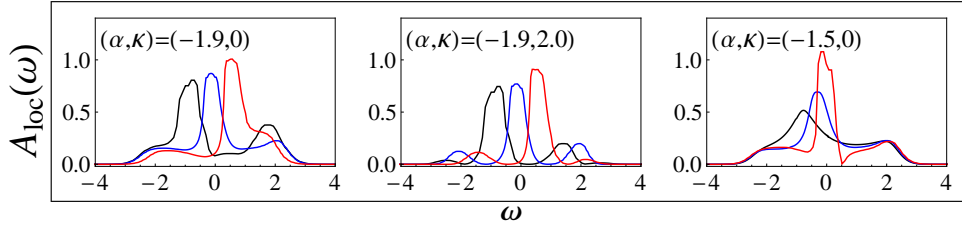
Figure 11: Local (momentum-integrated) spectral weight at frequency ω denoted by $A_{\text{loc}}(\omega)$ for three interesting cases: metallic phase without (left) and with (center) dipole coupling, for $\alpha = -1.9$, and the transition toward a Mott-insulator-like phase (right), for $\alpha = -1.5$ and no dipolar coupling. All cases are for $\Delta = 1.2$ and for three chemical potentials (dopings), in black, blue and red respectively: $\mu_0 = 0.81, 2.10, 2.70$ (left and center), $\mu_0 = 1.35, 1.70, 2.10$ (right). In the first two figures, we see the central, quasiparticle-like peak moving toward the upper band as the doping is increased; the figure with nonzero κ has gaps separating the quasiparticle from the bands as we already expect. In the rightmost figure, the quasiparticle is absent for low chemical potentials/dopings (black, blue); increasing the doping from black to blue curve does not produce a quasiparticle but just a spectral weight transfer from low to high frequencies. This signals that the system is approaching the insulating phase (but is not insulating yet because there is no gap in the center). All local spectra are obtained by inverse-Fourier-transforming the momentum-space spectra on a 4x4 grid of points in momentum space.

The source $\mathcal{S}$ mixes different Bloch waves:

$$\mathcal{S}_{(0)}^{(\mathbf{n})} = \left(E_{tt}^{(2)} \frac{\omega^2}{C_a^6 r^{6\gamma}} - E_{xx}^{(2)} \frac{k_x^2 + k_y^2}{C_a^2 r^{4\beta+2\gamma}} \right) \sum_{\mathbf{n}'} \psi_{(0)}^{(\mathbf{n}')}, \tag{44}$$

and the coefficients $\hat{M}_1, \hat{M}_2$ read

$$\hat{M}_1 = \begin{pmatrix} \frac{2\gamma\omega r^\beta + (\beta+\gamma)C_a k_x r^\gamma}{\omega r^{\beta+1} + C_a k_x r^{\gamma+1}} & 0 & 0 & -\frac{k_y}{C_a r^{\beta+\gamma}} \\ 0 & \frac{2\gamma\omega r^\beta - (\beta+\gamma)C_a k_x r^\gamma}{\omega r^{\beta+1} - C_a k_x r^{\gamma+1}} & -\frac{k_y}{C_a r^{\beta+\gamma}} & 0 \\ 0 & -\frac{k_y}{C_a r^{\beta+\gamma}} & \frac{2\gamma\omega r^\beta - (\beta+\gamma)C_a k_x r^\gamma}{\omega r^{\beta+1} - C_a k_x r^{\gamma+1}} & 0 \\ -\frac{k_y}{C_a r^{\beta+\gamma}} & 0 & 0 & \frac{2\gamma\omega r^\beta + (\beta+\gamma)C_a k_x r^\gamma}{\omega r^{\beta+1} + C_a k_x r^{\gamma+1}} \end{pmatrix}, \tag{45}$$

$$\hat{M}_0 = \begin{pmatrix} \frac{\omega^2}{C_a^4 r^{4\gamma}} - \frac{k_x^2}{C_a^2 r^{2\beta+2\gamma}} & 0 & \frac{\omega k_y}{C_a^3 r^{\beta+3\gamma}} + \frac{k_x k_y}{C_a^2 r^{2\beta+2\gamma}} & \frac{(\beta-\gamma)\omega k_y}{C_a \omega r^{\beta+\gamma+1} + C_a^2 k_x r^{2\gamma+1}} \\ 0 & \frac{\omega^2}{C_a^4 r^{4\gamma}} - \frac{k_x^2}{C_a^2 r^{2\beta+2\gamma}} & \frac{(\beta-\gamma)\omega k_y}{C_a \omega r^{\beta+\gamma+1} - C_a^2 k_x r^{2\gamma+1}} & -\frac{\omega k_y}{C_a^3 r^{\beta+3\gamma}} + \frac{k_x k_y}{C_a^2 r^{2\beta+2\gamma}} \\ \frac{\omega k_y}{C_a^3 r^{\beta+3\gamma}} - \frac{k_x k_y}{C_a^2 r^{2\beta+2\gamma}} & \frac{(\beta-\gamma)\omega k_y}{C_a \omega r^{\beta+\gamma+1} - C_a^2 k_x r^{2\gamma+1}} & \frac{\omega^2}{C_a^4 r^{4\gamma}} - \frac{k_x^2}{C_a^2 r^{2\beta+2\gamma}} & 0 \\ \frac{(\gamma-\beta)\omega k_y}{C_a \omega r^{\beta+\gamma+1} + C_a^2 k_x r^{2\gamma+1}} & -\frac{\omega k_y}{C_a^3 r^{\beta+3\gamma}} - \frac{k_x k_y}{C_a^2 r^{2\beta+2\gamma}} & 0 & \frac{\omega^2}{C_a^4 r^{4\gamma}} - \frac{k_x^2}{C_a^2 r^{2\beta+2\gamma}} \end{pmatrix}. \tag{46}$$

The coefficients $E_{tt}^{(2)}$ and $E_{xx}^{(2)}$ in the source term are the expansion coefficients of the metric, given in Eqs. (A.7) in Appendix A. Fortunately, we will not need their explicit form neither in the source nor in the matrices $\hat{M}_1, \hat{M}_0$; we are just interested in the general structure of the self-energy.

From now on we employ the WKB approximation (this was also done in [27] in absence of lattice) for two reasons (1) the scaling of elements of the coefficient matrix $\hat{M}_0$ is such that they usually give a deep potential well, hence we expect to have many bound states and high quantum numbers, precisely the regime where WKB applies (2) it is difficult to make

any analytical progress without WKB because the equations are so complicated. Introducing the tortoise coordinate s in the usual way [23–25] and equating the coefficient of the first derivative $\partial_s \psi$ to zero, we arrive at the condition:

$$\det\left(\hat{I}_{4\times4} + \frac{\partial s/\partial r}{\partial_r(\partial s/\partial r)}\hat{M}_1\right) = 0,\tag{47}$$

which determines the tortoise coordinate as a function of r. In our case, keeping only the leading scaling term in r, we get $s(r) \sim r^{2C_a\gamma}$. This gives the Schrödinger equation in the tortoise coordinate, with no first-derivative term:

$$\left(\partial_s^2 - \left(\frac{\partial r}{\partial s}\right)^2 \hat{M}_0\right)\psi_{(1)}^{(\mathbf{n})} = \left(\frac{\partial r}{\partial s}\right)^2 \mathcal{S}_{(0)}^{(\mathbf{n})}.\tag{48}$$

The solution in the classically allowed region is expressed in terms of the WKB momentum p:

$$\det\left(p^2\hat{I}_{4\times4} + \left(\frac{\partial s}{\partial r}\right)^2\hat{M}_0\right) = 0 \Rightarrow p \sim r^{-\beta}\sqrt{\omega^2 r^{2\beta} - (k_x^2 + k_y^2)r^{2\gamma}},\tag{49}$$

$$\psi_{(0)\text{IN/OUT}}^{(\mathbf{n})} = \frac{1}{\sqrt{p}}e^{\pm i\int p\,dr}.\tag{50}$$

The two solutions above, with $\pm$ in the exponent, are just the incoming and the outgoing solution at the horizon – the two independent solutions of the IR Schrödinger equation. For the IN solution the integration limits in (50) are $\int_{r_h}^{r}dr$ and for OUT they are $\int_{r}^{\infty}dr$. For the next step we again follow [4] and solve the inhomogeneous equation by definition: we write down the bulk-to-bulk propagator and integrate it over the source. Expressing the bulk-to-bulk propagator from the solutions (50) and their Wronskian W as

$$G_{\text{bulk}}(r,r') = \frac{1}{W}\left[\psi_{(0)\text{IN}}^{(\mathbf{n})}(r)\psi_{(0)\text{OUT}}^{(\mathbf{n})}(r')\Theta(r'-r) - \psi_{(0)\text{IN}}^{(\mathbf{n})}(r')\psi_{(0)\text{OUT}}^{(\mathbf{n})}(r)\Theta(r-r')\right],\tag{51}$$

we write $\psi_{(1)}^{(\mathbf{n})}(r) = \int dr' G_{\text{bulk}}(r,r')\mathcal{S}_{(0)}^{(\mathbf{n})}(r')$ and restrict the integration to the ϵ neighborhood of the horizon (we are deliberately sketchy here as [4] contains a detailed discussion). When everything is said and done and when we match the UV solution and read off the field theory propagator G_R from (28), we obtain

$$G_R^{(\mathbf{n})} \sim \frac{1}{\omega - v_F k_\perp - i\text{Im}\Sigma^{(\mathbf{n})}}, \qquad k_\perp \equiv |\mathbf{k} - \mathbf{k}_F|,\tag{52}$$

$$\text{Im}\Sigma^{(\mathbf{n})} \sim e^{-2I^{(\mathbf{n})}} + \tilde{k}^2\left(\sum_{\mathbf{n}'}e^{-2I^{(\mathbf{n}')}}\right) + \tilde{k}^4\left(\sum_{(n'_x,n''_y)}e^{-2I^{(n'_x,n''_y)}}\right) + \tilde{k}^4\left(\sum_{(n''_x,n'_y)}e^{-2I^{(n''_x,n'_y)}}\right)$$

$$+ \tilde{k}^4\left(\sum_{\mathbf{n}''}e^{-2I^{(\mathbf{n}'')}}\right) + \dots\tag{53}$$

$$\tilde{k}^2 \equiv \frac{\delta\mu}{\mu_0}\left(E_{tt}^{(2)}\frac{\omega^2}{C_a^6 r_h^{6\gamma}} + E_{xx}^{(2)}\frac{k^2}{C_a^2 r_h^{4\beta+2\gamma}}\right).\tag{54}$$

In the first line, the expansion around the Fermi surface at $\omega = 0$ and the Fermi momentum $\mathbf{k}_F$ obviously assumes that a sharp Fermi surface exists; this is true if bound states exist in the effective Schrödinger potential [46]. By I we denote the integral of the WKB momentum appearing in (50) which, from (49) scales as

$$I \sim \frac{|\mathbf{k}|^{\frac{2\gamma-1}{\gamma-\beta}}}{\omega^{\frac{\beta+\gamma-1}{\gamma-\beta}}},\tag{55}$$

and the notation $\mathbf{n}', \mathbf{n}'', (n'_x, n''_y)$ and the like is hopefully clear: in $\mathbf{n} \equiv (n_x, n_y)$ we have the lattice momentum $(k_x + 2\pi n_x Q, k_y + 2\pi n_y Q)$, in $\mathbf{n}'$ the momenta are shifted from $\mathbf{n}$ by $(\pm 1, \pm 1)$, in $\mathbf{n}''$ the shift is $(\pm 2, \pm 2)$, in (n'_x, n''_y) the possible shifts are $(\pm 1, \pm 2)$ and so on.

The above expression for the self-energy is the main analytical result of our perturbative expansion. So how does the peak width scale with frequency? In absence of lattice, only the first term in (53) survives and from (55) we come back to the conclusion of [27] that the self-energy is exponentially small at small ω if the exponent $\beta + \gamma - 1$ is positive (i.e. if $\alpha < -1$), or else it is always of order unity, even at $\omega = 0$, and there is no sharp quasiparticle. But upon adding the zone-mixing terms, the magnitude of Σ depends in a complex way both on ω and on the position in the $\mathbf{k}$ space. We can discern the following trends.

1. Exponential decay of $\exp(-2I^{(\mathbf{n})})$ for small ω (when $\beta + \gamma - 1$ is positive) can be partially compensated by the power-law factors in $\tilde{k}^{2n}$. True, these factors are suppressed by factors of $\delta\mu/\mu_0$ but they can add up to a non-negligible quantity. This explains the lack of a sharp peak in some cases when $\beta + \gamma > 1$, i.e. $\alpha < -1$.

2. If $2\gamma > 1$ (in particular if $2\gamma \gg 1$) and $|\mathbf{k}| < 1$ then the numerator in (55) can come closer to zero than the denominator so even for $\beta + \gamma > 1$ and very small ω the integral I can still be quite small, i.e. the self-energy can be of order unity. This explains the weakening of the quasiparticle peak along the $\Gamma X M \Gamma$ trajectory (for finite $|\mathbf{k}|$) in some figures.

3. The appearance of Hubbard-like bands comes from the competition of the ω^{2n} prefactors and the exponential $\exp(-2I^{(\mathbf{n})})$ at finite ω – for small ω the influence of the prefactors is negligible[18] but for larger ω the exponential factors are all of order unity in any case, so what matters is whether $\tilde{k}^2$ grows or decays with ω: from (54), the maximum (the band) is located roughly at $\omega \sim C_a^3 r_h^{3\gamma}$; of course such a maximum is broad as it comes from a sum of various power laws. Emphatically, this has nothing to do with the position of the *poles*, which the self-energy cannot influence, and the wide bumps are not poles anyway; they are finite maxima and come solely from the variation of the finite part of the propagator (large imaginary part of the self-energy means smaller spectral weight).

We have thus explained qualitatively the complex structure of the region with a quasiparticle in the "phase diagram" in Fig. 4. For now we will not attempt to understand the action of the dipole coupling κ analytically. In leading order expansions that we use in this subsection, κ never appears – naively one would think its influence is not important. However, κ shifts the effective momentum and thus influences the *position of the pole*, not just the self-energy. Such effects require a more thorough analytical treatment than we are able to perform at present.

A systematic study of MDCs is also beyond the scope of this paper. Perhaps more interesting than EDCs as they show the influence of the lattice more directly, they are also far more complicated, and show strong dependence on the lattice strength $\delta\mu/\mu_0$. We have looked at a few examples in Appendix D, but we leave a proper treatment for further work.

5 Green functions in Matsubara frequencies: comparison to the Hubbard model?

Encouraged by the detailed phenomenological understanding that we have achieved, we explore now to what extent are our findings in line with real-world lattice models of strongly

---

[18]If $\beta + \gamma - 1 > 0$ then the exponential smallness is not much influenced by power-law prefactors; if $\beta + \gamma - 1 < 0$ then the power-law prefactors are important but they do not exist in front of the first term, $\exp(-2I^{(\mathbf{n})})$, so the self-energy remains large.

correlated metals. A natural candidate is the Hubbard model on a square lattice. This famous Hamiltonian

$$H = -t \sum_{\langle i,j \rangle} \sum_{\sigma} \left(c_{i\sigma}^{\dagger} c_{j\sigma} + c_{j\sigma}^{\dagger} c_{i\sigma} \right) + U \sum_{i} n_{i\uparrow} n_{i\downarrow}, \tag{56}$$

is a prototype model for strongly coupled electron systems, showing a wide range of experimentally relevant phenomena: strange-metallic behavior, Mottness, superconductivity, various exotic orders. The hopping is over the neighboring lattice sites, the spin is $\sigma \in \{\uparrow, \downarrow\}$, and the crucial parameter is the Coulomb interaction strength U/t. A review and comparison of state-of-the-art techniques can be found in [32,35]. We stick to the basic Hubbard Hamiltonian, with no additional interactions, non-nearest-neighbor hoppings etc. – since any direct relation to holography is tentative at best, it makes no sense to fine-tune the model.

The idea is to compare the holographic two-point function to the correlation functions of the quantum Monte Carlo calculation (CTINT); therefore, unlike the previous section where we looked solely at the spectral function, i.e. the imaginary part of G_R, here we look at the whole propagator. The object of comparison is the Green function *in Matsubara frequency* $G(i\omega_n)$. This object is the direct outcome of the CTINT method and of most quantum Monte Carlo methods (although real-time quantum Monte Carlo methods exist [66–68], they are of recent origin and not much data has been accumulated so far). A detailed study of the two-point retarded Green function in Matsubara frequencies for the Hubbard model on the square lattice has been published in [69]. For comparison with holography we have used the data from that study, provided to us by the first author of [69]. The data consists of Green function values for a range of imaginary frequencies, computed in the doped Mott insulator regime with $U/t = 10$ in a range of occupancy values $n = 0.500, 0.475, 0.450, 0.425$ (set by tuning the chemical potential), and for temperatures $T = 0.3, 0.5, 0.7$ (in units of $4t$). The occupancy $n = 0.500$ represents the half-filling. From analytical continuation, this phase is believed to have a quasiparticle or at least a clear maximum near $\omega = 0$ [36–38] at low temperatures (compared to both the chemical potential and lattice wavevector) – but for our temperature range $(0.3 - 0.7)$ one expects that the quasiparticle is already barely visible. The fit to holographic data will nevertheless show a clear quasiparticle, a puzzle that we try to resolve at the end of the section.

5.1 The fitting procedure

In order to express the Green functions in Matsubara frequency $i\omega_n$, we start from the real-frequency functions obtained from holography and apply the well-known Hilbert transform

$$G_R(i\omega_n) = -\frac{1}{\pi} \int_{-\infty}^{\infty} d\omega \frac{\mathrm{Im} G_R(\omega)}{i\omega_n - \omega}. \tag{57}$$

This is simply an integral over real frequencies ω and presents no difficulties, unlike the analytical continuation necessary to arrive at real-frequency results from $G(i\omega_n)$. There we see one advantage of holography, which directly produces real-frequency Green functions. Details on the numerical integration of (57) can be found in Appendix E.

Although the Matsubara Green function is mathematically well-defined for any imaginary ω_n, in physical quantities at temperature T only the frequencies $2\pi(n+1/2)T$ show up, so only these points were computed in CTINT and consequently we also only compute the holographic $G(i\omega_n)$ for such points. The momenta **k** are chosen along the triangular high-symmetry path ΓXMΓ for the square lattice 4×4. Although the reference [69] contains also the 8×8 data, we have found it unnecessary to use these – the deviations between the holography and the Hubbard model are larger than the systematic finite-size errors so we would get similar results even if fitting to CTINT data for a larger lattice.

In the holographic model that we employ, the free parameters are the scaling exponent α (we still keep δ fixed) and the conformal dimension Δ, whereas in the Hubbard model the free parameter is U/t. We can also tune the chemical potential μ_0 and the temperature T but these are external parameters, which are tuned for a given Hamiltonian. The idea is that the combination (α, Δ) that determines the scaling and interactions defines the effective Hamiltonian and should be fit to the Hubbard U/t. The inclusion of Δ may be controversial: in holography it really characterizes the probe, i.e. the dimension of the operator O in the correlation function $\langle OO \rangle$ that we compute, not the dual field theory itself or its Hamiltonian. However, in a model of correlated electrons, the operator in the Green function is always the electron annihilation operator $c_{j\sigma}$ (on lattice site j and with spin σ), and in holography we always consider a probe Dirac fermion, so the requirement that the latter acts as a proxy for the former is effectively a constraint on the dual field theory (that the Dirac probe really probes the degrees of freedom of an elementary electron).

How to match the temperatures and the chemical potential? To that end we need to match the *units* in the two models as μ_0 and T are both dimensionful quantities. This can be done in two ways. One, brute force way is to scan not only the parameters (α, Δ) but also μ_0 and T for each $(U/t, n, T)$ triple in CTINT data. We have done this only with limited resolution as the dimension of the parameter space is quite large. The other way is to notice that the self-energy of the Hubbard model in real space (i.e. in the space of lattice sites j, l) $\Sigma_{jl}(i\omega_n)$ can be written as

$$\Sigma_{jl}(i\omega_n) = U\langle n\rangle \delta_{jl} + \Sigma_{\text{dyn}}(i\omega_n). \tag{58}$$

The first term is the static contribution from the mean-field Coulomb repulsion and the second term is dynamical and comes from quantum corrections. This term is known to drop to zero in the static limit ($i\omega_n \to \infty$); this was the reason that we needed the dynamical cutoff $\mathcal{D}$ in holography. Therefore, only diagonal terms remain in the static limit; off-diagonal elements are zero. The structure of the real-space propagator $(G_R)_{jl}$ is now

$$\left[G_R(i\omega_n)\right]_{jl} = \left[(i\omega_n - U\langle n\rangle)I - \mathcal{H} - \Sigma_{\text{dyn}}\right]^{-1}_{jl}, \tag{59}$$

where I and $G_R(i\omega_n)$ are the unit matrix and the propagator in real (lattice-site) space and $\mathcal{H}$ is the nearest-neighbor hopping matrix $\mathcal{H}_{jl} = t\delta_{|j-l|,1}$. The first term in (59) contributes only to the diagonal elements of G_R, the last term drops to zero in the static limit, so off-diagonal we only have the contribution of the hopping matrix $\mathcal{H}$ from which we can read off t. The algorithm is therefore:

1. Starting from the Matsubara Green functions $G(i\omega_n, \mathbf{k})$, perform the inverse Fourier transform in momentum to get the real-space function $G_{jl}(i\omega_n)$.

2. For the largest $i\omega_n$ available in the numerics, invert the real-space matrix to get $G^{-1}_{jl}(i\omega_n \to \infty)$.

3. From (59), the terms bellow/above the main diagonal of the result equal $\pm t$.

Once we have t, we directly tune T and μ for computing G_{AdS} to the same values as in CTINT (in the latter they are in units of $4t$). Since the holographic model is certainly not exactly the Hubbard model (at best it comes close), and may well have long-range interactions, the above procedure is not exact, but it serves as a decent estimate, and yields similar results as the brute force fit.

One last technical remark is in order before we describe the fitting procedure. In AdS/CFT literature, the spectral function is usually defined as the imaginary part of the trace of the retarded Green function: $A(\omega, \mathbf{k}) = -(1/\pi)\text{Tr Im}\, G_R(\omega, \mathbf{k})$.[19] This quantity is basis-invariant;

---

[19]Depending on convention the prefactor $-1/\pi$ might be different, but that is not essential now.

it does not depend on the basis chosen to describe the spinor. On the other hand, Hubbard model correlation functions obtained by quantum Monte Carlo are typically expressed in the spin basis, so in absence of magnetic field they are of the form $G_R = \text{diag}(G_{11}, G_{22})$ with $G_{11} = G_{22}$. For that reason, the notation G_R for the Hubbard model usually means $(G_R)_{\sigma\sigma}$ with σ up or down all the same. We could write everywhere in this section $\text{Tr}G_{\text{AdS}}$ on one hand and $(G_{\text{CTINT}})_{\sigma\sigma}$ on the other but that would clutter the notation too much. We have decided to use solely the trace, so both in real and imaginary frequencies we write the trace in front of G both for AdS/CFT and CTINT functions. Although the trace is not explicitly performed in CTINT, we know that this is the invariant quantity behind the element $G_{11} = G_{22}$ of the CTINT calculation. The only trouble is the mismatch in normalization: in CTINT conventions, the AdS/CFT result should be normed not to unity but to 2. We have corrected for this by explicitly renormalizing the AdS result by $1/2$. As a result, we compare the same type of Green functions.

Now we describe the fit of the intrinsic parameters of the model (α, Δ). We look for the combination which minimizes the merit function. The merit function M_d is just the normalized deviation of weight d between the holographic function G_{AdS} and the CTINT function G_{CTINT}:

$$M_d \equiv \frac{1}{N^d} \sum_{n,j} |\text{Tr}\delta G\left(i\omega_n, \mathbf{k}_j\right)|^d = \min.$$

$$\delta G \equiv G_{\text{AdS}}\left(i\omega_n, \mathbf{k}_j; \alpha, \Delta\right) - G_{\text{CTINT}}\left(i\omega_n, \mathbf{k}_j; U/t\right), \quad N \equiv \sum_{n,j} 1. \tag{60}$$

We have tried different weights $d = -2, -1, 1, 2$, with very similar results.[20] The solution corresponds to the minimum of M_d. As we discussed above, by G_{AdS} and G_{CTINT} we mean the full 2×2 matrices. The trace in front is the trace in the internal space of these matrices.

If we turn on also the dipole coupling κ, we should in principle perform a three-dimensional scan. In order to avoid that, we perform the scan in (α, Δ) for a few κ values between 0 and 5 (for larger κ the gap is too broad and clearly far from the Hubbard data), find that the κ value does not influence much the position (but only the depth) of the minimum in the (α, Δ) plane, and then do a detailed scan in κ just near these minima.

In hindsight, quantitative accuracy of the fit is not a great concern as the main limiting factor is the transition from $G(\omega)$ to $G(i\omega_n)$; the integral (57) erases a lot of information so several rather different solutions may all give a very good fit in Matsubara domain. Until we can find a different object for comparison (perhaps real-time G_R from real-time quantum Monte Carlo), it does not make sense to go for a high-resolution scan of the parameter space.

5.2 The solution

We first fix $\kappa = 0$ and perform the fit in the (α, Δ) space only. The motive is that it is useful to see if κ is essential or not for reproducing the Hubbard model results, and to know how much can we get from the minimal model. In Fig. 12 we plot the merit function M_2 for a range of (α, Δ) values. The landscape contains a few local minima, one of which is rather dominant as the global minimum at

$$(\alpha, \Delta)_{\text{sol}} = (-1.3 \pm 0.1, 1.20 \pm 0.05).$$

While in this case the global minimum is quite dominant, it is still in fact only by a factor of 5 better than the next smallest local minimum.

With nonzero dipolar coupling, the outcome is the Fig. 13. The local minima are pretty much in the same places as in Fig. 12 but the depths differ somewhat. In particular, the global

---

[20]It is often said that negative d works better, imposing strict constraints on large-$i\omega_n$ properties, which translate to the normalization of the real-ω spectral function, but we have seen little difference in our fits no matter what d is.
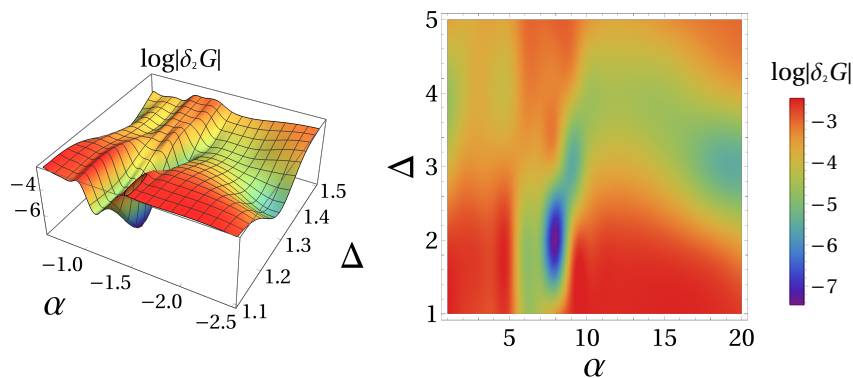
Figure 12: The squared norm of the difference $|\mathrm{Tr}\delta G|^2$ (M_2 function from (60)) between the holographic and CTINT Matsubara Green functions. For better viewing, we give both a 3D plot (left) and a density plot (right) with the same data. Several local minima are visible, but there is also a rather clear global minimum around $(\alpha, \Delta) = (-1.3, 1.2)$.
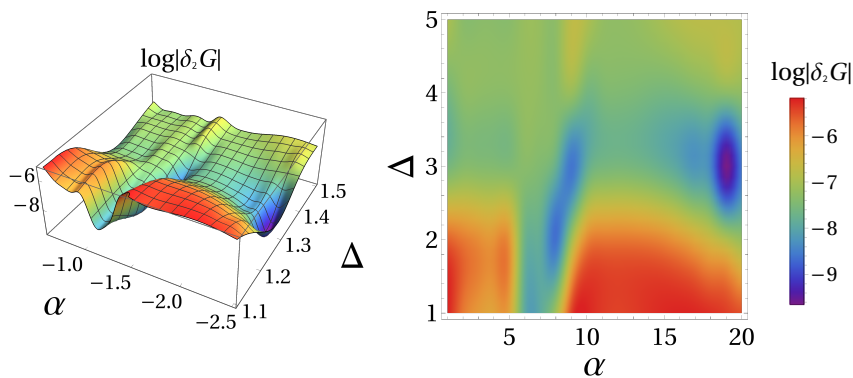
Figure 13: Same as Fig. 12 (squared norm of the difference $|\mathrm{Tr}\delta G|^2$ between the holographic and CTINT Matsubara Green functions) but for nonzero $\kappa = 1.5$. We have picked the κ value which yields the global minimum of the deviation (see the text for details of the fitting procedure for nonzero κ). The local minima remain in the same positions as for $\kappa = 0$ but their depths and consequently the position of the deepest minimum change; the global minimum is now at $(\alpha, \Delta) = (-2.3, 1.5)$.

minimum is now different and lies at

$$(\alpha, \Delta, \kappa)_{sol} = (-2.3 \pm 0.1, 1.30 \pm 0.05, 1.5 \pm 0.5).$$

The relatively large uncertainty on κ is simply due to the fact that once we move away from $\kappa = 0$ (and until we reach large values, around $4-5$), the solution is not very sensitive to κ. Therefore, even though the overall structure of the landscape is similar with $\kappa = 0$ and $\kappa > 0$, the minima can go up and down when κ becomes nonzero. Therefore, it is important to decide if κ should be fixed to zero (presumably by some symmetry) or not. Notice that both solutions are in the violet zone of the "phase diagram" in Fig. 4, with a quasiparticle (or at least something similarly-looking), separated from the upper and lower band by a soft gap.

The comparison of $\mathrm{Tr}G(i\omega_n)$ for AdS/CFT and Hubbard model is given in Fig. 14. In addition to the real and imaginary part of the propagator, we give also the absolute value of their difference. Notice that in the large-frequency regime the curves almost fall on top of each other as they should because the asymptotics is universal. At smaller frequencies, the real
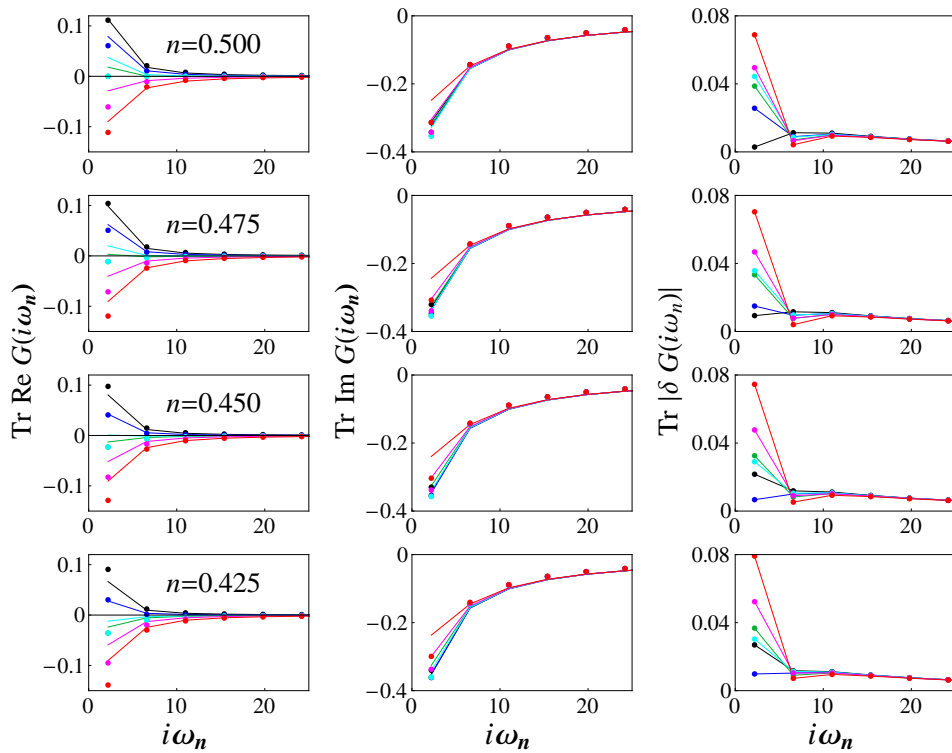
Figure 14: Real part (left) and imaginary part (middle) of the Matsubara Green function $\mathrm{Tr}G(i\omega_n)$, for the holographic fermion (solid lines) and for the QMC solution of the Hubbard model (circles), together with the module of the deviation between the two $|\mathrm{Tr}\delta G(i\omega_n)|$ (right; the lines are just to guide the eye). The functions are computed for the canonical Matsubara frequencies $i\omega_n$ and for six standard momentum values $((0,0)$ black, $(\pi/2,0)$ blue, $(\pi,0)$ cyan, $(\pi,\pi/2)$ magenta, (π,π) red, $(\pi/2,\pi/2)$ green$)$ along the high-symmetry line $\Gamma\mathrm{X}\mathrm{M}\Gamma$ of the unit cell. The holographic model is for the parameters yielding the best fit to the QMC data: $(\alpha,\Delta)=(-1.3\pm0.1,1.20\pm0.05)$, with no dipole coupling $(\kappa=0)$. The temperature is $T=0.7$.

part generally fares better than the imaginary part. Overall, there is a good agreement. The agreement is even better when κ is allowed to vary (though of course increasing the number of fit parameters nearly always yields better fits), as seen in Fig. 15. At the (π,π) point the agreement is much worse, just like for $\kappa=0$. At first glance, such an effect could be discarded as a mere artifact, but in the near-horizon analysis in subsection 4.2, we have shown below Eqs. (54-55) that special behavior near the corners of the Brillouin zone is in fact expected. However, this phenomenon is absent in the Hubbard model, hence this curve is never very well fit to the CTINT data.

While we need the Matsubara propagators for comparison, it is the real-frequency propagator which is of prime physical importance. The solution without dipole coupling is shown in Fig. 16, with momentum-integrated spectra $A_{\mathrm{loc}}(\omega)$ (top) and momentum-resolved spectra $A(\omega,\mathbf{k})$ (bottom). The overall structure of the spectrum in this regime is in fact known from previous subsections – quasiparticle plus the bands. The interesting fact, best seen from the integrated spectra, is that the chemical potentials corresponding to the four doping values of the Hubbard Hamiltonian are very close – the peak is barely moving upon dialing n. The chemical potentials (from highest to lowest n) are $\mu_0=(1.21,1.22,1.24,1.25)\pm0.01$, i.e. quite close to each other. A good fit as in Fig. 14 is obtained thanks to the large weight of the peak – slow
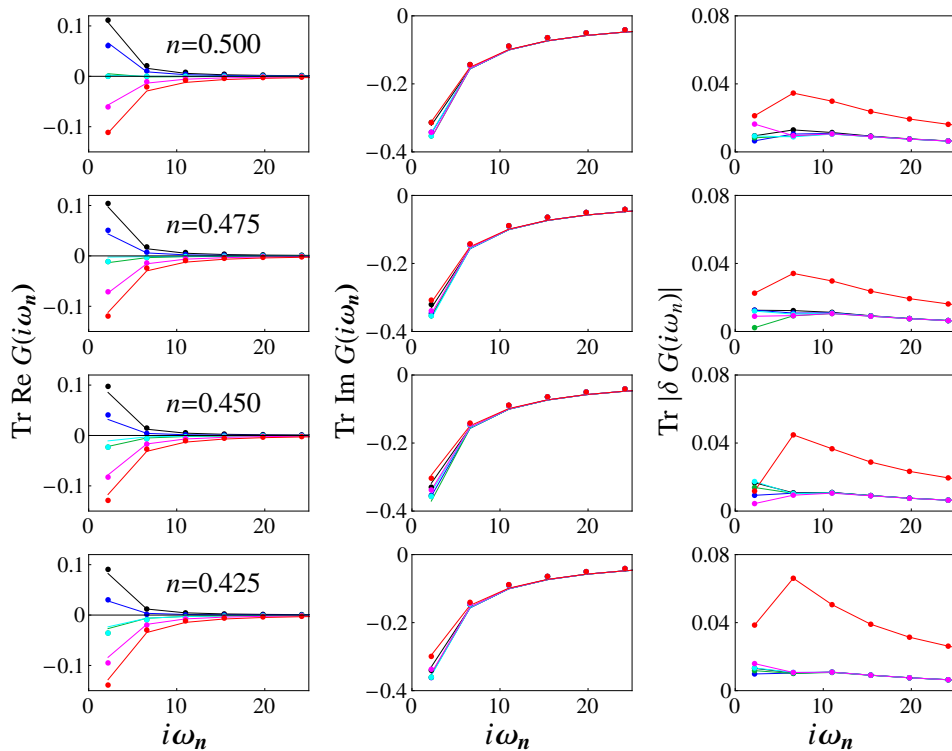
Figure 15: Same quantities as in Fig. 14 (real and imaginary part of $\mathrm{Tr}\,G(i\omega_n)$ for AdS/CFT and Hubbard models, and the module of the difference between the models) but with nonzero dipole coupling κ, for the three parameters yielding the best fit to the QMC data: $(\alpha, \Delta, \kappa) = (-2.3 \pm 0.1, 1.20 \pm 0.05, 1.5 \pm 0.5)$. The inclusion of dipolar coupling makes the gap between the bands and quasiparticle more prominent and allows for a better fit.

movement across the ω-axis is compensated by the fact that a lot of weight is moving, hence the broad interval of $\mathrm{Re}\,G(i\omega_n)$ values at small $i\omega_n$ (which roughly corresponds to the spectral weight asymmetry in real frequencies) is still reproduced. We will come back to the question how physical this solution is (in other words, is this really what is happening in the Hubbard model in order to produce the resultant Matsubara curves). The fits for the remaining two values of the temperature are given in Appendix E.

Finally, in Fig. 17 we appreciate the overall shape of the dispersion curve in the density plot for an intermediate temperature (A) and for a very high temperature $T = 10$ at six standard momenta (B). The lower temperature is not much of a surprise as we have already seen the general properties of $A(\omega, \mathbf{k})$ in Fig. 10. But the high-temperature plot provides another hint toward Hubbard physics: the curves evolve toward a Gaussian in ω, which is believed to happen also in the Hubbard model in the high-T limit [70]. We do not give the full density plot here as we have already demonstrated the temperature evolution in density plots in Fig. 7, and in particular because we want to compare to a Gaussian, which is easier to visualize for just a few momentum slices.

What is the physical significance of the solutions found? The fits are quite good and the landscape of the merit function (Figs. 12 and 13) is robust in the sense that the same 2-3 local minima always appear. However, these minima can become higher or lower when turning on κ. The spectra corresponding to these minima all contain the quasiparticle and the bands but in detail they differ. What is most suspicious when looking at Figs. 12 and 13 is that on average *nearly all points in the parameter space* have relatively small deviations from the CTINT
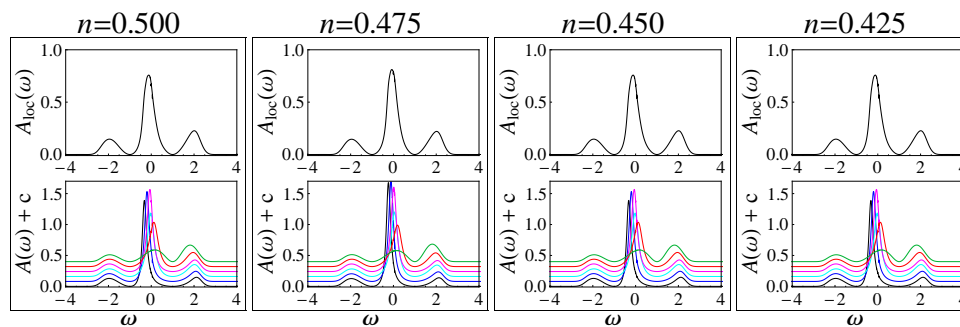
Figure 16: The local or momentum-integrated (top panel) and the momentum-resolved (bottom panel) spectral weight for the best fit of the holographic spectral function to the quantum Monte Carlo data for the Hubbard model, yielding the parameters $(\alpha, \Delta, \kappa) = (-2.3, 1.3, 1.5)$. The local spectrum shows the by now familiar structure lower band + quasiparticle + upper band. What is unexpected is that the chemical potentials for the four doping values are very close for each other: $\mu_0 = 2.10, 2.25, 2.40, 2.50$ (left to right), and indeed the local spectral function barely changes between $n = 0.500$ and $n = 0.425$. Similar conclusions follow also from the momentum-resolved spectra in the bottom row. The rough explanation is that the strong quasiparticle in the center can transfer a lot of spectral weight from $\omega < 0$ to $\omega > 0$ even for a minimal change of chemical potential.

solution and present relatively good fits! This suggests that the merit function is not very well chosen. Physically, the behavior we see in the spectra is expected for these values of n and U/t but only at much lower temperatures [37, 39]. We do not understand the origin of this systematic mismatch – when we determine the temperature in AdS/CFT by brute-force fitting we may well have large errors but we have also checked the units of temperature directly, by estimating the effective t value in holography. It seems that the temperature mismatch is physical and that the holographic system reacts differently to a heat bath. Another possibility is that the real-time spectra obtained by analytic continuation (e.g. in [37, 39]) contain large errors but that is less likely as many authors obtain similar results. We hope to understand this better in the future.

6 Discussion and conclusions

In our photoemission adventure we have gained a lot of knowledge on the phenomenology of holographic spectra on 2D lattices; we have also developed a few useful tools on the way. On the other hand, there is no sharp, golden-bullet conclusion on how exactly all of this relates to real-world systems, apart from the basic features – non-Fermi liquids, asymmetric and momentum-dependent self-energies, Hubbard-like bands and some (limited) signs of Mottness. More specifically, we have found the following robust features:

1. The quasiparticle peak, the bands and the strong momentum dependence of the spectrum are the three possible robust features of photoemission spectra on the hyperscaling-violating ionic lattice; they are not all present for all parameters, but may or may not be there as shown in the phase diagrams in Fig. 4. In absence of a quasiparticle, the central peak remains but becomes a wide bump, resembling a strange metal regime.

2. The quasiparticle pole is of similar origin as usual in holographic systems, stemming from a zero in the holographic source at the boundary. But the bands are novel – they
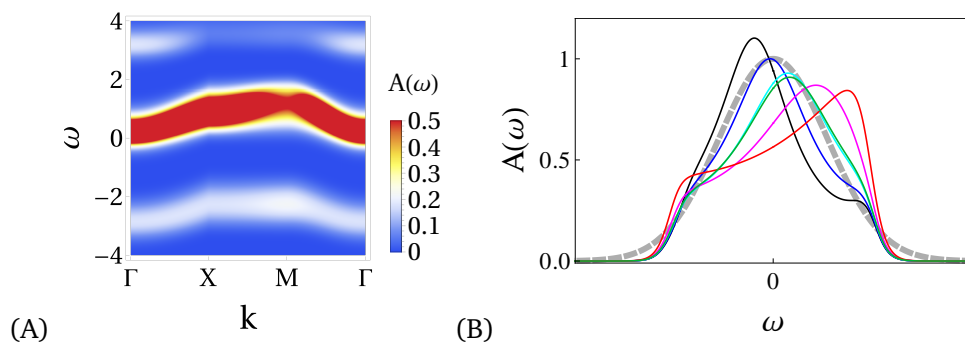
Figure 17: (A) Density plot for the spectral function $A(\omega, \mathbf{k})$ for the standard momentum set ($(0,0)$ black, $(\pi/2,0)$ blue, $(\pi,0)$ cyan, $(\pi,\pi/2)$ magenta, (π,π) red, $(\pi/2,\pi/2)$ green), for the best Hubbard fit with dipole coupling: $(\alpha, \Delta, \kappa) = (-2.3 \pm 0.1, 1.3 \pm 0.1, 1.5 \pm 0.5)$, at temperature $T = 0.5$. The central quasiparticle peak together with the upper and lower band is clearly seen, and the gaps between the bands and the center are rather hard. (B) Spectra $A(\omega)$ for the standard set of momenta (solid curves, black to green) for the same backgroud but with $T = 10$. At very high temperatures the spectrum evolves toward a single broad peak with a Gaussian profile – the gray dashed line is a Gaussian centered at the chemical potential $\omega = 0$. The fit is best for the blue curve, which has its maximum approximately at $\omega = 0$; for the others, we do not expect a zero-centered Gaussian to be a good fit except at large ω, which is precisely what we see.

can exist (separated from the central peak by soft gaps) even in absence of dipole coupling and arise from the umklapp terms in self-energy, which make its ω dependence nonmonotonic.[21]

3. Inhomogeneous and anisotropic (i.e., momentum-dependent) quasiparticle weight is also explained through the near-horizon analysis of umklapp terms in the self-energy. While it is somewhat at odds with the Hubbard model, it might have a role in some realistic strange metals.

4. The influence of the dipole coupling is to make the side bands more robust and the corresponding gaps harder. At larger couplings a soft central gap also appears, giving rise to a Mott-like regime (but the gap never fully opens for all momenta). We do not understand this analytically but it is likely related to the effective momentum shift and the zero-pole duality found for κ in homogeneous systems in [45, 59, 61].

5. The fit to the Hubbard model is surprisingly good, given the vast differences in microscopic physics from the holographic model. While the anisotropy of the spectrum always spoils the fit, the general structure is preserved, and the dipole coupling κ further helps to come closer to the Hubbard model. However, the fact the we have multiple local minima of the merit function, often with rather different real-frequency shapes, suggests that good fits to *Matsubara* functions do not mean that much.

In relation to the last point, we conclude that, quite generally, explicit fitting of the holographic Matsubara Green function to that of the quantum Monte Carlo calculations is not the best way to match the two. Essentially, we have attempted to circumvent the well-known unreliability of analytic continuation from imaginary to real frequencies by calculating the real-frequency

---

[21]We thank Jan Zaanen for asking this question, in particular how much the existence of bands hinges on the dipole coupling; it turns out that the dipole coupling strengthens the bands but is not a necessary condition.

functions directly (quite a natural thing to do in holography); in this way we work with perfectly reliable real-frequency functions, but when we try to compare to the Matsubara data from CTINT calculations, the problem shows up, just in reverse – it is easy to get a good fit but we do not know how relevant that is when it comes to real-frequency propagators. Still, the AdS/CFT curves pass several additional tests for the Hubbard physics (e.g. the single Gaussian limit at high temperatures), so we believe it makes sense to connect holographic models to lattice model Hamiltonians, but one has to find better merit functions and more appropriate objects for comparison. We would be interested to try with real-frequency Green functions obtained from the recently developed real-time Monte Carlo methods [66–68]. And it certainly makes sense to construct AdS duals of simpler and lower-dimensional models, i.e. an Anderson impurity, in a controlled way. Although it is unreasonable to expect that typical condensed matter lattice models have a controlled, microscopic gravity dual at all, work in this direction is still useful, as it can tell us which properties of these models are important.

On the technical side, quite a number of goodies employed in this work are likely useful also in different contexts. In particular, we have learned how the explicit ionic lattice influences the spectrum at finite Lifshitz ζ, i.e. for a general case of the "holographic scaling atlas" of [29,30]. The IR analysis with the matching to the UV that we have performed is in principle feasible in any background; it would be exciting to apply it to other AdS lattice models such as scalar lattices or the spontaneously generated charge density wave lattices (stripes, checkerboards and the like). These lattices are relevant also in the IR and we may expect further surprises. The UV cutoff that we employ, following [43] but making the cutoff fully holographic, is also a viable method for many purposes, allowing us to model multi-scale systems by coupling many AdS spaces in a similar vein as in [64].

On the qualitative, phenomenological side, our findings seem robust and in line with the general knowledge on strange metals [33,49,52]. The million dollar question is – is holography ready to answer specific condensed matter questions, i.e. to teach us something about a specific class of systems (like strange metals) rather than just general phenomenology as in this paper. It seems we are not there yet although we are much closer than a decade ago – papers like [52] as well as recent applications to transport phenomena have brought AdS/CFT closer to the lab than ever before. Our present work does not answer any smoking gun question in condensed matter, but it teaches us where to look further (other types of lattices, stronger lattices, near-horizon analysis like in this paper, various hyperscaling-violating systems as very robust and general) when trying to formulate and solve deep questions in quantum matter within the holographic framework.

Acknowledgments

A Coefficients of the IR expansion

At zeroth order (homogeneous solution), the scaling exponents (reprinted here for convenience from (10)) and the coefficients read (with $C_{rr}^{(0)} = 1/C_{tt}^{(0)}$ and $C_{xx}^{(0)} = 1$):

$$\beta = \frac{(\alpha + \delta)^2}{4 + (\alpha + \delta)^2}, \quad \gamma = 1 - \frac{2\delta(\alpha + \delta)}{4 + (\alpha + \delta)^2}, \tag{A.1}$$

$$\eta = -\frac{2(\alpha + \delta)}{4 + (\alpha + \delta)^2}, \quad \xi = \alpha\sqrt{\beta(1 - \beta)} + \beta + \frac{5}{4}, \tag{A.2}$$

$$C_{tt}^{(0)} = \frac{V_0 \left(1 + (\alpha + \delta)^2\right)^2}{2\left(1 + 2\alpha(\alpha + \delta)\right)\left(1 + (3\alpha - \delta)(\alpha + \delta)\right)}, \quad C_{xy}^{(0)} = C_{xr}^{(0)} = 0. \tag{A.3}$$

Now we can also explicitly relate the temperature to r_h and the parameters of the model:

$$T = \frac{V_0}{4\pi} \frac{\left(1 + \alpha^2 - \delta^2\right)\left(1 + (\alpha + \delta)^2\right)}{\left(1 + 2\alpha(\alpha + \delta)\right)\left(1 + (3\alpha - \delta)(\alpha + \delta)\right)} r_h^{2\gamma - 1}. \tag{A.4}$$

At first order, all inhomogeneous corrections are zero, but we can determine the exponents λ and ν of the off-diagonal metric terms and the homogeneous corrections:

$$\lambda = \frac{(\alpha + \delta)^2}{1 + (\alpha + \delta)^2}, \quad \nu = \frac{1 + 3(\alpha + \delta)^2}{2 + 2(\alpha + \delta)^2}, \quad C_{xx}^{(1)} = C_{xr}^{(1)} = \frac{1}{1 + (\alpha + \delta)^2}, \tag{A.5}$$

whereas $C_{xy}^{(0)}$ remains undetermined and the other first-order coefficients are all equal zero. Only at second order there are (x, y)-dependent corrections:

$$E_{tt}^{(2)} = F_{tt}^{(2)} = \frac{\pi}{1 + (\alpha + \delta)^2}, \quad E_{xx}^{(2)} = F_{xx}^{(2)} = -\frac{2\pi(1 + 2\alpha^2 + 2\alpha\delta)}{(1 + (\alpha + \delta)^2)^2}, \tag{A.6}$$

$$E_a^{(2)} = F_a^{(2)} = -\frac{\pi^2(\alpha + \delta)}{2\alpha\left(1 + (3\alpha - \delta)(\alpha + \delta)\right)\left(-1 + 2\delta(\alpha + \delta)\right)}. \tag{A.7}$$

This tells us two important things: (1) at leading order there are indeed no inhomogeneous terms and the scaling solution remains valid, which is also consistent with the numerical integrations and theoretical expectations from the literature (2) the fact that an inhomogeneous branch exists at higher order means that it is possible to match the IR solution to the UV asymptotics discussed in Eq. (12). We have not tried to do this matching explicitly but again the fact that numerics yields a solution de facto justifies this logic.

B Summary of the numerics

Throughout most of the paper, we solve both the Einstein-Maxwell-dilaton system and the probe Dirac equation with a pseudospectral collocation grid solver, based on the algorithms in [50] and [51]. The pseudospectral method, by now pretty standard in works on holographic lattices, is based on a series expansion of the unknown functions $Y(x)$ in some basis,[22] and a set of points x_i associated with that basis, so that the (truncated) expansion of the unknown functions exactly satisfies the differential equation at the points from this set. This idea is explained very well in [51], and the usual basis choices (that we also adopt) are the Chebyshev

---

[22]We denote schematically the independent variable(s) by x and the unknown function(s) by $Y(x)$. In our case x is a triple of coordinates and Y is a whole set of functions but for the sake of brevity we write Y and x as scalars in this brief summary.

polynomials for nonperiodic directions and the Fourier series for the periodic directions. The collocation algorithm is a specific realization of the pseudospectral idea where one stores the information on the series expansion of Y not as a set of series coefficients but as an array of values $Y_j = Y(x'_j)$ at some set of points x'_j (the sets x_i and x'_j are distinct). In this way one can show (e.g. [50] and references therein) that, for a set of so-called cardinal functions $C_j(x)$, the unknown function is approximated as

$$Y(x) \approx \sum_j Y(x'_j) C_j(x), \tag{B.1}$$

thus a linear system $\hat{L}Y = f$ where $\hat{L}$ is some differential operator and f are the sources, discretizes as

$$L_{ij}Y_j = f_i, \quad L_{ij} = \hat{L}C_j(x)|_{x=x'_i}, \quad Y_j = Y(x'_j), \quad f_i = f(x'_i). \tag{B.2}$$

The advantage is that the differentiation of the cardinal functions is very cheap: their values at the collocation points x'_i are tabulated for pretty much any meaningful basis and can be found in the appendices of [50]. The solution of a *linear* system then reduces to the inversion of L. The boundary conditions (Dirichlet or Neumann) along the radial (z) direction are enforced by replacing the first and last row in L_{ij} with the appropriate row vectors implementing the boundary condition (just as explained in [51]). Along x, y, the boundary conditions are periodic, so when using periodic basis functions they are automatically satisfied and no explicit boundary conditions are needed.

We use the Gauss-Lobatto grid, which consists of the extrema of the basis polynomials and the endpoints of the interval. The alternative is the Gauss-Chebyshev grid, consisting of zeros of the basis polynomials and no endpoints. For equations of motion in AdS, we consistently find the Gauss-Lobatto grid to be superior, as Gauss-Chebyshev is much more prone to artificial oscillations. This is apparently a special property of AdS: the general convergence properties of the two grids are known to be the same [50].

Since the EMD system is nonlinear, one further necessary ingredient is the Newton-Raphson iterative algorithm, i.e. expanding the nonlinear system $\hat{F}(Y) = f$ to first order in the variations $\delta Y^{(0)}$ around some initial guess $Y^{(0)}$ as

$$J^{(0)}\delta Y^{(0)} = -\hat{F}\left(Y^{(0)}\right) + f, \quad J^{(0)} \equiv \frac{\partial \hat{F}}{\partial Y}|_{Y=Y^{(0)}}. \tag{B.3}$$

This is a linear equation in $\delta Y^{(0)}$ that can be solved by a linear collocation solver by inverting the discretized Jacobian $J^{(0)}_{ij}$ in (B.3). We then update the function as $Y^{(0)} \mapsto Y^{(1)} \equiv Y^{(0)} + \delta Y^{(0)}$ and repeat the procedure until subsequent approximations are close enough in some norm: $\|Y^{(n)} - Y^{(n-1)}\| < \epsilon$. The matrix inversion is the costliest part of the whole procedure and we found it more efficient to adopt the Broyden's method instead [71, 72]. The idea here is to compute the inverse of the Jacobian *in the first iteration only* and in subsequent iterations to update directly the inverse, rather than the Jacobian itself. Denoting the inverse of the Jacobian in the n-th iteration by $I^{(n)} \equiv \left(J^{(n)}\right)^{-1}$, the secant formula and the matrix inversion lemma (Sherman–Morrison–Woodbury lemma) yield the equation

$$I^{(n+1)} = I^{(n)} + \frac{1}{\mathrm{Tr}\left[\left(\delta Y^{(n)}\right)^T \cdot I^{(n)} \cdot \delta F^{(n)}\right]} \left(\delta Y^{(n)}\right)^T \cdot I^{(n)} \cdot \left(\delta Y^{(n)} - I^{(n)} \cdot \delta F^{(n)}\right), \tag{B.4}$$

with

$$\delta F^{(n)} = F\left(Y^{(n+1)}\right) - F\left(Y^{(n)}\right). \tag{B.5}$$
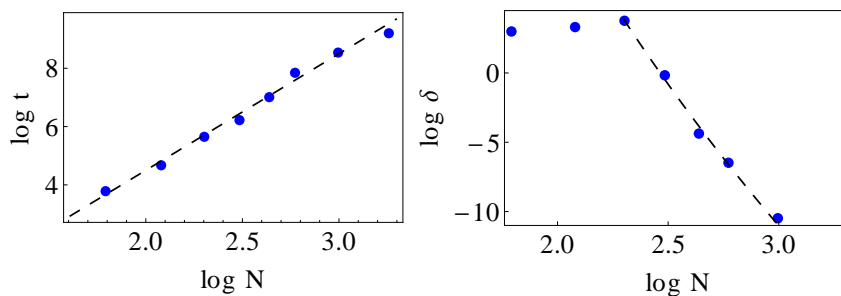
Figure 18: The running time in seconds (left) and the relative accuracy, i.e. relative deviation from the result on the largest lattice, here with $N = 26$ (right), for a number of lattice sizes. The running time grows as a power law, and the error drops sharply once we are over some critical lattice size (here about $N = 12$) and the finite-size effects stop.

Therefore, once we have $I^{(0)}$, everything proceeds by matrix multiplications only, with no further inversions. In this way the first iteration takes most time, and subsequent ones are much faster. An alternative formula is

$$I^{(n+1)} = I^{(n)} + \frac{1}{\|\delta F^{(n)}\|^2} \left(\delta F^{(n)}\right)^T \cdot \left(\delta Y^{(n)} - I^{(n)} \cdot \delta F^{(n)}\right), \tag{B.6}$$

which is generally believed [71] to be inferior to (B.4), but in some (infrequent) cases we find it actually more stable. Another possible method is to replace the inverse of the Jacobian by pseudoinverse, found by singular value decomposition (which can be programmed manually or invoked as the Mathematica function PseudoInverse). The decomposition runtime with pseudoinverse scales as mN^4 for an N-point grid with m iterations, unlike the naive inverse which scales as mN^6 and the Broyden's method which scales as $N^6 + (m-1)N^2$. Pseudoinverse is thus the fastest method but it is often not accurate enough, eventually producing large errors, so we avoid using it.

We demonstrate the convergence properties of the solver in Fig. 18 by plotting the running time and the relative error (with respect to the highest-resolution result) for a number of resolutions, for a test EMD equation.

In practice, we start by first fixing the gauge through the Einstein-DeTurck trick, explained in [51,73] and references therein. It makes the Einstein equations elliptic which is necessary to guarantee the numerical convergence. Then we usually perform a low-resolution run for typical parameter values on a desktop computer. Knowing the qualitative properties of the solution, we run a higher resolution calculation on a cluster for a range of parameter values of the EMD system of equations. Finally, we use the outcome as the background for solving the Dirac equations. The Dirac equations are solved in a single step of the pseudospectral solver, without iterations, as they are linear.

The semiholographic calculations (which are discussed in the next Appendix and which were not used in the main part of the paper but have proved valuable for a quick initial screening of the parameter space) were all performed on a desktop computer. All codes are implemented with double precision arithmetic.

C   Holography vs. semiholographies

While the fully consistent ionic lattice obtained by numerical solution of the partial EMD system is certainly preferable, we have experimented with two simpler approximations. We dub
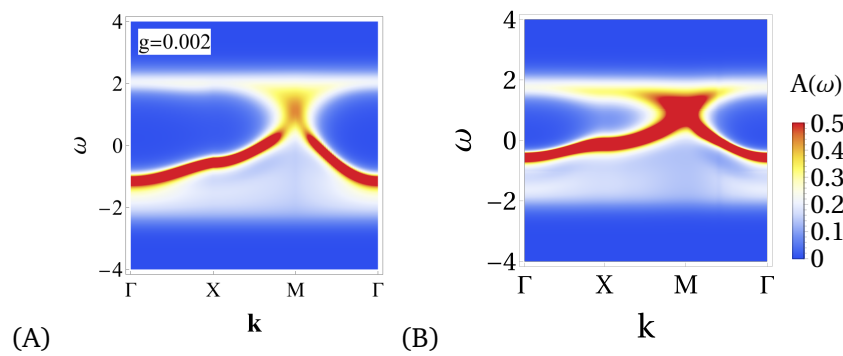
Figure 19: Semiholographic RPA Green function (A) and fully holographic Green function (B) for holographic parameters $(\alpha, \Delta) = (-1.40, 1.3)$. The hybridization for the semiholographic function is tuned to $g = 0.002$ in order to obtain a good approximation to the consistent holographic lattice calculation. As we see, for the appropriate hybridization values, semiholographic spectra reproduce all qualitative and even some quantitative features of the fully holographic spectra.

both semiholography, according to the paper [19] which pioneered this approach, however in detail they are quite different. The first is the true semiholography of the aforementioned paper, recently applied in [52] to experimental ARPES curves, and also in a hybridization-based theoretical model of strange metals [74,75]. To remind, the idea is to introduce a linear coupling between the holographic propagator $\mathcal{G}_R$ in a homogeneous background and a free electron on the lattice. The total action is then

$$S = S_{\text{AdS/CFT}}\left(\Psi^\dagger, \Psi\right) + \int dt \int d^2x \, \chi_{\mathbf{k}}^\dagger (i\partial_t - \epsilon(\mathbf{k})) \, \chi_{\mathbf{k}} + g \sum_{\mathbf{K}} \left(\chi_{\mathbf{k}}^\dagger \Psi_{\mathbf{k}+\mathbf{K}} + \Psi_{\mathbf{k}+\mathbf{K}}^\dagger \chi_{\mathbf{k}} \right). \quad (\text{C.1})$$

Here, $S_{\text{AdS/CFT}}$ is the action for the holographic fermion Ψ (in absence of lattice), χ is the free fermion on a square lattice with dispersion $\omega = \epsilon(\mathbf{k})$ and g is the hybridization between the two.[23] The resulting dressed retarded propagator of the lattice fermion $\mathcal{G}_R$ reads (in the RPA approximation):

$$\mathcal{G}_R(\omega, \mathbf{k}) = \frac{1}{\mathcal{G}_{0R}^{-1}(\omega, \mathbf{k}) - g^2 G_R^{-1}(\omega, \mathbf{k})} = \frac{1}{\omega - \epsilon(\mathbf{k}) - g^2 G_R^{-1}(\omega, \mathbf{k})}, \quad (\text{C.2})$$

where $\mathcal{G}_{0R}$ is the bare propagator of the same fermion χ (containing a quasiparticle pole), and G_R^{-1} is the inverse holographic propagator which now has the role of self-energy. We assume that g is real, i.e. $g = g^*$. Varying g and the holographic parameters (α, Δ) yields results similar to the full lattice calculation. We have *not* used this method neither when exploring the AdS model in Section 4 nor when fitting to the Hubbard model in Section 5. We comment upon it here because the resulting spectra look quite reasonable (we give one example in Fig. 19), and they provide a decent (though uncontrolled) approximation to the full lattice spectra.

Interestingly, the hybridization g also acts as a proxy of doping in the Mott-insulator-like regime, controlling the spectral weight transfer in absence of a quasiparticle. As an example we show a few spectra in Fig. 20 which all contain a soft gap around $\omega = 0$ with two bands around $\omega = \pm 4$. As we pump up the coupling g, the spectral weight passes from the lower to the upper band, while the gap remains approximately open. The gap-forming mechanism is different than in fully holographic lattices: the pole in the free propagator $\mathcal{G}_{0R}$ and the pole

---

[23]Of course, one should not confuse the coupling g with the determinant of the metric; it will always be clear from context which one we mean.
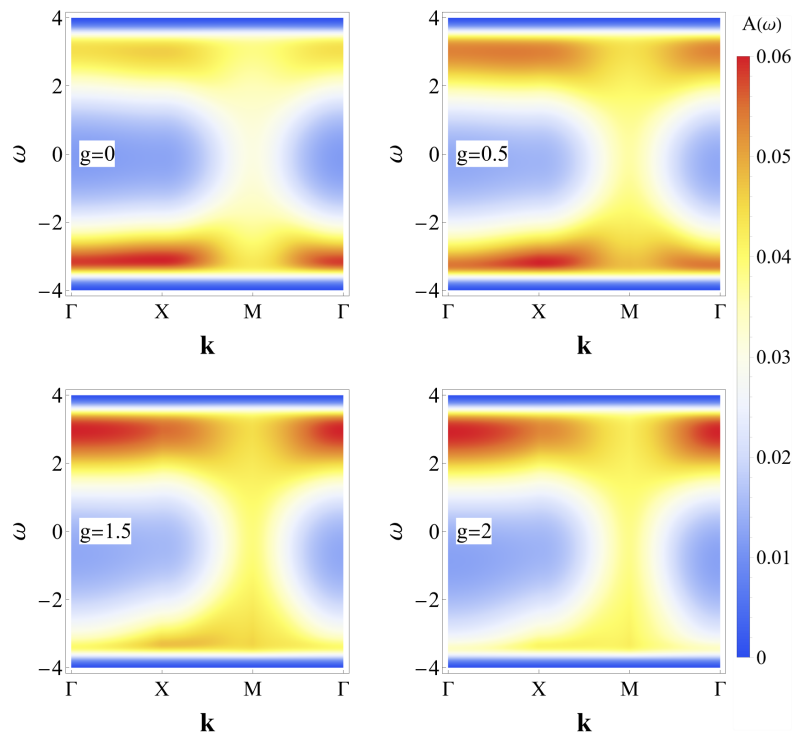
Figure 20: Semiholographic RPA Green function for four values of the hybridization g and for holographic parameters $(\alpha, \Delta) = (-0.65, 1.3)$. The structure of the spectrum resembles a Mott insulator: no central peak but a (rather soft) gap, and Hubbard bands at finite ω. This is a novel phenomenon in semiholography, however what happens is that the zero in G_R^{-1} (coming from the pole in the holographic propagator G_R) cancels the zero in the free fermion propagator. This is not what happens in true Mott systems, where the self-energy develops a pole.

in the holographic propagator G_R will approximately cancel each other in some interval of g. So what happens is that self-energy G_R^{-1} develops a *zero* which cancels the zero in the kinetic term, rather than self-energy developing a pole, as it happens in true Mott insulators.

To conclude, the main message is that semiholography may serve as a good *fit* in g to fully holographic Green functions, mimicking the true behavior quite well, however the physics behind it is different and cannot encapsulate true lattice effects.

Another approximation that we have used for a quick and dirty scan in the (α, Δ) plane is to integrate the right-hand side and the boundary conditions of the EMD equations over a single unit cell $(x, y) \in (-1/(2Q), 1/(2Q))$. In this way we obtain a system of ordinary differential equations (because the derivatives over x, y on the left-hand side also become trivial in this case) which we integrate using the same pseudospectral algorithm as for PDEs, but of course with just $\tilde{z}$ dependence the numerics is much easier. In the next step we write the stress-energy tensors and sources as the sum of the former (monopole or averaged) term and the quadrupole contribution (the dipole contribution is zero). This leads to the separation of variables and again results in a system of ordinary differential equations. Already the third (octupole) step results in a good approximation to the final solution. We have *never* used this method either for any of the production runs but we have used it to gain a quick glance over various corners of the parameter space. We will apply and describe in detail this scheme in a forthcoming work [76].
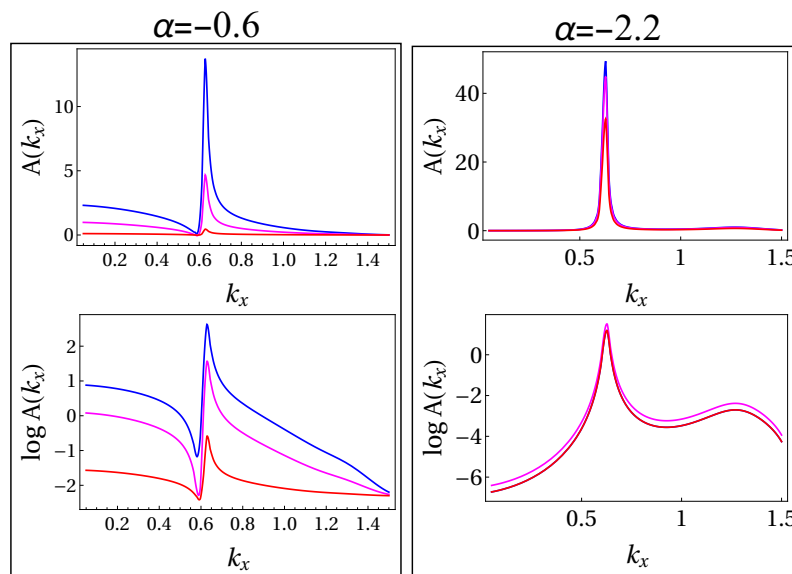
Figure 21: Three sections of momentum distribution curves (MDCs) $A(k_x, k_y)$ for $k_y = 0, 0.5, 1.0$ (blue, magenta, red), at $\omega = 10^{-3}$, for $\Delta = 1.4$ and $\alpha = -0.6$ (left) vs. $\alpha = -2.2$ (right). The curves capture a QP peak which exists for both cases; however the non-Fermi-liquid phase shows clear asymmetry of the peak, as opposed to the Fermi-liquid-like phase where the MDC peak is apparently Lorentzian.

D   A quick look at momentum distribution curves

We give here a few remarks on the difficult subject of MDC structure. Because of the interplay of the lattice and the Fermi surface shape and the magnitudes of $\mathbf{k}_F$ and the lattice period, the phenomenology of MDCs shows vast variety. We thus limit ourselves to just pointing at what MDCs look like for Fermi-liquid-like regime as opposed to the non-Fermi-liquid regime. We work solely at $\kappa = 0$ now.

In Fig 21, we show the difference between a typical MDC in the non-Fermi-liquid phase (left) and in the Fermi-liquid-like phase (right). In both cases the system has a quasiparticle (as we can see also from the "phase diagram" in Fig. 4). However, the asymmetric structure of the QP peak, the telltale sign of non-Fermi-liquid physics, is clearly present in the left, whereas the right-hand plot has a symmetric peak. Notice that in this case the asymmetry of the left-side plots is seen also in EDCs (e.g. Fig. 5), which is expected for the holographic model of our type, since it is known that both in homogeneous space [27] and in the presence of weak lattice (Section 4.2) our choice of the EMD action implies that overdamped peaks are always asymmetric also in energy. But MDCs provide a direct and general piece of evidence of the non-Fermi liquid physics.[24]

As a taste of the work to be done, we present in Fig. 22 three two-dimensional MDC plots, again near zero energy, roughly corresponding to the three cases of EDCs in Fig. 5: a sharp but asymmetric quasiparticle, a broad continuum with no quasiparticles, and a more symmetric, Fermi-liquidish quasiparticle. Unusually, sharp EDC for $\alpha = -0.7$ becomes a broad MDC, whereas a complete lack of quasiparticle for $\alpha = -1.0$ translates to strongly localized (though of course finite in amplitude) MDC curve. The third case ($\alpha = -2.2$) is sharp both in momentum and energy. This potentially very intriguing phenomenon will be the subject of further work.

---

[24]We thank an anonymous referee for reminding us of this criterion.
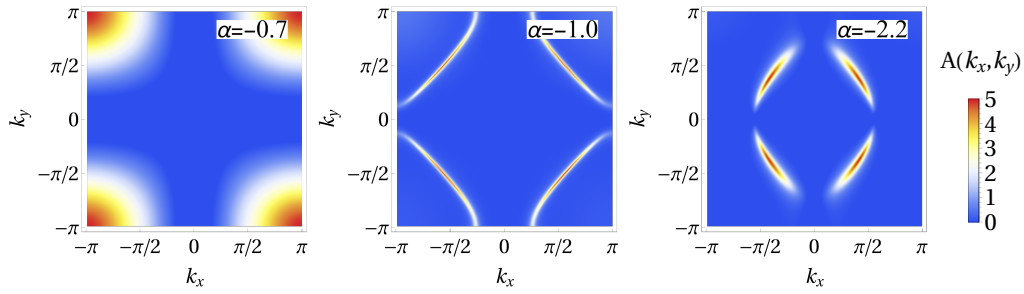
Figure 22: Two-dimensional plots of momentum distribution spectra $A(k_x, k_y)$ at $\omega = 10^{-3}$, for $\Delta = 1.3$ and $\alpha = -0.7$, $\alpha = -1.0$, $\alpha = -2.2$ (left to right). The first case has no sharp QP in momentum despite a sharp EDC. The second case is opposite to that: sharp momentum distribution even though we have shown that no sharp QP in energy exists. The final case looks close to a Fermi liquid.
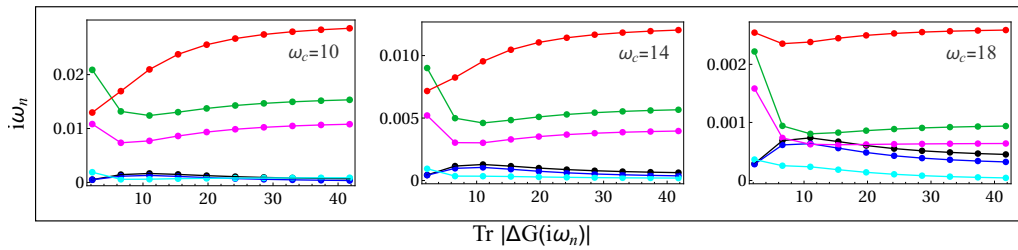
Figure 23: Absolute trace of the relative difference $\mathrm{Tr}|\Delta G(i\omega_n)|$ for three cutoff values ω_c, with respect to the largest cutoff we have tried $\omega_c = 22$. The spectra are computed for the six standard momentum values. Overall agreement is good, even for the largest cutoff employed.

E More on comparison to the Hubbard model

In this Appendix we discuss the practicalities of performing the Hilbert transform (57) numerically, we give some more data comparing the Green functions of the holographic lattice to those of the Hubbard model, and finally we show that the Hubbard-like bands are not present in absence of the lattice even with the dipole coupling κ turned on. In other words, the band require both the dipole coupling and the lattice.

E.1 Numerical implementation of the Hilbert transform

The numerical integration over frequencies in (57) has two nontrivial points: (1) the large-frequency limit $\omega \to \pm\infty$ (2) the vicinity of the QP peak. The first problem is resolved by imposing a large but finite cutoff so we really compute the integral $\int_{-\omega_c}^{\omega_c}$. The convergence is quite rapid already for $\omega_c \approx 10$ because of the boundary source $\mathcal{D}$, introduced in Eq. (16) and motivated in subsection 3.3, which acts as a UV regulator. One can estimate the UV convergence by comparing the results for different cutoff values. We have considered the cutoffs $\omega_c = 10, 14, 18, 22$. We have adopted the $\omega_c = 22$ results as reference values $G^{(0)}(i\omega_n)$ for the Matsubara propagator and calculated the relative difference $\Delta G(i\omega_n) \equiv |(G^{(i)}(i\omega_n) - G^{(0)}(i\omega_n))/G^{(0)}(i\omega_n)|$, where the indices $i = 1, 2, 3$ correspond to $\omega_c = 18, 14, 10$. In Fig. 23 we show the values of the relative difference for the three cutoff values, for the standard set of momenta and for randomly chosen parameter values $\alpha = 1.1, \Delta = 1.3$. We see that already for the smallest cutoff the relative difference is about one percent, thus our results are reliable.
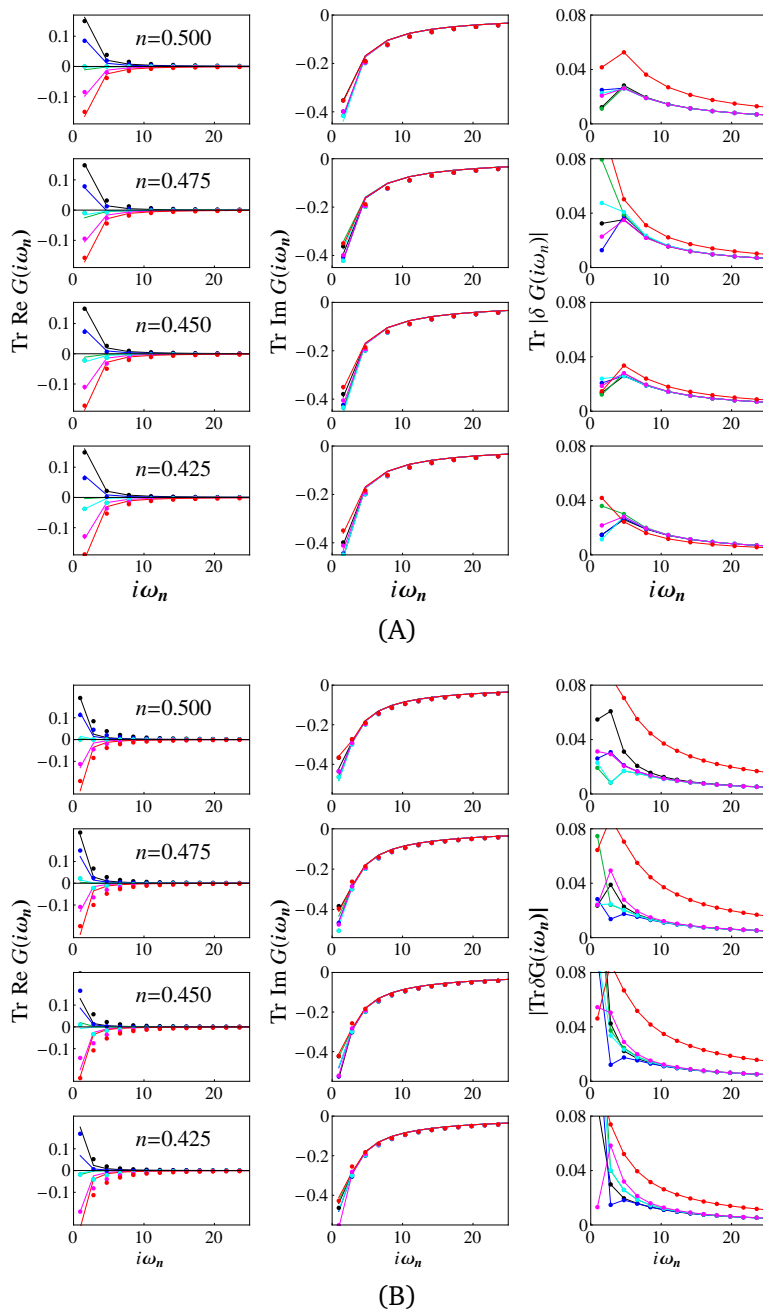
Figure 24: Same as Fig. 15 but for the temperature $T = 0.5$ (A) and $T = 0.3$ (B). At $T = 0.5$ the agreement is still quite good. For $T = 0.3$, the lowest temperature in the set of CTINT data that we have used, we see some systematic differences between the curves for small $i\omega_n$, which is absent on higher temperatures. This suggests differences in local features in real frequency, not really a surprise since the two models are microscopically distinct.

The second issue discussed above is essentially an IR problem: if the quasiparticle peak is very sharp, we need a much finer resolution when integrating near the peak; this is important as otherwise we do not get good large-$i\omega_n$ asymptotics. However, this is easily resolved by decreasing the integration step for by a factor $10 - 20$ near the peak maximum. Since this interval is very narrow (smaller than ~ 0.01), this presents no problems (the slowdown near the peak is significant but only constitutes a small part of the overall integration interval).

E.2 Additional data on fitting the holographic spectra to the Hubbard model

Now we give the comparison of the Matsubara Green functions for the holographic and for the Hubbard model for the remaining two temperatures, $T = 0.5$ and $T = 0.3$ (Fig. 24). At $T = 0.5$ the agreement is still very good but at the lowest temperature, $T = 0.3$, there are larger systematic differences. The agreement is the worst at small Matsubara frequencies, which correspond to local features of real-frequency G_R (large Matsubara frequencies correspond to global features, or properties of the integral $\int d\omega A(\omega, \mathbf{k})$). This simply means that detailed properties of the spectrum (which are best visible at low temperatures) differ between the AdS and Hubbard models. In the context of all our findings, this is expected. More interesting is the clear outlying status of the curve at $\mathbf{k} = (\pi, \pi)$, in the corner of the Brillouin zone. We have discussed in our WKB analysis why such points are expected to show diminished quasiparticle intensity. We thus understand the phenomenon in AdS but obviously it is something which does not happen in the Hubbard model.
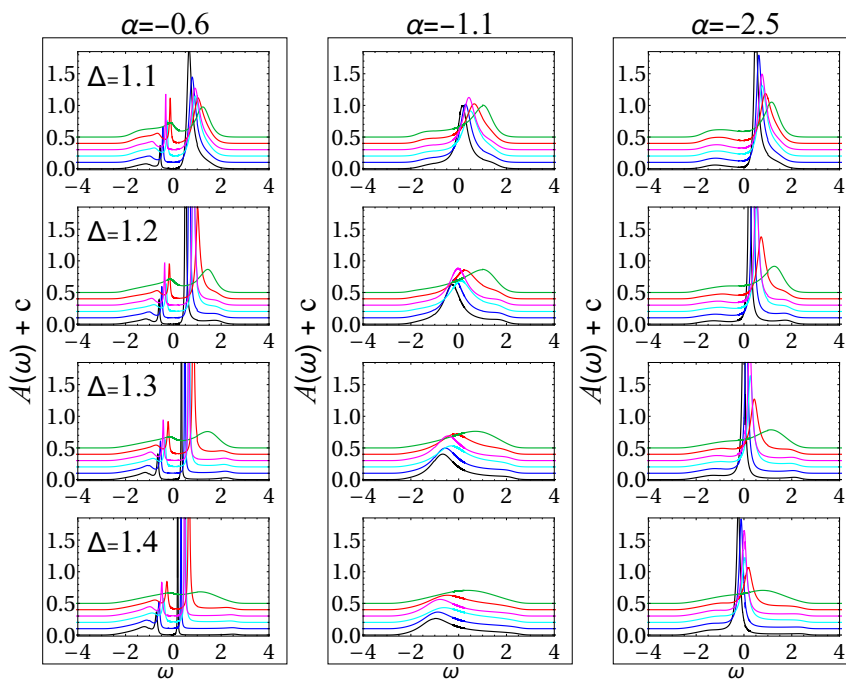
Figure 25: Energy spectra for the same values of $\alpha, \Delta, \kappa, \mu$ as Fig. 8 but in absence of lattice: $\delta\mu/\mu_0 = 0$. The gaps separating the left and right band from the central (quasiparticle) peak have almost vanished, in accordance with our expectation that the bands are well-separated thanks to the contributions of multiple Brillouin zones in the self-energy. The six momenta are chosen as $k/\mu_0 = 0, 0.5, 1.0, 1.5, 2.0, 2.5$.

E.3 Absence of Hubbard bands in a homogeneous system

We will now present numerical evidence that in absence of lattice and the umklapp contributions to the self-energy the Hubbard bands are not present (or at least are much less prominent). We simply take the same values of other parameters but put $\delta\mu = 0$, i.e. we work in homogeneous space. As an example, consider Fig. 25, obtained with the same parameters as Fig. 8, including the dipole coupling $\kappa = 1.5$, except for the absence of lattice. In this case, the momenta can take any real values and the natural unit is the chemical potential μ_0. While the overall structure of the spectrum does not differ too much from the weak lattice case for $\alpha = -1.1$ and $\alpha = -2.5$, there are no gaps and no band-like structures. For $\alpha = -0.6$, we

find the typical strong gap between two branches of the dispersion relation, both of them with sharp peaks; this is very different from the lattice result, and again has no broad bands (the only exception perhaps being the case $\alpha = -2.5, \Delta = 1.1$).

Note however that point 2 in subsection 4.2 provides an analytical argument for the same conclusion: that bands are a consequence of the umklapp terms in the Green function. Although that argument is clearly non-rigorous, it lends additional merit to the numerical reasoning in this Appendix.

References

[1] J. Zaanen, Y.-W. Sun, Y. Liu and K. Schalm, *Holographic duality in condensed matter physics*, Cambridge University Press, Cambridge, UK, ISBN 9781107080089 (2015), doi:10.1017/CBO9781139942492.

[2] M. Ammon and J. Erdmenger, *Gauge/gravity duality: Foundations and applications*, Cambridge University Press, Cambridge, UK, ISBN 9781107010345 (2015), doi:10.1017/CBO9780511846373.

[3] S. A. Hartnoll, A. Lucas and S. Sachdev, *Holographic quantum matter*, (arXiv preprint) doi:10.48550/arXiv.1612.07324.

[4] Y. Liu, K. Schalm, Y.-W. Sun and J. Zaanen, *Lattice potentials and fermions in holographic non Fermi-liquids: Hybridizing local quantum criticality*, J. High Energy Phys. **10**, 036 (2012), doi:10.1007/JHEP10(2012)036.

[5] A. Donos and S. A. Hartnoll, *Universal linear in temperature resistivity from black hole superradiance*, Phys. Rev. D **86**, 124046 (2012), doi:10.1103/PhysRevD.86.124046.

[6] G. T. Horowitz, J. E. Santos and D. Tong, *Further evidence for lattice-induced scaling*, J. High Energy Phys. **11**, 102 (2012), doi:10.1007/JHEP11(2012)102.

[7] Y. Ling, C. Niu, J.-P. Wu, Z.-Y. Xian and H. Zhang, *Holographic fermionic liquid with lattices*, J. High Energy Phys. **07**, 045 (2013), doi:10.1007/JHEP07(2013)045.

[8] T. Andrade, A. Krikun, K. Schalm and J. Zaanen, *Doping the holographic Mott insulator*, Nat. Phys. **14**, 1049 (2018), doi:10.1038/s41567-018-0217-6.

[9] S. Cremonini, L. Li and J. Ren, *Holographic fermions in striped phases*, J. High Energy Phys. **12**, 080 (2018), doi:10.1007/JHEP12(2018)080.

[10] S. Cremonini, L. Li and J. Ren, *Spectral weight suppression and Fermi arc-like features with strong holographic lattices*, J. High Energy Phys. **09**, 014 (2019), doi:10.1007/JHEP09(2019)014.

[11] F. Balm, A. Krikun, A. Romero-Bermúdez, K. Schalm and J. Zaanen, *Isolated zeros destroy Fermi surface in holographic models with a lattice*, J. High Energy Phys. **01**, 151 (2020), doi:10.1007/JHEP01(2020)151.

[12] A. Iliasov, A. A. Bagrov, M. I. Katsnelson and A. Krikun, *Anisotropic destruction of the Fermi surface in inhomogeneous holographic lattices*, J. High Energy Phys. **01**, 065 (2020), doi:10.1007/JHEP01(2020)065.

[13] A. Donos and J. P. Gauntlett, *Holographic Q-lattices*, J. High Energy Phys. **04**, 040 (2014), doi:10.1007/JHEP04(2014)040.

[14] Y. Ling, P. Liu, C. Niu, J.-P. Wu and Z.-Y. Xian, *Holographic fermionic system with dipole coupling on Q-lattice*, J. High Energy Phys. **12**, 149 (2014), doi:10.1007/JHEP12(2014)149.

[15] S. Chakrabarti, D. Maity and W. Wahlang, *Studying the holographic Fermi surface in the scalar induced anisotropic background*, Phys. Lett. B **827**, 136990 (2022), doi:10.1016/j.physletb.2022.136990.

[16] A. Donos and S. A. Hartnoll, *Interaction-driven localization in holography*, Nat. Phys. **9**, 649 (2013), doi:10.1038/nphys2701.

[17] A. Bagrov, N. Kaplis, A. Krikun, K. Schalm and J. Zaanen, *Holographic fermions at strong translational symmetry breaking: A Bianchi-VII case study*, J. High Energy Phys. **11**, 057 (2016), doi:10.1007/JHEP11(2016)057.

[18] H.-S. Jeong, K.-Y. Kim, Y. Seo, S.-J. Sin and S.-Y. Wu, *Holographic spectral functions with momentum relaxation*, Phys. Rev. D **102**, 026017 (2020), doi:10.1103/PhysRevD.102.026017.

[19] T. Faulkner and J. Polchinski, *Semi-holographic Fermi liquids*, J. High Energy Phys. **06**, 012 (2011), doi:10.1007/JHEP06(2011)012.

[20] V. P. J. Jacobs, S. Grubinskas and H. T. C. Stoof, *Towards a field-theory interpretation of bottom-up holography*, J. High Energy Phys. **04**, 033 (2015), doi:10.1007/JHEP04(2015)033.

[21] H. Liu, J. McGreevy and D. Vegh, *Non-Fermi liquids from holography*, Phys. Rev. D **83**, 065029 (2011), doi:10.1103/PhysRevD.83.065029.

[22] M. Čubrović, J. Zaanen and K. Schalm, *String Theory, quantum phase transitions, and the emergent Fermi liquid*, Science **325**, 439 (2009), doi:10.1126/science.1174962.

[23] T. Faulkner, H. Liu, J. McGreevy and D. Vegh, *Emergent quantum criticality, Fermi surfaces, and AdS$_2$*, Phys. Rev. D **83**, 125002 (2011), doi:10.1103/PhysRevD.83.125002.

[24] S. A. Hartnoll, D. M. Hofman and D. Vegh, *Stellar spectroscopy: Fermions and holographic Lifshitz criticality*, J. High Energy Phys. **08**, 096 (2011), doi:10.1007/JHEP08(2011)096.

[25] M. Čubrović, Y. Liu, K. Schalm, Y.-W. Sun and J. Zaanen, *Spectral probes of the holographic Fermi ground state: Dialing between the electron star and AdS Dirac hair*, Phys. Rev. D **84**, 086002 (2011), doi:10.1103/PhysRevD.84.086002.

[26] N. Iqbal, H. Liu and M. Mezei, *Semi-local quantum liquids*, J. High Energy Phys. **04**, 086 (2012), doi:10.1007/JHEP04(2012)086.

[27] N. Iizuka, N. Kundu, P. Narayan and S. P. Trivedi, *Holographic Fermi and non-Fermi liquids with transitions in dilaton gravity*, J. High Energy Phys. **01**, 094 (2012), doi:10.1007/JHEP01(2012)094.

[28] K. Goldstein, S. Kachru, S. Prakash and S. P. Trivedi, *Holography of charged dilaton black holes*, J. High Energy Phys. **08**, 078 (2010), doi:10.1007/JHEP08(2010)078.

[29] C. Charmousis, B. Goutéraux, B. S. Kim, E. Kiritsis and R. Meyer, *Effective holographic theories for low-temperature condensed matter systems*, J. High Energy Phys. **11**, 151 (2010), doi:10.1007/JHEP11(2010)151.

[30] B. Goutéraux and E. Kiritsis, *Generalized holographic quantum criticality at finite density*, J. High Energy Phys. **12**, 036 (2011), doi:10.1007/JHEP12(2011)036.

[31] B. Goutéraux and E. Kiritsis, *Quantum critical lines in holographic phases with (un)broken symmetry*, J. High Energy Phys. **04**, 053 (2013), doi:10.1007/JHEP04(2013)053.

[32] J. P. F. LeBlanc et al., *Solutions of the two-dimensional Hubbard model: Benchmarks and results from a wide range of numerical algorithms*, Phys. Rev. X **5**, 041041 (2015), doi:10.1103/PhysRevX.5.041041.

[33] S.-D. Chen et al., *Incoherent strange metal sharply bounded by a critical doping in Bi2212*, Science **366**, 1099 (2019), doi:10.1126/science.aaw8850.

[34] G. Rohringer et al., *Diagrammatic routes to nonlocal correlations beyond dynamical mean field theory*, Rev. Mod. Phys. **90**, 025003 (2018), doi:10.1103/RevModPhys.90.025003.

[35] T. Schäfer et al., *Tracking the footprints of spin fluctuations: A multimethod, multimessenger study of the two-dimensional Hubbard model*, Phys. Rev. X **11**, 011058 (2021), doi:10.1103/PhysRevX.11.011058.

[36] A. Georges, G. Kotliar, W. Krauth and M. J. Rozenberg, *Dynamical mean-field theory of strongly correlated fermion systems and the limit of infinite dimensions*, Rev. Mod. Phys. **68**, 13 (1996), doi:10.1103/RevModPhys.68.13.

[37] X. Deng, J. Mravlje, R. Žitko, M. Ferrero, G. Kotliar and A. Georges, *How bad metals turn good: Spectroscopic signatures of resilient quasiparticles*, Phys. Rev. Lett. **110**, 086401 (2013), doi:10.1103/PhysRevLett.110.086401.

[38] J. Vučičević, D. Tanasković, M. J. Rozenberg and V. Dobrosavljević, *Bad-metal behavior reveals Mott quantum criticality in doped Hubbard models*, Phys. Rev. Lett. **114**, 246402 (2015), doi:10.1103/PhysRevLett.114.246402.

[39] T. Ayral, J. Vučičević and O. Parcollet, *Fierz convergence criterion: A controlled approach to strongly interacting systems with small embedded clusters*, Phys. Rev. Lett. **119**, 166401 (2017), doi:10.1103/PhysRevLett.119.166401.

[40] A. Vranić et al., *Charge transport in the Hubbard model at high temperatures: Triangular versus square lattice*, Phys. Rev. B **102**, 115142 (2020), doi:10.1103/PhysRevB.102.115142.

[41] A. N. Rubtsov, V. V. Savkin and A. I. Lichtenstein, *Continuous-time quantum Monte Carlo method for fermions*, Phys. Rev. B **72**, 035122 (2005), doi:10.1103/PhysRevB.72.035122.

[42] E. Gull et al., *Continuous-time Monte Carlo methods for quantum impurity models*, Rev. Mod. Phys. **83**, 349 (2011), doi:10.1103/RevModPhys.83.349.

[43] U. Gürsoy, E. Plauschinn, H. Stoof and S. Vandoren, *Holography and ARPES sum-rules*, J. High Energy Phys. **05**, 018 (2012), doi:10.1007/JHEP05(2012)018.

[44] M. Edalati, R. G. Leigh and P. W. Phillips, *Dynamically generated Mott gap from holography*, Phys. Rev. Lett. **106**, 091602 (2011), doi:10.1103/PhysRevLett.106.091602.

[45] G. Vanacore, S. T. Ramamurthy and P. W. Phillips, *Evolution of holographic Fermi arcs from a Mott insulator*, J. High Energy Phys. **09**, 009 (2018), doi:10.1007/JHEP09(2018)009.

[46] T. Faulkner, G. T. Horowitz, J. McGreevy, M. M. Roberts and D. Vegh, *Photoemission "experiments" on holographic superconductors*, J. High Energy Phys. **03**, 121 (2010), doi:10.1007/JHEP03(2010)121.

[47] S. Sachdev, *Holographic metals and the fractionalized Fermi liquid*, Phys. Rev. Lett. **105**, 151602 (2010), doi:10.1103/PhysRevLett.105.151602.

[48] T. Andrade, A. Krikun and A. Romero-Bermúdez, *Charge density response and fake plasmons in holographic models with strong translation symmetry breaking*, J. High Energy Phys. **12**, 159 (2019), doi:10.1007/JHEP12(2019)159.

[49] J. Zaanen, *Planckian dissipation, minimal viscosity and the transport in cuprate strange metals*, SciPost Phys. **6**, 061 (2019), doi:10.21468/SciPostPhys.6.5.061.

[50] J. P. Boyd, *Chebyshev and Fourier spectral methods*, Dover Publications, Mineola, USA, ISBN 9780486411835 (2001), doi:10.1007/978-3-642-83876-7.

[51] A. Krikun, *Numerical solution of the boundary value problems for partial differential equations. Crash course for holographer*, (arXiv preprint) doi:10.48550/arXiv.1801.01483.

[52] S. Smit et al., *Momentum-dependent scaling exponents of nodal self-energies measured in strange metal cuprates and modelled using semi-holography*, (arXiv preprint) doi:10.48550/arXiv.2112.06576.

[53] S. S. Gubser, I. R. Klebanov and A. M. Polyakov, *Gauge theory correlators from non-critical string theory*, Phys. Lett. B **428**, 105 (1998), doi:10.1016/S0370-2693(98)00377-3.

[54] E. Witten, *Anti de Sitter space and holography*, Adv. Theor. Math. Phys. **2**, 253 (1998), doi:10.4310/ATMP.1998.v2.n2.a2.

[55] M. Henneaux, *Boundary terms in the AdS/CFT correspondence for spinor fields*, (arXiv preprint) doi:10.48550/arXiv.hep-th/9902137.

[56] R. Contino and A. Pomarol, *Holography for fermions*, J. High Energy Phys. **11**, 058 (2004), doi:10.1088/1126-6708/2004/11/058.

[57] I. R. Klebanov and E. Witten, *Ads/CFT correspondence and symmetry breaking*, Nucl. Phys. B **556**, 89 (1999), doi:10.1016/S0550-3213(99)00387-9.

[58] D. Guarrera and J. McGreevy, *Holographic Fermi surfaces and bulk dipole couplings*, (arXiv preprint) doi:10.48550/arXiv.1102.3908.

[59] M. Edalati, R. G. Leigh, K. W. Lo and P. W. Phillips, *Dynamical gap and cupratelike physics from holography*, Phys. Rev. D **83**, 046012 (2011), doi:10.1103/PhysRevD.83.046012.

[60] X.-M. Kuang, B. Wang and J.-P. Wu, *Dipole coupling effect of holographic fermion in the background of charged Gauss-Bonnet AdS black hole*, J. High Energy Phys. **07**, 125 (2012), doi:10.1007/JHEP07(2012)125.

[61] G. Vanacore and P. W. Phillips, *Minding the gap in holographic models of interacting fermions*, Phys. Rev. D **90**, 044022 (2014), doi:10.1103/PhysRevD.90.044022.

[62] B. Batell, T. Gherghetta and D. Sword, *The soft-wall standard model*, Phys. Rev. D **78**, 116011 (2008), doi:10.1103/PhysRevD.78.116011.

[63] N. Chagnet, V. Đukić, M. Čubrović and K. Schalm, *Emerging Fermi liquids from regulated quantum electron stars*, J. High Energy Phys. **08**, 222 (2022), doi:10.1007/JHEP08(2022)222.

[64] M. Fujita, Y. Hikida, S. Ryu and T. Takayanagi, *Disordered systems and the replica method in AdS/CFT*, J. High Energy Phys. **12**, 065 (2008), doi:10.1088/1126-6708/2008/12/065.

[65] M. Baggioli and O. Pujolàs, *On effective holographic Mott insulators*, J. High Energy Phys. **12**, 107 (2016), doi:10.1007/JHEP12(2016)107.

[66] J. Vučičević and M. Ferrero, *Real-frequency diagrammatic Monte Carlo at finite temperature*, Phys. Rev. B **101**, 075113 (2020), doi:10.1103/PhysRevB.101.075113.

[67] A. Taheridehkordi, S. H. Curnoe and J. P. F. LeBlanc, *Optimal grouping of arbitrary diagrammatic expansions via analytic pole structure*, Phys. Rev. B **101**, 125109 (2020), doi:10.1103/PhysRevB.101.125109.

[68] J. Vučičević, P. Stipsić and M. Ferrero, *Analytical solution for time integrals in diagrammatic expansions: Application to real-frequency diagrammatic Monte Carlo*, Phys. Rev. Res. **3**, 023082 (2021), doi:10.1103/PhysRevResearch.3.023082.

[69] J. Vučičević et al., *Conductivity in the square lattice Hubbard model at high temperatures: Importance of vertex corrections*, Phys. Rev. Lett. **123**, 036601 (2019), doi:10.1103/PhysRevLett.123.036601.

[70] A. Donos and C. Pantelidou, *Holographic transport and density waves*, J. High Energy Phys. **05**, 079 (2019), doi:10.1007/JHEP05(2019)079.

[71] R. Fletcher, *Practical methods of optimization*, John Wiley & Sons, New York, USA, ISBN 9780471915478 (1987), doi:10.1002/9781118723203.

[72] C. Broyden, *A class of methods for solving nonlinear simultaneous equations*, Math. Comput. **19**, 577 (1965), doi:10.1090/S0025-5718-1965-0198670-6.

[73] T. Andrade, *Holographic lattices and numerical techniques*, (arXiv preprint) doi:10.48550/arXiv.1712.00548.

[74] B. Douçot, A. Mukhopadhyay, G. Policastro and S. Samanta, *Linear-in-T resistivity from semiholographic non-Fermi liquid models*, Phys. Rev. D **104**, L081901 (2021), doi:10.1103/PhysRevD.104.L081901.

[75] S. Samanta, H. Swain, B. Douçot, G. Policastro and A. Mukhopadhyay, *A simple model for strange metallic behavior*, (arXiv preprint) doi:10.48550/arXiv.2206.01215.

[76] M. Čubrović, *Multipole expansions for inhomogeneous holographic systems*, In preparation.

CrossMark

Vortex dynamics of counterpropagting laser beams in photorefractive materials

Mihailo Čubrović[1] · **Milan Petrović[2,3]**

Abstract
We study vortex patterns of counterpropagating laser beams in a photorefractive crystal, with or without the background photonic lattice. The vortices are effectively planar and have two "flavors" because there are two opposite directions of beam propagation. In a certain parameter range, the vortices form stable equilibrium configurations which we study using the methods of statistical field theory and generalize the Berezinsky–Koster-litz–Thouless transition of the XY model to the "two-flavor" case. In the nonequilibrium regime, the patterns exhibit an Andronov–Hopf bifurcation which may lead to oscillations (limit cycle), chaos or decay to zero intensity due to radiation losses. We show how to iden-tify various pathways toward instability from intensity patterns, i.e. from experiment.

Keywords Vortex · BKT transition · Photorefractive optics · Statistical field theory

1 Introduction

Nonlinear optical systems are a rich arena for studies of various fundamental physi-cal phenomena. The strong response of the nonlinear optical medium to the propagation of light makes it a typical strongly correlated system, with many phenomena similar to those in other strongly interacting systems in areas such as condensed matter. Their com-plex dynamics offers an opportunity to study spatiotemporal chaos and optical turbulence

---

✉ Mihailo Čubrović
mcubrovic@gmail.com

Milan Petrović
petrovic@ipb.ac.rs

[1] Scientific Computing Laboratory, Institute of Physics, University of Belgrade, Pregrevica 118, Belgrade 11080, Serbia

[2] Institute of Physics, P. O. B. 57, Belgrade 11001, Serbia

[3] Texas A&M University at Qatar, Doha P.O.Box 23874, Qatar

 Springer

(Cross and Hohenberg 1993; Rabinovich et al. 2000). On the other hand, they often also exhibit stable, equilibrium confgurations in a certain parameter range, which are nautrally studied by statistical physics methods. Vortices and other topological configurations (Alexander et al. 2007; Anderson 2007; Fetter 2009), long-range order (Anderson 2007), quenched disorder and glassy behavior (Antenucci et al. 2015a, b; Ghofraniha 2015; Perret et al. 2012) are universal in a broad range of systems such as cold atoms (Bagnato et al. 2015; Malomed et al. 2016) and magnetic systems, and the relative simplicity of experiments in optics makes it an excellent testing ground for strongly coupled models.

In this paper we study a specific and experimentally realizable nonlinear optical system: laser beams counterpropagating (CP) through a photorefractive (PR) crystal. This means we have an elongated PR crystal (with one longitudinal and two transverse dimensions) and two laser beams shone onto each end. We thus effectively have two fields, one forward-propagating and one backward-propagating. The optical response of the crystal depends nonlinearly on the *total* intensity of both beams, which means the beams effectively interact with each other. This system has been thoroughly investigated for phenomena such as dynamical solitons (Denz et al. 2003; Petrović et al. 2011, 2005; Jović et al. 2008), vortex stability on the photonic lattice (Alexander et al. 2007; Terhalle et al. 2008; Čubrović and Petrović 2017) and topological invariants (Rechtsman et al. 2013).

We first recast the system in Lagrangian and then in Hamiltonian form so it can be studied as a field theory, which depends parametrically on the time *t*. Then we consider the time dynamics of the system and show that in a broad parameter range the patterns relax to a static configuration which can be studied within *equilibrium* field theory. By renormalization group (RG) analysis, we obtain the phase diagram of static vortex configurations. The phase diagram is obviously closely related to the famous Berezinsky–Kosterlitz–Thouless (BKT) vortex unbinding transition in the XY model (Berezinsky 1971; Kosterlitz and Thouless 1973) except that having two components of the field produces additional phases and phase transitions, due to forward–backward beam interaction. The analytical insight we obtain also allows us to avoid overextensive numerics – analytical construction of the phase diagram tells us which patterns can in principle be expected in different corners of the parameter space.

Next we focus on the nonequilibrium regime, classify the fixed points and study possible routes of instability. We emphasize the pictorial and "rule-of-thumb" criteria to recognize various instabilities, in order to facilitate experimental checks. At the end we will discuss the perspective of studying dynamical criticality, i.e. instablities which consist in moving from one vortex phase to another in real time, a phenomenon which is intimately connected to the difficult questions of quench dynamics and thermalization in many-body systems.

2 Counterpropagating beams in photorefractive medium: equations of motion

Consider a photorefractive crystal of length *L* irradiated by two paraxial head-on laser beams which propagate from the opposite faces of the crystal in the *z*-direction. Photorefractive crystals induce self-focusing of the beams—the vacuum (linear) wave equation is modified by the addition of a friction-like term, so the diffusion of the light intensity (the broadening of the beam) is balanced out by the self-focusing of the beam. The physical ground for this is the redistribution of the charges in the crystal due to the Kerr effect.
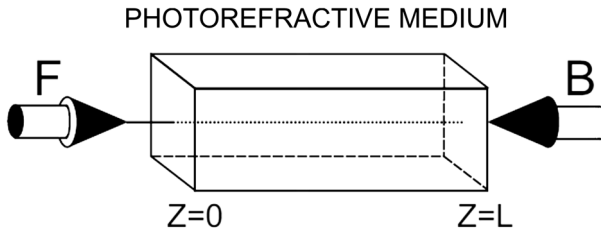
Fig. 1 Experimental setup for the study of the CP beams in the PR crystal. The crystal has the shape of a parallelepiped, and the beams propagate along the longitudinal, z-axis: the forward (F)-beam from $z = 0$ to $z = L$, and the backward (B)-beam the other way round. The intensity patterns can be observed at the transverse faces of the crystal, at $z = 0$ and $z = L$

The nonlinearity is contained in the change of the refraction index which is determined by the induced charge density. A sketch of the system is given in Fig. 1. Before entering the crystal, the laser beams can be given any desirable pattern of both intensity and phase. In particular, one can create vortices (winding of the phase) making use of the phase masks (Denz et al. 2003).

Assuming the electromagnetic field of the form $\mathbf{E} = e^{\iota\omega t + \iota \mathbf{q}\mathbf{r}}\left(Fe^{ikz} + Be^{-ikz}\right)$, we can write equations for the so-called envelopes F and B of the forward- and backward-propagating beams along the z-axis (the frequency, transverse and longitudinal momentum are denoted respectively by $\omega, \mathbf{q}, k$). The wave equations for F and B are now:

$$\pm \iota \partial_z \Psi_\pm(z;x,y;t) + \Delta\Psi_\pm(z;x,y;t) = \Gamma E(z;x,y;t)\Psi_\pm(z;x,y;t), \qquad (1)$$

where the plus and minus signs on the left-hand side stand for the forward- and backward-propagating component of the beam amplitude doublet $\Psi \equiv (\Psi_+, \Psi_-) \equiv (F, B)$, and Γ is the dimensionless PR coupling constant. From now on we will use $\alpha \in \{+, -\}$ to denote the two beams (F and B) and call it a flavor index, in analogy with field theory. The vorticity (winding number of the phase) will be called vortex charge as usual. The charge field E on the right-hand side of the equation is the electric field sourced by the charges in the crystal (i.e., it does not include the external electric field of the beams). Its evolution is well represented by a relaxation-type equation (notice that the derivative ∂_E is strictly negative) (Petrović et al. 2011):

$$\frac{\tau}{1 + I(z;x,y;t)}\partial_t E(z;x,y;t) + E(z;x,y;t) = -\frac{I(z;x,y;t)}{1 + I(z;x,y;t)}. \qquad (2)$$

Here, $I \equiv I_\Psi + I_x$ is the total light intensity at a given point, $I_\Psi \equiv |F|^2 + |B|^2$ is the beam intensity and I_x the intensity of the fixed background. The meaning of I_x is that the crystal is all the time irradiated by some constant light source, independent of the counterpropagating beams with envelopes F, B. The relaxation time is τ. The form of the nonlinearity accounts for the saturation of the crystal; notice that a simple quartic non-linear Schrödinger equation would not account for the saturation.[1] In the numerical calculations,

---

[1] One might also worry that a realistic crystal is anisotropic, while our equation is isotropic. Nevertheless, comparison to experiment (Neshev et al. 2004; Fleischer et al. 2004; Dreischuh et al. 2002) shows that this model is able to describe actual measurements rather well. Also, the effects of anisotropy can be suppressed in experiment by illuminating the crystal by *uniform* light for very long times before starting the experiment (Cohen et al. 2002).

we solve Eqs. (1), (2) with no further assumptions, using a slightly modified version of the beam propagation method (Sandfuchs et al. 2001). For analytical results we will need to transform them further assuming a vortex pattern. The Eq. (2) is completely phenomenological, but it excellently represents the experimental results (Denz et al. 2003). We will first consider the equilibrium regime, and then the nonequilibrium dynamics.

For slow time evolution (in absence of pulses), we can Laplace-transform the Eq. (2) in time ($E(t) \mapsto E(u) = \int_0^\infty dt e^{-ut} E(t)$) to get the algebraic relation

$$E(z;x, y;u) = -\frac{\Psi^\dagger \Psi + I_x - \tau E_0}{1 + \tau u + I_x + \Psi^\dagger \Psi} = -1 + \frac{1 + \tau u + \tau E_0}{1 + \tau u + I_x + \Psi^\dagger \Psi}. \quad (3)$$

The original system (1) can now be described by the Lagrangian:

$$\mathcal{L} = \imath \Psi^\dagger \sigma_3 \partial_z \Psi - |\nabla \Psi|^2 + \Gamma \Psi^\dagger \Psi - \Gamma(1 + \tau E_0 + \tau u) \log(1 + \tau u + I_x + \Psi^\dagger \Psi), \quad (4)$$

where σ_3 is the Pauli matrix $\sigma_3 = \text{diag}(1, -1)$. This has the form $\mathcal{L} = \imath \Psi^\dagger \sigma_3 \partial_z \Psi - |\nabla \Psi|^2 - V_{eff}(\Psi^\dagger, \Psi)$, i.e. the Lagrangian of a non-relativistic field theory (a two-component nonlinear Schrödinger field equation) in $2 + 1$ dimensions ($x, y; z$), where the role of time is played by the longitudinal distance z, and the physical time t (or u upon the Laplace transform) is a parameter.

3 Stable vortex configurations and the phase diagram

Following the same steps as for the textbook XY model we can arrive at an effective Hamiltonian for stable vortex configurations. For details we refer the reader to Čubrović and Petrović (2017). Assuming the vortex solution of the form

$$\Psi_{0\pm}(\mathbf{r}) = \psi_{0\pm}(r) e^{\imath \delta \theta_\pm(\phi) + \imath \theta_{0\pm}(\phi)}, \quad (5)$$

where $\theta_\pm(\phi)$ is the singular part of the phase and $\theta_{0\pm}(\phi)$ the regular part, we want to integrate out both the amplitude fluctuations and the regular part of the phase and arrive at a description of the systems solely in terms of vortex charges. This is done by expanding the Lagrangian (4) to quadratic order in both amplitude and phase fluctuations and integrating them out. Then the usual Legendre transform yields the vortex Hamiltonian:

$$\mathcal{H}_{\text{vort}} = \sum_{i<j} \left(g Q_{i\alpha} Q_{j\alpha} + g' Q_{i\alpha} \times Q_{j\beta} \right) \log r_{ij} + \sum_i \left(g_0 Q_{i\alpha} Q_{i\alpha} + g_1 Q_{i\alpha} \times Q_{i\beta} \right). \quad (6)$$

We denote the flavor $\pm$ by Greek indices, and the summation convention is understood.[2] Furthermore, we denote $Q_\alpha \times Q_\beta \equiv Q_{i+} Q_{j-} + Q_{i-} Q_{j+}$. The first term is the expected Coulomb interaction of vortices from the XY model (Berezinsky 1971; Kosterlitz and Thouless 1973); notice that only like-flavored charges interact through this term (because the kinetic term $|\nabla \Psi|^2$ is homogenous quadratic). The second term is the forward–backward interaction, also with Coulomb-like (logarithmic) radial dependence. This interaction is generated by the coupling of amplitude fluctuations $\delta \psi_\alpha(r)$ to the phase fluctuations. In a system without amplitude fluctuations, i.e. classical spin system, this term would not be generated. The third and fourth term constitute the energy of the vortex core. The self-interaction

---

[2] There is no difference between upper and lower indices as both flavors always enter the sum with positive sign.

constants g_0, g_1 are of course dependent on the vortex core size and behave roughly as $g \log a/\epsilon, g' \log a/\epsilon$, where ϵ is the UV cutoff. The final results will not depend on ϵ, as expected, since g_0, g_1 can be absorbed in the fugacity y (see the next subsection). Expressions for the coupling constants in terms of original parameters are given in Čubrović and Petrović (2017); they can be used to relate the theoretical phase diagram to experiment.

To describe the phase diagram, we will perform the renormalization group (RG) analysis. Here we follow closely the calculation for conventional vortex systems. We consider the fluctuation of the partition function $\delta\mathcal{Z}$ upon the formation of a virtual vortex pair at positions $\mathbf{r}_1, \mathbf{r}_2$[3] with charges $q_\alpha, -q_\alpha$, (with $\mathbf{r}_1 + \mathbf{r}_2 = 2\mathbf{r}$ and $\mathbf{r}_1 - \mathbf{r}_2 = \mathbf{r}_{12}$), in the background of a vortex pair at positions $\mathbf{R}_1, \mathbf{R}_2$ (with $\mathbf{R}_1 + \mathbf{R}_2 = 2\mathbf{R}$ and $\mathbf{R}_1 - \mathbf{R}_2 = \mathbf{R}_{12}$) with charges $Q_{1\alpha}, Q_{2\alpha}$. It is also convenient to replace the core self-interaction constants $g_{0,1}$ with the fugacity parameter defined as $y \equiv \exp\left[-\beta(g_0 + g_1) \log \epsilon\right]$. We also introduce the notation $\beta \equiv L$ in analogy with the inverse temperature β in standard statistical mechanics but of course the physical meaning of β in our system is very different: we have no thermodynamic temperature or thermal noise, and the third law of thermodynamics is not satisfied for the "temperature" $1/\beta$. We merely use the β-notation for reasons of formal similarity, not as a complete physical analogy.

This is a straightforward but lengthy calculation and we state just the resulting flow equations:

$$\frac{\partial g}{\partial \ell} = -16\pi(g^2 + g'^2)y^4, \quad \frac{\partial g'}{\partial \ell} = -2\pi gg'y^4, \quad \frac{\partial y}{\partial \ell} = 2\pi(1 - g - g')y. \tag{7}$$

Notice that if one puts $g' = 0$, they look very much like the textbook XY model RG flow, except that the fugacity enters as y^4 instead of y^2 (simply because every vortex contributes two charges). We can find fixed points analytically and then numerically integrate the flow equations to find exact phase borders. The fugacity y can flow to zero (meaning that the vortex creation is suppressed and the vortices tend to bind) or to infinity, meaning that vortices can exist at finite density. At $y = 0$ there is a fixed line $g + g' = 1$. This line is attracting for the half-plane $g + g' > 1$; otherwise, it is repelling. There are three more attraction regions when $g + g' < 1$. First, there is the point $y \to \infty, g = g' = 0$ which has no analogue in single-component vortex systems. Then, there are two regions when $g \to \infty$ and $g' \to \pm\infty$ (and again $y \to \infty$). Of course, the large g, g' regime is strongly interacting and the perturbation theory eventually breaks down. What happens when g, g' flow toward very large values is that the intensity at the vortex core becomes very large, so the lowest-order, quadratic Hamiltonian needs to be supplemented by higher-order terms in intensity fluctuations. To integrate them out, one needs to perform a diagrammatic expansion which leads to quartic- and higher-order terms in vortex charges Q_α in the effective vortex Hamiltonian [Eq. (6)], ultimately correcting the flow at large g, g' to flow toward finite values g_*, g'_* and g_{**}, g'_{**}.

The RG flows in the $g - g'$ plane are given in Fig. 2. The situation is now the following:

1. The attraction region of the fixed line is the vortex insulator phase (INS): the creation rate of the vortices is suppressed to zero. There is no vortex charge conservation.

---

[3] The boldface vectors are the coordinate vectors in the plane.
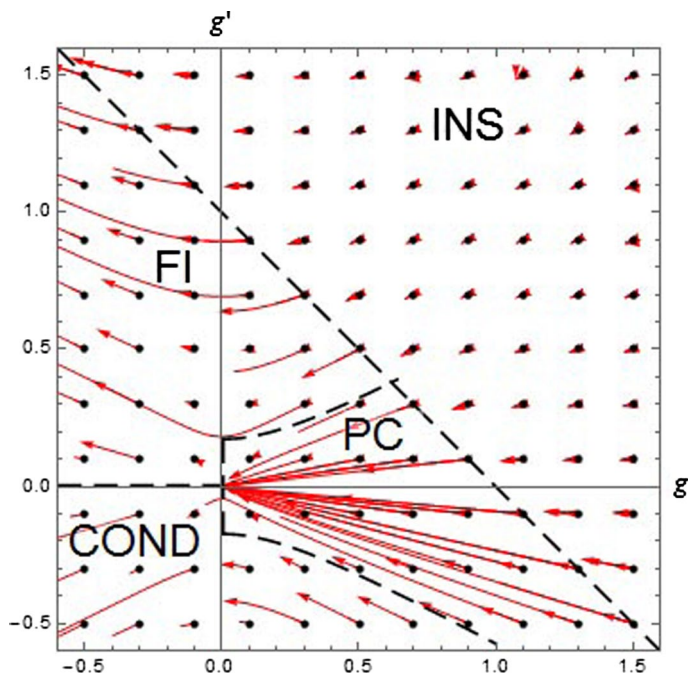
Fig. 2 Phase diagram for the clean system in the g–g' plane, at the mean-field level with RG flows. We show the flows for a grid of initial points, denoted by black dots; red lines are the flows. Four phases exist, whose boundaries are delineated by black dashed lines: conductor (COND), insulator (INS), frustrated insulator (FI) and perfect conductor (PC). The straight line $g + g' = 1$ is obtained analytically whereas the other phase boundaries can only be found by numerical integration of the flow Eq. (7). The flows going to infinity are the artifacts of the perturbative RG; they correspond to finite values which are beyond the scope of our analytical approach. Notice how the flows in the $g + g' > 1$ phase all terminate at different values

2. The zero-coupling fixed point attracts the trajectories in the vortex perfect conductor phase (PC): only the fugacity controls the vortices and arbitrary charge configurations can form. Each vortex charge, Q_+ and Q_-, is separately conserved.
3. In the attraction region of the fixed point with $g_* < 0$ and $g'_* > 0$ (formally they flow to $-\infty$ and $+\infty$, respectively), same-sign F- and B-charges attract each other and those with the opposite sign which repel each other. This is the frustrated insulator (FI): it conserves only the combination $Q_+ + Q_-$, and only vortices with charge $(Q_+, -Q_+)$ are stable.
4. The fixed point with $g_{**}, g'_{**} < 0$ (formally both flow to $-\infty$) corresponds to the conductor phase (COND). This phase preserves one of the charges, Q_+ or Q_-, i.e. either $(Q_+, 0)$- or $(0, Q_-)$-vortices proliferate.

In the half-plane $g + g' > 1$ every point evolves toward a different, finite point (g, g') in the same half-plane. In the other half-plane we see the regions of points moving toward the origin or toward one of the two directions at infinity. In the future we plan to apply this formalism also to multi-component vortices in Bose–Einstein condensates (Ma et al. 2016) and in particular in type-1.5 superconductors (Silaev and Babev 2012), where even more complex phenomena, including frustration, are observed as a consequence of multi-component interaction.

An interesting line of research consists in adding disorder to the above system. We consider this problem in Čubrović and Petrović ([2017]) and find that the system can be approximated by a random-coupling *and* random-field two-component XY-like model, related to the Cardy–Ostlund model ([1982]). The replica formalism (Castellana and Parisi [2015]) then predicts a glassy phase with slow dynamics, strong correlations and no long-range order. This is however a separate story and we will leave it out here. Interested readers can consult (Čubrović and Petrović [2017]) and look at related work in Antenucci et al. ([2015a], [b]).

4 Time-dependent regime

Here our goal is twofols. First, we have to show that at least for some boundary conditions and parameter values there is a stable fixed point of the time evolution, so that the system reaches a time-independent, equilibrium pattern. The reason is that the whole formalism of the previous chapter is only valid for such configurations, as it departs from equilibrium statistical mechanics. Second, we want to check other, non-static behaviors as they are interesting in their own right and experimentally relevant (but one should not expect them to be described by an equilibrium phase diagram like Fig. [2]).

Time dynamics can be studied in a straightforward way, making use of the relaxation Eq. ([2]) to write down the first-order evolution equations for $\Psi_\pm$:

$$\frac{\partial \Psi_\alpha^\pm}{\partial t} = -\frac{\Gamma}{\tau}\frac{((1+I)E + I)}{\alpha k - q^2 - \Gamma E}\Psi_\alpha^\pm, \quad \frac{\partial E}{\partial t} = -\frac{1}{\tau}((1+I)E + I). \tag{8}$$

This system has three equilibrium points. One is the trivial equilibrium with zero intensity ("0" point):

$$\left(\Psi_+^\pm, \Psi_-^\pm, E\right) = \left(0, 0, -\frac{I_x}{1+I_x}\right),$$

and the remaining two are related by a discrete symmetry $\Psi_\pm \mapsto \Psi_\mp$ ("$\pm$" points). The "+" point is

$$\left(\Psi_+^\pm, \Psi_-^\pm, E\right) = \left(\sqrt{\frac{E(1+I_x)+I_x}{1+E}}e^{\iota\phi_+}, 0, E\right),$$

and the "−" point has instead $\Psi_+ = 0$ and $\Psi_- = \sqrt{(E(1+I_x)+I_x)/(1+E)}\exp(\iota\phi_-)$. Notice that the phase $\phi_\pm$ remains free to vary so the "$\pm$" solutions support vortices. We first ask what is the stability criterion for a nontrivial solution, i.e. one of the "$\pm$" points, as this is the main criterion for the applicability of the equilibrium statistical mechanics methods in the previous section. Introducing the amplitudes of the fluctuations from equilibrium as $X_{1,3} = \Re\delta\Psi_\pm, X_{2,4} = \Im\delta\Psi_\pm, X_5 = \delta E$, we can do a first-order stability analysis as the system is non-degenerate. Rescaling $X_1 \mapsto (1+E_0)^{-3/4}\left(I_x + E_0\left(1+I_x\right)\right)^{1/2}$ and $t \mapsto t\left(\left(1+E_0\right)/\left(I_x + E_0\left(1+I_x\right)\right)\right)^{1/4}$, the equation of motion for the "$\pm$" point reads

$$\partial_t \begin{pmatrix} X_1 \\ X_5 \end{pmatrix} = \begin{pmatrix} -\frac{a_\pm}{\Gamma E_0 + k + q^2} & -1 \\ 1 & -\frac{a_\pm}{\Gamma E_0 + k + q^2} \end{pmatrix}\begin{pmatrix} X_1 \\ X_5 \end{pmatrix} + O(X_1^2 + X_5^2; X_2, X_3, X_4), \tag{9}$$
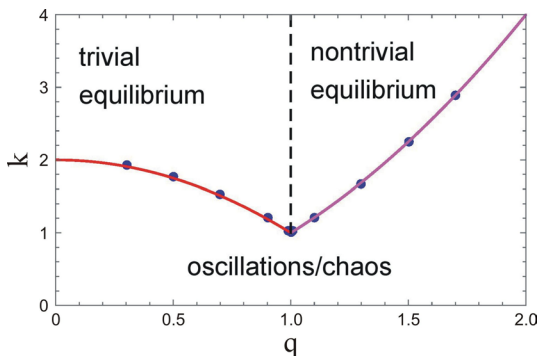
Fig. 3 Stability diagram in the q–k plane. The onset of instability for $k < k_c(q)$ is found numerically for a range of q values. The solid lines are the analytical prediction for the stability of the "0" point ($k_c = q^2$, magenta) and of the "+" point ($k_c = \Gamma E_0 - q^2 \approx \Gamma - q^2$, red). The black dashed line at $q = q_c \approx 1$ separates the stability regions of the two points. The domain of applicability of our main results is the top right corner (nontrivial equilibrium), above $k > k_{min} \sim 1/L$ and for not too large q values. Parameter values: $\Gamma = 2, I_x = 0$

with $a_\pm$ being some (known) *positive* functions of Γ, E_0, I_x (independent of k, q). This is precisely the normal form for the Andronov–Hopf bifurcation (Arnol'd et al. 1994), and the bifurcation point lies at $k = -\Gamma E_0 - q^2$. To remind, the bifurcation happens when the off-diagonal element in the linear term changes sign: the fixed point is stable when $a_\pm/(\Gamma E_0 + k + q^2)$ is positive. The sign of the nonlinear term determines the supercritical/subcritical nature of the bifurcation.[4]

Now the textbook analysis of the Andronov–Hopf bifurcation tells us that stable "+" equilibrium exists for $k > -\Gamma E_0 - q^2$ where E_0 is best found numerically. Exactly the same condition holds for the "−" point. For $k < -\Gamma E_0 + q^2$, dynamics depends on the sign of the nonlinear term in Eq. (9). For the positive sign we expect periodically changing patterns and for the negative sign (subcritical bifurcation), various possibilities arise: the system may wander chaotically between the "+" and the "−" points, or it may end up in the attraction region of the "0" point and fall onto the trivial solution with zero intensity. Naively, the attraction regions of the two fixed points ("±" and "0") are separated by the condition $-\Gamma E_0 - q^2 = q^2$, i.e. $q_c = \sqrt{-\Gamma E_0(\Gamma, \tau)/2}$, where we have emphasized that E_0 is in general non-universal. The actual boundary may be more complex however, as our analysis is based on finite-order expansion around the fixed points, which is not valid far away from them.

The numerical stability diagram is given in Fig. 3. The stability limit turns out to be $k > \Gamma - q^2$, i.e. $E_0 \approx -1$. The curves separating the attraction regions of the three equilibrium points follow exactly the quadratic scaling in q as predicted by the analytical stability analysis. The equilibrium region lies in the top right corner of the diagram (nontrivial equilibrium), above $k \approx 1/L$. This is where the patterns evolve towards static

---

[4] Negative sign means the fixed point is stable everywhere before the bifurcation and is replaced by a stable limit cycle after the bifurcation (supercritical). Positive sign means the fixed point coexists with the stable limit cycle before the bifurcation and the (X_1, X_5) plane is divided among their attraction regions; after the bifurcation there is no stable solution at all (subcritical). However, one should not take the stability in the whole (X_1, X_5) plane in the supercritical case too seriously. We have expand the equations of motion in the vicinity of the fixed points and the expansion ceases to be valid far away from the origin.

Fig. 4 Time evolution of the relaxation rate r for the various situations from Figs. 5 and 6, illustrating the relaxation to non-trivial (non-zero intensity) equilibrium, i.e. "±" fixed points (Fig. 5a, c, black), limit cycle (6a, blue), chaos (6b, red) and the relaxation to trivial (zero intensity) equilibrium, i.e. "0" fixed point (6c, green). In the main text we mainly study the cases like the black curves, where time-independent stable configurations are seen. The circles are data points from numerics and the lines are just to guide the eye
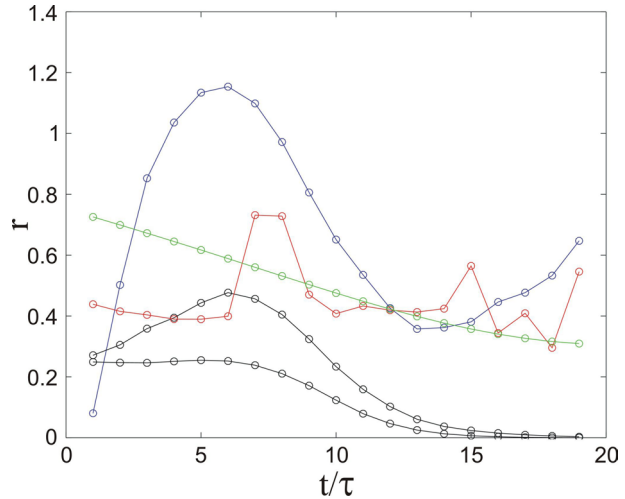
long-time configurations. The top left corner describes "boring" situations, when all light ultimately radiates away from the crystal and intensity drops to zero. The bottom region contains nontrivial dynamics: depending on parameters, it may contain a limit cycle (corresponding to oscillating patterns) or aperiodic wandering among an alphabet of unstable patterns (chaos).

Formally, both k and q can be any real numbers. In practice, however, k is discrete and its minimal value is of the order $1 / L$. The spatial momentum q lies between the inverse of the transverse length of the crystal (which is typically an order of magnitude smaller than L, i.e. minimal q can be assumed equal to zero) and some typical small-scale cutoff which in our case is the vortex core size.

Now we test our conclusions numerically. A convenient quantity to differentiate between different stability regimes is the relaxation rate

$$r \equiv \frac{1}{X}\frac{dX}{dt} = \frac{\sum_{x,y}|X(t_{j+1};x,y) - X(t_j;x,y)|^2}{\sum_{x,y}|X(t_j;x,y)|^2}, \tag{10}$$

which is expected to reach zero for a generic relaxation process, where in the vicinity of an asymptotically stable fixed point $X \sim X_{eq} + xe^{-rt}$ will be generically nonzero for a limit cycle or chaos, and will asymptote to a constant for the "0" point, where $X_{eq} = 0$ so we get $(1/X)dX/dt \sim r$.

Figure 4 summarizes these possibilities in terms of the relaxation rate r, whereas Figs. 5 and 6 show how the patterns evolve in some representative cases. The black curves in Fig. 4 show the situation which is in the focus of this work – the approach toward static equilibrium. This corresponds to the phases from Fig. 2. In Fig. 5 we see how the equilibrium configurations are reached (for three phases). In each case we start with a regular lattice of circular vortices. In the PC phase (Fig. 5a) the vortices expand somewhat but in principle retain the original configuration (and charges). The other two phases (Fig. 5b, c) have nontrivial transient dynamics and undergo the lattice inversion, but eventually (for times about $t \approx 20 - 25\tau$) they stabilize and form a static inverse lattice (with charges $(3, -3)$ in the FI case and with zero charge in the INS case).
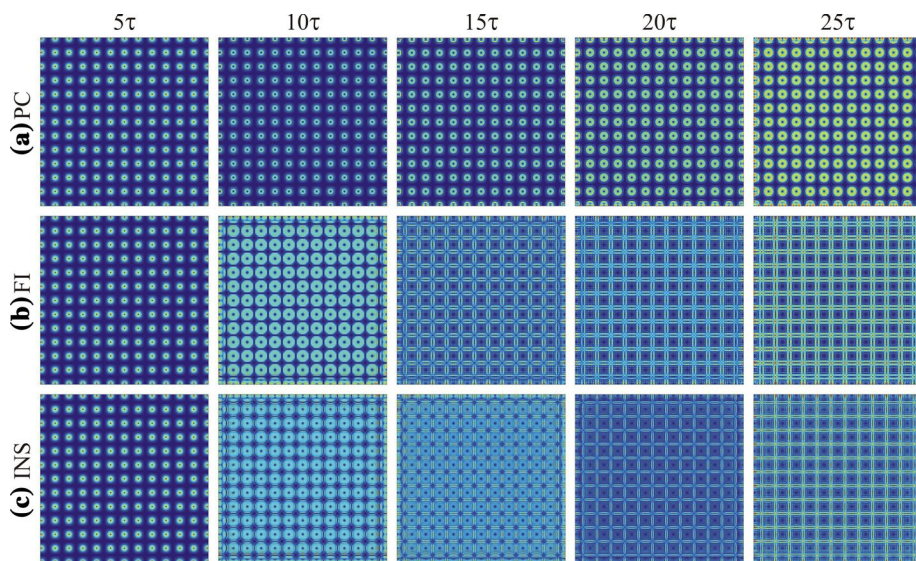
Fig. 5 Time evolution of patterns at five different times: **a** perfect conductor phase, **b** frustrated insulator phase and **c** insulator phase. In all cases the approach to equilibrium is obvious, and we expect that for long times a thermodynamic description is justified
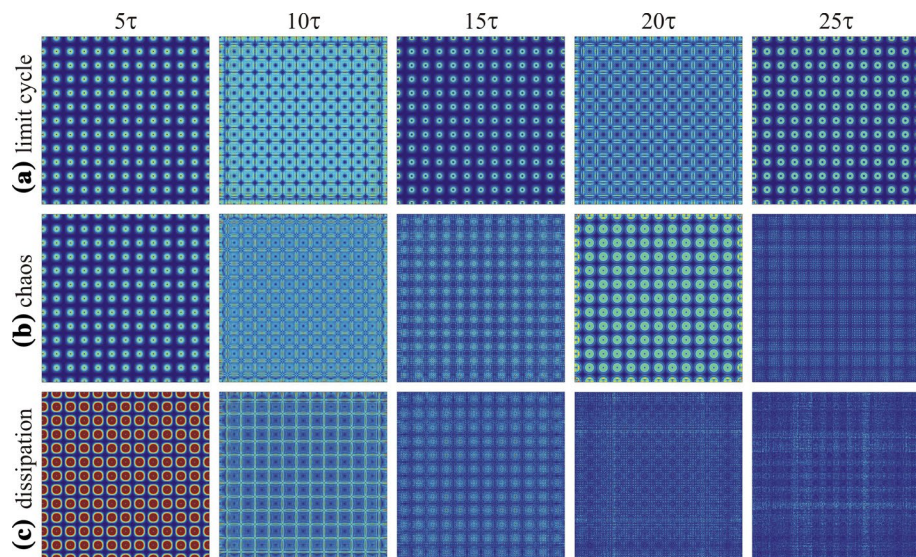
Fig. 6 Time evolution of non-equilibrium patterns. In **a** the limit cycle leads to permanent oscillatory behavior, in **b** wandering along the unstable manifold between the equilibrium points gives rise to chaos and in **c** dissipation wins and dynamics dies out. The parameters are the same as in the previous figure, except that the length L is increased thrice
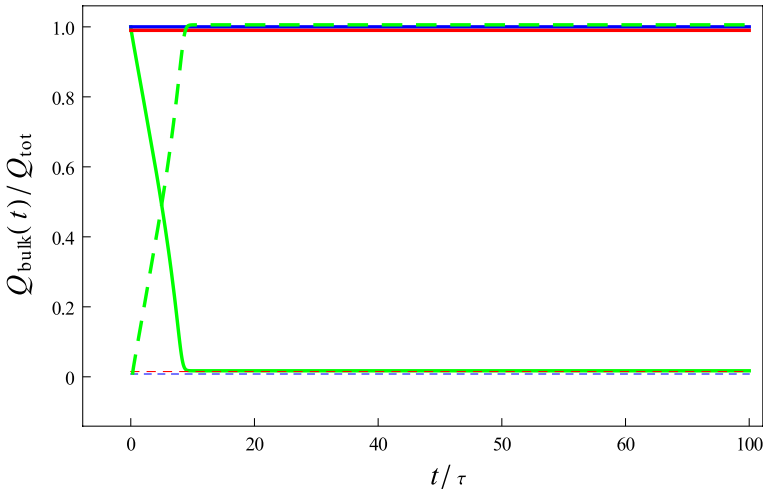
Fig. 7 Same systems as in Fig. 6 but now for the time dependence of the *F*-vortex charge in the bulk (full lines) and the vortex current flow through ther boundary (dashed lines). While the limit cycle (blue) and chaos (red) keep all vortex charge in the bulk, dissipation toward the trivial equilibrium (green) has a systematic vortex flow toward the edges. This is a finite-size effect which would not happen in an infinite field (but it does happen in real-world PR crystals which are, of course, finite)

The other curves in Fig. 4 describe dynamics which does not result in a nontrivial static pattern. The blue curve shows a limit cycle leading to periodic oscillations of the pattern, with half-period about 10τ. The corresponding patterns are seen in Fig. 6a, where we see how the vortex lattice keeps coming back to the original configuration at times $\approx 5\tau, 10\tau, 15\tau$. The red curve corresponds to the chaotic regime with aperiodic dynamics and no relaxation, as in Fig. 6b. Here the pattern keeps changing, wandering among the original lattice (for $t = 5\tau, 20\tau$), the inverse lattice (for $t = 10\tau$) and more or less incoherent patterns (for $t = 15\tau, 25\tau$). Finally, the green curve in Fig. 4 reaches a constant value of r. This corresponds to the pattern which radiates away in Fig. 6c, with total intensity being almost zero for $t > 20\tau$. Here one might wonder what happens to the vortex charge when the initially regular vortex lattice ends up as an incoherent, low-intensity configuration which obviously does not support vortices. The explanation is that the vortex charge flows outward, eventually reaching the edges of the crystal. The finite-size effects then invalidate the vortex charge conservation, as the usual proof that the winding number of the phase is a topological invariant crucially depends on considering the winding at infinity. Vortex charge thus dissipates at the edges. This is demonstrated in Fig. 7, which presents the same systems as in Fig. 6a–c but shows the ratio of the total bulk vortex charge $Q_{\text{bulk}}(t)$ to the total initial vortex charge Q_{tot}. Total initial charge is calculated by definition, as the integrated vorticity of the *F*-beam, $Q_{\text{tot}} = \int dx \int dy |\boldsymbol{\omega}_F|$, with

$$\boldsymbol{\omega}_F = \left(\cos\theta_F \partial_x \theta_F, \sin\theta_F \partial_y \theta_F\right), \tag{11}$$

and all the quantities are taken at $t = 0$. The integral $\int dx \int dy |\boldsymbol{\omega}_F|$ equals precisely the total *F*-vortex charge summed over all vortices. The bulk charge is computed by subtracting the integrated vorticity flow along the boundary:

$$Q_{\text{bulk}}(t) = Q_{\text{tot}} - \int_0^t dt' \oint d\mathbf{l} \cdot \boldsymbol{\omega}_F(t). \tag{12}$$

Figure 7 shows that the sum of the bulk charge and the vortex current through the boundary is preserved in all cases, including when chaos or dissipation makes the pattern incoherent. In the last case, however, all the vortex charge flows toward the boundaries – this is a finite-size effect which would be absent in infinite field but is observable in realistic PR-crystals which are of finite dimensions. In practice, the matters are even more complicated as the boundary surface carries also new physics (surface polarization etc.), so the starting equations of motion would have to be modified. We believe, however, that the basic picture of vortex charge dissipating at the boundary still remains, because the mapping from the internal $U(1)$ phase onto the loop in the coordinate plane is explicitly broken by the boundary (whatever its detailed physics might be), and the vortex charge nonconservation at the boundary follows from this breaking.

The next task is to consider in more detail the decay of an ordered phase, either to chaos or to a limit cycle (radiating away all intensity is likely a trivial process, fully described by the approximately constant decay rate). We plan to address this problem in further work, and to relate the results to the question of quench dynamics in vortex systems.

References

Alexander, T.J., Desyatnikov, A.S., Kivshar, Y.S.: Multivortex solitons in triangular photonic lattices. Opt. Lett. **32**, 1293–1295 (2007)

Anderson, P.W.: Two new vortex liquids. Nat. Phys. **3**, 160–162 (2007)

Antenucci, F., Conti, C., Crisanti, A., Leuzzi, L.: General phase diagram of multimodal ordered and disordered lasers in closed and open cavities. Phys. Rev. Lett. **114**, 043901 (2015a)

Antenucci, F., Crisanti, A., Leuzzi, L.: Complex spherical 2 + 4 spin glass: a model for nonlinear optics in random media. Phys. Rev. A **91**, 053816 (2015b)

Arnol'd, V.I., Afraymovich, V.S., Il'yashenko, Y.S., Shil'nikov, L.P.: Bifurcation Theory and Catastrophe Theory. Springer, Berlin (1994)

Bagnato, V.S., Frantzeskakis, D.J., Kevrekidis, P.G., Malomed, B.A., Mihalache, D.: Bose–Einstein condensation: twenty years after. Rom. Rep. Phys. **67**, 5–50 (2015)

Berezinsky, V.L.: Destruction of long range order in one-dimensional and two-dimensional systems having a continuous symmetry group. 1. Classical systems. Sov. Phys. JETP **32**, 493–500 (1971)

Cardy, J.L., Ostlund, S.: Random symmetry-breaking fields and the XY model. Phys. Rev. B **25**, 6899–6909 (1982)

Castellana, M., Parisi, G.: Non-petturbative effects in spin glasses. Nat. Sci. Rep. **5**, 8697 (2015). arXiv:1503.02103 [cond-mat.dis-nn]

Cohen, O., Lan, S., Harmon, T., Giordmaine, J.A., Segev, M.: Spatial vector solitons consisting of counter-propagating fields. Opt. Lett. **27**, 2013–2015 (2002)

Cross, M., Hohenberg, P.: Pattern formation outside of equilibrium. Rev. Mod. Phys. **65**, 851–1112 (1993)

Čubrović, M., Petrović, M.: Quantum criticality in photorefractive optics: vortices in laser beams and antiferromagnets. Phys. Rev. A **96**, 053824 (2017). arXiv:1701.03451 [physics.optics]

Denz, C., Schwab, M., Weilnau, C.: Transverse Pattern Formation in Photorefractive Optics. Springer, Berlin (2003)

Dreischuh, E., Chervenkov, S., Neshev, D., Paulus, G.G., Walther, H.: Generation of lattice structures of optical vortices. J. Opt. Soc. Am. B **19**, 550–556 (2002)

Fetter, A.L.: Rotating trapped Bose–Einstein condensates. Rev. Mod. Phys. **81**, 647–691 (2009)

Fleischer, J.W., Bartal, G., Cohen, O., Manela, O., Segev, M., Hudock, J., Christodoulides, D.N.: Observation of vortex-ring "discrete" solitons in 2D photonic lattices. Phys. Rev. Lett. **92**, 123904 (2004)

Ghofraniha, N.: Experimental evidence of replica symmetry breaking in random lasers. Nat. Commun. **6**, 6058 (2015). arxiv.org/abs/1407.5428 [cond-mat.dis-nn]

Jović, D.M., Petrović, M.S., Belić, M.R.: Counterpropagating pattern dynamics: from narrow to broad beams. Opt. Commun. **281**, 2291–2300 (2008)

Kosterlitz, J., Thouless, D.: The Kosterlitz–Thouless phase in a hierarchical model. J. Phys. C **6**, 1181–1203 (1973)

Ma, X., Driben, R., Malomed, B., Meoer, T., Schumacher, S.: Two-dimensional symbiotic solitons and vortices in binary condensates with attractive cross-species interaction. Nat. Sci. Rep. **6**, 34847 (2016). arXiv:1606.08579 [physics.optics]

Malomed, B., Torner, L., Wise, F., Mihalache, D.: On multidimensional solitons and their legacy in contemporary atomic, molecular and optical physics. J. Phys. B: At. Mol. Opt. Phys. **49**, 170502 (2016)

Neshev, D.N., Alexander, T.J., Ostrovskaya, E.A., Kivshar, Y.S.: Observation of discrete vortex solitons in opticlly induced photonic lattices. Phys. Rev. Lett **92**, 123903 (2004)

Perret, A., Ristivojevic, Z., Le Doussal, P., Schehr, G., Wiese, K.: Super-rough glassy phase of the random field XY model in two dimensions. Phys. Rev. Lett. **109**, 157205 (2012). arXiv:1204.5685 [cond-mat.dis-nn]

Petrović, M.S., Belić, M.R., Denz, C., Kivshar, YuS: Counterpropagating optical beams and solitons. Lasers Photonic Rev. **5**, 214–233 (2011). arXiv:0910.4700 [physics.optics]

Petrović, M., Jović, D., Belić, M., Schröder, J., Jander, P., Denz, C.: Two dimensional counterpropagating spatial solitons in photorefractive crystals. Phys. Rev. Lett **95**, 053901 (2005)

Rabinovich, M.I., Ezersky, A.B., Weidman, P.D.: The Dynamics of Patterns. World Scientific, Singapore (2000)

Rechtsman, M.C., Zeuner, J.M., Plotnik, Y., Lumer, Y., Podolsky, D., Dreisow, F., Nolte, S., Segev, M., Szameit, A.: Photonic Floquet topological insulators. Nature **496**, 196–200 (2013). arXiv:1212.3146 [physics]

Sandfuchs, O., Kaiser, F., Belić, M.R.: Self-organization and Fourier selection of optical patterns in a nonlinear photorefractive feedback system. Phys. Rev. A **64**, 063809 (2001)

Silaev, M., Babev, E.: Microscopic derivation of two-component Ginzburg–Landau model and conditions of ots applicability in two-band systems. Phys. Rev. B **85**, 134514 (2012). arXiv:1110.1593 [cond-mat.supr-con]

Terhalle, B., Richter, T., Desyatnikov, A.S., Neshev, D.N., Krolikowski, W., Kaiser, F., Denz, C., Kivshar, Y.S.: Observation of multivortex solitons in photonic lattices. Phys. Rev. Lett **101**, 013903 (2008)

P r o c e e d i n g s

of the

10th MATHEMATICAL PHYSICS MEETING:
School and Conference on
Modern Mathematical Physics

September 9 – 14, 2019, Belgrade, Serbia

Editors

B. Dragovich, I. Salom and M. Vojinović

Institute of Physics

Belgrade, 2020

SERBIA

CONTENTS

Review and Research Works

x

Fermions, hairy blackholes and hairy wormholes in anti-de Sitter spaces[*]

Mihailo Čubrović[†]

Center for the Study of Complex Systems,
Institute of Physics Belgrade, Serbia

Abstract

We discuss the existence, properties and construction (analytical and numerical) of hairy black holes with fermionic matter in asymptotically anti-de-Sitter space. The negative cosmological constant makes hairy black holes stable, and the nucleation mechanism can make the formation of hair at the horizon energetically and entropically preferable to conventional black holes. The difficulties intrinsic to fermions at finite density – the Pauli principle and exchange interactions – require some drastic approximations in calculating the stress-energy tensor and geometry. We will consider several methods on the market – Hartree-Fock, WKB, and fluid-mechanical methods, and consider the dual field theories of these constructions. Then we will apply the same methods to the construction of wormholes; fermions are a natural candidate for wormhole source matter as they have a Dirac sea of negative energies, and negative energy-momentum density is the condition for wormhole formation. The field theory interpretation of wormholes is still open but has to do with strongly entangled systems. The paper combines a pedagogical introduction to the basic methods and results (obtained in the last 10+ years) with an account of fresh research results, mainly on the wormhole applications and non-planar black holes.

1. Introduction

AdS black holes are a favorite topic, not only in relation to holography but also in general: AdS space behaves like a potential box, the cosmological constant provides an effective repulsive force at large distances and the existence of a boundary at spatial infinity makes bound states possible. All of

this brings about the famous result that hairy black holes are indisputably possible, and well-studied. In full (global) AdS space, one may have small black holes, which barely see the boundary and radiate like in asymptotically flat space, and large black holes, which reach an equilibrium state with the Hawking radiation at given temperature and remain stable forever (eternal AdS black holes). We will focus on the latter, as they can be treated as (semi)classical stationary systems. Clearly, just like the Hawking radiation, matter and gauge fields can likewise equilibrate between the black hole horizon and AdS boundary, possibly forming hair – by definition, it means nonzero density of some field (and possibly nonzero expectation values of other operators, like charge density, spin, etc) at the horizon itself. This in turn means that the geometry changes as opposed to the no-hair case: the hair itself enters the stress-energy tensor, and the outcome is a hairy black hole geometry, where a horizon still exists but with a different metric. At zero temperature, hair tends to remove extremal black holes in favor of zero-area horizons, with zero Bekenstein-Hawking entropy. We will soon discuss several explicit examples of this phenomenon.

   The above story acquires an additional dimension thanks primarily to the AdS/CFT correspondence (gauge/gravity duality) [1, 2, 3] – the fact that the bulk gravity physics is equivalent to a quantum field theory in flat space in one dimension less, whose operators act as boundary sources of the AdS (bulk) fields. The actions in AdS (with field Φ) and in CFT (with field O, which acts as a boundary source to Φ) are equal:

$$
\begin{aligned}
S_{\mathrm{AdS}} &= S_{\mathrm{CFT}} \\
S_{\mathrm{AdS}} &= \int \mathcal{D}\Phi \exp\left(-\int_{\mathrm{AdS}} d^{D+1}x\sqrt{-g}\mathcal{L}_{\mathrm{AdS}}\left(\Phi,\partial_\mu\Phi\right) + \oint_\partial d^D x\sqrt{-h}\mathcal{O}\Phi\right) \\
S_{\mathrm{CFT}} &= \int \mathcal{D}\mathcal{O} \exp\left(-\int d^D x\mathcal{L}_{\mathrm{CFT}}\left(\mathcal{O}\right)\right),
\end{aligned}
\tag{1}
$$

where we have denoted by ∂ the boundary of the AdS space, $g_{\mu\nu}$ is the AdS metric and $h_{\mu\nu}$ is the induced metric at the boundary. From now on, integrals over the bulk of AdS will be dnoted just by $\int$, understanding that the integral is over the whole space. At this place we do not intend to explain AdS/CFT and its applications in any detail; suffice to say that one can obtain thermodynamic potentials and correlation functions in field theory, which has found important applications in condensed matter theory, quantum chromodynamics and conformal field theory. Interested readers can consult [4, 5, 6] for reviews. In this work we deal with the gravity side of the correspondence – the formation of a hairy black hole with fermionic matter, which corresponds to a finite electron density phase in field theory. We assume the familiarity with the basic notions of AdS space and quantum field theory in curved spacetime, for example at the level of [7] and [8], respectively.

   Mathematically, the topic of this review is the solution of the coupled Einstein-Maxwell-Dirac system with the total action $S_{\mathrm{AdS}} = S_{\mathrm{bulk}} + S_\partial$.

The bulk action reads:

$$S_{\text{bulk}} = S_{\text{E}} + S_{\text{M}} + S_{\text{Dir}}$$

$$S_{\text{E}} = \int d^4x \sqrt{-g} \, (R+6)$$

$$S_{\text{M}} = -\int d^4x \sqrt{-g} \frac{\hat{F}^2}{4}$$

$$S_{\text{Dir}} = -\int d^4x \sqrt{-g} \left(\frac{1}{2} \bar{\Psi} D_\mu e_a^\mu \Gamma^a \Psi + \frac{1}{2} \bar{\Psi} e_a^\mu \Gamma^a \Psi + m \bar{\Psi}\Psi \right). \quad (2)$$

Here, $\hat{F}_{\mu\nu} = \partial_\mu A_\nu - \partial_\nu A_\mu$ is the electromagnetic (EM) field strength tensor, and the the cosmological constant in AdS$_4$ is $6/L^2$, where the AdS radius $L = 1$ is set to unity, as we will mainly work on the Poincare patch of AdS space, so all other dimensionful quantities can be expressed in terms of L. The Dirac bispinor Ψ has mass m and charge q, and the covariant derivative

$$D_\mu = e_\mu^a D_a = \partial_\mu - \frac{\imath}{8} \left[\Gamma^a, \Gamma^b \right] \omega_{ab}^\mu - \imath q A_\mu \quad (3)$$

depends on the spin connection ω_{ab}^μ and the gauge field A_μ, and the gamma matrices satisfy the usual relations $\left[\Gamma^a, \Gamma^b \right] = 2\eta^{ab}$, with the Minkowski metric η. We will be using the mostly plus convention. Obviously, $\Psi = 0$ is a solution, and in this case we get a Schwarzschild black hole if the EM field is also zero, or a charged Reissner-Nordstrom (RN) black hole for nonzero field strength. The question is, are there other solutions, with nonzero profile Ψ? Such solutions describe hairy black holes at finite temperature: the horizon is typically still there, but the geometry is changed. At zero temperature, the black hole might disappear. Since AdS space has a boundary, there is also a boundary contribution to the action, as in (1), depending on extrinsic curvature K, boundary cosmological constant λ and the boundary values of the fields:

$$S_\partial = \oint_\partial d^3x \sqrt{-h} \left[K - \lambda - \frac{1}{2} n_\mu A_\nu \hat{F}^{\mu\nu} - \frac{1}{2} \bar{\Psi}\Psi \right]. \quad (4)$$

The classical equations of motion do not depend on the boundary action. However, S_∂ is still important (1) to make sure there is a good action principle, i.e., that the on-shell solutions are indeed minima of the action[1] (2) to regularize any UV divergences (3) to get correct thermodynamics. The last point will be particularly important: one way to see that the hairy black hole and not the bald black hole is the true vacuum will be the fact that the action on the hairy solution is lower.

Solving the system (2) is a problem in quantum field theory at finite density. We work with classical general relativity (GR) and classical EM

---

[1]Remember that the (bulk) Euler-Lagrange equations are only a necessary condition for the minimum of the action.

field, but *fermions are never classical*; this is the first important lesson. The Pauli principle always introduces nonlocal correlations which show as the exchange interaction. Another way of saying this is that the pressure of a fermionic gas or fluid always includes the quantum contribution which is absent in both classical and bosonic gas; that is the reason that organized matter such as stars, planets, chairs and notebooks has rigidity and does not collapse onto itself. Therefore, even though we do gravity at $\hbar = 0$, the fermions even at leading order need to be tackled quantum-mechanically. This means calculating the *fermionic determinant*:

$$Z_{\mathrm{Dir}} = \int \mathcal{D}\bar{\Psi}\mathcal{D}\Psi e^{-S_{\mathrm{Dir}}} \text{ " } = \text{ " } [\det\left(D_\mu e_a^\mu \Gamma^a + e_a^\mu \Gamma^a D_\mu + m\right)]^{1/2}. \tag{5}$$

We have put the equality sign under quotation marks because the determinant is actually the product of the eigenenergies of all the modes (an infinity of them), which is not only badly divergent (that could be regulated) but is also impossible to calculate because of the *fermion sign problem*, the fact that the fermionic modes enter the path integral with a sign that can be plus or minus. This makes the measure in the path integral (5) non-probabilistic and makes it impossible to expand around a classical solution in a controlled way. Fortunately, the AdS metric turns out to simplify the problem enough that it can be tackled in a way which is tractable and, while of course not exact, can be systematically improved in a perturbative way. This is in fact the motivation behind AdS/CFT modelling of strongly correlated electron systems: the fermion sign problem is fatal for strongly coupled field theories in flat space, but in GR with AdS boundary conditions it transforms into a difficult but doable task.

Is the journey worthwhile? In line with the broad scope of the Belgrade Mathematical Physics Meetings, we have anticipated a broad readership of this paper and thus we have decided to give a very general and perhaps rather dry introduction to the topic of fermionic hairy black holes. This necessarily means that we will not touch upon the many interesting applications: AdS/CFT and its applications to quantum chromodynamics and condensed matter physics, the black hole information problem, the critical phenomena in gravitational collapse and the black hole solutions in string theory. We do discuss one special topic that we currently find very interesting: hairy wormholes generated by fermion matter, where many of the methods used for hairy black holes can be successfully applied. The main task of the paper is to provide a tutorial on the basic methodology and calculation techniques, bringing the reader to the point that he can understand and repeat the calculations from the literature and start doing his own. The existing literature is rather heterogenuous and there is no single text to recommend. We will give the references we deem particularly useful throughout the paper, without the pretention of being exhaustive; the choice of references is certainly dictated also by our prejudices and tastes.

Plan of the paper. In Section 2 we first explain the instabilities of AdS space and AdS black holes to a nonzero density profile of fermions, and in-

troduce the basic concepts that will keep appearing throughout the paper: effective potential and the bound states of the fermionic wavefunctions. In Section 3 we first treat the problem in the consistent one-loop (Hartree-Fock) approximation, calculating the determinant (5) by definition, from the individual wavefunctions for different states. We find this job surprisingly difficult – it is still an active research area. But we are able to give a qualitative picture of the outcome and sketch the phase diagram, depending on the chemical potential μ and fermion mass and charge m, q. As we move toward the high-fermion-density corner of the phase diagram, the things simplify. The simplest and "most classical" limit of the problem is the limit of large density. It is a rule of thumb that for fermions, the role of interactions diminishes as the density grows. At high density, WKB approximation works very well. At highest densities, we find semiclassical fluid with an equation of state that takes into account the fermionic pressure, similar in spirit to the Oppenheimer-Volkov equations for neutron stars. In section 4 we apply these methods to a different topic – hairy wormholes instead of black holes. This problem has recently gained notoriety and might carry some important messages for the black hole information problem. The final section sums up the conclusions.

2. Planar AdS black holes and fermion nucleation

In this and the next section we will focus on large planar black holes on the Poincare patch of AdS space. Large black holes can reach equilibrium with the AdS boundary so they do not emit Hawking radiation and can exist eternally. The Poincare patch of AdS_4 space is a coordinate chart with a single boundary on one end and interior on the other end. It does not cover the whole AdS space but is simpler to work with than global AdS and is good enough to desribe the instability at the horizon. The metric of pure AdS space witout a black hole is given by

$$ds^2 = r^2 \left(-dt^2 + d\vec{x}^2 \right) + \frac{dr^2}{r^2} = \frac{1}{z^2} \left(-dt^2 + d\vec{x}^2 + dz^2 \right) \qquad (6)$$

where $r = 1/z$ is the radial coordinate, t is time and $\vec{x} = (x, y)$ are the transverse coordinates. The AdS boundary is at $r = \infty$ ($z = 0$), and the interior is at $r = 0$ ($z = \infty$). From now on we will mainly use the z coordinate; we will always specify explicitly if a different radial coordinate is used. In AdS/CFT, the radial coordinate corresponds to the energy scale in field theory: the near-boundary region encodes for the physics at high energies, in the ultraviolet (UV), and the deep interior, with z large, is the infrared (IR). Even though we do not consider the CFT dual here, we will still adopt the UV/IR terminology.

In the presence of a point electric charge e we get a Reissner-Nordstrom (RN) black hole with the horizon at $z_h = 1$, with charge e, mass M and

temperature T:

$$ds^2 = \frac{1}{z^2}\left(-f(z)dt^2 + d\vec{x}^2 + \frac{dz^2}{f(z)}\right), \quad f(z) = 1 - Mz^3 + e^2 z^4$$

$$M = z_h^3 + e^2, \quad A = \frac{ez_h}{2\sqrt{\pi}}(1 - z/z_h)dt, \quad T = \frac{3z_h}{4\pi}\left(1 - \frac{e^2}{3z_h^4}\right) \quad (7)$$

For $e = 0$ we get the Schwarzschild AdS black hole, and for $e = \sqrt{3}z_h^2$ the black hole becomes extremal, with temperature $T = 0$. To see this, remember that the black hole temperature is given by $f(z \to z_H) = 4\pi T(z - z_H) + \ldots$, so plugging in f from above we indeed get the correct expression for T. Importantly, the near-horizon region of a black hole is an AdS space [7]. This IR AdS space (near $z = z_h$) has a priori nothing to do with the AdS asymptotics in the UV (near $z = 0$); it is there also for black holes in flat or dS space. At $T = 0$, rescaling $z - e/\sqrt{3} \mapsto 1/6\epsilon\xi$ and expanding in ϵ to lowest order gives the metric

$$ds^2 = \frac{1}{6}(-dt^2 + d\xi^2) + \frac{e^2}{3}d\vec{x}^2, \quad A_t = \frac{1}{\sqrt{6}\xi}. \quad (8)$$

The is $\mathrm{AdS}_2 \times R^2$ geometry, a direct product of AdS with a plane. At finite temperature, a similar rescaling can be worked out, yielding again an AdS_2 throat. Since the throat describes the near-horizon region, instabilities of the black hole can be figured out from possible instabilities of this IR AdS space. Once again, this is *not* the whole AdS_4, which is always stable far from the horizon, in the UV (otherwise our whole classical gravity approach crumbles down), it is just a region near the horizon, in IR.

In order to write the equations of motion, we have to choose a basis for the gamma matrices and the form of the Dirac bispinor (remember that only two out of four components are really independent degrees of freedom). A convenient representation is

$$\Gamma^0 = \sigma^1 \otimes \iota\sigma_2, \ \Gamma^1 = \sigma^1 \otimes \sigma_1, \Gamma^2 = \sigma^1 \otimes \sigma^3, \ \Gamma^z = \sigma^3 \otimes \hat{1}. \quad (9)$$

so that the Dirac equation in a spherically symmetric metric defined as $\mathrm{diag}(g_{tt}, g_{ii}, g_{ii}, g_{zz})$ gives two equivalent decoupled pairs of equations. Taking the Dirac bispinor in the form $\Psi = (\psi_1, \chi_1, \iota\chi_2, \iota\psi_2)^T$, the equations for $\psi_{1,2}$ read [9, 10]:[2]

$$\partial_z \psi_{1,2} \pm \hat{m}\psi_{1,2} - \left(\mp\hat{E} + \hat{k}\right)\psi_{2,1} = 0 \quad (10)$$

$$\hat{m} \equiv m\sqrt{g_{zz}}, \hat{\mu} \equiv \sqrt{\frac{g_{zz}}{-g_{tt}}}A_t, \ \hat{E} \equiv q\hat{\mu} + E\sqrt{\frac{g_{zz}}{-g_{tt}}}, \ \hat{k} \equiv \sqrt{\frac{g_{zz}}{g_{ii}}}k. \ (11)$$

---

[2]Since only two components of the Dirac bispinor are independent, the system for $\chi_{1,2}$ yields no new information.

We have Fourier-transformed the derivatives over time and transverse spatial dimensions as $\partial_t = -\imath\omega, \partial_x = \imath k_x, \partial_y = \imath k_y$, and we have exploited the spherical symmetry to set $k_x = k, k_y = 0$. The quantities $\hat{E}$, $\hat{k}$, $\hat{\mu}$ can be informally interpreted as "local" values of the energy, momentum and chemical potential, respectively. The "local" values equal E, k, μ at the AdS boundary, grow monotonously toward the horizon and diverge there, a consequence of the infinite redshift seen by a faraway observer. An important idea is to consider the Schrödinger form of the Dirac equation instead, differentiating (10) once with respect to z, decoupling the equations for $\psi_{1,2}$, and elliminating the first derivatives $\psi'_{1,2}$ by introducing the tortoise coordinate s instead of z. The resulting picture is that of a zero-energy Schrödinger equation, of the form $\partial_s^2 \psi_{1,2} - V_{\mathrm{eff}}(s)\psi_{1,2} = 0$, in an effective potential $V_{\mathrm{eff}}(s)$.[3] Near the horizon, the potential is constant at leading order [11]:

$$V_{\mathrm{eff}}(s \to -\infty) = \frac{m^2 + 12k^2/\mu^2 - 2q^2}{(q/\sqrt{2}+k)^2} + \dots \tag{12}$$

It is true that the Schrödinger form is only a consequence of the Dirac equation, not equivalent to it: extra conditions must be imposed on the Schrödinger solution to make it satisfy the Dirac equation. But the effective potential is great for qualitative insights and it contains the basic idea of the black hole instability in a very transparent way. The near-horizon potential can contain bound states if it is negative, hence the instability criterion for a fermionic mode with momentum k is that the numerator of (12) is negative. Fermions fill up the potential well starting from $k = 0$ up to some maximum k for which (12) reaches zero. Therefore, the instability first sets in when V_{eff} is negative for $k \to 0$, so we get our first rule-of-thumb prediction: the black hole will be surrounded by a gas of fermions and become hairy when

$$m < q\sqrt{2}. \tag{13}$$

But this is just one end of the potential well; what happens at the other end? Plugging in the pure AdS metric (6) into (12) we get

$$V_{\mathrm{AdS}}(s \to 0) = \frac{m^2 + m + k^2}{(k+\mu)^2} \frac{1}{s^2} + \dots, \tag{14}$$

which is always non-negative, and grows to infinity. This is good – there is never an instability in the far UV, and the fermionic hair can never come arbitrarily close to the AdS boundary. It also means that bound states in the interior will indeed exist whenever (13) is negative. The physical picture is the following: in the presence of EM and gravitational field of the black hole, fermions are pair-created. These pairs are virtual, and

---

[3]This is a simple exercise that we will do many times; the reader should be able to do the necessary (straightforward) calculations leading to the expression for $s(z)$ and $V_{\mathrm{eff}}(s)$.

they only have a finite probability of becoming long-living if the external potential energy is large enough. In that case, bound states form, and there is a solution of (2) with nonzero fermion density. In the literature, this is sometimes called fermion nucleation. For scalars, similar logic leads to the Breitenlohner-Freedman bound, which puts a constraint on the scalar mass for the stability of the UV (with fermions, as we have seen, UV is always stable), and in IR it similarly gives a criterion for forming hair [5]. We also see from (14) and Fig. 1 that the potential well becomes shallower as k grows, so the bound states only exist up to some maximum $k = k_F$ which is really the Fermi momentum of the bulk Fermi sea.

From (12,14) we can understand the behavior of the effective potential. In Fig. 1, we give the function $V(s)$ in the whole space, from $z = 0$ ($s = 0$), to $z = z_h$ ($s = -\infty$). The fermionic modes fill the potential well until they reach the energy $E = 0$. From (12), higher modes correspond to higher momentum k. The fermionic density is thus given by a sum over these bound states. The easiest case is in fact an extremely deep well: the energy levels are so dense and so numerous that they can be approximated by a continuum; this is called electron star limit. But the most interesting regime is the one with only a few wavefunctions, which really describes the transition to a hairy solution. This is a much harder nut to crack.
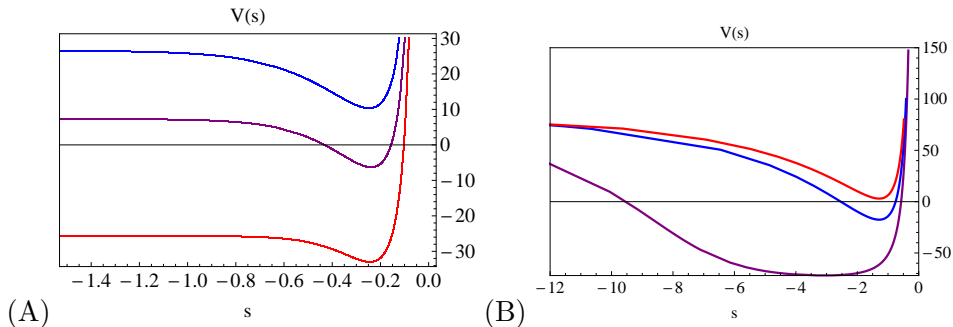

Figure 1: Effective potential V_{eff}, as a function of the tortoise coordinate $s \equiv \int_0^z dz g_{zz}(z)$, in the RN metric (A), and in the Lifshitz metric (B), for $q = 1$, $m = 0.4$, $\mu = 1$, and three momentum values increasing from violet to blue to red: $k = 1, 2, 3$ (A) and $k = 0, 5, 10$ (B). In both cases, the negative potential well becomes shallower and shallower and eventually disappears as k grows, so we fill the bulk Fermi sea up from $k = 0$ to some maximal $k = k_F$. In the black hole background, the potential is flat for $s \to -\infty$, which corresponds to the AdS$_2$ near-horizon region and signifies an instability as the bound states extend all the way to the horizon ($s = -\infty$). In the backreacted Lifshitz metric the potential grows for $s \to -\infty$, suggesting that deep IR is stable: the true vacuum is the Lifshitz geometry, not RN. Taken over from [14].

3. Fermionic hair

Now that we have convinced ourselves that hairy solutions, with finite fermion density, have to exist, we need to solve the full system of Einstein, Maxwell and Dirac equations to find them. Clearly, a more general ansatz for the metric than (7) is needed now, and we will write it as

$$ds^2 = -\frac{F(z)G(z)}{z^2}dt^2 + \frac{1}{z^2}d\vec{x}^2 + \frac{1}{F(z)z^2}dz^2, \tag{15}$$

leading to Einstein-Maxwell equations

$$1 - F + zF'/3 - T_{tt}^{\text{tot}}FG/3z^2 = 0 \tag{16}$$

$$G' + z(T_{tt}^{\text{tot}}/F^2 + T_{zz}^{\text{tot}}G) = 0 \tag{17}$$

$$A_t'' - G'/2GA_t' + qn\sqrt{G}/\sqrt{F}z^3 = 0, \tag{18}$$

where $T_{\mu\nu}^{\text{tot}}$ is the total stress-energy tensor, both from the electric field (which is easy to find) and from the fermions (which is our big problem). A typical situation in hairy problems is that formulating the physically meaningful boundary conditions is not so easy. Notice the Einstein equations are first-order, so we need one boundary condition for each function (F and G), whereas the Maxwell equation is second-order and requires two boundary conditions. Let us now summarize what boundary behavior we expect on physical grounds.

1. The AdS asymptotics for the metric and gauge field require $F(z \to 0), G(z \to 0) = 1, A_t(z \to 0) = \mu$. So far it's all simple.

2. The main puzzle for the IR geometry is – does the horizon disappear or not? At $T = 0$ we do not expect that the degenerate RN horizon can survive. So we do not expect zeros in F, G but we do expect their derivatives to vanish in order to have a smooth solution (finite derivatives at $z \to \infty$ would likely give divergent curvature). Thus at $T = 0$ we need $F'(z \to \infty) = G'(z \to \infty) = 0$ or, in other words, $F(z \to \infty) = \text{const.} + O(1/z)$ and likewise for G. At finite temperature, general GR arguments suggest there is a horizon at some $z = z_h$ satisfying $F'(z \to z_h) = 4\pi T$.

3. The IR behavior of the gauge field is related to the question: *is all the charge carried by the fermions, or the charge is shared between the fermions and the horizon?* The Gauss-Ostrogradsky theorem for the AdS space, with a UV boundary and either a horizon or a smooth far-away IR takes the form [12]:

$$\oint_\partial d^3x\sqrt{-h}|_{z \to 0} \star \hat{F} = \int d^4x\sqrt{-g}qn + \oint_{\text{IR}} d^3x\sqrt{-h_{\text{IR}}}|_{z=z_{\text{IR}}} \star \hat{F} \tag{19}$$

Here, $\star\hat{F}$ is the coordinate-invariant flux of the 2-form $\hat{F}$, and h_{IR} is the induced metric on the surface normal to the radial direction at

$z_{\mathrm{IR}} = z_h$ or $z_{\mathrm{IR}} = \infty$, depending on whether there is a horizon or not. In principle, the IR charge might be shared between the horizon and the fermions. However, we will find that in the semiclassical calculation there are no solutions where the charge is shared – any backreaction will always expell all the charge from the IR.

4. The boundary conditions for the Dirac equation present no problems and are pretty standard in AdS space [13]. In the UV, out of the two branches, we want the subleading one, with the motivation to preserve the AdS asymptotics, i.e., to perturb the space as little as possible in the UV. In particular, the near-boundary expansion of (11) gives

$$\psi_1(z \to 0) = \frac{E + \mu q - k}{2m - 1} A_2 z^{5/2-m} + B_1 z^{3/2+m} + \ldots$$

$$\psi_2(z \to 0) = A_2 z^{3/2-m} + \frac{E + \mu q + k}{2m + 1} B_1 z^{5/2+m} + \ldots, \quad (20)$$

so we pick $A_2 = 0$, as the leading contribution for $z \to 0$ comes from the $z^{3/2}$ term. In the IR, the metric determines the boundary conditions: if there is a horizon, we need $\Psi(z = z_h) \to 0$ for stability, if not, then to avoid infinite energy density at large z we require $\partial_z \Psi(z \to \infty) = 0$, for otherwise a nonconstant density profile would give rise to a diverging curvature. The attentive reader should be alarmed: this means two boundary conditions for each component (one in UV and one in IR), but the equations are only first-order. The resolution is that for given momenta, the energy is not arbitrary but fixed by the dispersion relation $E(k)$; thus solving the Dirac equation in an effective potential well introducs energy quantization, as one would expect.

What remains is to find the fermionic stress tensor. Since spinors couple to the spin connection e_a^μ and not directly to the metric, the stress tensor is expressed as

$$T_{\mu\nu} = \left\langle \frac{1}{4} e_{\mu a} \bar{\Psi} \Gamma^a D_\nu \Psi + (\mu \leftrightarrow \nu) \right\rangle, \quad (21)$$

and the expectation value $\langle \ldots \rangle$ reminds us that the fermions are never classical. At zero temperature, the state is pure and can be represented as the sum of (appropriately normalized) radial modes with energies E_ℓ, where ℓ is the radial quantum number, and the energies E_ℓ are all ≤ 0. At finite temperature, the state is mixed and gets a contribution from both positive and negative energies E_ℓ, with thermal weights $w_\ell = \exp(-\beta E_\ell)/Z$, the partition sum being $Z = \sum_\ell \exp(-\beta E_\ell)$. With this in mind, we can wrote out (21) as

$$T_{tt} \;\; = \;\; e_{t0} \sum_{\ell=1}^{N} w_\ell \int_0^{k_F} \frac{k dk}{(2\pi)^2} \left(\psi_{1;\ell}^\dagger \psi_{1;\ell} + \psi_{2;\ell}^\dagger \psi_{2;\ell} \right) (E_\ell + q A_t)$$

$$T_{ii} = e_{i1} \sum_{\ell=1}^{N} w_\ell \int_0^{k_F} \frac{kdk}{(2\pi)^2} \left(\psi_{1;\ell}^\dagger \psi_{1;\ell} - \psi_{2;\ell}^\dagger \psi_{2;\ell} \right) k$$

$$T_{zz} = e_{z3} \sum_{\ell=1}^{N} w_\ell \int_0^{k_F} \frac{kdk}{(2\pi)^2} \left(\psi_{1;\ell}^\dagger \partial_z \psi_{2;\ell} - \psi_{2;\ell}^\dagger \partial_z \psi_{1;\ell} \right). \tag{22}$$

For brevity, we write $\psi_{1,2;\ell} \equiv \psi_{1,2}(E\ell, k; z)$. We will consider in detail just the $T = 0$ case, when the weights w_ℓ effectively just pick the ground state and cut off all the others, but we will later discuss the results (without details of the calculations) also at finite T. The spectrum is discrete and gapped in the radial direction, so the integral $\int dE/2\pi$ becomes a sum, however in the transverse directions the system remains gapless, filling the whole (spherical) Fermi sea in the $k-$momentum space, as long as the dispersion relation $E(k) = E_\ell \leq 0$ is satisfied for some ℓ. The highest such k, for which $E_\ell = 0$, is the Fermi momentum k_F, and the possible momenta are $0 \leq k \leq k_F$. It is this continuous quantum number k that makes our life difficult. Here, indeed, our easy path comes to an end, because a self-consistent calculation of the wavefunctions certainly cannot be done in a closed form. Here we must resort to approximations. The number of occupied levels N is a good guide on the kind of approximation one needs to make. One can rephrase it as the ratio Q/q, where Q is the total fermion charge $\int d^4x \sqrt{-g} q \Psi^\dagger \Psi$. The thermodynamic limit, where the number of particles goes to infinity and the charge of an individual fermion to zero so that $N \to \infty, q \to 0, Q = Nq = $ const., is at one extreme. We expect that the problem approaches the classical regime in this case, and it will turn out to be true. The opposite limit is $Q/q = 1$, with just a single excitation, the hairy black hole at birth. We expect this to be likewise a simple limit, however it will turn out not to be quite true. In-between we dial between the quantum mechanics of $N = 1$ and the classical field theory of $N \to \infty$ [14].

Phase diagram. Before doing that, we can sum up our qualitative knowledge on a phase diagram (Fig. 2). From (12-14), bound states form for small enough m values (panel (A)); if (13) is valid beyond the probe approximation, the borderline is $m = q\sqrt{2}$. Left of this line there is a hairy solution, to the right of it the AdS$_2$ near-horizon region (and the whole RN black hole) remain. The hairy solutions are best described in different ways depending on the number of filled levels ($N = Q/q$); this is the topic od the rest of this section. One can also plot the situation at finite temperature (panel (B)). The phases remain the same; more precisely, the extremal black hole becomes a finite-temperature black hole, and the hairy solutions also smoothly develop a hairy horizon (thermal horizon with nonzero fermion density $n(z_h)$). What changes is the order of the phase transition: at $T = 0$ it is continuous, and at finite temperature it is discontinuous.
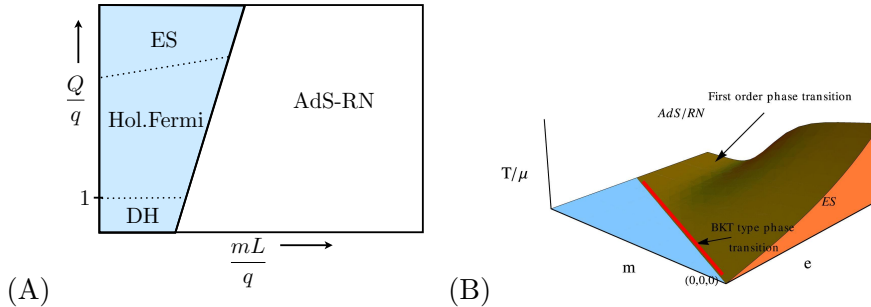
Figure 2: (A) Phase diagram as a function of the total-to-fermion-charge ratio Q/q (y-axis), and the fermion mass (in units of AdS radius L) over charge ratio mL/q (x-axis). For large masses, the effective potential is positive and the ground state is the bald RN black hole, with quantum critical dual field theory. For smaller masses, hair develops, which corresponds to a Fermi liquid in dual field theory. For $Q \sim q$ (few wavefunctions), the single-wavefunction Dirac hair approximation works; for $Q/q \to \infty$ we approach the semiclassical fluid (electron star) limit; between them there is a smooth crossover with unclear properties, both in AdS and in the holographic dual. Notice different notational conventions for the total charge from the main text (e vs. Q). Taken over from [15]. (B) Adding nonzero temperature as the third axis, we obtain also the thermal phase transitions between the black hole and the hairy solution, which are generically first order, smoothing out to an infinite order (BKT) transition at $T = 0$ – the red line in (B) is the bold black line between the RN and hairy (blue) region in (A).

3.1. Quantum hairy black holes

A controlled approximation is to solve the problem perturbatively, at one-loop order in fermionic fields. This is nothing but the textbook Hartree-Fock (HF) method, but in curved space. Dynamical spacetime makes a big difference: it introduces an additional strongly nonlinear component of the system, making the solution landscape larger and less predictable, and the UV and IR divergences can appear also in the Einstein equations and need explicit regulators. In fact, this is still an open problem – nobody has yet classified the solutions of the Einstein-Maxwell-Dirac system even in the Hartree-Fock approximation, and we do not know what surprises might lurk in this corner of the phase diagram. The HF electrodynamics contains two diagrams, a vacuum bubble that renormalizes the chemical potential

as $\hat{\mu}(z) \mapsto \hat{\mu}(z) + \delta\hat{\mu}(z)$ (the Hartree term):

$$\delta\hat{\mu}(z) \equiv q \sum_{\ell=1}^{N} \int \frac{kdk}{2\pi} \left(\psi_1^\dagger(E_\ell, k; z)\psi_1(E_\ell, k; z) + \psi_2^\dagger(E_\ell, k; z)\psi_2(E_\ell, k; z) \right)$$

(23)

and the exchange interaction (the Fock term). The explicit z-dependence of the Hartree correction is a gory reminder that the problem is solved in inhomogenous background. This is also the reason why already the Hartree correction is nontrivial: unlike the textbook situation where the shift $\delta\mu$ merely changes the numbers, here it is a radial function $\delta\mu(z)$ and its influence is also qualitative. So far, nobody even tried to do the whole HF calculation, and even just the Hartree term is not easy. We are plagued (1) by the UV divergences introduced by the modes close to $k = k_F$ which, as we have seen, peak most sharply near the boundary and can shatter the AdS space into pieces if not properly renormalized (2) by the IR divergences introduced by the modes with k close to zero, which extend far into large z values and can make the system unstable to forming a naked singularity.

Hard-wall Fermi liquid. The only case which is under good control is the hard-wall model of [12]: the UV divergences are resolved simply by not backreacting on the metric, i.e. solving just the Maxwell-Dirac system in fixed AdS metric (6) even without a black hole, and the IR divergences disappear by cutting off the space at some arbitrary z_0, so that we simply elliminate the IR region. The approximations are rather drastic, but they allow a complete solution. In pure AdS space, the solutions $\psi_{1,2}$ can be found analytically in terms of Bessel functions, the states form discrete and gapped bands, and we only have to solve the Maxwell equation (18). The outcome is given in Fig. 3. Hard wall acts as an infinite potential barrier, so the wavefunctions should die on it, and the condition $\psi_{1,2}(z_0) = 0$ determines the dispersion relation. The wall should not be charged, so in (19) the second term on the right-hand side equals zero, meaning that $A_t'(z_0) = 0$. The picture is that of a Fermi liquid, nicely filling the Fermi sea at momenta $k \leq k_F$ and having long-living quasiparticles. This model is an important starting point for more complicated setups, and has the advantage of being intuitive, but by itself is too simplistic. Indeed, we want to talk about hairy black holes, and here we don't even have one, as it is hidden behind the hard wall!

An attempt to study a simple setup but with a black hole was made in [16]. In this approach, we are limited to a single energy level, $\ell = 1$. This is justified only when the hair is just starting to form, right at the transition point. There is again no backreaction on metric, but the (fixed) metric is now taken to be the RN black hole. This is actually a big jump in difficulty: the wavefunctions oscillate near the horizon at any nonzero energy (Fig. 4(A)), so they can satisfy the IR boundary condition at any energy and momentum (we can always pick the phase so that $\psi'(z_h) = 0$), and the spectrum is continuous as there is no wall to create a gap. This

is what forces us to consider the single-mode case: with the gapped hard-wall model we could add a *finite* number of modes, but now there is a *continuum* of them, N going to infinity even for arbitrarily small Q/q. The only way out is to *assume* there one mode only and solve the resulting Dirac-Maxwell system. This setup is convenient for understanding the transition itself, which turns out to be discontinuous (first-order) at finite temperature (Fig. 4(B), and likely infinite-order (Berezinskii-Kosterlitz-Thouless, BKT) at zero temperature, as we shall soon see.
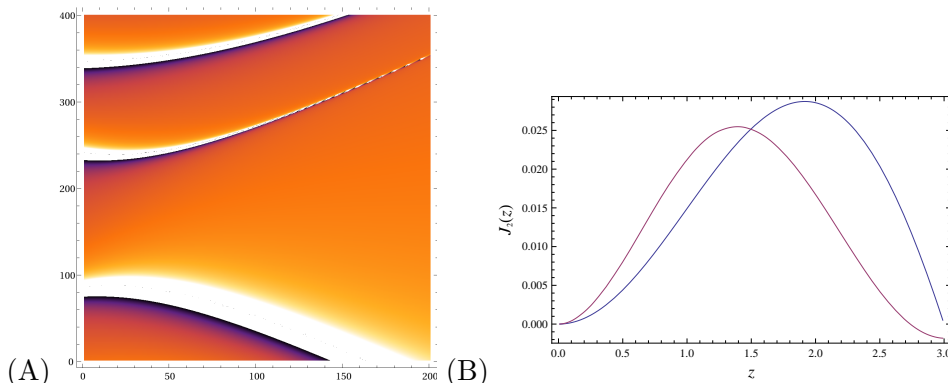

Figure 3: (A) Dispersion relation $E_\ell(k)$ for the first two electron bands $\ell = 1, 2$ in hard-wall AdS space, for $\mu = 1, m = 1, q = 2$. The first band from bottom is the hole band, not an an electron band – its contribution can be absorbed in the redefinition of the parameters and it does not contribute to hair. The colormap shows the resolvent of the Dirac operator, $(D_z\Gamma^z + \vec{D} \cdot \vec{\Gamma} - m - E)^{-1}$, thus the bright white regions show the places where the resolvent diverges and a discrete bound state is formed. The horizontal axis is the momentum and the vertical axis the energy, both in computational units. (B) Wavefunctions $\psi_{1,2}$ (here for $\ell = 1$ and $k = 1$) are smooth everywhere - what happen exactly at the horizon we do not know in this model, as the space is cut off at $z = 3$.

Quantum electron star. The single-mode approach has taught us a lesson: already at the level of the gauge field only, the changes from the finite fermion density are drastic, and the resulting stress tensor is large at the horizon, so a change of the black hole metric is certainly expected. However, when we try to solve the Einstein equatioons, things become almost intractable. Both UV and IR divergences appear: the former because the currents diverge in continuous space, and the latter because the discrete bands fuse into a continuum in IR. The latter issue is most easily regularized by a hard wall, but a hard wall does not make much sense if we want to backreact on geometry. The regularization of the UV divergences is systematically discussed in [17, 18] and the bottom line is that there is a logarithmic short-distance divergence which can be regularized by point
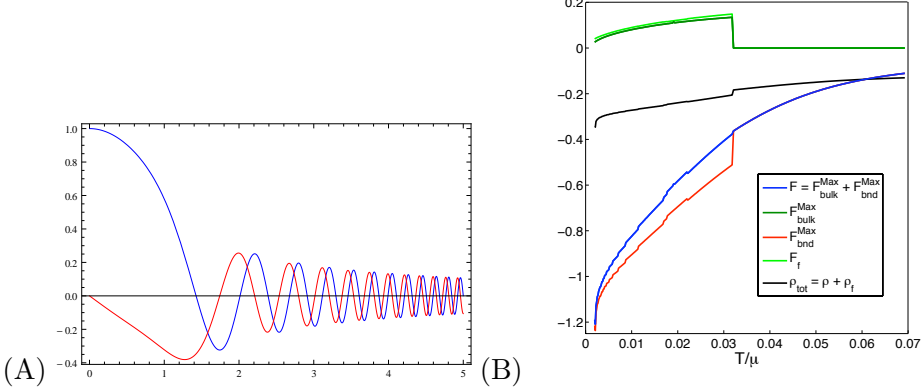
Figure 4: (A) Wavefunctions $\psi_{1,2}$in RN background, for $\ell = 1$ and $k = 1$, always oscillate and approach an essential singularity at the horizon, which indicates an instability: the metric changes and the degenerate horizon disappears. (B) The bulk action (or free energy F, from AdS/CFT correspondence) of the Maxwell (electric field), in blue, consists of the bulk and boundary contribution (dark green and red), the former practically identical to the contribution from fermions. All these are computed from the action (2-4). While the *total* free energy is continuous, it has a cusp, made manifest by the slight jump in density (black), a sign of first-order hair-forming transition.

splitting; in this procedure the cosmological constant becomes renormalized. This is not a drastic change: it will just change the numbers but not qualitative behavior. The IR problem is still unsolved. The approach of [18] is to put the system in global AdS space[4] whose radial slices are spheres, not planes, so the AdS radius provides a regulator. A perhaps more physical approach, motivated by consistent truncations from string theory, is to introduce a non-minimally coupled scalar, i.e., a dilaton that introduces a soft wall and suppresses the IR degrees of freedom in a continuous way, without an abrupt cutoff at some z_0, so the total bulk action is now

$$
\begin{aligned}
S_{\text{bulk}} &= \int d^4x \sqrt{-g} \left[R - V(\Phi) - \frac{1}{2}(\partial\Phi)^2 - \frac{Z(\Phi)}{4}\hat{F}^2 \right] - \\
&- \int d^4x \sqrt{-g}\bar{\Psi}\left(\frac{1}{2}D_a\Gamma^a e^\Phi + \frac{1}{2}e^\Phi D_a\Gamma^a + m \right)\Psi,
\end{aligned} \qquad (24)
$$

where the dilaton potential reproduces the AdS cosmological constant near the boundary, i.e., $\Phi(z \to 0) = 0$ and $V(\Phi \to 0) = 6, Z(\Phi \to 0) = 1$. It is not clear if one can ever remove the IR regulator. That is precisely the

---

[4]Dual field theory then lives on a sphere instad of a plane.

reason that we regard the dilaton regulator as more physical, since string theory constructions as a rule contain non-minimally coupled scalars, and the action (24) can be obtained by consistent truncation; whereas global AdS is essentially an ad hoc solution, though a very interesting one, with possible applications in AdS/condensed matter duality, where systems that live on surfaces (such as a sphere) appear naturally.

While this is still very much a work in progress,[5] preliminary results suggest that the RN-to-hairy-black-hole transition at zero temperature is an infinite-order (BKT) transition, where all derivatives of S remain smooth (Fig. 5). This is the point where the potential just starts deviating very slightly from the flat IR behavior in Fig. 1(A). At the end of this section we will try to understand this (still conjectural) numerical finding analytically.
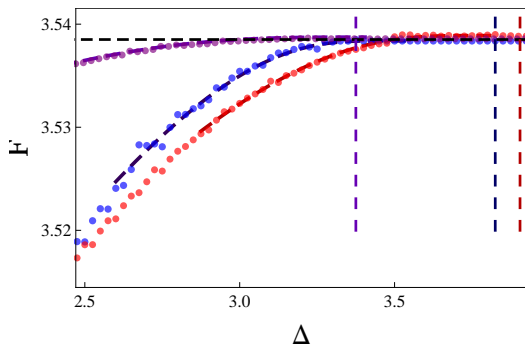

Figure 5: The bulk action (here denoted as free energy F, from AdS/CFT correspondence) as a function of the fermion mass (here denoted as $\Delta = 3/2 + m$) is very well fit by the BKT function $\exp(-c/\sqrt{\Delta_c - \Delta})$. The parameter c is determined by the chemical potential (we plot for three values $mu = 1.0, 1.5, 2.0$ in violet, blue, green). To the right of the transition point the action is independent of m as there is no hair, fermion density is zero, and so nothing depends on the fermion parameters. To the left of the transition point, the fermions form hair of nonzero density. Nobody knows yet how the near-horizon metric changes.

3.2.   WKB star and electron star

WKB approach. We have followed the logical chain of reasoning from the point where the hair starts growing, having $Q/q \sim 1$ and deforming the black hole just a slight bit, towards larger and larger hair, eventually reaching the regime $Q/q \gg 1$. But this last regime is the easiest to approach, as the fermions become as close to classical as they can possibly be. A good starting point is the controlled expansion in $\hbar$, where we solve the

---

[5]With N. Chagnet, V. Djukić and K. Schalm.

Dirac equation in the eikonal approximation or, in other words, the WKB approach [15]. We express the wavefunction as

$$\psi_{1,2} = e^{\imath\theta_\pm}/\sqrt{p}, \quad p \equiv \sqrt{\hat{E}^2 - \hat{m}^2 - \hat{k}^2}, \tag{25}$$

where p has the role of the canonical momentum. The wavefunction is nonzero between the turning points $z_\pm$, determined by the equation $p(z_\pm) = 0$. The explicit from of the phase $\theta_\pm$ as well as higher-order corrections to the phase can be found in [15], but the reader should in fact have no difficulty in deriving them, following the usual WKB procedure (though for the Dirac equation instead of the Schrödinger equation). Now the density and pressure are found by inserting the solution (25) into (22). The procedure can be iterated to obtain self-consistent solutions, but now we solve the whole system including the Einstein equations. It is instructive to plot the total on-shell action (2) as a function of temperature (remember that finite temperature is imposed through the corresponding boundary condition for the metric function F).[6] Fig. 6 plots the dependence $\mathcal{F}(T)$ in the vicinity of the transition value T_c: the derivative $\partial\mathcal{F}/\partial T$ undergoes a jump which is nothing but the entropy $\mathcal{S} \equiv \partial\mathcal{F}/\partial T$. We thus find a *first-order phase transition* at the point when Fermi hair starts forming. Of course, don't forget that the WKB approach is in fact *not* to be trusted very near the transition point: at the transition N changes from 0 to 1, which is far from the regime $N \ll 1$. But the qualitative insight that at finite temperature the system undergoes a non-symmetry-breaking transition is likely robust and we expect to prove it also within the more rigorous fully quantum-mechanical approach of the previous subsection. It is a hairy version of the celebrated Hawking-Page transition [19], and confirms the intuition that the high-tmeperature phase is always a black hole; but now, the low-temperature phase is not simply a gas, but a dense fluid in AdS.

Ploting the density and pressure in Fig. 7(A), one finds that for high values of N they tend to a constant value in deep interior. This motivates the fluid ansatz taken in the electron star limit, now to be considered.

Electron star. Electron star is a charged, AdS version of the neutron stars, described as perfect fluid by the Oppenheimer-Volkov equations. The idea is to *assume* that the fermionic matter is a perfect fluid, and then express the energy density ρ, pressure p and charge density n in terms of *integrals* over energy and momenta (i.e., assume that the bound states are infinitely close, and the gaps between them vanish). The fluid approximation thus becomes exact in the limit of $N \to \infty$, as we expect from a semiclassical approximation. Anticipating the current and stress tensor of the form

$$T_{\mu\nu} = (\rho + p)u_\mu u_\nu + p g_{\mu\nu}, \quad N_\mu = n u_\mu, \tag{26}$$

---

[6]In AdS/CFT, the bulk on-shell action $\mathcal{S}$ precisely equals the free energy $\mathcal{F}$ of the CFT side. But even without considering the details of the CFT, we can still make use of this interpretation to detect a phase transition in the system.

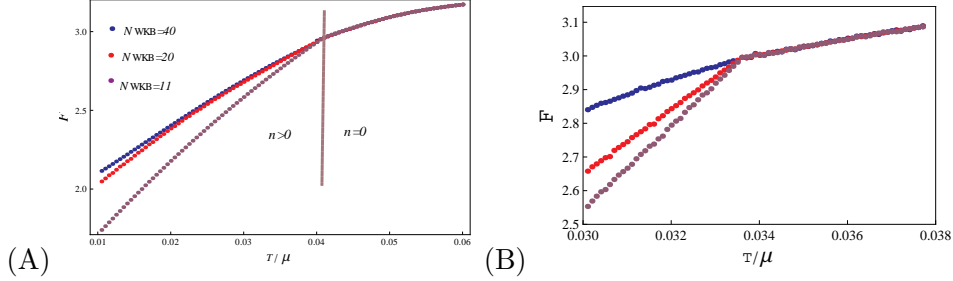(A)   (B)

Figure 6: (A) The on-shell action or free energy as a function of temperature, in the presence of fermions. For low temperatures, the fermion density is finite and the derivative $\partial\mathcal{F}/\partial T$ jumps at $T = T_c$, a sign of first-order transition with the development of the hair. This is in line with the Dirac hair result in the previous figure, and indeed for the lowest number of levels N_{WKB} the transition is the sharpest. In (B) we zoom in into the transition region.

we can write the density starting from (22) and making use of the optical theorem to relate it to the imaginary part of the Feynmann propagator G_F. This spells out as

$$
\begin{aligned}
\rho &= \int_0^{\hat{E}^2-k^2} \frac{dE}{2\pi} \int_0^{k_F} \frac{d^3k}{(2\pi)^3} \hat{E}\Im\mathrm{Tr}\imath\Gamma^0 G_F(E,k) \\
&= \int_0^{\hat{E}^2-k^2} dE \int \frac{k^2 dk}{4\pi^3} \frac{1}{2}\left(1-\tanh\left(\frac{\beta}{2}\hat{E}\right)\right)\mathrm{Tr}(\imath\Gamma^0)^2\delta\left(\hat{E}-\sqrt{k^2+m^2}\right) \\
&= \frac{1}{\pi^2}\int_m^{\hat{\mu}} dE E^2\sqrt{E^2-m^2}.
\end{aligned}
\tag{27}
$$

We similarly find the number density n, whereas the pressure need not be computed explicitly: since we work with an isotropic free Fermi fluid, its equation of state has to be $p = \rho - qn\hat{\mu}$. It is here that the approximate nature of the electron star with respect to the WKB star becomes obvious (Fig. 7): in WKB star there is an extra term in the pressure, coming from the nodes of the WKB wavefunction. One can check that the integral in (27) indeed approaches a constant as we go into deep interior. On the other hand, at some z_* when $\hat{\mu}(z_*) = m$ the density falls to zero: the star is a classical object and has a sharp border. So for $0 < z < z_*$ we continue the metric to the RN metric (the metric outside a charged isotropic object).

Since we can express n, ρ, p explicitly, we get a nice system of local ordinary differential equations in F, G, A_t, with all quantum expectation values pulled under the rug. This completes the circle, and brings another universal message: *due to Pauli principle, fermionic operators are never local, except in two extreme cases: when only one state is occupied (so the format of the Slater determinant is 1×1, i.e., it contains a single state), or*

when infinitely many states are occupied, so the Slater determinant turns into a classical, continuous probability density. In Fig. 7 we can see how the WKB solution captures the quantum "tails" near the turning points, which the electron star does not have. It is also instructive to compare this solution to the Oppenheimer-Volkov equations in flat space: in the latter case, $\hat{m} \sim 1/\sqrt{F}$ is always larger than $\hat{\mu} \sim 1/F\sqrt{G}$, unlike in AdS where $\hat{m} \sim 1/z\sqrt{F}$ and for $z > z_*$ it becomes smaller than the local chemical potential, so the integral in (27) has a nonzero range. This is because AdS acts like a potential box that can hold the charged fermions together against electrostatic repulsion. In flat space that does not happen, and we have only neutron stars, not electron stars.
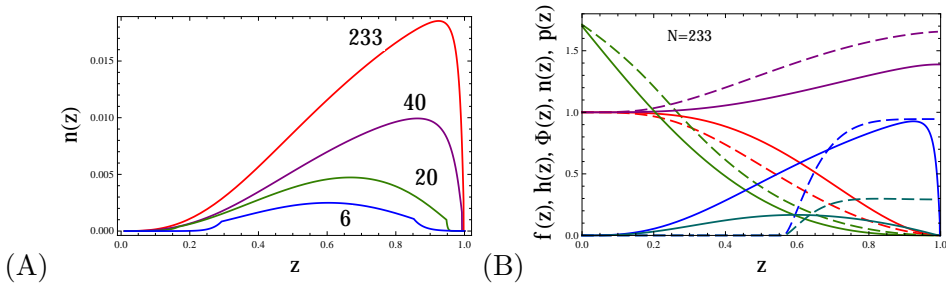

Figure 7: (A) Density of the finite temperature WKB star at various fillings N_{WKB}; besides the classically allowed region, there are also exponentially decaying tails in the classically forbidden region, where $V_{\mathrm{eff}} > 0$. (B) In the electron star (fluid limit), there are no such tails and the star has a sharp border. Taken over from [15]. (B) Comparison of the WKB solution (full lines) and the electron star solution (dashed lines) at the same chemical potential, fermion charge and mass. We plot the metric functions f, h (F, G in the main text) in red and violet, the gauge field Φ (A_t in the main text) in green, and density and pressure n, p in blue and dark green. The metric solutions do not differ much, despite the long quantum WKB tails, absent in the electron star.

3.3. Lifshitz metric, BKT transition and the missing pieces

In the framework of the electron star model, the Einstein-Maxwell equations can be solved analytically, thanks to the fact that, in deep IR, $n, \rho, p = $ const. and we can employ a scaling ansatz for the metric. The idea is to match the IR expansion around the scaling solution to the UV expansion around pure AdS. With ansatz of the form $g_{tt} \propto -1/z^{\alpha}$, $g_{ii} \propto 1/z^{\beta}$ and $g_{zz} = 1/z^2$ (one metric component we can fix at will as it amounts to picking the gauge for the metric), equations of motion give the IR solution

$$ds^2 = -\frac{1}{z^{2\zeta}}dt^2 + \frac{1}{z^2}d\vec{x}^2 + \frac{1}{z^{\zeta}}dz^2$$

$$A_t = \frac{1}{z^\zeta}, \quad \mathcal{L} = \frac{2}{z^{2\zeta}} + 6 - \partial_z A_t^2 - n A_t^2 - p_\perp, \tag{28}$$

where in the expression for the total Lagrangian density in the second line, we have inserted in the action (2) the solutions for the metric and the gauge field, as well as the constant (z-independent) solution obtained for ρ in (27) and similarly for n, p. Three important conclusions can be drawn: (1) the IR metric is scale-invariant, with anisotropic scaling of time and space, so that the scaling transformation has the form $t \mapsto \lambda t, \vec{x} \mapsto \vec{x}\lambda^{1/\zeta}$ (2) the on-shell Lagrangian density effectively describes a *massive vector field*, with mass squared equal to fermion density n (3) the fermionic contribution to the action equals the pressure. The second point agrees with the known result that Lifshitz black holes are generated by Proca fields [21], and what happens is the Abelian-Higgs mechanism: fermion density acquires a finite expectation value which in turn breaks the $U(1)$ symmetry, giving the photon a mass. The third point is expected within a fluid model, since the action of an ideal Lorentz-invariant (semi)classical fluid equals its pressure [7]. In the fluid limit we can also understand the first-order transition at finite temperature, because it is just a van der Waals-type liquid-gas transition.

We have seen that the thermal transition from RN to a Lifshitz black hole is of first order, and that the $T = 0$ transition is apparently a BKT (infinite order) transition. The latter is not quite clear yet because, as we have emphasized, nobody has yet managed to peek into the deep IR, it remains hidden behind the hard wall. But if we tentatively accept the numerical evidence for the infinite-order transition, can we understand it theoretically? The key lies in understanding how the AdS_2 throat disappears. The conformality-breaking mechanism of [22, 23] gives an idea, though the details are still missing. The crucial moment is that the near-horizon geometry is AdS_2. Right at the horizon ($s \to -\infty$) the potential is approximately constant. In the UV of the AdS_2 throat, which is around some finite value s_0, the potential behaves as $-c/(s - s_0)^2$. This inverse-square potential is known to describe conformal quantum mechanics when $c > -1/4$. For $c = -1/4$ the conformal invariance breaks. discrete states appear and the effective potential is not consistent unless regularized as

$$V_{\mathrm{eff}} = \frac{c}{(s - s_0)^2} - v\delta(s - s_0), \tag{29}$$

and the solution of the effective Schrödinger equation is

$$\psi(r) = c_+(s - s_0)^{\alpha_+} + c_-(s - s_0)^{\alpha_-}, \quad \alpha_\pm = \frac{1}{2} \pm \sqrt{c + \frac{1}{4}}, \tag{30}$$

and the ratio c_+/c_- is given in terms of Bessel functions $J_{1/2}$ and $J_{-1/2}$:

$$\frac{c_+}{c_-} = -\epsilon^{\alpha_- - \alpha_+} \frac{\gamma + \alpha_-}{\gamma + \alpha_+}, \quad \gamma = \sqrt{v} \frac{J_{1/2}(\sqrt{v})}{J_{-1/2}(\sqrt{v})} \tag{31}$$

The solution (30) diverges at $s = s_0$ unless we introduce a cutoff at some distance ϵ from s_0. Imposing the renormalization condition that c_+/c_- remains independent of ϵ, we get the β-function of the renormalization group as (ℓ being the RG scale):

$$\beta \equiv \frac{d\gamma}{d\ell} = (c + 1/4) - (\gamma + 1/2)^2. \tag{32}$$

And we're done: the fixed points of the above flow equation are easily found to be $-\alpha_\mp$. For $\gamma = -\alpha_\mp$ we get the solution for ψ from (30) with $c_\pm = 0$ respectively. The free energy scaling is obtained as $S_{\text{on-shell}} = \mathcal{F} \propto \int d\ell/\beta$, which gives just the form found in Fig. 5. However, the presence of both a hard-wall cutoff in z and the soft-wall dilaton, completely unaccounted for in the above analysis, clearly suggest more work is needed for everything to click together.

4. Wormholes with fermion hair

The lengthy review we have given so far is meant to be self-contained and helpful for those interested in understanding and contributing to the problem of black hole instabilities with fermionic matter. As we have seen, it contains some puzzling questions and is of more than technical interest (after all, the whole field has been active mostly for the last fifteen years or so). But we also want to point out that with the methodological powerhouse of the HF, WKB and fluid methods, one can tackle new problems. A recent issue where fermions at finite density seem very relevant is the search for traversable wormholes.

The motivation for this story lies mainly in the celebrated black hole information paradox: as far as we know, the Hawking radiation is thermalized, meaning that the information content of the matter falling into the black hole is lost. A possible way out or, at least, a way to better understand the issue, is to consider the maximally extended Carter-Penrose diagram of a black hole, which contains two horizons and two spacetimes. If transport between the two were possible, one could imagine that the information is not lost because the matter falling into one horizon is entangled with the matter on the opposite side. This is the idea of the ER=EPR conjecture [24]. In order to build a traversable wormhole, one needs negative that the stress-energy tensor averaged over a geodesic be negative, thus violating the so-called averaged negative energy condition (ANEC) [25, 26]. This will never happen with conventional classical matter. One needs either exotic fields or quantum corrections. Recently however, a few traversable wormholes have been realized with only standard-model matter. The most "conservative" is the setup of [27] which creates negative energy by considering a particle-hole symmetric spectrum of massless fermions in a mangetic monopole field: because of the negative Landau levels, the net energy is negative. The starting point is thus a pair of magnetically charged RN black holes with magnetic charges H and $-H$, with the hope that the

negative energy Landau levels will push the averaged stress tensor to large enough absolute values to open up a wormhole. In this way, [27] constructs a quasi-stationary (long-living) wormhole in *assymptotically flat* space. In AdS, negative energy density can easily be constructed by coupling the two boundaries nonlocally: in this way temporary wormholes, opening up for the finite duration of the pertrubation, can be constructed [28], and even eternal wormholes are possible but at the cost of much more exotic boundary CFTs and their couplings [29, 30, 31]. Here we are interested in making a wormhole in a more "down-to-earth" manner, by growing negative-energy fermion levels as in [27]. The task is to make such wormholes more stable, and to see if they survive at higher fermion density rather than just a single wavefunction as in [27]. Here the previously develped methods can help us.

Magnetic electron star. The crucial consequence of the magnetic field is the Landau quantization. The motion along the x-coordinate is quantized into discrete levels, whereas the motion along y is not quantized and introduces degeneracy. The quantization along x-axis makes our life somewhat easier – even without any IR cutoff the ground state wavefunction now has a discrete quantum number, the Landau level m_j. The magnetic field breaks the spherical symmetry of the wavefunctions down to cylindrical, so it is convenient to introduce the polar angles θ, ϕ:

$$ds^2 = -A(z)dt^2 + B(z)dz^2 + C(z)\left(d\theta^2 + \sin^2\theta d\phi^2\right) \tag{33}$$

and to pick a different gamma matrix basis: $\Gamma^0 = \imath\sigma_1 \otimes \hat{1}$, $\Gamma^1 = \sigma_2 \otimes \hat{1}$, $\Gamma^2 = \sigma_3 \otimes \sigma_1$, $\Gamma^3 = \sigma_3 \otimes \sigma_2$. Separating the variables and representing the wavefunction as

$$\Psi = \sum_{m_j=-j}^{j} \left(\psi_+\left(m_j; z\right), \psi_-\left(m_j; z\right)\right) \otimes \left(\eta_1\left(m_j; \theta\right), \eta_3\left(m_j; \theta\right)\right) e^{\imath m_j \phi}, \tag{34}$$

where j is the total number of Landau levels $j = (H - 1)/2$, we get the fully spin-polarized solution ($\eta_2 = 0$) for zero fermion mass:

$$\psi_{\pm}(m_j; z) = \exp\left(\pm\imath E(m_j)\int_0^z dz'\sqrt{\frac{B(z')}{A(z')}}\right), \tag{35}$$

$$\eta_1(m_j; \theta) = \frac{e^{\imath H \sin\theta/2}}{\sqrt{\sin\theta}}\left(\tan\frac{\theta}{2}\right)^{m_j}.$$

For nonzero mass, we can perform a Foldy-Wouthuysen transform starting from the above solution. Unlike the massless case considered in [27], the resulting stress-energy tensor will not be traceless, but that is precisely what will guve us extra stability. The reason this is consistent is the Landau quantization: the levels for different m_j are gapped from each other and

each Landau level can be treated as a single-particle solution which does not mix with other Landau levels. This results in the stress tensor

$$\langle T_{zz} \rangle = \frac{E_n}{(1+z^2)^2} \left(\sin 2\alpha - \cos 2\alpha \right), \quad \tan \alpha = -m/E(m_j). \qquad (36)$$

Fig. 8(A) shows the radial pressure T_{rr} as a function of energy, the outcome being that *positive* stress energy tensor is produced for $0 > E > -m$. In order to avoid this positive contribution, the Landau level spacing has to be large enough, i.e., larger than the mass gap (at zero mass this condition is trivially satisfied, as it simply means that any finite $E(m_j = 1)$ will do; this is the case studied in [27]). The simplest gapping mechanism we can think of is the chemical potential, i.e. an electrostatic field in addition to the magnetostatic one. The black hole thus has to become dyonic, with magnetic charge H and electric charge e. Assuming we have ensured the negativity of (36), we can write it in the form $T_{zz} = -\tau/(1+z^2)^2$, with τ a positive constant. Its magnitude roughly determines the size of the wormhole opening.
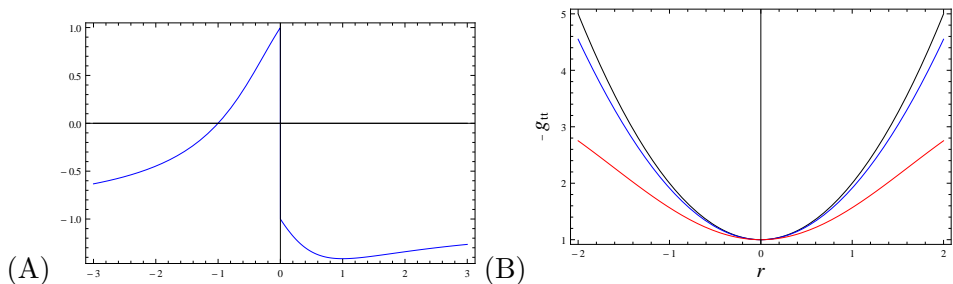

(A) (B)

Figure 8: (A) Radial component of the stress-energy tensor $\langle T_{rr} \rangle$ as a function of the (discrete) fermion energy E. Positive contribution only comes when $> E(m_j) > -m$. In order to avoid this range of energies we need a nonzero chemical potential (i.e., electric field, resulting in a dyonic black hole) to stabilize the wormhole with massive fermionic hair. (B) The solution for the metric component g_{tt} in the intermediate region, as a function of the radial coordinate r, for $\tau = 0, 0.05, 0.10$ (black, blue, red). Wormhole solutions (blue, red) are quantitatively very close to the unperturbed black hole (black) but qualitativrly different as there is no zero anymore.

Wormhole solution and matching. Having computed the stress-energy tensor (36), we can solve the Einstein equations. The strategy is again matching the expansions, but now we have three regions: the far region which is asymptotically AdS or even flat (we have mentioned that in the presence of magnetic field discrete bound states can form even in absence of AdS boundary), the intemediate region is a slightly perturbed near-horizon AdS$_2$ region of our magnetic RN geometry, and the inner region, the wormhole throat that opens up, turns out to be a *global* AdS$_2$ at leading order,

so it has a spherical boundary continuing onto the intermediate regions. The inner, near-global-AdS$_2$ metric in the form (33) at leading order reads

$$A(z) = R_0^2 \left[1 + z^2 - 8\pi\tau \left(z^2 + \left(3z + z^3 \right) \arctan z - \log \left(1 + z^2 \right) \right) \right]$$
$$B(z) = R_0^4/A(z), \quad C(z) = R_0^2 \left[1 + 8\pi\tau \left(1 + z \arctan z \right) \right]. \tag{37}$$

This solution is to be matched to the intermediate-region solution. Now large z corresponds to the wormhole mouth, i.e., the matching is to be done at large z, where small z is the "center" of the wormhole throat. The solution to match onto is the RN black hole metric:

$$ds^2 = -l^2 f(r) dt^2 + \frac{dr^2}{f(r)} + r^2 \left(d\theta^2 + \sin^2\theta d\phi^2 \right)$$
$$l = \frac{R_0}{2\pi^2\tau}, \quad R = \frac{r - \sqrt{\pi}\sqrt{e^2 + H^2}}{2\pi^2\tau}. \tag{38}$$

The solution thus exists for any choice of e and H. But for large e (in other words, for a large chemical potential), the density of the hair will increase significantly and we should repeat the WKB star or electron star approach. in AdS this is a simple matter, proving the stability of the configuration even at high densities. The interesting question is, can it work also in assymptotically flat space? In absence of magnetic field, the answer is certainly no – without an AdS boundary, there is nothing to equilibrate the electrostatic repulsion of electrons. But in the presence of magnetic field, one might obtain a stable charged hairy wormhole if the change in the near-horizon geometry is sufficient to effectively decrease the electrostatic energy density. This is the logical immediate task for future work.

We finish this short review of our work in progress on hairy wormholes with a somewhat more ambitious task. The dyonic wormhole model considered here is obviously quite simplistic and artificial. A much more realistic model is to start from a pair of Kerr black holes and see if these can open up a wormhole in a manner analogous to the scenario we have considered. In this case the magnetic field would be generated self-consistently by the (rotating) fermionic hair, removing the need for the magnetic monopole charge. Such an object would come much closer to realistic astrophysical matter.

5.   Instead of a conclusion

We have given a crack and practical review of the insights and technologies needed to describe and understand hairy black holes in anti-de Sitter space. The phase diagram in the presence of nonzero fermion density is quite rich, and it involves two deep and universal phenomena. First, the finite-temperature hairy black holes develop through a discontinuous phase

transition akin to the Hawking-Page transition (indeed, it is precisely the Hawking-Page transition but at finite density). The standard lore that at high enough temperatures black holes will always form is confirmed. Notice this is true at any fermion mass and charge, and thus at any occupation number, from a single wavefunction to the fluid limit, so the finding is definitely robust. Second, at zero temperature the transition is driven by the fermionic charge and/or chemical potential, i.e., electric charge of the black hole. In this case the black hole vanishes infinitely slowly, in a BKT transition that can be understood as the breaking of the one-dimensional conformal symmetry of the wavefunctions in the effectve inverse-square potential well. This is solely the consequence of the near-horizon physics, independent of the AdS boundary. Similar conformality-breaking infinite-order transitions are known in various backgrounds in string theory. Maybe one could relate the case described here to some consistent top-down model.

As mentioned in the Introduction, we have deliberately left out extensions and applications of the formalism described, for reasons of space and also generality of discussion. The field of applications closest to our experience is the AdS/CFT correspondence. Electrically charged black holes are dual to field theories at finite $U(1)$ density. The transition from a bald black hole to a hairy black hole is thus a transition between two phases at equal chemical potential. How do they differ then? We know that a black hole is dual to the Coulomb (deconfined) phase of some non-Abelian finite-temperature gauge theory [1, 4]; in the simplest setup coming from type IIB string theory, it is the $\mathcal{N} = 4$ supersymmetric $SU(N)$ theory. Coulomb phase means that the $U(1)$ charge is carried by $SU(N)$-gauge-charged operators, in our case fermions ("mesinos") and thus not visible to low-energy probes, since at low energies all operators are likely $SU(N)$-gauge-neutral. The hairy phase describes a dual field theory where the charge is carried by gauge-neutral operators ("baryons") and thus visible to probes such as a photon. This viewpoint was tried and confirmed in [11, 12, 15, 23]. It has realizations in condensed matter systems such as strange metals and heavy fermion materials. In this case, the gauge fields are emergent and arise from the spin-charge separation, and the transition between a black hole and a hairy geometry is a transition between a non-Fermi liquid, where most of the charge is carried by complicated excitatons that are nor directly seen in the spectrum, and a Fermi liquid where the fundamental degrees of freedom are just renormalized electrons. In QCD, this picture describes the phase diagram at intermediate energy scales and finite densities, where a black hole describes quark-gluon plasma, and a hairy solution describes either the color condensate or conventional barionic matter depending on the details of the model. One can learn a lot on AdS/condensed matter and AdS/QCD from [5, 6].

Finally, the search for wormhole solutions and how fermionic hair might stabilize them is likely to become very important in the future, in connection to the quantum information theory and the firewall, ER=EPR and other approaches to the black hole information problem. One can use much

of the formalism developed for hairy black holes, but the interpretation is still challanging. It is also unclear how realistic the wormhole proposal is if we work with only conventional, standard model matter, i.e. is it just an important proof of concept or a realistic model?

References

[1] J. Maldacena, *The large N limit of superconformal field theories and super-gravity*, Adv. Math. Theor. Phys. **2**, 231 (1998). [arXiv:hep-th/971120]

[2] S. S. Gubser, I. R. Klebanov and A. M. Polyakov, *Gauge theory correlators from non-critical string theory*, Phys. Lett. B **428**, 105 (1998). [arXiv:hep-th/9802109]

[3] E. Witten, *Anti de Sitter space and holography*, Adv. Math. Theor. Phys. **2**, 253 (1998). [arXiv:hep-th/9802150]

[4] O. Aharony, S. S. Gubser, J. Maldacena, H. Ooguri and Y. Oz, *Large N field theories, string theory and gravity*, Phys. Rep. **323**, 183 (2000). [arXiv:hep-th/9905111]

[5] J. Zaanen, Y.-W. Sun, Y. Liu and K. Schalm, *Holographic duality in condensed matter physics*, Cambridge University Press, 2015.

[6] M. Ammon and J. Erdmenger, *Gauge/gravity duality: foundations and applications*, Cambridge University Press, 2015.

[7] S. W. Hawking and G. F. R. Ellis, *The large-scale structure of space-time*, Cambridge University Press, 2010.

[8] N. D. Birrel and P. C. W. Davies, *Quantum fields in curved space*, Cambridge University Press, 1982.

[9] H. Liu, J. McGreevy, D. Vegh, "Non-Fermi liquids from holography", Phys. Rev. D **83**, 065029 (2011). [arXiv:0903.2477[hep-th]]

[10] M. Čubrović, J. Zaanen and K. Schalm, "String Theory, Quantum Phase Transitions and the Emergent Fermi-Liquid", Science **325**, 439 (2009). [arXiv:0904.1993[hep-th]]

[11] T. Faulkner, H. Liu, J. McGreevy and D. Vegh, *Emergent quantum criticality, Fermi surfaces, and AdS2*, Phys. Rev. D **83**, 125002 (2011). [arXiv:0907.2694 [hep-th]].

[12] S. Sachdev, *A model of a Fermi liquid using gauge-gravity duality*, Phys. Rev. D **84**, 066009 (2011). [arXiv:1107.5321 [hep-th]]

[13] W. Mück and K. S. Viswanathan, *Conformal field theory correlators from classical field theory on anti-de Sitter space: Vector and spinor fields*, Phys. Rev. **D58**, 106006 (1998). [arXiv:hep-th/9805145]

[14] M. Čubrović, Y. Liu, K.'Schalm, Y.-W. Sun and J. Zaanen, *Spectral probes of the holographic Fermi groundstate: Dialing between the electron star and AdS Dirac hair*, Phys. Rev. **D84**, 086002 (2011). [arXiv:1106.1798 [hep-th]]

[15] M. Medvedyeva, E. Gubankova, M. Cubrovic, K. Schalm, J. Zaanen, *Quantum corrected phase diagram of holographic fermions*, JHEP **2013**, 025 (2013). [arXiv:1302.5149[hep-th]].

[16] M. Čubrović, J. Zaanen, K. Schalm, *Constructing the AdS dual of a Fermi liquid: AdS Black holes with Dirac hair*, JHEP **2011**, 17 (2011). [arXiv:1012.5681[hep-th]]

[17] A. Allais, J. McGreevy and X. Josephine Suh, *Quantum electron star*, Phys. Rev. Lett **108**, 231602 (2012). [arXiv:1202.5308[hep-th]]

[18] A. Allais and J. McGreevy, *How to construct a gravitating quantum electron star*, Phys. Rev. **D88**, 066006 (2013). [arXiv:1306.6075[hep-th]]

[19] S. Hawking and D. Page, *Thermodynamics of black holes in anti de Sitter space*, Comm. Math. Phys. **87**, 577 (1977).

[20] S. A. Hartnoll, A. Tavanfar, *Electron stars for holographic metallic criticallity*, Phys. Rev. D **83**, 046003 (2011). [arXiv:1008.2828[hep-th]]

[21] K. Balasubramanian and J. McGreevy, *An analytic Lifshitz black hole*, Phys. Rev. D **80**, 104039 (2009). [arXiv:0909.0263[hep-th]]

[22] D. B. Kaplan, J.-W. Lee, D. T. Son, M. A. Stephanov, *Conformality Lost*, Phys. Rev. D **80**, 125005 (2009). [arXiv:0905.4752[hep-th]].

[23] M. Čubrović, *Confinement/deconfinement transition from symmetry breaking in gauge/gravity duality*, JHEP **2016**, 102 (2016). [arXiv:1605.07849[hep-th]]

[24] J. Maldacena and L. Susskind, *Cool horizons for entangled black holes*, Fortschr. Phys. **61** 781 (2013). [arXiv:1306.0533[hep-th]]

[25] M. S. Morris and K. Thorne, *Wormholes in spacetime and their use for interstellar travel: A tool for teaching general relativity* Am. J. Phys **56**, 395 (1988).

[26] D. Hochberg and M. Visser, *Null energy condition in dynamic wormholes*, Phys. Rev. Lett**81**, 746 (1998).

[27] J. Maldacena, A. Milekhin and F. Popov, *Traversable wormholes in four dimensions*, (2018). [arXiv:1807.04726[hep-th]]

[28] P. Gao, D. L. Jafferis and A. C. Wall, *Traversable wormholes via a double trace deformation*, JHEP **12**, (2017) 151. [arXiv:1608.05687[hep-th]]

[29] Z. Fu, B. Grado-White and D. Marolf, *A perturbative perspective on self-supporting wormholes*, Class. Quant. Grav. **36**, (2019) 045006. [arXiv:1807.07917[hep-th]]

[30] D. Marolf and S. McBride, *Simple perturbatively traversable wormholes from bulk fermions*, (2019). [arXiv:1908.03998[hep-th]]

[31] J. Maldacena and X.-L. Qi, *Eternal traversable wormhole*, (2018). [arXiv:1804.00491[hep-th]]

Учешће на конференцијама

[F1]

ICTP Workshop on String Theory, Holography, and Black Holes | (smr 3888)

Search

Search in Conferences:

Secretariat:

✉ smr3888@ictp.it

🕐 Starts **23 Oct 2023**
Ends **27 Oct 2023**
Central European Time

📍 **ICTP**
Budinich Lecture Hall (LB)

Strada Costiera, 11
I - 34151 Trieste (Italy)

Organizers

Ignatios ANTONIADIS (LPTHE - CNRS - Sorbonne University, France), Nikolay BOBEV (Institute for Theoretical Physics, KU Leuven, Belgium), Goran DJORDJEVIC (University of Nis, Serbia), Monica GUICA (CEA, Saclay, France), Kyriakos PAPADODIMAS (CERN, Switzerland), Local Organiser: Joan Elias Miro (ICTP)

An ICTP meeting 'in person'

The goal of this meeting is to discuss and consolidate recent advances in the vibrant research fields of string theory, holography, black hole physics, and cosmology. We will address important open problems through an active program of talks by well recognized scientific leaders in the field. In addition, we will organize an open discussion forum for researchers with close ties to the countries from the Balkan region and other parts of Eastern Europe in which we plan to brainstorm about future activities of the existing SEENET-MTP network, and other networking collaborations that will enhance the development of fundamental theoretical physics in these countries.

The workshop will have a series of review talks related to holography, string theory, black holes, as well as their interplay with topics in cosmology and particle physics. The aim will be to provide an overview of the recent developments and open challenges in these fields of fundamental physics while at the same time encouraging the participation of students and researchers with a wide spectrum of scientific interests (such as the ones in the Eastern European region). In addition to the review talks we plan a few shorter research presentations focused on new results and recent developments.

Topics:

- Black hole microstates in string theory and AdS/CFT
- Precision holography, string theory and supersymmetric localization
- Bounds on effective theories of gravity and interplay with bootstrap ideas in QFT
- Holography for non-AdS space-times
- Advances in strongly coupled QFT

We also envision ample time for discussion and informal interactions between the

ICTP school and workshop Примљено ×

Nikolay Bobev <nikolay.bobev@kuleuven.be>   пон, 26. сеп 2022. 00:42
коме mihailo.cubrovic

Преведи на: српски ×

Dear Mihailo,

We are in the process of organizing a two-week activity at the ICTP (Trieste) in September 2023 (precise dates to be fixed at a later time) and would like to include your name as a potential participant. At the moment you do not have to firmly commit to participating in this event but only indicate general interest and support for this activity by agreeing to be listed as a potential speaker or participant.

We plan to have a 1-week school followed by a 1-week workshop on topics related to string theory, holography, black hole physics and their applications. In addition to the scientific program, we also plan to use this event as a forum to discuss future activities that could strengthen the development of these research fields in the countries of (South) Eastern Europe (broadly defined).

We very much hope that you will support this initiative and, given that the ICTP application deadline is on Sep 30 2022, we would appreciate a quick answer..

Best regards,

Ignatios Antoniadis, Nikolay Bobev, Goran Djordjevic, Monica Guica, Joan Miro, Kyriakos Papadodimas

Mihailo Cubrovic <mcubrovic@gmail.com>   пон, 26. сеп 2022. 12:05
коме Nikolay

Dear Nikolay,

Thank you for your kind invitation, I'm happy to participate or to give a talk, it sounds like a good idea indeed. It's also useful to have an informal discussion on strengthening our fields in South/Eastern Europe

Best regards
Mihailo Čubrović

Nikolay Bobev <nikolay.bobev@kuleuven.be>   пон, 26. сеп 2022. 13:48

Scientific Calendar Event

GO TO SCIENTIFIC CALENDAR

Europe/Rome   Administration

Overview

Program

Speakers

Practical info

Material

📁 Final list of Participants

📁 Group photo

📁 How to choose your Time Zone

📁 Poster

Go to day ▾

Monday, 23 October 2023

| 08:30 - 09:00 | Registration and administration formalities |
| 09:00 - 17:30 | |

09:00   **Opening remarks** *5'*

09:05   **Quantum electrodynamics in two spacetime dimensions, 60+ years later** *2h0'*
Speaker: Silviu Pufu (Princeton University, USA)

11:05   **Coffee break** *40'*

11:45   **From Thermal 2pt Functions to Conformal Fishnet** *45'*
Speaker: Anastasios Petkou (Aristotle University of Thessaloniki, Greece)
Material: 📄 Slides

12:45   **Lunch** *1h45'*

14:30   **Low d singularities** *45'*
Speaker: Marija Tomašević (CPHT CNRS - Institut Polytechnique de Paris, France)
Material: 📄 Abstract 📄 Slides

15:15   **The Amazing Super-Maze** *45'*
Speaker: Iosif Bena (Centre d'Etudes de Saclay - CEA, Service de Physique Theorique, France)
Material: 📄 Abstract 📄 Slides

16:00   **Coffee break** *45'*

16:45   **Stringy effects in chaos** *45'*
Speaker: Mihailo Čubrović (Institute of Physics, Serbia)
Material: 📄 Abstract 📄 Slides

18:00 - 19:00   Welcome reception
Location: ICTP (Adriatico Guest House Cafeteria)

Tuesday, 24 October 2023

09:00 - 17:30

09:00   **Cosmology: recent progress, current status and future prospects** *2h0'*
Speaker: Marko Simonović (CERN Theoretical Physics, Switzerland)

11:00   **Group photo & Coffee break** *45'*

11:45   **On the thermodynamics of 4d Kerr-Newman black holes** *45'*

Speaker: Mihailo Čuborivć

Title: Stringy effects in chaos

Abstract: Black hole horizons and their holographic duals - strongly coupled thermal gauge theories - are well-known to exhibit fast scrambling and maximal chaos, which is best seen from their out-of-time ordered correlators. But the time is now ripe to look at chaos beyond classical gravity in the bulk. We will first look at D-brane dynamics in the framework of matrix models and show how stringy effects lead to sub-maximal chaos which in turn relates to the factorization problem in holography. We will also show how the infinite-matrix limit naturally leads back to black-hole-like fast scrambling. If time permits, we will also consider the opposite, perturbative regime by looking at the S-matrix of string-string scattering and find weak chaos with long-living states. This regime is disconnected from the fast-scrambling regime.

[F2]

https://mail.google.com/mail/u/0/#search/dragoljub/FMfcgzGxTNzPsfgpNDtkrRNJDqQKvhJD

Gmail

dragoljub

35 од много

HINT workshop predavanje Примљено ×

dgocanin <dgocanin@ipb.ac.rs>
коме Mihailo ▾

нед, 19. мај 2024. 14:54

Zdravo Mihailo,

Počeli smo (najzad) sa pozivanjem predavača za letnji HINT workshop od 22-26. jula na FF-u (poslao sam mail na hep-th, ne znam da li si na toj listu, poslaću uskoro i na phys4phys kada sakupimo sve invited speaker-e), pa želim da te i zvanično zamolim da budeš jedan od predavača.

Otvorili smo registraciju preko sajta HINT projekta:

https://hint.edu.rs/workshop/

I ne znam da li treba da ti pošaljem zvanično pozivno pismo u nekoj standardnoj formi?

Pozdrav,
Dragoljub

dgocanin <dgocanin@ipb.ac.rs>
коме Mihailo ▾

нед, 19. мај 2024. 16:10

Super, hvala! Nije hitno za naslov i apstrakt. Obavesticu te svakako o listi predavaca cim utvrdimo ko ce sve biti raspolozen, a i kako ce tematski biti podeljen workshop.

Pozdrav,
Dragoljub

On 2024-05-19 15:54, Mihailo Čubrović wrote:
> Hvala, rado ču biti predavač, HINT zvuči kao vrlo zanimljiva
> kombinacija tema! Evo upravo se registrovah. Za naslov i apstrakt
> moram još malo da razmislim, u stvari pomoglo bi i ako bih znao neka
> od imena predavača, da vidim šta bi se najbolje uklopilo.
>
> Mislim da mi ne treba nikakvo pozivno pismo, pozivna pisma sam
> prilagao jedino za izbor u zvanje a za to je mislim dovoljan i mail

Нов имејл

Примљено
Одложено
Важно
Ћаскања
Послато
Недовршено   1
Непожељно   15
Отпад

Категорије
    Друштвено
    Новости
    Форуми
    Промоције   1

Више

Ознаке

Више

HINT WORKSHOP
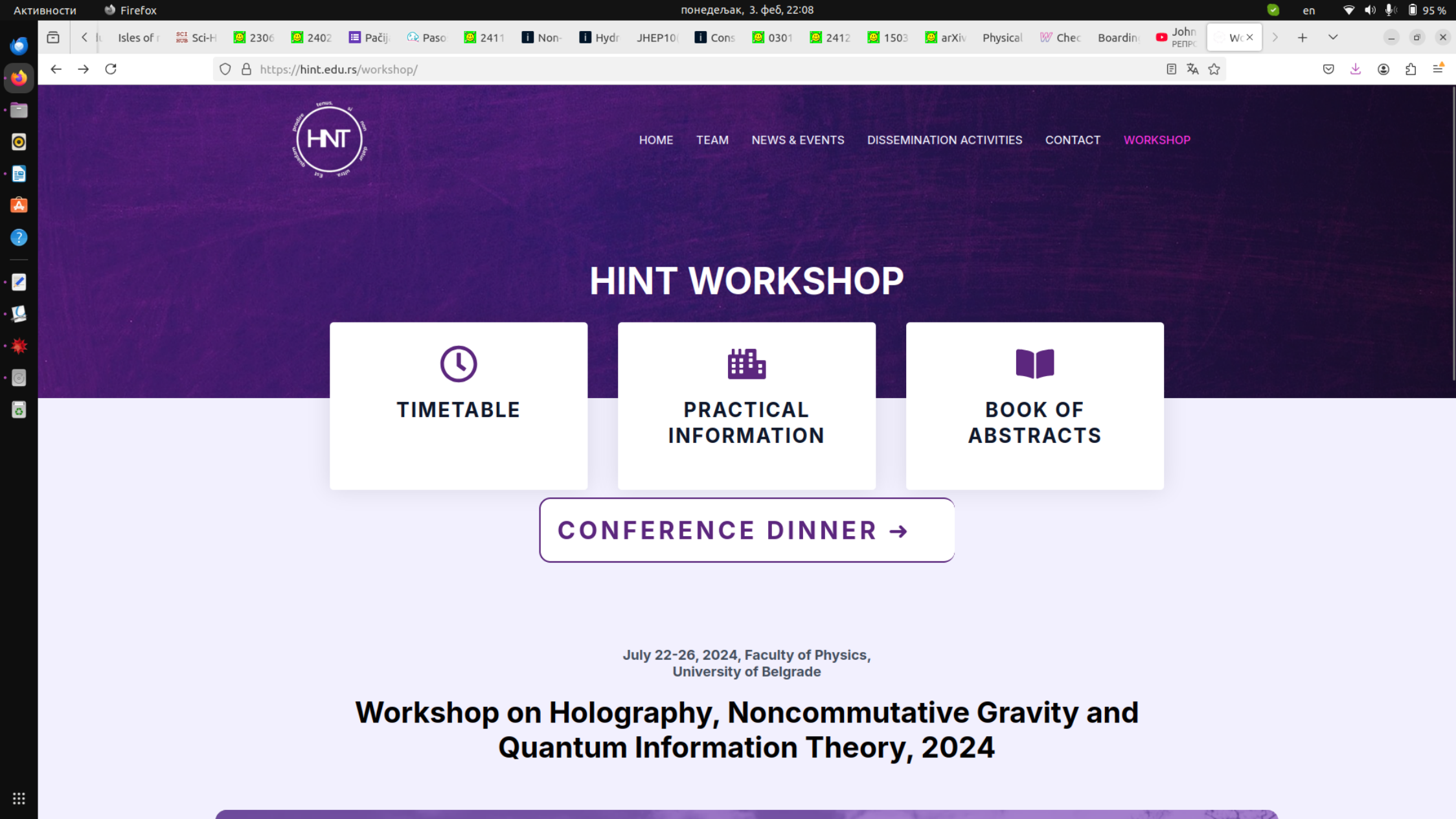
HOME TEAM NEWS & EVENTS DISSEMINATION ACTIVITIES CONTACT WORKSHOP

TIMETABLE

PRACTICAL INFORMATION

BOOK OF ABSTRACTS

CONFERENCE DINNER →

July 22-26, 2024, Faculty of Physics,
University of Belgrade

Workshop on Holography, Noncommutative Gravity and Quantum Information Theory, 2024

General Information

This workshop is intended for dissemination of the project results among the colleagues of the FIZFUB QTP Center and international collaborators.

Venue

Studentski Trg 12, Belgrade
Lecture Hall 661
Faculty of Physics, University of Belgrade

Contact

hint@ff.bg.ac.rs

Comittees

Scientific Advisory Comittee

- Professor *Fedele Lizzi*, Università di Napoli Federico II, Italy
- Professor *Časlav Brukner*, Faculty of Physics of the University of Vienna, Scientific Director of the Institute for Quantum Optics and Quantum Information (IQOQI) Vienna and member of SASA
- Professor *Đorđe Minić*, Virginia Tech, USA
- Professor *Rodrigo Olea*, Department of Physics, Universidad Andrés Bello, Chile
- Professor *Borivoje Dakić*, Faculty of Physics of the University of Vienna
- Professor *Nikola Paunković*, Departamento de Matemática Instituto Superior Técnico, Lisboa, Portugal
- Professor *Voja Radovanović*, Faculty of Physics, University of Belgrade

Local Organizing Comittee

Members of the HINT team

Time	Monday	Tuesday	Wednesday	Thursday	Friday
9:00-10:00	Registration/Opening				
10:00-11:00	Đorđe Minić	Mihailo Čubrović	Marko Vojinović	Flavio del Santo	Branislav Cvetković
11:00-11:30	Coffee break	Coffee break	Coffee break	Coffee break	Coffee break
11:30-12:15	Olivera Mišković	Rodrigo Olea	Igor Prlina	Dragan Prekrat	Nikola Konjik
12:15-12:30			Discussion/posters	Discussion/posters	Charlène Laffond
12:30-13:00	Discussion	Discussion			
13:00-15:00	Lunch break	Lunch break	Lunch break	Lunch break	Farewell cocktail
15:00-15:45	Ilija Burić	Iva Lovreković	Bastian Heß	Petar Tadić	
15:45-16:15	Nicolas Medina Sanchez	Vladan Đukić	Fatemeh Bibak	Anne-Catherine de la Hamette	
16:15-16:45	Coffee break	Coffee break	Coffee break	Coffee break	
16:45-17:15	Dušan Đorđević	Đorđe Bogdanović	Ana Đorđević	Carlo Cepollaro	
17:15-17:45	Discussion	Discussion	Discussion	Discussion	
17:45-20:00					
20:00		Conference dinner			

1 One hour talks

1. Đorđje Minić: *Quantum gravity as gravitized quantum theory*

   In this talk I will present the new understanding of quantum foundations based on the concept of quantum (modular) spacetime endowed with manifest non-locality that is consistent with causality. This view implies the consistency of the fundamental length/time and Lorentz symmetry, based on the principle of relative (observer-dependent) locality. The geometry of such quantum spacetime is encoded in the new concept of Born geometry. The problem of quantum gravity is then viewed from the perspective of a dynamical Born geometry. In this approach the quantum mechanical structures that are traditionally fixed, such as the Fubini-Study metric in the Hilbert space of states, become dynamical and so implement the idea of "gravitization of quantum theory". A specific test of this new approach to quantum gravity is based on intrinsic triple interference in a varying gravitational field, in a profound analogy with recent triple-path interference experiments performed in the context of nonlinear optics. I will emphasize that the intrinsic triple interference experiment in a varying gravitational field would deeply influence the present understanding of the kinematics of quantum gravity and quantum gravity phenomenology. I will also discuss the non-linear Talbot effect in this context as another striking phenomenological probe of gravitization of the geometry of quantum theory.

2. Olivera Mišković: *Asymptotic symmetries in the flat space and the electric-magnetic duality*

   We analyze asymptotic symmetries emerging at the null boundary of four-dimensional field theories in the flat space, not related to the bulk gauge transformations. We discuss consequences on the examples of the scalar field theory and electromagnetism.

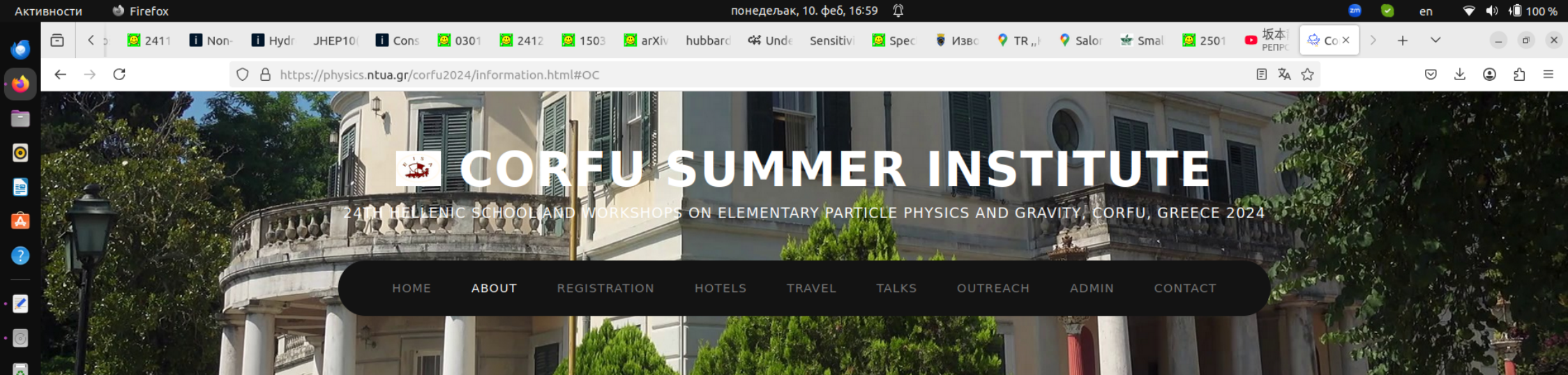3. Mihailo Čubrović: *Black holes and chaos in matrix models*

   We study the measures of chaos (out-of-time ordered correlators and energy level statistics) and magic (stabilizer Renyi entropy) in the black hole phase of the BFSS (type IIA) matrix model, which is conjectured to contain the full nonperturbative stringy physics of black holes. Deep in the black hole phase of the model, the physics is strongly chaotic and strongly quantum-mechanical. At the black hole-thermal gas transition, the collective modes give rise to a different mechanism of chaos. Inside the thermal gas phase, the magic also decreases and we end up with weakly chaotic, semiclassical dynamics. We discuss the implications of our findings for the black hole - string complementarity and compare them to our earlier findings for the IKKT (type IIB) matrix model and the factorization of the partition functions.

4. Rodrigo Olea: *Conformal Renormalization of anti-de Sitter gravity*

   Boundary counterterms are required to cancel the divergences in the bulk action of asymptotically AdS gravity. These boundary terms are prescribed by a systematic procedure known as Holographic Renormalization, developed in the context of AdS/CFT correspondence. In this seminar, we show that, in four and six bulk dimensions, these counterterms can also be obtained from a proper embedding of Einstein in Conformal gravity (Conformal Renormalization).

[F3]

CORFU SUMMER INSTITUTE

24TH HELLENIC SCHOOL AND WORKSHOPS ON ELEMENTARY PARTICLE PHYSICS AND GRAVITY, CORFU, GREECE 2024

Corfu2024

LINKS

Home

Cosmo School

Future Colliders

SM and Beyond

QG & Strings

DSU2024

Non-Com Geom
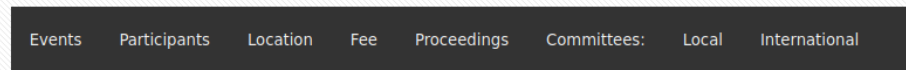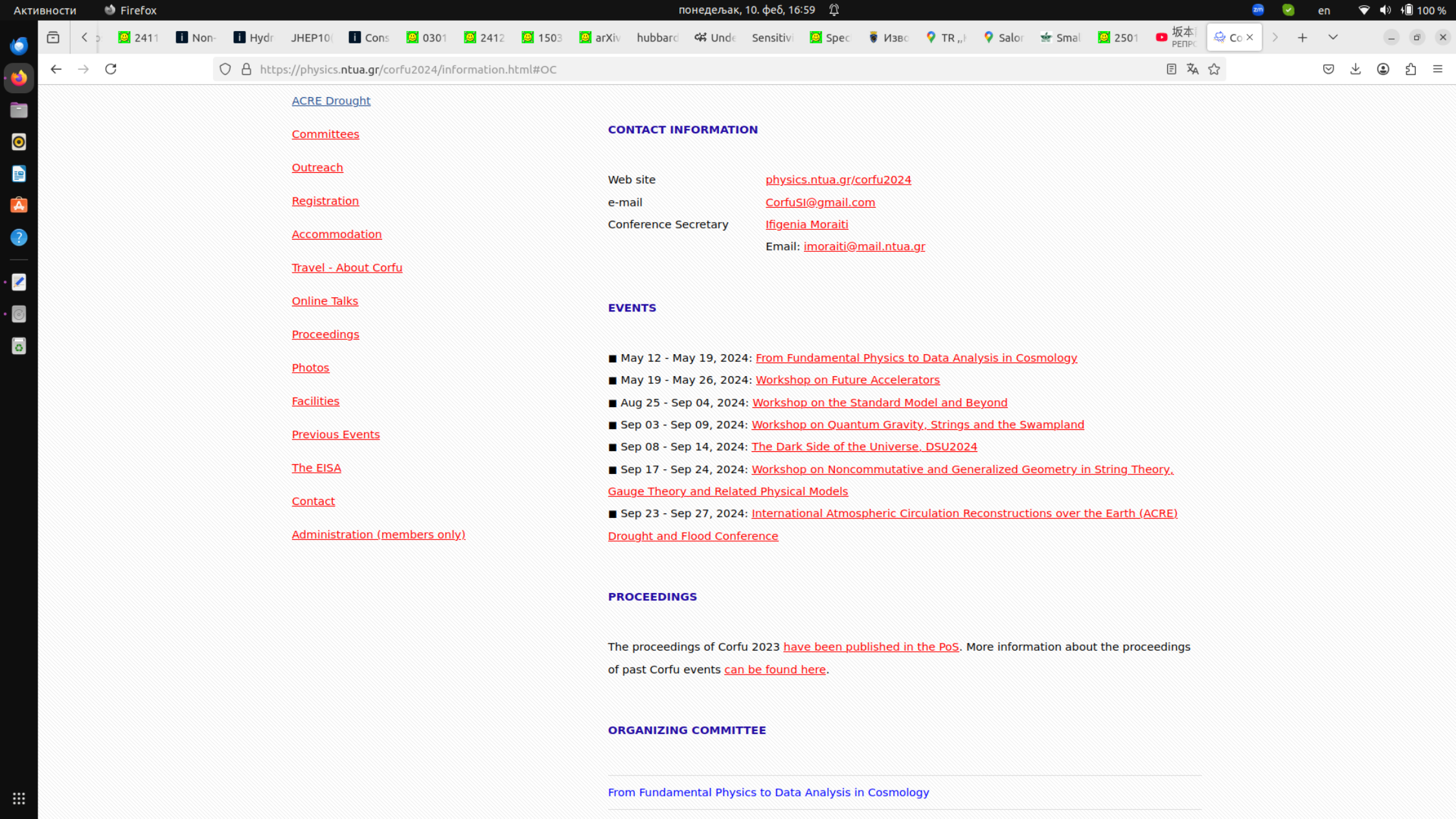
ACRE Drought

Committees

Outreach

Information

EVENTS, CONTACT INFORMATION, ORGANIZING COMMITTEES AND THE INTERNATIONAL SCIENTIFIC COMMITTEE

E I S A
European Institute for Sciences and Their Applications

Corfu Summer Institute
Hellenic School and Workshops on Elementary Particle Physics and Gravity
Corfu, Greece

Events   Participants   Location   Fee   Proceedings   Committees: Local   International

CONTACT INFORMATION

ACRE Drought

Committees

Outreach

Registration

Accommodation

Travel - About Corfu

Online Talks

Proceedings

Photos

Facilities

Previous Events

The EISA

Contact

Administration (members only)

CONTACT INFORMATION

Web site	physics.ntua.gr/corfu2024
e-mail	CorfuSI@gmail.com
Conference Secretary	Ifigenia Moraiti
	Email: imoraiti@mail.ntua.gr

EVENTS

■ May 12 - May 19, 2024: From Fundamental Physics to Data Analysis in Cosmology

■ May 19 - May 26, 2024: Workshop on Future Accelerators

■ Aug 25 - Sep 04, 2024: Workshop on the Standard Model and Beyond

■ Sep 03 - Sep 09, 2024: Workshop on Quantum Gravity, Strings and the Swampland

■ Sep 08 - Sep 14, 2024: The Dark Side of the Universe, DSU2024

■ Sep 17 - Sep 24, 2024: Workshop on Noncommutative and Generalized Geometry in String Theory, Gauge Theory and Related Physical Models

■ Sep 23 - Sep 27, 2024: International Atmospheric Circulation Reconstructions over the Earth (ACRE) Drought and Flood Conference
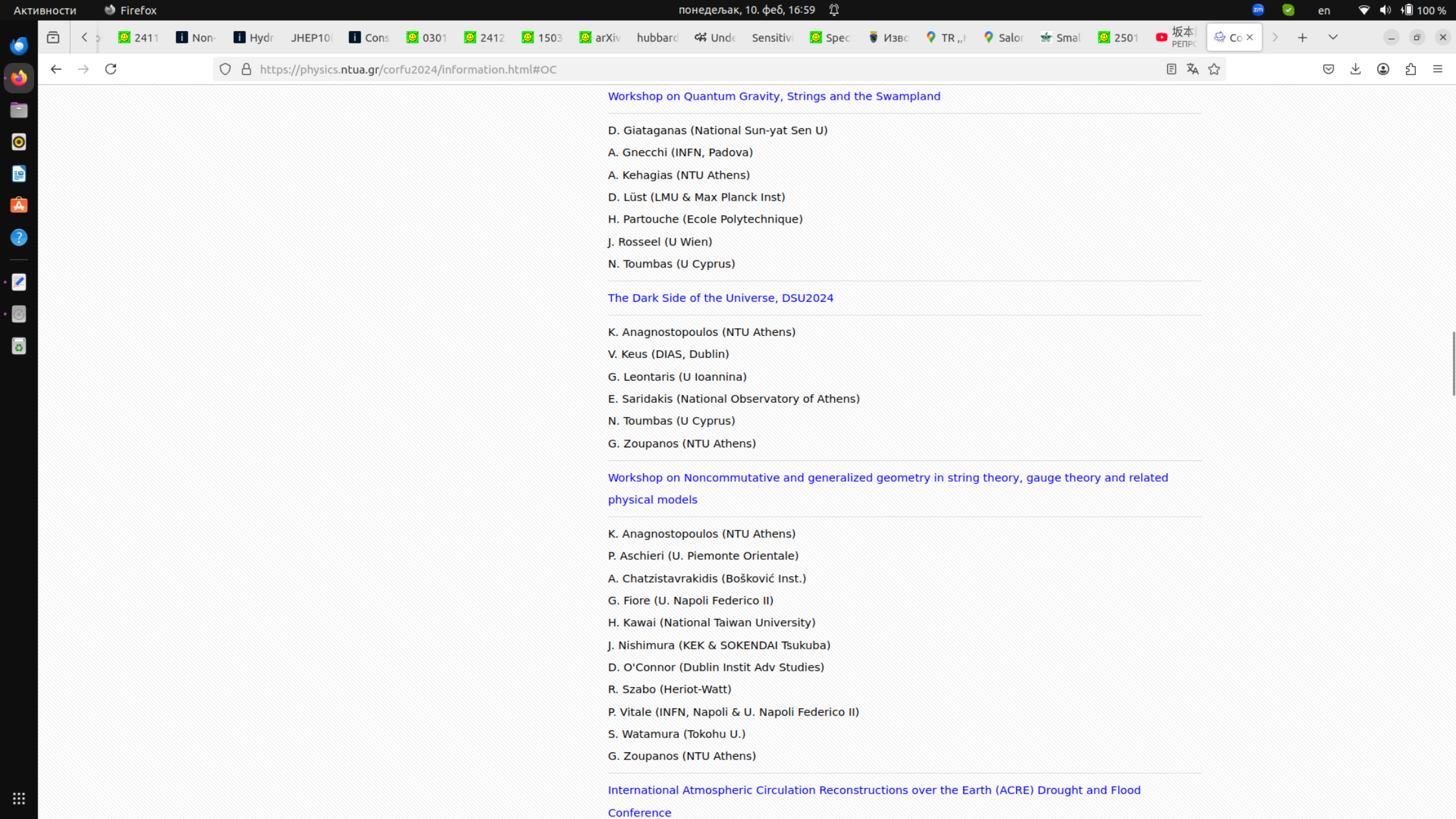
PROCEEDINGS

The proceedings of Corfu 2023 have been published in the PoS. More information about the proceedings of past Corfu events can be found here.

ORGANIZING COMMITTEE

From Fundamental Physics to Data Analysis in Cosmology

[Workshop on Quantum Gravity, Strings and the Swampland](#)

D. Giataganas (National Sun-yat Sen U)

A. Gnecchi (INFN, Padova)

A. Kehagias (NTU Athens)

D. Lüst (LMU & Max Planck Inst)

H. Partouche (Ecole Polytechnique)

J. Rosseel (U Wien)

N. Toumbas (U Cyprus)

[The Dark Side of the Universe, DSU2024](#)

K. Anagnostopoulos (NTU Athens)

V. Keus (DIAS, Dublin)

G. Leontaris (U Ioannina)

E. Saridakis (National Observatory of Athens)

N. Toumbas (U Cyprus)

G. Zoupanos (NTU Athens)

[Workshop on Noncommutative and generalized geometry in string theory, gauge theory and related physical models](#)

K. Anagnostopoulos (NTU Athens)

P. Aschieri (U. Piemonte Orientale)

A. Chatzistavrakidis (Bošković Inst.)

G. Fiore (U. Napoli Federico II)

H. Kawai (National Taiwan University)

J. Nishimura (KEK & SOKENDAI Tsukuba)

D. O'Connor (Dublin Instit Adv Studies)

R. Szabo (Heriot-Watt)

P. Vitale (INFN, Napoli & U. Napoli Federico II)

S. Watamura (Tokohu U.)

G. Zoupanos (NTU Athens)

[International Atmospheric Circulation Reconstructions over the Earth (ACRE) Drought and Flood Conference](#)

Gmail

🔍 corfu

16 од 19

Corfu 2024: Quantum Gravity, Strings and the Swampland, September 3 - 9 Примљено ×

Dimitrios Giataganas <dimitrios.giataganas@gmail.com>
коме ја

чет, 16. мај 2024. 06:35

Преведи на: српски ×

Dear Mihailo,

Within this year's program of the European Institute for Sciences and their Applications (EISA), we are organizing the event "Quantum Gravity, Strings, and the Swampland", which will take place on-site.

We would be delighted if you would like to participate and give a talk as a main speaker. The workshop will take place at the Mon Repos Estate in the island of Corfu, Greece, and the relevant dates are 3-9 of September 2024 (including arrival and departure dates). More information may be found on the webpage of the institute:
http://www.physics.ntua.gr/corfu2024/st.html
where you may also register.

~~██~~
~~██~~
~~██~~

We would be very happy to hear a positive answer from you and hopefully to welcome you to Corfu this coming September.

With our best wishes,
The organisers

--

Columbus Fellow and Assist. Professor,
National Sun Yat-sen University,
Taiwan
Web: https://sites.google.com/site/dgiataga/

Workshop on Quantum Gravity, Strings and the Swampland 2024

Venue: Lecture Hall

	Wednesday 4/9	Thursday 5/9	Friday 6/9	Saturday 7/9	Sunday 8/9
Chair:	Trigiante	Grana	Lopes Cardoso	Lozano	Giataganas
09:30 – 10:00	Registration	Faraggi	Reffert	Antoniadis	Cubrovic
10:00 – 10:30	Vandoren	Benakli	Brustein	Leontaris	Macpherson
10:30 – 11:00	Coffee Break	Coffee Break	Coffee Break	Coffee Break	Coffee Break
11:00 – 11:30	Grana	Orlando	Lozano	Marchesano	Kuipers
11:30 – 12:00	Grumiller	Papadoulaki	Jafferis	Florakis	Liatsos
12:00 –12:30	Antipin	Lopes Cardoso	Trigiante	Guarino	Coudarchet
12:30 – 16:30	12:30 – 13:00 Rosseel / Lunch Break	Lunch Break	Free Afternoon or Excursion	Lunch Break	Lunch Break
Chair:	Grumiller	Vandoren		Rosseel	Giataganas
16:30 – 17:00	Montella	Markou		Wang	Schachner
17:00 - 17.30	Herraez	Betzios		Kalogirou	Paraskevopoulou
17:30 – 18:00	Coffee Break	Coffee Break		Coffee Break	Coffee Break
18:00 – 18:30	Raptakis	Linardopoulos		Angius	Karageorgos
18:30 – 19:00	Masias	Raml		Discussion	Discussion

Detailed Program

Wednesday 4/9

Stefan Vandoren: "The landscape of freely acting orbifolds"
Mariana Graña: "Tadpole conjecture in non-geometric backgrounds"
Daniel Grumiller: "Carroll Swiftons"
Oleg Antipin: "Standard Model at large hypercharge"
Jan Rosseel: "Carroll gravity from the conformal approach"
Carmine Montella: TBA
Alvaro Herraez: "On the origin of species thermodynamics and the black hole-tower correspondence"
Emmanouil Raptakis: "Higher-derivative deformations of the ModMax theory"
Joaquin Masias: "Starobinsky Inflation and the Swampland"

Thursday 5/9

Alon Faraggi: "Mirror symmetry and spinor-vector duality"
Karim Benakli: Gravitinos, Modulinos & Neutrinos
Domenico Orlando: "What is the Large Charge Expansion?"
Olga Papadoulaki: Euclidean Wormholes in Holography
Gabriel Lopes Cardoso: "Weyl-Lewis-Papapetrou coordinates, self-dual Yang-Mills equations and the single copy"
Chrysoula Markou : "On the deep string spectrum"
Panos Betzios: "An inflationary cosmology from anti-de Sitter wormholes"
Georgios Linardopoulos: "B-type anomaly coefficients of holographic defects."
Thomas Raml: "Infinite distances, the scalar potential and the Ricci flow"

Friday 6/9

Susanne Reffert: "The large-charge expansion: recent progress and applications"
Ramy Brustein: "What's inside a black hole?"
Yolanda Lozano: "Recent developments in low dimensional holography"
Daniel Jafferis: 3d gravity and ensembles of CFTs
Mario Trigiante: "S-Fold Solutions to Type IIB Superstring Theory"

Saturday 7/9

Ignatios Antoniadis: TBA
George Leontaris: "Fibre Inflation in Large Volume Compactification"
Fernando Marchesano: "Yukawas and Neutrinos at infinite distance"
Ioannis Florakis: TBA
Adolfo Guarino: "Charting the Landscape of 3D Orientifold Flux Vacua"
Zhiwei Wang: "Probe Strongly Coupled Dark Sector via Gravitational Wave"
Antonis Kalogirou: "Thermal Effects in Ising Cosmology"
Roberta Angius: "Topological defects in K3 sigma models"

Sunday 8/9

Mihailo Cubrovic: "Weak chaos in the string-black hole scattering from classical to quantum"
Niall Macpherson: "G-structures for AdS2 solutions"
Folkert Kuipers: "Quantum Theory, Gravity and Higher Order Geometry"
Nikolaos Liatsos: "N=4 Supergravity with Local Scaling Symmetry in Four Dimensions"
Thibaut Coudarchet: "New families of scale separated vacua"
Andreas Schachner: "Candidate de Sitter vacua"
Antonia Paraskevopoulou: "Is M-theory Emergent?"
Leonidas Karageorgos: Renormalization of Composite operators & RG flow

[G2]
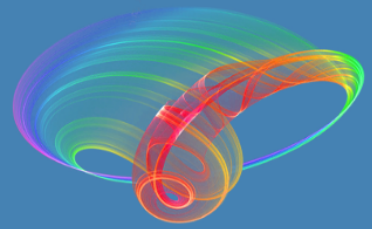
VI International School and Conference on Photonics
28 August - 1 September 2017, Belgrade, Serbia

PHOTONICA 2017

with 3 joint events: *MP1402-HERALD,*
MP1406-MultiscaleSolar and
H2020-MSCA-RISE-2015 CARDIALLY workshop

- Home
- About PHOTONICA
- Committees & Organizers
- News
- Deadlines/Important dates

- Topics & Program
- Speakers & Lectures
- Book of abstracts
- Posters presentations
- Manuscript submission for OQE ^{NEW!}
- Registration
- Abstract submission

- Venue
- Travel Information
- Accommodation
- Social program
- Gallery ^{NEW!}

- First announcement
- Second announcement
- Conference poster

- Sponsors
- Industrial presentation

Welcome to Belgrade

Dear Colleague,

You are cordially invited to participate at the **VI International School and Conference on Photonics - PHOTONICA2017** that will take place in Belgrade, Serbia (August 28 - September 1, 2017).

Conference group photograph!

COST Action MP1402 - HERALD
Atomic layer deposition and related ultra-thin film processes for advanced devices

COST Action MP1406 - MultiscaleSolar
Multiscale in modelling and validation for solar photovoltaics

H2020-MSCA-RISE-2015 CARDIALLY workshop
Capturing and quantitative analysis of multi-scale multi-channel diagnostic data

NEWS!

October 30th 2017.
Deadline for manuscript submission in OQE is extended until November 6th (October 31st, October 15th)

October 14th 2017.
Deadline for manuscript submission in OQE is extended until **October 31st**

PHOTONICA 2017

with 3 joint events: *MP1402-HERALD, MP1406-MultiscaleSolar* and *H2020-MSCA-RISE-2015 CARDIALLY workshop*

- Home
- About PHOTONICA
- Committees & Organizers
- News
- Deadlines/Important dates

- Topics & Program
- Speakers & Lectures
- Book of abstracts
- Posters presentations
- Manuscript submission for OQE NEW!
- Registration
- Abstract submission

- Venue
- Travel Information
- Accommodation
- Social program
- Gallery NEW!

- First announcement
- Second announcement
- Conference poster

- Sponsors
- Industrial presentation

- Links

- Contacts

Follow us!

Scientific Committee

- Aleksandar Krmpot, Serbia
- Antun Balaž, Serbia
- Arlene D. Wilson-Gordon, Israel
- Bojan Resan, Switzerland
- Boris Malomed, Israel
- Branislav Jelenković, Serbia
- Dejan Gvozdić, Serbia
- Detlef Kip, Germany
- Dragan Indjin, United Kingdom
- Edik Rafailov, United Kingdom
- Feng Chen, China
- Francesco Cataliotti, Italy
- Giannis Zacharakis, Greece
- Goran Isić, Serbia
- Goran Mašanović, United Kingdom
- Isabelle Philippa Staude, Germany
- Jelena Radovanović, Serbia
- Jerker Widengren, Sweden
- Jovana Petrović, Serbia
- Laurent Sanchez, France
- Ljupčo Hadžievski, Serbia
- Marco Santagiustina, Italy
- Milan Mashanović, United States of America
- Milan Trtica, Serbia
- Miloš Živanov, Serbia
- Milutin Stepić, Serbia
- Milivoj Belić, Qatar
- Nikola Stojanović, Germany
- Pavle Anđus, Serbia
- Peđa Mihailović, Serbia
- Radoš Gajić, Serbia
- Schaaf Peter, Germany
- Sergei Turitsyn, United Kingdom
- Suzana Petrović, Serbia
- Ticijana Ban, Croatia
- Vladana Vukojević, Sweden
- Zoran Jakšić, Serbia
- Željko Šljivančanin, Serbia

NEWS!

October 30th 2017.
Deadline for manuscript submission in OQE is extended until November 6th (October 31st, October 15th)

October 14th 2017.
Deadline for manuscript submission in OQE is extended until October 31st (October 15th)

September 21st 2017.

Vortices and topological structures in photorefractive materials

M. Čubrović[1] and M. Petrović[2]

[1]*Scientific Computing Lab, Center for the Study of Complex Systems, Institute of Physics, Belgrade, Serbia*
[2]*Institute of Physics, Belgrade, Serbia*
e-mail:mcubrovic@gmail.com

We consider the collective behavior and stability of topologically nontrivial patterns in laser beams propagating through a photorefractive crystal by analytical and numerical means. The photorefractive medium leads to the self-focusing of the beam, giving rise to complex stationary patterns for some choices of initial conditions. When two beams with winding phase (vortices) propagate from the opposite ends of the crystal, their interaction mimics the planar Heisenberg antiferromagnets and can be described by a phase diagram obtained from renormalization group analysis. Different phases are visually recognizable and can be identifed in numerical simulations. If the crystal has defects (holes), the long-range order is lost but individual vortices can still be stable in a pattern akin to a spin glass.

We then consider a deeper question: can such topological configurations behave as optical solitons, i.e. propagate through each other without interacting? With the counterpropagating vortex system considered above, this is obviously not the case as they interact and show collective behavior. The question is considered in the framework of the Lax pair formalism and the answer seems to be non-universal, depending strongly on the details of the propagation geometry and the properties of the crystal. The construction of such solutions remains attractive if elusive, because of the robustness of optical solitons to perturbations which are inevitable in experiment.

[G3]
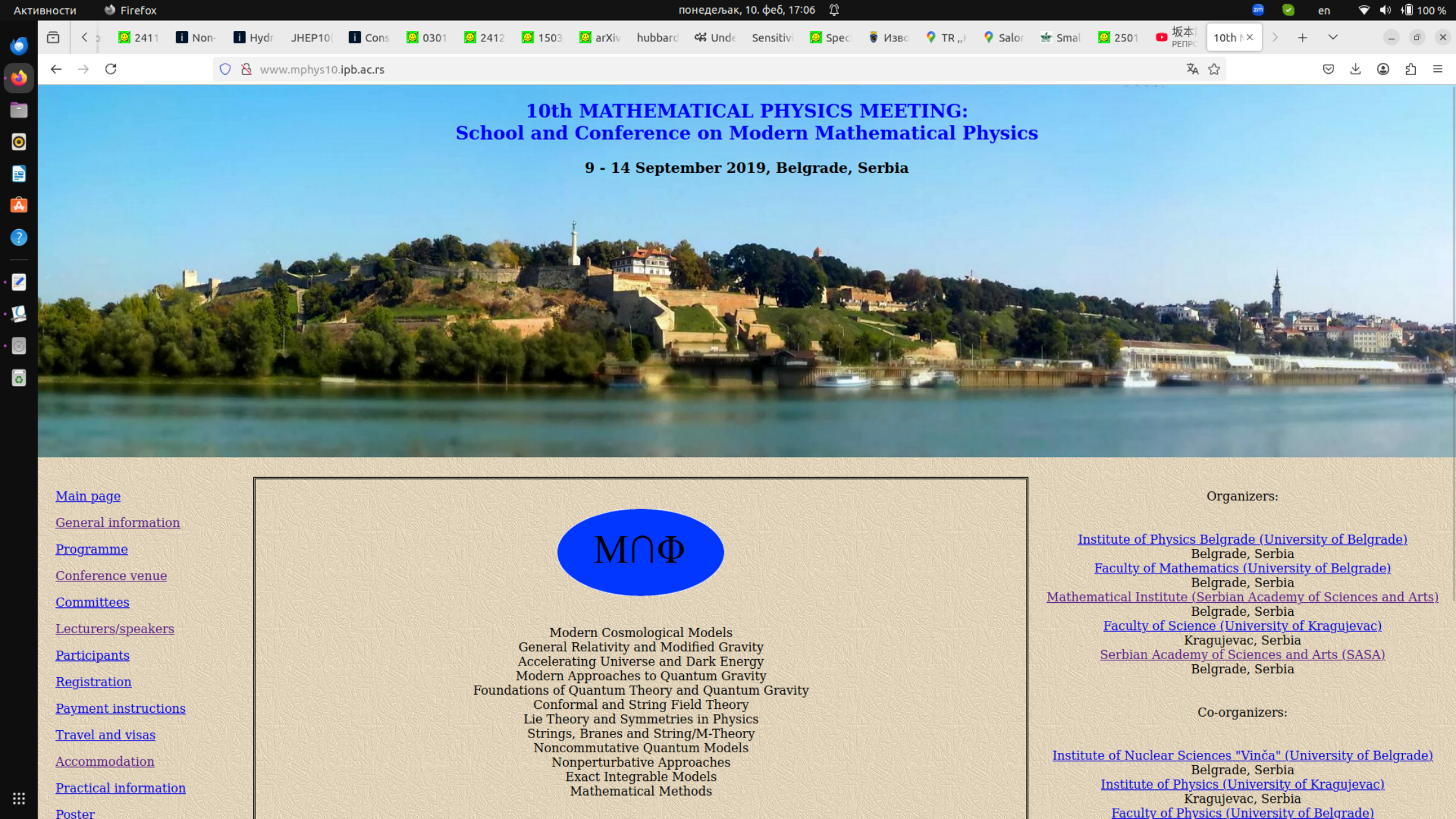
10th MATHEMATICAL PHYSICS MEETING:
School and Conference on Modern Mathematical Physics

9 - 14 September 2019, Belgrade, Serbia

- Main page
- General information
- Programme
- Conference venue
- Committees
- Lecturers/speakers
- Participants
- Registration
- Payment instructions
- Travel and visas
- Accommodation
- Practical information
- Poster

М∩Ф

Modern Cosmological Models
General Relativity and Modified Gravity
Accelerating Universe and Dark Energy
Modern Approaches to Quantum Gravity
Foundations of Quantum Theory and Quantum Gravity
Conformal and String Field Theory
Lie Theory and Symmetries in Physics
Strings, Branes and String/M-Theory
Noncommutative Quantum Models
Nonperturbative Approaches
Exact Integrable Models
Mathematical Methods

Organizers:

Institute of Physics Belgrade (University of Belgrade)
Belgrade, Serbia
Faculty of Mathematics (University of Belgrade)
Belgrade, Serbia
Mathematical Institute (Serbian Academy of Sciences and Arts)
Belgrade, Serbia
Faculty of Science (University of Kragujevac)
Kragujevac, Serbia
Serbian Academy of Sciences and Arts (SASA)
Belgrade, Serbia

Co-organizers:

Institute of Nuclear Sciences "Vinča" (University of Belgrade)
Belgrade, Serbia
Institute of Physics (University of Kragujevac)
Kragujevac, Serbia
Faculty of Physics (University of Belgrade)

Committees

International Advisory Committee

Ignatios Antoniadis (Paris, France)
Irina Arefeva (Moscow, Russia)
Milutin Blagojević (Belgrade, Serbia)
Loriano Bonora (Trieste, Italy)
Martin Cederwall (Goteborg, Sweden)
Branislav Cvetković (Belgrade, Serbia)
Marija Dimitrijević Ćirić (Belgrade, Serbia)
Nemanja Kaloper (Davis, USA)
Djordje Minic (Blacksburg, USA)
Viatcheslav Mukhanov (Munich, Germany)
Emil Nissimov (Sofia, Bulgaria)
Sergei Odintsov (Barcelona, Spain)
Dmitri Polyakov (Chengdu, China; Moscow, Russia)
Branislav Sazdovic (Belgrade, Serbia)
Paul Sorba (Annecy, France)
Alexei Starobinsky (Moscow, Russia)
Dejan Stojkovic (Buffalo, USA)
Mihai Visinescu (Bucharest, Romania)
Rade Zivaljevic (Belgrade, Serbia)
George Zoupanos (Athens, Greece)

International Organizing Committee

Vladimir Dobrev (Sofia, Bulgaria)
Radu Constantinescu (Craiova, Romania)
Branko Dragovich (Belgrade, Serbia)
Goran Djordjevic (Nis, Serbia)
Zoran Rakic (Belgrade, Serbia)
Djordje Sijacki (Belgrade, Serbia)
Marko Vojinović (Belgrade, Serbia)
Igor Volovich (Moscow, Russia)

Local Organizing Committee

Organizers:

Institute of Physics Belgrade (University of Belgrade)
Belgrade, Serbia
Faculty of Mathematics (University of Belgrade)
Belgrade, Serbia
Mathematical Institute (Serbian Academy of Sciences and Arts)
Belgrade, Serbia
Faculty of Science (University of Kragujevac)
Kragujevac, Serbia
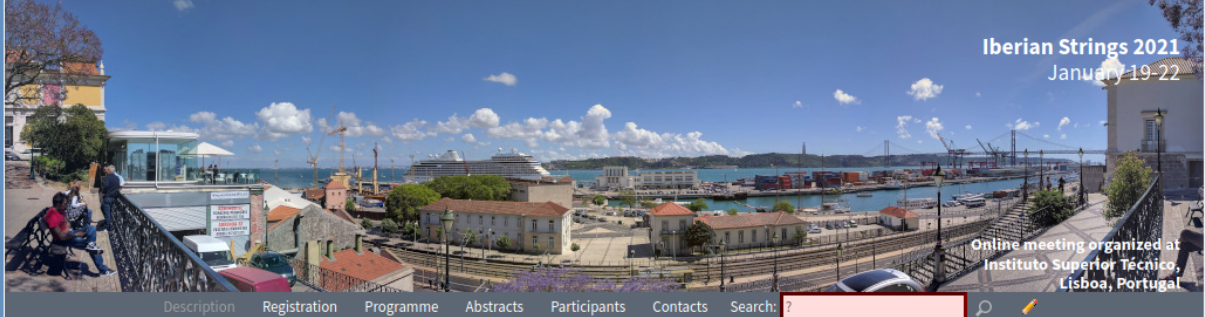Serbian Academy of Sciences and Arts (SASA)
Belgrade, Serbia

Co-organizers:

Institute of Nuclear Sciences "Vinča" (University of Belgrade)
Belgrade, Serbia
Institute of Physics (University of Kragujevac)
Kragujevac, Serbia
Faculty of Physics (University of Belgrade)
Belgrade, Serbia
Faculty of Sciences (University of Novi Sad)
Novi Sad, Serbia
School of Electrical Engineering (University of Belgrade)
Belgrade, Serbia
SEENET-MTP (Southeastern European Network in Mathematical and Theoretical Physics)
Nis, Serbia

10th Mathematical Physics Meeting: School and Conference on Modern Mathematical Physics
Belgrade, 9 – 14 September 2019

Timetable Tuesday (10.09.2019)

Time	Duration	Speaker	Title
9:20 – 10:00	40'	F. Toppan	*New issues in superconformal quantum mechanics*
10:00 – 10:40	40'	F. Sugino	*Highly entangled quantum spin chains*
10:40 – 11.10	30'		C o f f e e b r e a k
11:10 – 11:50	40'	I. Cotaescu	*Leptogenesis in a spatially flat Milne-type universe*
11:50 – 12:20	30'	S. Pacif	*An accelerating cosmological model from a parametrization of Hubble parameter*
12:20 – 12:40	20'	S. Bhatacharjee	*Role of particle creation mechanism on the collapse of a massive star*
12:40 – 13:00	20'	A. Mandal	*Thermodynamic study of Reissner-Nordstrom quintessence black hole*
13:00 – 15:30	150'		L u n c h b r e a k
15:30 – 16:00	30'	B. Nikolic	*From 3D torus with H-flux to torus with R-flux and back*
16:00 – 16:30	30'	M. Stetsko	*Black holes in the theory with nonminimal derivative coupling and some aspects of their thermodynamics*
16:30 – 17:00	30'	G. Samanta	*Wormhole modeling in general relativity*
17:00 – 17:30	30'		C o f f e e b r e a k
17:30 – 18:00	30'	M. Szydlowski	*Starobinsky cosmological model in Palatini formalism*
18:00 – 18:30	30'	M. Cederwall	*Extended geometry and tensor hierarchy algebras*
18:30 – 19:00	30'	M. Cubrovic	*Toward eternal traversable hairy wormholes*

[H8]

Iberian Strings 2021
January 19-22

Online meeting organized at Instituto Superior Técnico, Lisboa, Portugal

Description

The Iberian Strings 2021 meeting is the twelfth meeting of the *Iberian Strings* series, superseding previous editions of the *Workshop on Gravitational Aspects of Strings and Branes* and of *Northwest Strings*. These meetings bring together a large part of the string theory community of Spain and Portugal with the aim of discussing and sharing recent advances in the field of strings and branes. However, all string theorists working elsewhere too are highly welcome to participate in the meeting.

Iberian Strings 2021 is organized by Instituto Superior Técnico (Lisbon, Portugal) and will be an **online conference** running from January 19 till January 22, 2021. This will be the third time that IST has the pleasure of hosting Iberian Strings, after already having hosted Iberian Strings 2013 and of Iberian Strings 2017.

The present edition will feature 8 invited one-hour review lectures as well as a considerable number of shorter (30 minute) talks by participants. The review lecturers are listed below. PhD students are especially encouraged to participate in the meeting

In addition, this edition of Iberian Strings will feature two outreach colloquia on the experimental and theoretical aspects of the Physics Nobel Prize 2020, by Frank Eisenhauer (Max-Planck Institute for Extraterrestrial Physics, Garching) and Roberto Emparan (ICREA, Barcelona). The links to the two outreach colloquia are here and here.

Interested researchers can register to participate through the *Registration* page. Upon registration, participants will receive a Zoom access password for the online sessions.

To apply for a short talk, please follow the instructions under *Contacts*. The deadline for submission of abstracts is *January 4.*

This conference is supported by CAMGSD.

Lecturers

Johanna Erdmenger (Würzburg)
Jerome Gauntlett (London)
Yang-Hui He (City, University of London & University of Oxford)
Thomas Mertens (Ghent)
Malcolm Perry (Cambridge)
Daniel Hernández Ruipérez (Salamanca)
Lárus Thorlacius (Reykjavík)
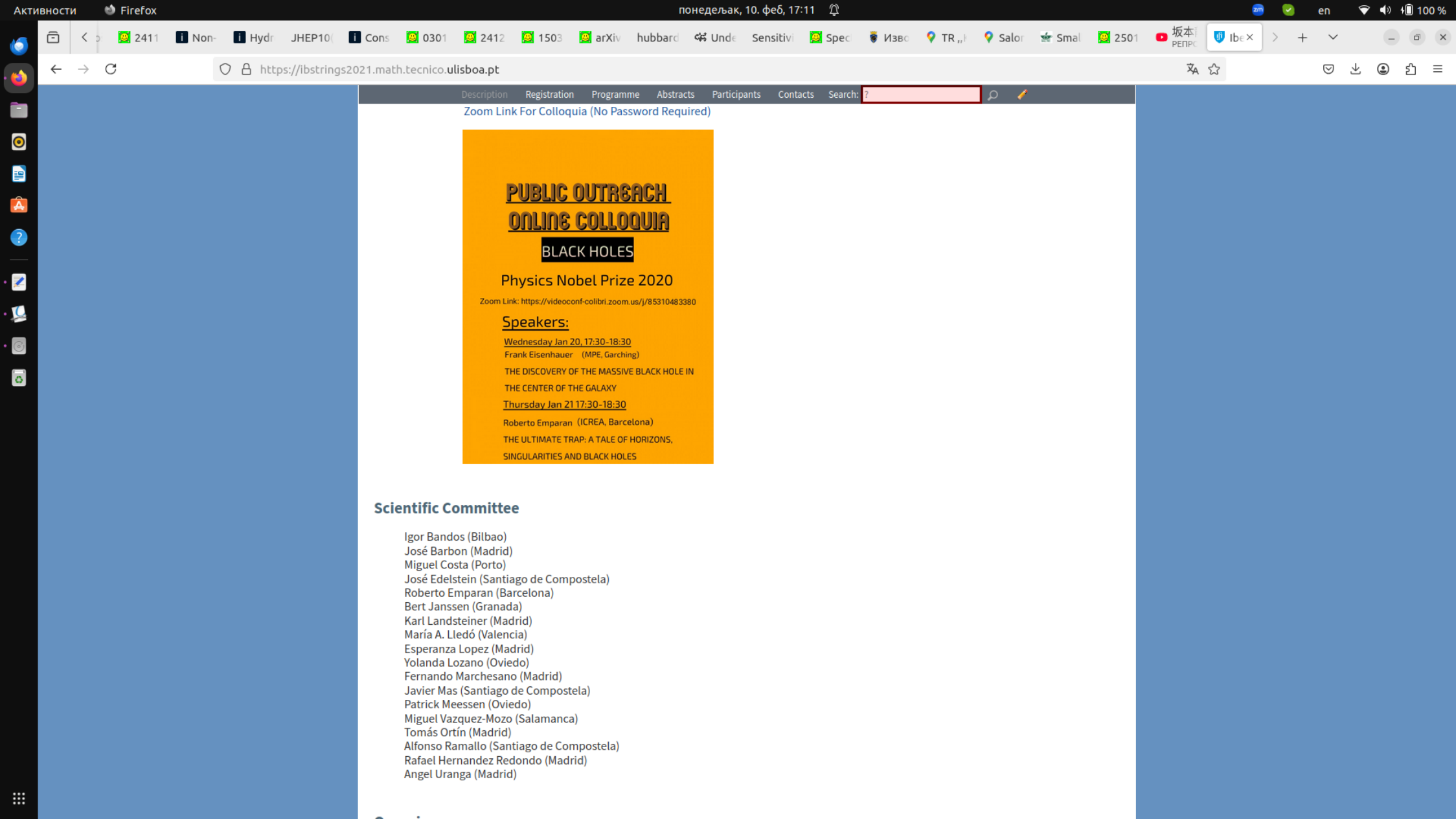
Zoom Link For Colloquia (No Password Required)

Scientific Committee

Igor Bandos (Bilbao)
José Barbon (Madrid)
Miguel Costa (Porto)
José Edelstein (Santiago de Compostela)
Roberto Emparan (Barcelona)
Bert Janssen (Granada)
Karl Landsteiner (Madrid)
María A. Lledó (Valencia)
Esperanza Lopez (Madrid)
Yolanda Lozano (Oviedo)
Fernando Marchesano (Madrid)
Javier Mas (Santiago de Compostela)
Patrick Meessen (Oviedo)
Miguel Vazquez-Mozo (Salamanca)
Tomás Ortín (Madrid)
Alfonso Ramallo (Santiago de Compostela)
Rafael Hernandez Redondo (Madrid)
Angel Uranga (Madrid)

Secure | https://ibstrings2021.math.tecnico.ulisboa.pt/programme

Iberian Strings 2021
January 19-22

Online meeting organized at Instituto Superior Técnico, Lisboa, Portugal

Description   Registration   Programme   Abstracts   Participants   Contacts   Search:
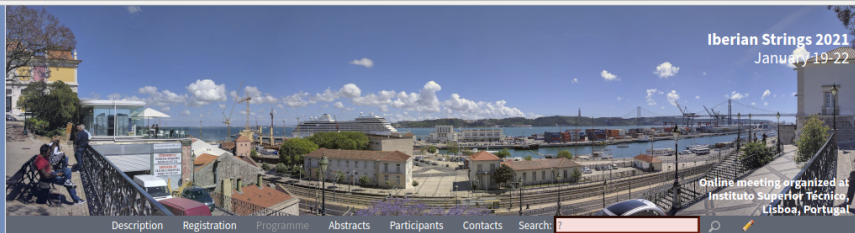
Programme

Move the mouse over the schedule to see start and end times and complete clipped titles.

	Tue, 19 Jan 2021	Wed, 20 Jan 2021	Thu, 21 Jan 2021	Fri, 22 Jan 2021
9-11	Malcom Perry — Soft Charges, Soft Hair and Black Hole Entropy	Johanna Erdmenger — Information geometry and QFT	Jerome Gauntlett — Geometric Extremization for AdS/CFT and Black Hole Entropy	Lárus Thorlacius — Entanglement islands
	David Mateos — Strong-coupling dynamics and entanglement in de Sitter space	Martin Sasieta — A Momentum/Complexity Correspondence	Anayeli Ramirez — 1/4 BPS AdS_2/CFT_2	Roberto Emparan — Quantum BTZ black hole
	Coffee break	Coffee break	Coffee break	Coffee break
11-13	Matteo Baggioli — How small hydrodynamics can go	Mihailo Cubrovic — Lyapunov spectra in traversable wormholes and their holographic duals	Salvatore Baldino — Seiberg-Witten theory, string theory and WKB analysis	Marija Tomasevic — Multi-mouth traversable wormholes
	Pablo Cano — Novel higher-curvature variations of R^2 inflation	Kevin Nguyen — Slow scrambling in extremal BTZ and microstate geometries	Gabriel Larios — Kaluza-Klein spectra and consistent truncations	Tomas Andrade — Violations of weak cosmic censorship in black hole collisions
	Mikel Sanchez Garitaonandia — Bubble Mergers from Holography	Johannes Lahnsteiner — A Non-Relativistic Limit of NS-NS Gravity	Mattia Cesaro — Kaluza-Klein fermion mass matrices from Exceptional Field Theory and $\mathcal{N}=1$ spectra	Martí Rosselló — Arithmetic of decay walls through continued fractions: a new exact dyon counting solution in $\mathcal{N}=4$ CHL models
	Yago Bea — New insights from Real-time Dynamics	Edvard Musaev — Non-abelian U-duality of M-theory background	Mario Herrero — Amplitudes Positivity and IR-UV connections in Graviton Exchange	Pablo Enmanuel León Torres — Massive supermembrane in ten non-compact dimensions
13-15	Lunch	Lunch	Lunch	Lunch

Secure | https://ibstrings2021.math.tecnico.ulisboa.pt//abstracts?abstract=6065#abstract-6065

Description   Registration   Programme   Abstracts   Participants   Contacts   Search:

Mihailo Cubrovic
University of Belgrade

Lyapunov spectra in traversable wormholes and their holographic duals

2021/01/20, 11:00 — 11:30

We study the decay of out-of-time-ordered correlators (OTOC) in an AdS traversable wormhole and its gravity dual, two coupled Sachdev-Ye-Kitaev models ("left" and "right" subsystem). The gravity calculation of OTOC involves perturbative equations more involved than for a black hole, as the perturbation has complex kinematics and can bounce back and forth through the wormhole many times. The outcome is a phase diagram with three regions. One is black-hole like with uniform exponential growth and the Lyapunov exponent $\lambda = 2\pi T$ ("the chaos bound"). The intermediate phase has OTOCs with a spectrum of different exponents for different operator modes, all below the maximal chaos bound. The third phase has exponentially small Lyapunov exponents, behaving as $\exp(-1/T)$, in accordance with a recent field-theory calculation in the literature. The Lyapunov spectrum carries more information than just the maximum exponent: it can be related e.g. to teleportation fidelity from left to right subsystem.

Frank Eisenhauer
Max Planck Institute for extraterrestrial Physics

The Discovery of the Massive Black Hole in the Center of the Galaxy. Outreach colloquium on the occasion of The Nobel Prize in Physics 2020

2021/01/20, 17:30 — 18:30

Outreach colloquium on the discovery of a supermassive compact object at the centre of our galaxy.

Black Holes are among the most mysterious objects in the Universe. They are so massive and compact that nothing - not even light - can escape their gravity. The 2020 Nobel Prize in Physics was awarded to Roger Penrose for showing that these exotic objects are a direct consequence of Einstein's general theory of relativity, and to Reinhard Genzel and Andrea Ghez for the discovery of such a monster in the center of our Galaxy. Our presentation will portrait the 40 year journey from the first indications to the overwhelming observational evidence for a extremely heavy and compact object in the Galactic Center, for which a supermassive black hole is the only known explanation. Using the world's largest telescopes and most advanced optics technology, astronomers can now follow the stars orbiting the central object, precisely measure its mass, and detect the stunning effects of general relativity. In our talk we will present both the spectacular observations and the technology behind.
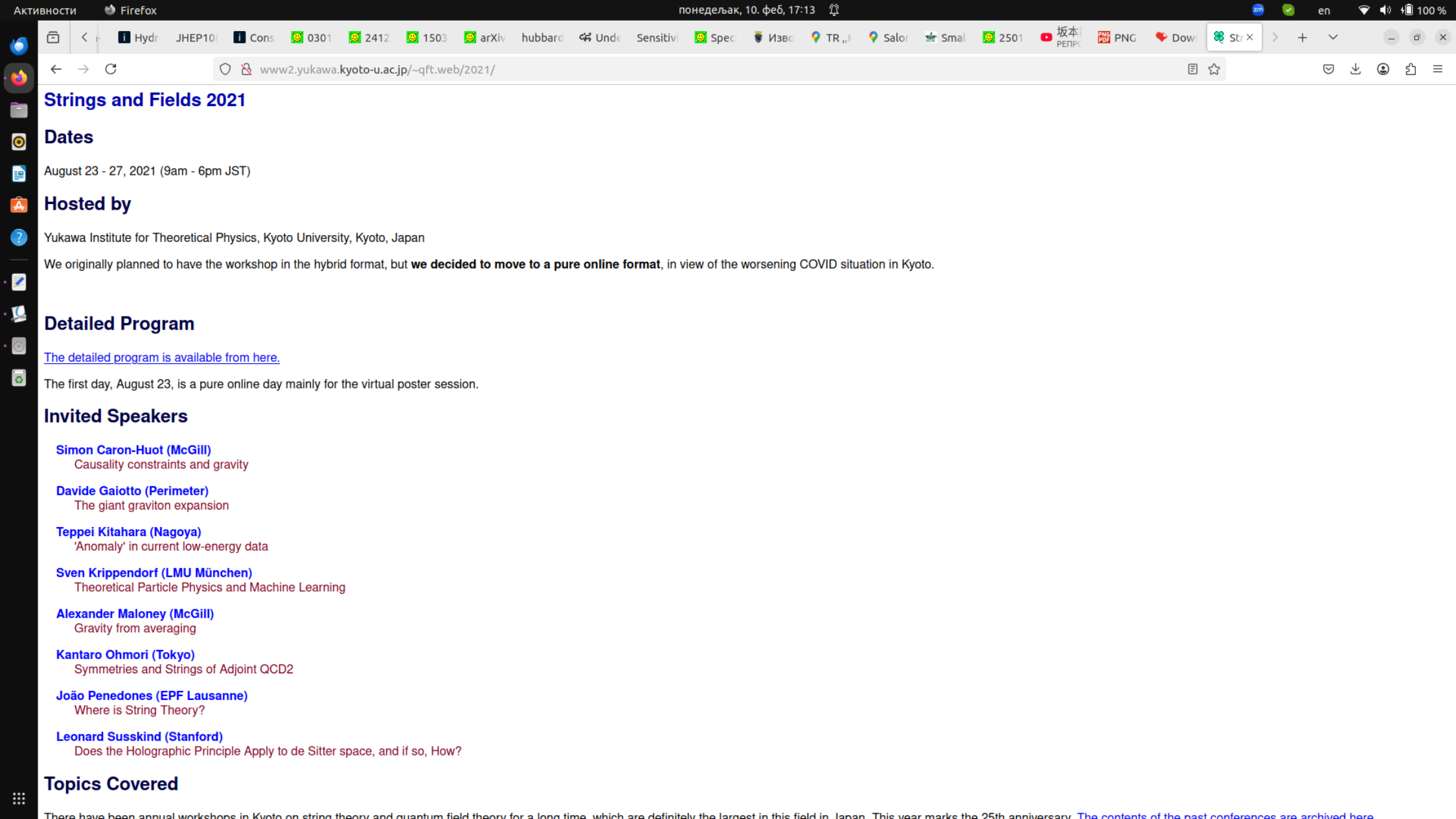
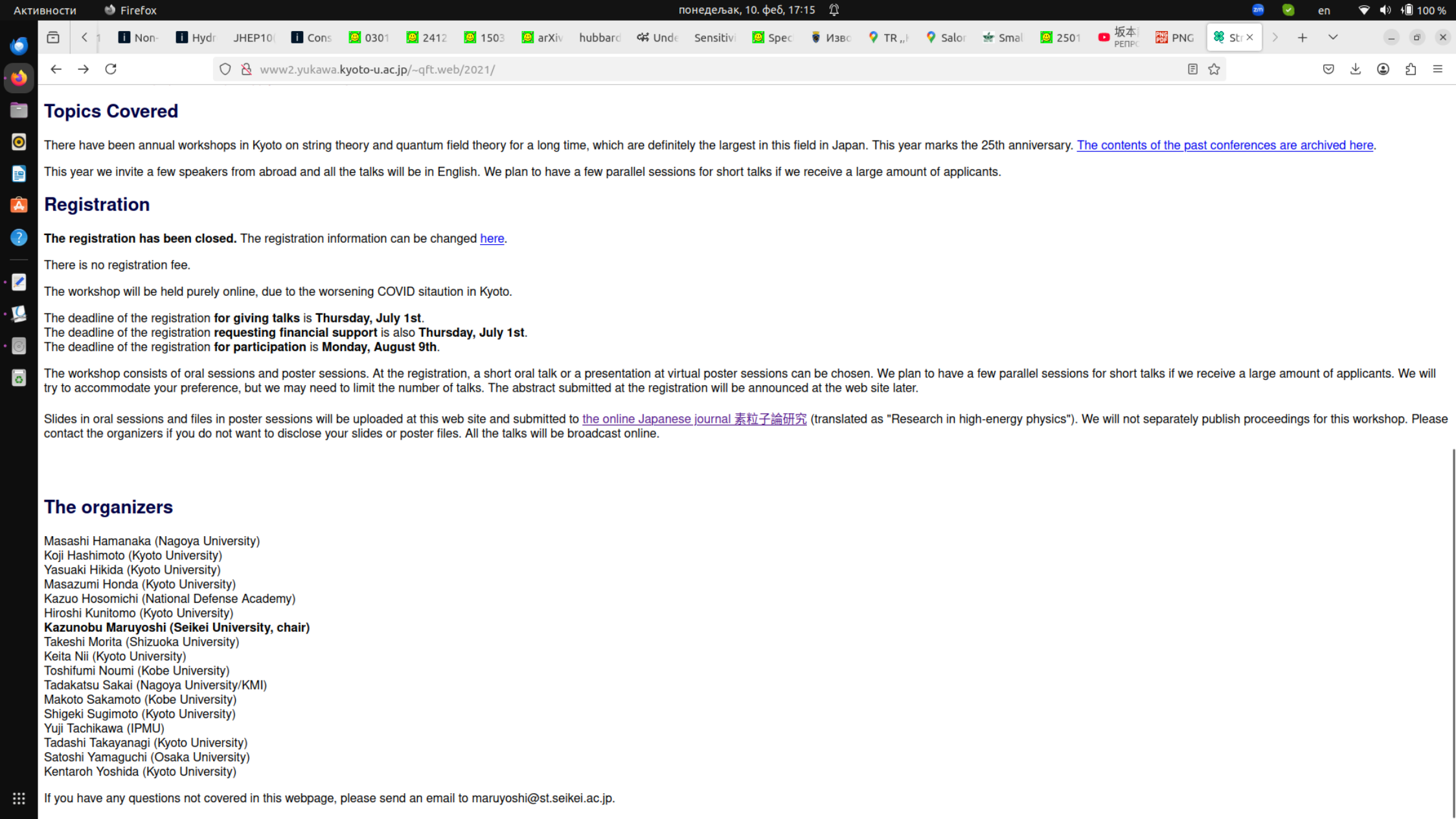### Zachary Elgood
Universidad Autónoma de Madrid

The first law of heterotic stringy black hole mechanics at zeroth order in α'

2021/01/22, 16:30 — 17:00

We re-derive the first law of black hole mechanics in the context of the Heterotic Superstring effective action compactified on a torus to leading order in α', using Wald's formalism, covariant Lie derivatives and momentum maps. The Kalb-Ramond field strength of this theory has Abelian Chern-Simons terms which induce Nicolai-Townsend transformations of the Kalb-Ramond field. We show how to deal with all these gauge symmetries deriving the first law in terms of manifestly gauge-invariant quantities. In the presence of Chern-Simons terms, several definitions of the conserved charges exist, but the formalism picks up only one of them to play a role in the first law. The derivation of a first law is a necessary step towards the derivation of a manifestly gauge-invariant entropy formula which is still lacking in the literature. In its turn, this entropy formula is needed to compare unambiguously macroscopic and microscopic black hole entropies.

[H9]

Strings and Fields 2021

Dates

August 23 - 27, 2021 (9am - 6pm JST)

Hosted by

Yukawa Institute for Theoretical Physics, Kyoto University, Kyoto, Japan

We originally planned to have the workshop in the hybrid format, but **we decided to move to a pure online format**, in view of the worsening COVID situation in Kyoto.

Detailed Program

The detailed program is available from here.

The first day, August 23, is a pure online day mainly for the virtual poster session.

Invited Speakers

Simon Caron-Huot (McGill)
Causality constraints and gravity

Davide Gaiotto (Perimeter)
The giant graviton expansion

Teppei Kitahara (Nagoya)
'Anomaly' in current low-energy data

Sven Krippendorf (LMU München)
Theoretical Particle Physics and Machine Learning

Alexander Maloney (McGill)
Gravity from averaging

Kantaro Ohmori (Tokyo)
Symmetries and Strings of Adjoint QCD2

João Penedones (EPF Lausanne)
Where is String Theory?

Leonard Susskind (Stanford)
Does the Holographic Principle Apply to de Sitter space, and if so, How?

Topics Covered

There have been annual workshops in Kyoto on string theory and quantum field theory for a long time, which are definitely the largest in this field in Japan. This year marks the 25th anniversary. The contents of the past conferences are archived here.

Topics Covered

There have been annual workshops in Kyoto on string theory and quantum field theory for a long time, which are definitely the largest in this field in Japan. This year marks the 25th anniversary. The contents of the past conferences are archived here.

This year we invite a few speakers from abroad and all the talks will be in English. We plan to have a few parallel sessions for short talks if we receive a large amount of applicants.

Registration

The registration has been closed. The registration information can be changed here.

There is no registration fee.

The workshop will be held purely online, due to the worsening COVID sitaution in Kyoto.

The deadline of the registration **for giving talks** is **Thursday, July 1st**.
The deadline of the registration **requesting financial support** is also **Thursday, July 1st**.
The deadline of the registration **for participation** is **Monday, August 9th**.

The workshop consists of oral sessions and poster sessions. At the registration, a short oral talk or a presentation at virtual poster sessions can be chosen. We plan to have a few parallel sessions for short talks if we receive a large amount of applicants. We will try to accommodate your preference, but we may need to limit the number of talks. The abstract submitted at the registration will be announced at the web site later.

Slides in oral sessions and files in poster sessions will be uploaded at this web site and submitted to the online Japanese journal 素粒子論研究 (translated as "Research in high-energy physics"). We will not separately publish proceedings for this workshop. Please contact the organizers if you do not want to disclose your slides or poster files. All the talks will be broadcast online.

The organizers

Masashi Hamanaka (Nagoya University)
Koji Hashimoto (Kyoto University)
Yasuaki Hikida (Kyoto University)
Masazumi Honda (Kyoto University)
Kazuo Hosomichi (National Defense Academy)
Hiroshi Kunitomo (Kyoto University)
Kazunobu Maruyoshi (Seikei University, chair)
Takeshi Morita (Shizuoka University)
Keita Nii (Kyoto University)
Toshifumi Noumi (Kobe University)
Tadakatsu Sakai (Nagoya University/KMI)
Makoto Sakamoto (Kobe University)
Shigeki Sugimoto (Kyoto University)
Yuji Tachikawa (IPMU)
Tadashi Takayanagi (Kyoto University)
Satoshi Yamaguchi (Osaka University)
Kentaroh Yoshida (Kyoto University)

If you have any questions not covered in this webpage, please send an email to maruyoshi@st.seikei.ac.jp.

| Jaydeep Kumar Basak | Indian Institute of Technology, Kanpur, India | Islands for Entanglement Negativity |

Plenary — Aug 25 04:30 Средњеевропско летње време - Aug 25 05:30 Средњеевропско летње време

| Masamichi Miyaji | UC Berkeley | Entanglement of Initial State and Pseudo Entanglement Wedge |
| Sotaro Sugishita | Nagoya University | Target space entanglement in quantum mechanics of fermions and matrices |

Parallel Slot A — Aug 25 07:00 Средњеевропско летње време - Aug 25 08:00 Средњеевропско летње време

| Sungjoon Kim | POSTECH | Non-unitary TQFTs from 3D N=4 rank 0 SCFTs |
| Ioannis Lavdas | LMU Munich | Boundaries and Topological Twists of 3d N=4 SCFTs |

Parallel Slot B — Aug 25 07:00 Средњеевропско летње време - Aug 25 08:00 Средњеевропско летње време

| Katsuta Sakai | KEK | Entanglement entropy in interacting field theories |
| Aranya Bhattacharya | Indian Institute of Science, Bangalore | Sub-region complexity of entanglement islands in AdS braneworld model |

Parallel Slot A — Aug 25 08:10 Средњеевропско летње време - Aug 25 09:10 Средњеевропско летње време

| Shuichi Yokoyama | Yukawa Institute for Theoretical Physics | Topologically protected phase factor, spin Chern-Simons theory and duality on lens space |
| Zhenghao Zhong | Imperial College London | 3d Mirrors of U & SU Quivers |

Parallel Slot B — Aug 25 08:10 Средњеевропско летње време - Aug 25 09:10 Средњеевропско летње време

| Satoshi Kanno | University of Tsukuba | Various generalizations of the matrix regularization |
| Mihailo Cubrovic | Institute of Physics Belgrade | Chaos and replica wormholes in the IIB matrix model |

We study the dynamics and statistics of the Ishibashi-Kawai-Kitazawa-Tsuchiya (IKKT) IIB matrix model. We first consider the spectrum and detect signs of level repulsion and quantum chaos. Then we expand perturbatively the partition function of the quenched model and find that, with an appropriately chosen quenching, the expansion contains wormhole terms akin to those in the time-frozen SYK model. We conjecture that such terms are crucial in describing the chaotic aspects of the IIB model.

Invited — Aug 25 09:40 Средњеевропско летње време - Aug 25 10:50 Средњеевропско летње време

| Sven Krippendorf | LMU München | Theoretical Particle Physics and Machine Learning |

Day 4

Invited — Aug 26 02:00 Средњеевропско летње време - Aug 26 03:10 Средњеевропско летње време

| Teppei Kitahara | Nagoya | 'Anomaly' in current low-energy data |

Plenary — Aug 26 03:20 Средњеевропско летње време - Aug 26 04:20 Средњеевропско летње време

| Hajime Otsuka | KEK | Hidden structures in the landscape of heterotic line bundle models |
| Naotaka Kubo | YITP | Non-perturbative Tests of Duality Cascades in Three Dimensional Supersymmetric Gauge Theories |

Plenary — Aug 26 04:30 Средњеевропско летње време - Aug 26 05:30 Средњеевропско летње време

| Hitoshi Murayama | UC Berkeley, Kavli IPMU | Can we "solve" gauge theories? |

Организација скупова и летњих школа
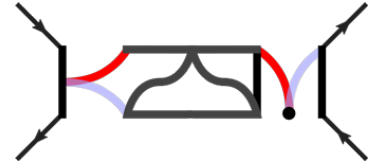
Online Workshop on Zoom, 23-25 May 2022

Zoom Links: <u>Day 1</u>, <u>Day 2</u>, <u>Day 3</u>

Strange metals: from the Hubbard model to AdS/CFT

Hosted by:
Institute of Physics Belgrade (IPB), Serbia
Key2SM project, funded by the *Science fund of the Republic of Serbia*

Organizers:

Dr Jakša Vučičević, Associate Research Professor (IPB)
Dr Mihailo Čubrović, Assistant Research Professor (IPB)

We aim to bring together the top experts approaching the same outstanding physical problem in two greatly different ways. The main subject will be the strange metallic behavior, as viewed from the perspective of the holographic theories and the microscopic theories based on interacting lattice models. Particular focus will be given to the direct comparison between the two general approaches. The workshop will also cover the specific realizations of the ubiquitous strange metal regime: in the cuprates and other strongly correlated materials, moire systems and cold atom simulators. The goal of the workshop is to provide a wider perspective on the theoretical work focusing on the strange metals, a better overview of the established phenomenology, and a connection of the strange metal to other phenomena in strongly correlated electronic systems.

Speakers:

Antoine Georges	Jake Ayres	Richard Davison
Waseem Bakr	Jan Zaanen	Aristomenis Donos
Rok Žitko	Koenraad Schalm	Mark Golden
Darko Tanasković	Blaise Goutéraux	Mihailo Čubrović
Thomas Schäfer	Alexander Krikun	Jakša Vučičević
Wéi Wú	Jie Ren	Aavishkar Patel

Schedule:

GMT+01 (Belgrade)	Day 1 (23/05/2022)	Day 2 (24/05/2022)	Day 3 (25/05/2022)
14h	14:45-15:00 | Intro by the organizers		
15h	15:00-15:45 | Antoine Georges	15:15-15:45 | Waseem Bakr	15:00-15:45 | Aavishkar Patel
	15:45-16:15 | Wéi Wú	15:45-16:15 | Jakša Vučičević	15:45-16:15 | Rok Žitko
16h	16:15-16:45 | Thomas Schäfer	16:15-16:45 | Darko Tanasković	16:15-16:45 | Jake Ayres
	16:45-17:15 | Break, general discussion	16:45-17:15 | Break, general discussion	16:45-17:15 | Break, general discussion
17h	17:15-18:00 | Jan Zaanen	17:15-18:00 | Blaise Goutéraux	17:15-18:00 | Koenraad Schalm
18h	18:00-18:30 | Mihailo Čubrović	18:00-18:30 | Richard Davison	18:00-18:30 | Jie Ren
	18:30-19:00 | General discussion	18:30-19:00 | Aristomenis Donos	18:30-19:00 | Alexander Krikun
19h		19:00-19:45 | Mark Golden	19:00-19:30 | Break, general discussion
		19:45-20:00 | General discussion	19:30-19:45 | Outro by the organizers

Full program:

Day 1

15:00-15:45
Antoine Georges
CCQ, Flatiron Institute, New York, USA & Collège de France, Paris, France

Doped SYK Models, Quantum Criticality and Strange Metal Behavior

15:45-16:15
Wéi Wú
Sun Yat-sen University, Guangzhou, China

Linear-in-temperature scattering rate in overdoped two dimensional Hubbard model

In this talk, we will discuss a recent numerical study on the overdoped Hubbard Model at low temperatures. We show that in the Hubbard model, the electron scattering rate γ(T) can display linear T- dependence as temperature T goes to zero. The T-dependent scattering rate is found in general isotropic on the Fermi surface, in agreement with recent experiments. We identify the antiferromagnetic fluctuations as the physical origin of the T-linear scattering rate in this system. Finally, we will also discuss briefly the T-linear electron scattering rate that shows up in the two dimensional periodic Anderson model.

revealed by holography showing how the Fermi-liquid generalizes into a densely many-body entangled affair [1], revealing the finite temperature physics through a "first principle" treatment of quantum thermalization. Guided by these insights, substantial progress has been made in recognizing various of these traits in experiments on the strange metal states of the high Tc superconductors.

[1]. J. Zaanen, arXiv:2110.00961 (2021).

18:00-18:30
Mihailo Čubrović
Institute of Physics Belgrade, Serbia

Spectral functions in holographic lattices and the Hubbard model

We compare the spectral functions of probe fermions on holographic square lattices to the Hubbard model spectra obtained from Quantum Monte Carlo CTINT simulations. We find that a minimal AdS setup which incorporates the Hubbard physics at the level of spectra consists of (1) inhomogenous bulk geometries with hyperscaling violation obtained by solving the Einstein-Maxwell-dilaton equations in the presence of the lattice (2) high-frequency dynamical cutoff which gives rise to sum rules (3) bulk dipole coupling which provides Mottness, a clear separation of the spectrum into IR (quasiparticle and Hubbard bands) and UV (exponentially decaying tails) scales. The fit of the holographic spectra to the Quantum Monte Carlo data is not strongly dependent on the specific choice of the bulk parameters as long as all the ingredients are present. We conclude that the key properties of spectral functions in the Hubbard model are not strongly dependent on microscopy, however they crucially depend on the presence of Motness, even in the Fermi liquid phase.

Day 2

15:15-15:45
Waseem Bakr
Princeton University, New Jersey, USA

Observation of strange metallicity in "hot" atomic Hubbard systems

The normal state of high-temperature superconductors exhibits anomalous transport and spectral properties that are poorly understood. Cold atoms in optical lattices have been used to realize the celebrated Fermi-Hubbard model, widely believed to capture the essential physics of these materials. The recent development of fermionic quantum gas microscopes has enabled studying the normal state of Hubbard systems with single-site resolution. I will start by introducing the atomic platform and reviewing experiments that have been done on measuring spin and density correlations. Next, I will describe the development of a technique to measure microscopic diffusion, and hence resistivity, in doped Mott insulators. We have found that this resistivity exhibits a linear dependence on temperature in an intermediate temperature regime, and it violates the Mott-Ioffe-Regel limit, two signatures of strange metallic behavior. I will compare our experimental results to state-of-the-art numerical techniques.
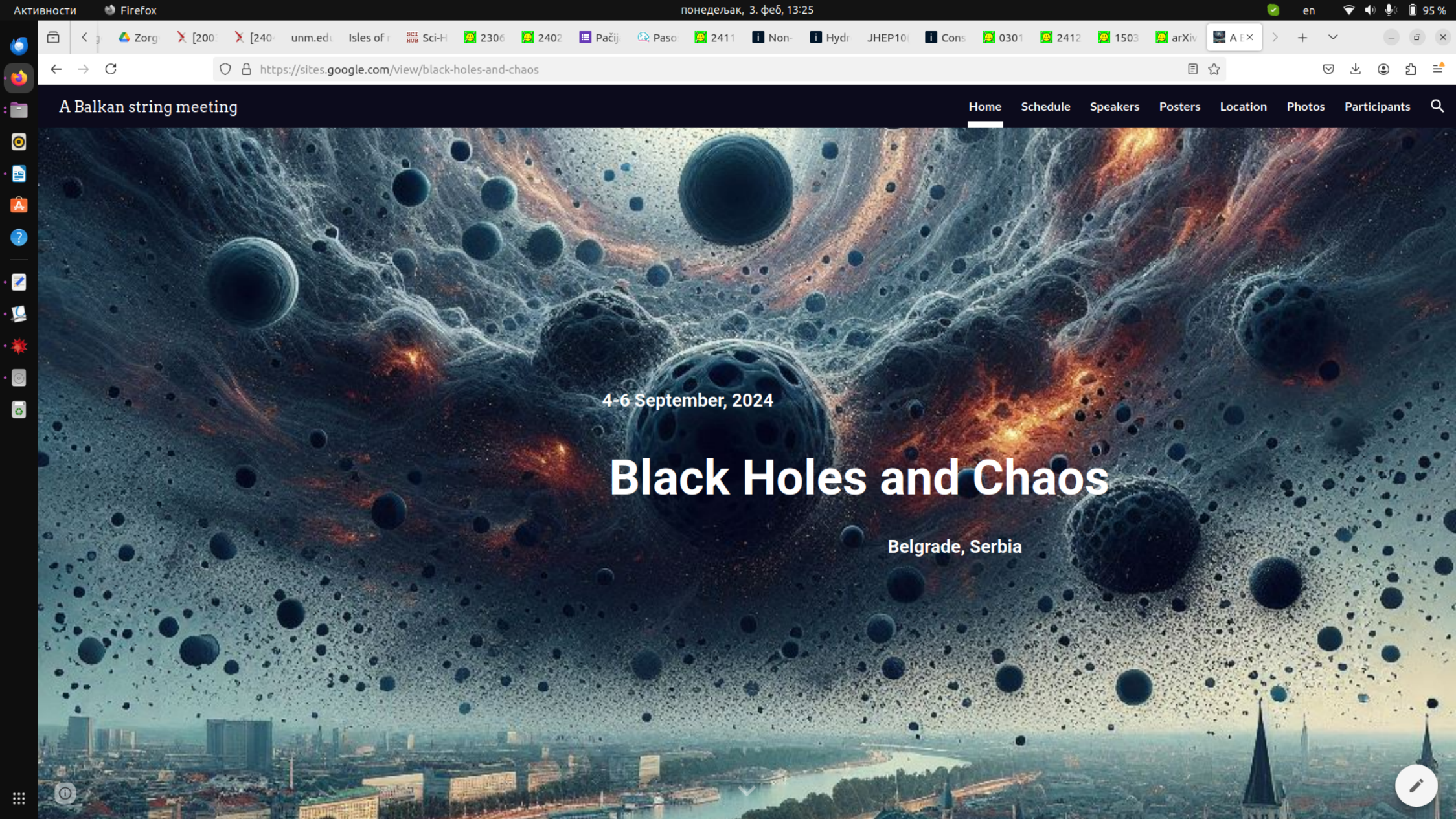
4-6 September, 2024

Black Holes and Chaos

Belgrade, Serbia
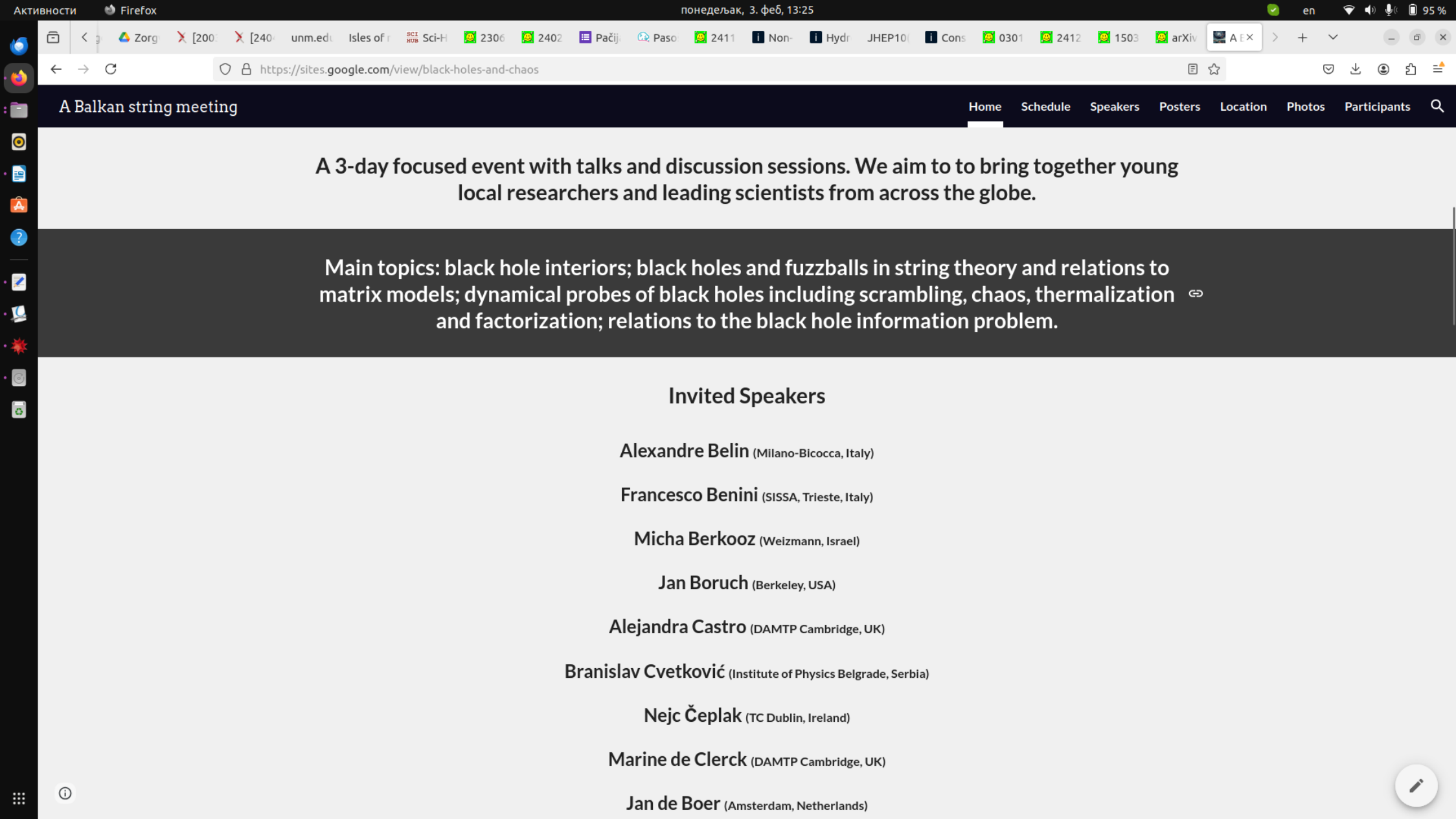
A 3-day focused event with talks and discussion sessions. We aim to to bring together young local researchers and leading scientists from across the globe.

Main topics: black hole interiors; black holes and fuzzballs in string theory and relations to matrix models; dynamical probes of black holes including scrambling, chaos, thermalization and factorization; relations to the black hole information problem.

Invited Speakers

Alexandre Belin (Milano-Bicocca, Italy)

Francesco Benini (SISSA, Trieste, Italy)

Micha Berkooz (Weizmann, Israel)

Jan Boruch (Berkeley, USA)

Alejandra Castro (DAMTP Cambridge, UK)

Branislav Cvetković (Institute of Physics Belgrade, Serbia)

Nejc Čeplak (TC Dublin, Ireland)

Marine de Clerck (DAMTP Cambridge, UK)

Jan de Boer (Amsterdam, Netherlands)
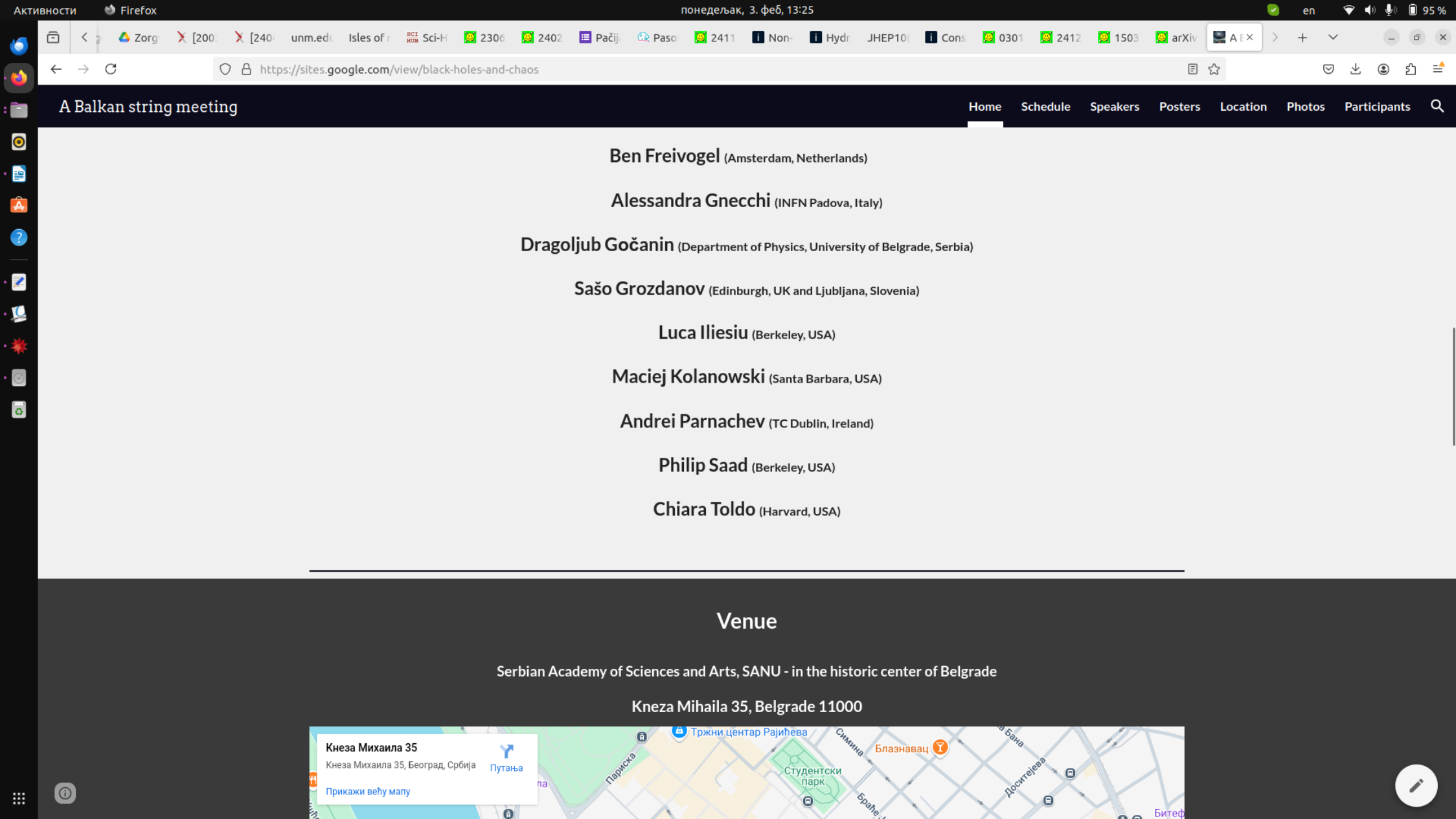
Ben Freivogel (Amsterdam, Netherlands)

Alessandra Gnecchi (INFN Padova, Italy)

Dragoljub Gočanin (Department of Physics, University of Belgrade, Serbia)

Sašo Grozdanov (Edinburgh, UK and Ljubljana, Slovenia)

Luca Iliesiu (Berkeley, USA)

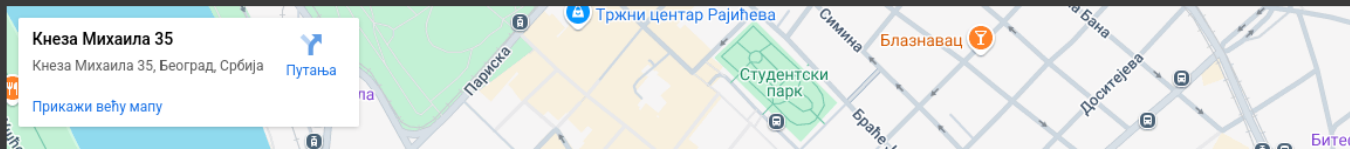Maciej Kolanowski (Santa Barbara, USA)

Andrei Parnachev (TC Dublin, Ireland)

Philip Saad (Berkeley, USA)

Chiara Toldo (Harvard, USA)

Venue

Serbian Academy of Sciences and Arts, SANU - in the historic center of Belgrade

Kneza Mihaila 35, Belgrade 11000

Organizers

COST action CA22113

Institute of Physics Belgrade, Serbia

Mathematical Institute of the Serbian Academy of Sciences and Arts, Belgrade, Serbia

Organizing Committee

Mihailo Čubrović

Institute of Physics Belgrade, Serbia

cubrovic@ipb.ac.rs

Marija Tomašević

University of Amsterdam, Netherlands

m.tomasevic@uva.nl

Kiril Hristov

Sofia University and INRNE, Bulgaria

khristov@phys.uni-sofia.bg

Branislav Cvetković

Institute of Physics Belgrade, Serbia

cbranislav@ipb.ac.rs

Sašo Grozdanov

University of Ljubljana, Slovenia, and University of Edinburgh, Scotland

saso.grozdanov@fmf.uni-lj.si

Vladan Đukić

Institute of Physics Belgrade, Serbia

djukic@ipb.ac.rs

A Balkan string meeting　　Home　Schedule　Speakers　Posters　Location

Speakers and Topics

Alexandre Belin : Discussion on ensemble averages in holography

Francesco Benini : Entanglement and symmetry breaking

Abstract: Entanglement asymmetry is a recently introduced quantum-information-based observable that detects symmetry breaking in quantum states on subsystems and out of equilibrium. After reviewing this observable, I will describe how to compute it in CFTs for a class of coherent states in a perturbative expansion. I will present explicit formulas for various subsystem geometries as well as for its time dependence, exhibiting in some cases the quantum Mpemba effect. The class of states we consider have a simple holographic description, allowing us to present a dual holographic computation of entanglement asymmetry. This might have interesting applications to the study of quantum properties of charged black holes.

Micha Berkooz : A chord path integral and chaos integrable phase transitions in DS-SYK

ⓘ

A Balkan string meeting   **Home   Schedule   Speakers   Posters   Location**

Abstract: In recent years, the Euclidean gravitational path integral has proven to be a reliable tool for studying quantum mechanical aspects of black holes. An important quantity that can help us probe whether black holes behave like conventional quantum mechanical systems is the supersymmetric index computed directly from the gravitational path integral. In this talk, I will discuss the issue of multicentered black hole contributions to the Euclidean path integral that computes the supersymmetric index at finite temperature. In the context of Einstein-Maxwell theory in 4d, I will explain how the multicentered generalization of the Kerr Newman black hole, called the Israel-Wilson solution, can be seen to satisfy the boundary conditions of the supersymmetric index and yields a regular contribution to the index. I will show how even though we perform the computations at finite temperature, the construction makes the value of the on-shell action depend only on the black hole charges, which can be viewed as a new form of the attractor mechanism. Finally, I will describe how we can extend the analysis to the most general solutions of N=2 4d supergravity, where the on-shell action becomes independent of the boundary values of the scalars. Time permitting, I will describe how the phenomenon of wall-crossing, in which the index jumps discontinuously as one crosses a codimension one wall in the space of asymptotic scalar moduli, arises from the perspective of the new finite temperature saddles.

Based on 2310.07763 and an upcoming work with Luca Iliesiu, Sameer Murthy and Joaquin Turiaci.

Alejandra Castro : Near-extremal black holes

Branislav Cvetković : Near horizon symmetry of extremal spacelike-stretched black holes

Abstract: We analyze the near horizon structure of the extremal spacelike stretched black holes, exact solutions of topologically massive gravity. We show that the algebra of improved canonical generator is realized as a single centrally extended Virasoro algebra. We obtain the entropy of the solution by using the Cardy formula and compare the results with the corresponding non-extremal case.

ⓘ

A Balkan string meeting   **Home   Schedule   Speakers   Posters   Location**

Abstract: The Fuzzball proposal is a proposal for the resolution of the information paradox and the entropy problem of black holes. It states that conventional black holes should be replaced by horizonless microstates whose number reproduces the black hole entropy and that can be, in principle, realised in string theory.

In this discussion session, I will review some of the general arguments in favour of and against the fuzzball proposal. I will then briefly talk about the construction of some explicit black hole microstates within supergravity, often called microstate geometries, and discuss some of their most important properties and how these differ from conventional black holes. I will conclude with some future directions and connections with other works.

Marine de Clerck : <u>Mixmaster chaos in AdS black hole interior</u>

Abstract: Amongst the most fascinating behaviours to arise from Einstein's equations is the onset of chaotic dynamics in the approach to certain cosmological singularities. This was analysed in detail in seminal work by Belinskii, Khalatnikov, Lifshitz (BKL) and others some fifty years ago. A consequence of these results is that the Schwarzschild interior solution near the singularity appears very fine-tuned and should give way for BKL-like dynamics in more generic black holes. In our recent work (arxiv:2312.11622), we construct a setup that realises the so-called 'mixmaster' chaotic dynamics in the interior of an AdS black hole. After a brief review of the BKL work, I will describe our holographic setup and discuss the peculiar symmetries appearing in this problem.

Jan de Boer : Discussion on black hole interiors

Ben Freivogel : Quantum fluctuations in black holes

~~symmetry breaking~~

Abstract: The presence of black holes in the low energy spectrum of the gravitational EFT signals fundamental properties of the UV-complete, quantum gravity theory. We show how black holes constructed from string theory can be exploited to investigate swampland constraints, through their thermodynamics. Finally, we discuss BPS states in relation to the breaking of supergravity one-form symmetries, associated to abelian vector fields.

Dragoljub Gočanin : Holographic exploration of exotic bulk geometries

Abstract: In the context of AdS/(B)CFT duality, we discuss the possibility of having Riemann-Cartan bulk geometry that involves torsion. This is a crucial step towards a better understanding of spin systems, such as Fermi liquids, in holographic terms, and is also a base for holographic analysis of noncommutative gravity - a theory that goes beyond the classical notions of spacetime geometry. Due to its rich structure, the main focus is on 5D Chern-Simons gravity and related models.

Sašo Grozdanov : Three facts about the spectra of holographic thermal field theories and black holes

Maciej Kolanowski : Looking at extremal black holes from very far away

Andrei Parnachev : Operator product expansion, geodesics and black hole singularities

Abstract: We observe features of black hole singularities in finite temperature holographic correlators. We also elucidate the relation between geodesics in AdS-Schwarzschild and the Operator Product Expansion in the boundary theory.

Philip Saad : Review of JT gravity

ⓘ

A Balkan string meeting   **Home**   **Schedule**   **Speakers**   **Posters**   **Location**

Abstract: From the perspective of classical gravity, a black hole is the simplest object we know of. At the same time, it possesses huge entropy, hinting at an incredibly complex microstructure: understanding this fact falls in the realm of quantum gravity. In this talk I will review recent results concerning the microscopics and the thermodynamics of fast spinning black holes in asymptotically flat and Anti-de Sitter space. In the first part, I will describe how recently developed techniques allow to compute the quantum corrections to the entropy of near-extremal Kerr black holes. I will show that the quantum-corrected near-extremal entropy exhibits $3/2 \log T$ behavior characteristic of the Schwarzian model, and predicts a lifting of the ground state degeneracy for the extremal Kerr black hole. In the second part, I will show the computation for the density of states for fast spinning black holes in AdS4, which admit a supersymmetric limit, and comment on the spectrum of near-BPS states and on the interpretation in terms of the dual 3d field theory.

ⓘ

Posters

Vasil Avramov (Sofia University)

Nielsen complexity of a TFD of a quantum harmonic oscillator in external magnetic field

Drawing on the growing links between quantum information theory and black hole physics, we explore the circuit complexity of a quantum
harmonic oscillator in the presence of an external magnetic field. By applying the Nielsen approach within the thermofield dynamics (TFD)
framework, we calculate the complexity of thermofield double states. Our analysis uncovers several notable characteristics of this complexity. Lastly, we derive the Lloyd bound for the system and demonstrate that it is upheld.

A Balkan string meeting **Home Schedule Speakers Posters Location**

An equivalence of three butterflies in Lifshitz background

In this work, we investigate two salient chaotic features, namely Lyapunov exponent and butterfly velocity, in the context of an asymptotically Lifshitz black hole background with an arbitrary critical exponent. These features are computed using three methods: entanglement wedge method, out-of-time-ordered correlator computation and pole-skipping. We present a comparative study of the aforementioned features where all of these methods yield exactly similar results for the butterfly velocity and Lyapunov exponent. This establishes an equivalence between all three methods for probing chaos in the chosen gravity background. Furthermore, we evaluate the chaos at the classical level by computing the eikonal phase and Lyapunov exponent from the bulk gravity. These quantities emerge as nontrivial functions of the anisotropy index. By examining the classical eikonal phase, we uncover different scattering scenarios in the near-horizon and near-boundary regimes. We also discuss potential limitations regarding the choice of the turning point of the null geodesic in our approach.

Marti Berenguer (Universidad Santiago de Compostela)

Floquet SYK wormholes

We study the non-equilibrium dynamics of two coupled SYK models, conjectured to be holographically dual to an eternal traversable wormhole in AdS2. We consider different periodic drivings of the parameters of the system. We analyze the energy flows in the wormhole and black hole phases of the model as a function of the driving frequency. Our numerical results show a series of resonant frequencies in which the energy absorption and heating are enhanced significantly and the transmission coefficients drop, signalling a closure of the wormhole. These frequencies correspond to part of the conformal tower of states and to the boundary graviton of the dual gravitational theory. Furthermore, we provide evidence supporting the existence of a hot wormhole phase between the black hole and wormhole phases. When driving the strength of the separate SYK terms we find that the transmission can be enhanced by suitably tuning the driving.

ⓘ

A Balkan string meeting   **Home   Schedule   Speakers   Posters   Location**

Chern-Simons and Boundaries: The Neverending Story

One concept that needs to be better understood in the holographic duality is the introduction of torsion in gravity theory. Furthermore, first order gravity formalism seems to be computationally simpler but conceptually more challenging to tackle. Chern-Simons gravity is an example of a theory where we can test different implications of the torsion tensor in the AdS/(B)CFT duality set-up. This poster presents some of our recent results in that direction.

Vladan Đukić (Institute of Physics Belgrade)

Trapping and Chaos in Bubbling AdS Spaces

We study the dynamics of null geodesics in 1/2 BPS bubbling AdS space. Building on prior research that established a connection between certain null geodesics confined to a specific (phase) plane and chaotic billiards, we extend the analysis to geodesics that are not restricted to a plane. We calculate the escape rate and Lyapunov exponent for trapped geodesics in these geometries. Our results show that in systems with large spatial dimensions, the Kolmogorov-Sinai entropy—representing the rate of information growth—is influenced by a non-zero escape rate, leading to a value lower than the Lyapunov exponent. Additionally, our findings validate, within numerical precision, the Gaspard-Nicolis relation, which links Kolmogorov-Sinai entropy, Lyapunov exponent, and escape rate.

Vladan Gecin (Institute of Physics Belgrade)

Holographic Lattices and Luttinger's Theorem

AdS/CFT correspondence can provide a novel, nonperturbative insight into strongly correlated materials. We solve numerically a system of Einstein-Maxwell-dilaton equations with periodic boundary conditions which describes strongly correlated matter at finite temperature and chemical potential on a square lattice. The metric in the deep interior is hyperscaling-violating, implying an anomalous scaling of thermodynamic quantities. We then compute the charge density of the system and inspect the validity of the Luttinger's theorem. The dependence of the charge density on doping and its profile confirm that the system is in metallic phase. However, the Luttinger's theorem is strongly violated, meaning that the system is a non-Fermi liquid, despite having stable quasiparticle peaks in the spectrum.

ⓘ

Hydrodynamics in 1d spin chains from a Holographic Perspective

Many physical systems admit a simplified description of their dynamics when examined at macroscopic scales. This simplified description—generally referred to as hydrodynamics—is governed by a restricted set of macroscopic observables that includes conserved quantities, Goldstone modes, and order parameters. An outstanding challenge in quantum many-body physics is finding this hydrodynamic description in terms of the microscopic variables. I will present a method inspired by holography for constructing the effective hydrodynamic description in the form of a transfer matrix and a set of hydrodynamically-relevant variables. The method proceeds by constructing an alternative representation of the operator dynamics in the form of a local (1+1)d "bulk" theory. I will show how the properties of the auxiliary bulk encode the existence of an effective local equation of motion of a given model, allowing for the extraction of hydrodynamic parameters like diffusion constants and characteristic thermalization scales. I will show results for various qubit and fermionic systems, and compare to the known literature.

Dragan Marković (Institute of Physics Belgrade)

Geometric and phase space (de)localization in a semiclassical Bose-Hubbard

chain

Anomalous diffusion is observed in the semiclassical approximation of the Bose-Hubbard model. We present a few crucial criteria for the

development of anomalous transport on long timescales. The criteria encapsulate both the initial geometry of the system (coordinate distribution of the particles) and the initial phase space statistics. We also find cases when diffusion breaks down completely (there is no

transport at all): it turns out that the operators which are sufficiently nonlocal exhibit no diffusion. In particular, this implies that (non-local) quantum corrections eventually destroy anomalous transport as we move away from the semiclassical regime.

ⓘ

Spectral Form Factor and Random Walks

This work examines the relationship between the spectral form factor (SFF) and planar random walks. The SFF is a measure used to identify the onset of quantum chaos and scrambling. We demonstrate that the moments of the SFF in generic quantum chaotic systems exhibit similar behavior to the moments of the distribution describing the positions of random walkers in the Euclidean plane. This similarity holds for the mean, variance, skewness, kurtosis, and all higher-order moments of the underlying probability distribution function. Additionally, we suggest a potential generalization of planar random walks that avoid intersections along the trajectory, and explore potential applications to integrable quantum systems.

Vasilii Pushkarev (Steklov Institute of Mathematical Sciences)

Signs for scalar field chaoticity

We study interesting but simple examples of models being integrable but exhibiting some features commonly attributed to chaotic dynamics. In the first case, we consider free massive scalar field dynamics in finite volume following a quench excitation and show that correlation function peak distribution is not necessarily exponential as expected but in some cases close to the level spacing distribution of Gaussian ensembles. In the second case, we generalize the free scalar field model on a curved background with the Dirichlet boundary conditions imposed (normal modes). In the case of BTZ spacetime, the appearance of the RMT profile for the spectral form factor was recently reported in literature. We discuss here massive field and the de Sitter spacetime case.

Juan Santos Suarez (Universidad de Santiago de Compostela)

Hamiltonian Forging of a Thermofield Double

The preparation of Thermofield Double states is of extreme importance due to its connection with wormhole teleportation. Following proposals in the literature we study its variational preparation as the ground state of an interacting Hamiltonian on the doubled Hilbert space. We focus on generic fermionic hamiltonians and find an exact solution for the quadratic case, which provides a warm start for the general case. The problem is naturally suited for the use of the entanglement forging strategy, in which only circuits of size N are required. We comment the case of SYK at the end.
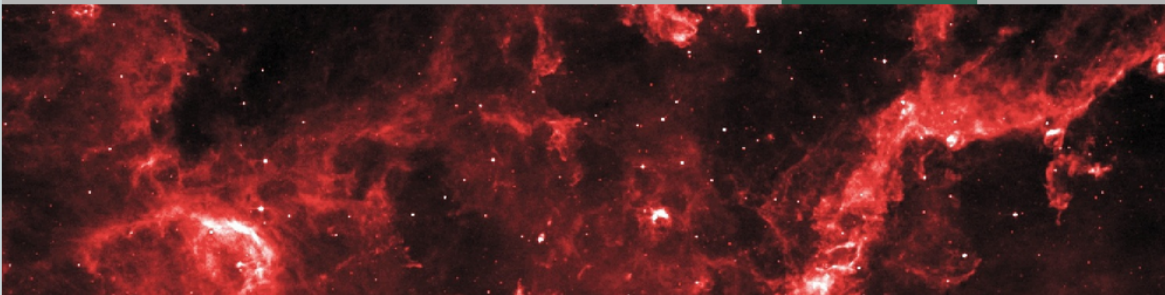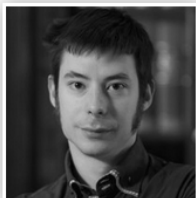
ⓘ

Petnica Summer Institute

Organizers

Mateja Bošković

Mateja is a postdoc working on gravitational wave probes in astro-particle physics and he has contributed to the organization of the school from 2022.

Institution: DESY, Hamburg, Germany

Email: mateja.boskovic (at) desy.de

Mihailo Čubrović

Mihailo is a researcher with interests at the interface of strongly correlated systems and high-energy theory. He has joined the PSI organizers in 2024.

Institution: Institute of Physics, Belgrade, Serbia

Email: cubrovic (at) ipb.ac.rs
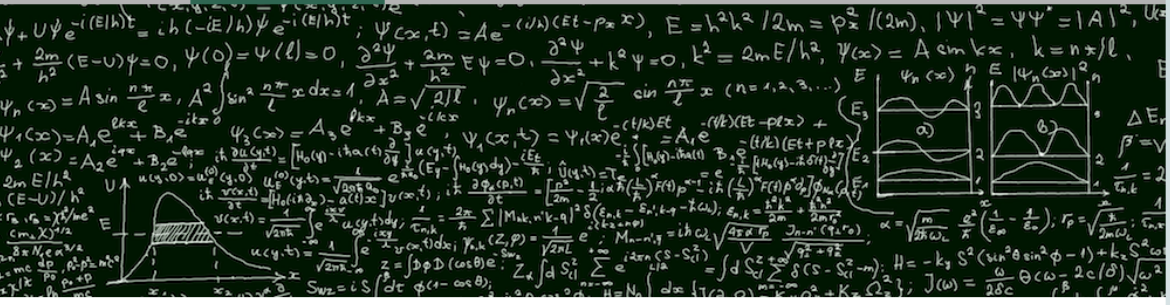
Ivan Milić

Contacts

Email address: psi (at) petnica.rs

Phone: +381 14 251180

Address: Manastirska 49, 14104 Valjevo, Serbia

Facebook

Petnica Summer Institute

PSI 2025 TH/PH

DESCRIPTION

Summer School on String Theory and Summer School on Gravitational Waves

On the theory and phenomenology tracks of PSI, we are organizing two schools in parallel—one on String Theory and the other on Gravitational Waves. The schools will take place at the end of July and the beginning of August. Information on dates, participation fees, and lecturers will be provided, and applications will open in winter 2025.

The aim: The schools aim to provide intensive and thorough courses on a broad range of topics in the fields of string theory and gravitational waves. The schools will not be limited to lectures but will also include daily discussion sessions, problem-solving, and independent work.

For whom: The schools are intended primarily for early graduate (MSc/junior PhD) students, although we will also consider motivated applications from senior undergraduates as well as more senior PhD students. Lectures will be given in English, and we welcome students from all around the world. In particular, we will provide a reduction in the participation fee for a number of regional students (Balkans/Southeast Europe), depending on budget constraints.

By whom: Lectures will be given by postdocs and senior researchers, while problem-solving sessions and project work will be tutored by senior PhD students. The lecturers will come from various European and US institutions.

PSI 2024

- **DESCRIPTION**
- PARTICIPANTS
- SCHEDULE
- NOTES
- PARTNERS

Posters

Summer School on High Energy Theory
# 1 August - 10 August, 2024

This year we are for the first time organizing two summer schools in parallel. One school is on High Energy Theory and the other on Cosmology (see the topics and lecturers below).

The aim: The schools aim to provide intensive and thorough courses on a broad range of topics in the field of high energy theory and cosmology. The schools are not limited only to lectures, but will also include daily discussion sessions, problem solving and independent work.

For whom: The schools are intended for senior undergraduate and early graduate (MSc / junior PhD) students mainly from the region of Southeast Europe. However, all lectures will be given in English, so we also welcome students from anywhere abroad.

By whom: Lectures will be given by senior PhD students, postdocs, but also by some senior researchers. Lecturers come from various European and US institutions.
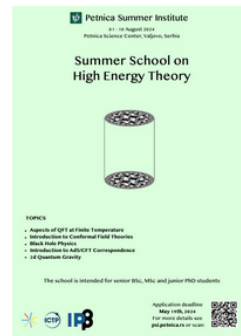
Topics

- Aspects of QFT at Finite Temperature
- Introduction to Conformal Field Theories
- Black Hole Physics
- Introduction to AdS/CFT correspondence
- 2d Quantum Gravity

Lecturers

- Lorenzo Di Pietro (University of Trieste)
- Roberto Emparan (University of Barcelona)
- Monica Guica (EPFL, Lausanne)
- Aditya Hebbar (Ecole Polytechnique, Paris)
- Jildou Hollander (University of Amsterdam)
- Marija Tomašević (University of Amsterdam)